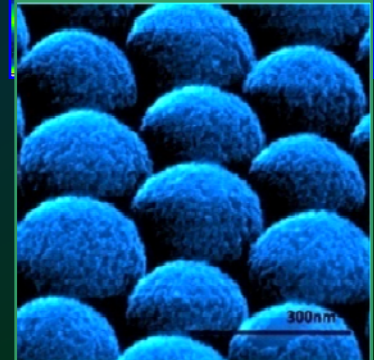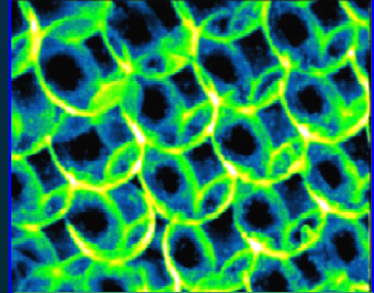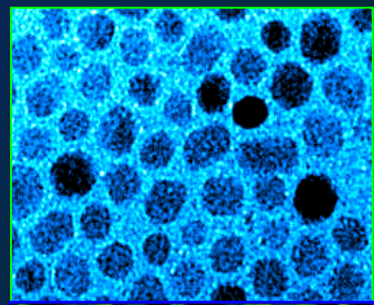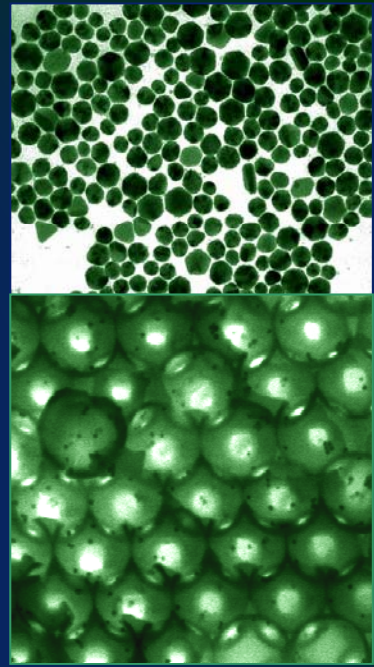Departament de Fisica,Facultat de Ciències
Universitat Autònoma de Barcelona

Oana Pascu

# Synthesis of Magnetic Nanoparticles and Strategies towards Magneto–Photonic Materials

DOCTORAL THESIS

May 2012

ICMAB CSIC Universitat Autònoma de Barcelona

Institut de Ciència de Materials de Barcelona

**UAB**

**Universitat Autònoma
de Barcelona**

Departament de Física, Facultat de Ciències

Programa de Ciència de Materials

Universitat Autònoma de Barcelona

Oana Pascu

# Synthesis of Magnetic Nanoparticles and Strategies towards Magneto–Photonic Materials

## DOCTORAL THESIS

Supervised by Dr. Anna Roig Serra and Dr. Gervasi Herranz Casabona

Tutor Prof. Javier Rodriguez-Viejo

to obtain the title of

PhD in Science

May 2012

at Institut de Ciència de Materials de Barcelona

**ICMAB**      **CSIC**

**Dra. Anna Roig Serra,** Investigadora Científica del CSIC i el **Dr. Gervasi Herranz Casabona,** Científic Titular del CSIC a l´Institut de Ciència de Materials de Barcelona,

CERTIFIQUEN:

Que n'Oana Pascu, Llicenciada en Química-Física per la Universitat ´´Babeş-Bolyai´´ Cluj-Napoca, Romania, ha dut a terme aquesta tesis doctoral sota la seva direcció i que porta per títol **"Synthesis of Magnetic Nanoparticles and Strategies towards Magneto-Photonic Materials",** la qual queda recollida en aquesta memòria per optar al grau de Doctor en Ciència en el Programa de Ciència de Materials.

I perquè així consti, signen el present certificat

Dra. Anna Riog Serra                    Dr.Gervais Herranz Casabona

Bellaterra, 10 de Abril de 2012

# Acknowledgements

The last four years I was spending in Catalonia were among the best years of my life. This is not exclusively due to the "very blue Mediterranean sea" but the wonderful people I met here. At this occasion, I would like to express my gratitude to all of them.

First of all, I would like to give thanks to my parents for encouraging and supporting me to come here and complete this PhD. Also, to the love of my life, my husband *Gergő* whom I met here and who completely changed my life. Without you I would not be here today. And moreover I am grateful to you for the critical corrections of the thesis. *Örülök, hogy ott voltál az Aula pont-ban...*

My infinite gratefulness to my supervisors Anna Roig and Gervasi Herranz, who admitted me doing research with them, who trusted me – sometimes more than myself, encouraged and supported me over these years and helped me to become a researcher.

Thank you Anna, from all my heart, for your inspiring ideas, for the "open door" and, most of all, for being such a sister I never had.

Special thanks to you, Gervasi, for your enthusiasm for my "opals", your teachings, the patience for explaining physics and your availability for scientific discussions.

I am grateful to Pep Fontcuberta for his very good scientific advices and suggestions.

The many hours spent at the institute would have been incomparably boring without the girls company: Elena, Nerea, Elisa, Carmen, Ana, Nina. Thank you girls!

It has been a pleasure to be able to work at ICMAB's facilities. In particular, I would like to mention the training and support that I always received from Judith Oró.

I give thanks to Roque for his time spent to measure magneto-optically the opals and for his help in data interpretation. It was an interesting and good experienced working with him.

I am also grateful to Marti Gich for his help and for his knowledge that shared with me; to Samuel Marre for his help in the Supercritical laboratory at the Chimie de la Matière Condensée de Bordeaux and for the chemistry discussions. Furthermore I thank to Susagna Ricart for her help and advices related to the experiments with the microwave reactor.

I would like to express my enormous thankfulness to Cyril Aymonier for accepting me to fulfill a fruitful and unforgettable three and half months research stage at Institut de Chimie de la Matière Condensée de Bordeaux. Many thanks for all in the Supercritical group for their kind welcome and in particular to Cedric, Thomas, Cinta, Iza, Matthieu for making me feel not alone.

Without the help of our collaborators from ICMM, we won't be here to present this thesis. I am grateful to Alvaro Blanco, Cefe Lopez, Victor Canalejas and Martin García for accepting the collaboration and for providing us with opals.

# *Motivation and Aim of the Thesis*

Today's society and our lifestyle progressively demand high speed technologies, for instance in telecommunication, data processing or microelectronics. According to the Optoelectronic Industry & Technology Development Association, the global internet traffic increases around 40-50% every year[1]. This leads to overwhelming stringent demands on the semiconductor technology in terms of physical space, power consumption, speed, waste heat and data transfer in the close future. Some solutions for these challenges can be achieved by replacing electrons with photons, which are faster information carriers (due to the absence of charge and mass), less costly and ensure negligible heat dissipation.

The 21$^{st}$ century is often referred as "the century of photons", giving an enormous importance to optics and photonics. "Photonics is the science and technology of the harnessing of light." (Pierre Aigrain, 1967). Nowadays, photonics plays an important role on sustainable economy by: i) reducing energy consumption by high-speed optical fibers networks, optical servers and switches used in computers and in telecommunication industry; ii) eco-efficient products such as light emitting diodes with less $CO_2$ emission and energy saving, organic/hybrid photovoltaics to generate "green" energy, lasers for rapid and efficient manufacturing, photonic sensors with less energy consumption; iii) biophotonics (application of light to living matter) for healthcare, by early detection of diseases with non-invasive, faster and more accurate imaging techniques. The current global photonic market is estimated to be 300 billion euros with an annual growth rate of 10% and with a share of 20% for Europe[2].

In addition, it is expected that nanotechnology will be ubiquitous in many industrial and society sectors such as Health, Information Technologies, Energy, Materials, Food, Environment or Instrumentation and that Materials is the market sector with the largest worldwide expected revenues.

The above mentioned, clearly provides sufficient motivation for the intense on-going research in photonics and in materials science to develop new functional devices with novel applications using materials tailored at the nanoscale. In this direction, photonic crystals are key materials which satisfy many of the technological needs. They were named as "semiconductors of light" by Eli Yablonovitch (1987). Photonic crystals (PCs) are composite materials with periodic modulation of the permittivity affecting the propagation of light, analogously to semiconductors affecting the propagation of electrons. The propagation of light with wavelength comparable with the periodicity of photonic crystals is forbidden, giving rise to the so-called photonic band gap (PBG). Propagation of light in one, two or three dimensions can thus be manipulated and effectively controlled by photonic crystals. An incomplete band gap can be obtained structuring the material in one or two dimensions. Nowadays the fabrication of 1D/2D-PCs has been successfully obtained for good quality photonic materials with long range structural order (essential for controlling the light propagation). In contrast, a complete photonic band gap for any orientation of the light wavevector can be achieved only in three dimensional structured materials. However, the

---

[1] Tatsuno, K. *"Future Challenges in the Photonics Market-Target at the Green Digital Economy"* Report presented at "Photonics 21", Brussels, Dec. 9. 2008.

[2] Kaierle, S. *Photonics Research in Europe. The European Technology Platform Photonics21*; European Laser Institute ELI: Fraunhofer, 2011.

fabrication of three dimensional materials is rather challenging, because of the difficulty of producing large area defect free 3D-PCs. The ambition is the manipulation of light driven by external controllable stimuli (e.g. pH, temperature, applied magnetic/electrical fields) using new materials, such as functionalized 3D photonic crystals, to convert them in new products, miniaturized optical devices with higher functionalities.

These challenges and the purpose to go beyond the state-of-the-art, set the motivation for this PhD thesis, which was supported by a two-years Intramural-CSIC project, entitled "Toward a new generation of magnetophotonic crystal (CRIMAFOT)" being the project partners groups at the Institut de Ciència de Materials de Barcelona (ICMAB-CSIC), Instituto de Ciencia de Materiales de Madrid (ICMM-CSIC) and Centro Nacional de Microelectrónica (CNM-CSIC). The project aimed to obtain an optical system responding to an external stimulus (magnetic field). Photonic crystal materials (two and three dimensions) were selected as the optical systems to be further functionalized with magnetic nanoparticles, to obtain magneto-photonic crystals (MPCs). This functionalization not only would enable the tunability of photonic band gap spectral position using an external magnetic field, but also would enable an enhanced magneto-optical response near photonic band-edge frequencies due to light-matter interaction. It has previously been demonstrated that the magneto-optical response of one-dimensional (1D) MPCs is significantly enhanced at band-edge frequencies. The achievement of high-quality 3D-MPCs is much more complex and the attainment of an optimal magneto-optical response, comparable to that of 1D-MPCs, remains a challenging issue and the work of this thesis goes in this direction. Three dimensional magnetophotonic crystals with enhanced magneto-optical response can be a suitable platform for the development, for instance, of a new generation of fast and compact optical isolators for optical transmission, drastically reducing their thickness and optical losses (advantageous for integrated optics).

Since the material's functionality was given (i.e., enhanced magneto-optical response at near-band edge wavelengths in 2D-MPCs and 3D-MPCs), some requirements in the magnetophotonic materials fabrication were established:

- Comprehensive knowledge of the magnetic nanoparticles: structural, morphological, magnetic and magneto-optical behavior in a disordered environment;
- The magneto-photonic crystal should contain superparamagnetic nanoparticles (within the range 5-20 nm) with the purpose to have high response at low magnetic field and zero response (no remanent magnetization) in the absence of the field;
- The system should contain sufficient magnetic material to give measurable magneto-optical response;
- The long-range ordered structure of original photonic crystal should be preserved in order to keep the optical properties after the magnetic functionalization;
- And if possible, to use sustainable methodologies in terms of high yield material production, easy and safe manufacturing, efficient in energy consumption and environmentally friendly.

Based on these requirements, the objectives of this PhD thesis have been: **1) to synthesize highly crystalline magnetic nanoparticles** (nickel, iron oxide and manganese ferrite) via a chemical method, to tune the nanoparticles size by playing with various experimental parameters and to study the stability of the obtained liquid magnetic colloids; **2) to fabricate magnetophotonic materials** by: i) bottom-up techniques – incorporating magnetic nanoparticles into a prefabricated photonic crystal (2D or 3D) and ii) top-down method – nanopatterning of magnetic composite material by lithographic techniques (electron beam

and nanoimprint lithography); 3) **to characterize the prepared photonic materials structurally and morphologically**; 4) **and to optimize magneto-photonic materials fabrication to ensure appropriate magneto-optical response**, namely enhanced magento-optical response near photonic band-edge frequencies.

The *PhD thesis report* is divided into six chapters:

**Chapter 1** provides a general introduction to magnetic nanoparticles, conventional photonic crystal materials and functionalized magnetophotonic crystals. Magnetic nanoparticles such as metal (nickel) and metal oxide (iron oxide and manganese ferrite) are discussed through their properties, synthesis, stabilization and applications. Photonic and magnetophotonic materials with their structural and optical/magneto-optical characteristics are presented.

**Chapter 2** describes the chemical synthesis of magnetic nanoparticles by three different pathways: thermal decomposition, microwave heating and continuous supercritical ethanol synthesis. The tunability of the nanoparticles size and stability of the magnetic colloids are studied. Structural, morphological and functional characterizations of the prepared nanoparticles are discussed.

**Chapter 3** deals with the fabrication of two-dimensional magneto-photonic materials by top-down (electron beam and nanoimprint lithography) and bottom-up (microwave-assisted deposition) approaches. For both strategies, an individual fabrication protocol was developed. Structural, morphological and functional characterizations of the fabricated materials are discussed.

**Chapter 4** describes the fabrication of three-dimensional magneto-photonic materials by bottom-up approaches using both *ex-situ* synthesized nanoparticles (vertical dip-casting deposition) and *in-situ* synthesized nanoparticles (microwave-assisted coating). Characterization and optimization of these materials are furthermore presented.

**Chapter 5** lists the main conclusions of the thesis and makes suggestions for future works.

**Chapter 6** includes the annexes. *Annex i.* lists the publications I have co-authored related to this thesis. *Annex ii.* includes a brief description of the experimental techniques used and protocols applied for samples preparation. *Annex iii. and iv* contains tables with detailed experimental conditions and measurements for magnetic nanoparticles and magnetic opals, respectively.

# Motivación y el Objetivo de la Tesis

El estilo de vida en nuestra sociedad exige una mejora constante de las prestaciones de dispositivos en diferentes ámbitos de las tecnologías de información, telecomunicaciones, informática o microelectrónica. Según la Asociación del Desarrollo para la Industria de Optoelectrónica, el tráfico mundial de datos en Internet aumenta alrededor de un 40-50% cada año. Esto debe conllevar, en un futuro cercano, a unas demandas cada vez más severas sobre tecnología de semiconductores, en términos de espacio físico, consumo de energía, velocidad, disipación y transferencia de datos. Algunas soluciones para estos desafíos se pueden lograr mediante la sustitución de electrones por fotones, que transportan la información más rápidamente (debido a la ausencia de carga y masa), con menos costeos y con una disipación de calor insignificante.

Se ha hablado del siglo XXI es referido a menudo como "el siglo de los fotones", dando una enorme importancia a la óptica y la fotónica. "La fotónica es la ciencia y la tecnología del uso de la luz." (Pierre Aigrain, 1967). Hoy en día, la fotónica juega un papel importante en la economía sostenible a través de: i) la reducción del consumo de energía con el uso de redes de fibra óptica de alta velocidad, servidores e interruptores ópticos utilizados en los ordenadores y en la industria de las telecomunicaciones, ii) eco-productos eficaces, tales como los diodos emisores de luz que reducen las emisiones $CO_2$ e implican un ahorro energético; la energía fotovoltaica orgánica/híbrida para generar energía "verde"; el láser para la fabricación rápida y eficiente de productos manufacturados; los sensores fotónicos con menor consumo de energía, iii) biofotónica (aplicación de la luz a la materia viva) para la asistencia sanitaria, mediante la detección precoz de enfermedades con técnicas de imagen no invasivas, más rápidas y más precisas. En la actualidad el mercado mundial de fotónica se estima en 300 millones de euros con una tasa de crecimiento anual del 10% y con una cuota del 20% para Europa.

Paralelamente, se espera que la nanotecnología vaya a ser omnipresente en numerosos sectores industriales y de sociales, tales como Salud, Tecnologías de la Información, Energía, Materiales, Alimentación, Medio Ambiente o Instrumentación y se prevee que los materiales sean el sector de mercado con los mayores ingresos.

Todos estos aspectos justifican la intensa investigación actualmente en curso en fotónica y en ciencia de materiales encaminada al desarrollo de nuevos dispositivos funcionales nanométricos. En este sentido, los cristales fotónicos son materiales importantes que pueden satisfacer muchas de las necesidades tecnológicas actuales. Fueron designados como "semiconductores de la luz" por Eli Yablonovitch (1987). Los cristales fotónicos son materiales compuestos que presentan una modulación periódica de la permitividad que condiciona la propagación de la luz, de la misma manera que la estructura periódica en los sólidos afecta la propagación de los electrones. La propagación de radiación electromagnética está prohibida para longitudes de onda dentro de un rango espectral de longitudes de onda comparables a la periodicidad de los cristales fotónicos, definiendo lo que se llama banda fotónica prohibida (PBG). Por tanto la propagación de la luz en una, dos o tres dimensiones puede ser manipulada y controlada eficazmente por materiales fotónicos. Una banda incompleta se puede obtener al estructurar el material en una o dos dimensiones (1D / 2D –PCs). Hoy en día se ha obtenido con éxito la fabricación de cristales 1D/2D de buena calidad con orden a largo alcance (esencial para el control de la propagación de la luz).

Asimismo, un bandgap completo que bloquea cualquier orientación del vector de luz se puede lograr solamente en materiales estructurados en tres dimensiones. Sin embargo, la fabricación de los materiales tridimensionales es bastante difícil, debido a la dificultad de producir grandes áreas sin defectos estructurales. Un objetivo ambicioso es poder sintonizar las propiedades ópticas del ópalo mediante estímulos externos controlables (por ejemplo, pH, temperatura, campos eléctricos y magnéticos) utilizando nuevos cristales fotónicos 3D funcionalizados que deriven en nuevos dispositivos ópticos miniaturizados con mayores funcionalidades.

El deseo de ir más allá en el estado de arte en cristales magneto- fotónicos es el que determina el motivo de esta tesis doctoral, que fue respaldada por un proyecto Intramural CSIC (CRIMAFOT) por un período de dos años titulado "Hacia una nueva generación de cristales magneto- fotónicos" entre grupos del Institut de Ciència de Materials de Barcelona (ICMAB-CSIC), Instituto de Ciencia de Materiales de Madrid (ICMM-CSIC) y el Centro Nacional de Microelectrónica (CNM-CSIC). El proyecto se propuso obtener un sistema óptico que responda a estímulos externos, en concreto, a campos magnéticos. Cristales fotónicos de dos y tres dimensiones fueron seleccionados como sistemas ópticos para ser funcionalizados con nanopartículas magnéticas para obtener cristales magneto-fotónicos (MPCs). La funcionalización de cristales fotónicos tuvo como objeto no solamente permitir los cambios en la posición espectral del bandgap utilizando un campo magnético externo, sino también permitir respuestas magneto-ópticas aumentadas a determinadas longitudes de onda debido a la interacción luz-materia. Previamente se ha demostrado que la respuesta magneto-óptica en un cristal fotònico 1D aumenta significativamente para frecuencias en el borde del bandgap. Sin embargo, lograr cristales 3D de alta calidad es mucho más complejo y, por lo tanto, conseguir una respuesta magneto-óptica óptima, comparable a la de los cristales magneto-fotónicos 1D, sigue siendo difícil. Los cristales magneto-fotónicos tridimensionales con una respuesta magneto-óptica aumentada pueden ser una plataforma adecuada para el desarrollo, por ejemplo, de una nueva generación de aislantes ópticos rápidos y compactos para transmisión en comunicaciones ópticas, disminuyendo drásticamente su espesor y en consecuencia las pérdidas ópticas (la cual es ventajoso para la óptica integrada).

A partir del objetivo sobre la funcionalidad del material (es decir, el aumento de la respuesta magneto-óptica en la zona de longitudes de onda de bordes de banda en cristales 2D y 3D), se establecen algunos de los requisitos en la fabricación de tales materiales:

• Amplio conocimiento de las nanopartículas magnéticas: comportamiento estructural, morfológico, magnético y magneto-óptico;
• El cristal fotónico debe contener nanopartículas superparamagnéticas (dentro del rango de 5-20 nm) con el propósito de tener alta respuesta a campos magnéticos bajos y cero respuesta (no hay magnetización remanente) en ausencia del campo;
• El sistema debe contener material suficiente para medir la respuesta magneto-óptica;
• La estructura ordenada de largo alcance debe ser conservada con el fin de mantener las propiedades ópticas a partir de la funcionalización magnética;
• Y si es posible, utilizar tecnologías sostenibles en términos de producción de material con un alto rendimiento, una fabricación fácil y segura, eficiencia en el consumo de energía y una mínima repercusión medio-ambiental.

En base a estos requisitos, los objetivos de esta tesis doctoral han sido : 1) **sintetizar nanopartículas magnéticas de alta cristalinidad** (níquel, óxido de hierro y ferrita de manganeso) a través de métodos químicos, con el fin de controlar el tamaño de las

nanopartículas a través de diversos parámetros experimentales y para estudiar la estabilidad de las soluciones coloidales magnéticas, 2) **la fabricación de materiales magneto-fotònicos** mediante: i) técnicas ¨bottom-up´´- para la incorporación de nanopartículas magnéticas en un cristal fotónico prefabricado (2D o 3D) y ii) métodos ¨top-down¨ -p.e., mediante técnicas litográficas (haz de electrones y litografía nanoimprint), 3) la **caracterización estructural y morfológica** de los materiales fotónicos preparados, 4) **optimizar la fabricación de los cristales magneto-fotónicos** para garantizar una respuesta magneto-óptica aumentada a longitudes de onda cerca del bandgap óptico.

La presente tesis está dividida en seis capítulos

**El capítulo 1** incluye una introducción general a las nanopartículas magnéticas, los materiales cristales fotónicos convencionales y funcionalizados (magneto-fotónicos). Las nanopartículas magnéticas de tipo metálico (níquel) y de óxido metálico (óxido de hierro y manganeso de ferrita) se describen a través de sus propiedades, la síntesis, estabilidad de las soluciones coloidales y sus aplicaciones. Se presentan los materiales fotónicos y magneto-fotónicos con sus características estructurales y óptica y magneto-óptica.

**El capítulo 2** describe la síntesis química de nanopartículas magnéticas por tres vías diferentes: la descomposición térmica, calentamiento por microondas y la síntesis continua en etanol supercrítico. El control del tamaño de las nanopartícula y la estabilidad de las soluciones coloidales magnéticas son analizadas. También se aborda la caracterización estructural, morfológica y funcional de las nanopartículas preparadas.

**El capítulo 3** está enfocado a la fabricación de los cristales magneto-fotónicos bidimensionales por técnicas de ´´top-down´´ (haz de electrones y la litografía por nanoimprint) y bottom-up (depósito de partículas magnéticas asistida por microondas). Para ambas estrategias se describe el protocolo de fabricación desarrollado, junto con la caracterización estructural, morfológica y funcional de los materiales fabricados.

**El capítulo 4** describe la fabricación de los materiales magneto-fotónicos tridimensionales mediante técnicas bottom-up basadas en dos estrategias, utilizando: i) nanopartículas sintetizadas *ex-situ* (método de dip-coating asistido por motor paso a paso) y ii) nanopartículas sintetizadas *in-situ* (depósito asistido por microondas).

**En el capítulo 5** se enumeran las principales conclusiones de la tesis y se hacen sugerencias para trabajos futuros.

**El capítulo 6** incluye los anexos. El anexo i. presenta la lista de las publicaciones relacionadas con esta tesis. El anexo ii. incluye una breve descripción de las técnicas experimentales utilizadas y protocolos aplicados para la preparación de las muestras. Los anexos III. y IV contienen las tablas detalladas con las condiciones experimentales y los datos de fabricación de nanopartículas magnéticas y ópalos magnéticos, respectivamente.

x

# *Motivatia si Scopul Tezei*

Societatea zilelor noastre si stilul nostru progresiv de viata necesita tehnologii avansate in special în sectoare ca telecomunicatiile, prelucrarea de date, microelectronica etc. Potrivit asociatiei "Optoelectronic Industry & Technology Development Association" traficul de internet la nivel mondial creste anual cu aproximativ 40-50%. Aceasta va afecta tehnologia de obtinere a semiconductorilor, noile cerinte coplesindu-o din punct de vedere a spatiului fizic, a consumului de energie, vitezei de transfer de date, etc. O solutie la aceste provocări ar putea fi înlocuirea electronilor cu fotonii , mult mai rapizi in transportul de informatie, (din cauza lipsei de sarcina si de masa), mai putin costisitori si cu o caldură pierduta neglijabila.

Secolul 21 este adesea mentionat ca "secolul fotonilor", prin importanta enorma oferita opticii şi fotonicii: "Fotonica este stiinta si tehnologia de valorificare a luminii." (Pierre Aigrain, 1967). In prezent, fotonica joaca un rol important in economia durabila prin: i) reducerea consumului de energie prin folosirea retele de fibre optice de mare viteza, a serverelor si switch-urilor optice utilizate in calculatoare si in industria de telecomunicatii; ii), "eco-produsele" cum ar fi diodele emitatoare de lumina cu emisie resusa de $CO_2$ şi eficiente energetic, celule fotovoltaice organice / hibride pentru generarea de "energie verde", lasere mai performante, senzori fotonici care opereaza cu consum mai mic de energie, etc; iii) Biofotonica pentru asistenta medicala (utilizarea luminii in aplicatii care vizează materia vie), pentru depistarea precoce, mai rapid si mai precis a bolilor dificil de diagnosticat prin tehnicile imagistice actuale. Piata actuala a fotonicii la nivel mondial este estimata la 300 de miliarde de euro, cu o rata anuala de crestere de 10% si cu o pondere de 20% pentru Europa[2].

De asemenea, este cunoscut faptul ca, nanotehnologia este deja omniprezenta in multe sectoare industriale si de societate, cum ar fii sanatate, tehnologiile informationale, energietice, obtinerea de materiale, a protectiei mediului, alimentatie, instrumentatie etc. Se asteapta o revenire în forta a sectorul materialelor pe pitata mondiala.

Toate cele mentionate anterior, sustin clar motivatiile pentru intensificarea cercetarilor in domeniile fotonicii si al stiintei materialelor, cu scopul de a dezvolta noi dispozitive functionale in vederea unor aplicatii noi, folosind materiale adaptate la scara nanometrică. In acest sens, cristalele fotonice sunt materiale "cheie" care pot satisafce multe dintre necesitatile technologice actuale. Ele au fost denumite de Eli Yablonovitch (1987) "semiconductori de lumina". Cristale fotonice (PC) sunt materiale compozite, cu modularea periodica a permitivitatii, perturband astfel propagarea luminii, similar cu perturbarea electronilor de catre semiconductori. Propagarea luminii cu lungimea de unda comparabila cu periodicitate cristalelor fotonice este blocata, ducand la aparitia asa-numitei benzi fotonice interzise (PBG). Astfel, propagarea luminii in una (1D), doua (2D) sau trei (3D) dimensiuni poate fi manipulata si controlata efectiv prin structura materialelor fotonice. O banda interzisa incompleta poate fi obtinuta prin structurarea materialului in una sau doua dimensiuni. Pana in prezent a fost obtinuta cu succes fabricarea cristalelor fotonice in una sau doua dimensiuni (1D/2D-PCs) prezentand o structura ordonata la distanta (esentiala pentru controlarea propagarii luminii). Dar, din punct de vedere al aplicatiilor practice, o banda fotonica interzisa completa pentru orice orientare a lungimii de unda a luminii este de

preferat. Aceasta poate fi realizata numai in materiale structurate tridimensional, dar fabricarea lor fara defecte structurale este foarte dificila. Prin folosirea acestor materiale in 3D, mai precis a cristalelo fotonice functionalizate in 3D, ambitia este de a manipula luminii cu jutorul unor stimuli externi (de exemplu, pH controlabil, temperatura, camp magnetic / electric) in ideea de a obtine produse noi cum ar fii dispozitive optice miniaturizate cu funcţionalitati mai complexe.

Aceste provocari au motivat aceasta teza de doctorat, sustinuta financiar pe durata de 2 ani de Proiectul National ”Intramural-CSIC” (CRIMAFOT) intitulat "Spre o noua generatie de cristale magneto-fotonice" avand ca parteneri grupuri de cercetare de la "Institut de Ciencia de Materials de Barcelona" (ICMAB-CSIC), "Instituto de Ciencia de Materiales de Madrid" (ICMM-CSIC) şi "Centro Nacional de Microelectronica" (CNM-CSIC). Proiectul a urmarit obtinerea unui sistem optic care sa raspunda la un camp magnetic exterior (considerat stimul extern). Ca si sisteme optice au fost selectate cristalele fotonice (in doua si trei dimensiuni) urmand ca acestea sa fie functionalizate cu nanoparticule magnetice pentru obtinerea cristalelor magneto-fotonice (MPCs). Aceasta functionalizarea nu numai ca ar permite controlarea pozitiei spectrale a benzii fotonice interzise cu ajutorul unui camp magnetic extern, dar ar permite înbunatatirea (marirea) raspunsului magneto-optic an apropierea marginii benzii interzise datorita cresterii interactiunii lumina-materie. A fost demonstrat anterior ca acest raspuns magneto-optic este îmbunatatit semnificativ în 1D – MPCs. Datorita complexitatii realizarii unui material fotonic in 3D, obtinera unui raspuns magneto-optic comparabil cu cel de 1D ramane o provocare. Scopul tezei a fost rezolvarea acestei provocari. Cristalele fotonice in 3D cu raspuns magneto-optic intensificat ar putea pot fi o baza adecvata pentru dezvoltarea, de exemplu, a unei noi generatii de izolatori optici compacţi (miniaturizati si cu pierderi optice meglijabile) pentru transmisia optica.

Deoarece s-a cunoscut functionalitatea materialul cautata, si anume un raspuns magneto-optic intensificat in apropierea marginii benzii interzise atat in materialele bi- cat si tridimensionale, de la inceput au fost stabilit unele cerinte de indeplinit:

• Cunoasterea cuprinzatoare a sistemuli de nanoparticule magnetice din punct de vedere structural, morfologic, a comportamenui magnetic şi magneto-optic intr-un mediu dezordonat.

• Cristalul magneto-fotonic sa contină nanoparticule superparamagnetice (cu dimensiuni între 5 si 20 nm), cu scopul de a obtine un raspuns rapid la camp magnetic de intensitate scazuta si raspuns nul in absenta unui camp.

• Cantitatea de material magnetic sa fie detectabila prin tehnicile folosite.

• Buna calitate a cristalului fotonic original să fie conservata, în vederea păstrarii proprietăţile optice si după functionalizarea materialului.

• Daca este posibil, de a folosii tehnologii de fabricare durabile: randament ridicat in producţia noului material, complexitate scazuta si munca neprimejdioasa, eficienta in consumul de energie si ecologica.

Tinand cont de aceste cerinte, obiectivele acestei teze de doctorat au fost :: **1) sintetiza de nanoparticule magnetice de mare cristalinitate** (nichel, oxid de fier şi ferita de mangan) utilizand metode chimice; controlul dimensiunilor nanoparticulelor cu ajutorul diferitilor parametrii experimentali si studiul stabilitatii sistemului coloidal magnetic (nanoparticule dispersate in mediu lichid). **2) Fabricarea materialelor magneto-fotonice** prin i) tehnica

"botom-up" –incorporarea nanoparticule magnetice într-un cristal fotonic prefabricat (2D sau 3D) şi ii) metoda "top-down" – sablonarea la scala nano a unui material magnetic compozit prin tehnici de litografie (cu fascicul de electroni şi nanoimprimare). 3) **Caracterizarea** structurala, morfologica si functionala a materialele fabricate; 4) **Optimizarea procesului de fabricare** pentru a asigura functionalitea dorita şi anume detectarea raspunsului magneto-optic si daca este posibil si intensificat (marit) la marginea benzii interzise.

Teza de doctorat este structurata in sase capitole:

**Capitolul 1** ofera o prezentare generala a nanoparticulelor magnetice, a cristalelor fotonice conventionale si a celor functionalizate, numite magneto-fotonice. In prima sectiune sunt discutate proprietatile, metodele de sinteza chimica si posibilele aplicatii ale nanoparticulele magnetice de interes, cum ar fi de metal (nichel) şi de oxid (oxid de fier şi ferita de mangan). Urmatoarele doua sectiuni, se refera la cristalele fotonice, fiind presentate caracteristicile lor structurale si fenomele fizice ce stau la baza proprietatilor lor optice si magneto-optice.

**Capitolul 2** descrie sinteza chimica a nanoparticuleo magnetice folosind trei strategii de sinteza: descompunerea termica la temperature inalta, folosirea microundelor ca si sursa de energie şi sinteza continuă in etanol supercritic. Se discuta controlul asupra dimensiunii nanoparticulei precum si stabilitatea coloizilor magnetici. Sunt descrise caracteriristicile structurale, morfologice şi funcţionale ale nanoparticulelor preparate.

**Capitolul 3** se ocupa cu fabricarea cristalelor magneto-fotonice in doua dimensiuni folosind pe de o parte tehnicile de litografie si pe de alta parte a noua metoda de depunere a materialului magnetic si anume depunere asistata de microunde. Pentru strategiile abordate, s-a dezvoltat un protocol de fabricatie. De asemenea nelipsitele caracterizari structurale, morfologice şi functionale ale materialelor fabricate sunt prezentate.

**Capitolul 4** descrie fabricarea si caracterizarea materialelor magneto-fotonice tridimensionale abordand doua strategii: Prima strategie va folosi nanoparticulele de nichel sintetizate anterior cu prezentarea mai multor variante de depunere pentru a gasi metoda optima. A doua strategie are in vedere sinteza nanoparticulelor metalice direct in interiorul structurii fotonice, folosind o metoda chimica sol-gel clasica si cea neconventionala, depunerea asistata de microunde. In scopul evaluarii calitatii materialului fabricat si in vederea optimizarii procesului, caracterizarea completa a materialelor este de asemenea presentata.

**Capitolul 5** prezinta principalele concluzii ale tezei de doctorat si face sugestii pentru lucrarile viitoare.

**Capitolul 6** include anexele: Anexa I.- publicatiile referitoare la această teză. Anexa II. – o scurta descriere a tehnicilor experimentale utilizate, precum şi protocoalele aplicate pentru pregătirea probelor. Anexele III. şi IV contin tabelele cu conditiile experimentale detaliate atat pentru obtinerea nanoparticulelor cat si a materialelor fotonice.

# Table of contents

Chapter 1.                                                    INTRODUCTION

*EXPERIMENTS, RESULTS AND DISCUSSIONS*

Chapter 2.                                            MAGNETIC NANOPARTICLES

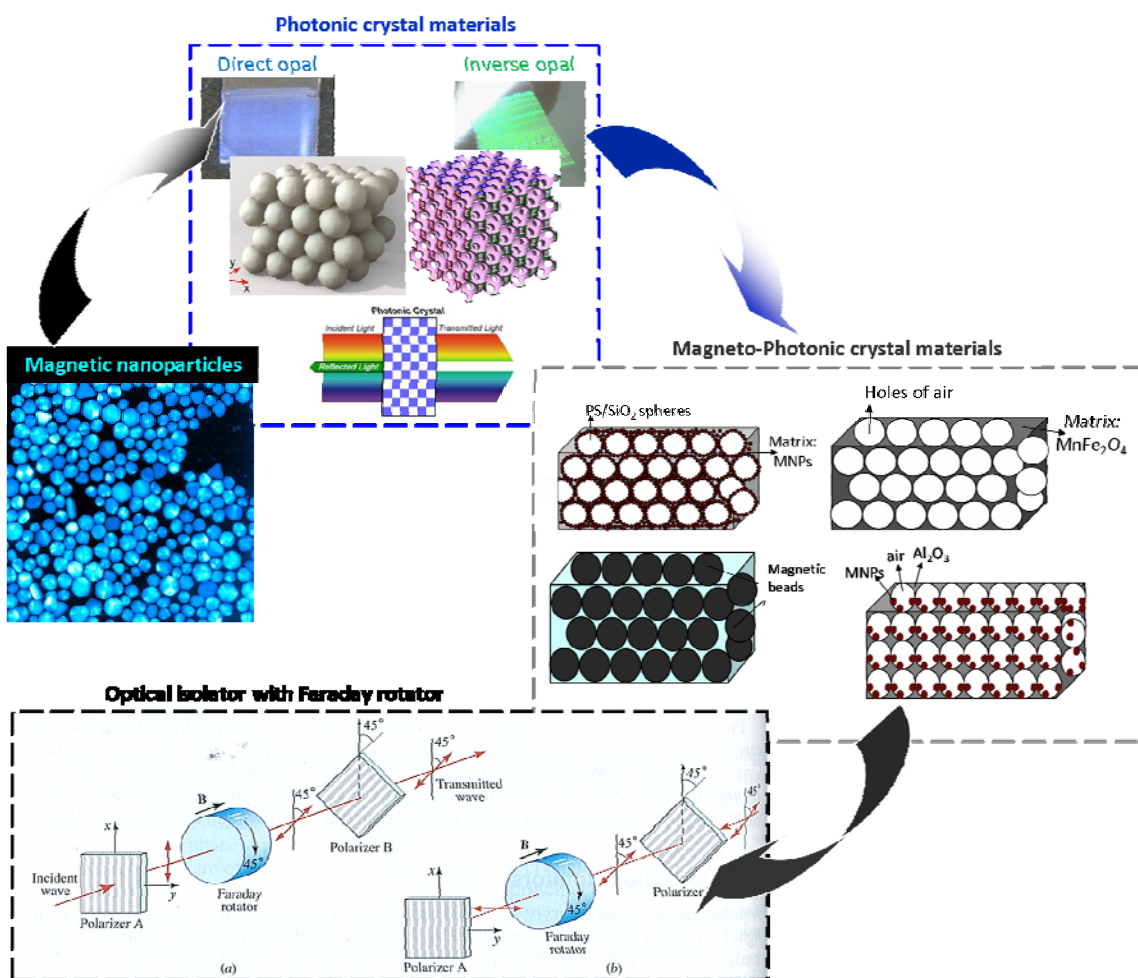Chapter 3.                          2D MAGNET0-PHOTONIC CRYSTAL MATERIALS

# *Attributions*

Here, I would like to acknowledge the people who have contributed to this thesis.

- **Jose Manuel Caicedo Roque** (ICMAB-CSIC, Laboratory of Multifunctional thin films and complex structures) performed the optical transmissivity and magneto-optical measurements by magnetic circular dichorism setup (MCD) and also the data analysis. We collaborated during the three year of my PhD thesis and he is co-author in several papers related to this thesis (presented in chapter 6.1).

- **Alvaro Blanco, Cefe Lopez, Victor Canalejas and Martin García** (ICMM. Photonic Crystals group) for their collaboration in providing the prefabricated opals, optical reflection of measurements of blank opals and also in functional (optical and magneto-optical) data interpretations of magnetic opals.

- **Antonio Garcia Martín** and **Gaspar Armelles** (CNM-CSIC) contributed to the evaluation and understanding of the magneto-optical results of magnetic opals.

- **Du Xing Chen** (UAB, Physics Dep. And ICREA) performed specific magnetic measurements for nickel nanoparticles and developed a model to calculate the size of magnetic nanoparticles from the magnetization curves.

- **Marti Gich** (ICMAB-CSIC, Nanoparticles and Nanocomposites group) performed the atomic layer deposition coating with alumina of several opals and the XRD data analysis by Rietveld refinement of iron oxide NPs synthesized by microwave route.

- **Cyril Aymonier, Samuel Marre** and **Yann Roig** (ICMCB, Supercritical fluid group, Bordeux) help me with the continuous supercritical reactor setup and trained me to use it. **Philippe Dagault** and **Eric Lebraud** (ICMCB) performed the TGA and XRD measurements of ferrite nanoparticles prepared by supercritical fluids.

- **Jordi Arbiol** (ICMAB, ICREA) performed the High Angle Annular Dark Field HAADF-STEM images and the Electron Energy Loss Spectroscopy (EELS) line profile of the $SiO_2$ opal sphere covered with $MnFe_2O_4$ nanoparticles.

- **Sonia Estradé** (LENS, MIND-IN2UB) and **Francesca Peiro** (LENS, MIND-IN2UB) performed the high resolution TEM images, Fast Fourier Transform (FFT) with the analysis of the crystallographic faceting planes of iron oxide nanoparticles prepared by microwave route.

- **Susagna Ricart** and **David Olid** trained me in using the microwave reactor.

- **Xavier Borissé**, trained me in using nanoimprint lithography.

- **Judit Oró** (ICMAB-CSIC) performed the TEM images and electron diffraction analyses of the synthesised nanoparticles and trained me to use the scanning electron microscope and electron beam lithography.

- **Miguel Rubio-Roy** (ICMAB, Laboratory of Multifunctional thin films and complex structures) fabricated the Au nanodisk arrays and performed the optical plasmon measurements.

- **Ondrej Vlasin** (ICMAB, Laboratory of Multifunctional thin films and complex structures) performed the magneto-optical characterization of corrugated 2D gold/dielectric material infiltrated with Ni nanoparticles.

- **Alejandro Goñi** (ICMAB), **Nicolas Tognalli and Alejandro Fainstein** (CNEA) provided the Au voids arrays.

- The magnetic characterization by SQUID of the materials was carried out by **Bernat Bozzo** at the low temperature lab of the ICMAB.

- **Francisco Javier Campos** and **Joan Esquius** (ICMAB-CSIC) performed the x-ray diffractograms in powder form. **Anna Crespi** (ICMAB-CSIC) performed the diffractograms in colloidal dispersion. X-ray diffraction analyses were done at the XRD lab of the ICMAB.

- Thermal gravimetric analysis were done by **Silvana Tomici** (URV) and **Jordi Balaque** (ICMAB)

# 1

# INTRODUCTION



**Photonic crystal materials**

Direct opal       Inverse opal

Photonic Crystal

Incident Light       Transmitted Light

Reflected Light

**Magnetic nanoparticles**

**Magneto-Photonic crystal materials**

PS/SiO₂ spheres       Holes of air       Matrix: MnFe₂O₄

Matrix: MNPs

Magnetic beads       MNPs   air   Al₂O₃

**Optical isolator with Faraday rotator**

Transmitted wave

B       Polarizer B       45°   45°

Incident wave

Polarizer A       Faraday rotator       45°

B       45°   45°

Polarizer

Faraday rotator       45°

Polarizer A

(a)       (b)

## 1.1 MAGNETIC NANOPARTICLES

### 1.1.1. Nanostructured materials and applications

Nanotechnology is commonly defined as the understanding, control, and restructuring of matter at nanometer scale (< 100 nm) to create materials with fundamentally new properties and functions[1]. It is expected that nanotechnology will be ubiquitous in many industrial and society sectors such as health, information technologies, energy, materials, food, environment or instrumentation and that materials is the market sector with the largest worldwide expected revenues. According to Cientifica company market report[2], the worldwide total government funding for nanotechnology research and development at the end of 2011 was around $65 billion and is going to rise up to $100 billion by 2014.

A major material science challenge is the design of functional nanostructured materials combining superior and novel tailored (physical or chemical) properties with versatile and reliable material's processing technologies. Nanostructured materials can be fabricated in many forms such as monodispersed nanoparticles, thin films containing at least one nano-dimensional component, two-dimensional nanosized structures created by lithographic methods or self-assembly of nano-components in three dimensions, etc.

Inorganic, organic or hybrid nanoparticles exhibiting interesting optical, electrical, magnetic and chemical properties are of interest not only for fundamental research but also for technological applications[1a, b, 3]. As a result, intense research has been done in the last decade on the synthesis of nanoparticles with sizes smaller than 50nm[4] and nanocolloids below 50 nm[3c, 5]. Special attention has been devoted to the careful control of shape, particle size, size distribution, structure and surface properties, all being dependent on the field of application.

Among all types of nanoparticles, magnetic ones are of huge importance for various fields such as magnetic fluids, drug delivery, bio-imaging, therapy, ultra-high magnetic storage devices, magneto-optical component in optoelectronic devices, magneto-photonic crystals, magnetic catalyst, environmental remediators, sensors etc[3a, b, 4a, 4d, 6].

Since magnetic nanoparticles such as nickel, iron oxide and manganese ferrite are the systems used in this Thesis, special attention will be devoted on the properties and synthesis of these materials.

### 1.1.2. Bulk *vs.* nano-dimension magnetic properties of nanoparticles

**Bulk properties**

Magnetism[4a, 4d, 7] arises from two characteristics of electrons in atoms: (1) the motion of the electrons in an orbit around the nucleus and (2) the motion of the spin of the electrons around its axis. Thus each electron has a spin and orbital magnetic moments which act as little magnets. When a material has a net magnetic moment, it is called a magnetic material such as transition metals: manganese, iron, cobalt, nickel. In these metals, the magnetic

moment arises from the spin motion due to the unpaired 3d[a] electrons ($3d^5 4s^2$ for Mn, $3d^6 4s^2$ for Fe, $3d^8 4s^2$ for Ni).

The magnetic moment per unit volume is called magnetization (M, expressed in units of A/m in SI or emu/cm$^{3}$[b] in cgs[c]) which changes by varying the magnetic field strength (H, A/m in SI and Oe in cgs). The magnitude of this response is the magnetic susceptibility ($\chi$, adimensional), given by the ratio $\chi$ = M/H. Materials can be classified according to their response to a magnetic field as: i) *diamagnetic* and *paramagnetic* materials (**Figure 1.1a**) without magnetization in the absence of a magnetic field; ii) *ferromagnets, antiferromagnets and ferrimagnets* in which below the temperature called Curie or Néel temperature a spontaneous magnetization takes place but in the absence of a magnetic field, above the Curie/Néel point (**Figure 1.1e**), the magnetic moments are randomly aligned as in paramagnetism. In the case of ferromagnetic materials (**Figure 1.1b**), magnetic moments with the same magnitude are aligned parallel to each other. When the moments are equal in magnitude but aligned antiparallel, the net magnetic moment is zero. This occurs in antiferromagnetic materials (**Figure 1.1c**). In a ferrimagnetic material, a net magnetic moment results from two types of atoms with magnetic moments of different strength and antiparellel alignment (**Figure 1.1d**). Both ferro-and ferrimagnets have a permanent magnetic moment, i.e. they have remnant magnetization ($M_r$) without the presence of an external magnetic field. Fe and Ni are ferromagnetic materials; magnetite ($FeFe_2O_4$), maghemite ($\gamma-Fe_2O_3$) and manganese ferrite ($MnFe_2O_4$) are ferrimagnetic materials.
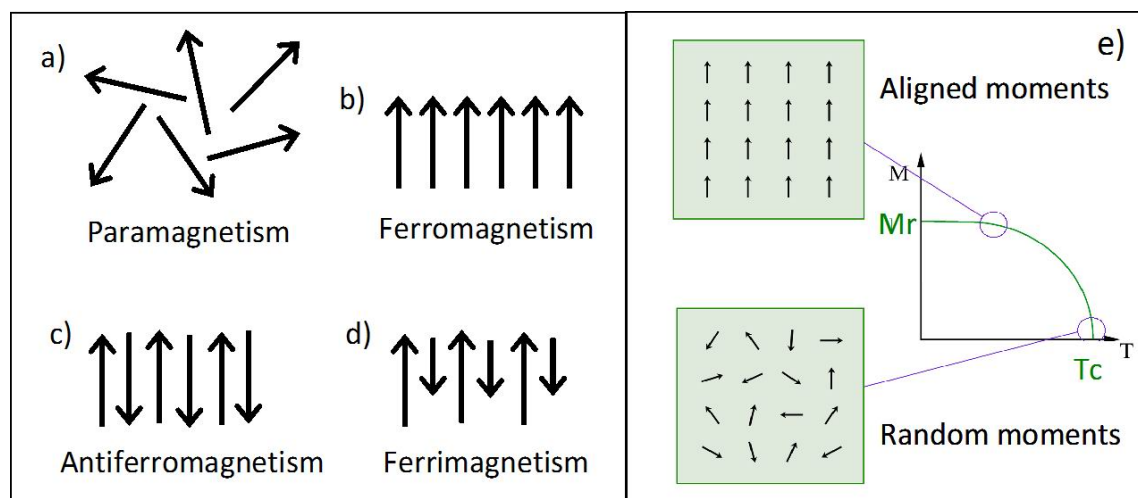


**Figure 1.1.** *Alignment of individual magnetic moments in different magnetism (**a-d**). Temperature-dependent magnetization of ferromagnetic material (**e**) where Mr is the remnant magnetization and Tc is the Curie temperature.*

Bulk ferromagnets consist of small regions, called domains separated by the domains walls (**Figure 1.2-lower inset**). Each domain has its own magnetization vector arising from the alignment of the magnetic moments within the domains. By applying a magnetic field at one

---

[a] *There are five orbital d-types* and according to Pauli's exclusion principle, one orbital can be occupied by only two electrons with opposite spins. The maximum number of electrons on 3d is 10.

[b] More often used for practical purposes is the mass magnetization expressed in emu/g units in cgs.

[c] *cgs:* centimeter, gram, second

point the material will become a single domain, due to domains displacement, reaching the magnetic saturation (saturation magnetization, $M_s$). The magnetization curve (**Figure 1.2**) displays a hysteresis loop. When the magnetic field is decreased, magnetization does not follow the initial curve, and at H = 0, not all domains return to their original orientations retaining a non-zero magnetization. This is called remnant magnetization ($M_r$). The external field required to bring this magnetization to zero is called coercivity ($H_C$).

### Properties at nano-level

Reducing the size of ferri-ferromagnetic materials to nano dimensions results in interesting magnetic properties[4a, 4d, 7-8]. While in bulk ferromagnets, domains are formed to reduce the magnetic free energy (magnetostatic energy), when reducing the material volume below a critical value, to create a domain wall would require more energy than to support the magnetic free energy of a single-domain state (so-called monodomain ferromagnetic particle) with all the spins aligned in the same direction.
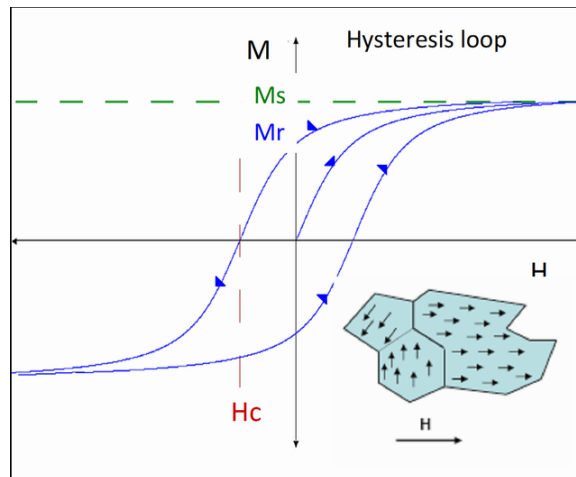


*Figure 1.2. Magnetic hysteresis loop (M vs. H) of bulk ferromagnetic material with domains (lower inset).*

The energy of atoms in a crystal depends on the orientation of magnetic moments respect to the crystallographic axis: a minimum energy is along the easy magnetization direction and vice-versa. The energy responsible to hold the magnetic moments along a certain direction is the magnetic anisotropy energy, expressed by $E(\theta) = K_{eff}V_P \sin\theta$, where $V_P$ is the particle volume, $K_{eff}$ is the effective anisotropy constant and $\theta$ is the angle between the easy axis and magnetization. For monodomain ferromagnetic particles (i.e. below critical size), two equivalent energies along the easy direction of magnetization are separated by the energy barrier ($K_{eff}V_P$) (**Figure 1.3a**). When the particles size is further decreased, the thermal energy ($K_BT$) becomes greater than the energy barrier resulting in magnetization flipping, and the system enters in superparamagnetic state (**Figure 1.3b**). In this state, every nanoparticle is a single domain and behaves like a giant paramagnetic atom. In the presence of a magnetic field, will present a large susceptibility with no remnant magnetization nor coercivity (essential for various applications) (**Figure 1.3c**). For an ideal superparamagnetic system, the

magnetization obeys the Langevin function, $M = M_s \cdot (coth\alpha - 1/\alpha)$, where $\alpha = (m_0 H)/(k_B T)$ and $m_0 = M_s V_p$ (magnetic moment of one particle). Superparamagnetic behavior takes place above a temperature called blocking temperature ($T_B$, K). If the particle magnetic moment reverses at shorter times than the experimental measurement time scale (about 100s in SQUID magnetometry), the system is in a superparamagnetic state, otherwise it is in blocked state. $T_B$ is influenced by the nanoparticle size and size polydispersity and can also be modified by the
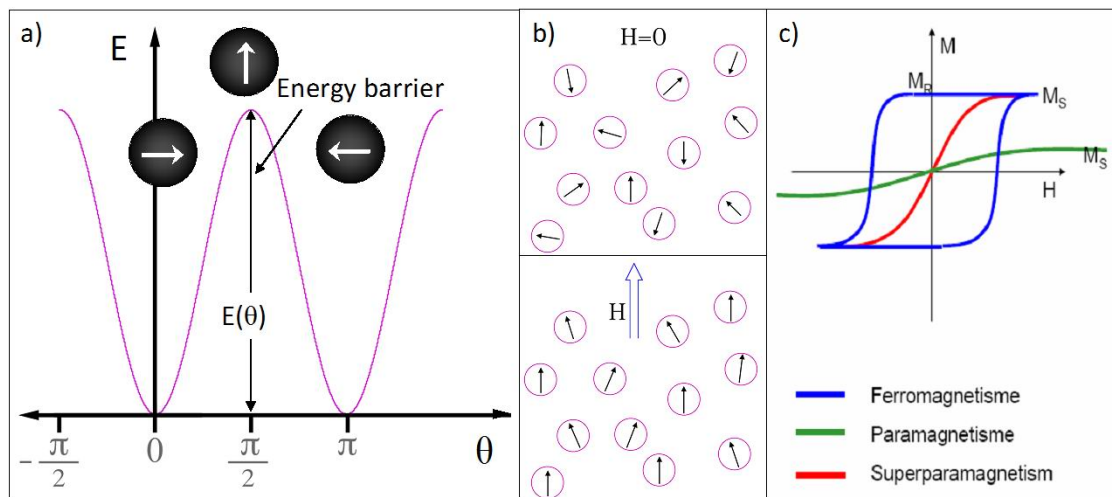


interparticle interactions.

*Figure 1.3. Magnetic characteristics of monodomain ferromagnets: (a) magnetic anisotropy energy depending on magnetic moment orientation; the white arrows represent spin states (magnetic moments); (b) superparamagnetic system in absence and presence of magnetic field; (c) magnetization curves of different magnetisms.*

## 1.1.3. Synthesis and stabilization of monodispersed magnetic nanoparticles

**Synthesis methods**

Magnetic properties of nanoparticles are directly influenced by the preparation methods. By choosing a fabrication method [4, 6a, 9], the size, shape, cristallinity, surface energy and surface chemistry of the nanoparticles can be controlled and tuned. Many physical (top-down) and chemical (bottom-up) approaches can be employed for magnetic nanoparticles preparation, according to the desired applications. If the interest is to study the intrinsic novel properties of individual magnetic nanoparticles and not in an interacting system, one must look at the preparation of stable monodispersed nanoparticles (one aim of this thesis). According to Murray [10a, 10], samples with standard deviations (size distribution) $\sigma \leq 5$ % in diameter are referred to as monodispersed and the term *nanocrystals* (NCs) is reserved for structures with well-characterized core, while the term *nanoparticles* (NPs) is more general, denoting an amorphous or inherently multidomain inorganic core. But many times, the term "nanoparticles" is used as synonym of nanocrystals and the same we do in this thesis, using nanoparticles for well crystalline monodomain materials.

Since our interest is in nickel and ferrites (iron oxide and manganese ferrite), among all methods (physical or chemical) used for the preparation of magnetic nanoparticles, we

will focus in this section in the most popular methods to prepare the aforementioned materials.

Without entering in details, we mention a few *physical methods* [6a, 4a, 9b], such as condensation on a substrate by metal evaporation (e.g. Ni), laser pyrolysis (e.g. maghemite/magnetite), electrodeposition (e.g. Ni), atomic layer deposition (e.g. Ni, oxides), chemical vapor deposition (iron oxides), sputtering (e.g. oxides), and inert gas condensation (e.g. Ni), grinding of microcrystallites power (e.g.ferrites), etc. It has to be mentioned that these methods are not able to produce individual, non–interacting nanoparticles and the use of a substrate is a must and in addition, these techniques are costly.

On the contrary, nearly monodispersed nanoparticles can be prepared by *solution-phase chemical synthesis* that allows the addition of a stabilizer (surfactant) as a shell around the magnetic core. This shell can (i) prevent agglomeration and surface oxidation of monodispersed nanoparticles, (ii) stabilize the nanoparticles long–term in liquid media and (iii) change the surface chemistry. A requirement for the preparation of monodispersed nanoparticles, according with the classical La Mer mechanism[11], is a fast nucleation step followed by a slow controlled growth of the existing nuclei. This can be achieved via *thermal decomposition* methods, based on decomposition of a metallic precursor (usually organometallic) in organic solvent at high reaction temperature ( 100– 320 $^{o}$C)[4d]. The Murray group developed the *hot-injection*[10a,10] a landmark work in the colloidal chemical synthesis of nanocrystals. It involves a very fast injection of the organometallic precursor into a hot mixture of coordinating solvent (150-300 $^{o}$C), making the solution highly supersaturated instantaneously. The bulky coordinating solvent, binding to the metal atoms, retards the crystal formation while keeps, the supersaturation a while. This allows a control over nucleation and colloidal crystal growth. The size distribution control is driven by the initial supersaturation (kinetic process) and requires a very reactive precursor in order to induce a fast supersaturation after its injection. Through this method, highly crystalline nanoparticles with size distribution $\sigma \sim 5\%$ can be achieved but has the limitation of the precursors' type and in addition the reaction could be dangerous and not suitable for large scale synthesis.

To overcome these drawbacks, Hyeon group[4c] have developed a more reliable synthesis route for the preparation of uniform nanoparticles in the same thermal decomposition route, namely the *heat-up* method. It involves a slow heating of the reaction mixture (organo-metallic precursor with surfactants and solvent) from room to high temperature (up to 320 $^{o}$C), followed by material aging (minutes or hours). The difference over hot-injection is that between the precursor decomposition and formation of nanoparticles, there is an intermediate step, in which the surfactant is forming an intermediary complex that delays the nucleation promoting instead the accumulation of intermediary species (monomers). When the nucleation energetic barrier is reached by the system, nucleation and growth start suddenly and within 10 minutes of the start of nucleation, the nanoparticles' mean size increases and simultaneously decreased the size distribution. In this heat-up method, the size distribution is kinetically driven, as for hot-injection, the stable intermediate species (meaning a high monomers concentration) being essential for the size distribution control. The advantages of this method is that allows a

much wider choice of precursors, not only organometallic but also metal salts, is less dangerous and it can be performed at larger scale.

Both hot-injection and heat-up, are suitable for iron oxide, ferrites or Ni NPs and the resulting nanoparticles are dispersable in organic media using steric surfactant(s)[4c, 9a, 9d] . A very good quality material are produced, but requires inert atmospheres, the surfactants, high reaction temperature involving high energy consumption and a long preparation time (hours or 1 day).

If biological applications are envisaged, the nanoparticles are required to be stabilized in aqueous media. For that, either a ligand transfer for the NPs prepared by thermal decomposition is employed, or the NPs are synthesized directly in aqueous media. The later is called *co-precipitation*[4a, 4d, 6a, 9b,12] and also is a widely used method for the synthesis of iron oxide and ferrites nanoparticles. Compared with thermal decomposition, co-precipitation is much simpler; it uses water as solvent, mild reaction temperature and shorter reaction time (order of minutes). It is based on the reaction between the aqueous solution of metal salts with alkali (base) solution under magnetic stirring in inert atmospheres at room or higher temperature (20-90 °C). For nanoparticles stabilization an electrostatic surfactant is added during or after the nanoparticles synthesis. The final nanoparticles' size, shape and composition are influenced by various experimental parameters such as, the type of precursors salt (nitrate, chloride, sulfate), the ratio between precursor cations $M^{2+}/M^{3+}$, the reaction media pH, the ionic strength of the media, reaction temperature and unfortunately rather polydisperse nanoparticles can be prepared.

An other synthesis method is the *two-phase route*[4a, 4d, 6a, 9b], namely water-in –oil or oil-in-water microemulsions, consisting in nanodroplets (up to 50 nm) of water or oil dispersed in the other phase, stabilized by a surrounding layer of surfactant at the water-oil interface. For instance for the preparation of ferrites nanoparticles[4d], the aqueous solution of metal salt precursors are forming the water droplets in oil media (e.g toluene, in reverse micelles process). The size of the droplets and subsequently the size of the future nanoparticles will depend on the molar ratio between water and the surrounding surfactant, the precursor's concentration and also on the water to oil volume ratio. Nanoparticles can be produced by different mechanisms such as i) identical water droplets containing the precursors will collide, coalesce and finally the precipitate will be confined in the micelle; ii) addition of a reducing or precipitating agent into the solution containing the dissolved metallic precursor. However, this method presents some drawbacks: limitation of the working window (reagents choice), lower yield than thermal decomposition or co-precipitation, broad size distribution and limitation to scaling up.

*Sol-gel process* [4a,10b,13] is another chemical route used for synthesis of metal oxides nanoparticles. The classical way consists in hydrolysis and condensation of an alkoxide precursor in solution leading to the formation of gel. Slower and controlled hydrolysis reaction results in smaller nanoparticles. The size and phase are also influenced by the initial solution composition, pH and temperature. Limitation of the classic sol-gel method is the contamination with the byproducs, and the need of post-treatment to improve the cristallinity of the material. Conventional sol-gel is used for the preparation of ferrite NPs, or nanocomposites (e.g. silica-iron oxide aerogels or oxide@silica nanoparticles)[14]. An improvement of the classic route, is the *microwave-assisted nonhydrolytic sol-gel route*[15]

using organometallic precursors (acetate, acetylacetonate ligands) in organic solvent (benzyl alcohol) with the formation of M–O–M matrix. This method has the advantage of using non-conventional heating source (microwave energy) which is faster, high yield, with no need of prost-treatment producing highly crystalline materials comparable with thermal decomposition. Due to the versatility of microwave-heating, apart from the nonhydrolytic way, the synthesis can be performed using water, polyols or ionic liquids as green solvents[16].

The last synthetic method that it is worth to be mentioned is *high pressure hydrothermal* route[4a, 4d], relying i) on the ability of water at elevated pressures and temperatures to hydrolyze and dehydrate metal salts, and ii) the very low solubility of the resulting metal oxides in water at these conditions to generate supersaturation and subsequently fine crystals formation. Parameters such as pressure, temperature, reaction time, and the precursor–product system can be tuned to maintain high nucleation rates and to control the growth. It is considered environmentally friendly and with the possibility of scaling up but with the drawback of a medium yield and a formation mechanism not fully understood.

In this thesis, the chemical synthesis methods chosen for the preparation of magnetic nanoparticles of interest are the following:
1. Thermal decomposition based on heat-up method for the synthesis of Ni NPs;
2. Microwave-assisted nonhydrolytic sol-gel route for the preparation of iron oxide and manganese ferrite NPs;
3. Continuous supercritical ethanol synthesis of iron oxide and manganese ferrite NPs.


**Stabilizations of magnetic colloids**


Stable magnetic colloids are a prerequisite for many applications. The stability implies individually dispersed nanoparticles and long term stability without agglomerations or precipitation in liquid media[4c, d, 6a, 9a]. Due to the large surface to volume ratio, nanoparticles tend to aggregate in solution in order to reduce their surface energy. Additionally, the metal nanoparticles, such as Ni, Co, Fe, are very easily oxidized in the presence of oxygen. Therefore, development of strategies to stabilize the magnetic nanoparticles in liquid media by controlling the surface chemistry is important. The surface functionalization can be done using organic substances (surfactants, polymers, proteins) or inorganic (silica, gold, $TiO_2$), resulting in a core@shell nanoparticles

Surfactant or polymers are often used to stabilize monodispersed magnetic nanoparticles by steric or electrostatic repulsion in liquid media to balance the attractive magnetic and van der Waals forces between the magnetic nanoparticles. In general, the steric surfactant or polymer with functional groups such as carboxyl, phosphate, and sulfate are chemically bonded to the magnetic nanoparticles surface forming a very stable organic shell **(Figure 1.4a)**. Usually, in the case of electrostatic coating, if the electric potential associated with the double layer (positively and negatively charged) **(Figure 1.4b)** is sufficiently high, the electrostatic repulsion prevents the agglomeration. But by increasing the ionic strength of the media, or by decreasing the surface charge, the system can be destabilized and the particles will agglomerate and eventually precipitate. Moreover, the electrostatic shell is mainly physisorbed at the nanoparticles surface, without offering a very

good protection for long term stability. The organic coating has the drawback that does not stand very high temperatures (the organic decomposes up to 500 °C). Other coatings alternatives are for instance the use of Pt, Au, silica, oxide or carbon shell. Steric and electrostatic coatings were used as our stabilization approaches, being suitable with the thesis purpose,
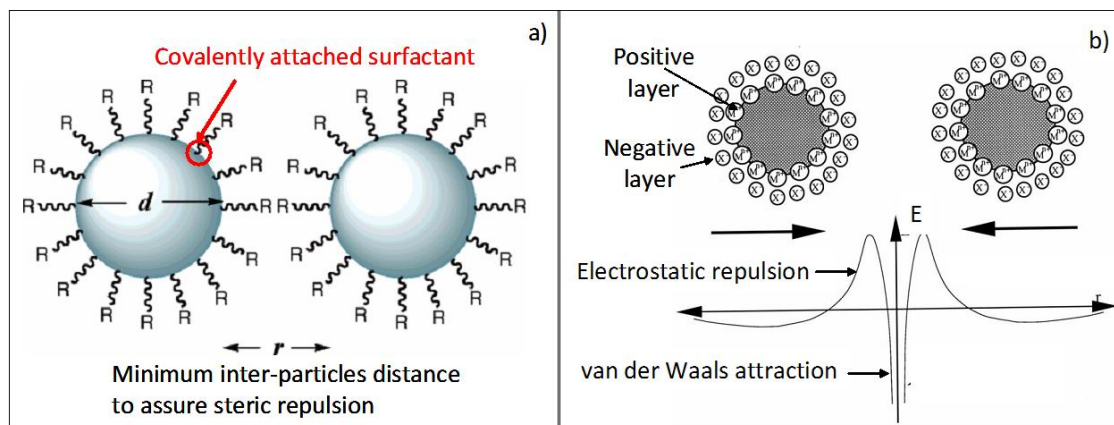


**Figure 1.4**. *Different types of stabilization of nanoparticles in liquid media: steric[17] (a) and electrostatic[6a] (b)*

## 1.2 PHOTONIC CRYSTAL MATERIALS

### 1.2.1 Photonics in our future

Photonics encompass the generation, detection and management of light through guidance, manipulation, amplification and most importantly, its utilization for the benefit of mankind (definition given by the eminent French scientist, Pierre Aigrain).

An interesting "decade forecast" was made in 2004 by the Optoelectronic Industry & Technology Development Association (OITDA)[18] about a world-wide market prediction for the future of photonic products. The prediction (**Figure 1.5**) was based on a future social life characterized by three features: 1) less birth rate & longer life, 2) sustainability, and 3) borderless economy. According to this, the photonic market will be about 4 times bigger in 2015 than in 2002 where photonic-energy (green energy), solid-lighting and medical-care will be dominant. This forecast is in good agreement with a more recent report of the European Commission[19] about the important role of photonics today providing innovative products and services for relevant societal challenges such as globalization, climate change or ageing society. Many photonic products rely on the development of a new generation of tailored, multifunctional photonic materials with novel properties. Their manufacture is vital for the information technology of the 21st century that requires more compact, cheap and energy efficient devices. Recent progress has led to spectacular advances in light flow and light-matter interaction control through photonic crystal technology[20], photonic crystal fibers[21], plasmonics[22] and optical metamaterials[23].
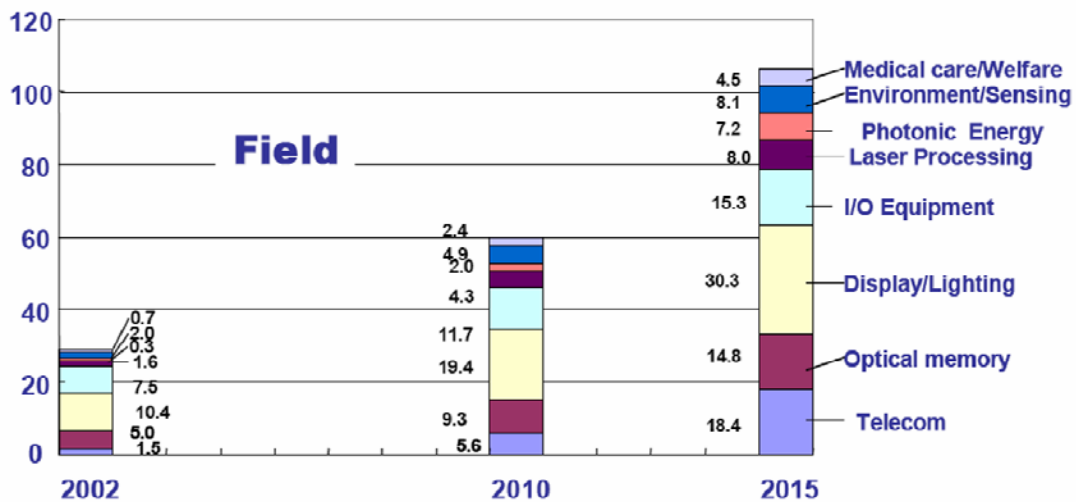
**1.5** *World wide photonics market prediction (OITDA)* [18] *(X axes –represents billion of $ and Y axis-years)*

## 1.2.2 Photonic crystal structure and the photonic effect

The harnessing of light has attracted interest for a long time. "λ-Photonics" in one word means the control of photons at the wavelength scale within the tiniest possible space during the longest possible time[24]. This can be done by structuring the matter in such way to tailor light-matter interaction and obtain engineered electromagnetic responses.

Photonic crystals, named "semiconductors of light" by Eli Yablonovitch (1987), are artificial crystal structures that can be used to manipulate the light, through the so-called band gap[20] analogously to the manipulation of electron propagation in solids such as the semiconductors. In the latter, the electronic band gaps are forbidden for narrow range of energies that electrons cannot occupy. A similar structure but at larger scale is involved in photonic crystal materials in which the light with wavelengths (energies) inside the band gap cannot propagate through the crystal.

**Natural and engineered photonic structures**

Photonic crystals present iridescences as a result of light diffraction. Sophisticated examples of these materials can be found in nature, in the form of optical reflectors (e.g., in gemstones and animals) that have resulted from millions of years of evolutionary "fine-tuning"[25].

For instance, the first "photonic crystal fiber" (two-dimensional photonic crystal, 2D–PCs) was identified in nature in a marine sea-mouse, a worm-type, covered with iridescent hairs and spines which behave as photonic crystal fibers with air holes (**Figure 1.6a–c**). At different orientation of the hairs/spines respect to the light source[25], their color changes. The iridescence of the peacock feathers is also due to 2D–PCs structure. Three-dimensional (3D–PCs) opal structure can be found, for instance, in the gemstone named opal or opalized fossils (**Figure 1.6d, e**) and in some live animals such as beetles. In weevil-*Metapocyrtus sp.*, the metallic body coloration visible from every direction (**Figure 1.6f, g**) is due to the direct opal structure made of 250 nm chitin spheres in hexagonal close-packing order. In weevil-

*Eupholus nickerli sp.,* the same body color can be found but with an inverse opal structure consisting of empty spheres in a chitin matrix **(Figure 1.6h, i)**.
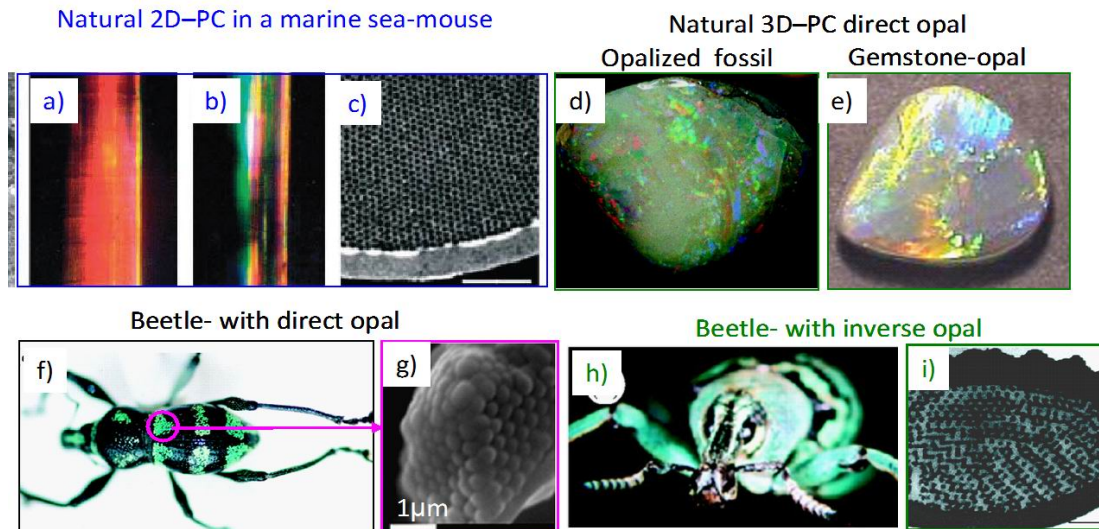


**Figure 1.6.** *Examples of photonic crystal structures in nature.* **a–b)** *show the color of a spin at different light incidence angle;* **c)** *TEM image of a cross-section of sea-mouse hair;* **d)** *bivalved Mollusca found in Australia;* **e)** *gemstone used for jewelry;* **f)** *beetle with the spots made of direct opal;* **g)** *SEM image of direct opal structure;;* **h)** *beetle with a color given by chitin inverse opal;* **i)** *TEM image of inverse opal structure in the transverse section of beetle foot (all images except e) adapted from ref*[25] *)*

Engineered photonic crystals[20, 24, 26] (PCs) are composite materials with periodic modulation of the permittivity, by alternating materials with high and low refractive indexes. The periodicity of dielectric materials can be in one, two or three dimensions, with these materials being named: one dimensional (1D–PCs), two dimensional (2D–PCs) and three dimensional (3D–PCs) photonic crystals, respectively.

Artificial photonic materials can present some of the following structures:

➤ 1D–PCs are sandwich-type structures, alternating different dielectric layers/films **(Figure 1.7a)**;

➤ 2D–PCs consist of a periodic array of air holes (cylinders) in a dielectric medium (polymer, semiconductor) **(Figure 1.8a)** or of a monolayer of self-assembled spheres (PS, PMMA, $SiO_2$, etc

➤ 3D–PCs can be fabricated in different forms. On the one hand, the woodpile structure consisting of high dielectric constant rods assembled such that the contact points form a diamond lattice **(Figure 1.7b)** or a spiral ones **(Figure 1.7c)**. On the other hand, the structure named opal; either direct opal, made of full spheres (PS, PMMA, $SiO_2$, $TiO_2$, etc) self-assembled in three dimension **(Figure 1.8c)** with air voids within the structure, or inverse opal, obtained from the direct opal by filling the air voids with a dielectric material and followed by the removal of the spheres. The resulted structure has air spheres in a dielectric matrix **(Figure 1.8e)**.

### Physical phenomenon of photonic band gap

The interfaces between the dielectric media behave as light-scattering centers due to the high refractive index contrast.
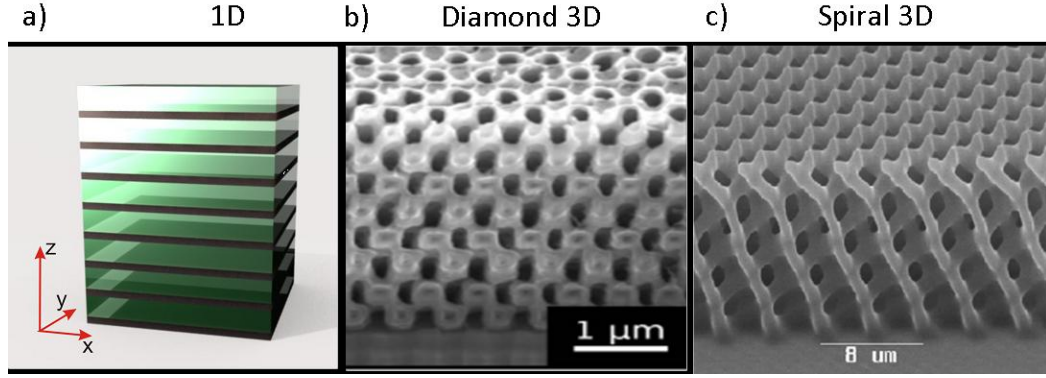
*Figure 1.7.* Schematic representation of 1D and 3D–PCs

The light can "sense" the change in refraction index as it transmits through the structure and is both refracted and partially reflected back on each dielectric interface. The subsequent interference can be either constructive or destructive depending on the light wavelength. A perfect cancellation in all direction for a wavelength comparable with the photonic crystal periodicity forbids that wavelength to propagate through the crystal. The band of the forbidden wavelengths is commonly referred as a *photonic band gap* (PBG).

Without entering into many details, some notions are important to be discussed in order to better understand the physical phenomenon that lies beneath the photonic band gap effect. The behavior of light in PCs is governed by Maxwell's equations[26c, 27] and in the absence of charges and current a simplified form is the electromagnetic wave equation (Eq.1.1):

$$\nabla \times \left( \frac{1}{\varepsilon} \nabla \times \vec{H} \right) = \left( \frac{\omega}{c} \right)^2 \vec{H} \qquad \text{(Eq.1.1)}$$

where $\vec{H}$ is the magnetic field of the photon, $\omega$ is the frequency, $c$ is the speed of light and $\varepsilon$ is the permittivity. If the permittivity is periodic (as in photonic crystals), the eingensolutions of eq 1.1 have the form of series of function $\omega_n(k)$, which can be viewed as successions (n) of energies $\omega$ for every wavevector $k$. The collections of all solutions $\omega_n(k)$ is called the band structure[26c]. For the wavevector $k$, the values at $(k \pm 2\pi/a)$ are identical to those at $k$, where $a$ is the lattice periodicity[d]. Therefore wavevector $k$ can be confined to the first Brillouin zone (BZ)[e]. Since $k$ is a continuous value, $\omega_n(k)$ varies continuously as $k$ varies.. The band structure of a PC can be represented by the wavevector as a function of energy (a/$\lambda$). The different panels in the band structures represent the path between the high symmetry points[f] ($\Gamma$, X, L, W) in the reciprocal space[g] and correspond to the propagation directions (wavevector $k$). **Figure 1.8** illustrates the band structures for: i) 2D–PCs consisting of air cylinders in a dielectric media (refractive index of 3.6)[26c] (**Figure 1.8a,b**); ii) direct 3D–PCs made of spheres

---

[d] *Lattice periodicity* (a): the length scale in which the variation of the refractive index takes place.

[e] *First Brillouin zone*: a region of reciprocal space closer to the origin than to any other reciprocal lattice point.

[f] *High symmetry points*: are the midpoints of the segments joining the origin to its nearest neighbours in the reciprocal lattice.

[g] *Reciprocal lattice*: a lattice (in a wavevector space) of whose points generate plane waves with the periodicity of the direct lattice.

of polystyrene (refractive index of 1.45)[28] (**Figure 1.8c,d**); and iii) inverse 3D–PCs consisting of air spheres in a dielectric matrix (refractive index of 4.1)[29]. (**Figure 1.8e,f**). As it can be seen, there are frequencies $\omega$ inside the Brillouin zone where no photon modes are available for any value of the wavevector $k$ in the direction of propagation, giving the region of photonic band gap (PBG). Gaps open at the edge of first BZ and the corresponding energy is $\omega = (ck)/n$, thus, the gaps found at different directions, occur at different energies. If the photonic crystal structure presents different periodicities in different directions, the band gaps will open at very different energies and will hardly be overlapped. Pseudo or partial PBG (**Figure 1.8d**) appears when the periodicity is the same for some directions while a full PBG (**Figure 1.8b, f**) can be obtained only with identical periodicity in all directions. This can be achieved in inverse 3D–PCs toward the face–centered cubic (fcc) lattice[29a]

The refractive index contrast ($\delta n$) is defined as the ratio between the higher ($n_h$) and lower ($n_l$) refractive index. If this ratio is higher than $2^{26a}$, then most probably, a full PBG is formed. In these, the ideal structure typically consists of an inverse opal – spheres of air in a dielectric matrix to both obtain the greatest dielectric contrast and reduce the losses associated with light propagation in optical materials others than air.
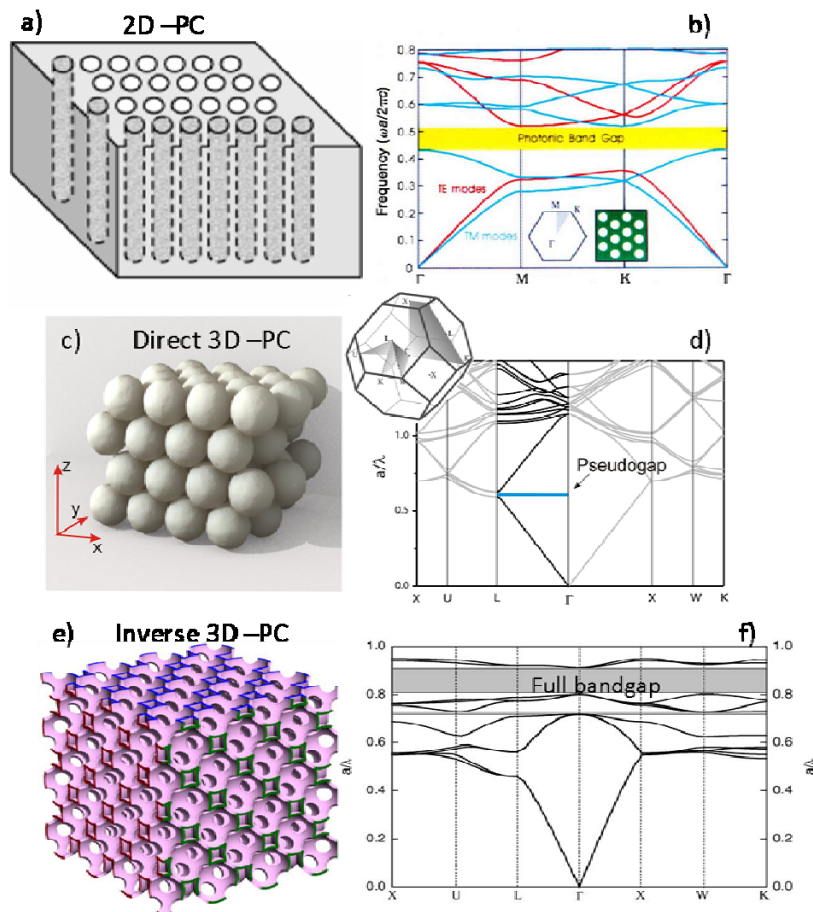


***Figure 1.8.*** *Band structures calculated along the high symmetry points defining the Brillouin zone for different photonic structures: 2D –PC (**a**) and its band structure (adapted from ref[26c]) (**b**); fcc structure of a direct opal (**c**) and its band structure containing a pseudo PBG along the ΓL direction (**d**) (image adapted from ref[28]); fcc structure of an inverse opal (**e**) and its band structure containing a full PBG[29](**f**).*

**Photonic band gap effect**

At the photonic band gap edges, the bands (propagating waves) along certain directions flatten and the energy velocity equal to the group velocity of light ($v_g$, eq.1.2) is considerably reduced (tending to 0). This implies an increase of the optical path meaning that the time taken by electromagnetic wave to traverse the sample is dramatically increased enhancing the light-matter interaction.

The group velocity can be written as:

$$v_g = d\omega/dk \qquad\qquad (Eq.\ 1.2)$$

From the free photon behavior ($\omega = (ck)/n$), the refractive index can be deduced as:

$$n = (c \cdot k)/\omega \qquad\qquad (Eq.\ 1.3).$$

Combining eq. 1.2 and eq. 1.3 gives:

$$n = c/v_g \qquad\qquad (Eq.\ 1.4)$$

where $c$ is the speed of light. The so-called optical path can be calculated as the product of refractive index and the path of light. Close to the band edges, the optical path goes to infinity. This provides a way to enhance the optical responses at specific wavelengths. This effect can be exploited for instance, in magneto-optical materials (**Section 1.3.3**), being one of the aims of this thesis.

## 1.2.3 Optical characterization

Since our interest was mainly in 3D–PCs, direct and inverse opal-like structures, the discussions and examples below are referred to these structures.

Bragg diffraction of the visible light is the main feature of PBG materials and can be used for material characterization by testing order and cristallinity. Since the spheres in the opal are in the order of the wavelength, interference will lead to Bragg diffraction. By measuring the optical spectra (reflection and transmission), the positions of the Bragg peaks related to the PBG wavelength can be detected. **Figure 1.9** presents the structure of a polystyrene (PS) direct opal with the typical fcc compact arrangement of the spheres and the corresponding optical spectra measured for the outer (111) facet[27a, 30]. Due to the Bragg diffraction caused by (111) plane (**Figure 1.9b**) of the fcc lattice, the band structure will open a pseudo PBG (**Figure 1.9c**). The spectral position of this PBG can be clearly seen by the Bragg peak position, visible in both in reflection (R) and in transmission (T) (**Figure 1.9d, e**). When the opal is ideal (defect-free), the sum of R and T gives 1. The fabrication methods, however, may provide some defects within the structure producing scattering and the propagation becoming diffused. Consequently, the Bragg peak in the optical spectra broadens and R and T do not add up to $1^{[27a, 29b]}$.

The optical spectra do not only give information about the spectral position (wavelength) of the PBG but, also, permits to estimate the effective refractive index ($n_{eff}$) of the material. There are several formulas used to calculate $n_{eff}$ , namely: The *Bragg's law*, expressing the position of the maximum reflection peak [31] is:

$$\lambda_{max} = 2d_{hkl}\sqrt{n_{eff}^2 - \sin^2\theta} \qquad\qquad (Eq.1.5)$$

where $\lambda_{max}$ is the wavelength of the maximum stop band; $d_{hkl}$ is the interplane distance corresponding to the scattering lattice periodicity; $\theta$ is the angle of the incident light with the fcc lattice; and $n_{eff}$ is the average (effective) refractive index of the photonic material.
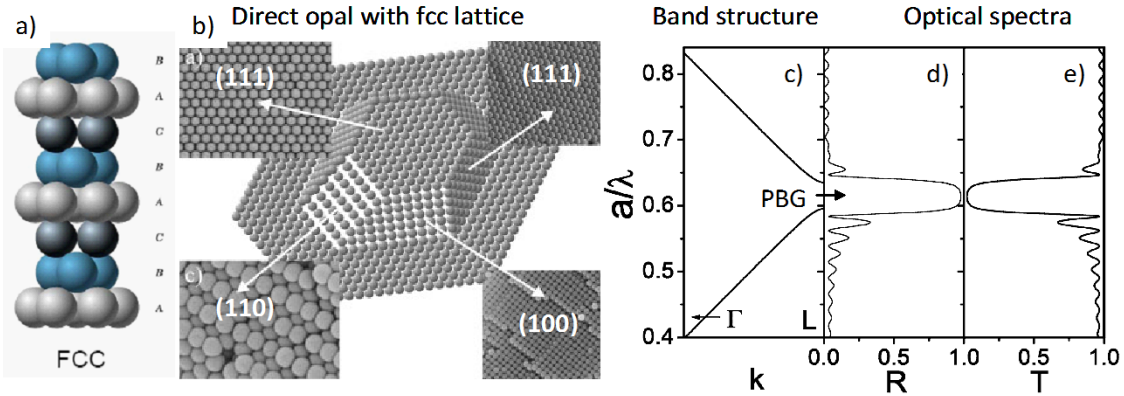


***Figure 1.9.*** *Photonic material characterization: (**a**) structure of the face-centered cubic lattice (ABCABC); (**b**) SEM images of the fcc lattice with facets (111), (110), and (100) belonging to fcc structure* [30]; *(**c**) band structure for the Bragg diffraction by (111) facets; (**d-e**) reflection and transmission spectra with the Bragg peak where the PBG was formed* [27a].

$n_{eff}$ can be determined according to Eq.1.6:

$$n_{eff}^2 = \sum n_i^2 f_i \qquad n_i = \sqrt{\varepsilon_i} \qquad (Eq.1.6)$$

where $n_i$ corresponds to the refractive index of component i in the photonic material and $\varepsilon_1$ is the dielectric constant of component i with the filling fraction $f_i^{ch}$. For a close-packed fcc structure made up from spheres of different materials, the value of $f$ is 0.74 (74%) while air occupies 26% of the volume.

The interplane distance ($d_{hkl}$) can be calculated by the next formula (Eq.1.7):

$$d_{hkl} = \frac{a}{\sqrt{h^2 + k^2 + l^2}} \qquad (Eq.1.7)$$

where a is the lattice parameter (in close-packed structures, a is determined directly by the sphere diameter ($\phi$) as a = $(2)^{1/2}$ $\phi$), (hkl) are the important planes in the fcc structure. For (111) plane, the interplane distance is calculated as (Eq.1.8):

$$h = k = l = 1 \rightarrow d_{111} = \frac{a}{\sqrt{3}} \qquad (Eq.1.8)$$

Since Bragg diffraction is caused by the (111) plane for an fcc arrangement, the average refractive index can be calculated at known values of diameters of the spheres composing the opal and the spectral position of the Bragg peak, according to Eq.1.9:

$$\lambda_{111} = 2d_{111}\sqrt{n_{eff}^2} = 2\sqrt{\frac{2}{3}}\phi n_{eff} = \left(\frac{8}{3}\right)^{\frac{1}{2}}\phi n_{eff} \qquad (Eq.1.9)$$

Eq. 1.6 is too simplistic to describe the optical properties of composite materials. In such case, a more precise way to determine the effective refractive index ($n_{eff}^2 = \varepsilon_{eff}$) is to use effective medium approximations, such as Maxwell-Garnett equation (eq. 1.10) and Bruggeman's symmetric effective medium theory [32] (eq. 1.11).

---

[h] *Filling fraction:* the volume fraction occupied by the dielectric material in the photonic structure.

*Maxwell-Garnett equation*
$$\frac{\varepsilon_{eff} - 1}{\varepsilon_{eff} + 2} = f_1 \frac{\varepsilon_1 - 1}{\varepsilon_1 + 2} + f_2 \frac{\varepsilon_2 - 1}{\varepsilon_2 + 2} \qquad \text{(Eq.1.10)}$$

*Bruggeman's symmetric effective medium theory:*
$$0 = f_1 \frac{\varepsilon_1 - \varepsilon_{eff}}{\varepsilon_1 + 2 \cdot \varepsilon_{eff}} + f_2 \frac{\varepsilon_2 - \varepsilon_{eff}}{\varepsilon_2 + 2 \cdot \varepsilon_{eff}} \qquad \text{(Eq.1.11)}$$

where $\varepsilon_{eff}$ is the average permittivity of the photonic material and $\varepsilon_1$ and $\varepsilon_2$ are the permittivity of each component in the system with the corresponding filling fractions $f_1$ anf $f_2$. Always the sum of $f_i$ is 1.

All the above equations are valid for a conventional photonic crystal material. When the photonic structure is functionalized, a third component is introduced in the initial binary system. In our case, the third component was the magnetic nanoparticles. These equations allowed us to calculate the effective refractive index of the magneto-photonic system and the filling fraction of the magnetic component. The results are discussed in **Chapter 4.2.3** , **4.4.3**.

## 1.2.4 Fabrication technologies and potential applications

Nanophotonics[33] is an emerging science and engineering of light-matter interaction at the nanometer/sub-wavelength scale. By exploiting the unique physical and chemical properties of the matter at the nanoscale, nanophotonics enables new photonic functionalities that can be converted into new products such as miniaturized devices with potential applications in telecommunications, sensing, lasers, optoelectronics chips, photonic integrated circuits, lighting, etc. Without the ambitious of being exhaustive this part briefly discusses the most relevant examples of 2D and 3D– PCs [24, 26a, 26c, 27b, 34].

Nowadays, the fabrication of 1D/2D-PCs has successfully been evolved by producing good quality photonic materials with long range structural order (essential for controlling the light propagation), at high volume and low cost by standard lithopgraphic technologies used in the electronic industry[26a, 35]. Due to these characteristics, they are of interest for potential applications in data storage and optical communications[23-24, 34b] **(Table 1.1)**. However, even higher materials performance can be achieved by using 3D-PCs (due to the full control of light wavevector in all directions) which would be more appropriate for future society needs. Up to date, the efficient micro-fabrication of 3D-PCs at large scale still presents a scientific challenge. So far, only a few fabrication technologies have been investigated **(Table 1.1)**.The main objective is to find an economic and rapid way to produce uniform and defect-free 3D nanostructures at large scale[35-36].

## 1.3 MAGNETO-PHOTONIC CRYSTAL MATERIALS

## 1.3.1 Tuning the optical properties of photonic materials

The functionalities of the opal like photonic crystals, fabricated by self-assembly method, can be enhanced if their optical properties can be tuned by an external stimulus[26a, 27b].

*Table 1.1 Summary of technologies used for 2D– and 3D–PCs fabrication and potential applications*

| PCs type | Fabrication technologies | Possible applications |
|---|---|---|
| 2D | Lithography: electron-beam (EBL), X-ray, focused-ion beam (FIB), nanoimprint (NIL), Self-assembly, Templating[26a, 34b] | micro-cavity lasers, efficient wave guides and cavities, optical fibers, superprism, supercollimators, sensors security labeling , paints, coatings [23-24, 34b, 34d, 37,38], etc. |
| 3D | Lithography: laser-guided, interferometric, holography, ion beam, self-assembly, Langmuir-Blodgett deposition, colloidal crystal templating[26a, 35, 39,27b, 36, 40]. | Optoelectronic devices: zero-treshold lasers, optical isolators, switching, low-loss waveguides, high-efficiency light-emitting diodes, photonic chips. Sensors (environmental remediation, health), solar cells, fuel cells, photovoltaic (energy conversion), storage[19, 27b, 34c, 39b, c, 41]. |

This can be achieved either by changing the lattice parameter of the structure or by an appropriate tuning of refractive index of the materials components. A summary of the external stimuli used in different approaches[26a, 27b] is presented in **Table 1.2.**

If the ambition is to manipulate the light by external controllable stimuli using new materials, one must look on reversibility, speed of tuning of optical properties and new functionalities. For this purpose, **"magneto-photonic crystal materials" (MPCs)** are very good candidates. They are photonic crystal materials functionalized with a magnetic component to respond to an external magnetic field. Their versatility lies not only in the control of path, direction, polarization and wavelength of light by external magnetic field but, also, in the remarkable magneto-optical properties accompanied by the enhancement of magneto-optical response near photonic band gap edge.

*Table 1.2 Summary of external stimuli used for tuning optical properties of photonic materials (reviews[26a, 28b])*

| External stimulus | Variation of refractive index of constitutive materials | Variation of lattice parameter of the structure |
|---|---|---|
| Light | *photo-tunable system:* -colloidal particles containing photoionizable or photopolymerizable molecules; -direct opal infiltrated with photochromic dye | - |
| Temperature | -direct and inverse opals filled with liquid crystals; -semiconductor core/shell colloidal particles self-assembled | *Volume phase transition:* -PS opal (direct or inverse) by annealing at different temperatures (around its $T_G$) |
| Stress/strain | - | -highly deformable polymeric opals (e.g. elastomers) |
| Electric field | - ferroelectric inverse opals (e.g. barium strontium titanate, lead lanthanum zirconate titanate) | -opal of $SiO_2$ beads filled with metalopolymer, immersed in electrochemical cell |
| Magnetic field | - opals filled with magneto-optical component by varying the strength of magnetic field | -rotation of ferromagnetic inverse opal placed in water; -self-assembly of a ferrofluid |

Since the aim of this thesis was to fabricate 3D magneto-photonic materials with enhanced magneto-optical response, the next sections are addressed to the brief presentation of employed fabrication techniques (especially for 3D), magneto-optical effect and possible applications of MPCs.

## 1.3.2 MPCs fabrication methods

The fabrication of 1D/2D–MPCs has been successfully realized in good-quality magneto-photonic materials with long range structural order (essential for controlling the light propagation). The fabrication of 3D–PCs, however, is quite challenging due to the requirements of defect-free and large area production. In the case of 3D-MPCs, it is even more difficult to go beyond the sate-of–the art. So far, a few methods have been used to produce 3D-MPCs with a defect-free structural order of hundreds of $\mu m^2$ in surface and up to 100 $\mu m$ in thickness[39a]. However, it is further demanded to both increase the area (i.e. for high quality materials) with ensuring a relatively high transmissivity of the magnetic content and reduce fabrication costs for making the future applications of magneto-photonic integrated devices feasible.

There are a few types of 3D–PCs which have been used for fabrication of 3D–MPCs: artificial direct opals, inverse opals and functionalized or core/shell colloidal crystals. The magnetic component can be introduced either by physical or chemical methods.

In *physical methods*[42] the voids of a direct opal (spheres of polystyrene, silica) are filled with the magnetic component, in the form of thin film e.g. by atomic layer deposition (ALD), sputtering, pulsed laser deposition, molecular beam epitaxy, electrodepositon, followed by the removal of the spheres. The result is a structure with air holes in a magnetic matrix. The main advantage of these methods is the precise control of infiltration degree, infiltration uniformity and desired magnetic composition. However, they are costly, time consuming and the magnetic component is in the film form and not monodispersed magnetic nanoparticles.

In *chemical methods*[42b, 43, 44], the voids of a direct/inverse opal (solid material), in most cases, are infiltrated either with liquid colloids of pre-synthesized magnetic nanoparticles (e.g. Ni, Co, iron oxide, manganese ferrite) or with solution of metallic precursors resulting in *in-situ* nanoparticles formation. Adding the magnetic component in the form of nanoparticles has the advantage that the nanoparticles present superparamagnetic behavior for certain sizes i.e., they ensure high response at low magnetic field and lack of remnant magnetization once the field is removed that are a requisite for optoelectronic devices. Additional, a better control over size, shape, polydispersity and subsequently magnetic properties of the nanoparticles can be achieved. Unfortunately, this method also has some drawbacks such as: a non-uniform infiltration within the structure; accumulation of nanoparticles on the surface causing diffuse light scattering, associated with the decrease of material transmissivity; damage of the structure during infiltration and further processing. These drawbacks, however, can be overcome by the judicious design and proper choice of the fabrication method, as it is presented in this thesis.

The alternatives to solid MPCs are the liquid MPCs produced by self-assembly in (aqueous or non–aqueous) solution of magnetic colloidal particles under the influence of an external magnetic field[36, 45,45a, 46]. The colloidal particles can be ferrofluids or core/shell particles where the magnetic core (e.g. clusters of small nanoparticles) is coated with a polymeric or silica shell. By a proper functionalization of the colloidal particles surface, the colloids self-assemble in a photonic structure under a magnetic field and, thus, the periodicity and optical properties can be tuned by varying the strength of the magnetic field.

Besides the advantages of reversibility and relatively fast tuning, liquid MPCs also present some drawbacks such as the liquid media (although this can be turned into advantage by fabricating response polymer composites, liquid displays or sensors) and the size of the colloid, being limited to maximum 200 nm and related to the control of the wavelength (closer to ultraviolet than to visible range). A summary of the different fabrication methodologies reported in the literature is presented in Table 1.3.

*Table 1.3 Fabrication methods for 1D, 2D and 3D–MPCs.*

| MPCs type | Magnetic material | Non-magnetic material | $\Phi_{sphere/hole}$ (nm) | Fabrication method | Ref. |
|---|---|---|---|---|---|
| 1D | Bi-YIG | SiO$_2$ | | RF magnetron→ annealing 700°C | R[42a] |
| | Bi-YIG | air | 200 | -Selective area epitaxy using a Al$_2$O$_3$ mask→ etching→ annealing→ pore structre | R[42a] |
| 2D | MnFe$_2$O$_4$ ferrofluid | SiO$_2$ | | -Kerosene base ferrofluid injected into a hexagonal shaped SiO$_2$ shell under a magnetic field | R[45e] |
| | Ni | air | 320, 457, 780 | -PS opal template→electrodepositing of Ni→ removing the template | R[42c] |
| 3D | Dysprosium nitrate/ iron porfyrin | SiO$_2$ | 250, 260 | -Infiltration of the voids of direct SiO$_2$ opal with glycerol solution of dysprosium nitrate or aqueous solution of iron porfyrin | R[43a, 43c] |
| | Bi-YIG, TGG, *TAG | SiO$_2$ | 300 | -Infiltration of the voids of direct SiO$_2$ opal with aqueous solution of metallic nitrate precursor → drying → annealing | R[42a] |
| | Fe$_3$O$_4$ / γ–Fe$_2$O$_3$NPs | SiO$_2$, PS | 134, 26o, 300, 680 | -Self-assembly of core/shell spherical/ellipsoids colloids (Fe$_3$O$_4$ /SiO$_2$) | R[45b, 46a, 46c] |
| | Fe$_3$O$_4$ NPs (20 nm), Co | SiO$_2$ | 290, 300, 545 | -Infiltration of the voids of direct SiO$_2$ opal with aqueous solution of metallic salts / nitrates precursor → heating →drying | R[43b, 43d-f] |
| | γ–Fe$_2$O$_3$ | SiO$_2$ | | -SiO2 direct / inverse opal infiltrated with aqueous solution of iron oxide NPs | R[44a, 46b] |
| | Iron oxide | PMMA | 183, 268, 413 | -PMMA direct opal infiltrated with ethylene glycol solution of metal nitrate precursor→ heating above T$_G$ | R[44b] |
| | Fe$_3$O$_4$ NPs (10 nm) | PS, SiO$_2$, polyelectrolite | 30–180 | -Polymer or silica capped superparamagnetic clusters, self assembled in aqueous, alkanol or non-polar solutions under a magnetic filed | R[45a, 45c, d, 45f, 46c, 47] |
| | Ni | PS, SiO$_2$ | 250, 460, 530 | -Direct opal template→electrodepositing of Ni→ removing the template | R[42d-g] |

Bi-YIG – bismuth substituted yttrium iron garnet; TGG–terbium gallium garnet; TAG–terbium aluminium garnet; T$_G$–glass transition temperature * –TGG has a very high Verdet constant and thus the Fraday rotation achieved is over 45°

## 1.3.3 Magneto-optical effects and applications

**General concept**

The magneto-optical phenomenon[48] refers to the interaction between light and matter in magnetized media. It was first discovered by Michael Faraday (1845) and reverend J. C. Kerr and the magneto-optical effects were then named after them as *Faraday Effect* (observed in transmission of light through a material) or *Kerr effect* (observed on reflection of light from a material).

      *The Faraday Effect or Faraday rotation.* The propagation of linearly polarized light in a magnetic material can be described in terms of its decomposition into two circularly polarized waves, one with left-hand (LCP) and the other with right-hand (RCP) polarization. These propagate at different speeds within the material (the indices of refraction of the right- and left- handed circularly polarized light become different when a material is magnetized). The waves, upon emergence from the magnetized material, re-combine but with a net phase offset due to the difference in propagation speed. Thus the plane of linearly polarized light is rotated with an angle. The direction of rotation is dependent on the direction of the magnetic field but not on the direction of light propagation. The rotation is thus non-reciprocal.

      The *magneto-optic Kerr effect* is similar to the Faraday effect, however it describes changes in polarization of light that is *reflected* from a magnetized material.

In region of absorption, the magnetic field can induce not only *differences in index of refraction* for plane polarized light in different directions (left and right) *correlated with magnetic optical rotation* (MOR ) or Faraday rotation, but also *differences in absorption* of left circularly polarized light (LCP) and right circularly polarized (RCP) light , which differences give rise *to elliptically polarized light[49]*. The difference in absorption (named dichroism) between LCP light and RCP light, induced in a sample by a strong magnetic field oriented parallel to the direction of light propagation can be measured by *magnetic circular dichroism (MCD) spectroscopy[49a]*

      The propagation in z-direction of the circularly polarized waves (left and right), can be defined by their electric vector (according to absorption theory within electric dipole approximation) (eq.1.12)[49b].

$$E_{\pm}(z,t) = E_0^0 \exp\left[i\omega\left(t - n_{\pm} \cdot z/c\right)\right] \qquad \text{(Eq.1.12)}$$
$$\omega = 2\pi\upsilon, \quad n_{\pm} = n - ik_{\pm}$$

where + and – denote the RCP and LCP light respectively; c is the speed of light, t is the time, z is direction of propagation, $n_{\pm}$ is the complex refractive index and $k_{\pm}$ –absorption coefficient. If the circularly polarized wave have the same absorption coefficient, then $k+ = k$ if they are different $k+ \neq k_{-}$ the media is dichroic. Thus in a dichroic media, the electric vector is elliptically polarized and traces out an ellipse, symbolized with $\Psi$ for a wave vector that travels a distance l along the z-direction[49a].

      The tangent of $\Psi$ being the ratio of minor axis to major axis of ellipse, it can be written as eq.1.13[49a]

$$\tan \Psi = \frac{\left(\left|E_-\right| - \left|E_+\right|\right)}{\left(\left|E_-\right| + \left|E_+\right|\right)} \approx \Delta k \cdot \pi \upsilon / c \qquad \text{(Eq.1.13)}$$

where $\Delta k = k_- - k_+$, defining the circular dichorism.

Based on this, MCD is the used method to study the magnetic optical activity. The difference between MCD and the commonly used spectroscopic techniques based on an applied magnetic field such as nuclear magnetic resonance (NMR) is that the former is rather based on the wavelength dependent absorption of circularly polarized light to form electronic exited states than the resonance between spin states.

In this thesis, the magneto-optical activity either of magnetic colloidal dispersion or magneto-photonic materials was measured by MCD homemade set-up (**Chapter 6.2. A.ii.9**). In our configuration the signal detected was proportional with the dichroic signal (eq.1.14)

$$\text{MCD signal} = \frac{\left(I_{RCP} - I_{LCP}\right)}{\left(I_{RCP} + I_{LCP}\right)} \qquad \text{(Eq.1.14)}$$

where $I_{RCP}$ and $I_{LCP}$ are the right– and left–circularly polarized light transmitted through the magnetic material, respectively

**Potential applications**

The optical isolators[50] (i. e. Faraday isolators) rely on the Faraday rotation principle (**Figure 1.10**) i.e. when a ray of light is passed through a magnetized material and then reflected back through it, the rotation doubles; therefore the optical isolators (passive magneto-optic devices) only allow the light to travel in one direction. They are useful tools in optical transmission, for instance, to protect the laser source from back-reflection that may cause damage to the source by amplitude fluctuation, frequency shift, instabilities etc.
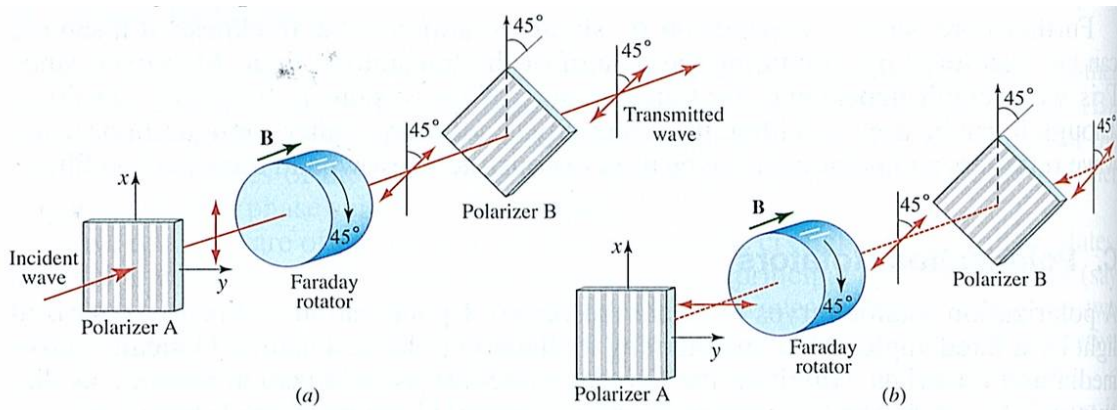


**Figure 1.10** *Schematization of an optical isolator device. (**a**) Forward mode – the propagation of light is parallel with the magnetic field. The light is linearly polarized by an input polarizer (A) and consequently passed through the Faraday rotator. At end, the plane of polarization is rotated clockwise by 45°. (**b**) Reverse mode – the light travels backwards through the isolator. It enters the output polarizer (B) which polarizes the light at 45° with respect to the input polarizer (A), then passes through the Faraday rotator rod while the plane of polarization is rotated another 45° clockwise. The net rotation is 90° with respect to the input polarizer (ref[48a]).*

Faraday rotators[50] in the market are made of terbium-gallium –garnet (TGG) single crystal, with dimensions (including the polarizers) of e.g. 60 mm of diameter x 120 mm of length [50b] Due to the very high Verdet constant of TGG, rotation angles over 45° can be achieved. These isolators, however, are still not small enough to be considered for the next generation of integrated magneto-optics devices. Three dimensional magnetophotonic crystals with an enhanced magneto-optical response can be suitable for the development of novel, fast and compact optical isolators[43a] by drastically reducing their thickness and optical losses. Other applications[34d, 41b, 51] to be taken into considerations are: high-speed sensors, future optical transistors, photonic chips, optical circulator, ultra-high speed spatial light modulator, optical computers, etc.

**Magneto-photonic effect in MPCs**

How does the photonic structure influence the magneto-optical effects? At the edges of PBG, the light is considerably slowed down (group velocity tends to zero). As a consequence, the time taken by the electromagnetic wave to traverse the sample (the optical path) is dramatically increased (tends to infinite) enhancing the light-matter interaction. When the photonic crystal contains a magnetic material, by applying a magnetic field and due to the slow light effect, the light interacts stronger with the magnetic material. This has a direct influence on magneto-optical response of the material, enhancing the magneto-optical Faraday and Kerr effects[51a, 52] (by it's directly dependence on optical path).

This enhancement at the edges of the photonic bandgap has been demonstrated experimentally by Inoue group[52b, c] in 1D-MPCs made of Bi-TYIG/$SiO_2$ multilayer films **(Figure 1.11a)**. Reports on the magneto-optical characterization of 3D–MPCs have revealed some features of the photonic crystal stop-band which have generally been interpreted as a moderate increase of the magneto-optical activity around those frequencies[42a, b, 43e, f, 44c] **(Figure 1.11b)**. On the contrary, as discussed in this Thesis (Chapter 4), a strong modification/ enhancement of magneto-optical effects near the photonic bandgap edge could be achieved[32b, 53]. by using two different 3D–MPCs fabrication strategies: (1) infiltration of $Al_2O_3$ inverse opal with *ex-situ* synthesized Ni NPs [15b] and (2) *in-situ* deposition of $MnFe_2O_4$ and iron oxide NPs on $Al_2O_3$ inverse opal and $SiO_2$ direct opal, respectively)[32b, 53].
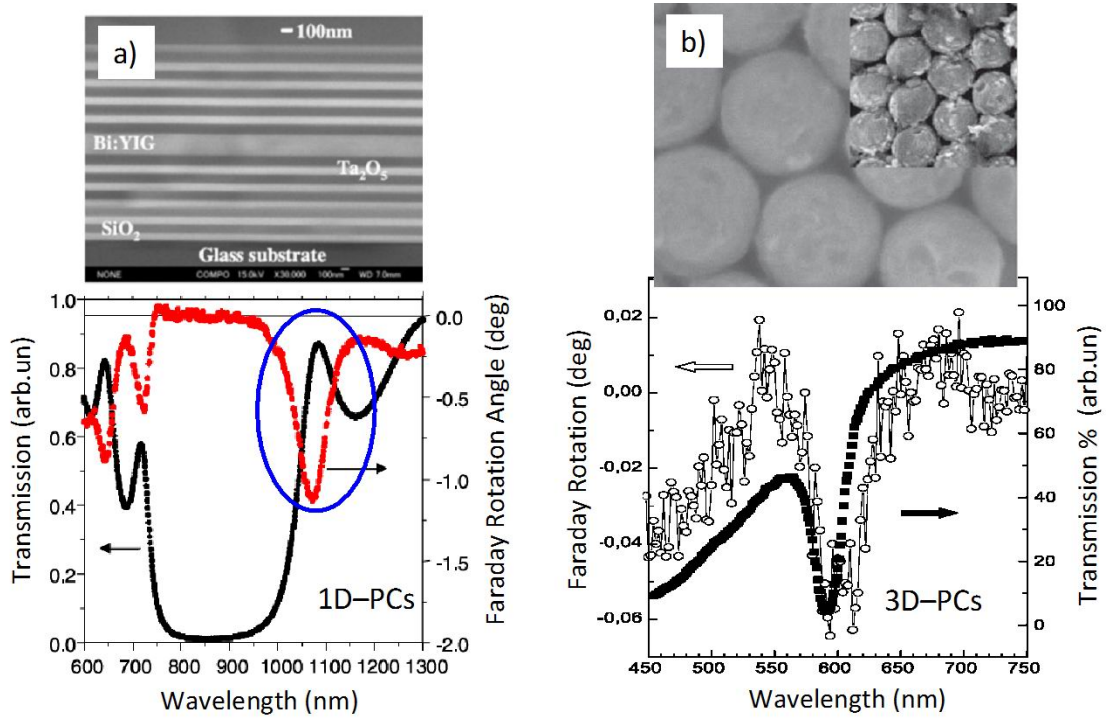
**Figure 1.11** *Optical (transmission) and magneto-optical (Faraday rotation angle) response of (**a**) one-dimensional* [52b, c] *and (**b**) three-dimensional* [42a, b] *. MPCs. The enhancement of magneto-optical effect is highlighted with blue color (**a**).*

## 1.4 REFERENCES

1.      (a) Inorganic Nanoparticles Synthesis, Applications and Perspectives. Altavilla, C.; Ciliberto, E., Eds. CRC Press Taylor & Francis Group: New York, 2011; p. 558; (b) Nanoparticles: From Theory to Applications. Schmid, G., Ed. WILEY-VCH Verlag GmbH & Co. KGaA: Weinheim, 2004; p. 422; (c) Kulisch, W.; Freudensten, R.; Ruiz, A.; Valsenia, A.; Sirghi, L.; Ponti, J.; Colpo, P.; Rossi, F., Nanostructured Materials for Advanced Technological Applications: A brief Introduction. In *Nanostructured Materials for Advanced Technological Applications*, Reithmaier, J. P., Ed. Springer Science + Business Media B.V: 2009; pp 1-34.

2.      Harper, T. *Global Funding of nanotechnology & its impact -Report*, Cientifica: London, 2011.

3.      (a) Altavilla, C., Magnetic Nanoparticles for Drug Delivery. In *Inorganic Nanoparticles Synthesis, Applications and Perspectives*, Altavilla, C., Ciliberto, E., Ed. CRC Press Taylor & Fracis Group: 2011; pp 313-343; (b) Frey, N. A.; Sun, S., Magnetic Nanoparticle for Information Storage Applications. In *Inorganic Nanoparticles Synthesis, Applications and Perspectives*, Altavilla, C.; Ciliberto, E., Eds. CRC Press Taylor & Francis Group: 2011; pp 33-69; (c) Pichot, C., Reactive Nanocolloids for Nanotechnologies and Microsystems. In *Colloidal Nanoparticles in Biotechnology,*, Elaissari, A., Ed. John Wiley & Sons, Inc: Hoboken, 2008.

4.      (a) Teja, A. S.; Koh, P.-Y., Synthesis, properties, and applications of magnetic iron oxide nanoparticles. *Progress in Crystal Growth and Characterization of Materials* **2009**, *55*, 22-45; (b) Xia, Y.; Xiong, Y.; Lim, B.; Skrabalak, S. E., Shape-Controlled Synthesis of Metal Nanocrystals: Simple Chemistry Meets Complex Physics? *Angewandte Chemie International Edition* **2009**, *48* (1), 60-103; (c) Kwon, S. G.; Hyeon, T., Colloidal Chemical Synthesis and Formation Kinetics of Uniformly Sized Nanocrystals of Metals, Oxides, and Chalcogenides. *Accounts of Chemical Research* **2008**, *41* (12), 1696-1709; (d) Lu, A.-H.; Salabas, E. L.; Schuth, F., Magnetic Nanoparticles: Synthesis, Protection, Functionalization, and Application. *Angewandte Chemie International Edition* **2007**, *46*, 1222 – 1244.

5.      Katz, E.; Shipway, A. N.; Willner, I., Biomaterial-Nanoparticle Hybrid Systems: Synthesis, Properties, and Applications. In *Nanoparticles: From Theory to Application.*, Schmid, G., Ed. WILEY-VCH Verlag GmbH & Co. KGaA: Weinheim, 2006; pp 368-421.

6.      (a) Talapin, D. V.; Shevchenko, E. V.; Weller, H., Synthesis and Characterization of Magnetic Nanoparticles. In *Nanoparticles: From Theory to Application*, Schmid, G., Ed. WILEY-VCH Verlag GmbH & Co. KGaA: Weinheim, 2004; pp 199-238; (b) Polshettiwar, V.; Luque, R.; Fihri, A.; Zhu, H.; Bouhrara, M.; Basset, J.-M., Magnetically Recoverable Nanocatalysts. *Chemical Reviews* **2011**, *111*, 3036–3075; (c) Ho, D.; Sun, X.; Sun, S., Monodisperse Magnetic Nanoparticles for Theranostic Applications. *Accounts of Chemical Research* **2011**, *44* (10), 875-882; (d) Guo, S.; Dong, S., Metal nanomaterial-based self-assembly: Development, electrochemical sensing and SERS applications. *Journal of Materials Chemistry* **2011**, *21* (42), 16704-16716.

7.      Koksharov, Y. A., Magnetism of Nanoparticles: Effects of Size, Shape, and Interactions. In *Magnetic Nanoparticles.*, Gubin, S. P., Ed. WILEY-VCH Verlag GmbH & Co.: Weinheim, 2009; pp 197-254.

8.      Krishnan, K. M.; Pakhomov, A. B.; Bao, Y.; Blomqvist, P.; Chun, Y. G., M.; Griffin, K.; Ji, X.; Roberts, B. K., Nanomagnetism and spin electronics: materials, microstructure and novel properties. *Journal of Materials Science* **2006,** *41,* 793–815.

9.      (a) Murray, C. B.; Sun, S.; Gaschler, W.; Doyle, H.; Betley, T. A.; Kagan, C. R., Colloidal synthesis of nanocrystals and nanocrystal superlattices. *IBM J. RES. & DEV.* **2001,** *45* (1), 47-56; (b) Gubin, S. P.; Koksharov, Y. A.; Khomutov, G. B.; Yurkov, G. Y., Magnetic nanoparticles: preparation, structure and properties. *Russian Chemical Reviews* **2005,** *74* (6), 489 - 520; (c) Kolesnichenko, V. L., Synthesis of Nanoparticulate Magnetic Materials. In *Magnetic Nanoparticles.*, Gubin, S. P., Ed. WILEY-VCH Verlag GmbH & Co.: Weinheim, 2009; pp 25-58; (d) Niederberger, M.; Pinna, N., Surfactant-assisted synthesis. In *Metal Oxide Nanoparticles in Organic Solvents—Synthesis Formation, Assembly and Application,* Niederberger, M., Ed. Springer: London, 2009; pp 19-52.

10.     Murray, C. B.; Kagan, C. R.; Bawendi, M. G., Synthesis and characterization of monodisperse nanocrystals and close-packed nanocrystal assemblies. *Annual Reviews of Matererials Science* **2000,** *30,* 545–610.

11.     Lamer, V. K., Dinegar, R. H., Theory, production and mechanism of formation of monodispersed hydrosol *Journal of American Chemical Society* **1950,** *72* (11), 4847-4854.

12.     Qu, H.; Caruntu, D.; Liu, H.; O'Connor, C. J., Water-Dispersible Iron Oxide Magnetic Nanoparticles with Versatile Surface Functionalities. *Langmuir* **2011,** *27* (6), 2271-2278.

13.     Niederberger, M.; Pinna, N., Aqueous and Nonaqueous Sol-Gel Chemistry Metal Oxide Nanoparticles in Organic Solvents. Springer London: 2009; pp 7-18.

14.     Taboada, E.; Solanas, R.; Rodríguez, E.; Weissleder, R.; Roig, A., Supercritical fluid assisted one-pot synthesis of biocompatible core($\gamma$-Fe$_2$O$_3$)@shell(SiO$_2$) nanoparticles as high relaxivity T$_2$-contrast agents for Magnetic Resonance Imaging. *Advanced Functional Materials* **2009,** *19* (14), 2319-2324

15.     Bilecka, I.; Niederberger, M., Microwave chemistry for inorganic nanomaterials synthesis. *Nanoscale* **2010,** *2,* 1358–1374.

16.     (a) Yin, S.; Luo, Z.; Xia, J.; Li, H., Microwave-assisted synthesis of Fe$_3$O$_4$ nanorods and nanowires in an ionic liquid. *Journal of Physics and Chemistry of Solids* **2010,** *71,* 1785-1788; (b) Kokorin, A., *Ionic Liquids: Theory, Properties, New Approaches.* InTech: Rijeka, 2011; p 748; (c) Polshettiwar, V.; Varma, R. S., Fundamentals of Aqueous Microwave Chemistry. In *Aqueous Microwave Assisted Chemistry: Synthesis and Catalysis,* Polshettiwar, V.; Varma, R. S., Eds. Royal Society of Chemistry: 2010; pp 1-9; (d) Hu, H.; Yang, H.; Huang, P.; Cui, D.; Peng, Y.; Zhang, J.; Lu, F.; Lian, J.; Shi, D., Unique role of ionic liquid in microwave-assisted synthesis of monodisperse magnetite nanoparticles. *Chemical Communications* **2010,** *46* (22), 3866-3868.

17.     Dahl, J. A.; Maddux, B. L. S.; Hutchison, J. E., Toward Greener Nanosynthesis. *Chemical Reviews* **2007,** *107,* 2228-2269.

18.     Tatsuno, K. *"Future Challenges in the Photonics Market"-Target at the Green Digital Economy-*; Optoelectronic Industry & Technology Development Association: Brussel, 2008; p 17.

19.        Kaierle, S. *PhotonicsResearch in Europe. The European Technology PlatformPhotonics21*; European Laser Institute ELI: Fraunhofer, 2011.

20.        Yablonovitch, E., Photonic Crystals semiconductors of light. *Scientific American* 2001, pp 47–55.

21.        Russell, P., Photonic Crystal Fibers. *Science* 2003, *299*, 358–362.

22.        Maier, S. A., *Plasmonics: Fundamentals and Applications.* Springer-Verlag: 2007.

23.        Lourtioz, J.-M., Photonic crystals and metamaterials. *Comptes Rendus Physique* 2008, *9*, 4–15.

24.        Viktorovich, P.; Drouard, E.; Garrigues, M.; Leclercq, J. L.; Letartre, X.; Romeo, P. R.; Seassal, C., Photonic crystals: basic concepts and devices. *Comptes Rendus Physique* 2007, *8*, 253–266.

25.        Parker, A. R., Natural photonics for industrial inspiration. *Philosophical Transactions of The Royal Society A: Mathematical Physical and Engineering Sciences* 2009, *367*, 1759–1782.

26.        (a) Kasap, S.; Capper, P., Nano-Engineered Tunable Photonic Crystals in the Near-IR and Visible Electromagnetic Spectrum: Materials for Optoelectronics and Photonics. In *Springer Handbook of Electronic and Photonic Materials*, Kasap, S.; Capper, P., Eds. 2006; Vol. Part D, pp 997–1020; (b) Busch, K.; von Freymann, G.; Linden, S.; Mingaleev, S. F.; Tkeshelashvili, L.; Weneger, M., Periodic nanostructures for photonics. *Physics Reports* 2007, *444*, 101–202; (c) Joannopoulos, J. D.; Villeneuve, P. R.; Fan, S., Photonic crystals: putting a new twist on light *Nature* 1997, *386* (13), 143–149.

27.        (a) Galisteo López, J. F. An Optical Study of Opals based photonic crystals. Universidad Autónoma de Madrid, Madrid, 2005; (b) Galisteo-López, J. F.; Ibisate, M.; Sapienza, R.; Froufe-Pérez, L. S.; Blanco, Á.; López, C., Self-Assembled Photonic Structures. *Advanced Materials* 2011, *23* (1), 30–69.

28.        Garcia Lopez, M. Self Assembled Photonic-Plasmonic Crystals for Light control at the Nanoscale. Santiago de Compostela, Madrid, 2011.

29.        (a) Lopez, C., Three-dimensional photonic bandgap materials: semiconductors for light. *JOURNAL OF OPTICS A: Pure and Applied Optics* 2006, *8*, R1–R14; (b) Galisteo-Lopez, J. F.; Garcia-Santamaria, F.; Golmayo, D.; Juarez, B. H.; Lopez, C.; Palacios-Lidon, E., Design of photonic bands for opal-based photonic crystals. *Photonics and Nanostructures – Fundamentals and Applications* 2004, *2*, 117–125.

30.        Lopez, C., Material Aspects of Photonic Crystals. *Advanced Materials* 2003, *15* (20), 1679–1704.

31.        (a) Lopez, C.; Vazquez, L.; Meseguer, F.; Mayoral, R.; Ocana, M.; Miguez, H., Photonic crystal made by close packing $SiO_2$ submicron spheres. *Superlattices and Microstructures* 1997, *22* (3), 399–405; (b) Chiappini, A.; Armellini, C.; Chiasera, A.; Ferrari, M.; Fortes, L.; Clara Gonçalves, M.; Guider, R.; Jestin, Y.; Retoux, R.; Nunzi Conti, G.; Pelli, S.; Righini, G. C., An alternative method to obtain direct opal photonic crystal structures. *Journal of Non-Crystalline Solids* 2009, *355*, 1167–1170; (c) Yamada, Y.; Ishii, M.; Nakamura, T.; Yano, K., Artificial black opal fabricated from nanoporous carbon

spheres. *Langmuir* **2010**, *26* (12), 10044-10049; (d) Ruhl, T.; Spahn, P.; Hellmann, G. P., Artificial opals prepared by melt compression. *Polymer* **2003**, *44*, 7625–7634.

32.  (a) Doyle, W. T., Electrical and optical properties of dense composites. *Journal of Applied Physics* **1999**, *85* (4), 2323-2329; (b) Caicedo Roque, J. M.; Pascu, O.; López-García, M. n.; Canalejas, V. c.; Blanco, A. l.; López, C.; Fontcuberta, J.; Roig, A.; Herranz, G., Magnetophotonic Response of Three-Dimensional Opals. *ACS Nano* **2011**, *5* (4), 2957-2963.

33.  Ghoshal, S. K.; Sahar, M. R.; Rohani, M. S.; Sharma, S., Nanophotonics for 21st Century. In *Optoelectronics- devices and applications*, Tredeep, P., Ed. InTech: 2011; pp 576-630.

34.  (a) Joannopoulos, J. D.; Johnson, S. G.; Winn, J. N.; Meade, R. D., *Photonic crystals: molding the flow of light*. Princeton University Press: Singapour, 2008; (b) Wang, X.; Wang, Z. L., Photonic Crystals and Devices. In *Scanning Microscopy for Nanotechnology*, Wang, Z. L.; Weilie, Z., Eds. Springer: New York, 2006; pp 281-305; (c) Boldov, I.; Orlova, N.; Kargapolova, I.; Kuchyanov, A.; Shelkovnikov, V.; Plekhanov, A., Optical Sensors Based on Opal Film and Silica Nanoparticles Modified with a Functional Dye. In *Advances in Chemical Sensors*, Wang, W., Ed. InTech: 2012; pp 29-46; (d) Passaro, V. M. N.; Troia, B.; La Notte, M.; De Leonardis, F., Chemical Sensors Based on Photonic Structures. In *Advances in Chemical Sensors*, Wang, W., Ed. InTech: 2012; pp 89-120.

35.  Xu, D.; Chen, K. P.; Ohlinger, K.; Lin, Y., Holographic Fabrication of Three-Dimensional Woodpile-type Photonic crystal Tempates using Phase Mask Techniques. In *Recent Optical and Photonic Technologies*, Kim, K. Y., Ed. InTech: 2010; pp 71-88.

36.  Stein, A.; Li, F.; Denny, N. R., Morphological Control in Colloidal Crystal Templating of Inverse Opals, Hierarchical Structures, and Shaped Particles. *Chemistry of Materials* **2008**, *20*, 649–666.

37.  (a) Kwon, S.-H.; Sünner, T.; Kamp, M.; Forchel, A., Optimization of photonic crystal cavity for chemical sensing. *Optics Express* **2008**, *16* (16), 11709-11717; (b) Makarova, M.; Vuckovic, J.; Sanda, H.; Nishi, Y., Silicon-based photonic crystal nanocavity light emitters. *Applied Physics Letters* **2006**, *89*, 221101-3.

38.  (a) Zhu, L.; Chak, P.; Poon, J. K. S.; DeRose, G. A.; Yariv, A.; Scherer, A., Electrically-pumped, broad-area,single-mode photonic crystal lasers. *Optics Express* **2007**, *15* (10), 5966-5975; (b) Kolle, M.; Salgard-Cunha, P. M.; Scherer, M. R. J.; Huang, F.; Vukusic, P.; Mahajan, S.; Baumberg, J. J.; Steiner, U., Mimicking the colourful wing scale structure of the Papilio blumei butterfly. *Nature Nanotechnology* **2010**, *DOI: 10.1038/NNANO.2010.101*, 1-5.

39.  (a) Lee, J. A.; Ha, S. T.; Choi, H. K.; Shin, D. O.; Kim, S. O.; Im, S. H.; Park, O. O., Novel Fabrication of 2D and 3D Inverted Opals and their Application. *Small* **2011**, *7* (18), 2581–2586; (b) Raub, A. K.; Bruek, R. J., Large area three-dimensional phootonic crystals with embeded waveguides. *Journal of Vacuum Science & Technology B Microelectronics and Nanometer Structures* **2010**, *28* (6), C6O38-C6O44; (c) Nelson, E. C.; Dias, N. L.; Bassett, K. P.; Dunham, S. N.; Verma, V.; Miyake, M.; Wiltzius, P.; Rogers, J. A.; Coleman, J. J.; Li, X.; Braun, P. V., Epitaxial growth of three-dimensionally architectured optoelectronic devices. *Nature Materials* **2011**, *DOI: 10.1038/NMAT3071*, 1-6.

40.  (a) Zhang, Y.; Wang, J.; Huang, Y.; Song, Y.; Jiang, L., Fabrication of functional colloidal photonic crystals based on well-designed latex particles. *Journal of Materials Chemistry* **2011**, *21*,

14113-14126; (b) Oh, J. R.; Moon, J. H.; Yoon, S.; Park, C. R.; Do, Y. R., Fabrication of wafer-scale polystyrene photonic crystal multilayers via the layer-by-layer scooping transfer technique. *Journal of Materials Chemistry* **2011,** *21,* 14167–14172.

41.      (a) Quan, F., Green Photonics. *Journal of Optics A: Pure and Applied Optics* **2012,** *14,* 024001-4; (b) Light Propagation Controlled in Photonic Chips: Major Breakthrough in Telecommunications          Field.          *Science          Daily*          2011,          p http://www.sciencedaily.com/releases/2011/07/110710132825.htm.

42.      (a) Inoue, M.; Uchida, H.; Nishimura, K.; Lim, P. B., Magnetophotonic crystals – a novel magneto-optic material with artificial periodic structures. *Journal of Materials Chemistry* **2006,** *16,* 678-684; (b) Inoue, M.; et al., Magnetophotonic crystals. *Journal of Physics D: Applied Physics* **2006,** *39* (8), R151; (c) Torrado, J. F.; Gonzalez-Diaz, J. B.; Armelles, G.; Garcia-Martin, A.; Altube, A.; Lopez-Garcia, M.; Galisteo-Lopez, J. F.; Blanco, A.; Lopez, C., Tunable magneto-photonic response of nickel nanostructures. *Applied Physics Letters* **2011,** *99,* 193109-193111; (d) Napolskii, K.; Sapoletova, N.; Eliseev, A.; Tsirlina, G.; Rubacheva, A.; Gan'shina, E.; Kuznetsov, M.; Ivanov, M.; Valdner, V.; Mishina, E.; van Etteger, A.; Rasing, T., Magnetophotonic properties of inverse magnetic metal opals. *Journal of Magnetism and Magnetic Materials* **2009,** *321,* 833-835; (e) Sapoletova, N.; Makarevich, T.; Napolskii, K.; Mishina, E.; Eliseev, A.; van Etteger, A.; Rasing, T.; Tsirlina, G., Controlled growth of metallic inverse opals by electrodeposition. *Physical Chemistry Chemical Physics* **2010,** *12* (47), 15414-15422; (f) Pardavi-Horvath, M.; Makeeva, G. S.; Golovanov, O. A., Interactions of Electromagnetic Waves With 3-D Opal-Based Magnetophotonic Crystals at Microwave Frequencies. *IEEE Transactions on Magnetics* **2011,** *47* (2), 341-244; (g) Yu, X.; Lee, Y. J.; Furstenberg, R.; White, J. O.; Braun, P. V., Filling Fraction Dependent Properties of Inverse Opal Metallic Photonic Crystals. *Advanced Materials* **2007,** *19* (13), 1689-1692.

43.      (a) Koerdt, C.; Rikken, G. L. J. A.; Petrov, E. P., Faraday effect of photonic crystals. *Applied Physics Letters* **2003,** *82* (10), 1538-1540; (b) Kodama, T.; Nishimura, K.; Baryshev, A. V.; Uchida, H.; Inoue, M., Opal photonic crystals impregnated with magnetite. *Physical State Solide* **2004,** *241* (7), 1597–1600; (c) Sabataitytea, J.; Simkienea, I.; Rezaa, A.; Babonasa, G.-J.; Vaisnorasb, R.; Rastenieneb, L.; Kurdyukovc, D.; Golubevc, V., Studies of opal crystals infiltrated with iron porphyrin. *Superlattices and Microstructures* **2008,** *44,* 664–669; (d) Grudinkin, S. A.; Kaplan, S. F.; Kartenko, N. F.; Kurdyukov, D. A.; Golubev, V. G., Opal-Hematite and Opal-Magnetite Films: Lateral Infiltration, Thermodynamically Driven Synthesis, Photonic Crystal Properties. *The Journal of Physical Chemistry C* **2008,** *112* (46), 17855-17861; (e) Pavlov, V. V.; Usachev, P. A.; Pisarev, R. V.; Kurdyukov, D. A.; Kaplan, S. F.; Kimel, A. V.; Kirilyuk, A.; Rasing, T., Optical study of three-dimensional magnetic photonic crystals opal/Fe3O4. *Journal of Magnetism and Magnetic Materials* **2009,** *321* (7), 840-842; (f) Šimkiene, I.; Reza, A.; Kindurys, A.; Bukauskas, V.; Babonas, J.; Szymczak, R.; Aleshkevych, P.; Franckevičius, M.; Vaišnoras, R., Magnetooptics of opal crystals modified by cobalt nanoparticles. *Lithuanian Journal of Physics* **2010,** *50* (1), 7-15; (g) Inoue, M.; Fujikawa, R.; Baryshev, A.; Khanikaev, A.; Lim, P. B.; Uchida, H.; Aktsipetrov, O.; Fedyanin, A.; Murzina, T.; Granovsky, A., Magnetophotonic crystals. *Journal of Physics D: Applied Physics* **2006,** *39* (8), R151.

44.      (a) Caicedo, J. M.; Taboada, E.; Hrabovský, D.; López-García, M.; Herranz, G.; Roig, A.; Blanco, A.; López, C.; Fontcuberta, J., Facile route to magnetophotonic crystals by infiltration of 3D inverse opals with magnetic nanoparticles. *Journal of Magnetism and Magnetic Materials* **2010,** *322* (9-12), 1494-1496; (b) Sadakane, M.; Horiuchi, T.; Kato, N.; Takahashi, C.; Ueda, W., Facile Preparation of

Three-Dimensionally Ordered Macroporous Alumina, Iron Oxide, Chromium Oxide, Manganese Oxide, and Their Mixed-Metal Oxides with High Porosity. *Chemistry of Materials* **2007**, *19*, 5779-5785; (c) Pavlov, V. V.; Usachev, P. A.; Pisarev, R. V.; Kurdyukov, D. A.; Kaplan, S. F.; Kimel, A. V.; Kirilyuk, A.; Rasing, T., Enhancement of optical and magneto-optical effects in three-dimensional opal/$Fe_3O_4$ magnetic photonic crystals. *Applied Physics Letters* **2008**, *93* (7), 072502-3.

45.      (a) Ge, J.; He, L.; Goebl, J.; Yin, Y., Assembly of Magnetically Tunable Photonic Crystals in Nonpolar Solvents. *Journal of the American Chemical Society* **2009**, *131* (10), 3484-3486; (b) Ding, T.; Song, K.; Clays, K.; Tung, C.-H., Fabrication of 3D Photonic Crystals of Ellipsoids: Convective Self-Assembly in Magnetic Field. *Advanced Materials* **2009**, *21*, 1936–1940; (c) Ge, J.; Yin, Y., Magnetically Tunable Colloidal Photonic Structures in Alkanol Solutions. *Advanced Materials* **2008**, *20*, 3485–3491; (d) Ge, J.; Hu, Y.; Yin, Y., Highly Tunable Superparamagnetic Colloidal Photonic Crystals. *Angewandte Chemie International Edition* **2007**, *46*, 7428 −7431; (e) Yang, S. Y.; Hornga, H. E.; Shiaoa, Y. T.; Hongb, C.-Y.; Yangc, H. C., Photonic-crystal resonant effect using self-assembly ordered structures in magnetic fluid films under external magnetic fields. *Journal of Magnetism and Magnetic Materials* **2006**, *307*, 43-47; (f) Xu, X.; Friedman, G.; Humfeld, K. D.; Majetich, S. A.; Asher, S. A., Synthesis and Utilization of Monodisperse Superparamagnetic Colloidal Particles for Magnetically Controllable Photonic Crystals. *Chemistry of Materials* **2002**, *14*, 1249-1256.

46.      (a) Fang, M.; Volotinen, T. T.; Kulkarni, S. K.; Belova, L.; Rao, K. V., Effect of embedding $Fe_3O_4$ nanoparticles in silica spheres on the optical transmission properties of three-dimensional magnetic photonic crystals. *Journal of Applied Physics* **2010**, *108* (10), 103501; (b) Libaersa, W.; Kolaric, B.; Vallée, R. A. L.; Wongd, J. E.; Woutersa, J.; Valeva, V. K.; Verbiest, T.; Clays, K., Engineering colloidal photonic crystals with magnetic functionalities. *Colloids and Surfaces A: Physicochemical and Engineering Aspects* **2009**, *339*, 13-19; (c) Xu, X.; Friedman, G.; Humfeld, K. D.; Majetich, S. A.; Asher, S. A., Synthesis and Utilization of Monodisperse Superparamagnetic Colloidal Particles for Magnetically Controllable Photonic Crystals. *Chemistry of Materials* **2001**, *14* (3), 1249-1256.

47.      Ge, J.; He, L.; Goebl, J.; Yin, Y., Assembly of Magnetically Tunable Photonic Crystals in Nonpolar Solvents. *Journal of American Chemical Society* **2009**, *131* (10), 3484-3486.

48.      (a) Saleh, B. E. A.; Teich, M. C., *Fundamanetals of photonics*. Wiley Interscience 2007; p 1177; (b) Pustelny, S. Nonlinear magneto-optical effects. Jagiellonian University, Krak¶ow, 2007.

49.      (a) Mason, M. R., *A Practical Guide to Magnetic Circular Dichroism Spectroscopy*. John Wiley & Sons, INC. Publication: Hoboken (New Jersey), 2007; p 218; (b) Stephens, P. J., Magnetic Circular Dichroism. *Annual Review of Physical Chemistry* **1974**, *25* (1), 201-232.

50.      (a) www.thorlabs.com, Free-Space Optical isolators; (b) http://www.leysop.com/faraday.htm, Faraday Optical Isolators.

51.      (a) Inoue, M.; Baryshev, A. V.; Khanikaev, A. B.; Dokukin, M. E.; Chung, K.; Heo, J.; Takagi, H.; Uchida, H.; Lim, P. B.; Kim, J., Magnetophotonic materials and their applications. *IEICE TRANS. ELECTRON.* **2008**, *E91-C* (10), 1630-1638; (b) Dissanayake, N.; Levy, M.; Chakravarty, A.; Heiden, P. A.; Chen, N.; Fratello, V. J., Magneto-photonic crystal optical sensors with sensitive covers. *Appllied Physics Letters* **2011**, *99*, 091112-3.

52.     (a) Lyubchanskii, I. L.; Dadoenkova, N. N.; Lyubchanskii, M. I.; Shapovalov, E. A.; Rasing, T., Magnetic photonic crystals. *Journal of Physics D: Applied Physics* **2003,** *36*, R277–R287; (b) Fedyanin, A. A.; Aktsipetrov, O. A.; Kobayashi, D.; Nishimura, K.; Uchida, H.; Inoue, M., Enhanced Faraday and nonlinear magneto-optical Kerr effects in magnetophotonic crystals. *Journal of Magnetism and Magnetic Materials* **2004,** *282*, 256-259; (c) Zhdanov, A. G.; Fedyanin, A. A.; Aktsipetrov, O. A.; Kobayashi, D.; Uchida, H.; Inoue, M., Enhancment of Faraday rotation at photonic-band-gap edge in garnet-based mangetophotonic crystals. *Journal of Magnetism and Magnetic Materials* **2006,** *300*, e253-e256.

53.     Pascu, O.; Caicedo, J. M.; López-García, M.; Canalejas, V.; Blanco, A.; López, C.; Fontcuberta, J.; Roig, A.; Herranz, G., Ultrathin conformal coating for complex magneto-photonic structures. *Nanoscale* **2011,** *3*, 4811-4816.

# EXPERIMENTS, RESULTS AND DISCUSSIONS

*"De nu o simţi te strǎduieşti degeaba,*
*De un pui suflet n-o sǎ meargǎ treaba"*


*(''Unless you feel, nought will you ever gain;*
*unless this feeling pours forth from your soul*
*with native pleasing vigour to control*
*the hearts of all your hearers, it will be in vain'')*
*Goethe –FAUST*

# 2

# MAGNETIC NANOPARTICLES

## Preamble of chapter 2

Since we aimed at fabricating magnetic nanoparticles as monodispersed colloids, being used further for functionalization of two or three dimensional photonic-crystal materials the control over their size, polydispersity and appropriate magnetic properties such as high saturation magnetization, high magnetic susceptibility and superparamagnetic behavior at room temperature were desirable. Both *ex-situ* syntheses of the nanoparticles with control over their size and polydispersity and *in-situ* deposition of nanoparticles over the photonic materials were the criteria when choosing the most suitable chemical synthetic pathways. In addition, due to the fragility of the photonic material, the approaches causing no damage in the structure of the photonic materials, requiring no post-synthesis material processing were preferable.

Taking into account these requirements, three synthetic pathways were used for the synthesis of metallic and metal oxides magnetic nanoparticles:

**1) Thermal decomposition** reactions of metal complexes carried out in high-boiling-point organic solvents and the in presence of surfactants produced excellent quality nanoparticles with small sizes, narrow particle size distributions and high cristallinity. This method is suitable for the production of metallic and metal oxide nanoparticles with the resulting material having long time stability in organic solvents. In the case of magnetic colloids, two different applications can be highlighted, namely, biomedical applications (e.g., contrast agents MRI, magnetic hyperthermia therapies, guided drug delivery)[1] and the fabrication of novel magneto-photonic colloidal crystals[2], the latter being of our interest. Thermal decomposition, however, has some associated drawbacks such as it requires working under an inert atmosphere, high reaction temperature and rather long processing times (3-4 hours). These shortcomings result in high energy and time consumption and in a low amount of material produced (in each batch, typically in the order of 100 mg). In this study, the stable hexane dispersion of **Ni nanoparticles** produced by this method is used for the infiltration of photonic crystals (inverse opals) giving an enhancement of magneto-optical response of the magneto-photonic material (see **Chapter 4.2**).

**2) Microwave-assisted chemistry** is getting very attractive in all areas of synthetic chemistry because it can boost some competitive advantages over other fabrication methods. It is fast, it produces high yields, it is easy to operate and efficient in terms of energy consumption and environmentally friendly. By this method, **ferrite (MnFe$_2$O$_4$, FeFe$_2$O$_4$) magnetic nanoparticles** with good crystillinity, small size, good polydispersity and comparable magnetic properties to the ones obtained by the thermal decomposition method can be prepared. In addition to the stabilization of nanoparticles in organic solvents, they can be easily dispersable in water without a laborious ligand exchange step. Microwave heating has been used not only for organic[3] and inorganic[4] nanoparticles synthesis but also for the fabrication of high quality nanocrystals and large scale defect-free complex nanostructures with controllable morphologies and surfaces[5]. Other intricate nanoarchitectures, such as nanoporous materials[6] and superstructures[5] have also been reported. Moreover, this route allowed us in-situ deposition of **manganese ferrite and iron oxide nanoparticles** over photonic crystal materials[7], resulting in a very good quality material with enhanced magneto-photonic properties (**Chapters 3.4 and 4.4**).

**3) Continuous supercritical fluids synthesis** because its properties such as mass-transfer (diffusivity and viscosity) similar to those of gases, density and solvation capabilities more similar to liquids and zero surface tension, represents an excellent reaction media. Due to the reaction at high temperature and high pressure, the overall synthesis rate is very large offering thus good conditions for nanoparticles[8] or more complex nanomaterials fabrication[9]. In addition, if the interest is in an eco-friendly scalable technology that employs inexpensive, harmless chemicals and solvents, then the supercritical fluids seems to be the perfect choice.

# 2.1 METHODOLOGY

## 2.1.1. Synthesis methods: experimental set-up and methodology

### 1. Thermal decomposition-Ni nanoparticles

**Chemicals:** The following reagents were used in the chemical synthesis without any further purification: nickel(II) acetylacetonate (Ni(acac)$_2$, 95% Aldrich), oleylamine (tech.gr., 70%, Aldrich), trioctylphosphine (TOP, tech.gr., 90%, Aldrich), oleic acid (reagent gr., 99% (GC), Sigma-Aldrich), n-hexane anhydrous (95%, Sigma-Aldrich), ethanol absolute (Panreac).

**Nickel nanoparticles (Ni NPs) synthesis:** Nickel nanoparticles were synthesized by high-temperature organo-metallic decomposition route. It is a heat-up method[10] involving a slow heat-up of the reaction mixture (organo-metallic precursor with surfactants and the solvent) from room to high temperature. Then the reaction is held at the aging temperature for a specific time (minutes or hours) before cooling down to room temperature. A short description of the experimental set-up is shown in **Figure 2.1**. As for the heating source, oil bath for the first heating step with magnetic stirring (1a) and a heating mantle for the second heating step without stirring (1b) were used. The chemical reaction took place in a two-neck round-bottom flask of 20 mL (7) connected through a condenser (6) to the vacuum (4) and inert gas –argon (3) lines, assuring an air-free reaction environment.

An adapted procedure from those reported by Chen *et al.*[11] and Murray *et al.*[10a] was used. In a typical synthesis (considered as A type), 1 mmol (0.257 g) of Ni(acac)$_2$ was added to 7ml oleylamine, 2 mmol (0.63 ml) oleic acid (OAc) and 1 mmol (0.45 ml) trioctylphosphine (TOP). The mixture was magnetically stirred at room temperature for a few minutes. During the mixing, five cycles of argon/vacuum pumping and flushing were applied to assure an inert atmosphere. Afterwards, the system was heated up to 130°C under a flow of high purity argon and magnetically stirred. During the heating, the mixture changed its color from blue turquoise (specific for dissolved Ni precursor) to very clear green (decomposed precursor). The mixture was kept at 130°C for 20 minutes, followed by further heating up to reflux point (250°C) and maintained at this temperature for additional 30 minutes. When the reaction mixture was slowly heated up, the color of the solution was slowly changing from green to dark green and finally to black. When the heating rate was higher (12°C/min), the color change (from green to black) was almost instantaneous. After cooling the solution to room temperature, the nanoparticles were precipitated by adding extra ethanol, followed by two-times centrifugation. The precipitate was dried in an oven (at 70°C) overnight, redispersed in an organic non-polar solvent (hexane) and finally kept in hexane as a concentrated dispersion that was used for further characterizations.

Thermal decomposition synthesis set-up
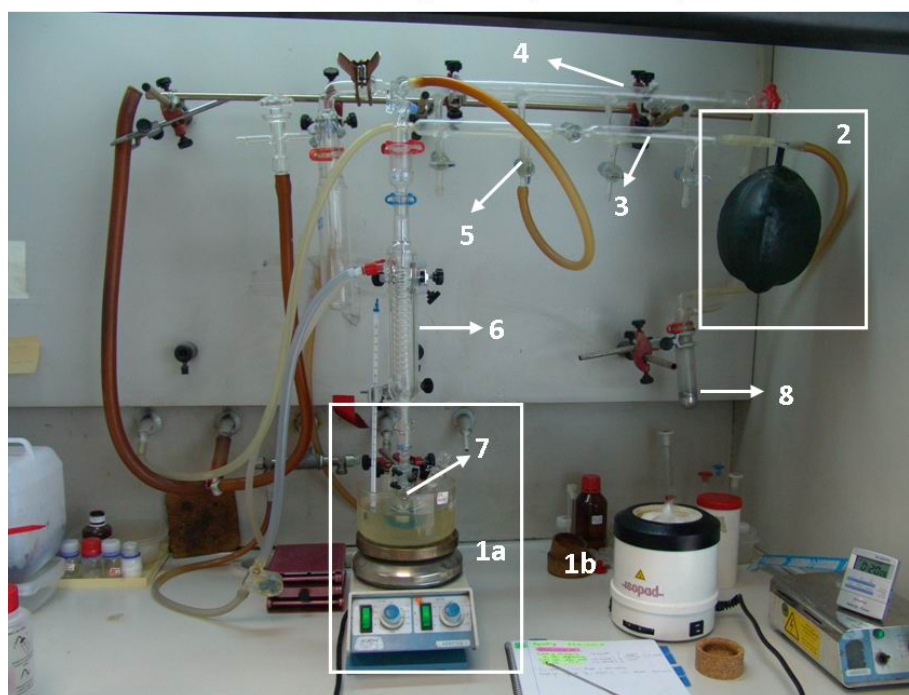


1. Heating source: a) oil bath for first step heating ($T_1$ = 130°C)
   b) heating mantle for second step heating ($T_2$ = 250°C).
2. Argon reservoir.
3. Argon line.
4. Vacuum line.
5. Vacuum/ argon valve.
6. Condenser with water refrigeration.
7. Reaction round-bottom flask.
8. Hg bubbler

**Figure 2.1.** *Our laboratory experimental set-up used for the synthesis of nickel nanoparticles (ICMAB-lab number 3.20)*

## 2. Microwave-assisted sol-gel chemistry – Ferrite (MnFe$_2$O$_4$, FeFe$_2$O$_4$) NPs

**Chemicals.** The following chemicals were purchased from Sigma-Aldrich and were used without any purification: iron(III) acetylacetonate (Fe(acac)$_3$, 97 %), iron(II) acetylacetonate (Fe(acac)$_2$), oleic acid (OAc) (analytical standard), oleylamine (OAm) (technical grade, 70 %), manganese(II)acetate tetrahydrated (Mn(ac)$_2$.x4H$_2$O, 99%), benzyl alcohol, hexane (anhydrous, 95 %), ethanol, trimethyl ammonium hydroxide (TMAOH, 25wt. % water solution), dodecyl trimethyl ammonium bromide (DTAB), sodium citrate and deionised water.

**Microwave-assisted chemistry**[4c, 12]. Microwave heating is based on the ability of some compounds to absorb electromagnetic energy and to transform it into heat. While a domestic microwave has a multimode cavity producing a non-homogeneous heating, the one for chemical synthesis is specially designed for a single mode resulting in uniform heating of the cavity. Compared to other conventional heating methods (e.g., heating plates, oil bath),

microwave radiation affects only the solvent and reactants, passing through the reaction vessel without heating it and avoiding temperature gradients. Thus by internal heating, the temperature is increased in the whole volume simultaneously and uniformly. Besides drastically decreasing the required time for the synthesis, the technique offers a combination of kinetics and selectivity characteristics and shows several advantageous features. The most important are (i) the acceleration of the chemical reaction rate; (ii) heating selectivity (e.g., polar substances absorb electromagnetic radiation and are intensively heated while the non-polar ones do not absorb); and (iii) greater movement of the molecules, higher diffusivity and collision probability due to the induced molecular vibration and the subsequent temperature increase, facilitating the conformal deposition onto intricate frames.

**Experimental set-up.** The microwave experiments were carried out in a CEM Discover reactor (Explorer 12-Hybrid) (**Figure 2.2**) operated at a frequency of 2.45 GHz (corresponding to a wavelength of 12.25 cm) and at a power of 200/300 W. For a typical run the parameters that can be controlled are the reaction temperature ($T_{set}$), the time at the constant $T_{set}$ ($t_{set}$) and the maximum power input (200 or 300 W) used for the heating step. The microwave reactor was connected to a computer that regulated the temperature during the chemical reaction (monitored by a volume-independent infrared sensor) by adjusting the power intput (**Figure 2.2-lower panel**). One of the limitations of single-mode apparatus is that only one vessel can be irradiated at a time. However, considering 30 minutes as the maximum employed time per batch, 8 experiments (8 batches) in microwave route could be run in 4 h (being the time necessary to produce a single batch of material using the thermal decomposition). After completion of the reaction, the mixture was rapidly cooled (up to 3 minutes) by compressed $N_2$ (being a built-in cooling feature of the apparatus). Another advantage of such reactor lies in its automatic sampling by an automatic arm (**Figure 2.2**) making the apparatus more user-friendly and safe.

***Synthesis of (MFe₂O₄; M = Mn, Fe) nanoparticles.*** For this synthesis, a non-aqueous sol-gel chemical reaction, similar to the one reported by Niederberger et al.[13], was followed. The most relevant difference in our case was the use of surfactants (steric OAc or electrostatic DTAB and/or TMAOH) as stabilizers, either during or after the synthesis, in order to assure monodispersity and long-term stability of the NPs.

*1) Manganese ferrite nanoparticles (MnFe₂O₄ NPs).* Briefly, in a typical reaction 0.15 mmol of $Fe(acac)_3$, 0.075 mmol of $Mn(ac)_2$ and oleic acid (0.45 mmol) were dissolved in anhydrous benzyl alcohol (1.5 ml) at 60°C ($T_1$) for 5 minutes in the microwave reactor under magnetic stirring for complete dissolution of the precursors. The mixture has a transparent dark-red colour. The mixture solution was further heated in the same microwave reactor to 160°C ($T_{set}$) and the temperature was kept stable for 5 min ($t_{set}$). Then, the solution was automatically cooled down to 50°C by compressed $N_2$ in approximately 3 min. The final suspension was black. The nanoparticles were separated by adding ethanol (40 ml), followed by centrifugation at 4000 rpm during 20 min. The supernatant from this first centrifugation was discharged and the precipitate, dispersed in 2 ml hexane with 10 μl oleic acid was centrifuged again at 4000 rpm during 20 min. No precipitate was separated but instead all the nanoparticles remained in the clear dark brown solution forming a colloidal dispersion.
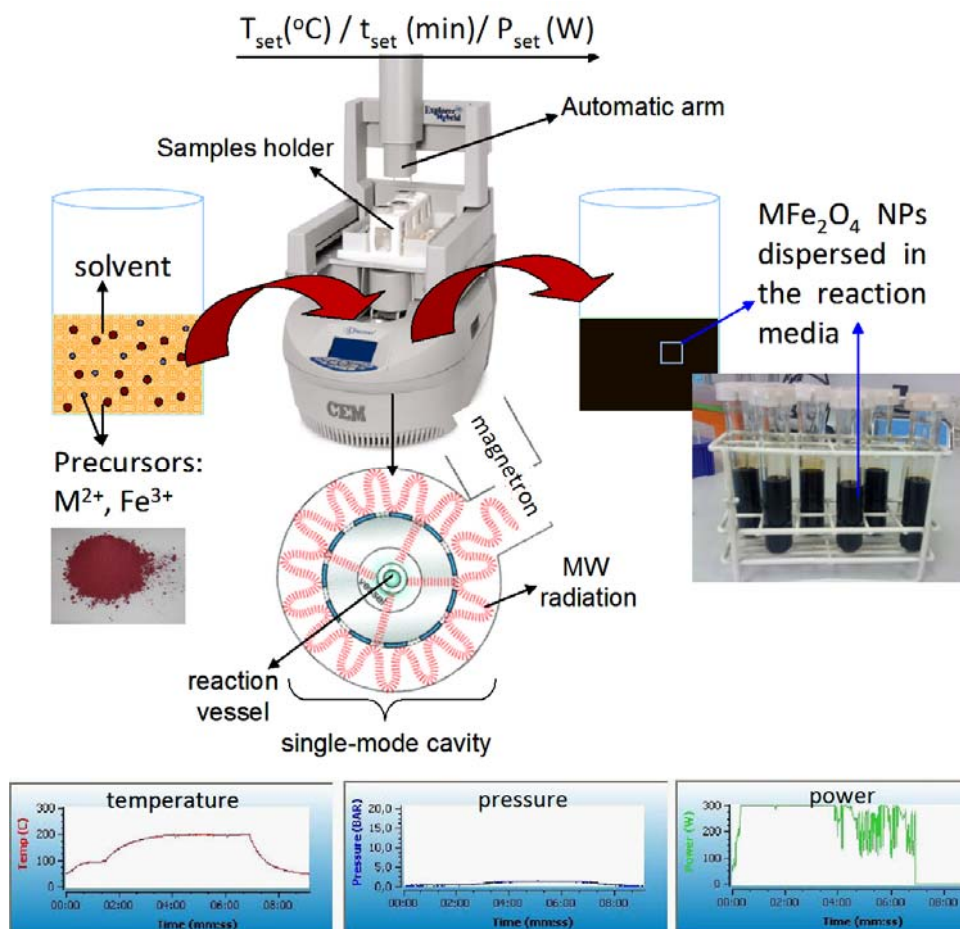
**Figure 2.2.** *Laboratory microwave reactor setup used for the synthesis of ferrite nanoparticles (ICMAB-Nanostructuration platform, Lab 4).*

The nanoparticles were labelled as *A_MW.MnFe$_2$O$_4$_x* and used for further analysis, where x indicates the different batches following the same procedure. A different batch of MnFe$_2$O$_4$ NPs was prepared using the same synthesis procedure but without adding oleic acid in the initial mixture. To separate the nanoparticles, almost the same protocol was applied. 40 ml ethanol containing 15 μl of oleic acid was added to the final black suspension and centrifuged at 4000 rpm during 20 min. The supernatant was discharged and the precipitate was re-dispersed in 2 ml hexane containing 10 μl of oleic acid and then centrifuged at 4000 rpm during 20 min. Because no precipitate was separated, the clear dark brown solution, labelled *B_MW.MnFe$_2$O$_4$_x,* was used for further analysis.

*2) Iron oxide nanoparticles (γ-Fe$_2$O$_3$/FeFe$_2$O$_4$).* Similar synthesis procedure to the one for MnFe$_2$O$_4$ was used. Nanoparticles labelled as *C_MW.iron oxide_x* were obtained by mixing 0.23 mmol of Fe(acac)$_3$, 0.12 mmol Fe(acac)$_2$ and 0.69 mmol oleic acid with 4.5 ml benzyl alcohol. A different batch was prepared using the same iron (III,II) precursors but without the presence of oleic acid in the synthesis. The latter was added at the end of reaction in a similar way as for the sample B_MW_X and labelled as *E_MW.iron oxide_x-organic.* To study the influence of the iron precursor as well as to compare with the thermal decomposition method, other batches were prepared using only iron(III) precursor, namely

Fe(acac)$_3$. Nanoparticles labelled as *D_MW.iron oxide_x* were obtained by mixing Fe(acac)$_3$ (0.35 mmol) and oleic acid (1.05 mmol) dissolved in 4.5 ml anhydrous benzyl alcohol. For all three batches, the same synthetic parameters and separation procedure as in case of MnFe$_2$O$_4$ synthesis were applied. For the batch *D_MW.iron oxide_6.2* using 123.6 mg of Fe precursor, 22 mg of iron oxide nanoparticles were obtained giving a mass reaction yield of 79 %. Another batch, labelled as *E_MW.iron oxide_X-water* was prepared using Fe(acac)$_3$ (0.35 mmol) dissolved in 4.5 ml anhydrous benzyl alcohol but without adding oleic acid in the initial mixture. Instead, at the separation step, 20 μl of TMAOH together with 40 ml of acetone were added and centrifuged at 6000 rpm for 20 min. The supernatant was discharged and the magnetic precipitate, after drying the sample overnight in an oven at 70°C, was re-dispersed in 2 ml distillate water containing 10 μl of TMAOH. The as-prepared dispersion had a pH = 11 that was adjusted to 7 by nitric acid.

Additionally, a study was done to compare iron oxide nanoparticles produced by the microwave heating method and by thermal decomposition using both the same stabilizers and precursor concentration.

## 3. Continuous supercritical ethanol synthesis –Ferrite (MnFe$_2$O$_4$, FeFe$_2$O$_4$) NPs

**Chemicals.** The following chemicals were purchased from Sigma–Aldrich and were used without any purification: iron(III) acetylacetonate (Fe(acac)$_3$, 97%), manganese(II) acetate tetrahydrated (Mn(ac)$_2$·4H$_2$O, 99%), oleic acid (OAc) (analytical standard), oleylamine (OAm) (technical grade, 70%), ethanol absolute.

**Continuous supercritical ethanol synthesis (cscEtOH)** is a chemical approach based on the thermolysis method. The metal–organic precursor is thermally decomposed in the supercritical fluids inducing high supersaturation with monomers and subsequently resulting in nanoparticle formation[9c, 14]. For the synthesis of ferrite (MnFe$_2$O$_4$, Fe$_3$O$_4$) nanoparticles, the cscEtOH used by us was a new approach whereas the procedure was partially adapted from wet-chemical synthesis[15] (thermal decomposition method for the synthesis of ferrite nanoparticles) and supercrtitical methanol synthesis[8b]. For the preparation of iron oxide nanoparticles, we used iron nitrate precursor (Fe(NO$_3$)$_3$) and surfactants OAc and OAm in the molar ratios of 1:3:3, all dissolved in ethanol solvent (synthesis *A_cscEtOH.Fe$_3$O$_4$*). In a **second approach,** we changed the iron precursor for iron acetylacetonate (Fe(acac)$_3$) while keeping both surfactants at the same molar ratios (synthesis *B_cscEtOH.Fe$_3$O$_4$*). For the synthesis of MnFe$_2$O$_4$, similar procedures were used with the addition of Mn(ac)$_2$ precursor in a molar ratio 1:2 to iron precursor (synthesis *A_cscEtOh.MnFe$_2$O$_4$ and B_cscEtOH.MnFe$_2$O$_4$*).

**Experimental set-up.** The chemical reaction was carried out in a continuous reactor (**Figure 2.3**). In the laboratory setup, high-pressure pumps (HPP) (200 bar) inject the solvents with the precursor(s) and surfactant(s) at room temperature and at same flow rates (Q$_1$) into the T-type mixture point and sequentially the mixture into the reactor. The chemical reaction took place in the tubular reactor made of stainless steel (with length and inner diameter of 1 m and 0.8 mm, respectively) and immersed into a silicone oil bath at 260°C. The inlet flow rate (Q$_2$) was chosen to ensure a residence time of 90 s. The pressure in the reactor (200 bar)

was controlled by a back-pressure regulator (BPR). The formed nanoparticles were recovered in liquid form through the exit tube of the reactor at room temperature where the reaction stopped.

*1) Synthesis of iron oxide nanoparticles (Fe₃O₄).* In a typical reaction, $Fe^{3+}$ precursor was dissolved in 100 ml ethanol at a concentration of $2x10^{-2}$ M and was introduced into the high-pressure pump (HPP-1). In parallel, HPP-2 was filled with ethanol (150 ml) containing the surfactants OAc and Oam, each at a concentration of $6x10^{-2}$ M ($Fe^{3+}$:OAc:OAm of 1:3:3). The two solutions, each at a flow rate of 450 μl /min, met in the mixing point at room temperature. The mixture was pumped through the heated reactor at 900 μl /min. When the outlet solution was dark, with a black precipitate responding to a magnet, the magnetic nanoparticles were formed. The nanoparticles were then separated by adding extra ethanol (in 3x dilution) followed by centrifugation at 6500 rpm for 30 min. The supernatant was discharged and the precipitate was dried overnight and subsequently redispersed in hexane containing 10 μl oleic acid. The prepared materials (*A_cscEtOH.Fe₃O₄_x* and *B_cscEtOH.Fe₃O₄_x* for $Fe(NO_3)_3$ and $Fe(acac)_3$ precursors, respectively) were studied by further characterization (**Section 2.4**).

*2) Synthesis of manganese ferrite nanoparticles (MnFe₂O₄).* Similar procedure to the one for $Fe_3O_4$ synthesis was used except that the precursor solution ($2.1 \times 10^{-2}$ M) consisted of .$Mn(ac)_2$ and $Fe(NO_3)_3/Fe(acac)_3$ (*A_cscEtOh.MnFe₂O₄_x* / *B_cscEtOH.MnFe₂O₄_x*). The separation procedure was the same as above.

## 2.1.2 Characterization techniques

Several characterization methods were used to study the properties of the nanoparticles:

*Structure and morphology (shape/size)* – by X-ray diffraction (**XRD**), selected area diffraction patterns (**SADP**), transmission electron microscope (**TEM and CryoTEM**) and high resolution TEM images (**HRTEM**). The mean diameter and polydispersity of each system were determined by adjusting a particle size histogram of over 200-300 counts (measured from TEM images using the imageJ© software) to a Gaussian distribution.

*Surface chemistry and stability (in solvents/in time)* – different techniques were used in order to understand the chemical properties of nanoparticles surfaces. First, the presence of some functional groups, covalently bonded to the nanoparticles surface was detected by infrared spectroscopy (AT-IR). Secondly, the amount of the organic compounds that form the nanoparticles protective shell was determined by thermogravimetric analysis (**TGA**), which gives the weight percentage of surfactants on the nanoparticles surface. And finally, dynamic light scattering (**DLS**) was used to investigate the hydrodynamic size (which embraces the metal core together with the surfactant shell and a layer of solvent close to the particle) of nanoparticles suspended in liquid media and also can be used as a complementary technique to TEM.
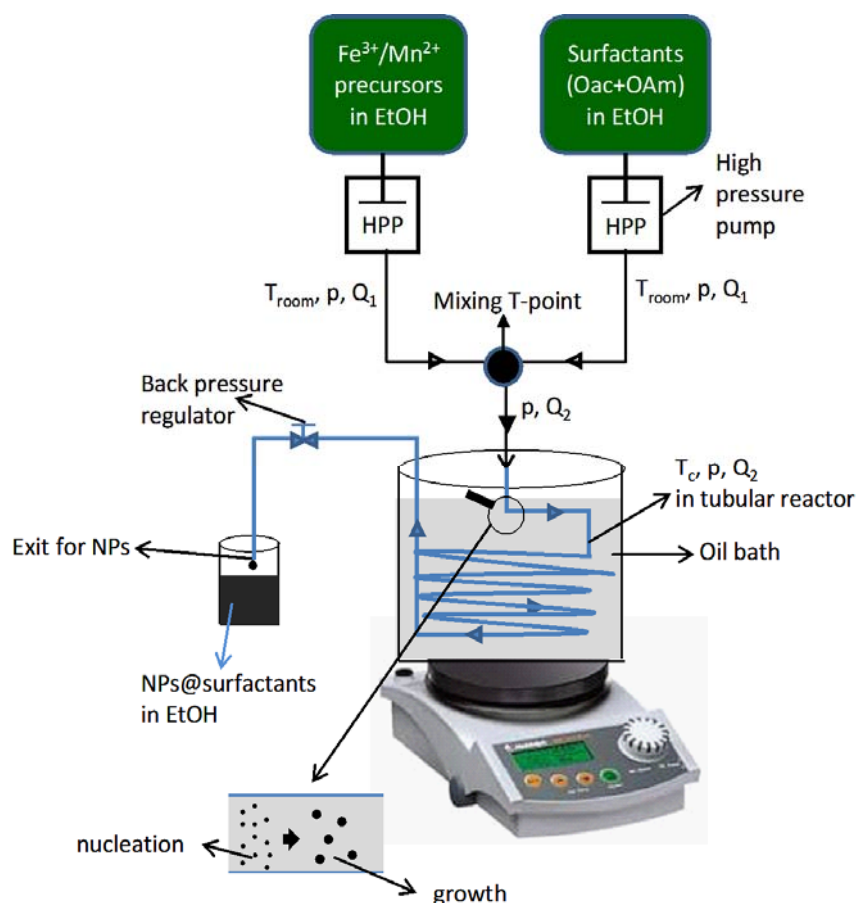
**Figure 2.3.** *Laboratory cscEtOH setup for ferrites nanoparticles synthesis (ICMCB-CNRS, Lab.).*

In order to have an idea about the size of the nanoparticles, it is not necessary to perform TEM analysis for each experiment and DLS measurements can be done instead. DLS was also used to monitor the long-term stability of nanoparticles dispersion (the particle aggregation after a few months could be monitored by both the shift of peak maximum and peak width).

*Magnetic and magneto-optical behavior* – by superconductive quantum interference device (**SQUID**) magnetometer giving information about magnetization vs. magnetic field (M(H)) at room (300K) and low (5K) temperatures and magnetization vs. temperature at zero field cooled (ZFC) and field cooled (FC). The magnetic properties of nanoparticles were also explored by probing their magneto-optical responsiveness at wavelengths in the visible spectra (400–800 nm). For that purpose, we measured their magneto-optical properties using magnetic circular dichroism (**MCD**) spectroscopy.

A brief description of each technique with their sample preparation procedures can be found in **Chapter 6.2.A.ii.**

## 2.2 THERMAL DECOMPOSITION–NICKEL (Ni) NPs

### 2.2.1. Synthesis and size control

**Nanoparticles formation mechanism**

Nickel nanoparticles were synthesized by thermal decomposition, as described above (**section 2.1.1.1**). In this method[10, 16], the relevant parameters playing a role in nanoparticle syntheses are the temperature, heating rate, aging time, quantity and the type of selected surfactant. By changing one of these parameters, the size, and in some cases the shape of nanoparticles can be tuned. The surfactant (ligand) does not only control the size and shape of nanoparticles but also stabilizes the colloids in solvents and prevents the metal surface from further oxidation. Kinetic studies for this method, reported by Hyeon group[10b], revealed a three-step mechanism for the synthesis of nanocrystals with size control:

1.  As metal precursors thermally decompose, monomers accumulate in the solution while nucleation is retarded due to the high chemical potential of nucleus. In our procedure (see **Figure 2.4**), this step coincides with the first heating step (20 min at $T_1$ of 130°C) and it is confirmed by color change from blue turquoise to green.
2.  Below the aging temperature ($T_2$, 250°C), the solution is supersaturated with monomers. At around 240°C (in our experiments), the nucleation energy barrier is overcome and burst nucleation occurs rapidly (color change from green to black); a few monomers form one crystal particle (nucleus) and its concentration suddenly increases with the decrease of monomer supersaturation level. At this point, the smaller and unstable nuclei dissolve and only the large nuclei survive in solution being capable to withstand the decrease of supersaturation.
3.  At the end of the second phase, the nucleation stops because of the consumption of monomers and the third phase begins. This takes place during the aging time (in our case 30 minutes at 250°C). In the beginning, the supersaturation level is still high enough to support the crystal particle growth by continued diffusion-controlled growth[a]: the larger particles grow slower than the smaller ones. If there is no additional nucleation during diffusion-controlled growth, size focusing with mean size increasing occurs. When no monomers are left, the smaller particles may dissolve and the released monomers may precipitate on the larger particles (Ostwald ripening). In this case, the larger particles grow faster (counteracting the focusing effect) and size distribution broadening occurs.

The bottleneck of the thermal decomposition process can be considered the phases 2 and 3 in which the heating rate is very important. The faster the heating rate, the more dominant the particles focusing effect. Moreover, while a kinetically controlled process produces spherical nanoparticles, a slow reaction would lead to a thermodynamic process and thus, to faceted and bigger particles, being the outer planes the ones with the lowest surface energy[17].

---

[a] The crystal can lose its monomers in solution (dissolution) or can grow by receiving the extra monomers from solution (precipitation).
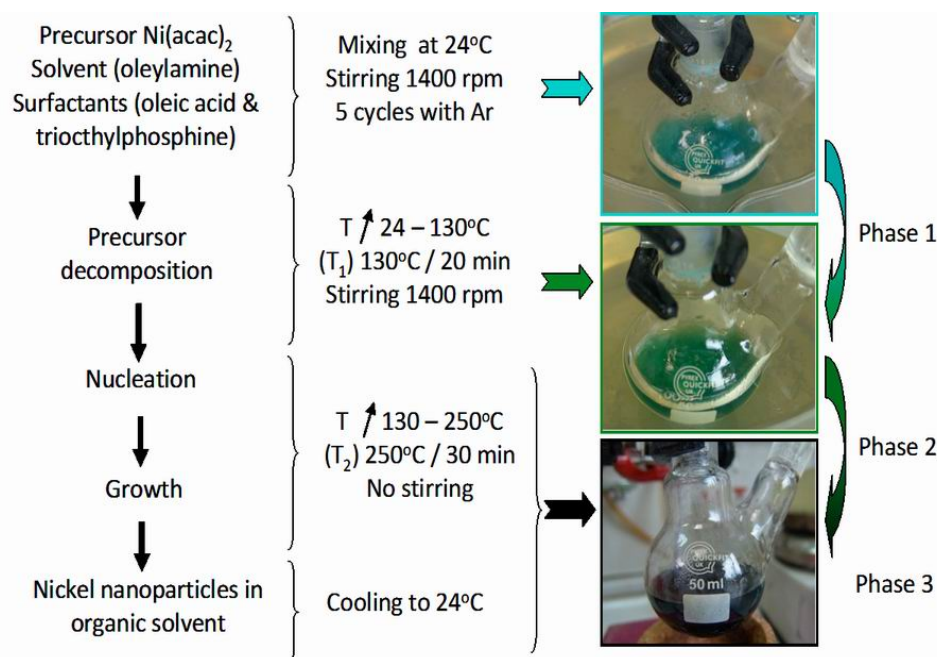
***Figure 2.4.*** *Experimental procedure for the synthesis of nickel nanoparticles.*

It is obvious that for high quality material production (small, spherical nanoparticles in the superparamagnetic domain), several experimental details have to be taken into account. First, a supersaturated solution with monomers is desirable, i.e., the nuclei formation should be as high as possible once the energy barrier is overcome. This could be obtained by a proper choice of temperature ($T_1$) and time (see below). On the other hand, other important issues are the heating rate and temperature ($T_2$) stability (related with phases 2 and 3 of the synthesis mechanism). At a high heating rate, the fast color change from green to black assures uniform nanoparticles production. As for the temperature stability, a small deviation of $T_2$ ($\pm 10°C$) during the aging time can broaden the polydispersity and should be avoided.

It is worth to emphasize some aspects related to the reduction mechanism of metallic nickel formation. This mechanism is not clearly understood, but a possible explanation supported by earlier reports[10b, 18] is the following (**Figure 2.5**): by mixing metallic acetylacetonate precursor with an alkyl amine as solvent in the presence of surfactants (TOP and OAc), an intermediary complex of Ni–oleylamine is first formed, due to the binding affinity of the amine with the metal surface. The solvent oleyalmine does not only facilitate the precursor decomposition by the cleavage of the acetylacetonate ligand by $CO_2$ removal, but also acts as a reducing agent[10b, 18c, 19]. On the other hand, the presence of surfactants is necessary to provide enough stabilization effects on the control of particle growth, since oleylamine is not able to do it. TOP with its phosphorous-terminated group coordinates reversibly with the Ni surface sites[10a] inhibiting the particle growth. At the same time, OAc is able to bind covalently to the surface with the carboxylate group ($-COO^-$) and the stability of the monomers–oleic acid complexes increases and consequently the nucleation is hindered, resulting in a lower number of nuclei and therefore a lower number of particles, but larger in size. Consequently, a competition between two surfactants appears. The control of this competition with its effects will be discussed in the section–surfactant influence.
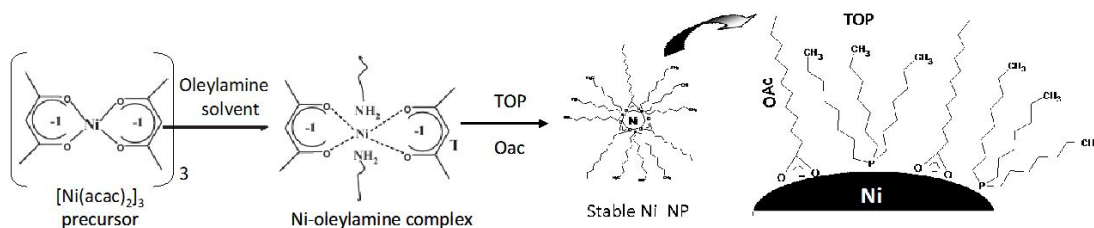
*Figure 2.5. Reduction mechanism for metallic Ni nanoparticles formation.*

## Experimental conditions

Because our interest was in Ni nanoparticles to be used for the fabrication of magneto-photonic materials, our goal was to produce nanoparticles with the following characteristics: spherical shape, small size (in the range of 6 – 17 nm), superparamagnetic behavior at room temperature, with high magnetic susceptibility and high saturation magnetization. Thus different experimental parameters such as the reaction temperature and surfactant amount were varied to study their influence on the final particle size and size distribution and to find the optimal experimental parameters for the production of the targeted nanoparticles. **In Table 2.1**, experimental data with different reaction parameters for nickel nanoparticles synthesis are shown. Synthesis *A_TD.Ni_x* was considered as the standard one, being adapted from the work of Chen et al.[11]. This reaction was made in the presence of the surfactants as discussed earlier **(Section 2.1.1.1)**. In the absence of surfactants, the synthesis was labeled as synthesis *B_TD.Ni_x*. By changing the temperature of the heating steps, synthesis *C_TD.Ni_x* was obtained. Finally, by playing with the molar ratio between the two surfactants, synthesis *D_TD.Ni_x* was performed. The nickel nanoparticles were labeled according to the synthesis type, where x is the batch number in each synthesis. A detailed description of each experiment is presented in Annex iii **(Chapter 6.3. Table A.iii.1)**

*Table 2.1. Experimental conditions corresponding to different synthesis types of Ni NPs.*

| Synthesis | Reaction parameters | | | |
| --- | --- | --- | --- | --- |
| | Temperature | | Molar ratio | Molar ratio of |
| | $T_1$ (°C) | $T_2$ (°C) | Ni(acac)$_2$ : surfactants | surfactants Oac : TOP |
| *A_TD.Ni_x ( x : 1–4, 14)* | 130 | 250 | 1 : 3 | 2 : 1 |
| *B_TD.Ni_x( x : 5–6)* | 130 | 250 | 1 : 0 | 0 : 0 |
| *C_TD.Ni_x ( x : 7–9, 15)* | 130 | 215 | 1 : 3 | 2 : 1 |
| | 170 | 215 | | |
| | 170 | 250 | | |
| *D_TD.Ni_x ( x : 11–13, 16)* | 130 | 250 | 1 : 3 | 3 : 0 |
| | | | | 0 : 3 |
| | | | | 1 : 2 |
| | | | | 1.5 : 1.5 |

## Structural analysis

Before discussing the influence of reaction parameters (temperature and surfactant), it was necessary to analyze the nanoparticles crystalline phase and size. As it was expected, X-ray diffraction (XRD) patterns **(Figure 2.6)** of the colloids exhibit the four characteristic peaks

corresponding to the fcc nickel lattice planes (111), (200), (220) and (311). No presence of peaks for crystalline nickel oxide or the metastable Ni hcp phase could be detected when nanoparticles were synthesized in the presence of surfactants (**Figure 2.6a, c, d**). In the synthesis with no surfactants (*B_TD.Ni_6*), neither hcp Ni or oxides peaks on the nanoparticles surface were observed, but some additional sharp peaks were detected which could be attributed to possible contamination during sample preparation (**Figure 2.6b**). In the literature, for the same reaction (*B_TD.Ni_6*), a phase transition of Ni from fcc to metastable hcp phase was reported for different temperatures such as of 240–260°C[11, 20] or above 280°C[21]. The lattice parameter values calculated from Maud refinement (**Table 2.2**) were found very close to the lattice constants of of bulk fcc nickel (3.53)[21]. It can thus be concluded that our material was pure nickel for all the synthesis procedures. From the width of the XRD reflection peaks we calculate the average crystalline size ($<\Phi>_{XRD}$) using the Scherer equation (**Chapter 6.2.A.ii.1**). These values are listed in **Table 2.2**. Large crystalline domains give sharp reflection peaks (**pattern b on Figure 2.6**), while a decrease in $<\Phi>_{XRD}$ results in a broadening of the reflection peaks (**patterns a, c and d on Figure 2.6**).
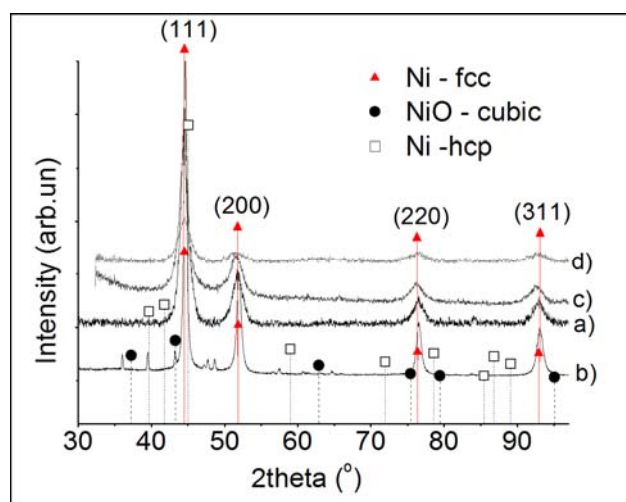


*Figure 2.6*. Comparison of XRD patterns of the Ni nanoparticles synthesized by different synthesis: *(a)* A_TD.Ni_4, *(b)* B_TD.Ni_6, *(c)* C_TD.Ni_9 and *(d)* D_TD.Ni_16, with the bulk phases of fcc Ni, hcp Ni and cubic NiO.

Because we were interested in using these nanoparticles for the infiltration of photonic crystals, we chose two different sizes of Ni nanoparticles (8 and 15 nm) for a more detailed characterization. To check the stability of Ni nanoparticles against their oxidation in time, an XRD analysis for these two systems was carried out 10 months after their synthesis. During this period, the nanoparticles were stored in hexane. As it can be clearly seen in **Figure 2.7**, no NiO has been detected by XRD.Nevertheless, from the magnetic data and using a core–shell model[22], we identified a self–limiting nonmagnetic shell of around 1 nm (see Section 2.2.3). Once it was certified that our material had the desired phase (fcc nickel) a subsequent analysis was done to check the influence of reaction temperature on the material quality.
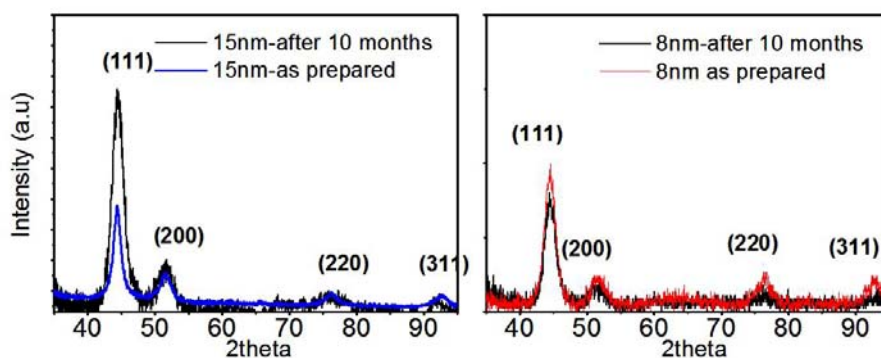
**Figure 2.7.** *Comparison of XRD patterns of the Ni nanoparticles <Φ>*$_{TEM}$ *of 8 and 15 nm) as prepared and after 10 months of storage.*

## Influence of temperature

As it was mentioned previously, the parameters to be taken into account for a high quality material production were: i) first heating step temperature ($T_1$) and time to attain a high monomers supersaturation level; ii) high heating rate (from $T_1$ to $T_2$) with a constant temperature ($T_2$) to assure small nanoparticles with uniform size distribution.

Temperatures ($T_1$) of 130°C (for 20 min) (*A_TD.Ni_3*) and 170°C (for 20 min) (*C_TD.Ni_15*) were tested (**Figure 2.8**). It was found that in the case of *C_TD.Ni_15* smaller nanoparticles (mean size of 19.6 nm) with a size distribution below 10% (**Chapter 6.3 Table A.iii.1**) were produced. The smaller size with better size distribution could be related to the larger accumulation of monomers in the solution. Chemically it is known that a higher temperature (170°C in our case) increase the decomposition rate of the metal precursor and consequently, the rate of the monomers formation is increased as well. Thus, a higher $T_1$ will produce a higher concentration of the monomers during the 20 min, which results in the formation of more and smaller nanoparticles, as found experimentally.
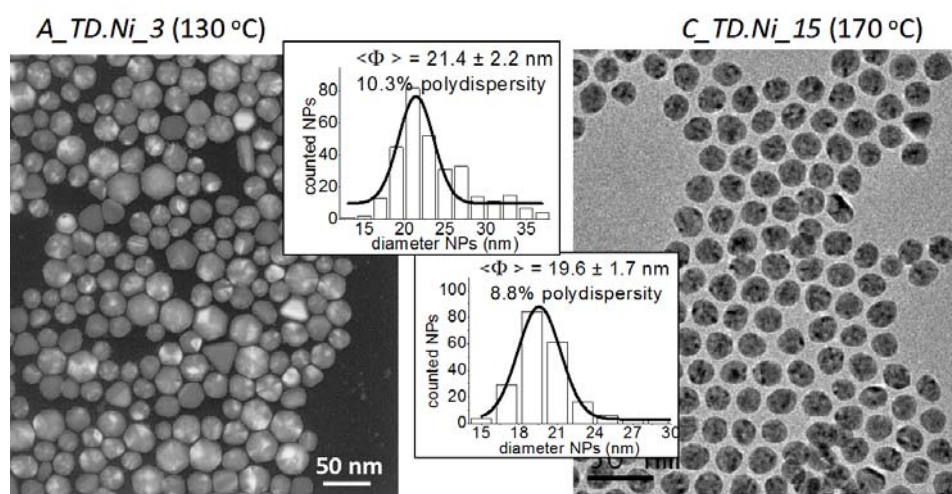


**Figure 2.8** *The influence of $T_1$ on the size and polydispersity of Ni nanoparticles.*

Sequentially, heating rates (from 130 to 250°C) of 6°C/min (*A_TD.Ni_1*) and 12°C/min (*A_TD.Ni_2*) were evaluated. It was observed that the lower rate –ensuring a

50

thermodynamically controlled process– gave faceted, bigger nanoparticles of 19.3 nm compared to the faster heating rate, kinetically controlled process that resulted in more spherical nanoparticles of 17 nm (**Figure 2.9**). When $T_2$ fluctuates during the aging period, the focusing effect is diminished due to an Ostwald ripening process. **Figure 2.10** shows an illustrative TEM image of the material (*A_TD.Ni_14*) produced during 30 minutes fluctuating $T_2$ (243–255°C).
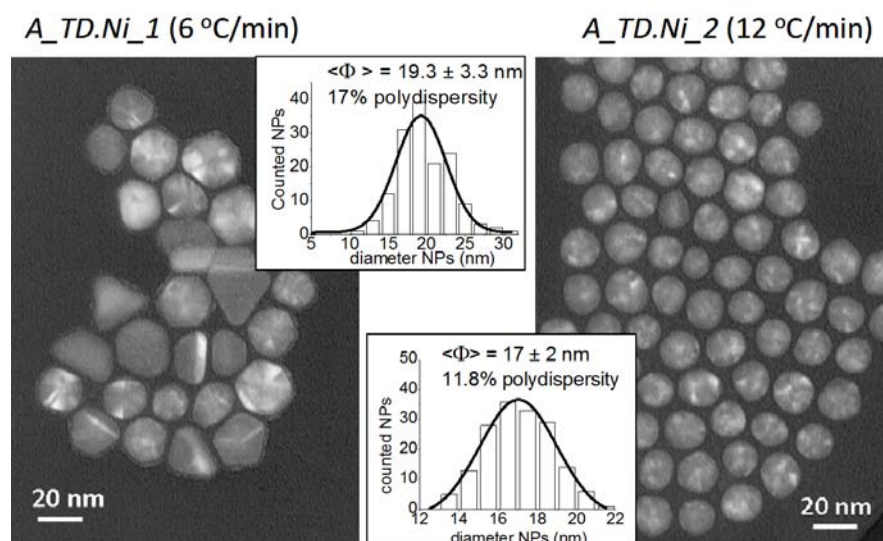


***Figure 2.9***. *The influence of heating rate on the size, shape and polydispersity of Ni nanoparticles*
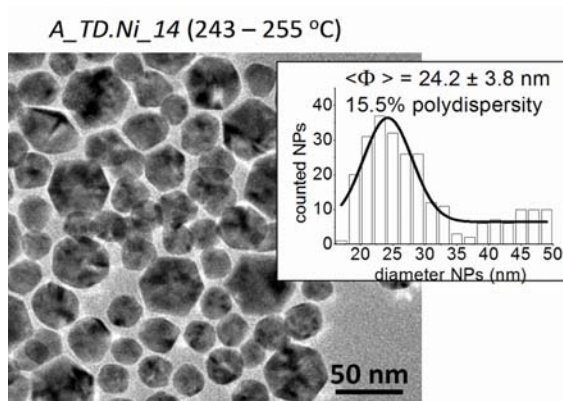


***Figure 2.10***. *The influence of a non-constant reaction temperature ($T_2$) on the polydispersity of Ni NPs.*

Finally, the effect of $T_2$ value on nanoparticles formation was investigated. As it was experimentally observed in case of $T_2$ of 250°C, the change of solution color from green to black (nucleation) took place at a temperature of around 240°C. The same temperature for fcc Ni formation from $Ni(acac)_2$ was also reported by Goto et al.[21]. When $T_2$ was set to 215°C, no Ni nanoparticles were formed (*C_TD.Ni_7, 8*) that is consistent with the former observation. In the literature it has been reported that a temperature of 215°C was enough for the formation of Ni nanoparticles[23] if the precursor was nickel acetate instead of nickel acetylacetonate, this being attributed to the lower decomposition temperature of the former (220°C)[21].

By using the standard synthesis (A-type), adapted from the literature, with the surfactants OAc and TOP with molar ratio Oac : TOP of 2:1, Ni nanoparticles of mean size ~

15 nm were produced, this being almost at the size limit imposed by our requirements. Thus, in order to synthesize smaller nanoparticles of mean size ~ 14 nm, other parameter had to be changed. This was the surfactant type and quantity. Its influence will be discussed in the next section.

**Influence of surfactants**

The presence and type of surfactants are crucial in colloidal organometallic synthesis. In the particular case of magnetic nanoparticles (metallic or ferrites), due to the strong magnetic interactions, the presence of surfactant as a protective shell against agglomeration is a must. To produce monodispersed metallic magnetic nanoparticles, an intensive research has been done, in particular by the Murray group[10a, 24]. They demonstrated that using a pair of surfactants –one strongly bound (oleic acid) and one weakly bound (trialkylphosphine) to the nanoparticles surface– the growth, stability and oxidation of the nanoparticles can be controlled. Trialkylphosphine reversibly coordinates metal surface sites, slowing down the particles growth. Ligands with larger carbonic tails or bulkier types (e.g., TOP) cause a steric hindrance in the ions adsorption resulting in the production of smaller NPs. It has been furthermore reported that for short-chain ligands (e.g., tributylphosphine), the precursor $M(acac)_2$ shows a higher reactivity favoring the production of larger particles[18d]. Oleic acid, when used alone, hinders the nucleation by binding so tightly to the particle surface, and therefore impeding the formations of a larger number of nuclei but favoring their growth[17], although other authors reported contradictory findings [25]. Using together, OAc with TOP, a competition between slowing down and favoring the particles growing will occur, and the resulted size of nanoparticles will depend on the amount of each surfactant used.

In this study, the molar ratio of the strongly (OAc) and weakly bound surfactant (TOP) was varied and thus the size and shape of the Ni nanoparticles could be tuned. **Figure 2.11**, shows the TEM images of Ni nanoparticles prepared with different molar ratios of the two surfactants. The nanoparticles synthesized in the absence of surfactants (*B_TD.Ni_6*, **Figure 2.11a**) had a large mean size of ~100 nm but well defined (faceted) shapes, as it was expected. When adding only the strongly bound surfactant (in $Ni(acac)_2$ : OAc molar ratio of 1:3) *(D_TD.Ni_10)*, one may expect the size of nanoparticles to be decreased because the seeds surface are then better stabilized and so the growth become more difficult[10a, 23, 25]. In contrast to this, two populations were found: one predominant, formed of large, stable clusters (possibly, aggregated nanoparticles) with a mean size of ≈150 nm, but without a well defined shape; and a small population formed of individual, spherical-like nanoparticles, with mean size of 13 nm, particularly present on the clusters surface (see **Figure 2.11b**). When the weakly bound surfactant (TOP) was added to the reaction mixture in the molar ratio OAc:TOP of 2:1 (*A_TD.Ni_4*, **Figure 2.11c**), a good quality of Ni nanoparticles with a mean diameter of 15.5 nm and small size distribution (8.4 %) were produced. As it was expected, the presence of TOP slowed the growth of nanoparticles. Their shape was still faceted but with a tendency to spherical. Next, the pair of surfactants was maintained but their molar ratio was changed to 1:1 (*D_TD.Ni_13*, **Figure 2.11d**). By this way, smaller nanoparticles with a mean size of ~ 11 nm were obtained while the good

polydispersity was maintained (13 %) and the shape became more spherical. Increasing further the amount of TOP (Oac:TOP of 1:2) (*D_TD.Ni_12*, **Figure 2.6e**) resulted in smaller, mostly spherical shaped nanoparticles of 8.8 nm. Finally, when TOP was employed alone (*D_TD.Ni_11*, **Figure 2.11f**), 8 nm spherical nanoparticles were produced. These experiments proved that the size of Ni nanoparticles could be decreased by increasing the amount of TOP (**Table 2.2**). The shape of nanoparticles changed slightly as their size decreased becoming less faceted and more spherical. This was in agreement with previous reports[10a,23].
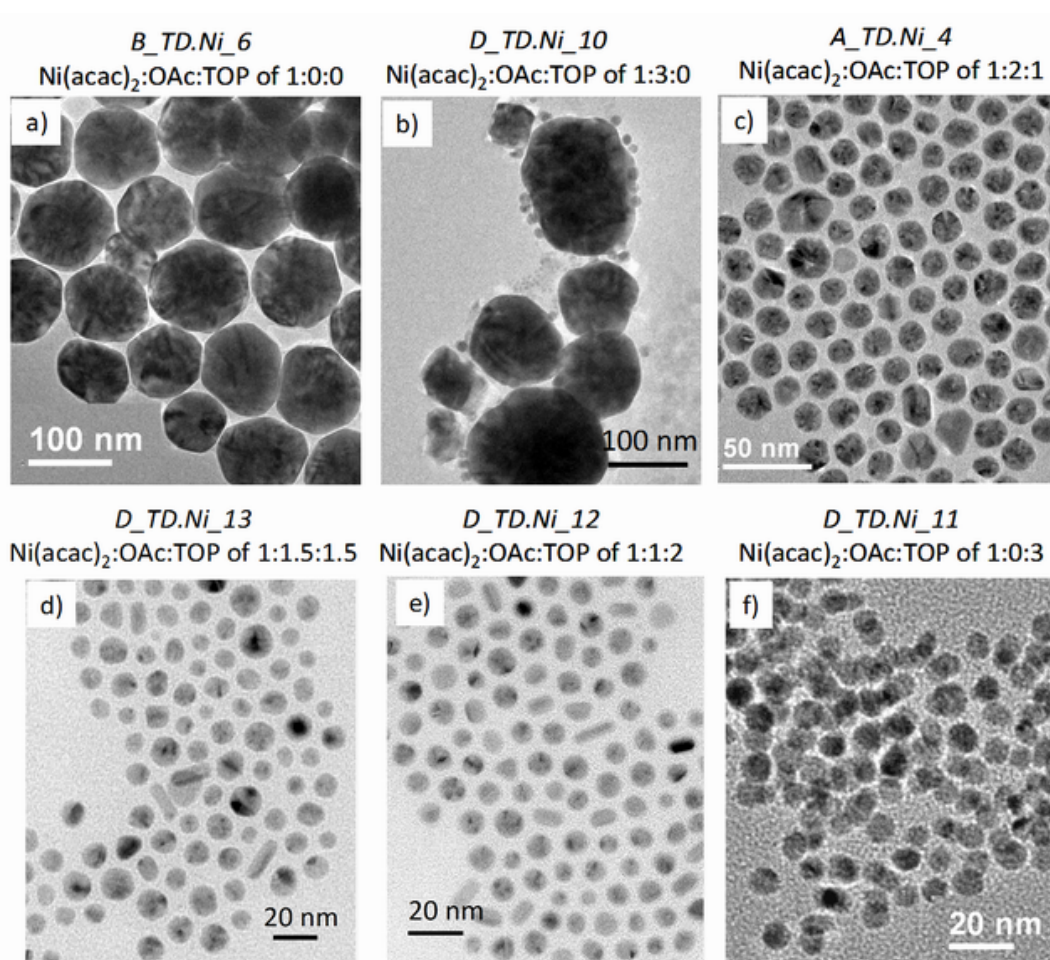


***Figure 2.11.*** *TEM images of Ni nanoparticles synthesized in the absence and presence of surfactants with different molar ratios*

***Table 2.2*** *Structural and morphological data for the as synthesized Ni nanoparticles.*

| Material | Molar ratio Ni(acac)$_2$: OAc:TOP | $<\Phi>_{TEM}$ (nm) | Size distribution (%) | $<\Phi>_{XRD}$ (nm) Scherer eq. | Cell lattice (Å) |
|---|---|---|---|---|---|
| *B_TD.Ni_6* | 1 : 0 : 0 | 102 ± 10 | 9.8 | 11.9 | 3.524 |
| *D_TD.Ni_10* | 1 : 3 : 0 | 150 and 13.3 ± 2.1 | 15.8 | 24.5 | 3.521 |
| *A_TD.Ni_4* | 1 : 2 : 1 | 15.5 ± 1.3 | 8.4 | 7.5 | 3.531 |
| *D_TD.Ni_13* | 1 : 1.5 : 1.5 | 11.1 ± 1.5 | 13.5 | 5.3 | 3.588 |
| *D_TD.Ni_12* | 1 : 1 : 2 | 8.8 ± 1.4 | 15.9 | 4.5 | 3.610 |
| *D_TD.Ni_11* | 1 : 0 : 3 | 8 ± 1 | 12.5 | 4.3 | 3.611 |

Concerning the microstructure of nanoparticles, multiple crystalline domain orientations can be appreciated in the HRTEM image of 15 nm Ni NPs (**Figure 2.12**) and the SAED image (**Figure 2.12 inset**) revealed a multi-spot pattern with the spots equally distant from the center which could be associated with multiple-twinned NPs[10a, 26]. This observation was supported by the $<\Phi>_{XRD}$ value resulting from the Scherer formula of the (111) diffraction peak (**Table 2.2**) which was about half the size of that found from TEM. Similar observations were reported by other authors[23, 27].
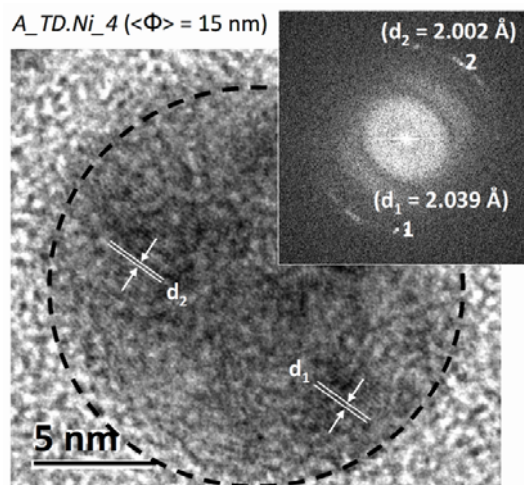


**Figure 2.12.** *HRTEM image of a single Ni nanoparticle of 15 nm and its selected area electron diffraction pattern as inset (SAED) .The distances $d_1$ and $d_2$ are closed to interplanar (111) distance..*

## 2.2.2 Colloidal dispersions and stability

Monodispersed colloids with long time stability are desirable. These can be achieved by the proper choice of surfactant quantity/type and by appropriate choice of dispersion media. This section deals with the study on monodispersion stability in time in different media. Those were chosen according to their polarity index values, from non polar (0) to polar (8).

For a better understanding of this section, a few details from the experimental procedure are reminded: from the final reaction solution, the nanoparticles coated with surfactants were precipitated by adding extra ethanol, followed by two times centrifugation in order to remove any free surfactants from the material; the precipitate was dried in an oven (at 70°C) overnight and than redispersed in hexane and used for further characterization (DLS, TGA). This separation process ensured that no free surfactant was in the media, and only the organic shell remained at the nanoparticles surface.

**Study of nickel nanoparticles-hexane dispersion stability in time**

DLS (**Chapter 6.2.A.ii.6**) was used to determine the hydrodynamic radius (metal-core, surfactant shell and a layer of solvent close to the particle) of nanoparticles in the dispersion media and to monitor the stability of nanoparticles dispersion in time (possible particle aggregation after a few months could be monitored by both the shift of the DLS peak maximum and broadening).

One of the most important factors that have to be taken into account as a possible cause of aggregations[b] is the size of the nanoparticles. In the case of magnetic nanoparticles, aggregation takes place due to the strong magnetic interaction. By increasing their size, the dipolar coupling increases and when its strength overcomes the steric hindrance (caused by the surfactant shell), the particles will aggregate. Two years after their synthesis, we observed that Ni nanoparticles with a diameter larger than 19 nm (**Chapter 6.3 Table.A.iii.1**) were not anymore re-dispersable in hexane due to the presence of very big (visible at naked eye) aggregates. With the same surfactant shell (molar ratio OAc:TOP of 2:1), nanoparticles with a diameter in the range of 18–13 nm were found partially re-dispersable. The smallest nanoparticles with a mean size around 8 nm were completely re-dispersable with monodispersed characteristics (**Figure 2.13**). It can be thus concluded that by decreasing the Ni nanoparticles size, long-term stability can be ensured.
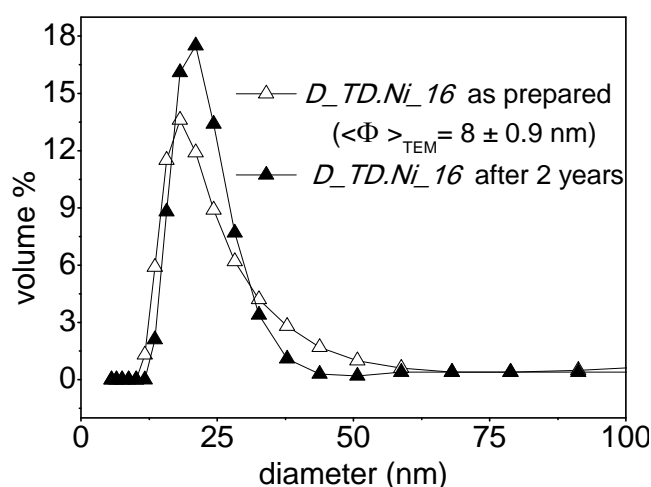


*Figure 2.13. DLS analysis of monodispered nanoparticles of 8 nm as prepared and after 2 years of storage after 2 years of storage*

Other factors which could affect the monodispersity are the surfactant type and its quantity at the nanoparticle surface. A strong (covalent or coordination) binding can preserve the organic shell even for months/years. On the contrary, nanoparticles with physisorbed surfactant are susceptible to lose the protective shell relatively fast –due to the reversible sorption/desorption effects between the nanoparticles surface and media– and so agglomeration occurs. The organic shell thickness can be controlled by using ligands with larger carbonic tails, i.e., the dipole-dipole interaction can be minimized.

Thermogravimetric analyses (TGA) (**Chapter 6.2.A.ii.4**) were performed in order to provide both quantitative data for the surfactant mass (weight loss, %) at the nanoparticles surface and qualitative information about the bonding strength of the surfactant. A stronger bond (chemisorption) is associated with weight losses at higher temperature while a weaker bond (physisorbed specimens) had weight losses at lower temperature[28]. The weight loss profiles are presented in **Figure 2.14** and the experimental values are listed in (**Chapter 6.3. Table A.iii.1**). Up to 200°C, the remained solvent evaporated and between 200°C and 600°C, desorption and decomposition of the organic coating (OAc and TOP) took place [24b, 29]. It can

---

[b] *Agglomerates*: a group of particles held together by relatively weak forces (Van der Waals, capillary) that may break apart upon processing (sonication). *Aggregates*: a discrete group of particles in which the individual components are not easily broken apart, being strongly bounded together. (definitions given by American Society of Testing and Materials).

be clearly seen that except for the larger Ni nanoparticles (150 nm), the weight loss drops in 2 or 3 steps attributed to the physisorbed (at lower temperature of 260°C) and chemisorbed (at higher temperatures of 420°C and 500°C) surfactants[28, 30]. From these profiles, it was not possible to determine which surfactant corresponds to which step(s), probably due to their similar chemical structure.



**Figure 2.14.** Thermogravimetric analysis (TGA): weight loss percentage plotted as a function of temperature for five sizes of Ni NPs.
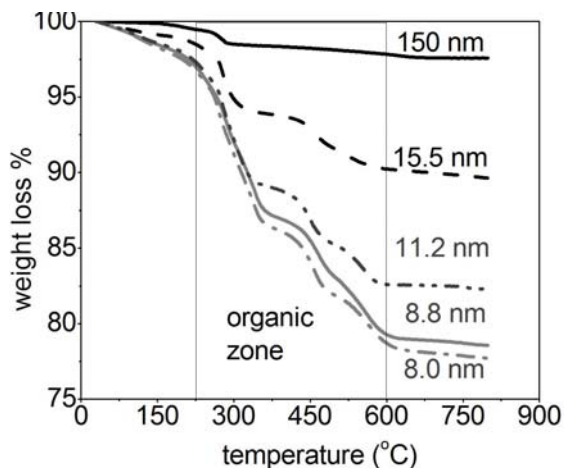
Instead of running the TGA characterization for each different Ni NPs, it may be useful to predict the surfactant weight loss as function of the NP size. A simple mathematical model was found to describe the relationship of these two parameters (Eq. 2.1):

$$y = \frac{k_1}{\left(<\Phi>_{TEM} + k_2\right)^2}$$

(Eq. 2.1)

where y is the weight loss (%), $<\Phi>_{TEM}$ is the Ni NP diameter (nm) and $k_1$ and $k_2$ are the model constants found to be 4080 nm$^2$ and 6.387 nm, respectively (calculated by the *Solver* function of Microsoft Excel). **Figure 2.15** shows that the model fits well the experimental data. The second power hyperbolic-type correlation (with boundary condition of y = 100% when no NPs are present) might be a result of the inverse relationship between NPs diameter and total NPs surface area (since the same amount of Ni precursor were used in each TGA experiment).



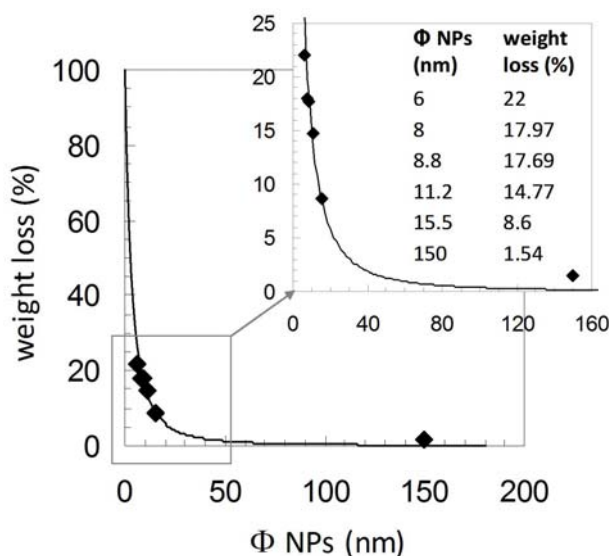| Φ NPs (nm) | weight loss (%) |
|---|---|
| 6 | 22 |
| 8 | 17.97 |
| 8.8 | 17.69 |
| 11.2 | 14.77 |
| 15.5 | 8.6 |
| 150 | 1.54 |

**Figure 2.15.** *Correlation between Ni NPs size and surfactant weight loss (from TGA) fitted by the hyperbolic function.*

$$\% \, weight \, loss = \frac{4080}{\left(<\Phi>_{TEM} + 6.387\right)^2}$$

### Stability study of 8 nm Ni nanoparticles in different dispersion media

From the TGA data we assumed that the Ni nanoparticles had the organic shell formed of chemisorbed oleic acid and physisorbed TOP species. Due to the apolar tail of surfactants (see Figure 2.5), the nanoparticles surface is non-polar and thus non-polar media will preserve the nanoparticles monodispersity. This was verified by DLS measurements of 8 nm Ni nanoparticles (*D_TD_Ni_16*) in solvents with different polarities[c]. In **Figure 2.16**, the solvents used are listed in the increasing order of polarity (given in parentheses for each solvent).
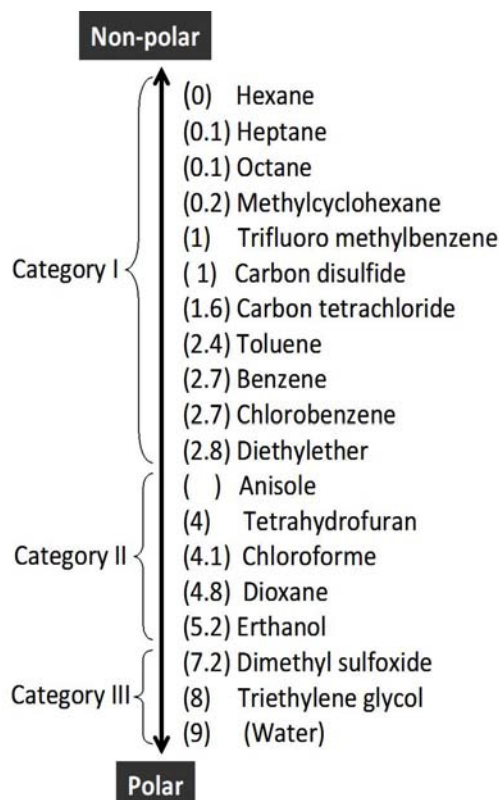


*Figure 2.16. Organic solvents studied as dispersion media.*

These solvents could be classified into three categories:

*Category I:* non-polar solvents with polarity index below 3 which keeps the nanoparticles individually dispersed, giving the maximum DLS peak position at $<\Phi>_{HYD}$ of $20 \pm 4$ nm (**Figure 2.17a–b**).

*Category II:* slightly polar (polarity index of 4–5) or polar (polarity index > 5) solvents in which nanoparticles are partially redispersable, forming smaller (below 400 nm) or bigger (above 400 nm) aggregates (**Figure 2.17c, d**).

*Category III:* some other solvents with rather high polarities (e.g., acetone, acetonitrilie, diethylamine) in which the nanoparticles cannot be redispersed and no DLS measurements could be done.

To confirm the formation of agglomerates/aggregates, SEM analysis of an evaporated drop of diluted dispersion on carbon grid support was performed. The SEM images (**Figure**

---

[c] *Polarity index:* degree of interaction of the solvent with various polar test solutes.

**2.18**) show examples for the different Ni nanoparticles states which were strongly dependent on the solvent polarity. However, the observed agglomerates sizes were somewhat different from the DLS data that could be due to the sample preparation procedure (**Chapter6.2.A.ii.3**).
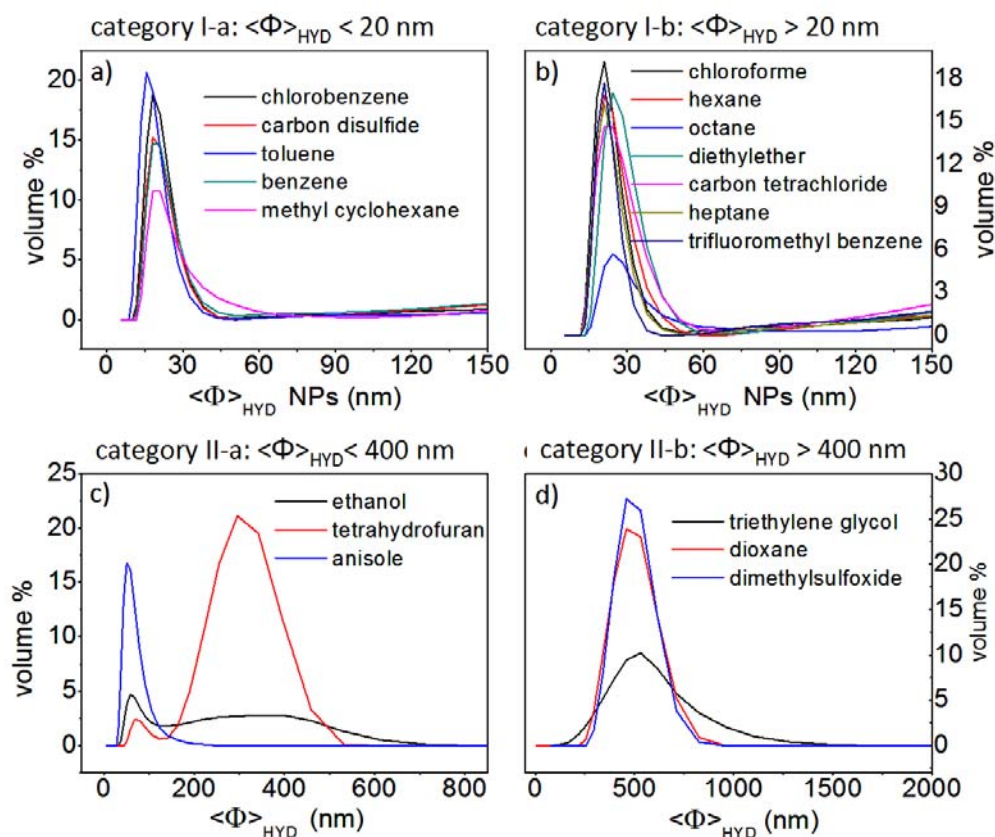


*Figure 2.17. Dynamic Light Scattering (DLS) analysis of the 8 nm Ni nanoparticles system in solvents with different polarity indexes of 0–3 (**a,b**), 4–5 (**c**) and >5 (**d**)*
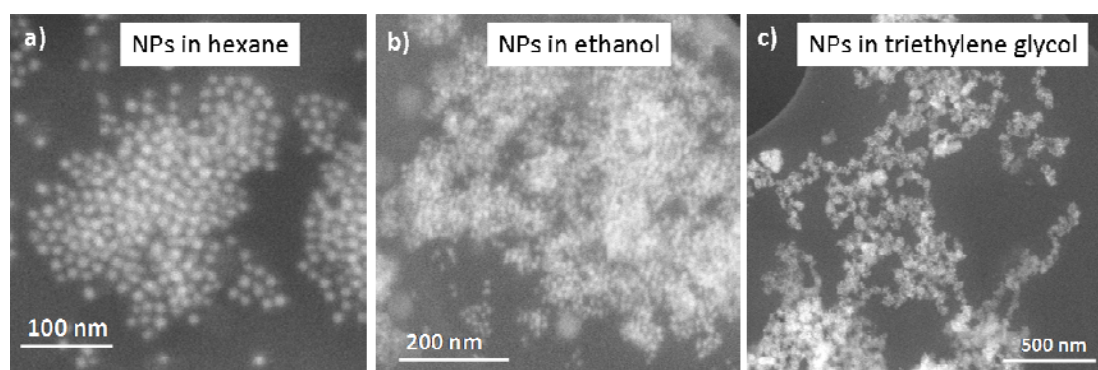


*2.18. SEM images of 8 nm Ni nanoparticles states in various dispersion media: monodispersed NPs in hexane (**a**), agglomerated NPs (**b**) and aggregated NP (**c**).*

## 2.2.3 Magnetic and magneto-optical study of Ni nanoparticles in stable colloidal dispersions.

For a better understanding of this subchapter, it is important to recall a few objectives of this thesis. We were primarily interested to have an optical system that responds to a magnetic field and secondarily to find new functionalities which could be applied in e.g., optical

communication, such as integrated optical devices. Our strategy was to use photonic crystals as optically ordered systems in which we incorporate a magnetic material in the form of magnetic nanoparticles. As for the new functionality, we looked for enhanced magneto-optical response at the edges of the photonic band gap.

In order to achieve these objectives, some requirements had to be fulfilled:

1. Comprehensive knowledge of the magnetic nanoparticles system: structural, morphological, magnetic and magneto-optical behavior in a disordered system;

2. The magneto-photonic crystal should contain superparamagnetic nanoparticles in order to have high response to low magnetic field and zero response (remnant magnetization) in the absence of the field;

3. The system should contain sufficient magnetic material in order to give a magneto-optical response;

4. The long-range ordered structure of the original photonic crystal should be preserved.

This section focuses on the study of magnetic and magneto-optical behavior of nanoparticles. In order to fulfill the requirements (2–4), we have chosen the two most suitable systems out of all Ni nanoparticles synthesized, namely, the Ni nanoparticles of 8 (*D_TD.Ni_16*) and 15 nm (*A.TD.Ni_4*).

The classical method used for magnetic characterization of nanoparticles is superconductive quantum interference device (SQUID) magnetometry (**Chapter 6.2 A.ii.8**). A drawback of this method is not only that it is a long procedure (preparation + measurements) but, also, uses a high quantity (few mg) of nanoparticles in powder form relatively to the low amount of material produced per batch (typically, in the order of 100 mg). Since in a wide range of applications the nanoparticles are commonly dispersed in liquids, a fast magnetic characterization technique able to probe small quantities of material dispersed in liquid carriers is of interest. Because of the growing research of magnetic colloids used for biomedical applications, the use of techniques to both measure diluted concentrations of magnetic nanoparticles and correlate the magnetic response of these liquids with particle aggregation or surface particle functionalization would also be welcomed. Our work[31] presented in the second part of this chapter is a contribution toward these purposes. A novel home-made magneto-optical set-up, was used for the rapid magneto-optical characterization of nanoparticles stabilized in liquid media. In order to prove the goodness of this method, SQUID measurements were also performed for comparison sake.

**Magnetic characterization by SQUID magnetometry**

SQUID measurements of temperature and field dependent magnetization of the synthesized nanoparticles were acquired to assess the superparamagnetic blocking temperature ($T_B$, K), saturation magnetization (Ms, emu/g) and coercivity (Hc, Oe). The magnetic units of emu/g Ni were based on the mass of metallic Ni (excluding the surfactant mass). **Figure 2.19a** presents the M(H) magnetization loops measured at room temperature for the whole series of Ni nanoparticles of different sizes (Ms values are listed in **Chapter 6.3 Table A.iii.1**). The graph shows increasing saturation magnetization with increasing the size and Ms nearly reached the bulk value (Ms = 57.6 emu/g) for particles of about 100 nm. These data were

interpreted in terms of a core-shell model[27, 32] (discussed below). Measurements of the temperature-dependent magnetization (M *vs* T) in 50 Oe field during heating after zero-field cooling (ZFC) are shown in **Figure 2.19b.** For nanoparticles with mean size smaller than 20 nm, the ZFC magnetization increases with the temperature until it reaches a maximum value corresponding to the blocking temperature ($T_B$, K) **(Chapter 6.3 Table A.iii.1).** Above this temperature, the thermal energy becomes larger than the magnetic energy barrier and the nanoparticles enter in the superparamagnetic domain. In case of nanoparticles larger than 20 nm, ZFC magnetization increases slower with the temperature while the field-cooling (FC) magnetization hardly changes. The splitting ZFC–FC magnetization curves reach a crossing point around 300 K, indicating a $T_B$ value above room temperature.
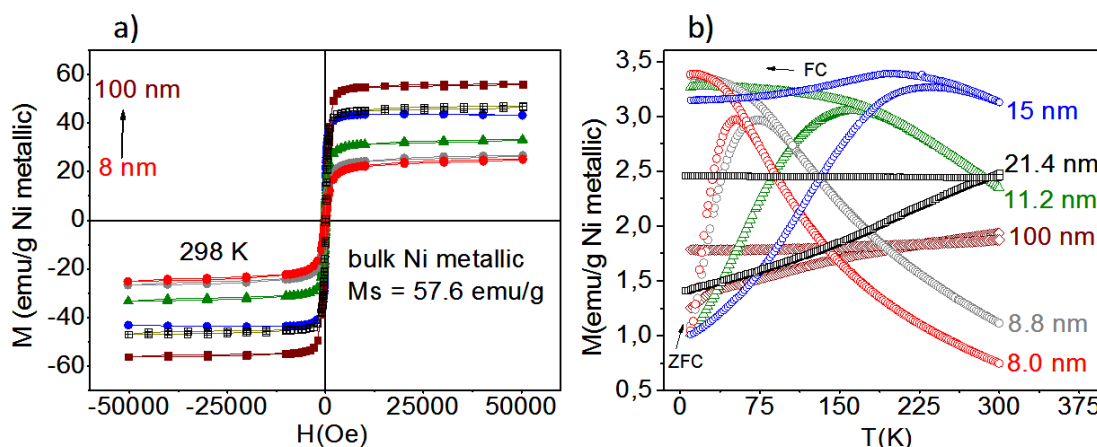


***Figure 2.19.*** *SQUID M(H) magnetization loops:* ***(a)*** *measured at room temperature for a whole series of Ni nanoparticles;* ***(b)*** *ZFC–FC plots measured at 50 Oe;*

### Core-shell model

In an ideal superparamagnetic system, the magnetization obeys the Langevin function (eq. 2.2)

$$M = M_S \cdot (\coth\alpha - 1/\alpha) \qquad (Eq.2.2)$$

where $\alpha$ is given by the expression $\alpha = \dfrac{m_0 \cdot H}{k_B \cdot T}$ with $m_0$ being the particle magnetic moment,

$$m_0 = M_S \cdot V_{NP} \qquad (Eq.2.3)$$

$M_s$ = saturation magnetisation and $V_{NP}$ – nanoparticle volume, $k_B$ –Boltzmann constant and T –temperature. From the measurements of magnetization curves M(H) it is thus possible the calculation of the particle magnetic moment and subsequently the particle magnetic volume (eq.2.3). Eq.2.2 can be applied in case of negligible anisotropy energy. However, a real superparamagnetic system is not isotropic in its properties, having anisotropic contributions energies. These could arise from the nanoparticles shape, lattice deformation at the particles surface, the crystalline structure itself (magnetocrystalline anisotropy), stressed imposed by the enviromement[33]. Thus the finite-size and surface effects can drastically change magnetic properties of nanoparticle in comparison with corresponding "bulk" counterpart[33-34].

By decreasing the nanoparticles size, the particles saturation magnetization decrease with respect to the bulk value, as we experimentally observed. This is explained mostly by the called dead layer theory, based on the existence of a nonmagnetic shell, surrounding the ferro/ferrimagnetic core. Due to the high surface to volume ratio in nanoparticles: the spins at the surface are canted and do not contribute to the total magnetic moment of the particle[35] leading the decrease of nanoparticles Ms.

We applied a core-shell model for Ni nanoparticles of different sizes assuming the presence of a constant effective nonmagnetic shell ($d_0$). We have considered that the nanoparticle magnetic moment is proportional to $(R–d_0)^3$ (formula presented in **Chapter 6.3. A.iii.2**), R being the nanoparticle radius determined by TEM. By plotting the saturation magnetization of nanoparticles (emu) measured by SQUID and normalized to the number of nanoparticles per sample ($N_{NPs}$) *versus* radius it was found a linear correlation (**Figure 2.20**). This confirmed the validity of model –the nickel core surrounded by a fix nonmagnetic shell, and permitted to calculate the thickness of $d_0$ to be ~1 nm.
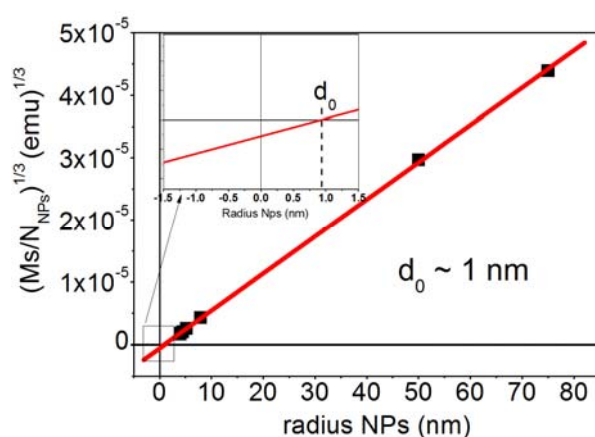


***Figure 2.20.*** *The core-shell model applied to different sizes of Ni nanoparticles.*

To verify on the existence of an antiferomagnetic NiO shell (not detected by XRD measurements) which might lead to an exchange bias with the ferromagnetic core we performed the following experiments: we dried samples of 8 nm nanoparticles overnight at 70°C either under oxygen or argon atmosphere. Subsequent measurements of the magnetization at 5 K of both samples (**Figure 2.21**) indicated that their saturation magnetization values are virtually identical. In addition, the SQUID experiments performed after field-cooling conditions (H=50 kOe), particularly sensitive to exchange bias, indicate that the loops are well centered at zero-field (see the inset in **Figure 2.21**), and thus there is no evidence of exchange bias[27] and, by extension, of the formation of an antiferromagnetic (likely NiO) surface layer in any of the material of 8 and 15 nm Ni nanoparticles. It is interesting to mention that particles in hexane are even more protected since this solvent is not oxidizing and is commonly used to prevent nanoparticles oxidation.
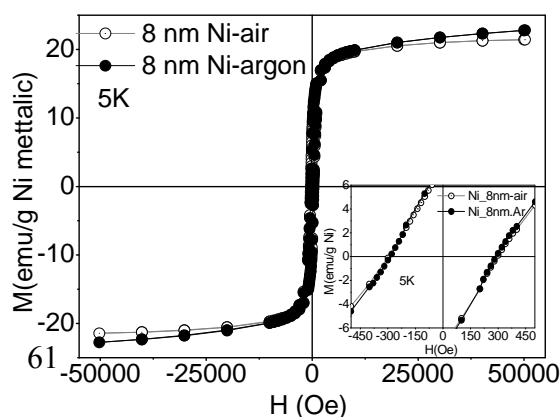
***Figure 2.21*** *SQUID M(H) magnetization loops measured at 5 K for 8 nm Ni nanoparticles dried overnight at 70°C in air and argon atmospheres; the inset shows a zoom of the low-field region of the loop.*

A more detailed analysis regarding the size determination of superparamagnetic nanoparticles from magnetization curves was made by our collaborator Prof. Chen. A core-shell model based on the Langevin function and considering a log-normal particle volume distribution has been applied. The model consisted in a ferri/ferromagnetic core (with bulk saturation magnetization) and a paramagnetic shell (with a given paramagnetic susceptibility) expressed by the eq.2.4.

$$M(H) = \int_0^\infty p(v; \eta, \sigma) v^{-1} \left[ M_s v_c L(x) + v_s \chi_{pm} H \right] dv \qquad (Eq.2.4)$$

where $p(v, \eta, \sigma)$ is the particle volume distribution, $M_s \cdot v_c \cdot L(x)$ is the superparamagnetic core contribution ($M_s$ = bulk saturation magnetization, $v_c$ = core volume and $L(x)$ corresponds to the Langevin function and $v_s \cdot \chi_{pm} \cdot H$ is the paramagnetic shell contribution ($v_s$ = shell volume, $\chi_{pm}$ = paramagnetic susceptibility and H = applied field). Applying this model to small iron oxide nanoparticles (~ 6 nm) the magnetically determined average size was in agreement with the results from TEM and XRD and it was determined a shell dimensions to be around 0.3 nm[22a]. Also the saturation magnetization of the core was found to be the same as bulk.

This core-shell model was also applied for nickel nanoparticles of around 8 nm (*D_TD.Ni_11*)[22b] the results showing some differences respect to iron oxide behaviour[22a]. The magnetically determine mean size of the core-shell system was in agreement with TEM measurements, but the calculated nonmagnetic layer was larger of a 1.6 nm. Additionally, for the nickel superpamagnetic system has been found that the ferromagnetic nickel core had a larger saturation magnetization than the bulk nickel. This enhanced moment respect to bulk was observed for very small nanocrystal sizes (~ 2 nm) which have less than 400-500 atoms[34b]. The interpretation[34b] was that ferromagnetic metals, especially 3d type have a moment with the magnitude influenced by the band structure. Near surface, the magnitude of the magnetic moment per atom is changing drastically with distance from the surface due to the band narrowing (as a result of reduced coordination of atoms at the surface).

### Magneto-optical characterization

This methodology is based on the magnetic circular dichroism (MCD) spectroscopy (**Chapter 6.2 A.ii.9**), measuring the relative difference of optical absorption between right- and left-circularly polarized light as a function of the wavelength[36] (**Figure 2.22**). In non-magnetic materials, this difference is null while in magnetic materials, the MCD signal is proportional to the value of the net magnetization. The procedure outlined here allows a magnetic characterization that, depending on specific experimental conditions (e.g., the maximum applied magnetic field and type of magnetic source), may be even a few orders of magnitude faster than the commonly used SQUID magnetometry. An additional advantage of MCD is the possibility of analyzing the magnetic properties of nanoparticle colloidal dispersions *in situ* in industrial production lines.
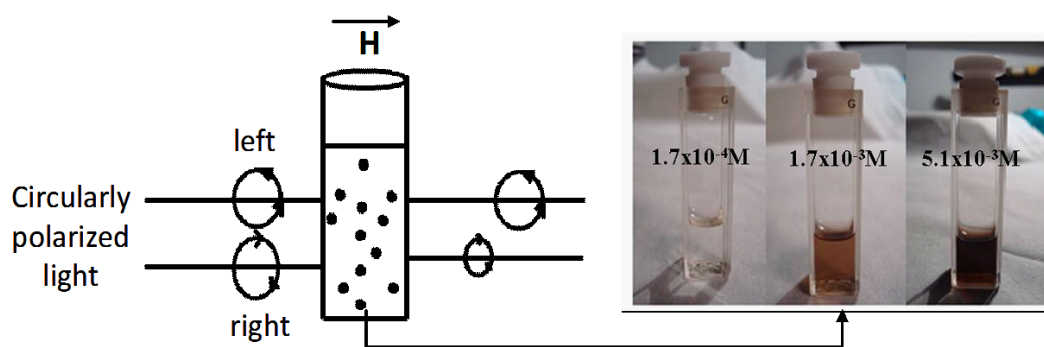
**Figure 2.22.** *Schematic representation of the MCD measurement method. The lower panel shows the photo of couvettes with different concentrations of Ni NPs dispersion.*

Moreover, MCD measurements preserve the stability of the colloidal dispersion (particles are individually dispersed and do not cluster). This was visualized by DLS measurements of the dispersion run before and after MCD (**Figure 2.23**). Plotting the size distribution vs. number % for the two sets of nanoparticles of 8 (**Figure 2.23a**) and 15 nm (**Figure 2.23b**) (using them at the same concentration) indicates that the MCD measurement did not result in a peak shift. Moreover a time effect experiment, by maintaining the application of strong magnetic field (0.6 T) for1 h on the 8nm Ni NPs colloidal dispersion (**Figure 2.23a**) neither had a detectable influence on the nanoparticle stability
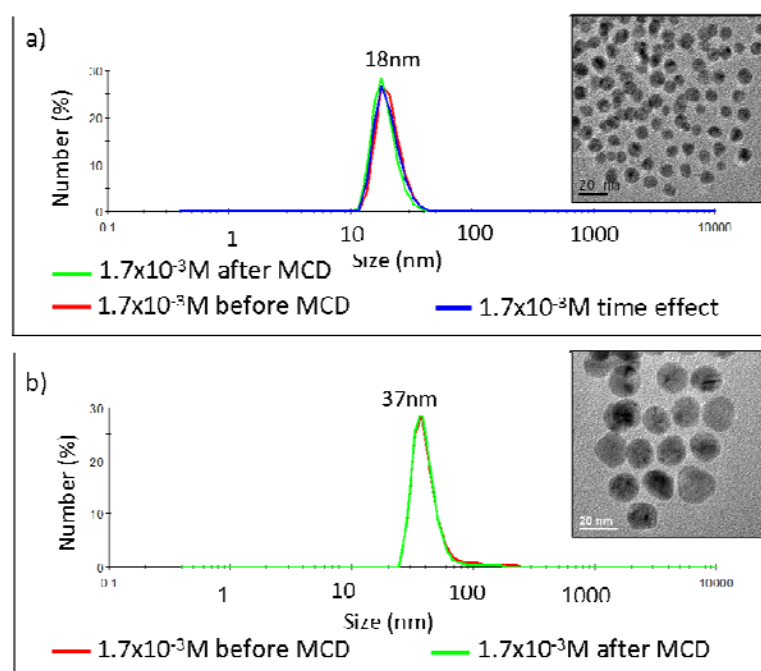


**Figure 2.23.** *DLS measurements of dispersions of 8 nm (**a**) and 15 nm (**b**) Ni NPs before and after their MCD analysis.*

MCD spectroscopy furthermore provides information that is not accessible by SQUID magnetometry: the spectral MCD response probes the electronic structure of the system with photons of different energies. We thus have the possibility to directly monitor changes of the electronic structure with the nanoparticle size. Two model systems, consisting of Ni nanoparticles of two different sizes (8 and 15 nm) dispersed in hexane, were used. In the

first set of experiments, we set the range of NP concentrations to be within $10^{-5}$–$10^{-2}$ M. Concentrations below $10^{-5}$ M were found too diluted and the magneto-optical signal was too weak for a proper analysis. In case of concentrations above $10^{-2}$ M, the magnetic field ($|H|$ = 6 kOe) promoted the aggregation of nanoparticles in clusters thereby distorting the magnetic hysteresis loops and precluding the analysis of the intrinsic nanoparticles properties. **Figure 2.24a** shows the recorded magneto-optical loops for the two extreme concentrations of $10^{-5}$ and $10^{-2}$ M. The loop measured at concentration of $10^{-2}$ M shows an anomalous shape (the upper and lower branches of the loops do not coincide) that departs significantly from the superparamagnetic behavior observed for more diluted dispersions.

Once determined the concentration window measurements, five different concentrations were carried out (1.7x$10^{-4}$, 1.7x$10^{-3}$, 2.6x$10^{-3}$, 4x$10^{-3}$ and 5.1x$10^{-3}$ M). For each concentration, Ni nanoparticles with sizes of 8 and 15 nm were measured. The spectral dependence of the magneto-optical hysteresis loops and the raw data for one selected concentration (1.7x$10^{-3}$) for both Ni sizes is illustrated in **Figure 2.24b**. As expected, the magnitude of loops is a strong function of the probe light wavelength. This data can provide straightforward information on certain magnetic characteristics of the system such as remnant magnetization, coercive field and anisotropy. For the investigated nanoparticle sizes it could be observed that the remnant magnetization was less than about 1% of the saturated value and the coercive field was virtually null, indicating that these colloidal dispersions exhibited a superparamagnetic behavior, even with the short time scale of the measurement. It has to be noted that due to the superparamagnetic properties of these liquids, the application of any magnetic field during the synthesis of nanoparticles does not affect the shape of the magneto-optical loops since the colloidal dispersions loose their magnetic memory, and the moments of nanoparticles are randomly oriented at zero field once the magnetic field is removed.
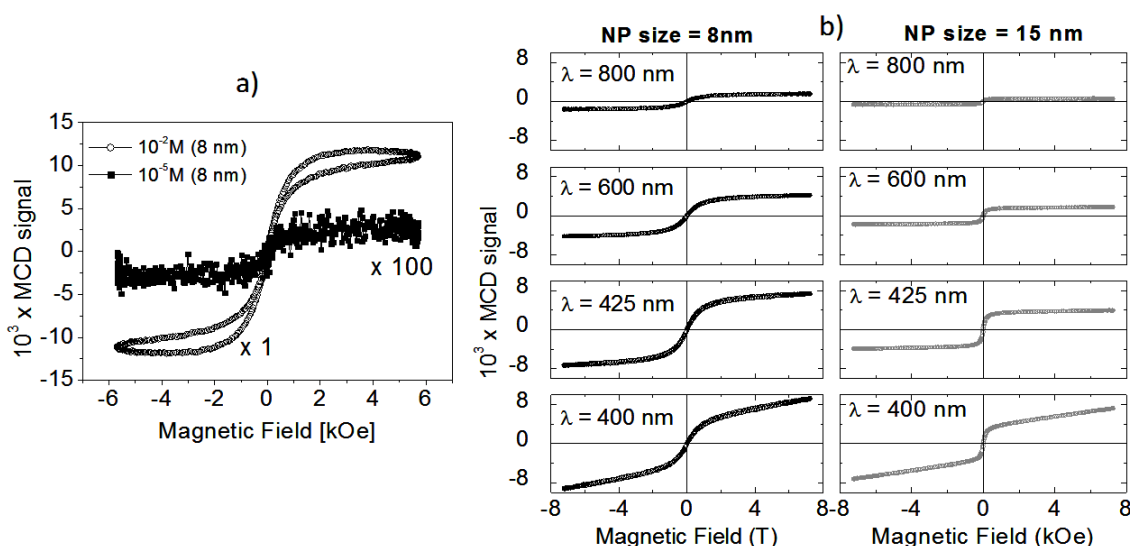


***Figure 2.24.*** *(a) Magneto-optical loops of 8 nm Ni NPs colloidal dispersions for the two extreme concentrations of $10^{-5}$ and $10^{-2}$ M. The data corresponding to $10^{-5}$ M are magnified by a factor 100 (b) The raw magneto-optical hysteresis loops recorded at selected wavelengths and at the same concentration (1.7x$10^{-3}$ M).*

When the normalized magneto-optical (MCD) hysteresis loops of the two sets of nanoparticles dispersions (measured at $\lambda$ of 425 nm) and the normalized magnetization SQUID loops are plotted together, it can be seen that the two techniques gave superimposable normalized loops (**Figure 2.25**). The NP size effects can be proved by the different anisotropy fields of 1.5 kOe and 5 kOe required to saturate the magnetization of 15 nm and 8 nm nanoparticles, respectively. The hysteresis loops thus confirmed that the set of smaller nanoparticles dispersions are more difficult to saturate than the bigger ones.

*Figure 2.25. Comparison of the normalized loops obtained by the two characterization techniques (SQUID and MCD).*
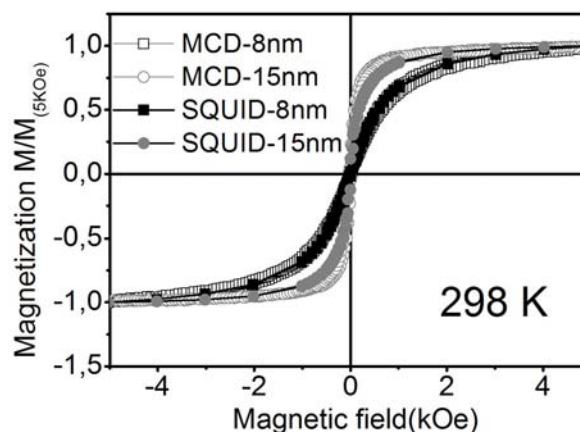


In order to obtain the saturation value from MCD signal *vs.* H measurements, the background magneto-optical signal –originated from the contributions of glass container and hexane solvent– was subtracted from the raw measured signal. Then, for five different concentrations and for two different NP sizes, we plotted the saturated (maximum) values of the MCD hysteresis loops as a function of wavelength within the range of 400–800 nm (**Figure 2.26a**). It can be observed that the spectral shape is very similar for all concentrations and NP sizes exhibiting a maximum[d] at $\lambda$ of 450 nm (photon energy of about 2.75 eV). The observed magneto-optical spectra are in agreement with previous works that report features in the Ni optical dielectric response close to this energy [37]. Plotting the MCD values –referred to the same $\lambda$ – at the different concentrations, a linear relationship is observed (**Figure 2.26b**). When $\lambda$ is varied, the linear correlation remains and only the slope changes (**Figure 2.26c**). Error bar was estimated around 5% of the average MCD value for the more diluted concentrations while it decreased to around 1% for the more concentrated dispersions. These experiments confirm that the methodology presented here provides a straightforward tool to determine with large accuracy the concentration of Ni nanoparticles dispersed in liquid media. It is worth to mention that for these specific experimental conditions, given the sensitivity of MCD setup to detect signals below $10^{-3}$M, NP concentrations as small as 1 $\mu$g/ml can be detected.

---

[d] It is important to note that the MCD is proportional to the net magnetization and therefore, any eventual nonmagnetic or antiferromagnetic shell formed on the nanoparticle does not contribute to the magneto-optical signal.
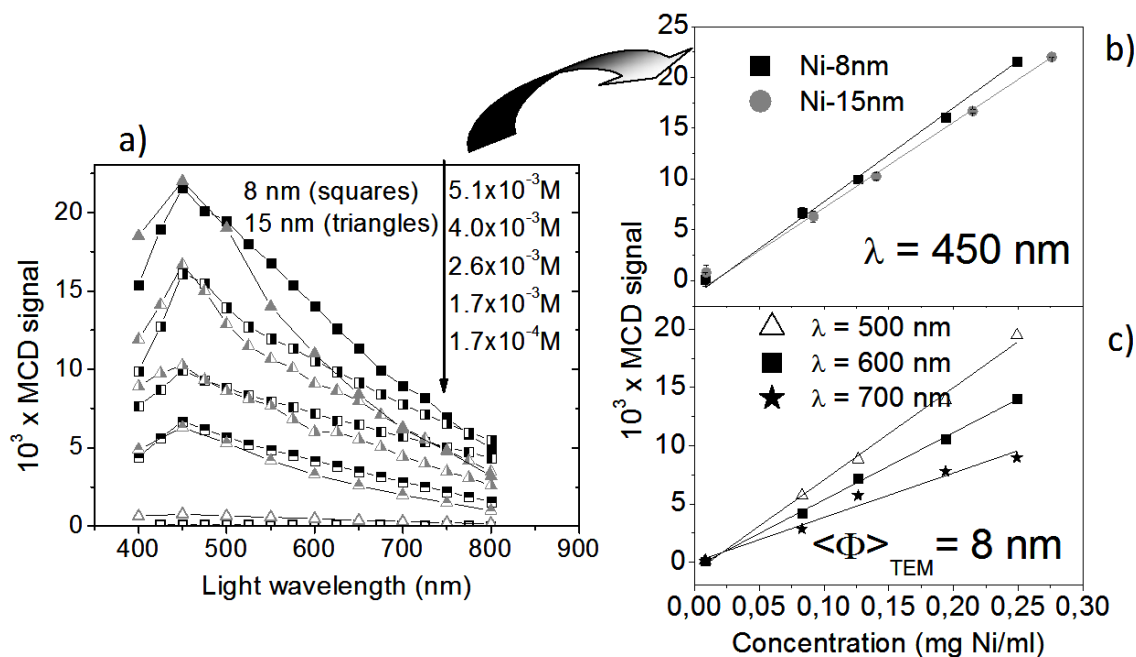
**Figure 2.26. (a)** *Magneto-optical signal as a function of wavelength and function of Ni NPs colloidal dispersion concentration for the two sets of nanoparticles.* **(b)** *Linear correlation between the magneto-optical response and Ni concentration measured at λ of 450 nm.* **(c)** *Linear correlation between the magneto-optical response and Ni concentration measured at different wavelengths for NPs of 8 nm.*

## 2.3 MICROWAVE–ASSISTED SOL–GEL CHEMISTRY – FERRITE NANOPARTICLES

### 2.3.1 General concepts of microwave-assisted nanoparticles synthesis

To produce functional materials with better or at least comparable properties than the existing ones while using fewer resources, less time and less toxic reagents (i.e., a cheaper, faster and cleaner synthesis) is in high demand[38]. Microwave-assisted chemistry is getting very attractive in all areas of synthetic chemistry because it can boost some competitive advantages over other fabrication methods. It is fast, it produces high yields, easy to operate, efficient in terms of energy consumption and environmentally friendly. From the mid–eighties, it has been extensively used in organic synthesis[3a, 3c]. In particular, Niederberger's group was a pioneer in demonstrating the versatility of this method for the synthesis of inorganic nanoparticles[3b, 4e, 12d, 39]. It has to be mentioned that microwaves are not able to induce chemical reactions –the photon energy of 0.0016 eV corresponding to the microwave operation frequency (2.45 GHz) is too low to break chemical bonds– but can be a very efficient heating tool. Microwave-assisted chemistry will thus be referred hereafter as a microwave dielectric heating process. For a better understanding **(Chapters 2.3, 3.3 and 4.4)** and also for a proper design of future experiments, a brief introduction about microwave working principles is presented.

66

Basic principles of microwave heating

Microwave radiation is an electromagnetic radiation that can be divided into electric and magnetic components, the former being responsible for dielectric heating. The heating mechanism involves two processes: (1) dipolar polarization and (2) ionic conduction
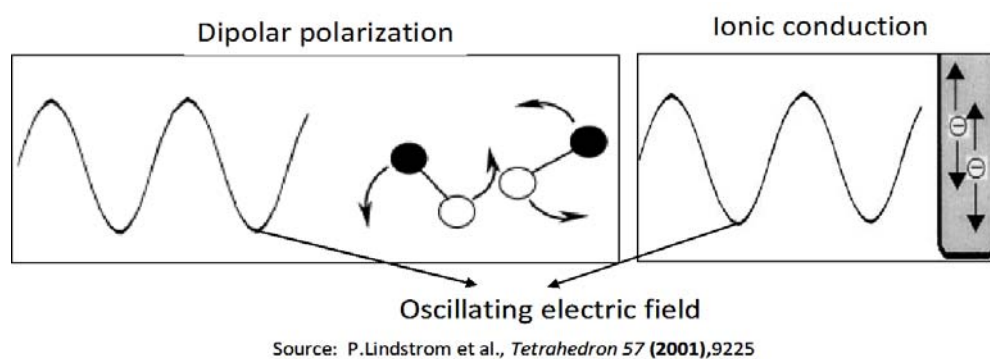


Source: P.Lindstrom et al., *Tetrahedron 57* **(2001)**,9225

**Figure 2.27.** *The main components of microwaves dielectric heating mechanism.*

Based on the theory available in the literature[3a, 12a, b, 40], a brief description of these mechanisms is the following:

**1)** Due to the oscillating field, the dipoles attempt to realign themselves in the electric field by rotation (in phase with the field). Their ability to align with the field is influenced by the irradiation frequency and liquid viscosity. For a very high frequency, the dipole does not have time to realign thus no heating occurs. The same happens when the time to change the direction of the field is longer than the dipole rotation. When the frequency is at value of interest (2.45 GHz in case of the microwave reactor) the dipoles have time to respond to the field, therefore rotate, but do not have sufficient time for completing the rotation due to the faster change of the field, generating a phase difference between the field and dipole orientations. This result in an energy lost in the form of heat through molecular friction and collision producing dielectric heating. The amount of heat generated is directly related to the ability of dipoles to align themselves with the frequency of the applied field.

**2)** During ionic conduction, the dissolved charged particles or ions oscillate back and forth under the influence of microwave irradiation, collide with the neighbor particles and ions and finally create heat. This heat effect is much stronger than of dipolar polarization and can be more advantageous for nanoparticles synthesized in ionic liquids[3c, 12c].

Two fundamental parameters define the dielectric properties of materials[40b]: the dielectric constant[e] ($\varepsilon'$) and dielectric loss[f] ($\varepsilon''$). The ratio of these two parameters gives the dielectric loss tangent ( $\varepsilon''/\varepsilon' = \tan \varepsilon$ ) that indicates the ability of a material to convert electromagnetic energy into heat at a given frequency and temperature. The efficient absorption and rapid heating of reaction media thus require high $\tan \varepsilon$ values such as of ethylene glycol (1.350), ethanol (0.941) and benzyl alcohol (0.667), etc. A more detailed list of organic solvents with different absorbing properties is presented in the **Chapter 6.3 Table A.iii.3.** Solvents with

---

[e] *Dielectric constant:* indicates the ability of media to be polarized by the electric field.
[f] *Dielectric loss:* indicates the efficiency of electromagnetic radiation conversion into heat.

relatively high loss tangent values (that is needed e.g., for nanoparticles production) have a short penetration depth[g] that may be problematic for industrial up-scale of the microwave process. In certain cases, solvents or other molecules with no permanent dipole moment and with transparency for microwave irradiation can also be used for microwave heating as long as they applied with other microwave-absorbent reagents in the reaction mixture. This can be useful for a selective heating mechanism offering the possibility of complex materials fabrication. It is worth mentioning that for most solvents, absorption of microwave irradiation decreases with the temperature (reduced bulk viscosity leads to reduced molecular friction), i.e., the reaction temperature may be limited in the microwave heating method. This is not the case for ionic liquids whereas the heat is generated by ionic conduction and absorption of microwave irradiation increases with the temperature.

## 2.3.2. Synthesis of ferrite nanoparticles

### Microwave-assisted non-hydrolytic sol-gel chemistry

Within microwave heating process for inorganic (e.g. metal oxide) nanoparticles preparation, Niederberger's group[4e, 12d, 39, 41] has developed a surfactant-free nonhydrolytic sol-gel[h] chemistry route based on the chemical transformation of metal oxide precursors (metal halides, alkoxides, acetates or acetylacetonates) into a metal oxide network in various organic solvents (alcohols, amines, aldehydes or ketones). These procedures gave access to a wide variety of binary, ternary and doped metal oxide nanoparticles with controllable crystallite shapes and sizes. They furthermore reported that the use of a coordinating organic solvent –as alternative to surfactant– has the following advantages: i) simpler approaches (the reaction mixture consists of precursor and solvent); ii) lower reaction temperature, up to 200°C; iii) products with higher purity. The organic solvent can act as reactant, control agent for particles growth, capping agent preventing agglomeration and source of oxygen for metal-oxide materials [42]. It has also been found that both the organic species with their organic side reactions[43] and experimental parameters (precursor concentration, reaction time and temperature)[44] strongly influence the structural and morphological characteristics of the inorganic material.

### Nanoparticles formation mechanism

According to the classical theory (thermal decomposition method), the formation of inorganic nanoparticles in solution involves two processes: nucleation and growth. A crucial prerequisite for monodispersed nanoparticles formation is to separate nucleation from growth, as already mentioned in **Section 2.1.1** in thermal decomposition, when the solution is supersaturated with monomers (phase 1), the burst nucleation takes place rapidly and

---

[g] *Penetration depth:* defined as the point where 37% of the initially irradiated microwave power is still present.

[h] By definition, the *classic aqueous or nonaqueous sol-gel process* is based on the formation of a sol (dispersion of colloidal particles in a liquid) followed by further reaction into a gel (a porous inorganic network enclosing a continuous liquid phase). The *sol-gel synthesis of metal oxide nanoparticles* can be considered rather a sol-precipitation process despite its sol-gel term due to the formation of metal-oxygen network at nanometer level.

large number of nuclei is produced (phase 2) that is followed by the growth of crystal particles through continued diffusion-controlled growth process (phase 3). If there is no additional nucleation during the aging time, size focusing with mean size increasing occurs. By increasing the aging temperature and time, the nanoparticles will grow further because of the Ostwald ripening process (coarsening). In the case of thermal decomposition, the whole process, including the cooling of reaction mixture, takes around 4 hours.

For microwave method, a schematization of the two possible mechanisms in the absence of coarsening effect (**Figure 2.28**) would be[12b]: i) fast burst nucleation with the formation of smaller nanoparticles with small size distribution; ii) a slower nucleation with the formation of bigger nanoparticles. For both mechanisms, the final nanoparticle size is determined by the amount of precursors introduced into the reaction mixture. Unfortunately, up to date, the MW effect is still a subject of controversy and intense debates and the whole process has not a unified theory.
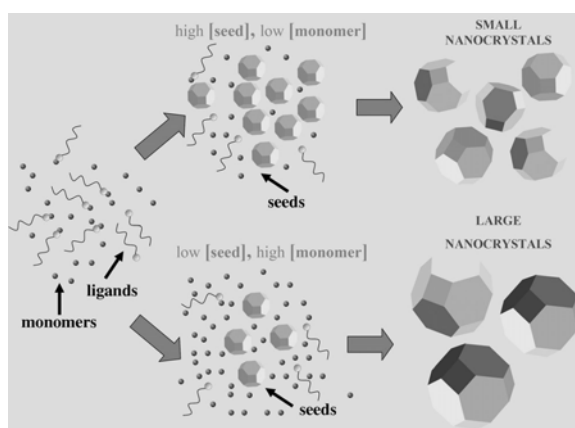


*Figure 2.28. The most possible mechanisms of size control obtained in microwave-assisted nanocrystals synthesis in the absence of Ostwald ripening effect*[12b]

Due to the very fast process in microwave heating (~ 25 minutes including cooling), a clear distinction between nucleation and growth is very difficult to make. Based on our experimental observation, the intention was to make a comparison regarding the nanoparticles formation mechanism between thermal decomposition and microwave heating methods. For this purpose in **Figure 2.29** we present a schematization of the two processes for producing ferrite nanoparticles.

To avoid confusions, a clear distinction has to be made:

1) *Thermal decomposition* (**Figure 2.29a**) consists in three experimental steps. Step 1–the reaction mixture (containing the organometallic precursors, solvent and surfactant) was heated under magnetic stirring up to 200°C ($T_1$) and kept at this temperature 2h. To reach the 200°C, it took 40 min. During this time (40 min) precursor dissolution followed by its decomposition and subsequently monomer accumulation with their solution supersaturation occurred (phase1). Around 180°C nucleation started (phase 2) with limited diffusion growth process of nanoparticles during the 2h at 200°C. Step 2– the mixture was further heated fast ~ 10 minutes to the reaction temperature of 300°C ($T_2$) and then kept 1 h at this temperature (step 3), aging period with the size focusing and nanoparticles growth (phase 3).

2) *Microwave heating* (**Figure 2.29b**) consists in similar three experimental steps with the following differences: Step 1 – the reaction mixture (containing the organometallic precursors, solvent and surfactant) were heated very fast (1 minute) to $T_1$ of 60°C and kept 5 minutes. In these 6 minutes, precursors dissolution occurs but the temperature is not high enough to decompose the precursors. Step 2– the mixture was directly heated ($t_{heating}$) to the reaction temperature of 160°C ($T_2 = T_{set}$) and kept at this temperature a few minutes (ranging 5–15 minutes) ($t_{set}$) being considered step 3. We assume that during heating time to reach the $T_{set}$, precursors decomposition and monomers accumulation might occur (phase 1 of the mechanism) including the nucleation around 140°C (phase 2). Step 3 is similar with the aging time in thermal decomposition corresponding the growth of nanoparticles (phase 3) with the difference that in microwave additional nucleation could take place.
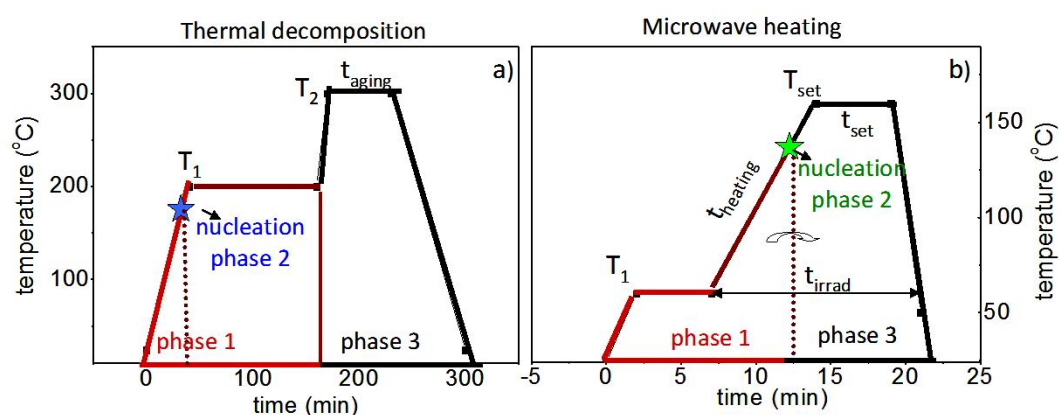


**Phase 1**: dissolution and decomposition of the precursors with monomers accumulation
**Phase 2**: ⭐ Burst nucleation (T ~ 180 °C) (a)
       ⭐ Burst ( T ~ 140 °C) or slow nucleation (T in the range of 140-160 °C) (b)
**Phase 3**: Growth of nanoparticles by size focusing and/or Ostwald ripening (a)
       Additional nucleation and simultaneously growth of nanoparticles by Ostwald ripening (b)

*Figure 2.29* Schematization of nanoparticles formation mechanisms by: *(a)* thermal decomposition and *(b)* microwave syntheses.

*Set time* ($t_{set}$) is a parameter that can be controlled in the microwave–heating process. It is an input data of the program and refers to the time at constant reaction temperature ($T_{set}$). *Heating time* ($t_{heating}$) is the time needed to heat the solution mixture up to the reaction temperature ($T_{set}$) and depends on the power input used (200 W or 300 W in our case). Furthermore, we observed that it plays a crucial role in nucleation. A drawback of our microwave process was the impossibility of full control over $t_{heating}$. It was experimentally observed that under the same reaction conditions, $t_{heating}$ showed a fluctuation of a few minutes from day to day. Therefore for a more accurate interpretation of the results, we used the experimental parameter named *irradiation time* ($t_{irrad}$, $t_{irrad} = t_{set} + t_{heating}$). Moreover, as we experimentally observed, a burst nucleation occurs when the heating time ($t_{heating}$) from $T_1$ (60°C) to $T_{set}$ (160°C) was very short (< 5 min; achieved by using a maximum power of 300 W) suggesting a fast precursor decomposition rate. At 200 W, less microwave energy was absorbed and the precursor conversion rate was decreased (correlating to a longer $t_{heating}$).

This resulted in less monomers[i] formation and subsequently a slower nucleation along a temperature range of 140–160°C took place. This affected nanoparticles growth, increasing their polydispersity: due to the additional nucleation during the aging time ($t_{set}$), the nanoparticles will grow further because of the Ostwald ripening process.

Based on these observations, the bottleneck of the microwave heating route similar with thermal decomposition can be considered the phase 2 and 3 of the mechanism in which the power input with directly influenced on $t_{heating}$ and $t_{irrad}$ seems to play an important role in the final nanoparticles size and quality.

For producing high quality ferrite nanoparticles, one has to take into account several experimental parameters that have an influence on the final material. For example, the nanoparticles size (diameter) depends on:

> precursor concentration $C_{Fe(acac)3}$ (M);
> irradiation time ($t_{irrad}$) (min) including $t_{heating}$ and $t_{set}$;
> reaction temperature ($T_{set}$) (°C);
> maximum power used (200 or 300 W) with its direct influence on heating rate ($t_{heating}$);
> presence/absence and type of surfactant during synthesis.

Their influence will be discussed in more details in **section 2.3.3**

### Experimental conditions

For the synthesis of $MFe_2O_4$ (M = Mn, Fe) nanoparticles, a non–aqueous sol–gel chemical reaction, similar to the one reported by Niederberger et al.[13], was followed. The most relevant difference in our case was the use of surfactants (steric OAc or electrostatic DTAB and/or TMAOH) as stabilizers, either during or after the synthesis, in order to assure monodispersity and long–term colloidal stability of the NPs. Additionally, for comparison purposes, a study was done to compare iron oxide nanoparticles produced by the microwave heating method and by thermal decomposition, using both the same stabilizers and precursor concentration[45]. In case of $MnFe_2O_4$ nanoparticles, a study on irradiation time influence[46] and deposition over different nanostructures[7] was undertaken, since such nanoparticles were used for the fabrication of 2D[46] or 3D[7] magneto-photonic crystal materials, which will be discussed in the next chapters (**Chapters 3.3 and 4.4**).

Five series of experiments were performed to study the influence of several parameters on the synthesis such as; the precursor type and concentration, irradiation time, reaction temperature and the presence/absence of surfactant(s).

**Table 2.3** summarizes the experimental conditions used in microwave heating for manganese ferrite and iron oxides nanoparticles production (detailed data for each experiment can be found in **Chapter 6.3 Table A.iii.4**). During $MnFe_2O_4$ nanoparticles syntheses (labeled *A_MW.MnFe₂O₄_x* and *B_MW.MnFe₂O₄_x*), the irradiation times ($t_{irrad}$), the presence/absence of oleic acid surfactant were varied and the reaction temperature ($T_{set}$ of 160°C) and irradiation power of 200 W (determining the $t_{heating}$) were constant. During iron oxide nanoparticles syntheses the influence of precursor type ($Fe^{3+}$, $Fe^{2+}$) and

---

[i] *Monomers*: defined as the chemical subunits contributing to crystal growth by either condensation onto or dissolution from the nanoparticle surface.

concentration, $t_{irrad}$, amount and type of surfactants (steric or electrostatic), $T_{set}$, different irradiation power (200 or 300W) on nanoparticles formation was investigated (*C_MW.iron oxide_x and D_MW.iron oxide_x, E_MW.iron oxide_x*). For each type of synthesis, a few experiments were performed and x corresponds to the experiment number.

*Table 2.3. Experimental conditions for different syntheses of ferrites NPs.*

| Synthesis | Precursors molar ratio M$^{2+}$(Mn or Fe) : Fe$^{3+}$ | Molar ratio Fe$^{3+}$ : OAc or DTAB | Microwave set parameters | | | $t_{irrad}$ (min) |
|---|---|---|---|---|---|---|
| | | | $T_{set}$(°C) | $t_{set}$ (min) | Power (W) | |
| *A.MW.MnFe$_2$O$_4$_x* | 1:2 | 1:3 (OAc) | 160 | 45s–5 | 200 | 4–12 |
| *B.MW.MnFe$_2$O$_4$_x* | 1:2 | 1:0 | | | | 6–21 |
| *C.MW.iron oxide_x* | 1:2 | 1:3 (OAc) | 160 | 3–5 | 200 | 10–21 |
| *D.MW.iron oxide_x* | 0:3 | 1:3 (OAc) | 160 | 1–10 | 200 | 8–25 |
| | | 1:a:b * | 200 | 15 | 300 | 17–20 |
| *E.MW.iron oxide_x* | 1:2 | 1:0 | 160 | 3 | 200 | 11 |
| | 0:3 | 1:0 | 160–200 | 5 | 300 | 6–17 |

* a–OAc, b–DTAB, with the molar ratios a:b of 2.5:0; 1.5:1; 1:1.5; 0:2.5.

## 2.3.3. The structure and morphology of ferrite nanoparticles

### Structural analysis

Powder X-ray diffraction (XRD) patterns of MnFe$_2$O$_4$ and iron oxide (**Chapter 6.3 Table A.iii.4**) are presented in **Figure 2.30**. Concerning MnFe$_2$O$_4$, all reflections (**Figure 2.30a**) could be indexed with those of the cubic inverse spinel manganese ferrite phase (ICDD PDF075-0035). For iron oxide, the distinction between magnetite and maghemite was not possible due to the very close reflection peaks of the two standards (ICDD PDF019-0629 and PDF039-1346) and the broad reflection peaks observed for the as-prepared iron oxide nanoparticles (**Figure 2.30b**). Moreover, the lattice parameters obtained from Rietveld refinement were 8.364 ± 0.001 Å for iron oxide systems, which is an intermediate value between the lattice constants of the two phases in bulk form, 8.350 Å for maghemite and 8.396 Å for magnetite [47]. Titration analyses revealed the presence of only 5 % of Fe$^{2+}$ in all *D_MW.iron oxide_6.10* in comparison with an expected 33% for pure magnetite. We thus conclude that our materials consist of a mixture of the two phases and will be referred hereafter as iron oxide nanoparticles. The crystalline domains calculated from the peak broadening refinements gave 2.76 ± 0.01 nm for *A_MW.MnFe$_2$O$_4$_5.2*, 5.41 ± 0.02 nm for *D_MW.iron oxide_6.10*. Moreover, the measured lattice spacing from the selected area electron diffraction (SAED) patterns (**Figure 2.30 right images**) are in good agreement with the XRD data for MnFe$_2$O$_4$ and iron oxide respectively.
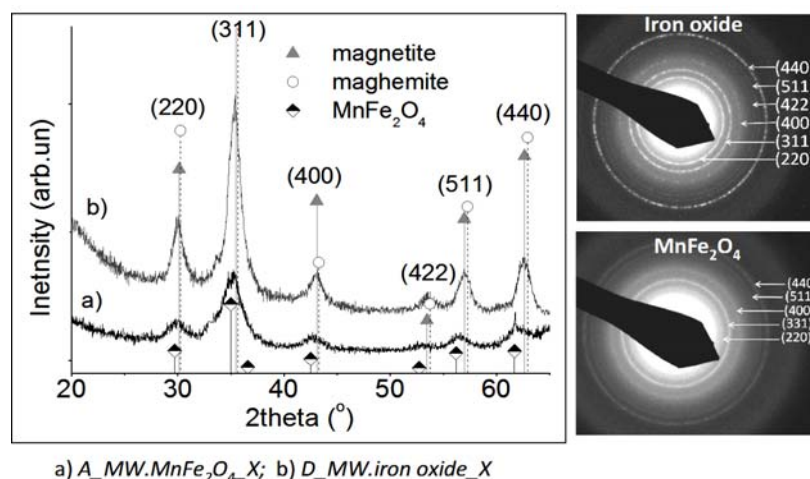
a) A_MW.MnFe$_2$O$_4$_X; b) D_MW.iron oxide_X

**Figure 2.30.** X-ray diffraction and SAED patterns corresponding to MnFe$_2$O$_4$ (**a**-exp.5.2) and iron oxide (**b**-exp 6.10) NPs synthesized by microwave heating.

### Influence of cation type and precursor concentration

In our standard procedure, Fe$^{3+}$ precursor was mixed with M$^{2+}$ (Mn, Fe) precursor in benzyl alcohol and in presence/absence of oleic acid surfactant (molar ratio of Fe$^{3+}$: OAc of 1 : 3).By varying the cation while the total precursor concentrations (0.13–0.15 M), reaction temperature (160$^o$C) and irradiation time (10 $\pm$1 min) were the same, we obtained similar nanoparticles size. The applied cations molar ratios were the following: Fe$^{3+}$:Mn$^{2+}$ of 2:1 (*A_MW.MnFe$_2$O$_4$_5.2*, **Figure 2.31a**); Fe$^{3+}$:Fe$^{2+}$ of 2:1(*C_MW.iron oxide_6.18*, **Figure 2.31b**); Fe$^{3+}$:Fe$^{2+}$ of 3:0 (*D_MW.iron oxide_6.13*, **Figure 2.31c**) and the size of the prepared nanoparticles were 3.9 $\pm$ 0.7 nm (Fe$^{3+}$:Mn$^{2+}$), 5 $\pm$ 1.1 nm (Fe$^{3+}$:Fe$^{2+}$) and 5 $\pm$ 2.5 nm (Fe$^{3+}$), respectively.
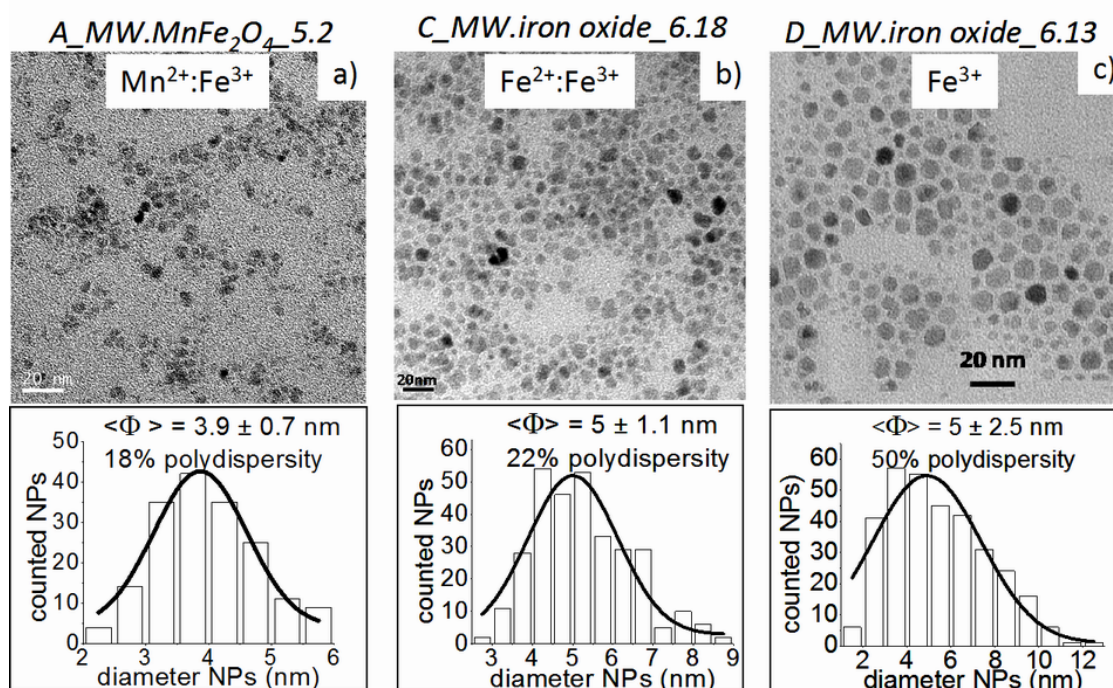


**Figure 2.31.** TEM images of ferrite nanoparticles synthesised with different cations. The lower insets show NPs size distributions by Gaussian fitting.

When the precursor concentration is higher, the nanoparticles are larger as observed for both thermal decomposition[48] and microwave heating [44] processes. This correlation was confirmed in our study for iron oxide: under similar synthesis conditions ($T_{set}$ of 160°C and irradiation time of 10 min). Fe(acac)$_3$ concentrations of 0.13 M (*D_MW.iron oxide_6.2*), 0.1 M (*D_MW.iron oxide_6.6*) and 0.072 M (*D_MW.iron oxide_6.13*) resulted in nanoparticles sizes of 6.7 ± 2 nm, 5.5 ± 1.4 nm and 5 ± 2.5 nm, respectively. Detailed experimental data can be found in **Chapter 6.3 Table A.iii.4.**

**Influence of irradiation time ($t_{irrad}$) and reaction temperature ($T_{set}$)**

Niederberger's group reported that in *surfactant-free non-aqueous sol-gel chemistry*, the supersaturation with monomers results from an organic reaction including the following two steps[43]: (1) fast dissolution of the precursor that is facilitated by the microwave energy directly transferred to the reactants; (2) enhanced alcoholisis reaction[j] between the acetylacetonate ligand and benzyl alcohol solvent[49]. This promotes a fast production of monomers and consequently an earlier nucleation. Since the surface of oxides nuclei is covered by hydroxyl groups, known for microwave-absorbing capabilities, the local surface temperature increases, producing the so-called "hot spots" and thus the particles surface is activated for further condensation reactions, i.e., metal-oxygen-metal bond formation, representing the main mechanism of nanoparticles growth.

The *irradiation time* ($t_{irrad}$) controls the size of nanoparticles. For iron oxide, two examples are presented (**Figure 3.32**): the same $T_{set}$ of 200°C and $t_{irrad}$, of 8 min (*D_MW.iron oxide_6.23*, **Figure 3.32a**) and 25 min (*D_MW.iron oxide_6.22*, **Figure 2.32b**) resulted in 4 and 11 nm respectively.



a) *D_MW.iron oxide_6.23*    b) *D_MW.iron oxide_6.22*

$t_{irrad}$ of 8 min, $T_{set}$ of 200°C    $t_{irrad}$ of 25 min, $T_{set}$ of 200°C

20 nm    20 nm
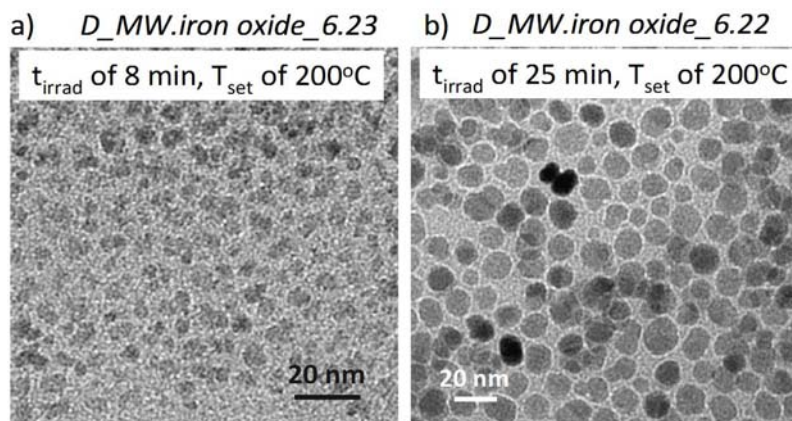
*Figure 2.32. Influence of $t_{irrad}$ on nanoparticles size*

The same effect of $t_{irrad}$ over NPs size was furthermore observed for the synthesis in the absence of surfactant. For instance (*E_MW.iron oxide_6.21*) resulted in nanoparticles size of 5.5 nm with a polydispersity of 14.5%, while 21 min (*E_MW.iron oxide_6.33*), gave 6.8 nm and 19%, respectively.

For the synthesis of nanoparticles in benzyl alcohol solvent and in the absence of surfactant (e.g. ZnO) was found that NPs growth follows the Lifshitz–Slyozov–Wagner (LSW) model

---

[j] *Alcoholisis* a reaction in which a chemical bond (C –C) is broken by the addition of alcohol.

(describing the Ostwald ripening process)[43a]. We have been verified if this model could be applied for our ferrite nanoparticles but synthesized in the presence of oleic acid surfactant, in particular for iron oxide nanoparticles. According to the LSW theory, adapted for our reaction, the diffusion limited coarsening can be described by eq.2.5:

$$r^3 - r_0^3 = k \cdot t_{irrad} \qquad \text{(Eq. 2.5)}$$

where $r_0$ is the average particle radius (nm) at $t_{irrad}$ zero, r is the average particle radius (nm) produced at $t_{irrad}$ (min) and k is the first-order growth rate constant (nm$^3$/min). In **Figure 2.33**, the (volumetric) growth of iron oxide NPs (synthesized at 160°C, 200 W, in presence of oleic acid and at $Fe^{3+}$ :OAc molar ratio of 1:3) is plotted in the function of $t_{irrad}$. The linear correlation between $r^3$ and $t_{irrad}$ gives a growth constant (k) of 4 nm$^3$/min. According to this, the LSW theory of diffusion limited coarsening can also be applied for iron oxide nanoparticles growth in the presence of surfactant.
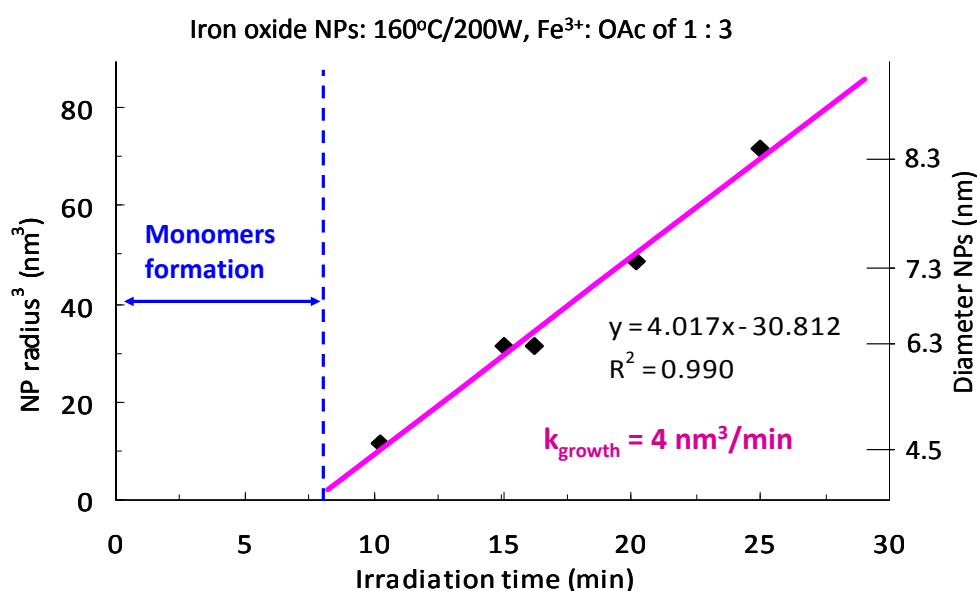


**Figure 2.33.** *Correlation between the iron oxide radius$^3$ (measured by TEM) and irradiation time.*

Beside $t_{irrad}$, the other crucial parameter affecting the crystal size is the *reaction temperature*. Such in case of the thermal decomposition method, in microwave heating, higher reactor temperature gives bigger NPs size. At an irradiation power of 300 W and $t_{irrad}$ of ~7 min, the $T_{set}$ values of 160°C (*E_MW.iron oxide_6.19*), 180°C (*E_MW.iron oxide_6.20*) and 200°C (*E_MW.iron oxide_6.21*) resulted in the NPs sizes of 3.5 ± 0.7 nm, 4.4±0.6 nm and 5.5 ± 0.8 nm, respectively.

### 3D plots of the influence of two variables on nanoparticles size

Although the microwave process may seem easy to be performed at first glance, the interpretation of the results can be difficult due to the numerous (both dependent and independent) variables in the NP formation. In contrast to thermal decomposition, in microwave heating, it was not possible to vary one of the experimental parameters and keep

the others constant at the same time; at least, one of these conditions was a dependent variable during NP synthesis. For example, a higher initial $C_{Fe(acac)3}$ contributes to shorter $t_{heating}$ (and $t_{irrad}$); a higher $T_{set}$ generates longer $t_{heating}$ at the same power input, etc. **Figures 2.34 and 2.35** tried to illustrate the influence of two-two variables on the prepared nanoparticles size. Unfortunately, no clear tendencies in NP diameter variation could be observed. In order to plot the NP size function surfaces, a more detailed experimental design is required. This was not the aim of the thesis but could be included as a future work.



*Figure 2.34*. 3D plot of the influence of variables $C_{Fe(acac)3}$ and $t_{irrad}$ on nanoparticles size.
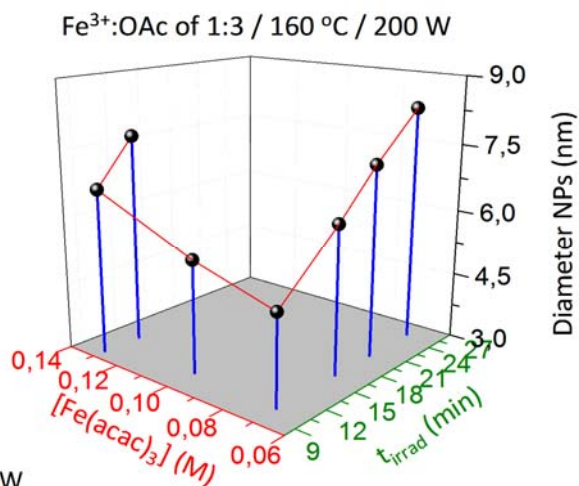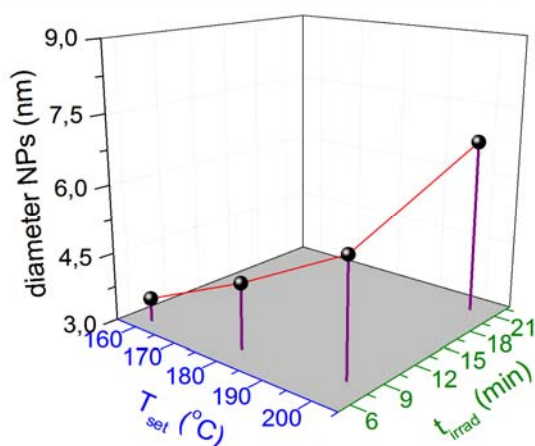


*Figure 2.35*. 3D plot of the influence of variables $T_{set}$ and $t_{irrad}$ on nanoparticles size.

**Influence of surfactants type on size and nanoparticles monodispersity**

As presented in thermal decomposition method, the surfactants (consisting of a coordinating polar head group and a long alkyl chain as a tail) adsorb reversibly to the surfaces of the growing nanoparticles providing a dynamic organic capping layer that stabilizes them in solution and also mediates their growth. The use of two surfactants with different binding affinities to the nanoparticles surface or with selectivity towards specific crystal facets, allow us the control over crystal size, size distribution and morphology. An important point which has to be kept in mind when employing surfactants in microwave heating is the fact that often the organic stabilizers could be potential reactants taking part in the chemical reactions[3b].

Very good quality spinel ferrites nanoparticles ($MFe_2O_4$, M = Fe, Mn, Co), have been produced by thermal decomposition method using oleic acid and oleylamine as surfactants

in the molar ration $Fe^{3+}$: OAc : OAm of 1:3:3[15]. We tried to use in microwaves both stabilizers (OAc and OAm) in the same molar ratio for the synthesis of $MnFe_2O_4$ nanoparticles (*A_MW.MnFe2O4_5.1*) but unfortunately the reaction did not work well:

- The reaction mixture reached the $T_{set}$ of 160°C, very slowly (8 min), showing the presence of non microwaves absorbing components formed perhaps during heating, as by-products of organic side reactions[42, 43b].

- The yield was small (a few black precipitate).

- After 3 steps centrifugation, the magnetic precipitate was partially re-dispersable in hexane with DLS measurements showing two peaks corresponding to two differentiated population (**Figure 2.36 –the plot of full squares**).

By employing just oleic acid for the $MnFe_2O_4$ synthesis (*A_MW.MnFe2O4_5.2*, *Figure 2.31a*), the reaction mixture reached the $T_{set}$ of 160°C faster with a better reaction yield. DLS measurement (**Figure 2.36 –plot of empty squares**) showed just one peak attributed to monodispersed nanoparticles and TEM analysis revealed $MnFe_2O_4$ nanoparticles with small size of 3.9 ± 0.7 nm.
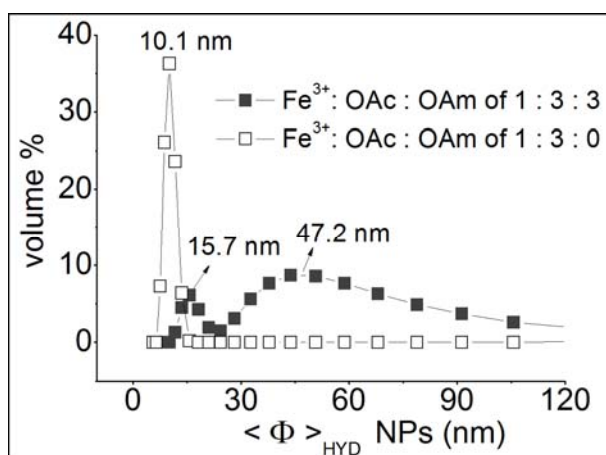


***Figure 2.36**. DLS data of the $MnFe_2O_4$ nanoparticles synthesized in the presence of one (empty squares) and two (full squares) surfactants.*

Considering these results, oleic acid was a better choice to be used as a stabilizer during chemical synthesis either for $MnFe_2O_4$ or iron oxide nanoparticles. Also we have investigated the possibility of adding the surfactant after the reaction was completed and the use of non-polar or polar surfactants to yield the direct stabilization in organic or aqueous media of the nanoparticles. For $MnFe_2O_4$ nanoparticles synthesised in the absence or in the presence of the oleic acid, the size was found similar (**chapter 6.3 Table A.iii.4**). As an example, $MnFe_2O_4$ synthesised in the absence of oleic acid (*B_MW.MnFe2O4_8.2*) had a mean value of 3.8 ± 0.8 nm and the presence of the surfactant gave a value of 3.9 ± 0.7 nm (*B_MW.MnFe2O4_5.2*). Iron oxide synthesised in the absence of surfactant was 5.5 ± 0.8 nm (*E_MW.iron oxide_6.21*) and in the presence of surfactant was 4 ± 0.8 nm (*D_MW.iron oxide_6.23*). Thus, the microwave approach gave the possibility of adding a surfactant either at the beginning or at the end of the chemical reaction and still maintaining the small sizes and monodispersity of the nanocrystals.

**Figure 2.37** shows the DLS measurements to monitor the monodispersity of iron oxide nanoparticles in different media (organic/water) as prepared and after a few months of liquid storage. For nanoparticles dispersed in hexane and synthesized in the presence of oleic

acid, the distributions at preparation (**Figure 2.37a**) show a maximum around 13.5 nm irrespective of the precursors used, a mixture of Fe(acac)$_3$ and Fe(acac)$_2$ (*C_MW.iron oxide_6.18*) or only Fe(acac)$_3$ (*D_MW.iron oxide_6.10*). When adding steric (oleic acid) (*E_MW.iron oxide_2.13*) or electrostatic surfactants (TMAOH) (*E_MW.iron oxide_6.25*) after the nanoparticles are formed, the peak positions also coincide (monodispersity is preserved) although the peak is slightly shifted to a larger value (around 15.7 nm). The width of the distribution for the nanoparticles dispersed in hexane (hex) is similar in all cases. The nanoparticles dispersed in water (w) show a larger polydispersity likely due to a bigger tendency of nanoparticle agglomeration in water. By checking the stability of nanoparticles a few months later (**Figure 2.37b**), we found out that: i) the nanoparticles synthesised in the presence of surfactant (*C_MW.iron oxide_6.18 and D_MW.iron oxide_6.10*) preserve the monodispersity, the DLS peak had the same value of 13.5 nm; ii) the monodispersity is lost and nanoparticles tend to aggregate, when the surfactant was added after the nanoparticles were formed. In the case of the steric surfactant (*E_MW.iron oxide_2.13*), smaller aggregates (DLS showed a peak at around 24 nm) were forming during the four month of hexane storage. Nanoparticles capped with electrostatic surfactant formed larger aggregates in time (DLS peak at ~ 32 nm). An explanation could be that the steric surfactant (oleic acid) used during chemical reaction makes stronger bonds (covalent type) with the nanoparticles surface, preserving the chemisorbed organic shell longer time. But the simply physical mixing of the formed nanoparticles with the steric/electrostatic surfactant will create a predominantly physisorbed organic shell which could in time be lost much more easily than the chemisorbed one. We should then conclude that although microwaves produce particles of nanometer size without the need of surfactants to hinder the particle growth, a given amount of surfactant must be used, preferably during the synthesis reaction, in order to achieve long time monodispersity.
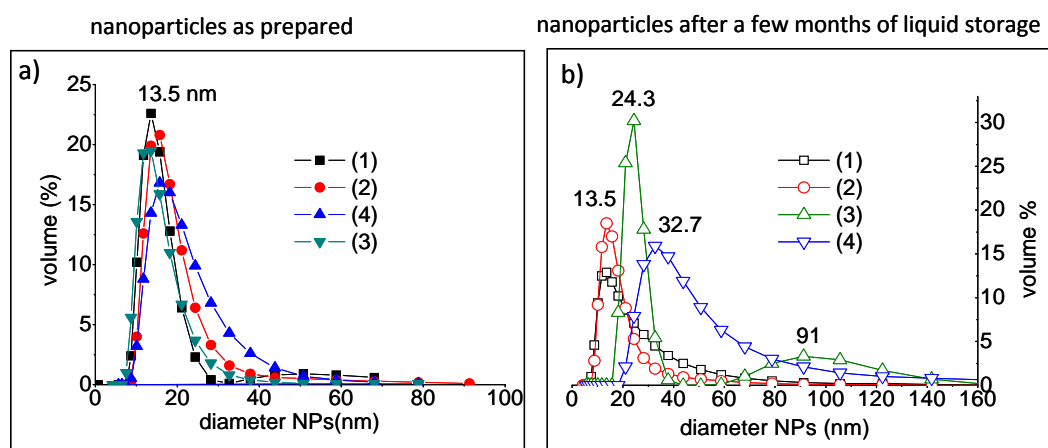


(1)  *C_MW.iron oxide_6.18*.hex; (2) *D_MW.iron oxide_6.10*.hex
(3) *E_MW.iron oxide_2.13.hex*; (4) *E_MW.iron oxide_6.25*.w

*Figure 2.37*. *DLS measurements corresponding to the stability of iron oxide nanoparticles synthesised by microwave in the presence/absence of stabilizers.*

The surfactant can be also used as shape-controlling agent with selectivity towards specific crystal facets. In this regards, an ionic surfactant known to absorb selectively to certain facets of the spinel ferrite, inducing strongly faceted nanoparticles formation is dodecyl trimetyl ammonium bromide (DTAB)[50]. It is a strong cationic surfactant (**Figure 3.38)** which can

absorb electrostatically (with its head group) to the {100} facets inhibiting its growth and therefore causing a more rapidly growth along {111} direction and thus producing elongated morphology[50a, b]. The nanoparticles shape will be very much influenced by the amount of cationic surfactant used. With the proper molar ratio of precursor to surfactant, rice-like structures magnetite[50a] or ferrite nanorods[50b] have been produced.
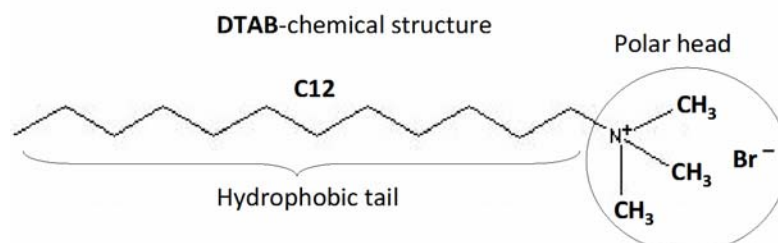


*Figure 2.38* The structure of the cationic surfactant.

In the following work our intention was to fabricate by microwave heating route, iron oxide nanorods or Au_iron oxide heterostructures, reported for the conventional high-temperature organometallic decomposition method[50b]. We adapted for microwave a synthesis reported by George. C et al.[50b, 51]. To get heterostructures of spherical Au with ferrite nanorods, the authors used the nucleation of Fe ions (from decomposition of iron carbonyl) over preformed gold nanoparticles in the presence of surfactants oleic acid, oleylamine and the cationic one dodecyl dimethyl ammonium bromide (DDAB). The presence of DDAB induced a rod-shaped growth of the ferrite domain on each Au seed.

In our experiments (*D.MW_iron oxide_6.27 – 6.33*) we used Fe(acac)$_3$ precursor combined with oleic acid and a similar cationic surfactant, dodecyl trimetyl ammonium bromide (DTAB), at $T_{set}$ of 200 °C, $t_{set}$ of 15 min, $t_{irrad}$ in the range 17–21 min and maximum power output of 300 W. But contrary to the expected[50b, 51], roughly spherical nanoparticles were produced. The surprise was that using DTAB alone during synthesis, we produced larger nanoparticles of ~ 11 nm with a better defined shape (*D.MW_iron oxide_6.27*) (**Figure 2.39b**) than the nanoparticles of mean size ~ 5.5 nm and undefined shape (*D.MW_iron oxide_6.28*) (**Figure 2.39c**) produced when oleic acid was used alone. Using together the two surfactants and varying the molar ration between them (**Figure 2.39d and e**), nanoparticles with mean size of 8.3 (*D.MW_iron oxide_6.29*) and 9.2 nm (*D.MW_iron oxide_6.30)* respectively were obtained. Keeping the same experimental conditions, the nanoparticles prepared in the absence of both surfactants showed spherical shape and mean size of ~ 6.8 nm (*D.MW_iron oxide_6.33,* **Figure 2.39a**).
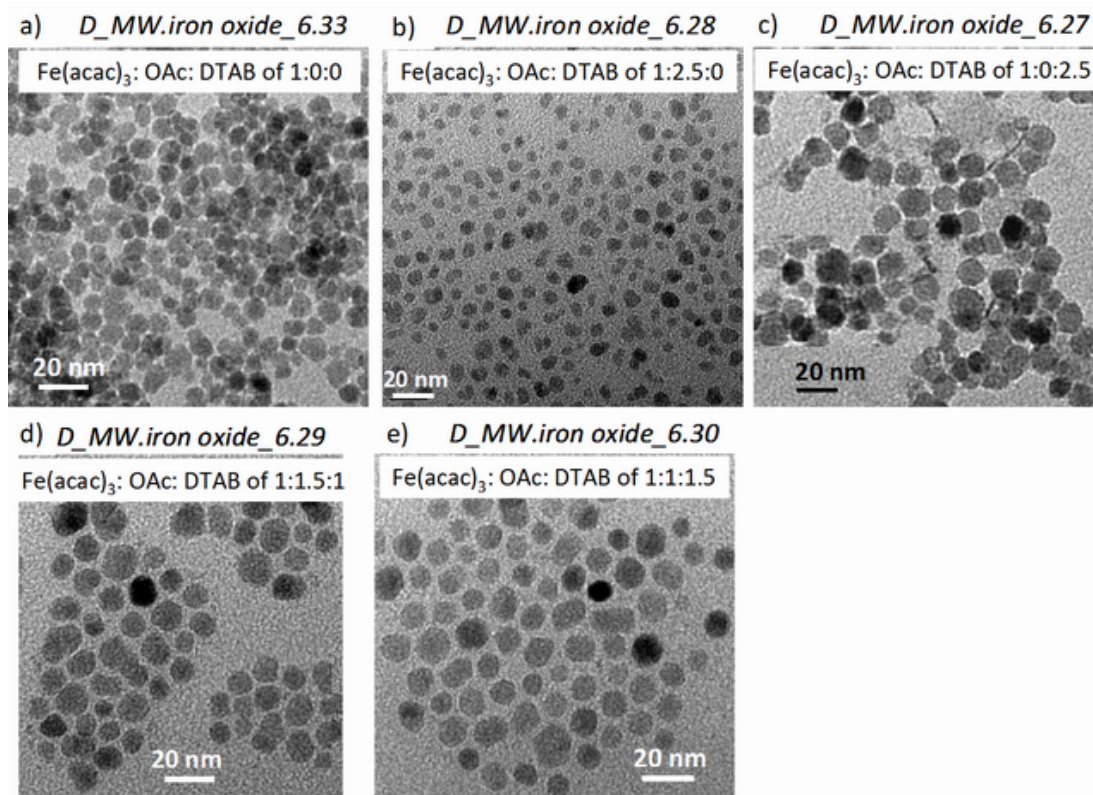
**Figure 2.39** *TEM micrographs of iron oxide nanoparticles synthesized in the absence and presence of surfactants with different molar ratios, $T_{set}$ of $200\,°C$ / $300$ W/ $t_{irrad}$ of 17–21 min.*

How can we interpret these results? As was discussed earlier, the main mechanism of nanoparticles growth was assumed to be the condensation reaction between hydroxyl groups present on the nuclei surface. In the absence of any surfactant (**Figure 2.40a**), just hydroxyl groups can be found at the nanoparticles surface which activates the surface by creating the "hot spots". By adding a surfactant in the reaction mixture, the surface functional groups could be changed and thus activate/inactivate the surface for further condensations reactions.

1.  By adding only oleic acid (**Figure 2.40b**), is possible that it chemisorbs onto the particles surface through a bi-dentate bond as was found for similar synthesis, discussed in **Section 2.3.4.** Thus it could happen that not many hydroxyl groups will be left on the surface to promote the condensation reaction and subsequently no further growth of particles will occur. Moreover, the non-polar tail of the oleic acid being part of the organic shell around nanoparticles and also being transparent to the microwave radiations could inactivate the surface by decreasing the local surface temperature with respect to the bulk solution.

2.  By adding the cationic surfactant (**Figure 2.40c**), which electrostatically adsorbs to the nuclei surface, not only it preserves the hydroxyl groups but also increases the charges of the shell with the extra $N^+$ and $Br^-$ ions from the DTAB, promoting a higher absorption of the microwave radiation. As a consequence, the surface local temperature will be higher so the condensation reaction rate will increase, resulting in a much faster growth of the nanoparticles.

3. By adding the two surfactants, we assume that the two mechanisms (1&2) could take place, competing, and this will dictate the size of the final nanoparticles.
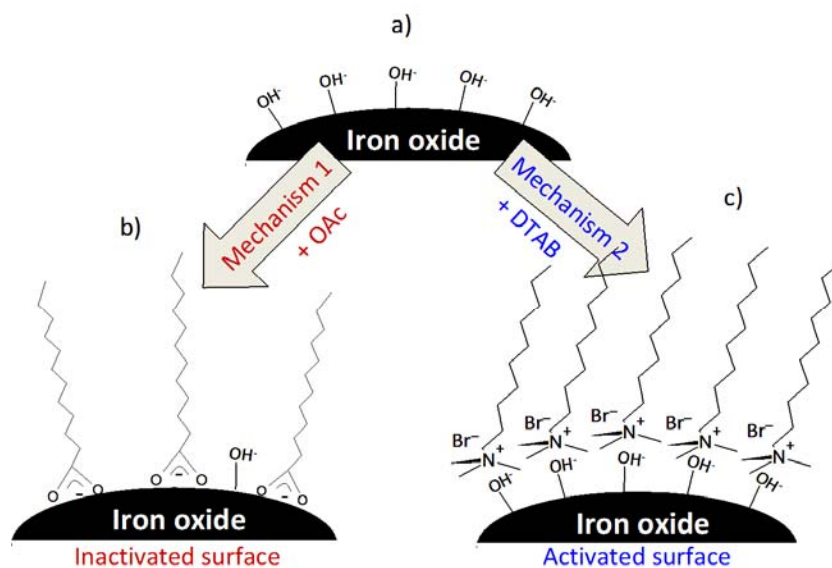


***Figure 2.40.*** *Two possible mechanisms for the nanoparticles synthesis by microwave heating using steric or electrostatic stabilizers.*

## 2.3.4. Comparison with thermal decomposition –iron oxide case

In this section we present on the comparison of the physico-chemical properties of iron oxide nanoparticles of comparable sizes around 6 nm fabricated by microwave-assisted synthesis and by thermal decomposition method. We present that both methods allowed us preparing monodisperse crystalline nanoparticles with a high saturation magnetization value although microwave nanoparticles presented more irregular shapes and higher polydispersity than those obtained by thermal decomposition. A relevant difference was the smaller surface reactivity of the nanoparticles resulted from the microwave route. We observed that the difference in surface reactivity have resulted from the lower energy of the crystallographic faceting planes. Such characteristic can be worth considering depending on the targeted final application, in particular when long time aggregation or particle growth is undesirable. A simplified life cycle analysis for the two preparation routes is included as a preliminary framework towards nanoparticles eco-design. In terms of cost, a positive balance for the microwave synthesis was clearly attained

**Iron oxide by the two methods**

To compare the properties of the iron oxide nanoparticles resulted from microwave and thermal decomposition synthesis, the same iron precursor, $Fe(acac)_3$, concentration (0.072M) and surfactant (oleic acid in the molar ratio to $Fe^{3+}$ of 3 to 1) added at the reaction mixture, were used. Microwave nanoparticles were stabilized using oleic acid while oleic acid and oleylamine at 1:1 molar ratio were used in thermal decomposition. For the easier

understanding of the comparison, the labels for the iron oxide prepared by the both method, are *(iron oxide)$_{MW.C}$* and *(iron oxide)$_{TD}$*. The organically stabilized nanoparticles were subsequently transfer to water by a ligand exchange procedure (subscript MW.C_water and TD_water) described elsewhere[45], for possible biomedical applications.

To visualize the synthesised materials, the corresponding TEM images with size distribution histograms are presented in **Figure 2.41**. At first glance only slight differences in the size and shape of nanoparticles can be observed although a higher polydispersity value is found for the nanoparticles prepared by the microwave route. A possible explanation in the case of microwave synthesis could be that the effective separation of nucleation and the growth is not as well defined as in the case of the thermal decomposition method where two well separated temperatures differentiate the two processes (160–180°C for the nucleation and 300 °C for the particle growth by size focusing)[16b].

The average diameters obtained by TEM (counting 250-300 particles) are larger than the sizes of the coherent diffraction domains extracted from the Rietveld refinement of XRD patterns **(Table 2.4)**. Such differences are indicative of the decreased cristallinity of the nanoparticle surfaces and calculating $100 \ (<\Phi>_{TEM} - <\Phi>_{XRD}) \ /<\Phi>_{TEM}$, values close to 15 % were obtained for both systems. The comparable cristallinity of (iron oxide)$_{MW.C}$ and (iron oxide)$_{TD}$ rules out that the differences in surface reactivity presented below could originate from different overall cristallinity and can instead be ascribed to intrinsic characteristics of the nanoparticles surfaces resulting after each synthesis.

**Table 2.4.** *The measured diameters size and standard deviations of the nanoparticles using different techniques. Cluster sizes of the water stabilized nanoparticles after ligand exchange and after 30 days (subscript 30d) are included.*

| Material | Nanoparticles monodispersed in organic media | | | | Clusters of nanoparticles in water | |
|---|---|---|---|---|---|---|
| | $<\Phi>_{XRD}$ (nm) | $<\Phi>_{TEM}$ (nm) | $<\Phi>_{HYD}$ (nm) | $M_S$ (emu/g) | $<\Phi>_{HYD}$ (nm) | $<\Phi>_{HYD-30d}$ (nm) |
| *(iron oxide)$_{TD}$* | 4.60 ± 0.01 | 5.3 ± 0.9 | 10.8 ± 1.5 | 62 | 28 ± 3 | 49 ± 3 |
| *(iron oxide)$_{MW.C}$* | 5.40 ± 0.02 | 6.3 ± 1.5 | 12.7 ± 1.5 | 60 | 22 ± 0.5 | 23 ± 1 |



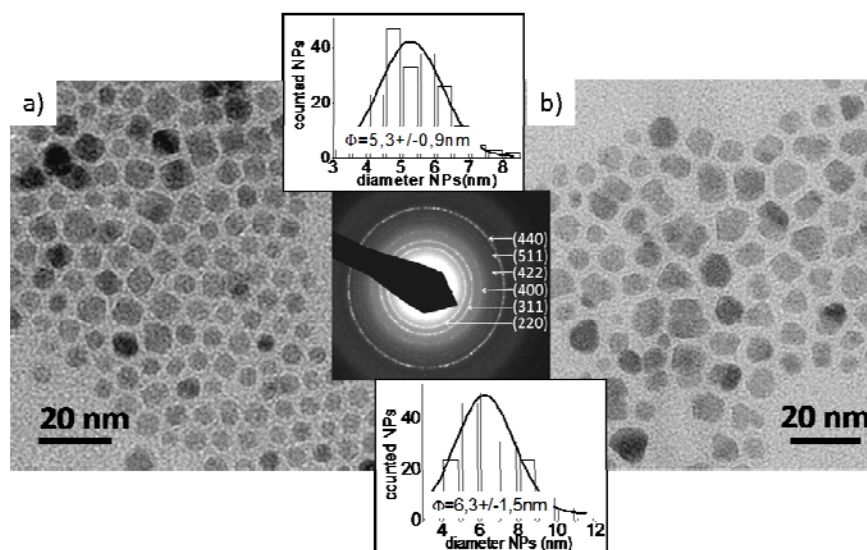**Figure 2.41** *Iron oxide nanoparticles synthesized by microwave route and thermal decomposition: (a) (iron oxide)$_{TD}$ and (b) (iron oxide)$_{MW.C}$. Size distributions, fitted to a Gaussian function are included as insets (a-b). Inset (a-b) represents the selected area electron diffraction (SAED) pattern.*

## Surface chemistry and reactivity

A more detailed look at the morphology of the nanoparticles showed that in the case of thermal decomposition a large fraction of nanoparticles were monocrystalline and spherical/hexagonal in shape, with only a small number of larger rectangular ones (**Figure 2.42a**). High-resolution TEM investigations revealed that the crystallographic faceting planes of the hexagons presented high Miller indexes (202, 220 and 022) and thus higher surface energy (**Figure 2.42b**).The high-index planes usually have higher surface energy ($\gamma$),and for the face-centred-cubic phase this sequence $\gamma$ {111}< $\gamma$ {100}< $\gamma$ [52]< $\gamma$ {220}[53] can be generated from the distance between those planes and the central Wulff's point[54]. In contrast microwave particles presented a more irregular shape, lobular-like, but still a main fraction was monocrystalline. In this case the crystallographic faceting planes were of low Miller indexes {110, 001, 112} (**Figure 2.42d**) conferring lower surface reactivity to the microwave nanoparticles.
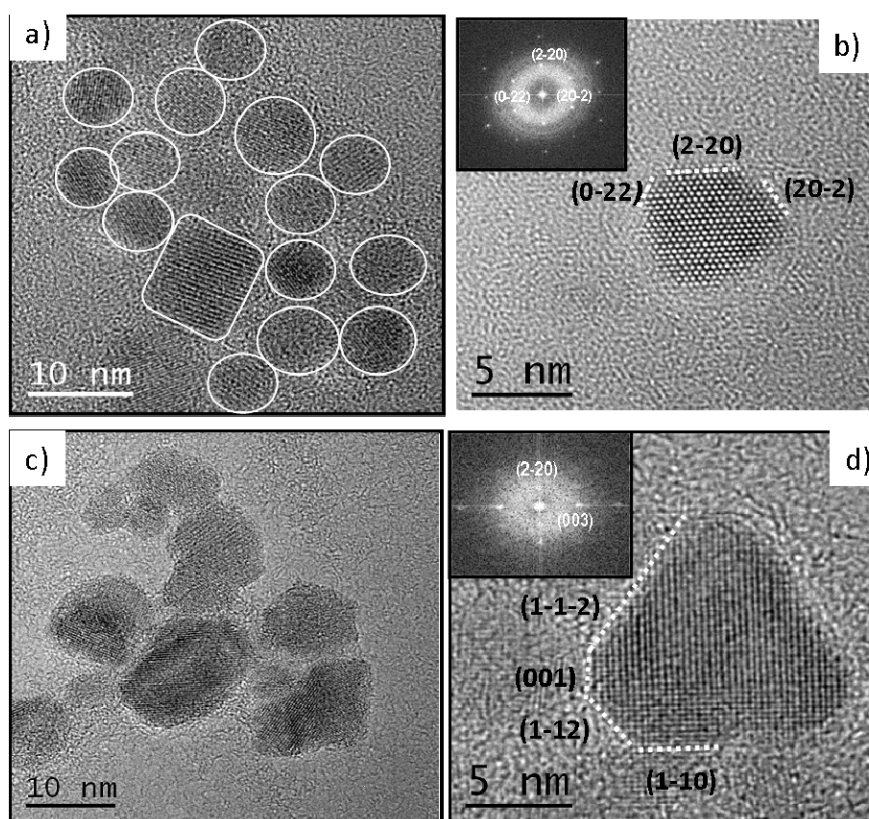


***Figure 2.42***. *HRTEM images: (**a**) several (iron oxide)$_{TD}$ nanoparticles where the regular shape is evidenced, (**b**) a hexagonal (iron oxide)$_{TD}$ nanoparticle in the{111} zone axis condition, faceting planes are indicated (the inset corresponds to the Fast Fourier Transform (FFT), (**c**) several (iron oxide)$_{MW\_C}$ nanoparticles where the irregular shape is evidenced, (**d**) a lobular (iron oxide)$_{MW\_C}$ nanoparticle in the [52] zone axis condition, faceting planes are indicated (the inset corresponds to the FFT).*

The more reactive surface of the (iron oxide)$_{TD}$ system could be also evidenced by the Cryo-TEM analysis of the nanoparticle clusters formed after their transfer from organic media to water. The images (**Figure 2.43**) show that the clusters of (iron oxide)$_{TD\_water}$ have more

dendritic and ramified structures than those of (iron oxide)$_{MW.C\_water}$ which are more compact and rounded in shape.
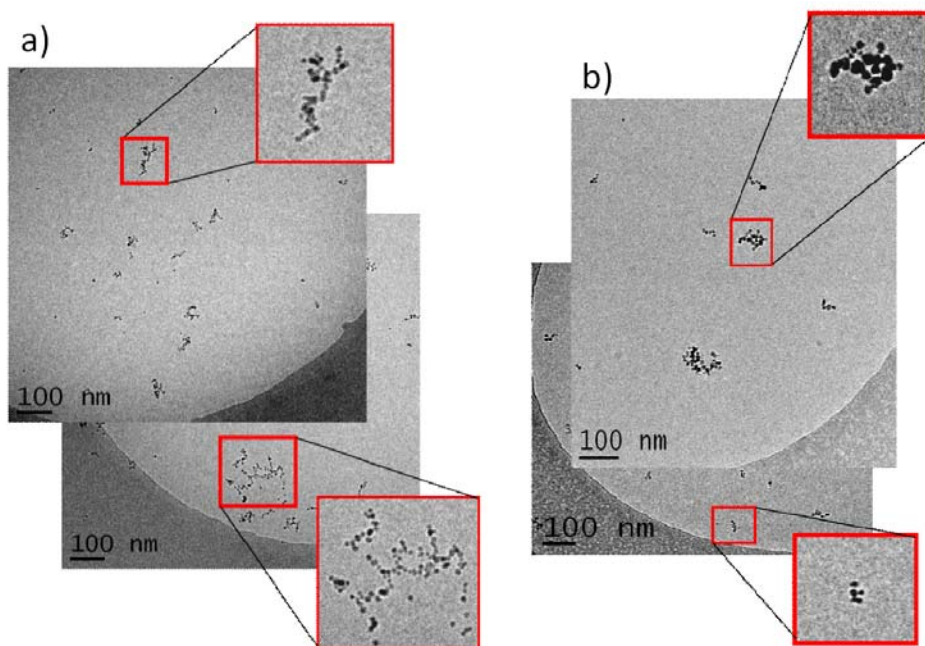


***Figure 2.43*** *Cryo-TEM micrographs of the clusters formed after solvent exchange from organic to aqueous media:* **(a)** *the (iron oxide)$_{TD\_water}$ system forming dendrite shape clusters and* **(b)** *the (iron oxide)$_{MW.C\_water}$ system forming more compacted and rounded clusters.*

Secondly, we have been interested in investigating how the differences in surface reactivity can be identified or finger printed by several other techniques. Dynamic light scattering (DLS) measurements, thermo gravimetric analysis (TGA) and infrared spectroscopy (IR) were further used to collect information on the surface chemistry of the nanoparticles. DLS measurements and the photograph of a cuvette with a clear brown solution are shown in **Figure 2.44a**. The hydrodynamic diameter ($<\Phi>_{HYD}$) which includes the magnetic core ($<\Phi>_{TEM}$) and the organic shell (length of the oleic acid ~2 nm) is in all cases larger than the diameter determined by TEM. Considering one monolayer of surfactant, the hydrodynamic diameter can be approximated as $<\Phi>_{HYD} = <\Phi>_{TEM} + 4$ nm[55]. DLS gives a $<\Phi>_{HYD}$ value of 10.8 $\pm$ 1.5 nm for *(iron oxide)$_{TD}$* which is in good agreement with the one monolayer approximation. In the case of *(iron oxide)$_{MW.C}$* the $<\Phi>_{HYD}$ value is larger (12.7 $\pm$ 1.5 nm) and can be approximated as $<\Phi>_{TEM} + 6$ nm. This can be attributed to a quasi–bilayer or interdigitated bilayer configuration, due to the chemisorbed (chemical bonding of carboxylate groups to the surface $Fe^{3+}$) and physisorbed ligands (oleic acid molecules inserted between adjacent coordinated oleic acid)[28, 56]. The hydrodynamic diameter of particle clusters formed in aqueous solutions was measured by DLS at the moment of the solvent exchange (**Figure 2.44a**) and after one month. It was found that the (iron oxide)$_{MW.C\_water}$ system formed more stable aggregates than the (iron oxide)$_{TD\_water}$ one. Indeed, repeating the measurement after one month, the (iron oxide)$_{TD\_water}$ clusters showed a size increase of about 40 % but the size for (iron oxide)$_{MW\_water}$ clusters remained constant: the hydrodynamic diameter of (iron oxide)$_{MW.C\_water}$ clusters was 22 $\pm$ 0.5 nm after the solvent exchange and 23 $\pm$ 1 nm after one month while the hydrodynamic diameter of (iron oxide)$_{TD\_water}$ clusters

increased from $28 \pm 3$ nm to $49 \pm 3$ nm after one month. Again, this finding also supports the higher reactivity of (iron oxide)$_{TD}$ nanoparticles.

      To support the hypothesis of mono or interdigitated layer, thermo gravimetric analyses were performed aiming to qualitatively studying the bonding strength of the surfactant. A stronger bond (chemisorption) is associated with weight losses at higher temperature while a weaker bond (physisorbed specimens) present weight losses at lower temperatures[28]. Therefore, one single step of mass loss in the TGA profile is expected when chemisorption is predominant and two or more steps when physisorbed and chemisorbed molecules are present[28, 30]. The TGA curves are shown in **Figure 2.44b**. The 200 – 500°C temperature range was considered as the surfactant desorption zone. Below 200 °C, the slight weight loss is due to the solvent evaporation, from 200°C onwards the free oleic acid starts to desorb[57]. In the range 200 – 500°C only one step was observed for *(iron oxide)$_{TD}$* (**Figure 2.44–black line**) with a 17 % weight loss, associated with chemisorption of oleic acid. In contrast, two steps were observed for *(iron oxide)$_{MW.C}$* (**Figure 2.44b–orange line**) suggesting the existence of both chemisorbed and physisorbed molecules. In the 200 – 300°C range a first step of 19.6 % weight loss is observed (step I) followed by a second one 19.5 % between 300 – 500°C (step II).
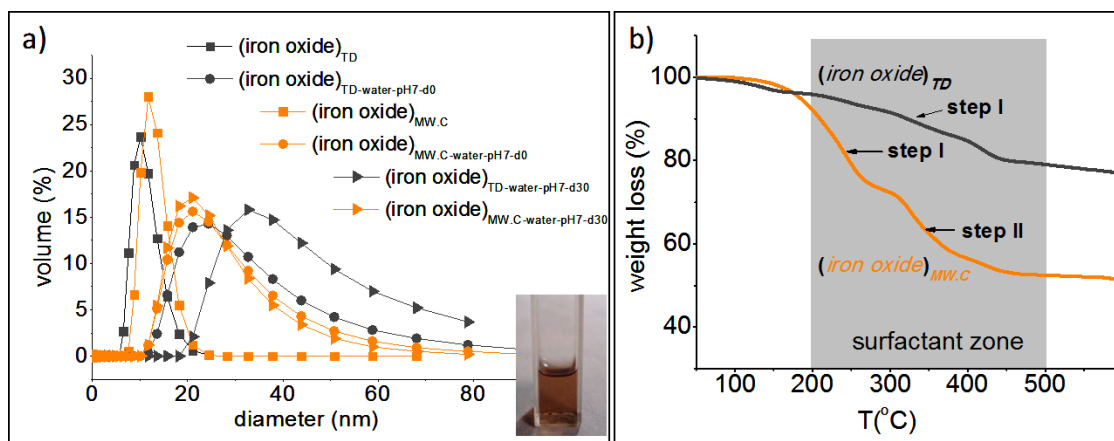


***Figure 2.44.*** *(a)* *Dynamic light scattering measurements on a stable colloidal dispersion of the synthesized nanoparticles.* *(b)* *Thermo gravimetric analysis.*

Using the experimental weight loss % values it is possible to quantify the number of surfactant molecules (physisorbed or chemisorbed) per nanoparticle. Among the different approximations that can be found to assess it[30, 56], we have chosen the following relation[30b]:

$$\text{weight loss}\% = 100\,\frac{m_s}{m_{NP} + m_s} = 100\,\frac{\dfrac{\pi d^2 \cdot M_s}{a \cdot N_A}}{\dfrac{1}{6}\pi d^2 \cdot \rho_{maghemite} + \dfrac{\pi d^2 \cdot M_s}{a \cdot N_A}} \qquad \text{(Eq. 2.6)}$$

where $m_s$ is the mass of the surfactant and $m_{NP}$ is the mass of the inorganic magnetic core, the weight loss % can be taken from a TGA run, $\rho_{maghemite} = 5.49$ g/cm$^3$, the molecular mass of oleic acid is $M_S = 282.5$ g and $N_A$ is the Avogadro's number. Considering that the average number of surfactant molecules ($n_S$) onto the magnetic particle surface is given by eq. 2.7,

where $d$ = $<\Phi>_{TEM}$ (TEM diameter of the nanoparticles) and $a$ = surface area occupied by one surfactant molecule.

$$n_S = \frac{A_{NP}}{A_S} = \frac{4\pi r^2}{a} = \frac{\pi d^2}{a} \qquad \text{(Eq. 2.7)}$$

Substituting (eq.2.7) in (eq.2.6) the expression for surfactant coverage is the following:

$$n_S = \frac{\text{weight loss}\% \cdot \frac{1}{6}\pi d^2 \cdot \rho_{maghemite} \cdot 6.023}{M_S\left(1 - \frac{\text{weight loss}\%}{100}\right)} \qquad \text{(Eq. 2.8)}$$

The same equation was used to calculate the number of physisorbed ($n_S^{Ph}$) and chemisorbed ($n_S^C$) molecules. Knowing the number of surfactant molecules per nanoparticle one can calculate the surface grafting coefficient ($\zeta$) which gives the density of surfactant molecules per square nm [30a]. **Table 2.5** gathers the surfactant coverage ($n_S^{Ph}$ and $n_S^C$) using eq.2.8 and the grafting coefficients ($\zeta^C$ and $\zeta^{Ph}$) that give additional information about the arrangement of those surfactant molecules. In the case of *(iron oxide)$_{TD}$* the grafting coefficient is 3.6 molecules/nm$^2$. This is close to the expected theoretical maximum value for a complete monolayer of chemisorbed oleic acid onto a nanoparticle surface [39] and in agreement with the value of 3.5 molecules/nm$^2$ experimentally obtained by Tomoaia-Cotisel *et al.* [42]. For (iron oxide)$_{MW.C}$ the chemisorbed grafting coefficient is smaller (3.0 molecules/nm$^2$), indicating that the surfaces of these nanoparticles present lesser number of active sites for oleic acid chemisorption.

These results indicate once more that the surface reactivity of (iron oxide)$_{TD}$ is greater than that of (iron oxide)$_{MW.C}$. Moreover, the physisorbed grafting coefficient obtained for (iron oxide)$_{MW.C}$ (3.0 molecules/nm$^2$ ) is comparable to the corresponding chemisorbed one, as expected for interdigitated structures. One can expect this physisorbed shell to be stable against cleanings due to the hydrophobic interaction between the carbonyl chains of chemisorbed and physisorbed oleic acid molecules.

*Table 2.5* *Thermogravimetric data of iron oxide nanoparticles synthesized by the two methods. Parameters characterising the nanoparticles surface coverage that have been calculated from these data and the particle size are included.*

| material | $<\Phi>_T$ EM (nm) | $A_{NPs}$ (nm$^2$) | $<\Phi>_{HYD}$ (nm) | Weight loss % | | $n_S^{Ph}$ molec/ NP | $n_S^C$ molec/ NP | $\zeta^{Ph}$ molec/ nm$^2$ | $\zeta^C$ molec / nm$^2$ | Obs• |
|---|---|---|---|---|---|---|---|---|---|---|
| | | | | step I | step II | | | | | |
| *(iron oxide)$_{MW.C}$* | 6.3 ± 1.5 | 125 | 12.7 ± 1.5 | 19.6 | 19.5 | 374 | 371 | 23 | 3 | IML$_{Ph+C}$ |
| *(iron oxide)$_{TD}$* | 5.3 ± 0.9 | 88 | 10.8 ± 1.8 | 17 | – | – | 314 | | 3.6 | ML$_C$ |

•*ML$_C$*= monolayer of chemisorbed surfactant molecules on the NP surface

•*IML$_{Ph+C}$*= interdigitated layers formed by one monolayer of chemisorbed surfactant with an inserted physisorbed layer

$A_{NP} = \pi <\Phi>_{TEM}^2$ ; $\zeta^{Ph} = n_S^{Ph} / A_{NP}$; $\zeta^C = n_S^C / A_{NP}$

These findings are also supported by the infrared spectra (IR) displayed in **Figure 2.45**. When comparing the iron oxide nanoparticles prepared by the two methods, the presence of two sharp bands at 2925 and 2855 cm$^{-1}$ in all four spectra is attributed to the stretching of $CH_2$ (asymmetric and symmetric) and -$CH_3$ of saturated alkyl chain fragments. The peak at 1710 cm$^{-1}$ found in free oleic acid and also in *(iron oxide)$_{MW.C}$* nanoparticles is due to the free carboxylic group, which in the case of nanoparticles, indicates the presence of oleic acid physisorbed at the surface. The absence of the aforementioned peak in the spectra of *(iron oxide)$_{TD}$* shows that in this case there is no free physisorbed surfactant. Instead, the presence of both asymmetric and symmetric carboxylate stretch at 1526 and 1412 cm$^{-1}$ for *(iron oxide)$_{MW.C}$* and at 1543 and 1403 cm$^{-1}$ for (iron oxide)$_{TD}$ indicates that oleic acid is chemisorbed onto the particles surface through a bi-dentate bond, in agreement with our interpretation of TGA curves. The strong peak at 583 cm$^{-1}$ for both types of nanoparticles is characteristic for the Fe-O bond of the nanoparticles core.
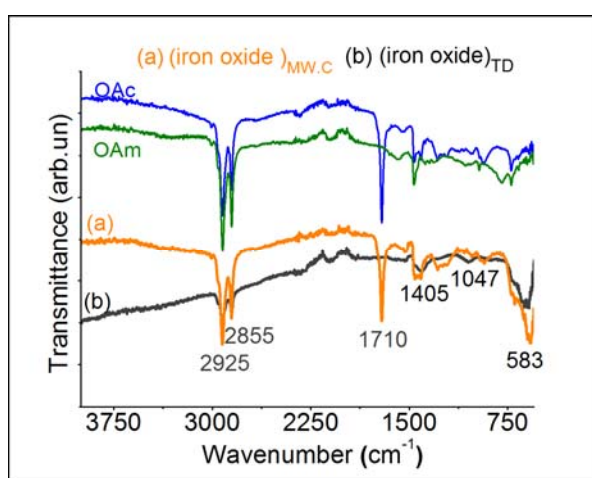


*Figure 2.45. Infrared spectra of the free surfactants and of the iron oxide systems: (a) (iron oxide)$_{MW.C}$ and (b) (iron oxide)$_{TD}$.*

### Life Cycle Analysis

The Life Cycle Analysis (LCA) of a product/material should provide the tools and methodology to assess and quantify the impact of a specific product/material[58]. LCA thus defines the boundaries for the conception of an environmentally-benign product/material and it constitutes the starting framework for the concept of eco-design. Without having the ambition of performing a LCA for our materials, we have made a comparative study in terms of material yield and resources involved to produce 1 g of iron oxide nanoparticles by microwave and thermal decomposition methods. The results are gathered in Table 3 which contains: i) the energy (computed by the time needed for the chemical reaction to take place at a given temperature) and time consumption; ii) the potential toxicity of the reagents used not only for human body but also for environment and iii) an estimation of the production cost (in Euros). The reaction yield is similar in both cases although a slightly smaller yield was found for the microwave method.  It is to note that by increasing the microwave heating temperature, from 160$^o$C to 200$^o$C, the yield increased up to 85 %. To produce 1 g of iron oxide by thermal decomposition takes three times longer (a batch of 130 mg takes 160 min) than by microwaves (a batch of 22 mg takes 15 min). Moreover, since the working

temperature, heating power and reaction time is much lower in the case of the microwave synthesis; the energy consumption of this technique is reduced by a factor of 10 as compared to thermal decomposition. Regarding the safety of the reagents, benzyl alcohol and benzyl ether are both harmful if inhaled or absorbed through the skin[59]. Benzyl alcohol in small quantity is non-threatening but benzyl ether may cause long-term environmental damage. Oleic acid may be harmful in big quantities (>230mg/kg) and oleylamine is corrosive[60]. Then, the presence of oleylamine and benzyl ether in thermal decomposition method makes this approach more environmentally burdening compared to the microwave method.

The production costs have been estimated considering the prices of reagents and energy[61]. It turns out that the production of 1 g of iron oxide nanoparticles is 40 % cheaper by microwaves than by the thermal decomposition method. In addition the microwave synthesis does not require working under inert atmosphere and can yield stable dispersions in either polar or non-polar solvents. Other synthetic methods, namely from oleate complexes also use inexpensive and environmentally friendly compounds and can produce large-scale nanoparticles of excellent quality

*Table 2.6. Precursors and synthetic parameters to produce 1 g of iron oxide nanoparticles by microwave and thermal decomposition methods.*

| Synthesis Information | MICROWAVE (iron oxide)$_{MW.C}$ | Thermal Decomposition (iron oxide)$_{TD}$ |
|---|---|---|
| Iron Precursor (g) | Fe(acac)$_3$–5.6 g | Fe(acac)$_3$–5.4 g |
| Solvent (ml) /safety | benzyl alcohol (204.5ml)/ harmful[60], non-toxic[59] | benzyl ether (183ml) /harmful & dangerous for environment |
| Surfactant (ml) /safety | oleic acid (15ml) / irritant[60] | oleic acid (15ml) /irritant + oleylamine (15ml) /corrosive[60] |
| Reaction Yield (%) | 79% | 82% |
| Time (min) | 682 min (~11h) | 1756 min (~29h) |
| Maximum Temperature (° C) | 160 °C | 300 °C |
| Energy consumption (kWh) | 2.3 kWh | 20.5 kWh |
| Price (reagents + energy) | 166 euros | 274 euros |
| Working atmosphere | no need to work in an inert atmosphere | need to work in an inert atmosphere |
| Colloidal stability | organic / aqueous media | organic media |

## 2.3.5. Magnetic properties

The magnetic properties of ferrites nanoparticles were evaluated by magnetisation *vs* magnetic field measurements at 300 K, 5 K and zero-field-cooled (ZFC), field-cooled (FC) temperature dependent magnetization curves. **Figure 2.46a–b** shows typical magnetization curves for superparamagnetic nanoparticles with no hysteresis loop neither remnant magnetization nor coercivity at room temperature. The magnetic units of emu/g for both systems (manganese ferrite and iron oxide) were based on the mass of metal oxide core (excluding the surfactant mass). The saturation magnetization increases with the nanoparticles sizes. In the case of manganese ferrite, Ms has a value of 44 emu/g for a mean size of 4.9 nm (*B_MW.MnFe$_2$O$_4$_2.11*), 41 emu/g for 3.9 nm (*A_MW.MnFe$_2$O$_4$_5.2*) and 16 emu/g for the smallest nanoparticles (3.2 nm) (*A_MW.MnFe$_2$O$_4$_4.3*). These values are larger

than those found in some previous reports[4f, 62] but, as expected, smaller than that of the bulk (i.e. 110 emu/g at room temperature). The values determined experimental for Ms respect to the iron oxide size are the following: 74 emu/g for ~11 nm (*D_MW.iron oxide_6.22*), 59 emu/g for ~ 6.3 nm (*D_MW.iron oxide_6.15*), 44 emu/g for ~ 5 nm (*E_MW.iron oxide_6.18*) and 35 emu/g for ~ 3.5 nm (*E_MW.iron oxide_6.19*). For the other experiments which have produced similar size nanoparticles, the Ms is summarize in the **Chapter 6.3 table A.iii.4** with the difference that the unit emu/g correspond to the mass of nanoparticles weighted, with the surfactant mass included (no TGA analysis available for the all experiments).

Superparamagnetism at room temperature was also confirmed by the ZFC-FC magnetization curves (**Figure 2.46a-b –left insets**). For the all ferrite nanoparticles synthesised by microwave heating, the ZFC magnetization increases with the temperature until reaching a maximum value corresponding to the blocking temperature ($T_B$). Above this temperature, the thermal energy ($K_B T$) becomes larger than magnetic energy barrier and the nanoparticles enter in the superparamagnetic domain. It can be seen that $T_B$ is increasing with the nanoparticles size, as was expected. For very small nanoparticles with small size distribution, the ZFCFC peak has a sharp shape, as could be observed for $MnFe_2O_4$ and also iron oxide (3.5 nm). With the increasing in size and polydispersity also the ZFCFC shape is broadening, being in good agreement with the TEM measurements.

By comparing Ms of around 6 nm iron oxide nanoparticles prepared by microwave and thermal decomposition, the magnetizaton are similar as 59 emu/g and 62 emu/g respectively, pointing to the high degree of cristallinity of both systems. The temperature dependent magnetic measurements also show that the magnetic susceptibility at low field is about 40 % larger for (iron oxide)$_{MW.C}$ than for (iron oxide)$_{TD}$. It is important to highlight here that from the magnetic point of view iron oxide nanoparticles prepared by a simple technique as microwave synthesis can be as good as those prepared by more complex and costly thermal decomposition (comparable saturation magnetization) or even outperform the latter in some respects (higher magnetic susceptibility at low field). In these regards the microwave technique is clearly superior compared to other simple synthetic techniques such as co-precipitation witch tend to yield less well crystallised iron oxide nanoparticles with much lower saturation magnetization saturations[63].
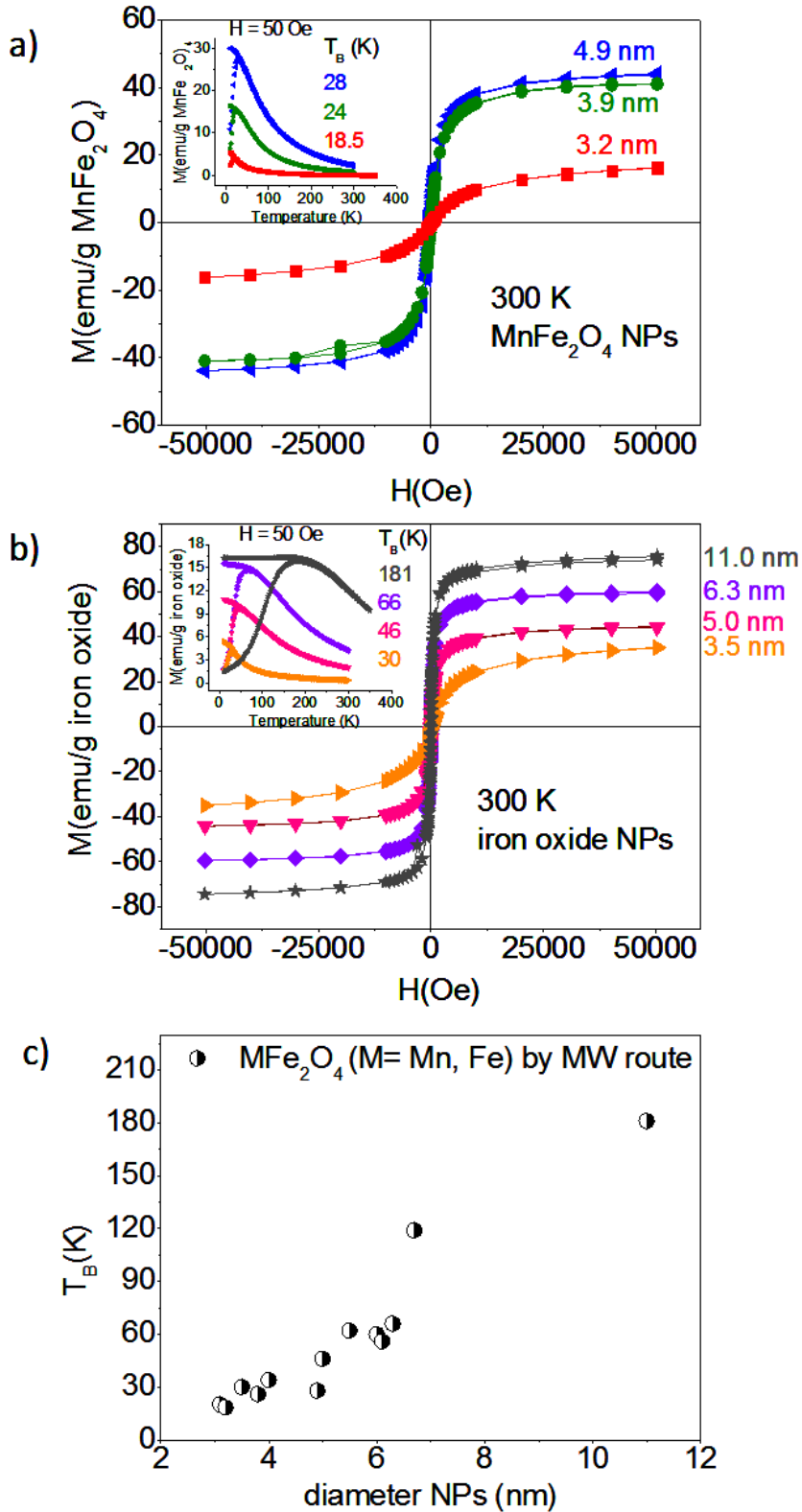
**Figure 2.46.** *Magnetic characterization of the manganese ferrite (**a**) iron oxide (**b**) nanoparticles. Comparison of M(H) at 300 K and ZFC–FC (**a**-**b**-insets) between different sizes. (**c**) Size dependence of the blocking temperature of ferrite nanoparticles*

# 2.4  CONTINUOUS  SUPERCRITICAL  ETHANOL  SYNTHESIS– FERRITE ($MnFe_2O_4$, $Fe_3O_4$) NPs

This work was part of a 3 months PhD research stage in Bordeaux (France) at Institut de Chimie de la Matière Condensée de Bordeaux (ICMCB-CNRS) within Supercritical Fluids group. Due to the short period of time and the novelty of the approach, we performed just a few experiments and the processing results are still in progress. However, the results seem to be promising and this could open new ways in the near future for nanoparticles preparation at industrial scale. In this section a brief presentation of the results will be done, with a more detailed investigation to be accomplished as future work.

## 2.4.1 Synthesis in supercritical fluids

The term supercritical fluid (SCF) refers to a substance that is above both its critical temperature and pressure. When the substance is placed within supercritical (SC) region only a single phase exists  and the fluid exhibits mixed properties of the normal liquid and gas: gas-like transport properties i.e. diffusivity and viscosity, surface tension zero while keeping the liquid–like density and the capabilities to dissolve other substances. By small variation of temperature and pressure, these physical properties can be continuously adjusted from gas to liquid[9c, 64] (**Figure 2.47**). The local organization of SCF, containing both gas and liquid like density, is a dynamic one and these density fluctuations give the high fluid compressibility.
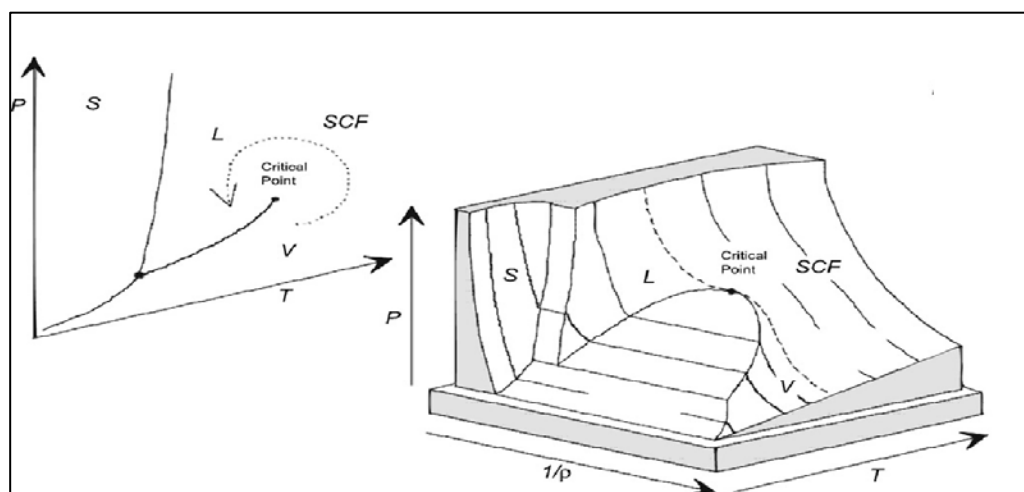


***Figure 2.47*** *State surface of a pure component: p-pressure, T-temperature,  –density, S–solid, L–liquid, V–vapor, SCF–supercritical fluid[64]*

These unique features make supercritical fluids (SCF) attractive solvents in chemical processes for the preparation of nanoparticles[8] or complex functional nanomaterials[9]. Moreover, the rapid heating rate, high reaction rate, high temperature and short residence time lead the production of nanoparticles through a burst nucleation process followed by crystal growth[8c, 65]. When the reaction is performed in a continuous way, it is believed[65a] that

the nucleation takes place in the mixing point in the case of preheated reagent streams and the further crystal growth and aggregation occur in the reactor[9d, 66]. But little is known about the chemical reactions taking place during nanoparticles formation at high temperature and pressure. A drawback of the continuous setup is that due to the nanoparticles aggregation, coagulation may appear at the inner walls, ending with a blocked reactor[8f] even it is claimed that the high density of SCF may avoid the aggregation[8e]. The use of surfactants during SCF synthesis could overcome the nanoparticles aggregation [8a, 8f], even so the coagulation is not completely removed as was observed in our experiments. Small changes in temperature and pressure of the SCF results in large density changes and thus the reaction kinetics, the thermodynamical properties of the reaction media and subsequently the size and shape of the synthesized nanoparticles can be controlled by varying the main operating parameters (pressure, temperature, nature of solvent(s) and reagent(s), concentration of reagents, residence time)[8a, 67].

In this work, we varied the residence time, the precursor type and the surfactant quantity. The summary of the experimental conditions is presented in **Table 2.7.**

*Table 2.7. Experimental conditions for different syntheses of ferrites NPs in cscEtOH*

| Material label | Before mixing | | | | | After mixing | | | | |
| | Precursor(s) (P) in EtOH | | Surfactants in EtOH | | $Q1$ ($\mu l$/ min) | $C_{Pf}$ (M) | $T_c$ (°C) | $p_c$ (Bar) | $R_t$ (min) | $Q1$ ($\mu l$/ min) |
| | type | $C_{Pi}$ (M) | molar ratio | $C_{SI}$ (M) | | | | | | |
| A_cscEtOH. Fe₃O₄_x | Fe(NO₃)₃ | $2 \cdot 10^{-2}$ | OAc:OAm 1:1 | $6 \cdot 10^{-2}$ | 675 225 450 | $1 \cdot 10^{-2}$ | 260 | 200 | 1 3 1'30s | 1350 450 900 |
| B_cscEtOH. Fe₃O₄_x | Fe(acac)₃ | $2 \cdot 10^{-2}$ | OAc:OAm 1:1 PEG (M_w=400) | $6 \cdot 10^{-2}$ | 450 | $1 \cdot 10^{-2}$ | 260 | 200 | 1'30s | 900 |
| A_cscEtOH. MnFe₂O₄_x | Fe(NO₃): Mn(ac)₂ 2:1 | $2 \cdot 10^{-2}$ | OAc:OAm 1:1 | $6 \cdot 10^{-2}$ | 450 | $1 \cdot 10^{-2}$ | 260 | 200 | 1'30s | 900 |
| B_cscEtOH. MnFe₂O₄_x | Fe(acac)₃ : Mn(ac)₂ 2:1 | $2 \cdot 10^{-2}$ | OAc:OAm 1:1 0:0 | $6 \cdot 10^{-2}$ | 450 | $1 \cdot 10^{-2}$ | 260 | 200 | 1'30s | 900 |

Here we report the synthesis of monodispersed ferrite ($MnFe_2O_4$, $Fe_3O_4$) nanoparticles using a novel approach of continuous supercritical ethanol synthesis in the presence of surfactants (oleic acid and oleylamine) as stabilizing agents. Kim group[8b] reported the synthesis of iron oxide nanoparticles in continuous supercritical methanol using iron nitrate precursor ($Fe(NO_3)_3$) in the absence of any stabilizers. By using a high reaction temperature (400°C) and pressure (300 Bar), they obtained magnetite nanoparticles of mean size around 21 nm but with a broad size distribution and aggregated. Employing the supercritical ethanol as reaction media in a batch reactor, with an organo-metallic precursor (acetate or acetylacetonate-as ligand) and a stabilizer (long-chain amine) co-solubilised in ethanol, a

variety of inorganic nanostructured materials, metal oxide among others, were prepared[8a]. In this procedure, the authors used oleylamine as stabilizer in the molar ratio to precursor of 15/30 to 1 and a temperature of 350°C. It is known that oleylamine is corrosive and environmentally harmful [60] so it is advisable the use of it in small quantity. It is important to be highlighted that the main difference in our approach was the use of ethanol and a small quantity of surfactants, at a lower temperature (260°C) more favorable for a "greener" technology compared with the previous reports. Moreover, the synthesized nanoparticles were superparamagnetic at room temperature.

## 2.4.2 Characterization

### Structure and morphology

Powder X-ray diffraction (XRD) patterns of $MnFe_2O_4$ and iron oxide nanoparticles are presented in **Figure 2.48**. The reflections peaks of pattern c ($B\_cscEtOH.MnFe_2O_4\_1bis$) were indexed with those of the cubic inverse spinel manganese ferrite phase (ICDD PDF075-0035) with the lattice parameter of 8.467 ± 0.002 Å. Although the reflection peaks of the bulk magnetite and maghemite are very close and therefore in the case of small nanoparticles (broad reflections peaks) it is very difficult to make a clear distinction, for the iron oxide nanoparticles (**Figure 2.48 patterns a and b**), the reflections peaks were attributed to those of magnetite phase (ICDD PDF019-0629). The lattice parameters values obtained from Maud refinement were 8.390 ± 0.005 Å for ($A\_cscEtOH.Fe_3O_4\_3$) and 8.400 ± 0.004 Å for ($B\_cscEtOH.Fe_3O_4\_1$), very close to the lattice constants of the phases of bulk magnetite (8.396 Å). We thus conclude that our materials consist of a predominant magnetite phase and will be referred hereafter as $Fe_3O_4$ nanoparticles. The size of the crystalline domains calculated from the peak broadening refinements gave 4.12±0.04 nm for ($A\_cscEtOH.Fe_3O_4\_3$), 7.72±0.07 nm for ($B\_cscEtOH.Fe_3O_4\_1$) and 9.77±0.08 nm for ($B\_cscEtOH.MnFe_2O_4\_1bis$).
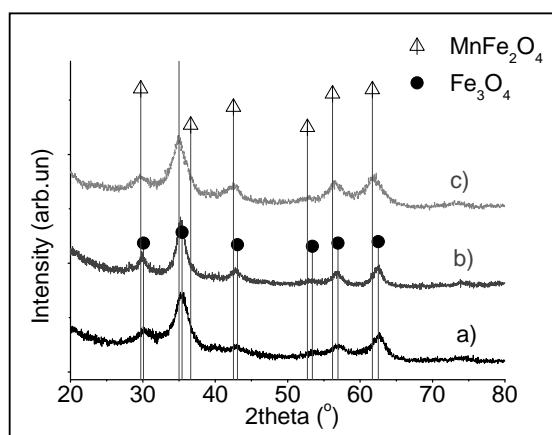


**Figure.2.48** *X-Ray patterns of magnetic nanoparticles synthesized in cscEtOH: (a) (A_cscEtOH.Fe₃O₄_3) from Fe(NO₃)₃; (b) (B_cscEtOH.Fe₃O₄_1) from Fe(acac)₃ precursors; (c) for (B_cscEtOH.MnFe₂O₄_1bis) was used Fe(acac)₃+ Mn(ac)₂ precursors. The three patterns are in agreement with the corresponding bulk materials.*

Size, polydispersity and shape of the ferrite nanoparticles have been further investigated by TEM. **Figure 2.49** shows TEM micrographs, for the nanoparticles synthesised in cscEtOH. Iron oxide nanoparticles (*A_cscEtOH.Fe₃O₄_3* and *B_cscEtOH.Fe₃O₄_1*) were obtained from two different precursors, $Fe(NO_3)_3$ and $Fe(acac)_3$ in the presence of a mixture of surfactants, oleic acid and oleylamine, using the same experimental procedures. As can be seen in **Figure 2.49a** and **2.49b** the mean size is very similar around 6 nm, with good polydispersity of 23 % and 25 % (**2.49a and 2.49b upper insets**), but a difference in shape can be observed. The nanoparticles synthesized from nitrate precursor, present a more irregular shape in comparison with those synthesized from acetylacetonate precursor which tend to be more rounded.
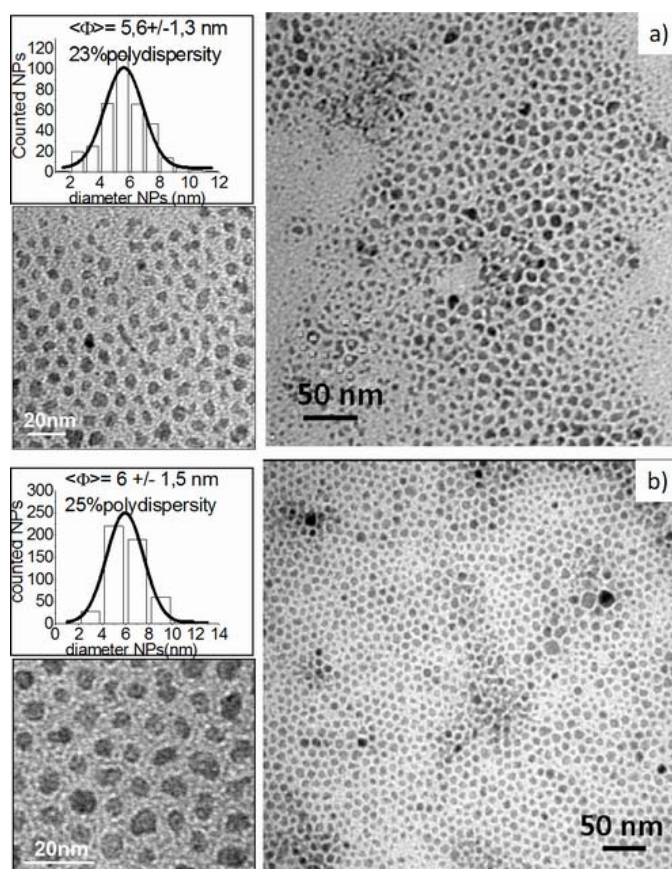


***Figure.2.49*** *TEM images with Gaussian fitting for size distribution in the case of Fe₃O₄ synthesized in cscEtOH: (**a**) A_cscEtOH.Fe₃O₄_3 and (**b**) B_cscEtOH.Fe₃O₄_1*

By using $Fe(acac)_3$ as precursor, small, almost spherical iron oxide nanoparticles resulted. Adding to it $Mn(ac)_2$ precursor while keeping the same all the others parameters $MnFe_2O_4$ have been synthesized. Surprising was, that on the contrary to the iron oxide, the synthesis of manganese ferrite in the presence of both stabilizers (OAc and OAm) did not worked. In the presence of just one surfactant, oleic acid, a very small yield was obtained and two populations of nanoparticles have been detected by TEM analysis (*B_cscEtOH.MnFe₂O₄_2*, (**Figure 2.50b**). When the synthesis was performed in the absence of any stabilizer, good quality nanoparticles with a mean size around 7 nm and 16% polydispersity resulted (*B_cscEtOH.MnFe₂O₄_1bis*, **Figure 2.50a**). In the case of iron oxide synthesised from iron nitrate precursor, we observed that $<\Phi>_{TEM}$ was greater than $<\Phi>_{XRD}$(nm). This could indicate the decrease of crystallinity of the nanoparticles surface. On the contrary, when iron

acetylacetonate was used as precursor for both, $Fe_3O_4$ and $MnFe_2O_4$ nanoparticles synthesis, $<\Phi>_{TEM}$ was only slightly smaller than $<\Phi>_{XRD}$. We interpreted this as mono-crystalline nanoparticles
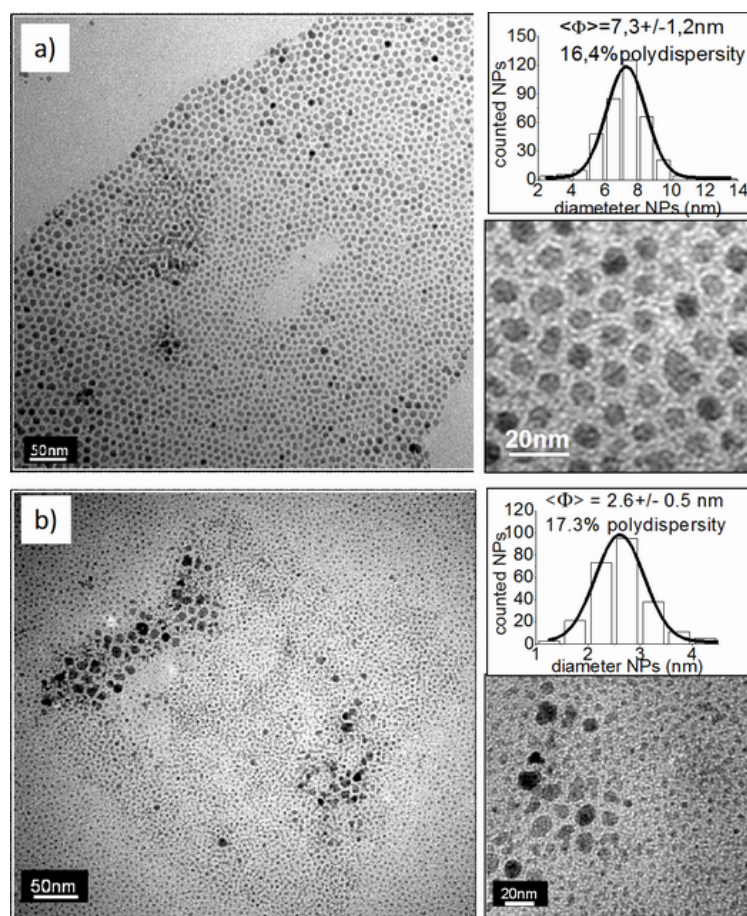


**Figure.2.50** *TEM images and size distribution by a Gaussian fitting for in the case of $MnFe_2O_4$ synthesized in cscEtOH: (a) B_cscEtOH.MnFe$_2$O$_4$_1bis and (b) B_cscEtOH.MnFe$_2$O$_4$_2.*

Mono-dispersity and time stability of the hexane colloidal dispersion were also monitored by DLS (**Figure 2.51a, c, e**) as size distribution by volume %. The nanoparticles synthesised in the presence of surfactants (**Figure 2.51a and c**) are more stable in time, the values of the maximum peaks position for the as prepared materials and after six month are very close, (**Table 2.8**), due to the presence of chemisorbed oleic acid, as we also observed for the others two synthetic methods (discussions In Section 2.2 and 2.3). This was confirmed by the surfactant weight loss % measurements using the thermo gravimetric analysis. **Figure 2.51b, d, f** presents the TGA curves with the corresponding derivatives and surfactant zone. For *A_cscEtOH.Fe$_3$O$_4$_3* (**Figure 2.51b**) the two steps weight loss are clearly visible. The derivative shows a first weight loss at around 243°C and a second at 366°C. In the case of *B_cscEtOH.Fe$_3$O$_4$_1*, the presence of two steps is not so clear and the derivative shows a very board peak with a minimum at ~ 355°C (**Figure 2.51d**). These two high temperatures, 366 and 355 °C suggest the presence of chemisorbed surfactant. The situation was different when the nanoparticles were synthesised in the absent of surfactant, but added after the nanoparticles were formed, in order to have a stable colloidal dispersion (*B_cscEtOH.MnFe$_2$O$_4$_1bis*). The weight loss (**Figure 2.51f**) starts at much lower temperature respect to the nanoparticles synthesized in the present of surfactant, suggesting the presence

95

of physisorbed surfactants (**see discussions Section 2.3.3**). Because the mixing was done at room temperature, no chemical bond between oleic acid and iron oxide surface was formed and this resulted in aggregates formation after a few months of liquid storage. The same effect was observed for the ferrite nanoparticles synthesised by microwave route in the absence of surfactant (**Section 2.3.2**). After six month, the hexane colloidal dispersion of $MnFe_2O_4$ showed just aggregates of mean size around 100 nm (**Figure 2.51e**).
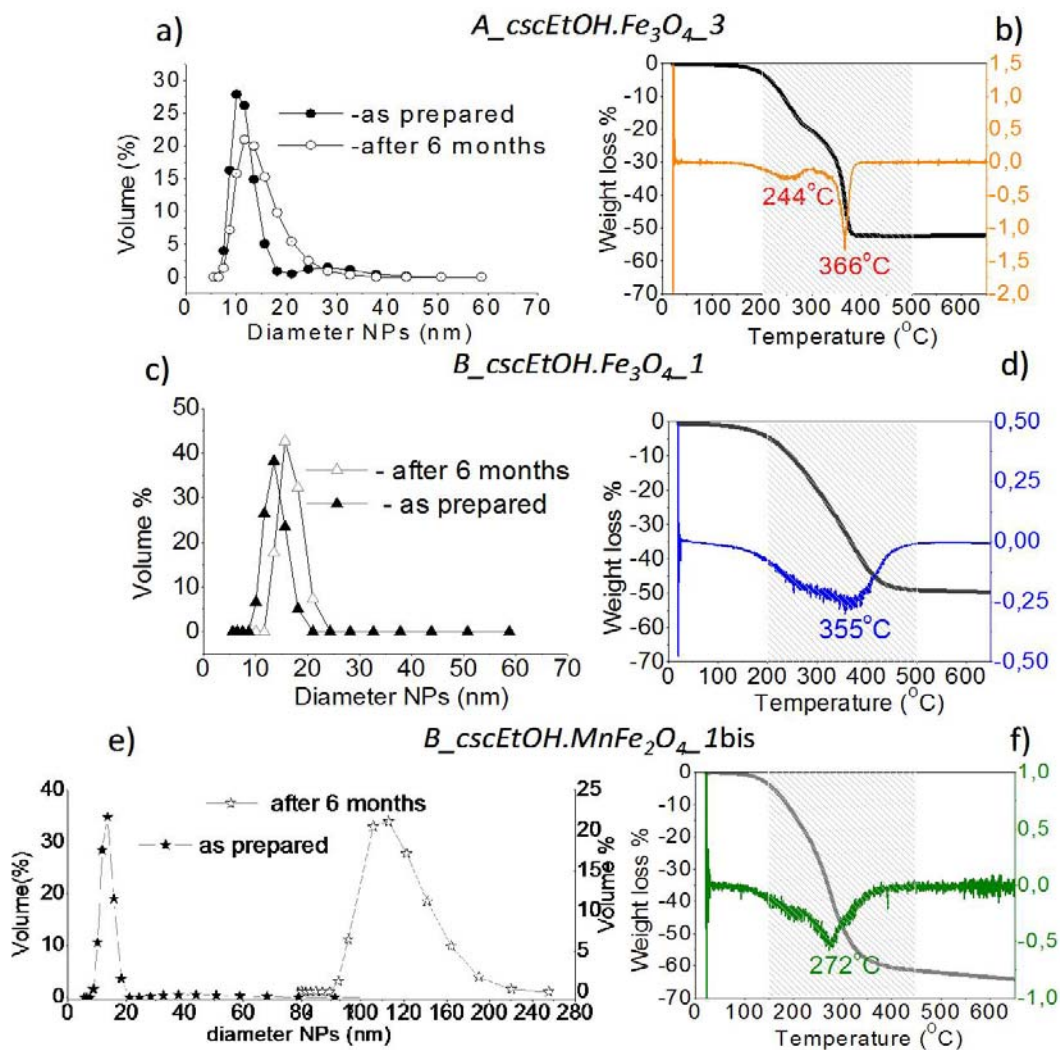


***Figure.2.51*** *DLS and TGA analysis of ferrite nanoparticles synthesized by cscEtOH procedure.*

**Magnetic characterization.**

The magnetic properties of ferrite nanoparticles were evaluated by magnetisation *vs.* magnetic field measurements at 300 K, 5 K and zero–field–cooled (ZFC), field–cooled (FC) temperature dependent magnetization curves. **Figure 2.52** shows typical magnetization curves for superparamagnetic nanoparticles with no hysteresis loop neither remnant magnetization nor coercivity at room temperature. Superparamagnetism is also confirmed by the ZFC–FC magnetization curves (**Figure 2.52a and 2.52b left insets**).
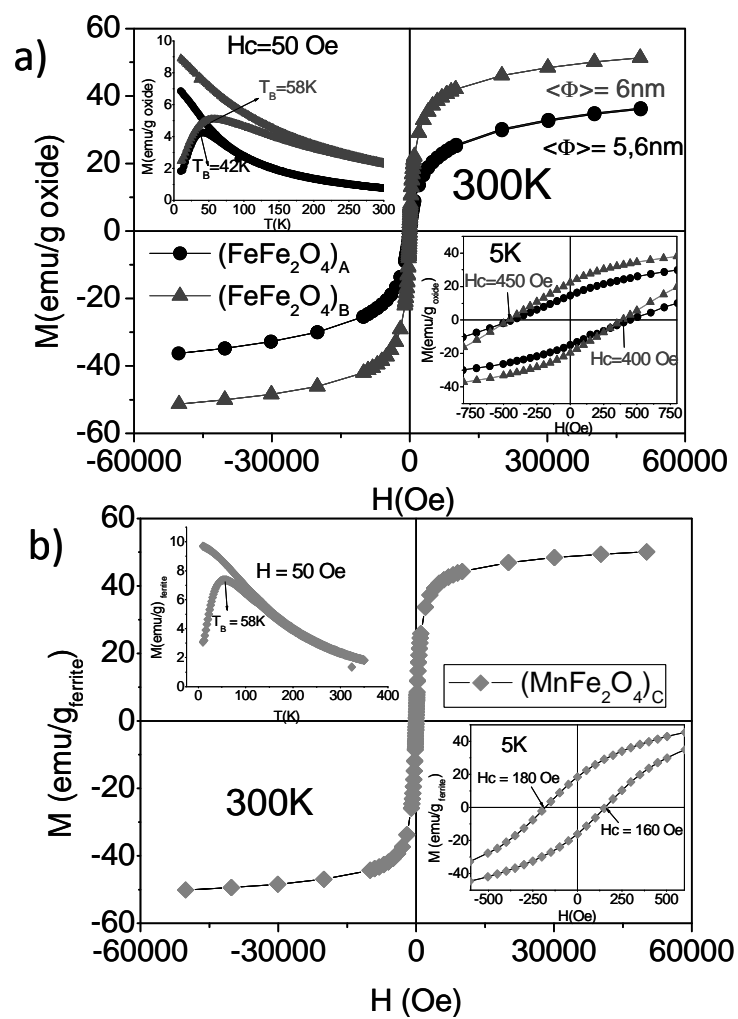
**Figure2.52** Magnetometry data. Hysteresis loops at 300K, 5K for the Fe₃O₄ (a) and MnFe₂O₄ NPs(b)

# 2.5. REFERENCES

1.      Parak, W. J.; Gerion, D.; Pellegrino, T.; Zanchet, D.; Micheel, C.; Williams, S. C.; Boudreau, R.; Gros, M. A. L.; Larabell, C. A.; Alivisatos, A. P., Biological applications of colloidal nanocrystals. *Nanotechnology* 2003, *14* (7), R15.

2.      (a) Ge, J.; Hu, Y.; Yin, Y., Highly Tunable Superparamagnetic Colloidal Photonic Crystals. *Angewandte Chemie International Edition* 2007, *46* (39), 7428-7431; (b) Ge, J.; He, L.; Goebl, J.; Yin, Y., Assembly of Magnetically Tunable Photonic Crystals in Nonpolar Solvents. *Journal of the American Chemical Society* 2009, *131* (10), 3484-3486.

3.      (a) Perreux, L.; Loupy, A., A tentative rationalization of microwave effects in organic synthesis according to the reaction medium, and mechanistic considerations. *Tetrahedron* 2001, *57* (45), 9199-9223; (b) Garnweitner, G.; Niederberger, M., Organic chemistry in inorganic nanomaterials synthesis. *J. Mater. Chem.* 2008, *18*, 1171-1182; (c) Martinez-Palou, R., Ionic liquid and microwave-assisted organic synthesis: a green and synergic couple. *J. Mex. Chem. Soc.* 2007, *51* (4), 252-264.

4.      (a) Tsuji, M.; Hikino, S.; Matsunaga, M.; Sano, Y.; Hashizume, T.; Kawazumi, H., Rapid synthesis of Ag@Ni core–shell nanoparticles using a microwave-polyol method. *Materials Letters* 2010, *64* (16), 1793-1797; (b) Yamauchi, T.; Tsukahara, Y.; Sakata, T.; Mori, H.; Yanagida, T.; Kawaic, T.; Wada, Y., Magnetic Cu-Ni (core–shell) nanoparticles in a one-pot reaction under microwave irradiation. *Nanoscale* 2010, *2*, 515–523; (c) Xiao, L.; Shen, H.; von Hagen, R.; Pan, J.; Belkoura, L.; Mathur, S., Microwave assisted fast and facile synthesis of $SnO_2$ quantum dots and their printing applications. *Chemical Communications* 2010, *46* (35), 6509-6511; (d) Nekooi, P.; Akbari, M.; Amini, M. K., CoSe nanoparticles prepared by the microwave-assisted polyol method as an alcohol and formic acid tolerant oxygen reduction catalyst. *International Journal of Hydrogen Energy* 2010, *35* (12), 6392-6398; (e) Bilecka, I.; Niederberger, M., New developments in the nonaqueous and/or non-hydrolytic sol-gel synthesis of inorganic nanoparticles. *Electrochimica Acta* 2010, *55* (26), 7717-7725; (f) Bilecka, I.; Kubli, M.; Amstad, E.; Niederberger, M., Simultaneous formation of ferrite nanocrystals and deposition of thin films via a microwave-assisted nonaqueous sol–gel process. *Journal of Sol-Gel Science and Technology* 2011, *57* (3), 313-322.

5.      (a) Ai, Z.; Deng, K.; Wan, Q.; Zhang, L.; Lee, S., Facile Microwave-Assisted Synthesis and Magnetic and Gas Sensing Properties of Fe3O4 Nanoroses. *The Journal of Physical Chemistry C* 2010, *114* (14), 6237-6242; (b) Hu, X.; Yu, J. C., High-Yield Synthesis of Nickel and Nickel Phosphide Nanowires via Microwave-Assisted Processes. *Chemistry of Materials* 2008, *20* (21), 6743-6749; (c) Chen, S. Q.; Wang, Y., Microwave-assisted synthesis of a $Co_3O_4$-graphene sheet-on-sheet nanocomposite as a superior anode material for Li-ion batteries. *Journal of Materials Chemistry* 2010, *20* (43), 9735-9739.

6.      (a) Tompsett, G. A.; Conner, W. C.; Yngvesson, K. S., Microwave Synthesis of Nanoporous Materials. *ChemPhysChem* 2006, *7* (2), 296-319; (b) Yacou, C.; Ayral, A.; Giroir-Fendler, A.; Fontaine, M.-L.; Julbe, A., Hierarchical porous silica membranes with dispersed Pt nanoparticles. *Microporous and Mesoporous Materials* 2009, *126* (3), 222-227.

7.      Pascu, O.; Caicedo, J. M.; López-García, M.; Canalejas, V.; Blanco, A.; López, C.; Fontcuberta, J.; Roig, A.; Herranz, G., Ultrathin conformal coating for complex magneto-photonic structures. *Nanoscale* **2011**, *3*, 4811-4816.

8.      (a) Pahari, S. K.; Adschiri, T.; Panda, A. B., Synthesis of monodispersed nanocrystalline materials in supercritical ethanol: a generalized approach. *Journal of Materials Chemistry* **2011**, *21* (28), 10377-10383; (b) Veriansyah, B.; Kim, J.-D.; Min, B. K.; Kim, J., Continuous synthesis of magnetite nanoparticles in supercritical methanol. *Materials Letters* **2010**, *64*, 2197–2200; (c) Kim, J.; Kim, D.; Veriansyah, B.; Kang, J. W.; Kim, J.-D., Metal nanoparticle synthesis using supercritical alcohol. *Materials Letters* **2009**, *63*, 1880–1882; (d) Zhao, D.; Wu, X.; Guan, H.; Han, E., Study on supercritical hydrothermal synthesis of $CoFe_2O_4$ nanoparticles. *Journal of Supercritical Fluids* **2007**, *42*, 226–233; (e) Jung, J.; Perrut, M., Particle design using supercritical fluids: Literature and patent survey. *Journal of Supercritical Fluids* **2001**, *20*, 179–219; (f) Byrappa, K.; Ohara, S.; Adschiri, T., Nanoparticles synthesis using supercritical fluid technology – towards biomedical applications. *Advanced Drug Delivery Reviews* **2008**, *60*, 299–327.

9.      (a) Cooper, A. I., Porous materials and supercritical fluids. *Advanced Materials* **2003**, *15*, 1049-1059; (b) Cansell, F.; Aymonier, C., Design of functional nanostructured materials using supercritical fluids. *Journal of Supercritical Fluids* **2009**, *47*, 508–516; (c) Aymonier, C.; Marre, S., New trends in inorganic materials science using supercritical fluids - from nanopowders to more complex nanoarhitectures. In *Supercritical fluids and Materials*, Aymonier, C.; Cansell, F.; Fouassier, O., Eds. Arcachon, 2007; (d) Reverchon, E.; Adamia, R., Nanomaterials and supercritical fluids. *Journal of Supercritical Fluids* **2006**, *37*, 1-22.

10.     (a) Murray, C. B.; Sun, S.; Gaschler, W.; Doyle, H.; Betley, T. A.; Kagan, C. R., Colloidal synthesis of nanocrystals and nanocrystal superlattices. *IBM J. RES. & DEV.* **2001**, *45* (1), 47-56; (b) Kwon, S. G.; Hyeon, T., Colloidal Chemical Synthesis and Formation Kinetics of Uniformly Sized Nanocrystals of Metals, Oxides, and Chalcogenides. *Accounts of Chemical Research* **2008**, *41* (12), 1696-1709.

11.     Chen, Y.; Peng, D.-L.; Lin, D.; Luo, X., Preparation and magnetic properties of nickel nanoparticles via the thermal decomposition of nickel organometallic precursor in alkylamines. *Nanotechnology* **2007**, *18*, 505703 (6pp).

12.     (a) Polshettiwar, V.; Varma, R. S., Fundamentals of Aqueous Microwave Chemistry. In *Aqueous Microwave Assisted Chemistry: Synthesis and Catalysis*, Polshettiwar, V.; Varma, R. S., Eds. Royal Society of Chemistry: 2010; pp 1-9; (b) Baghbanzadeh, M.; Carbone, L.; Cozzoli, P. D.; Kappe, C. O., Microwave-Assisted Synthesis of Colloidal Inorganic Nanocrystals. *Angewandte Chemie International Edition* **2011**, *50* (48), 11312-11359; (c) Yin, S.; Luo, Z.; Xia, J.; Li, H., Microwave-assisted synthesis of $Fe_3O_4$ nanorods and nanowires in an ionic liquid. *Journal of Physics and Chemistry of Solids* **2010**, *71*, 1785-1788; (d) Bilecka, I.; Niederberger, M., Microwave chemistry for inorganic nanomaterials synthesis. *Nanoscale* **2010**, *2*, 1358–1374.

13.     Bilecka, I.; Kubli, M.; Amstad, E.; Niederberger, M., Simultaneous formation of ferrite nanocrystals and deposition of thin film via a microwave-assisted nonaqueous sol-gel process. *J. Sol-gel Sci. Technol.* **2011**, *57*, 313-322.

14.     Aymonier, C.; Loppinet-Serani, A.; Reveron, H.; Garrabos, Y.; Cansell, F., Review of supercritical fluids in inorganic materials science. *Journal of Supercritical Fluids* **2006**, *38* (242–251).

15.     Sun, S.; Zeng, H.; Robinson, D. B.; Raoux, S.; Rice, P. M.; Wang, S. X.; Li, G., Monodispersed MFe$_2$O$_4$ (M = Fe, Co, Mn) Nanoparticles. *Journal of American Chemical Society* **2004,** *126,* 273-279.

16.     (a) Hyeon, T., Chemical synthesis of magnetic nanoparticles. *Chem. Commun.* **2003,** 927-934; (b) Lamer, V. K.; Dinegar, R. H., Theory, production and mechanism of formation of monodispersed hydrosol *Journal of American Chemical Society* **1950,** *72* (11), 4847-4854; (c) Talapin, D. V.; Shevchenko, E. V.; Weller, H., Synthesis and Characterization of Magnetic Nanoparticles. In *Nanoparticles: From Theory to Application,* Schmid, G., Ed. WILEY-VCH Verlag GmbH & Co. KGaA: Weinheim, 2008; (d) Park, J.; Joo, J.; Kwon, S. G.; Jang, Y.; Hyeon, T., Synthesis of Monodisperse Spherical Nanocrystals. *Angewandte Chemie International Edition* **2007,** *46* (25), 4630-4660; (e) Sun, S.; Zeng, H.; Robinson, D. B.; Raoux, S.; Rice, P. M.; Wang, S. X.; Li, G., Monodisperse MFe$_2$O$_4$ (M = Fe, Co, Mn) Nanoparticles. *Journal of the American Chemical Society* **2003,** *126* (1), 273-279.

17.     Taboada, E. Synthesis of γ-Fe$_2$O$_3$-SiO$_2$ composite nanoparticles targeting magnetic resonance imaging and magnetic hyperthermia applications. Universitat Autonoma de Barcelona, Bellaterra, 2009.

18.     (a) Park, J.; Kang, E.; Son, S. U.; Park, H. M.; Lee, M. K.; Kim, J.; Kim, k. w.; Noh, H.-J.; Park, J.-H.; Bae, C. J.; Park, J.-G.; Hyeon, T., Monodisperse nanoparticles of Ni and NiO: synthesis, characterization, self-assembled superlattices, and catalytic applications in the Suzuki coupling reaction. *Advanced Materials* **2005,** *17* (4), 429 -434; (b) Lee, I. S.; Lee, N.; Park, J.; Kim, B. H.; Yi, Y.-W.; Kim, T.; Kim, T. K.; Lee, I. H.; Paik, S. R.; Hyeon, T., Ni/NiO Core/Shell nanoparticles for selective binding and magnetic separation of histidine-fagged proteins. *Journal of American Chemical Society* **2006,** *128,* 10658-10659; (c) Chen, Y.; Luo, X.; Yue, G.-H.; Luo, X.; Peng, D.-L., Synthesis of iron–nickel nanoparticles via a nonaqueous organometallic route. *Materials Chemistry and Physics* **2009,** *113,* 412-416; (d) Li, Y.; Afzaal, M.; O'Brien, P., The synthesis of amine-capped magnetic (Fe, Mn, Co, Ni) oxide nanocrystals and their surface modification for aqueous dispersibility. *Journal of Materials Chemistry* **2006,** *16,* 2175-2180.

19.     Han, M.; Liu, Q.; He, J.; Song, Y.; Xu, Z.; Zhu, J., Controllable Synthesis and Magnetic Properties of Cubic and Hexagonal Phase Nickel Nanocrystals. *Advanced Materials* **2007,** *19,* 1096-1100.

20.     Wang, H.; Jiao, X.; Chen, D., Monodispersed Nickel Nanoparticles with Tunable Phase and Size: Synthesis, Characterization, and Magnetic Properties. *Journal of Physical Chemistry C* **2008,** *112* (48), 18793-18797.

21.     Goto, Y.; Taniguchi, K.; Omata, T.; Otsuka-Yao-Matsuo, S.; Ohashi, N.; Ueda, S.; Yoshikawa, H.; Yamashita, Y.; Oohashi, H.; Kobayashi, K., Formation of Ni$_3$C Nanocrystals by Thermolysis of Nickel Acetylacetonate in Oleylamine: Characterization Using Hard X-ray Photoelectron Spectroscopy. *Chemistry of Materials* **2008,** *20* (12), 4156-4160.

22.     (a) Chen, D.-X.; Sanchez, A.; Taboada, E.; Roig, A.; Sun, N.; Gu, H.-C., Size determination of superparamagnetic nanoparticles from magnetization curve. *Journal of Applied Physics* **2009,** *105,* 083924-6; (b) Chen, D.-X.; Pascu, O.; Roig, A.; Sanchez, A., Size analysis and magnetic structure of nickel nanoparticles. *Journal of Magnetism and Magnetic Materials* **2010,** *322,* 3834–3840.
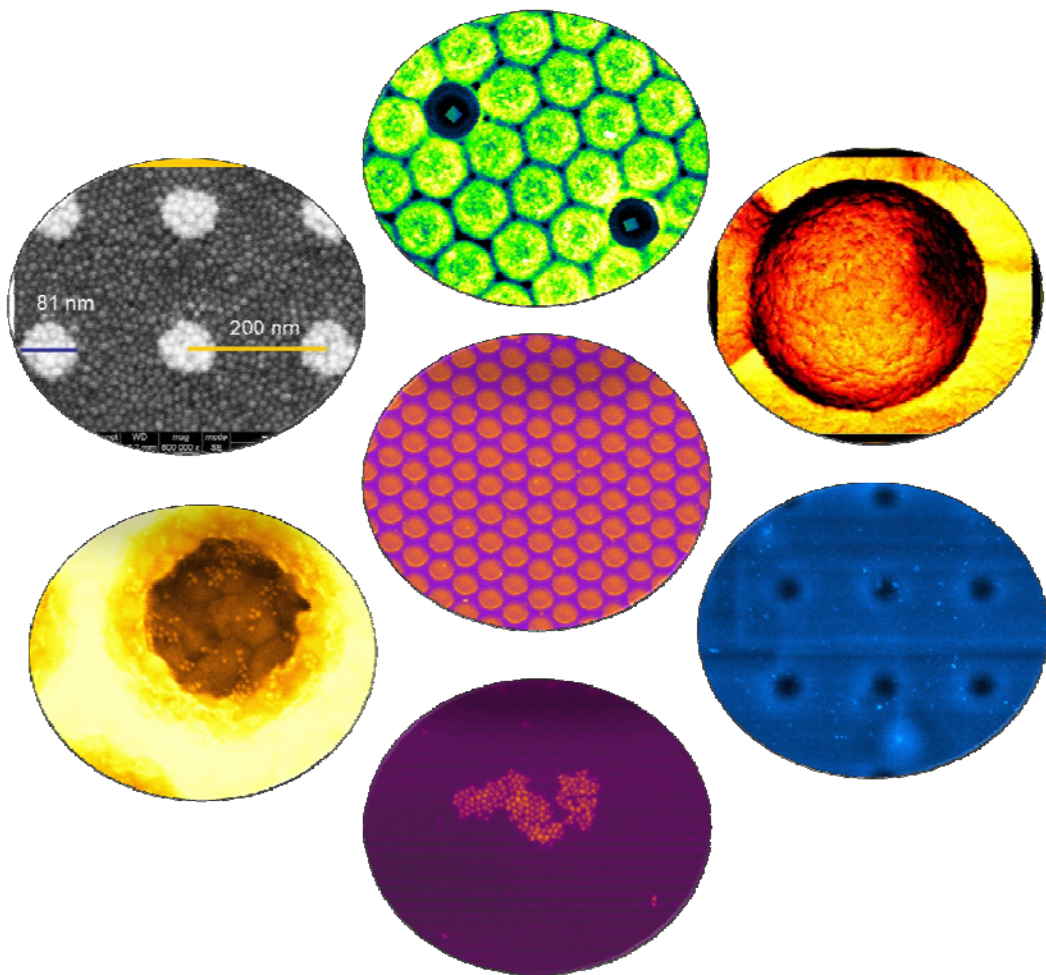
23.      Winnischofer, H.; Rocha, T. C. R.; Nunes, W. C.; Socolovsky, L. M.; Knobel, M.; Zanchet, D., Chemical Synthesis and Structural Characterization of Highly Disordered Ni Colloidal Nanoparticles. *ACS Nano* **2008**, *2* (6), 1313-1319.

24.      (a) Sun, S.; Murray, C. B., Synthesis of monodisperse cobalt nanocrystals and their assembly into magnetic superlattices. *Journal of Applied Physics* **1999**, *85* (8), 4325-4330; (b) Perez-Dieste, V.; Castellini, O. M.; Crain, J. N.; Eriksson, M. A.; Kirakosian, A.; Lin, J.-L.; McChesney, J. L.; Himpsel, F. J.; Black, C. T.; Murray, C. B., Thermal decomposition of surfactant coatings on Co and Ni nanocrystals. *Applied Physics Letters* **2003**, *83* (24), 5053-5055.

25.      Hou, Y.; Kondohb, H.; Ohtab, T.; Gaoa, S., Size-controlled synthesis of nickel nanoparticles. *Applied Surface Science* **2005**, *24*, 218-222.

26.      Marks, L. D., Experimental studies of small particle structures. *Reports on Progress in Physics* **1994**, *57* (6), 603.

27.      Johnston-Peck, A. C.; Wang, J.; Tracy, J. B., Synthesis and Structural and Magnetic Characterization of Ni(Core)/NiO(Shell) Nanoparticles. *ACS Nano* **2009**, *3* (5), 1077-1084.

28.      Zboril, R.; Bakandritsos, A.; Mashlan, M.; Tzitzios, V.; Dallas, P.; Trapalis, C.; Petridis, D., One-step solid state synthesis of capped g-Fe2O3 nanocrystallites. *Nanotechnology* **2008**, *19*, 095602 (8pp).

29.      (a) Limaye, M. V.; Singh, S. B.; Date, S. K.; Kothari, D.; Reddy, V. R.; Gupta, A.; Sathe, V.; Choudhary, R. J.; Kulkarni, S. K., High Coercivity of Oleic Acid Capped $CoFe_2O_4$ Nanoparticles at Room Temperature. *The Journal of Physical Chemistry B* **2009**, *113* (27), 9070-9076; (b) Khanna, P.; Srinivasa Rao, K.; Patil, K.; Singh, V.; Mehta, B., One-pot synthesis of oleic acid-capped cadmium chalcogenides (CdE: E = Se, Te) nano-crystals. *Journal of Nanoparticle Research* **2010**, *12* (1), 101-109; (c) Ghosh, M.; Biswas, K.; Sundaresan, A.; Rao, C. N. R., MnO and NiO nanoparticles: synthesis and magnetic properties. *Journal of Materials Chemistry* **2006**, *16* (1), 106-111.

30.      (a) Viali, W. R.; Alcantara, G. B.; Sartoratto, P. P. C.; Soler, M. A. G.; Mosiniewicz-Szablewska, E.; Andrzejewski, B.; Morais, P. C., Investigation of the Molecular Surface Coating on the Stability of Insulating Magnetic Oils. *J. Phys. Chem. C* **2010**, *114*, 179-188; (b) Parekh, K.; Upadhyay, R. V.; Belova, L.; Rao, K. V., Ternary monodispersed $Mn_{0.5}Zn_{0.5}Fe_2O_4$ ferrite nanoparticles: preparation and magnetic characterization. *Nanotechnology* **2006**, *17*, 5970-5975.

31.      Pascu, O.; Caicedo, J. M.; Fontcuberta, J.; Herranz, G.; Roig, A., Magneto-Optical Characterization of Colloidal Dispersions. Application to Nickel Nanoparticles. *Langmuir* **2010**, *26* (15), 12548-12552.

32.      Chen, D. X.; Pascu, O.; Roig, A.; Sanchez, A., Size analysis and magnetic structure of nickel nanoparticles. *Journal of Magnetism and Magnetic Materials* **2010**, *322* (24), 3834-3840.

33.      Koksharov, Y. A., Magnetism of Nanoparticles: Effects of Size, Shape, and Interactions. In *Magnetic Nanoparticles*, Gubin, S. P., Ed. WILEY-VCH Verlag GmbH & Co. KGaA: Weinheim, 2009; pp 197-254.

34.      (a) Talapin, D. V.; Shevchenko, E. V.; Weller, H., Synthesis and Characterization of Magnetic Nanoparticles. In *Nanoparticles: From Theory to Application*, Schmid, G., Ed. WILEY-VCH Verlag GmbH & Co. KGaA: Weinheim, 2004; pp 199-238; (b) Kodama, R. H., Magnetic nanoparticles. *Journal of Magnetism and Magnetic Materials* **1999,** *200,* 359-372.

35.      (a) Parker, F. T.; Foster, M. W.; Margulies, D. T.; Berkowitz, A. E., Spin canting, surface magnetization and finite-size effects in $\gamma$-$Fe_2O_3$ particles. *Physical Review B* **1993,** *47* (13), 7885-7891; (b) Zhang, H. T.; Wua, G.; Chen, X. H.; Qiu, X. G., Synthesis and magnetic properties of nickel nanocrystals. *Materials Research Bulletin* **2006,** *41,* 495-501.

36.      (a) Stephens, P. J., Magnetic Circular Dichroism. *Annual Review of Physical Chemistry* **1974,** *25* (1), 201-232; (b) Caldwell, D.; Thorne, J. M.; Eyrrng, H., Magnetic Circular Dichroism. *Annual Review of Physical Chemistry* **1971,** *22,* 259-&.

37.      Amekura, H.; Takeda, Y.; Kishimoto, N., Magneto-optical Kerr spectra of nickel nanoparticles in silica glass fabricated by negative-ion implantation. *Thin Solid Films* **2004,** *464-465,* 268-272.

38.      Biello, D., Will 10 Bilion people Use Up the Planet's Resources? Scientific American. *Scientific American* **2011,** *May 25.*

39.      Djerdj, I.; Arcon, D.; Jaglicic, Z.; Niederberger, M., Nonaqueous synthesis of metal oxide nanoparticles: Short review and doped titanium dioxide as case study for the preparation of transition metal-doped oxide nanoparticles. *Journal of Solid State Chemistry* **2008,** *181,* 1571– 1581.

40.      (a) Lindstrom, P., Bernard Wathey,J. T., Westman, J., Microwave-assisted organci synthesis –a review. *Tetrahedon* **2001,** *57,* 9225-9283; (b) Gabriel, C.; Gabriel, S.; Grant, E. H.; Halstead, B. S. J.; Mingosb, D. M. P., Dielectric parameters relevant to microwave dielectric heating. *Chemical Society Reviews* **1998,** *27,* 213-223; (c) Gupta, M.; Paul, S.; Gupta, R., General Characteristics and Applications of Microwaves in Organic Synthesis. *Acta Chimica Slovenia* **2009,** *56,* 749–764.

41.      Niederberger, M.; Pinna, N., Aqueous and Nonaqueous Sol-Gel Chemistry Metal Oxide Nanoparticles in Organic Solvents. Springer London: 2009; pp 7-18.

42.      Niederberger, M.; Pinna, N., Solvent-Controlled Synthesis Metal Oxide Nanoparticles in Organic Solvents. Springer London: 2009; pp 53-95.

43.      (a) Bilecka, I.; Elser, P.; Niederberger, M., Kinetic and Thermodynamics Aspects in the Microwave-Assisted Synthesis of ZnO Nanoparticles in Benzyl Alcohol. *ACS Nano* **2009,** *3* (2), 467-477; (b) Niederberger, M.; Pinna, N., Reaction Mechanism Metal Oxide Nanoparticles in Organic Solvents. In *Metal oxides,* Springer London: 2009; pp 97-127.

44.      Bilecka, I.; Djerdj, I.; Niederberger, M., One-minute synthesis of crystalline binary and ternary metal oxide nanoparticles. *Chemical Communications* **2008,** (7), 886-888.

45.      Pascu, O.; Carenza, E.; Gich, M.; Herranz, G.; Roig, A., Surface reactivity of iron oxidxe nanoparticles by microwave-assisted synthesis; comparison with the thermal decomposition route. *Journal of Materials Chemistry* **2012,** *submitted.*

46.     Pascu, O.; Gich, M.; Herranz, G.; Roig, A., 2D Magnetic Frames Obtained by the Microwave-Assisted Chemistry Approach. *European Journal of Inorganic Chemistry* **2012**, *DOI: 10.1002/ejic.201101244.*

47.     Cornell, R. M.; Schwertmann, U., The iron oxides: structure, properties, reactions, occurrences and uses. VCH, W., Ed. 2003.

48.     Zeng, H.; Rice, P. M.; Wang, S. X.; Sun, S., Shape-Controlled Synthesis and Shape-Induced Texture of MnFe$_2$O$_4$ Nanoparticles. *Journal of American Chemical Society* **2004**, *126*, 11458-11459.

49.     Mutin, P. H.; Vioux, A., Nonhydrolitic processing of oxide-based materials: simple routes to control homogeneity, morphology and nanostructure. *Chemistry of Materials* **2009**, *21*, 582-596.

50.     (a) Rajendran, R.; Muralidharan, R.; Santhana Gopalakrishnan, R.; Chellamuthu, M.; Ponnusamy, S. U.; Manikandan, E., Controllable Synthesis of Single-Crystalline Fe$_3$O$_4$ Nanorice by a One-Pot, Surfactant-Assisted Hydrothermal Method and Its Properties. *European Journal of Inorganic Chemistry* **2011**, *2011* (35), 5384-5389; (b) George, C.; Genovese, A.; Qiao, F.; Korobchevskaya, K.; Comin, A.; Andrea, F.; Marras, S.; Roig, A.; Zhang, Y.; Krahnea, R.; Manna, L., Optical and electrical properties of colloidal (spherical Au)-(spinel ferrite nanorod) heterostructures. *Nanoscale* **2011**; (c) Bakshi, M. S.; Thakur, P.; Sachar, S.; Kaur, G.; Banipal, T. S.; Possmayer, F.; Petersen, N. O., Aqueous Phase Surfactant Selective Shape Controlled Synthesis of Lead Sulfide Nanocrystals. *Journal of Physical Chemistry C* **2007**, *111*, 18087-18098.

51.     George, C.; Dorfs, D.; Bertoni, G.; Falqui, A.; Genovese, A.; Pellegrino, T.; Roig, A.; Quarta, A.; Comparelli, R.; Curri, M. L.; Cingolani, R.; Manna, L., A Cast-Mold Approach to Iron Oxide and Pt/Iron Oxide Nanocontainers and Nanoparticles with a Reactive Concave Surface. *Journal of American Chemical Society* **2011**, *133*, 2205–2217.

52.     http://www.sciencedaily.com/releases/2011/09/110915113752.htm, Carbon nanoparticles break barriers -- And That May Not Be Good. *Science Daily* 2011.

53.     (a) Su, D.; Horvat, J.; Munroe, P.; Ahn, H.; Ranjbartoreh, A. R.; Wang, G., Polyhedral Magnetite Nanocrystals with Multiple Facets: Facile Synthesis, Structural Modelling, Magnetic Properties and Application for High Capacity Lithium Storage. *Chemistry – A European Journal* **2012**, *18* (2), 488-497; (b) Xia, Y.; Xiong, Y.; Lim, B.; Skrabalak, S. E., Shape-Controlled Synthesis of Metal Nanocrystals: Simple Chemistry Meets Complex Physics? *Angewandte Chemie International Edition* **2009**, *48* (1), 60-103.

54.     Wu, W.; He, Q.; Jiang, C., Magnetic Iron Oxide Nanoparticles: Synthesis and Surface Functionalization Strategies. *Nanoscale Research Letters* **2008**, *3*, 397-415.

55.     Zhang, L.; He, R.; Gu, H.-C., Oleic acid coating on the monodisperse magnetic nanoparticles. *Applied Surface Sience* **2006**, *253*, 2611-2617.

56.     De Palma, R.; Peeters, S.; Van Bael, M. J.; Van den Rul, H.; Bonroy, K.; Laureyn, W.; Mullens, J.; Borghs, G.; Maes, G., Silane Ligand Exchange to Make Hydrophobic Superparamagnetic Nanoparticles Water-Dispersible *Chem. Mater.* **2007**, *19*, 1821-1831.

57.     Roca, A. G.; Morales, M. P.; O'Grady, K.; Serna, C. J., Structural and magnetic properties of uniform magnetite nanoparticles prepared by high temperature decompositon of organic precursors. *Nanotechnology* **2006,** *17,* 2783-2788.

58.     (a) Baccile, N.; Babonneau, F.; Thomas, B.; Coradin, T., Introducing eco-desing in silica sol-gel materials. *Journal of Materials Chemistry* **2009,** *19,* 8537-8557; (b) Khanna, V.; Zhang, Y.; Grubb, G.; Bakshi, B. R., Assesing the Life Cycle Environmental Implications of Nanomanufacturing: Opportunities and Challenges. In *Nanoscience and Nanotechnology Environmental and Health Impact,* Grassian, V. H., Ed. John Wiley & Sons, Inc.: Hoboken, 2008; pp 19-43; (c) Ngo, M. A.; Smiley-Jewell, S.; Aldous, P.; Pinkerton, K. E., Nanomaterials and the Environment. In *Nanoscience and Nanotechnology Environmental and Health Impact,* Grassian, V. H., Ed. John Wiley & Sons, Inc.: Hoboken, 2008; pp 3-19.

59.     Nair, B., Final report on the safety assessment of Benzyl Alcohol, Benzoic Acid and Sodium Benzoate. *International Journal of Toxicology* **2001,** *20* (3), 23-50.

60.     http://www.sigmaaldrich.com/catalog/product/, In *Sigma -Aldrich,* 2012.

61.     http://www.energy.eu/, In *For the reagents, Sigma-Aldrich prices were taken in consideration. 0.0952 €/kWh energy price was assumed according to  Europe´s energy Portal ( industrial consuption for Spain),* 2011.

62.     Wang, W.-W., Microwave-induced polyol-process synthesis of $M^{II}Fe_2O_4$ (M=Mn, Co) nanoparticles and magnetic properties. *Materials Chemistry and Physics* **2008,** *108,* 227-231.

63.     Morales, M. P.; Veintemillas-Verdaguer, S.; Montero, M. I.; Serna, C. J.; Roig, A.; Casas, L.; Martínez, B.; Sandiumenge, F., Surface and Internal Spin Canting in $\gamma$-$Fe_2O_3$ Nanoparticles. *Chemistry of Materials* **1999,** *11* (11), 3058-3064.

64.     Carlès, P., A brief review of the thermophysical properties of supercritical fluids. *Journal of Supercritical Fluids* **2010,** *53,* 2-11.

65.     (a) Lam, U. T.; Mammucari, R.; Suzuki, K.; Foster, N. R., Processing of Iron Oxide Nanoparticles by Supercritical Fluids. *Ind. Eng. Chem. Res* **2008,** *47,* 599-614; (b) Ventosa, N., Preparation of micro and nanoparticulate molecular materials using compresed fluids. In *Supercritical fluids and Materials,* Aymonier, C.; Cansell, F.; Fouassier, O., Eds. Arcacon, 2007.

66.     Choia, H.; Veriansyaha, B.; Kima, J.; Kima, J.-D.; Kang, J. W., Continuous synthesis of metal nanoparticles in supercritical methanol. *Journal of Supercritical Fluids* **2010,** *52,* 285–291.

67.     Moisan, S.; Marty, J.-D.; Cansell, F.; Aymonier, C., Preparation of functional hybrid palladium nanoparticles using supercritical fluids: a novel approach to detach the growth and functionalization steps. *Chemical Communications* **2008,** 1428–1430.

# 3

# 2D MAGNETO–PHOTONIC MATERIALS

## *Preamble of chapter 3*

Structuring the matter is a versatile way to manipulate light propagation in media and to obtain engineered electromagnetic responses. Examples of tailoring light–matter interactions are found in different fields of photonics, from metamaterials to photonic crystals[1] and surface plasmons in corrugated metal/dielectric interfaces[2]. Although three dimensional photonic crystals (3D–PC) have a higher potential for applications (due to the full control of light along the three dimensions), two-dimensional photonic crystals (2D–PC) with high quality structural order over large areas are easier to fabricate with existing lithographic methods. Therefore, two dimensional structures are of interest for potential applications in data storage, optical communications (more detailed in **Chapter 1.2**).

In this chapter, we are presenting the work related to 2D-PC materials, consisting of a periodic array of air holes in a dielectric medium (polymer, Au) or monolayer of self-assembled spheres (PS) that forms a planar waveguide with the vertical confinement of photons. For most applications, the tunability of PC's optical properties is required, either by locally changing the periodic structure, by an appropriate choice of the refractive index of the component materials or by using external stimuli[3]. As already mentioned, our goal is an optical system (2D or 3D photonic crystal) that responds to a magnetic field as the external stimulus. At the same time, photonic structures are being investigated as an ideal platform to have enhanced magneto-optical response[4]. To achieve these potentials, our approach was to incorporate a magnetic component in the form of magnetic nanoparticles. With these functionalized photonic materials we targeted i) potential tunability of photonic band gap spectral position; ii) the enhancement of magneto-optical response near photonic band-edge frequencies and iii) possible applications in new integrated optic devices [5]( e.g optical isolators).

To achieve that, three strategies have been considered concerning 2D constructs:

**1) 2D magnetic patterned nanocomposites by lithographic techniques**. Polymers play an important role for developing materials for photonics[6]. They are inexpensive, compatible with patterning methods (e.g. lithography)[7], possess useful optical properties, can be combined with inorganic materials (quantum dots, nanoparticles) applicable for hybrid composites[8] or even can be used as templates[1b]. In this section we present a preliminary work related to the fabrication of patterned hybrid nanocomposites by mixing ex-situ synthesized magnetic nanoparticles with pre-made polymer solution (polymethyl methacryalte-PMMA) followed by patterning with lithographic techniques, electron beam (EBL) and nanoimprint (NIL). These apporaches line , unfortunately, were not suitable to achieve our aim. The amount of magnetic nanoparticles in the hybrid polymeric film was found insufficient to give a magnetic signal. However, with the corresponding optimization, this strategy could yield appropriated 2D magneto-photonic materials.

**2) Gold array (nanocavities/nanodisks) infiltrated with magnetic nanoparticles** (collaboration work, see attributions). There is a great interest in the combination of resonant optical material with magnetic properties in a single nanostructure leading to new functionalities[2a, 9]. By incorporating ex-situ synthesized magnetic nanoparticles (Ni) into a plasmonic structure (Au void templates or Au nanodisk arrays) we found that the magneto-optic spectra at visible wavelengths are strongly modified compared to the spectra of nanoparticles randomly distributed on flat non-patterned surfaces. In particular, the magneto-optical response is enhanced for wavelengths at which surface plasmons are excited on the patterned metal/dielectric interfaces. This feature is important for fabrication of new materials exhibiting large magneto-optic responses. Only a brief description is presented, a deep analysis of the optical/magneto-optical properties of these systems being out of the scope of this Thesis.

**3) 2D array of magnetic hollow spheres by microwave heating method.** The fabrication of intricate 2D porous architecture using sacrificial scaffolds has recently attracted attention because of the interesting displayed optical, optoelectronic, magnetic, electric or catalytic properties [10]. In this consideration we present the fabrication of complex macroporous magnetic frames using a synthetic approach based on microwave heating. Only in a few minutes, a stoichiometric and homogeneous conformal nanometric coating of superparamagnetic

nanoparticles was grown onto a 2D monolayer formed by self-assembled PS colloids. No post-treatment was required; the sacrificial template was removed simultaneously with the magnetic nanoparticles formation while the structural order at large scale was preserved. The 2D character of these systems and the associated intrinsically extremely low magnetic load, makes their magneto-optical characterization very challenging and, indeed, we were not able to detect signals above the noise level. The functionalities of these materials are not discussed, then, in this Thesis, but they will be taken into account as a future work.

# 3.1   2D MAGNETIC PATTERNED NANOCOMPOSITES BY LITHOGRAPHIC TECHNIQUES

The two-dimensional photonic crystals (2D PC) consist of a 2D periodic array of air holes in a dielectric medium (semiconductor or polymer) or a monolayer of self-assembled spheres (PS, SiO$_2$, PMMA). These materials are attractive due to the simplicity of their manufacturing compared to 3D structures (Chapter 4), since conventional lithography techniques, such as electron-beam or nanoimprint and self-assembling approaches are suitable for their fabrication. Their optical properties (**Chapter 1.2**) such as spectral position of the photonic band gap can be tuned by: i) a proper geometry (e.g., lattice parameters, holes diameters); ii) choosing appropriately the refraction index of the constituent materials and iii) adding new functionalities to photonic materials, for instance magneto-optical component by impregnation with magnetic material in the form of magnetic nanoparticles.

Among the different lithographic methods, we chose to use electron-beam lithography (EBL) and nanoimprint lithography (NIL) for the following reasons: i) both methods have been applied successfully for 2D PCs fabrication, as reported in the literature[7a, b, 7d, 11]; ii) polymethyl methacrylate (PMMA) is the common polymeric material used as a resist that, due to its advantageous properties (it is inexpensive, possesses useful optical properties, can be combined with inorganic materials and can be used in hybrid composites[7e, 8, 11e]), plays an important role in the fabrication of polymeric photonic crystals[6]. At ICMAB we had access to the EBL whereas I could benefit of the NIL lithographic facilities at IMB-CNM (Insitut de Microelectronica de Barcelona.

Since we were interested in a photonic material that responds to magnetic field, hybrid organic (PMMA)-inorganic (Ni NPs) nanocomposites, patterned as 2D photonic structures was considered to be an appropriate system which could open new ways for 2D magnetophotonic materials fabrication. This strategy is challenging since it requires a large homogeneity in the nanoparticles distribution within the hybrid composite film and at the same time, high magnetic content.

We attempted two approaches:

*Approach 1 (***Figure 3.1***)*–patterning the PMMA film by EBL and NIL followed by drop casting a dispersion of magnetic nanoparticles (synthesis and characterization described in **Chapter 2.2**).

*Approach 2 (***Figure 3.1***)*– directly patterning by both techniques the nanocomposites of the PMMA film doped with magnetic nanoparticles. It is worth mentioning that the latter approach deserves further effort since that the preliminary results presented in section 3.1.3 were considered only partially but I foresee it as a very promising materials fabrication methodology.
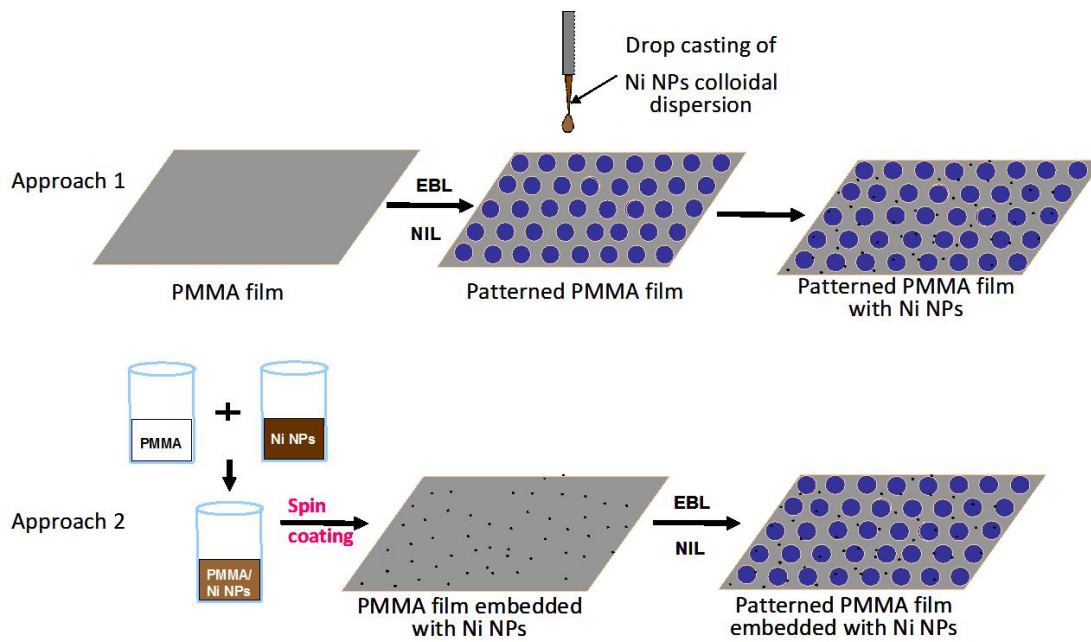
**Figure 3.1.** *Schematic representation of the approaches used for 2D magnetophotonic materials fabrication.*

## 3.1.1. Electron-beam (EBL) and nanoimprint lithography (NIL) –Basic principles

The word "lithography" comes from the Greek "lithos" ("stone") and "grapho" ("to write"). In the beginning, it was associated to a printing method used for text and later books, maps, poster manufacturing. Nowadays, the concept is extended to the processing of materials at much smaller lengths down to the nanometre, and micro- and nanolithography refer to patterning methods for structuring materials on fine scale, smaller than 10 μm (microlithography) or 100 nm (nanolithography). Lithography as a patterning tool defines mainly two dimensional features and can use mask/mold or direct writing.

**Electron-beam lithography**[12] (**Figure 3.2**) can be used for direct writing, consisting of scanning a beam of electrons across a substrate covered with an electrons sensitive resist film (spin-coated onto the substrate), PMMA polymer in our case, thus depositing energy in the desired pattern (designed previously, by software).The advantages of EBL over NIL are that the patterned designs are almost unlimited and can be rapidly and easily modified *in-situ*. Due to the deposited energy, the polymer is chemically modified and in case of PMMA, the covalent bonds within the polymer are broken with the formation of oligomers and monomers (**Figure 3.3**) which are further removed by the developer (organic solvent capable of dissolving the fragmented polymer). The energy deposited during exposure creates a latent image that is materialized during chemical development[a]. The process therefore leaves a patterned resist on the substrate that is either or not used for further processing (transferred into the sample using either metal lift-off or etching). There are two types of resists, with

---

[a] *Development*: the irradiated sample is immersed into a developer solution (consisting of a mixture of organic solvents) that dissolves the exposed (positive resist) or unexposed (negative resist) polymer.

positive or negative tone. The one with positive tone produces the same image as the pattern drawn by the e–beam (positive image), while the negative resist produces the reverse image (negative image). Due to the required high resolution (less than 20 nm), a specialized technique for creating extremely fine pattern is required for applications such as opto-electronic, photonic, optical devices, quantum structures etc . Its most important limitations are the geometric aberration, longer time processing, limited writing area; the interactions between beam and resist affects the resolution (damaging the desired pattern); and, it is not suitable for mass production (each machine can only make one structure at a time).
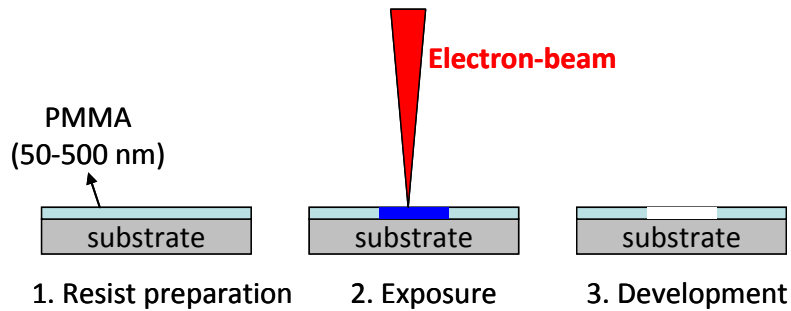


**Figure 3.2.** *Working principle of electron–beam lithography.*

In **nanoimprint lithography**[13] or hot embossing lithography, the pattern of the solid stamp is transferred into a thermoplastic material (PMMA in our case) while the film is heated above its glass transition temperature. The heated and viscous polymer flows and fills the mold with applying high pressure **(Figure 3.3)**. After cooling, the mold is removed and the pattern is either the final product or it is used as a nano–scale mask for further wafer processing.
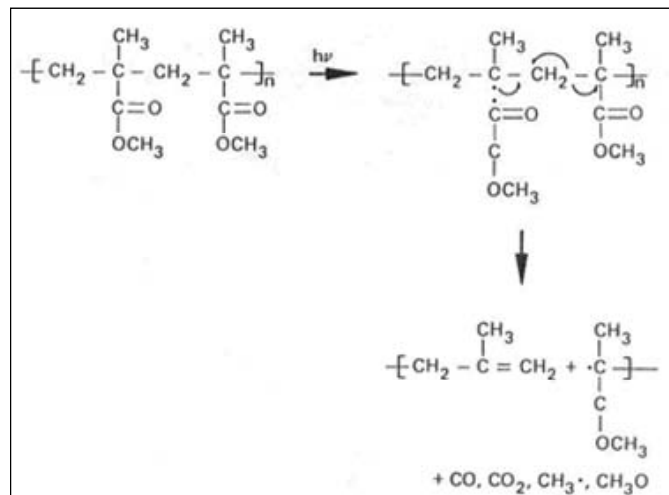


**Figure 3.3.** *Irradiation with electron–beam breaks the polymer into fragments (oligomers, monomers, free radicals).*

Since pattern fabrication in NIL is not based on modification of chemical structure of resist under the irradiation, as it is for EBL, resolution is not limited by the factors such as wave diffraction, scattering, interference, backscattering, development (as are for EBL). For these reasons, the features by NIL are no limited (e.g. 10 nm dot array with 40 nm periodicity have been fabricated or even lower), the limited being the features on the mold[14]. Thus, the resolution (better than 10 nm), low cost, simplicity and high fidelity in nanoscale pattern

transfer make this technique attractive for fabrication of nanostructures on large scale for nanoelectronics, photonics and biotechnology. The template (stamp) is usually made on Si, SiO$_2$ by electron-beam lithography. The quality of the nanoimprint depends on several experimental parameters such as the working temperature, viscosity of melt, adhesion of polymer to template. The most common polymer used is PMMA but the technique is also compatible with other polymeric materials, functional materials, silicon, glass or metal films.
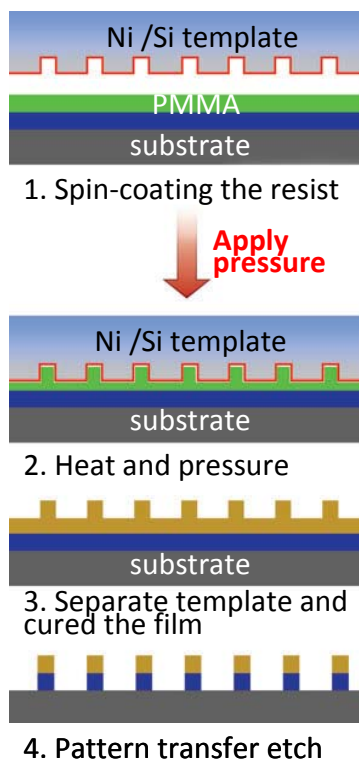


**Figure 3.4.** *Working principle of Nanoimprint lithography*[13]

## 3.1.2. Experimental methodology

**Electron-beam lithography** *(Approach 1)*

We have used EBL based on a scanning electron microscopy (SEM) accessible at ICMAB. The FEI Quanta 200 FEG from FEI is a state-of-the-art field emission microscope that allows nanometre level inspection of materials and by RAITH electron-beam, nano-lithography can also be performed **(Figure 3.5)**. For EBL, an electronic interface is attached to SEM in order to control the deflection and interruption of the beam, while the electron source, focusing system, and the sample support are provided by SEM[12]. The whole process is computer-controlled by the ELPHY PLUS program. The important parameters to be taking into account for the patterning process are: the resist profile (roughness, edge) and thickness; the energy and intenisty of electrons; the interaction of electrons with the solid leading to proximity effects[b];

---

[b] *Proximity effect*: the absorbed dose is not confined to the area where beam has been driven and therefore the areas in the central zone of the feature will receive additional energy
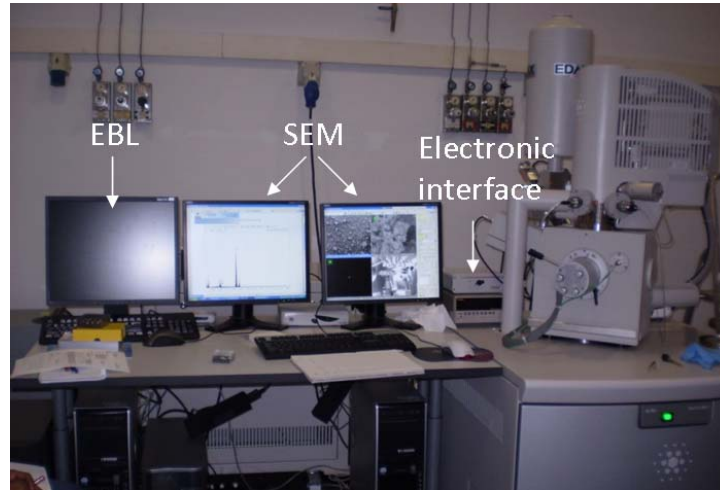
*Figure 3.5. EBL coupled with SEM, available at ICMAB.*

the irradiation process (acceleration voltage $V_{acc}$, area dose[c], exposure dose[d], dose fraction[e] and dwell time[f] $T_{dwell}$) (**Figure 3.6**); and the development conditions (time). In the writing process, the electron beam, with a circular section (spot) and gaussian intensity is driven along straight lines, process named scans. In order to reproduce the design features, the exposure consist in filling the areas (according to the design pattern) using a finite number of scans[12].



| Area dose (AD) | SPL dose (LD) | Dot dose (DD) |
|---|---|---|
| $AD = I_{beam} \cdot T_{dwell} / s^2$ ($\mu As/cm^2$) | $LD = I_{beam} \cdot T_{dwell} / s$ ($pAs/cm$) | $DD = I_{beam} \cdot T_{dwell}$ ($pAs$) |

*Figure 3.6. Expressions for the concepts: area dose, line dose and dot dose[12]*

We tried two different EBL exposure modes[7d, 11b]: the conventional mode, named *multispot (pixel-by-pixel)*, in which each design circle (area), representing the future hole in the PMMA resist is the result of the exposure consisting in filling the area with many electron

---

[c] *Area dose:* the amount of charge per unit area corresponding to each hole in the design pattern (introduced in the software (Elphy).

[d] *Exposure dose:* established as the number of incoming electrons (amount of charge per unit area) that are needed to fully develop the resist thickness, whatever is the shape of the pattern.

[e] *Dose fraction:* the number that multiplying with the area dose gives the delivery (exposure) dose in each feature.

[9] *Dwell time:* the time for what the electron beam remains in each pixel to deliver the correct dose.

beam spots with the diameters ten times smaller than the desired hole diameter (**Figure 3.7a**). The non-conventional *singlespot* (*dot*), in which each design circle (future hole) is realized by a single exposure with a single electron beam spot with a diameter comparable to the size of the desired hole diameter (**Figure 3.7b**).

The experimental parameteres varied for both exposure modes were: $V_{acc}$, in the range of 5–30 kV; spot size (in general, a spot of 3 was used); area dose, in the range of 100–300 $\mu C/cm^2$; step size, of 0.02 or 0.01; dose fraction, in the range of 0.2–10; dwell time, of $\leq$ 2 ms. The intensity of the beam was measured once at the beginning of the experiment, and could fluctuate from experiment to experiment. The PMMA, usually used for EBL, was in the commercially available liquid form (2% anisole) with a molecular weight of 950 K and was spin coated onto a silicon wafer substrate to have a 100 nm thickness. The developments was prepared by immersing the patterned sample first into the developper (mixture of MIBK:IPA of 1:3) for 50 s and then into the stopper IPA for 30 s, followed by nitrogen drying.



**a) Multispot mode**

Electron beam spot with the diameter $d_{spot}$

$d_{spot}$

Design circle diameter ($\Phi_{circle}$)

To produce the future single hole → the circle is filled with many electron beam spots. $10 \times d_{spot} \sim \Phi_{circle}$

**b) Singlespot mode**

$d_{spot}$

Design circle diameter ($\Phi_{circle}$)

To produce the future single hole → the circle is filled with a single electron beam spot. $d_{spot} \sim \Phi_{circle}$
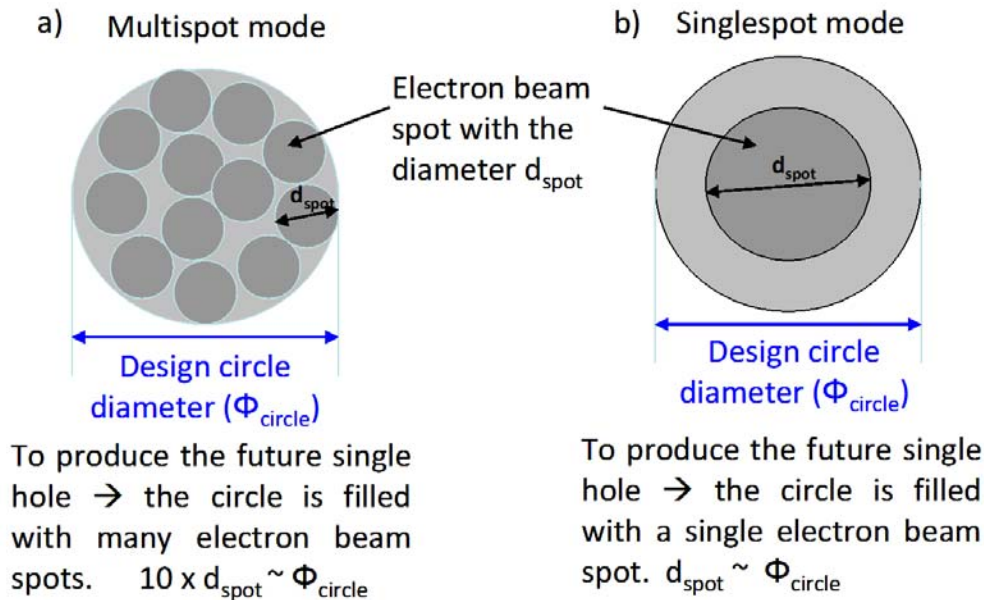
*Figure 3.7. EBL exposure modes*

Elphy program gives the possibility to vary some of the irradiation parameters while the rest can be calculated. For example, in *multispot mode*, by introducing the intensity (nA), area dose ($\mu C/cm^2$) and $V_{acc}$ (kV), the program automatically calculates the dwell time (ms) and step size. In this case, the hole dimensions and periodicity are given in the design pattern. We used holes of 350-600 nm diameter and a periodicity of 600-700 nm. In *singlespot mode*, the pattern contains only the periodicity (600 nm in this case) and after introducing the intensity and $T_{dwell}$, the dot diameter with the corresponding dose will be calculated by the program. But the proper dose is determined during exposure process and depends on interrelated parameters such as resist type, temperature, beam energy and intensity. In section 3.1.3, the most relevant results with the optimized controlling parameters are presented.

**Nanoimprint lithography** *(Approach 1)*

The whole work related to nanoimprint was carried out in the clean room of the IMB–CNM using an OBDUCAT NIL–4–SS model nanoimprinter system (**Figure 3.8**). The patterning process was computer controlled by the program NIL-4 System control.



*Figure 3.8. NIL available at the clean room of the IMB–CNM institute.*

The NIL process is much simpler than EBL and involves only three experimental parameters: pressure, temperature and time. In a typical process cycle, two steps were applied: (1) heating up to 160 °C at 0 bar and keeping this temperature for 100 s; (2) maintaining the temperature at 160 °C at a pressure of 40 bar for 300 s, followed by cooling down to 80 °C when the mold was released from the sample.

The PMMA used for NIL had a molecular weight of 35 K and was spin coated to have a thickness of 200 nm. We used a silicon mold (provided by CNM) with pillars of 120 nm height, diameter of 300-500 nm and periodicity of 1 μm in square array in a trial experiment (**Figure 3.9**). The PMMA was slightly thicker than the pillar height on the mold in order to protect the mold from touching the substrate. The referred results are presented in section 3.1.3



*Figure 3.9.  AFM image of silicon mold used for patterning by NI*

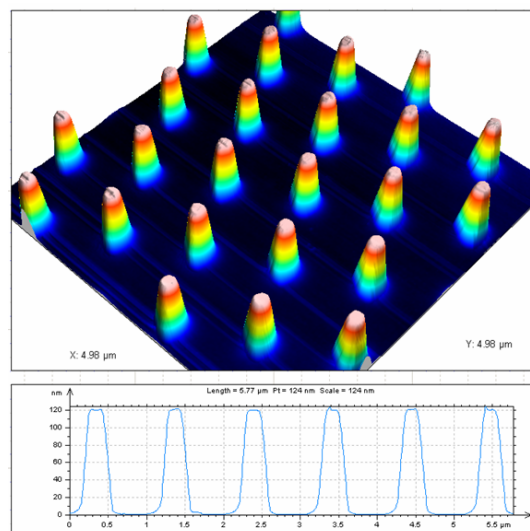### Magnetic hybrid nanocomposites *(Approach 2)*

Nanocomposites, in the form of hybrid inorganic-organic materials, can be homogeneous or heterogeneous materials with one of the components being in the nanometer range. The multiphase structure of these materials with improved or unusual features makes them very attractive for multifunctional material designing with innovative industrial applicabilities (electronics, mechanics, energy, environment, biology[8a] – and possibly, photonics). Depending on the nature of interaction between the organic and inorganic components, hybrid materials can be classified into two categories[8a, 15] : (1) the cohesion of the whole structure is given by weak hydrogen, van der Waals or ionic bonds and (2) the two components are linked together through strong chemical covalent bonds.

Our approach was to prepare magnetic nanocomposites by physical method (included in the first category) – mixing a preformed polymer (PMMA) with pre synthesized magnetic nanoparticles in colloidal dispersion. The reasons were the followings: i) accessibility, the polymers required for the lithography techniques were commercially available and in our laboratory, we synthesized magnetic nickel nanoparticles, ii) a chemical method for the nanocomposites was out of the question, since the Ni nanoparticles synthesis requires high temperature that is not compatible with a preformed PMMA polymer. On the other hand the strategy of *in-house* PMMA polymer synthesis around the magnetic nanoparticles was not considered since it was very difficult to obtain the polymer molecular weight exactly required for lithography and far from the group expertises.

PMMA is a hydrophobic polymer with the structure presented in **Figure 3.3**. It dissolves in the non-polar anisole that is miscible with hexane (the dispersion media for the 8 nm Ni NPs). Based on this, we tested different types of mixtures:

**Type I**: mixing 0.1 ml PMMA (950K, 2% anisole) with 0.1 ml Ni/hexane ($C_{Ni}$ of $10^{-2}$ M) at room temperature by a shaker.

**Type II**: adding 0.25 ml Ni/hexane ($C_{Ni}$ of $1.7 \times 10^{-2}$ M) drop by drop to 0.5 ml PMMA (950K, 2% anisole, heated at 50 °C) under magnetic stirring followed by stirring at 50 °C for 2.5 h.

**Type III a**: adding 20 μl Ni/hexane ($C_{Ni}$ of $10^{-1}$ M) drop by drop to 1 ml heated (at 60 °C for 15 min) PMMA (550K [16] and 35K NIL) under magnetic stirring followed by stirring at 60 °C for 2.5 h (nanocomposites labeled as *EBL-4* and *NIL-5*).

**Type III b**: adding 5 μl Ni/hexane ($C_{Ni}$ of $3.7 \times 10^{-1}$ M) drop by drop to 0.5 ml heated ( at 60 °C for 15 min) PMMA (550K [16] and 35K (NIL) under magnetic stirring followed by stirring at 60°C for 2.5 h (nanocomposites labeled as *EBL-7* and *NIL-8*).

**Type III c**: A very concentrated Ni-hexane colloidal dispersion was evaporated and over the dried NPs, 2 μl of oleic acid and 0.5 ml PMMA were added under magnetic stirring and heating (60 °C, 2 h) (nancomposites labeled as *EBL-11* and *NIL-11*) . The materials labeled as *EBL-12* and *NIL-12* contain half of the magnetic amount used for to the nanocomposites *EBL-11* and *NIL-11,* respectively.

The summary of the obtained nanocomposite film are presented in **Table 3.1.**

*Table 3.1. Summary of the prepared materials by EBL and NIL techniques and their processability.*

| Mixing type | label | mg Ni@surfactant / ml nanocomposite | Deposition mode /silicon wafer | Film quality * | Patterning |
|---|---|---|---|---|---|
| Type I | *EBL–1* | 0.3 mg/ml | Drop casting with micropipette | Bad/not uniform film | NO |
| Type II | *EBL–2* | 0.33 mg/ml | Drop casting with micropipette | Bad/not uniform film | NO |
| Type III a | *EBL–4* | 0.12 mg/ml | Spin-coating (3000rpm/45s, baked at 180°C /2 min ) | Good/ uniform film | YES |
| | *NIL–5* | 0.12 mg/ml | Spin-coating (3000rpm/35s, baked at 150°C /2 min) | Good/ uniform film | YES |
| Type III b | *EBL–7* | 0.35 mg/ml | Spin-coating (3000rpm/35s, baked at 150°C /2 min) | Bad/not uniform film | NO |
| | *NIL–8* | 0.22 mg/ml | Spin-coating (3000rpm/40s, baked at 140°C /2 min) | Good/ uniform film | YES |
| Type III c | *EBL–12* | 13 mg/ml | Spin-coating (3000rpm/40s, baked at 140°C /2 min) | Bad/not uniform film | NO |
| | *NIL–12* | 19,5 mg/ml | Spin-coating (3000rpm/40s, baked at 140°C /2 min) | Bad/not uniform film | NO |
| | *EBL–11* | 26 mg/ml | Spin-coating (3000rpm/40s, baked at 140°C /2 min) | Bad/not uniform film | NO |
| | *NIL–11* | 38 mg/ml | Spin-coating (3000rpm/40s, baked at 140°C /2 min) | Bad/not uniform film | NO |

* film quality, refers to the deposition uniformity (the same thickness of the film). Optically, this can be seen as single color (for the same thickness) or more colors (for different thickness-not uniform).

## 3.1.3. Results and discussions

Two different approaches were tried for both lithographic methods in order to fabricate 2D magnetophotonic crystals (**Figure 3.1)**. *Approach 1* includes patterning of the PMMA film (EBL/NIL) followed by infiltration (drop casting method using a micropipette) with colloidal dispersion of magnetic nanoparticles. *Approach 2,* is a direct patterning (EBL/NIL) of PMMA film doped with magnetic nanoparticles.

### Approach 1–EBL: multispot mode

The 2D photonic crystal was designed to be operative at visible wavelengths. In this consideration, we patterned hexagonal array with periodic air hole spacing at 600–700 nm and holes diameter ($\Phi$) in the range of 350–600 nm using both exposure modes.

For the fabrication of photonic materials, PMMA should have good verticality, meaning that the developed area (dissolved PMMA) in the cross-sectional image looks as a cylinder with vertical sidewalls and high dimensional accuracy[11b] (**Figure 3.10b)**. This can be obtained by a high electron energy (high $V_{acc}$) that gives a long penetration depth into the

PMMA resist with negligible proximity effect due to the secondary electron induced exposure[7c].
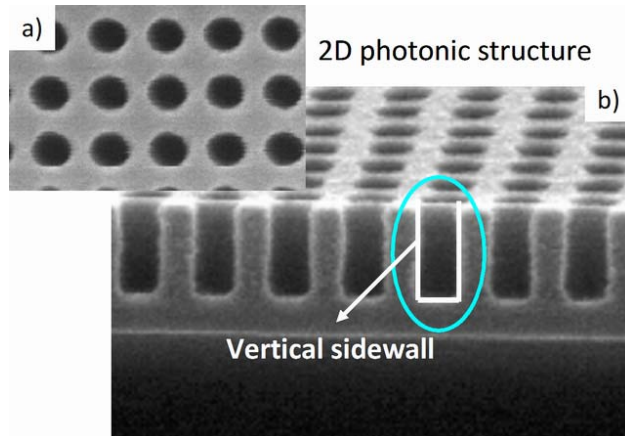


**Figure 3.10.** *SEM images of the surface (**a**) and cross-section (**b**) a 2D photonic structure fabricated by EBL techniques using the single mode exposure and $V_{acc}$ of 50 KV[11b]*

In our experiments, an acceleration voltage of 30 kV (the maximum for the setup) was used. The other important parameters were the dose exposure and dose fraction. These play an important role in determining the real dimension of the structure because they are correlated to the electron scattering together with the secondary electron emission[7a]. Consequently, the same design irradiated with different exposure doses (area dose multiplied with dose fraction) gave different dimensions for the structure (slightly different from the design dimensions) (**Figure 3.11**).

In case of an area dose of 100 μC/cm$^2$ (**Figure 3.11a**), the hole was only partial with a diameter of around 450 nm, smaller than the 600 nm design. This means that this energy was not enough to penetrate the resist and to break the polymer in smaller parts which can be dissolved in the developer (MIBK:IPA). By doubling the exposure dose, a good pattern was obtained with a hole diameter of around 650 nm and periodicity of 800 nm (**Figure 3.11b**). These conditions seemed to be appropriate for approach 2 as well.



Pattern:
holes of Φ = 600nm
periodicity = 700nm
100 μm x 100 μm

$V_{acc}$ = 30 KV
Area dose = 100 μC/cm$^2$
Dose fraction = 1
Exposure dose = 100 μC/cm$^2$

$V_{acc}$ = 30 KV
Area dose = 100 μC/cm$^2$
Dose fraction = 2
Exposure dose = 200 μC/cm$^2$
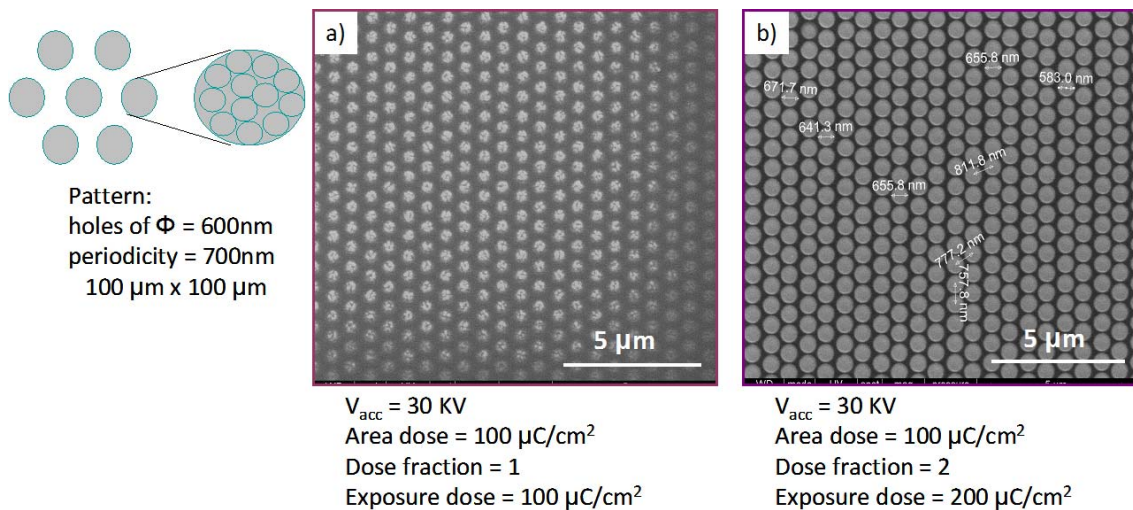
**Figure 3.11.** *Multispot mode with different exposure doses of 100 μC/cm$^2$ (**a**) and 200 μC/cm$^2$ (**b**)*

118

The pattern was further used for infiltration by drop casting using hexane dispersion of 8 nm Ni NPs. Unfortunately, the PMMA patterned film, with a molecular weight of 950 k and perhaps without cross-linking (that harden the polymer) together with the additional exposure to the electron–beam for image acquiring, become weak and did not stand the organic solvents. The hexane containing the Ni NPs dissolved the whole PMMA film and the structure was destroyed (**Figure 3.12**). Although the PMMA used for NIL patterning was not exposed to electron beam, is dissolving as well in hexane. An explanation could be the much smaller molecular weight of the polymer of 35 k that makes it easily soluble in organic solvents. Thus, does not matter if the PMMA film (with both molecular weight of 950 k and 35 k) is patterned or not, it is not hard enough to be insoluble in hexane. Based on this founding, the *approach 1* (**Figure 3.1**) can be considered not appropriate for 2D magnetophotonic fabrication.
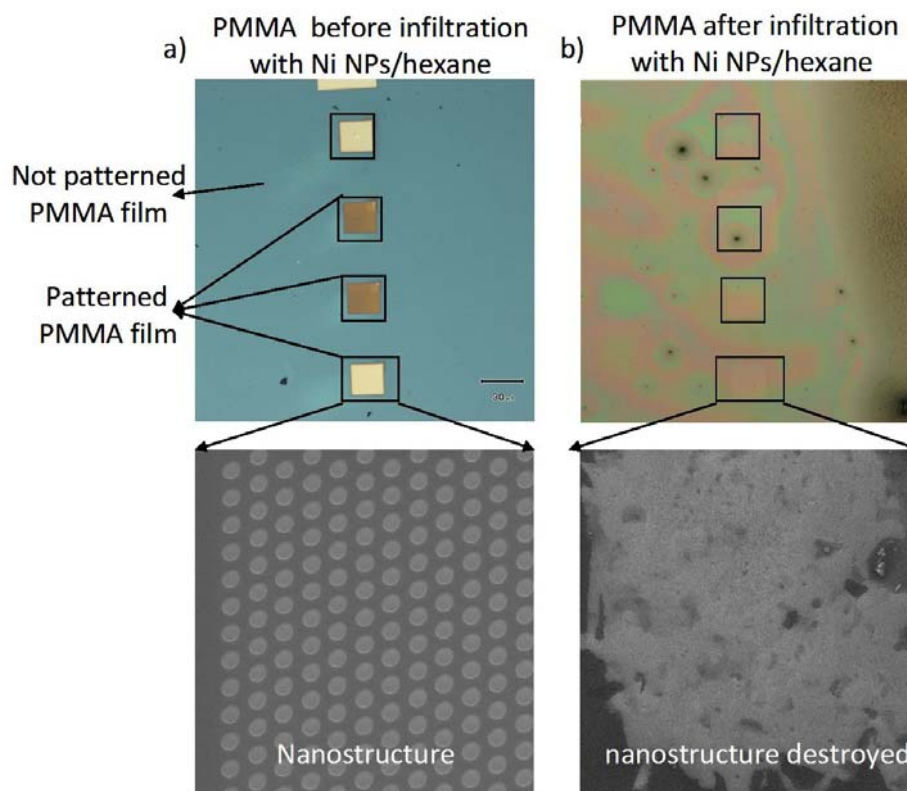


*Figure 3.12. PMMA pattern before and after infiltration with hexane dispersion of Ni NPs*

**Approach 1–EBL: singlespot mode**

Regarding the singlespot mode, we optimized the irradiation parameters in order to be further used for nanocomposite patterning (*Approach 2*). This patterning process is faster[7c, d, 11b] and gives better structures. As it was mentioned, the design contains only the periodicity value while the dot dose is calculated by the program, correlated with the intensity and $T_{dwell}$ (**Figure 3.5**). In this mode, we varied the dose fraction to control the dose of the feature and subsequently the dot diameter. In **Figure 3.13**, three patterns at different doses are presented.

**Pattern:**
periodicity = 600nm
100 µm x 100 µm

a)

3 µm

$V_{acc}$ = 30 KV
Dot dose = 0.22 pC
Dose fraction = 5
$T_{dwell}$ = 2 ms
$I_{beam}$ = 0.1079 nA

b)

3 µm

$V_{acc}$ = 30 KV
Dot dose = 0.23 pC
Dose fraction = 2
$T_{dwell}$ = 2 ms
$I_{beam}$ = 0.115 nA

c)

3 µm

$V_{acc}$ = 30 KV
Dot dose = 0.23 pC
Dose fraction = 1
$T_{dwell}$ = 2 ms
$I_{beam}$ = 0.115 nA

*Figure 3.13. Dot method with different doses of 1.1 pC (a), 0.46 pC (b) and 0,23 pC (c) used to pattern the PMMA film.*

As it can be seen, a dose of 0.22 x 5 = 1.1 pC (**Figure 3.13a**) is too high for the feature. The doses of 0.46 pC (**Figure 3.13b**) and 0.23 pC (**Figure 3.13c**) seem to create a good pattern.

For a more detailed characterization, AFM analysis was performed to determine the hole diameter, depth and periodicity. The results are presented in **Figure 3.14**. The profile analysis showed an oval rather than a circular structure for both doses, and a mean hole diameter of around 503 nm and 390 nm were found for 0.46 pC and 0.23 pC doses, respectively. The periodicity values were found slightly larger than the design value (600 nm) but still in the desired range (670 nm and 660 nm for 0.47 pC and 0.23 pC, respectively). A significant difference was observed in the depth of the holes. The thickness of the not patterned PMMA film was 100 nm while t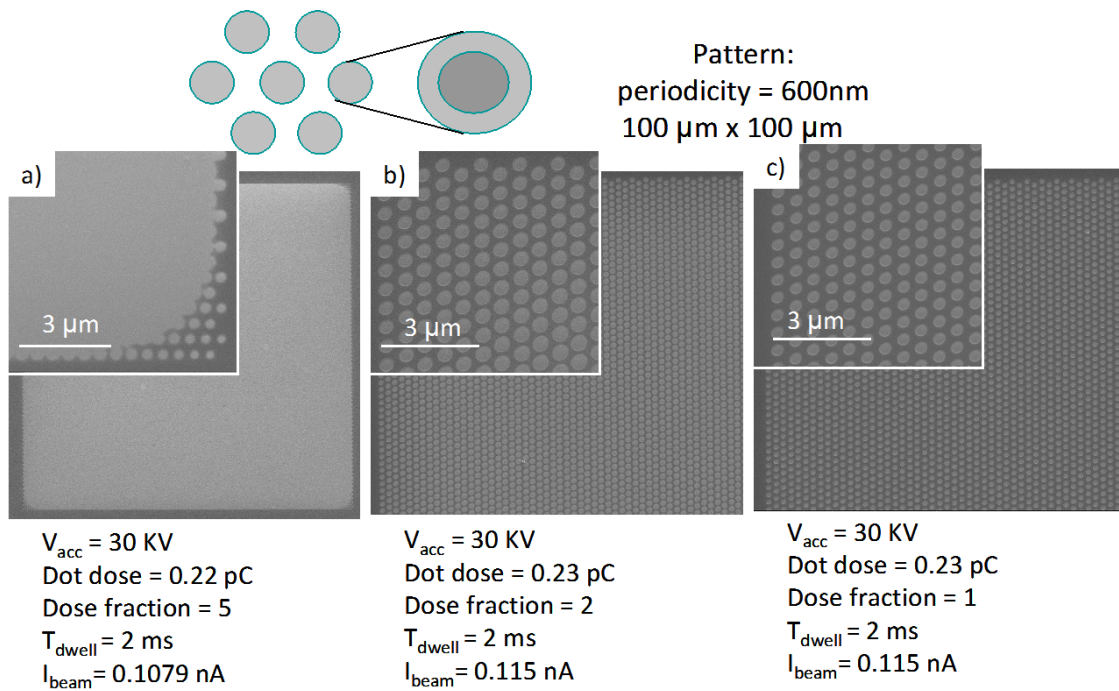he AFM profile analysis showed a mean depth of the air hole of ~87 nm for the smaller dose and ~37 nm for the bigger dose. In both cases, the sidewalls show verticality and the bottom of the holes is almost flat suggesting that this dot approach could be a good method for 2D magnetophotonic materials fabrication by *Approach 2.*

### Approach 2-magnetic nanocomposites

Although the anisole (solvent for polymer) and hexane (solvent for NPs) are miscible, with the physical mixing approach in our case, Ni NPs agglomerates in the host PMMA with 950 K molecular weight (**Figure 3.15**). Similar results have been reported by others for PMMA doped with CdSe@ZnS NPs[11e]. The authors explained the agglomeration as a consequence of a bad compatibility of the phosphine (TOPO) surfactant layer at the NCs surface with the host polymer. This explanation could be also applied for our results, since the Ni NPs are covered by a layer containing phosphine (TOP) and oleic acid surfactants.
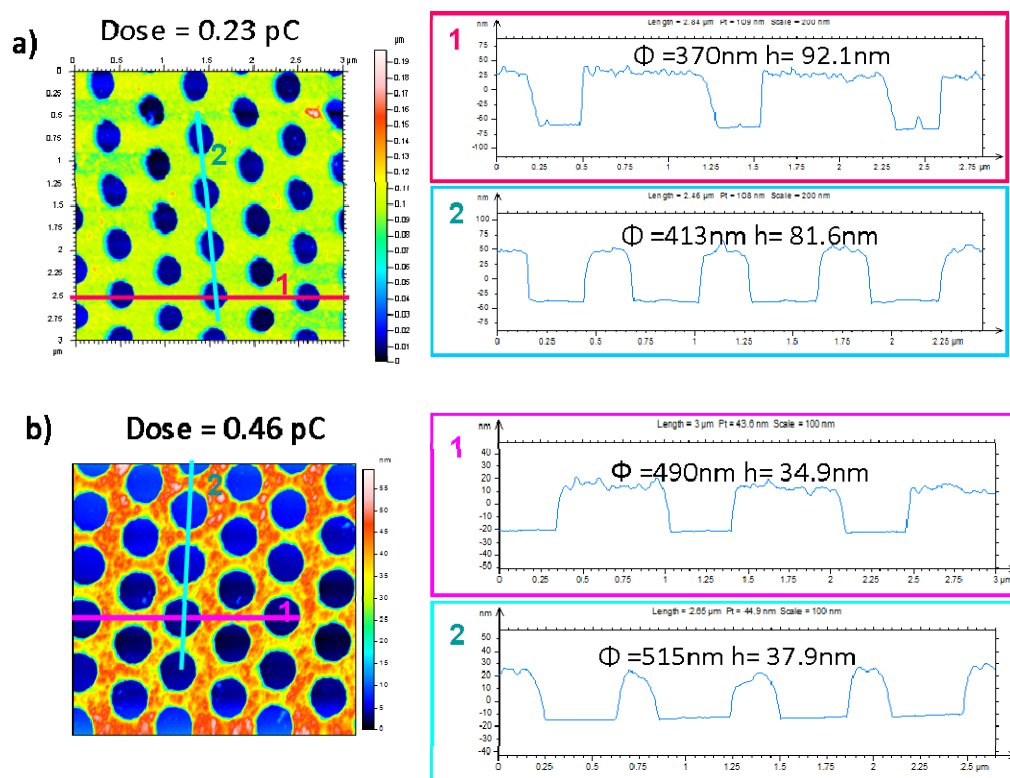
**Figure 3.14.** AFM profile analysis of the nanostructures obtained by single dot approach using two different doses.

To overcome this difficulty and to have a homogeneous distribution of NPs in the polymer environment, some authors [12e, 15] have suggested to make a chemical interaction between the polymer and NPs surface. This could be possible by functionalization of polymer with amine or carboxyl groups, both being able to strongly bind to the nanoparticles surface, resulting so in homogeneous hybrid nanocomposites[11e].
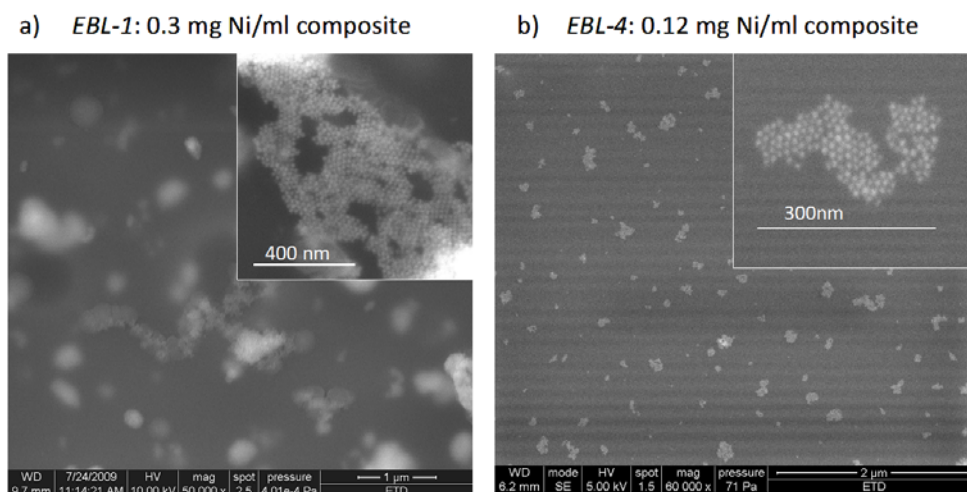


**Figure 3.15.** SEM images of nanocomposites, PMMA 950 k doped with different amount of 8 nm Ni NPs.

We have found that changing the molecular weight of the PMMA polymer, from 950 k to 35 k, we can obtain a homogeneous distribution of 8 nm Ni NPs in the polymeric film, without modifying the NPs surface and using the same mixing procedure. By increasing the amount of NPs, the homogenity of the nancomposite is still preserved (**Figure 3.16**). The Ni NPs appear as bright spots in the SEM images. An explanation for our success could be the smaller molecular weight of the polymer used, being correlated with polymer linearity and with a much more space between the polymer chains and therefore a better individual dispersion of nanoparticles.
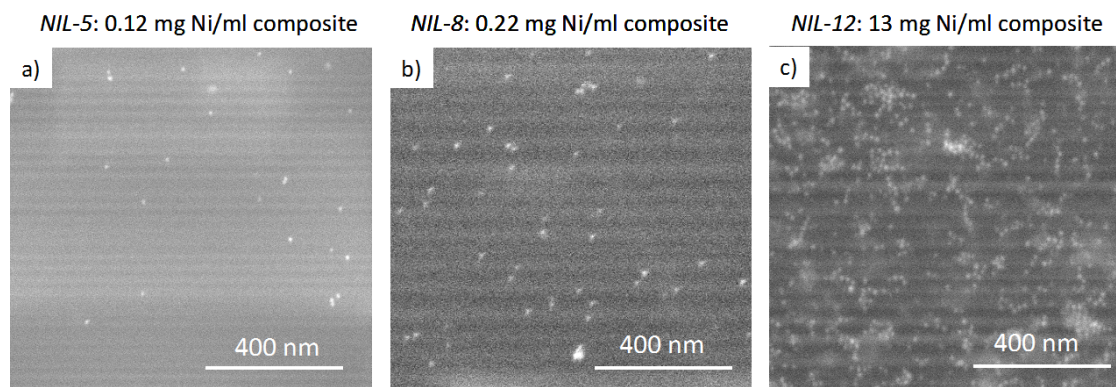


*Figure 3.16.* SEM images of nanocomposites, PMMA 35 K doped with different amount of 8 nm NiNPs

## Approach 2– patterning the nanocomposites by EBL and NIL

To pattern the most uniform magnetic nanocomposite film, we have used first the EBL patterning parameters found to be optimal with respect to our requirements in the case of pure PMMA film (**Section 3.1.3**). These parameters are summarized in the following table.

*Table 3.2. Summary of the patterning conditions found as optimal for pure PMMA film*

| Exposure parameters used for pure PMMA film | Exposure mode | |
|---|---|---|
| | Multispot | Singlespot |
| Pattern periodicity (nm) | 700 | 600 |
| Pattern area (μm x μm | 100 x 100 | 100 x 100 |
| $\Phi_{hole}$ (nm) | 600 | – |
| $V_{acc}$ (kV) | 30 | 30 |
| $I_{beam}$ (nA) | – | 0.115 |
| Area / dot dose ($\mu C/cm^2$ or pC) | 100 | 0.23 |
| Dose fraction | 2 | 1 |
| $T_{dwell}$ (ms) | – | 2 |

We chose the material labeled as *EBL–4* for patterning. Unfortunately, these parameters did not work for the hybrid materials due the roughness of the film, the changed density and subsequently the electron-solid interaction. Thus, other experimental conditions were necessary to find. With the changed parameters, the multispot mode did not work very well (no defined patterns could be obtained neither for $V_{acc}$ of 30 kV nor 5 kV). The singlespot mode seemed more appropriate to define a good photonic structure. Two of the patterns found to be optimal for magnetic nanocomposites patterning are shown in **Figure 3.17**. In these patterns, the holes diameters and periodicities obtained were 460 ±20 nm and 650–

700 nm, respectively (**Figure 3.17a**) and 400±20 nm and 650-700 nm, respectively (**Figure 3.17b**), both being suitable for our requirements.
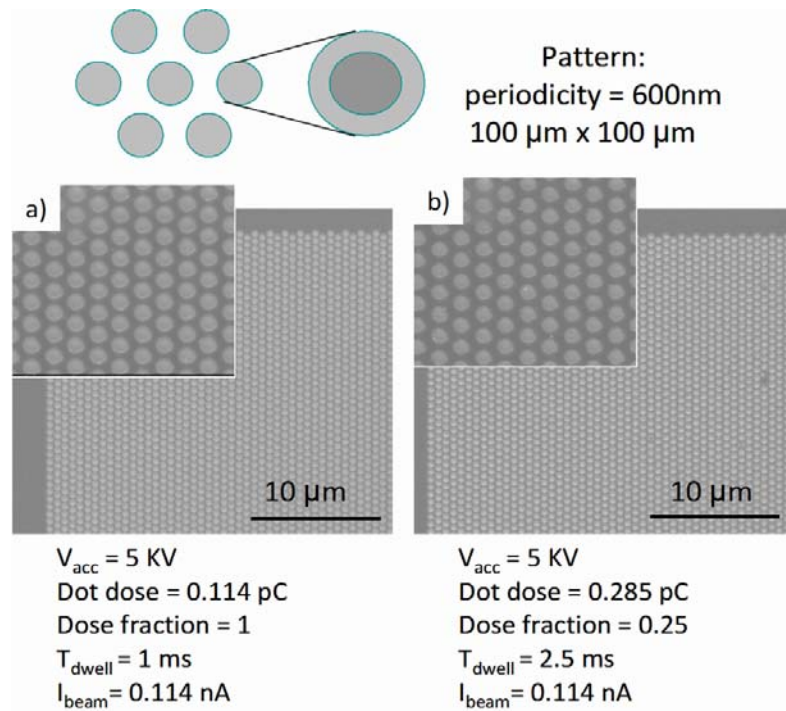


**Figure 3.17.** *SEM images of nanocomposites patterned by EBL-singlespot approach and using two different doses of 0.114 pC (a) and 0.071 pC (b).*

For NIL techniques, the nanocomposite labeled NIL–8 was used (parameters presented in the methodology section). The pattern obtained is shown in **Figure 3.18**, being the almost exact replica of the mold (**Figure 3.9**) as followings: i) the mold pillars were 120 nm height and the replica presented holes of 100 nm depth; ii) the pillar base diameter was 500 and the corresponding hole diameter was 500 nm; iii) the periodicity of 1 μm in square array of the mold was preserved in the replica, too.
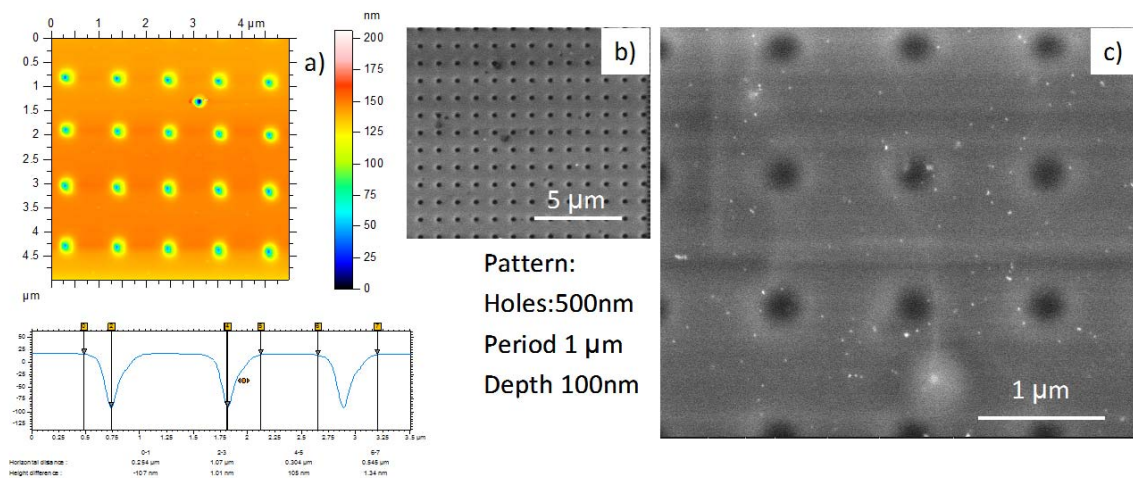


**Figure 3.18.** *Magnetic nanocomposites (NIL–8) with the corresponding AFM image with its profile analysis (a) and SEM images (b and c) of The pattern dimension were given by the profile analysis.*

The patterned magnetic nanocomposites, *EBL-4 and NIL-8* were subjected to optical (Annex, A.ii.7) and magneto-optical measurements (Annex, A.ii.9). Unfortunately no optical photonic band gap was found for both EBL-4 and *NIL-8* material (**Figure 3.19**) and the magnetic amount of 0.12 mg/ml (*EBL-4) and of 0.22 mg/ml (NIL-8)* in the hybrid nanocomposite was not enough to give a magnetic signal. Further we increased very much (almost 100 times) the magnetic content of 13 mg/ml (EBL-12) and 19,5 mg/ml (NIL-12) with the goal of obtaining a magnetic response. Unfortunately due to the high content of solid component (the magnetic nanoparticles) within the liquid polymer, the density and roughness of the mixture was changed considerable respect with the pure PMMA and this affected the spin-coating, being impossible to obtain a uniform film on an area, large enough to be patterned (by both EBL and NIL). But with the appropriate optimization of magnetic content in the hybrid mixture, could be obtained a uniform film that can be pattern. A suggestion would be that the magnetic amount to be within the range 1 -5 mg/ml (for EBL) and 1-10 mg/ml (for NIL) (as a future work).
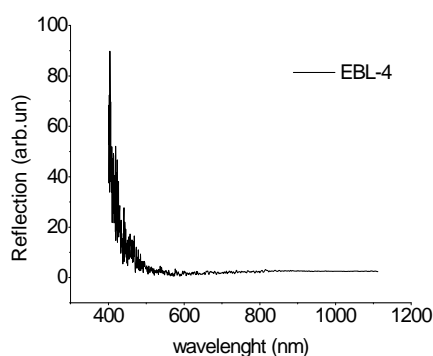


**Figure 3.19.** *No photonic band gap can be observed by reflectivity measurements*

## 3.2 GOLD ARRAY (NANOCAVITIES / NANODISCKS) INCORPORATED WITH MAGNETIC NANOPARTICLES (collaboration work)

An alternative method of enlarging the magneto-optical signal is not to exploit photonics, but plasmonics[2a]. Surface plasmon resonances are light waves trapped at the dielectric/metal interfaces due to the resonant and collective oscillation of free electrons. The most attractive property of plasmons is their ability to concentrate the energy of light into small regions at a metal-dielectric surface, providing thus extremely large light-matter interactions. The incorporation of magneto-optical materials into photonic-plasmonic structures[17] provides, then, a pathway for tailoring the magneto-optical spectral response and enhancing the

magneto–optical signal at the wavelengths for which the plasmons are excited. This gave rise to a collaboration work, briefly presented in this section.

**Methodology and materials morphology**

We have coated corrugated gold (nanoholes and nanodisks array)/dielectric interfaces with magnetic (nickel and iron oxide) nanoparticles, yielding relatively low density nanoparticle coatings and surface coverage ($\approx 6\% - 50\%$).

The Au nanovoids and Au nanodisk arrays were provided by our collaborators (see attributions) and the fabrication methodology was presented elsewhere[18]. Also optical and magneto–optical measurements were performed by my physicists' colleagues (see attributions). The *ex-situ* chemical synthesis of magnetic nanoparticles (Ni and iron oxide) was described in Section 2.1–thermal decomposition and microwave heating and the experimental condition can be found in Table A.iii.1 and A.iii.2). The Au void and nanodisk arrays were infiltrated by vertical dipping into the hexane colloidal dispersion of Ni (*D_TD.Ni_16*) and iron oxide (*D_MW.iron oxide_6.14*) nanoparticles, respectively for a few hours. TEM micrographs with a high resolution images and electron diffraction area (as upper and lower insets) of the infiltrated nanoparticles are presented in **Figure 3.20a and b**.
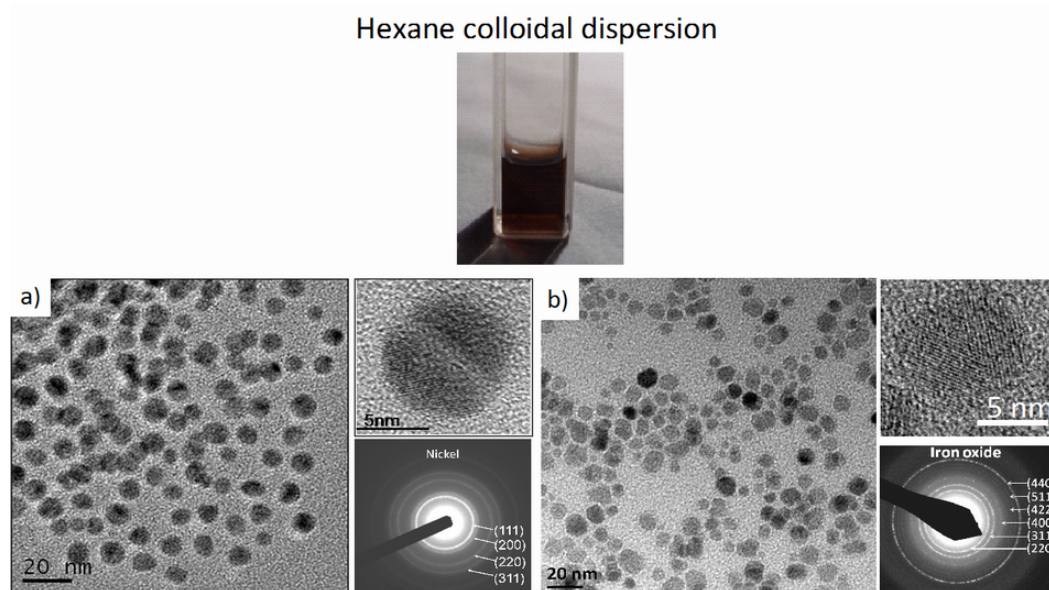


***Figure 3.20.*** *TEM micrographs of 8 nm magnetic nanoparticles: (**a**) Ni and (**b**) iron oxide. High resolution TEM of the both NPs presented as upper insets a and b. SEDA pattern as lower insets*

In **Figure 3.21a and b** the SEM imaging on the Au void template allows discerning the presence of Ni nanoparticles, better seen inside the void cavities (**Figure 3.21b**) as white spots. The surface nanoparticle density was estimated to be around $10^{-3}$ nanoparticles/nm$^2$, equivalent to a surface coverage of $\approx 6\%$. Concerning the Au nanodisk arrays (**Figures 3.21 c-e**), the white disks are Au and the iron oxide nanoparticles (smaller granules) are covering almost completely the Au array. Their surface density was estimated to be significantly larger than that found in the Au voids, around $5\times10^{-3}$ nanoparticles/nm$^2$ and surface coverage $\approx 50\%$.
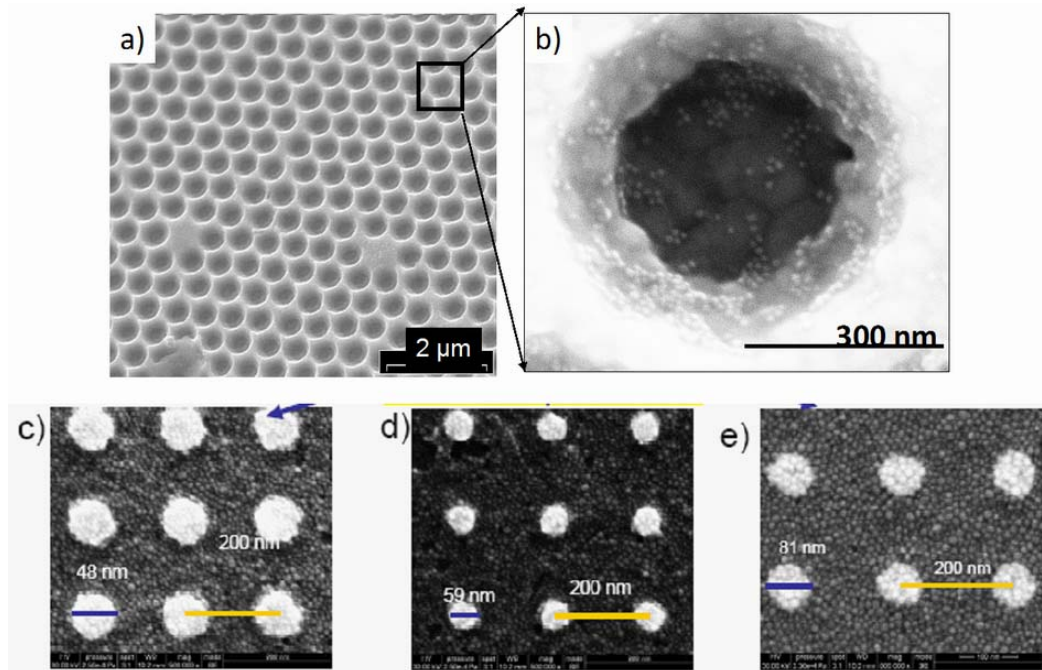
*Figure 3.21. SEM images of Au nanoholes (a, b) and nanodisks with different diameters (c-e) array infiltrated with magnetic NPs*

## Magneto-optical behavior

Without entering in details, neither for magneto-optical phenomenon description (presented in more details in **Chapter 1.3)** nor for optical and magneto-optical measurements procedures (described elsewhere[18]) in this part we want to highlight the magneto-optical behavior found in a hybrid systems, consisted of a magneto-optical material embedded in a plasmonic structures. Because the optical and magneto-optical measurements were done in reflections, the magneto-optical response is described by Kerr effect, rotation ($\theta$) and ellipticity ($\varepsilon$) (**Chapter 1.3**).

The magneto-optical activity was determined by measuring the Kerr rotation ($\theta$) and ellipticity ($\varepsilon$) at room temperature with a homemade setup in the range of wavelengths $\approx$ 390 – 850 nm in polar configuration by probing the magneto-optical signals with s- and p-polarized light incident at angles close to the normal to the surface. (**Figure 3.22**)
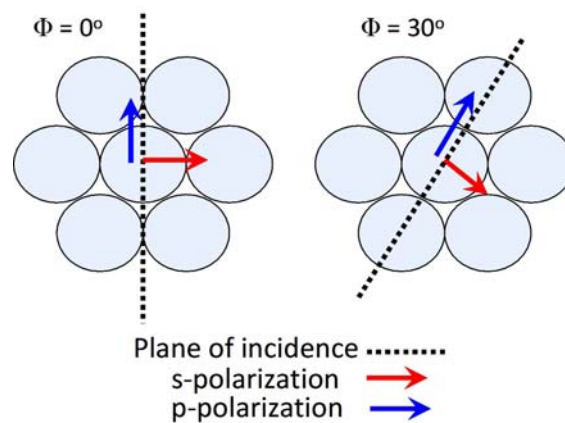


*Figure 3.22. Schematization of the geometry of the reflection measurements; $\Phi$ is the azimuth angle.*

From these measurements, we obtained the absolute value of the Kerr angle:

$$\left|\eta_{s,p}\right| = \left(\theta_{s,p} + i\varepsilon_{s,p}\right)^{\frac{1}{2}} \qquad \text{(Eq.3.1)}$$

for s-polarized light  (**Figures 3.23 a, e**) and p- polarized light (**Figure 3.23 c**) for both Au-voids and Au-disks arrays. We used $\left|\eta_{s,p}\right|$ as a probe of the coupling of the magneto-optical activity and plasmonic excitations.

On the other hand, we could probe the excitation of plasmons by measuring the reflection coefficients $\left|r_{ss}\right|$ and $\left|r_{pp}\right|$, directly drawn from the reflectance spectra (wavelengths $\approx 400 - 800$ nm (**Figure 3.23b, d, f**). To ascertain the effects of plasmons on the magneto-optical spectra, we recorded the optical and magneto-optical spectra by focusing the light inside the patterned areas (voids and disks, where plasmons are excited), as well outside, in non patterned areas (where plasmons are absent).
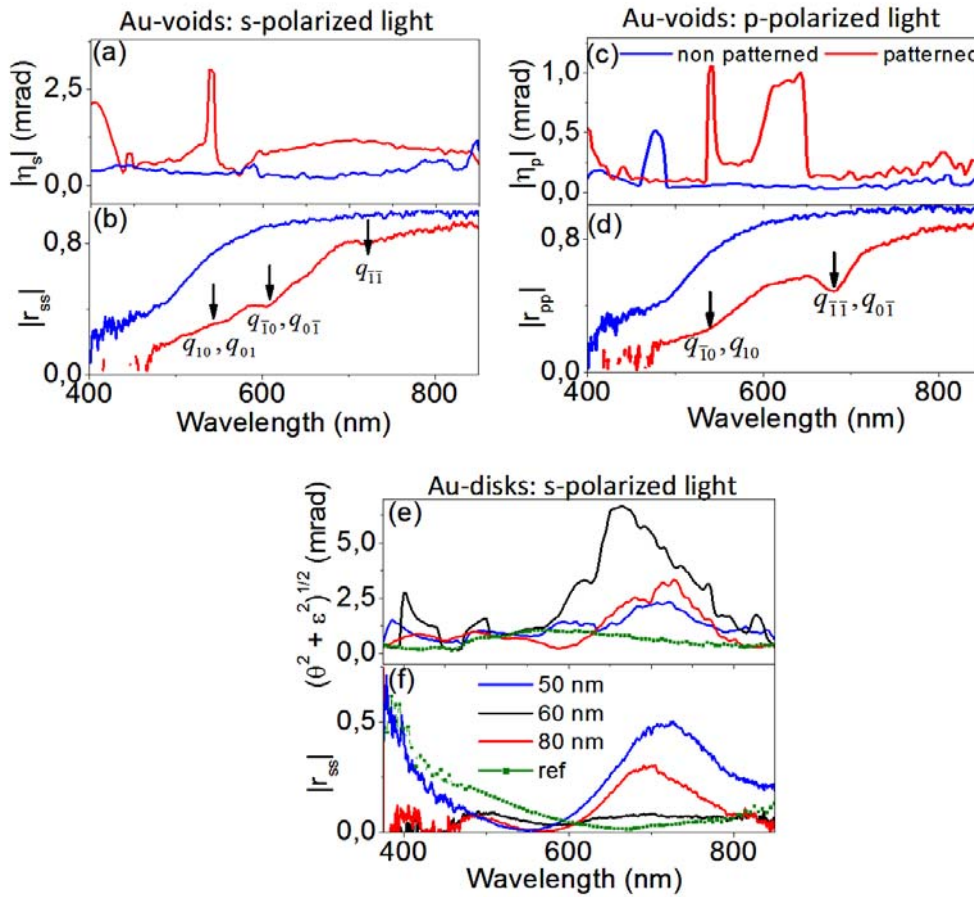


**Figure 3.23.** *Plots of the Kerr angles $|\eta_s|$ (**a, e**), $|\eta_p|$(**c**) and the diagonal reflectance coefficients $|r_{ss}|$(**b, f**) and $|r_{pp}|$(**d**) measured in the Au voids and Au-disks arrays, respectively.*

From reflectance spectra, we have inferred that delocalized (Bragg mode) plasmons are excited when light is focused inside the Au void patterns, whereas localized plasmons are excited in the Au nanodisks (Ref. M. Rubio submitted). Thus, the wavelengths at which delocalized  plasmons are excited in the Au void patterns are inferred by the appearance of dips in the reflectance spectra, and are indicated by arrows in the curves of $\left|r_{ss}\right|$ (**Figure 3.23b**) and $\left|r_{pp}\right|$ (**Figure 3.23d**). We observed for the Au-voids with Ni NPs system, that the Kerr angles $\left|\eta_s\right|$, $\left|\eta_p\right|$ (**Figure 3.23a, c**) are particularly enhanced in the patterned areas with

respect to the non–patterned regions for wavelengths close to excited Bragg modes (for s–polarized light: $q_{10}, q_{01}$ at $\lambda \approx 540$ nm and $q_{\bar{1}\bar{1}}$ at $\lambda \approx 700$ nm and for p–polarized: $q_{\bar{1}\bar{1}}, q_{0\bar{1}}$ at $\lambda \approx 540$ nm and $q_{\bar{1}0}, q_{10}$ at $\lambda \approx 630$ nm). A similar effect can be found for the Au nanodisk arrays infiltrated with iron oxide nanoparticles **(Figure 3.23 e, f)**, where localized plasmons are excited. It can be observed that the Kerr angle is strongly peaked at wavelengths at $\lambda \approx$ 720 nm for disks $d \approx 50$ and 80 nm, and at $\lambda \approx 670$ nm for $d \approx 60$ nm, with maximum values that reach up to $|\eta_s| \approx 6.7$ mrad **(Figure 3.23e)**. We have thus demonstrated that the coupling of the magneto–optical activity of magnetic nanoparticles with localized plasmon excitations of the Au nanovoids/nanodisk arrays gives way to a significant modification of the magneto–optical spectral response and to an enhancement of the magneto–optical activity[18].

Our results proof the potential of surface plasmons to generate large magneto–optical signal enhancements at specific wavelengths and to design promising strategies to modify the spectral optical responses of magneto–optical materials. Hybrids systems composed of magnetic nanoparticles with corrugated metal/dielectric surfaces offer a promising strategy for new applications in sensing, where the detection of very small changes of polarization of light can be exploited to sense the presence of nano–objects.

# 3.3 2D ARRAYS OF MAGNETIC HOLLOW SPHERES BY MICROWAVE–ASSISTED DEPOSITION

Fabrication of nanostructured materials by using sacrificial scaffolds, against which another material is deposited by mimicking the original template, has been demonstrated as effective approach towards achieving complex 2D and 3D porous architectures[19]. Templating over polymer colloids is a commonly used strategy to achieve long–range order, although it presents the drawback of having to remove the template either by solvent dissolution, etching, or calcination, which in turn could damage the intended hollow structure.

Microwave energy is becoming a very attractive tool in all areas of synthetic chemistry. As was mentioned **(Chapter 2.3)** it can be used not only for organic and inorganic nanoparticles synthesis but also for the fabrication of large–scale defect–free complex nanostructures with controllable morphologies and surfaces[20].

In this section we describe a facile and fast microwave–assisted sol–gel chemistry approach to produce 2D hollow magnetic frames using sacrificial templates[21]. The method has allowed us to grow in just a few minutes, a stoichiometric and homogeneous conformal nanometric coating of manganese ferrite on a polystyrene (PS) spheres coated with a thin layer of alumina ($Al_2O_3$) over an area of half a square centimeter. No post–treatment was required, the sacrificial template being removed simultaneously with the formation of magnetic nanoparticles.

## 3.3.1. Fabrication process

The microwave heating setup and working principle were described in **Sections 2.1 and 2.3.** Here we present briefly the experimental conditions used for deposition of *in-situ* synthesized magnetic nanoparticles over 2D monolayers. We used a template of polystyrene beads covered with a thin $Al_2O_3$, self-assembled in one monolayer with an area of 5x5 mm onto a glass slide substrate.

The $Al_2O_3$ layer was deposited by atomic layer deposition (Savanah 100 system by Cambridge Nanotech). Reactants for alumina growth, i.e. trimethylaluminum (TMA) and water were kept at room temperature. The PS monolayer was placed in the ALD chamber at 100°C, under a $N_2$ flow of 20 sccm and exposed to continuous TMA and water pulses (0.15 s each). Every TMA/water cycle was followed by a waiting time of 8 s, to ensure the complete reaction of the species on the exposed surface of the sample and evacuation of the non reacted ones. Hundred cycles were performed as the rate of alumina growth is about 0.1 nm per cycle, which yields an alumina layer of 10 nm.

The microwave-assisted deposition was performed in the microwave reactor by vertically immersing the template in the reaction solution by using a 10-mL closed pressurized vessel. The reaction media contained the organometallic precursors, iron(III) acetylacetonate ($Fe(acac)_3$) and manganese(II) acetate ($Mn(ac)_2$) (molar ratio of Fe/Mn = 2:1) with a total concentration of 0.1–0.15 M in anhydrous benzyl alcohol. During a typical run, the power was automatically adjusted to heat the sample to 160 °C ($T_{set}$), and the temperature was kept stable for 2, 5, or 10 min ($t_{set}$). After the reaction took place, the solution was automatically cooled to 50 °C by compressed nitrogen. The opal was washed with ethanol, in order to clean the surface and dried with nitrogen. The as prepared material was used for further characterizations.

Non-attached nanoparticles were also separated from the reaction media. Briefly, the reaction solution was mixed with excess EtOH (in a volume ratio of 1:3) and surfactant (20 μL, oleic acid for organic dispersion) followed by centrifugation at 6000 rpm for 30 min. The supernatant was discharged, and the precipitate redispersed in hexane (2 mL) containing oleic acid (10 μL) followed by centrifugation at 6000 rpm for 15 min. No precipitate was separated, and the stable dark brown solution was used for further analysis, the nanoparticles were labeled as *B_MW.MnFe$_2$O$_4$_8.2 and B_MW.MnFe$_2$O$_4$_8.5* (**Chapter 6.3 Table A.iii.4.**).The structure of the 2D materials was analyzed by SEM spectroscopy, described in **Annex A.ii.3.** The $MnFe_2O_4$ NPs were characterized by XRD (**Chapter 6.2 A.ii.1**), TEM (**Chapter 6.2 Aii.2**) and SQUID (**Chapter 6.2 A.ii.8**). A schematic representation of the synthesis steps and the resulting magnetic frames is displayed in **Figure 3.24.**

## 3.3.2. Results and discussions

The two-dimensional polystyrene colloidal template, vertically immersed in a solution containing the solvent and the organometallic precursors, was subjected to microwave radiation for a few minutes.
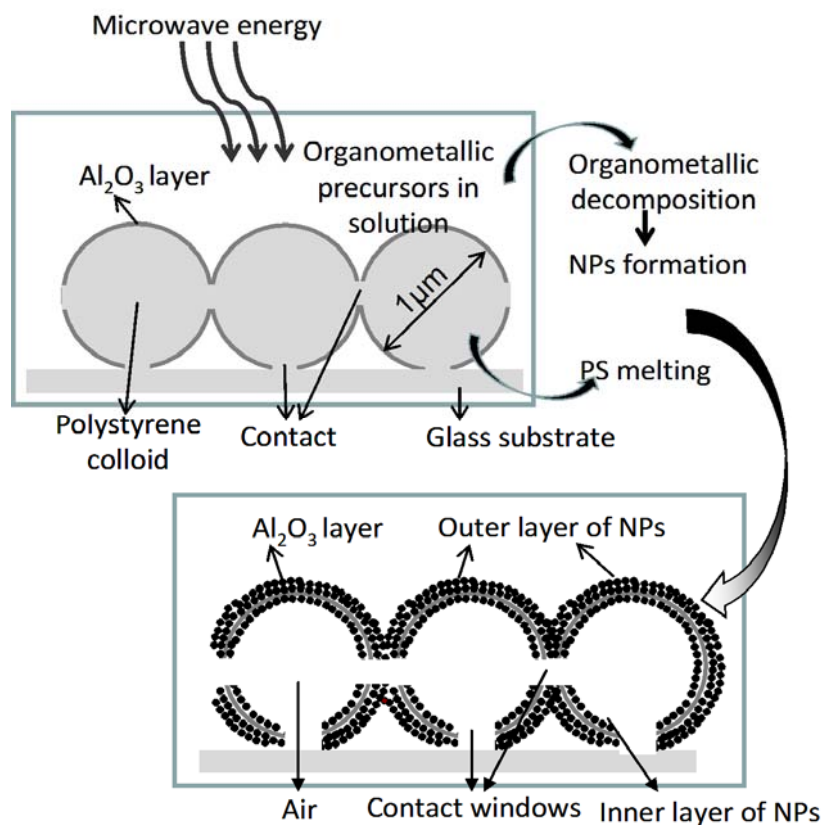
*Figure 3.24. Schematic representation of the fabrication process.*

The solvent (benzyl alcohol), being a polar substance, absorbs the microwave radiation and increases its temperature, which promotes the decomposition of the organometallic precursor and nanoparticles formation. By coating the PS spheres with a thin layer of an oxide ($Al_2O_3$ in this case), we gain two additional advantageous effects. Firstly, because PS has a glass transition at about 95–100 °C[22] and starts melting above this temperature[23], the PS template melted during the microwave synthesis at 160 °C and thus the $Al_2O_3$ frame kept the mechanical stability of the structure. Secondly, the hydroxyl surface terminations of the alumina efficiently absorb the microwave energy, which activates the surface and selectively promotes nucleation and growth of the magnetic nanoparticles on it. Thus, a final 2D hollow structure with a conformal magnetic coating was obtained. When the 2D template is made only of PS spheres, a non polar compound, the coating was not effective, and the template was not mechanically strong during particle deposition.

### *In-situ* synthesized $MnFe_2O_4$ magnetic nanoparticles

Prior to the discussion of the characteristics of the magnetic frames, the characterization of the nanoparticles is reported. As explained in the **Section 3.3.1**, non-attached $MnFe_2O_4$ nanoparticles (*B_MW.MnFe₂O₄_8.5)* could be separated from the reaction media by adding oleic acid once the reaction had taken place and thus stable colloidal dispersions in hexane were obtained after centrifugation and washing steps[24]. Transmission electron microscopy **(Figure 3.25a)** reveals small nanoparticles with good polydispersity and a rather irregular shape. A size distribution, fitted to a Gaussian function, gives an average size of 4.060.8 nm **(Figure 3.25b)**. The low polydispersity in the distribution of particle sizes is most probably a consequence of the rather uniform formation of nuclei as well as the uniform nanoparticle

growth in the microwave reactor. The powder X-ray diffractogram (inset of **Figure 3.25a**) and selected area electron diffraction pattern (SADP) (**Figure 3.25c**) can be indexed with that of the cubic inverse spinel manganese ferrite phase (ICDD PDF075-0035). The magnetic properties of the nanoparticles were evaluated by measuring the magnetization vs. the magnetic field strength at 300 K (**Figure 3.25d**) and the zero-field-cooled (ZFC), field-cooled (FC) magnetization curves (**Figure 3.25d inset**) vs. temperature. The absence of remnant magnetization at room temperature indicates the superparamagnetic character of the nanoparticles. The low blocking temperature at 26 K corresponds to very small nanoparticles, which is in agreement with the TEM data.
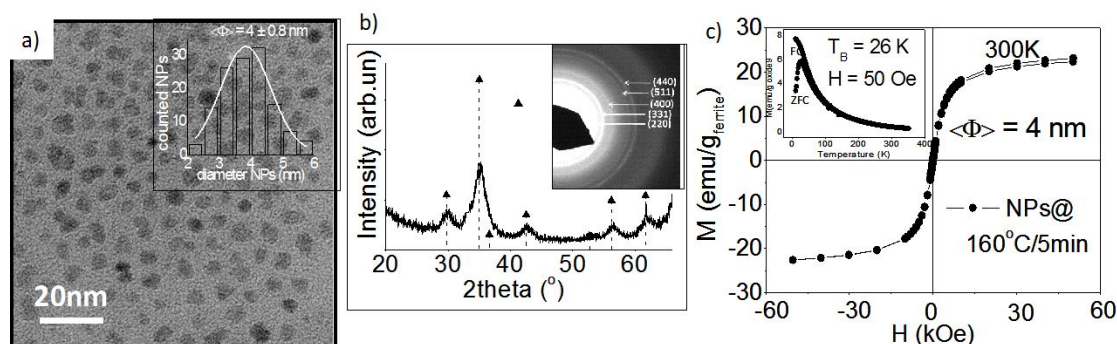


**Figure 3.25.** MnFe$_2$O$_4$ nanoparticles stabilized in organic media. **(a)** TEM image of monodisperse nanoparticles stabilized with oleic acid; the inset shows the powder X-ray diffratogram of these nanoparicles, **(b)** size distribution fitted to a Gaussian function, **(c)** the corresponding electron diffraction pattern, **(d)** magnetometry data; M(H) at room temperature and ZFC–FC curves at 50 Oe.

## 2D hollow magnetic frames

With regard to the 2D magnetic frames, the first observation was that the thickness of the coating can be controlled by the duration of the chemical reaction. Scanning electron microscopy (SEM) was used to study the surface of the magnetic frames at different reaction times (**Figure 3.26**). The PS template covered by the thin Al$_2$O$_3$ shell (about 10 nm) presents a very smooth surface (**Figure 3.26a and inset**); the reaction at 160 °C for 2 min resulted in partial coverage of the template (bright spots on the sphere surface) (**Figure 3.26b and inset**). The reaction with the precursor concentration (0.15 M) at the same temperature (160 °C) but with a longer reaction time (5 min) produces a complete conformal coating (**Figure 3.26c**). Higher magnification (**inset of Figure 3.26c**) confirmed that the layer was conformal, continuous and consisted of small nanoparticles. By increasing the reaction time to 10 min, the coverage increased to such an extent that the nanostructures were no longer evident and a continuous film was formed instead. At that point, if the growth continues, every sphere starts pushing against its neighbors, and cracks begin to appear in the nanostructure, as clearly seen in **Figure 3.26d.**
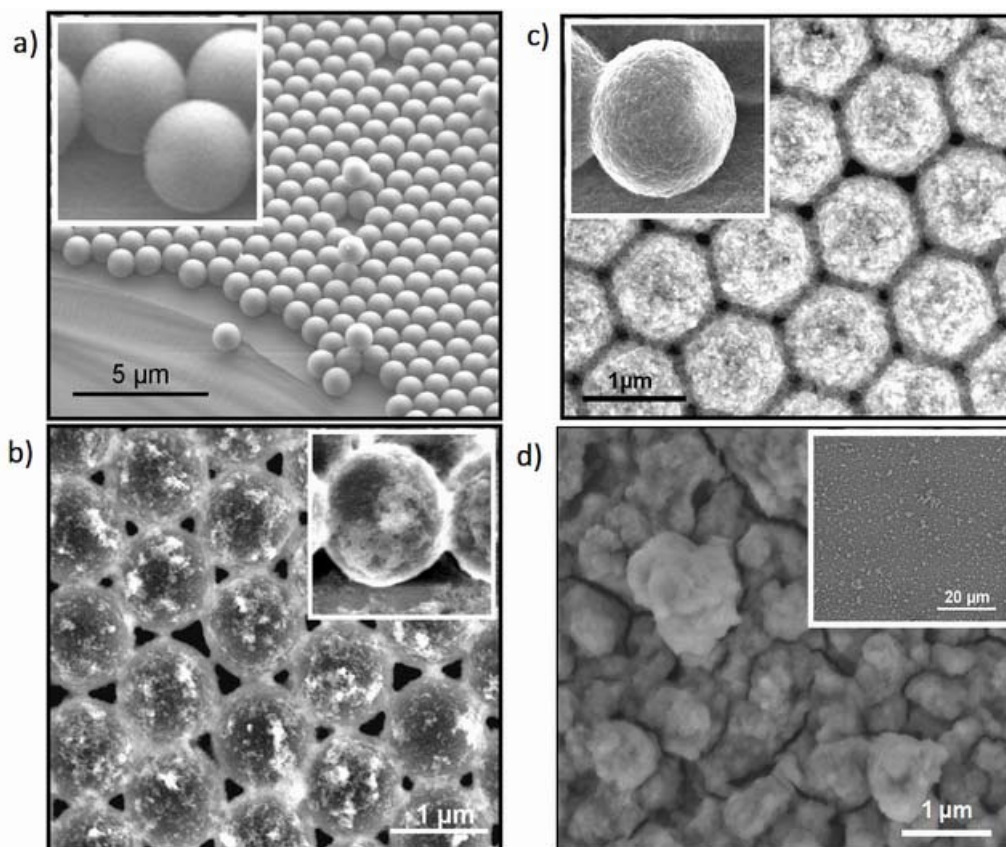
*Figure.3.26* The various coverage thicknesses depending on the duration of the chemical reaction are visualized by SEM micrographs. (a) The pristine opal (b) Partial magnetic coverage of the opal obtained at 160 °C/2 min; (c) Homogeneous magnetic coverage of the 2D template obtained at 160 °C/5 min (d) A thick magnetic film is formed at 160 °C/10 min over the 2D template

The next issue is what happens to the PS template during the chemical reaction that forms the nanoparticles. A close observation of the pristine template reveals that the PS spheres are in contact, and, therefore, the alumina will not be deposited on these contact areas (**Figure 3.24 and Figure 3.26**). Because PS is not very soluble in benzyl alcohol[25], we assumed that the disappearance of the PS during microwave heating resulted from a melting process. Since the microwave experiment was a very fast process – the full cycle did not took longer than 15 min – we can also safely assume that the melting of the PS and the nucleation and growth of the nanoparticles occurred simultaneously. When the PS melted, the contact areas between two PS spheres became contact windows, which allowed the diffusion of the organometallic precursors inside the spheres and consequently the formation of nanoparticles at the inner side of the alumina took place. This could be verified by the images taken from a transversal section across the templates (**Figure 3.27**). In the case of a 2-min reaction, it can be seen that the PS was only partially melted, and a small quantity of nanoparticles uniformly distributed (bright spots) inside the spheres can be observed (**Figure 3.27a**). By increasing the reaction time to 5 min, more nanoparticles are deposited on the outer shell and inner shell, a large fraction of the PS was melted, which left big voids, and a small fraction of the PS re-crystallized at the center of the spheres in the form of small cubes (**Figure 3.27b**)[26]. For a 10- min reaction time, the majority of the PS was melted, and large aggregates of nanoparticles accumulated at the center of the sphere (**Figure 3.27c**).
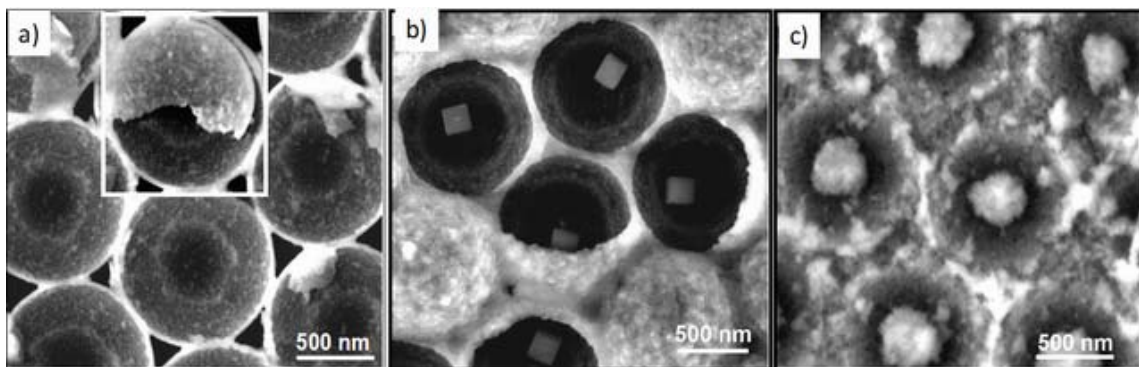
*Figure 3.27. SEM images of the transversal section across the spheres, which reveals the morphology within the hollow spheres. (a) The material with a bright $Al_2O_3$ shell (160 °C/2 min); the white spots uniformly distributed on the inner wall are nanoparticles. (b) Spheres with a thicker deposition within the spheres (5 min reaction). The cube inside is made of PS melted and recrystallized during the reaction. (c) After a 10-min chemical reaction under microwaves MW, the PS spheres disappear completely. The white spots inside the spheres are nanoparticle aggregates.*

To certify the coverage of the PS colloidal template with magnetic material, elemental analysis by energy dispersive X-ray spectroscopy (EDX) of the different materials was performed (**Figure 3.28**). The spectrum of the pristine template on a glass substrate is displayed in **Figure 3.28a;** naturally, iron and manganese peaks are not present. **Figure 3.28b** shows the spectrum, obtained at 160 °C over 10 min, of a thick magnetic film that completely covers the template, in which the Fe and Mn peaks are clearly visible. **Figure 3.28c–A** corresponds to the spectra (the scanned area represented by the square A of the template covered by a thinner ferrite layer, prepared at 160 °C over 5 min, and the intensity of the Fe and Mn peaks is smaller than in the previous case. Finally, **Figure 3.28c–B** corresponds to the spectrum of a cube inside the sphere (marked with a white cross), which reveals that no Mn and Fe is present in this area.
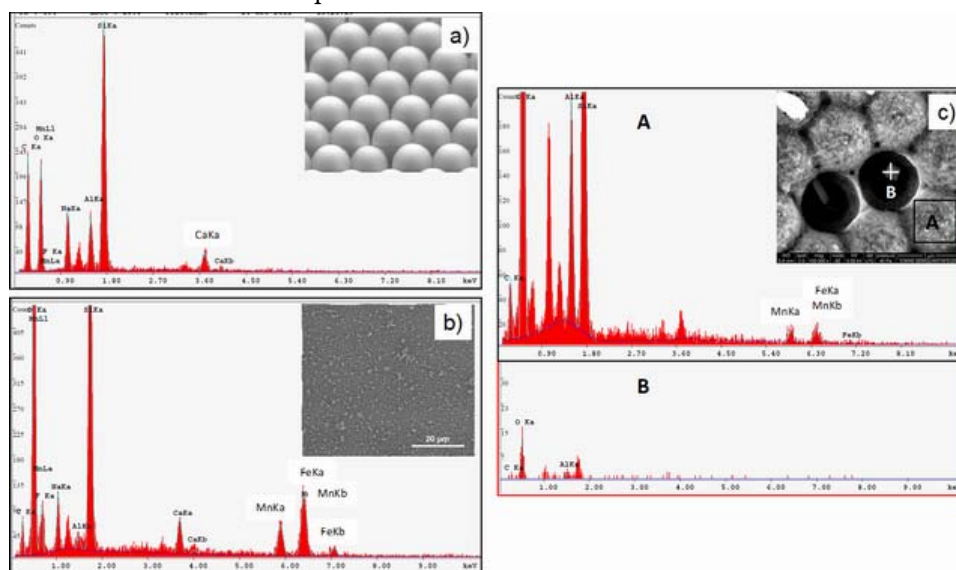


*Figure 3.28. EDX spectra for different materials: (a) the template of pristine PS + Al2O3 on a glass substrate; (b) magnetic film completely covering the template obtained at 160 °C/10 min; (c–A) spectra corresponding to the template covered by a ferrite layer at 160 °C/5 min. (c–B) spectra for the cube inside the sphere, no Mn and Fe are present.*

We have presented on a facile, rapid, and inexpensive microwave- assisted approach to fabricate large areas of high– quality, hollow, two-dimensional magnetic frames using sacrificial colloidal templates. We have proved that in addition to short reaction times, the technique offers other characteristics in terms of reaction kinetics, molecular diffusion, and selectivity, which can be used to enhance the potentiality of such a synthetic chemistry approach. The method has allowed the growth, in just a few minutes, of a stoichiometric and homogeneous conformal nanometric manganese ferrite coating of tenths of square millimeters. The coating thickness can be controlled by controlling the time of the reaction. No post-treatment was required – the sacrificial template is removed simultaneously as the magnetic nanoparticle coating is formed.

## 3.4 REFERENCES

1.        (a) Lourtioz, J.-M., Photonic crystals and metamaterials. *Comptes Rendus Physique* **2008**, *9*, 4-15; (b) Galisteo-López, J. F.; Ibisate, M.; Sapienza, R.; Froufe-Pérez, L. S.; Blanco, Á.; López, C., Self-Assembled Photonic Structures. *Advanced Materials* **2011**, *23* (1), 30-69.

2.        (a) Haglund, R. F. J., Nonlinear optical physics and applications of the plasmonic response in metal nanoparticles. In *Photon-based Nanoscience and Nanobiotechnology*, Dubowski, J. J.; Tanev, S., Eds. Spriger-Verlag: 2006; pp 67–96; (b) Maier, S. A., *Plasmonics: Fundamentals and Applications*. Springer-Verlag: 2007.

3.        Yerushalmi, R.; Scherz, A.; van der Boom, M. E.; Kraatz, H.-B., Stimuli responsive materials: new avenues toward smart organic devices. *Journal of Materials Chemistry* **2005**, *15*, 4480–4487.

4.        Inoue, M.; Uchida, H.; Nishimura, K.; Lim, P. B., Magnetophotonic crystals - a novel magneto-optic material with artificial periodic structures. *Journal of Materials Chemistry* **2006**, *16*, 678-684.

5.        Inoue, M.; Baryshev, A. V.; Khanikaev, A. B.; Dokukin, M. E.; Chung, K.; Heo, J.; Takagi, H.; Uchida, H.; Lim, P. B.; Kim, J., Magnetophotonic materials and their applications. *IEICE TRANS. ELECTRON.* **2008**, *E91-C* (10), 1630-1638.

6.        Paquet, C.; Kumacheva, E., Nanostructured polymers for photonics. *Materials Today* **2008**, *11* (4), 48-56.

7.        (a) Chen, A.; Wang, B. Z.; Chua, S. J.; Wilhelmi, O.; Mahmood, S. B.; Saw, B. T.; Kong, J. R.; Moser, H. O., Patterning of two-dimensional photonic crystal structures by nanoimprint lithography. *International Journal of Nanoscience* **2006**, *5* (4&5), 559—563; (b) Schift, H.; Park, S.; Jung, B.; Choi, C.-G.; Kee, C.-S.; Han, S.-P.; Yoon, K.-B.; Gobrecht, J., Fabrication of polymer photonic crystals using nanoimprint lithography. *Nanotechnology* **2005**, *16*, S261-S265; (c) Wu, C.-S.; Lin, C.-F.; Lin, H.-Y.; Lee, C.-L.; Chen, C.-D., Polymer-based photonic crystals fabricated with single-step electron-beam lithography. *Advanced Materials* **2007**, *19*, 3052-3056; (d) Stomeo, T.; Passaseo, A.; Cingolani, R.; De Vittorio, M., Fast nanopatterning of two-dimensional photonic crystals by electron beam lithography. *Superlattices and Microstructures* **2004**, *36*, 265-270; (e) Martiradonna, L.; Stomeo, T.; De Giorgi, M.; Cingolani, R.; De Vittorio, M., Nanopatterning of colloidal nanocrystals emitters dispersed in a PMMA matrix by e-beam lithography. *Microelectronic Engineering* **2006**, *83*, 1478–1481.

8.        (a) Samudrala, S. K.; Bandyopadhyay, S., Development of Hybrid Nanocomposites for Electronic Applications. In *Hybrid Nanocomposites for Nanotechnology*, Merhari, L., Ed. Springer Science + Business Media: 2009; Vol. part II, pp 231-287; (b) Pal, M.; De, A., Polymer–Iron Oxide Based Magnetic Nanocomposites. In *Hybrid Nanocomposites for Nanotechnology*, Merhari, L., Ed. Springer-Verlag Berlin Heidelberg: 2009; pp 455-506; (c) Ferreira, R. A. S.; André, P. S.; Carlos L.D. , Organic–inorganic hybrid materials towards passive and active architectures for the next generation of optical networks. *Optical Materials* **2010**, *32*, 1397–1409.

9.        (a) Levin, C. S.; Hofmann, C.; Ali, T. A.; Kelly, A. T.; Morosan, E.; Nordlander, P.; Whitmire, K. H.; Halas, N. J., Magnetic Plasmonic Core Shell Nanoparticles. *ACS Nano* **2009**, *3* (6), 1379–1388; (b)

Yu, Q.; Guan, P.; Qin, D.; Golden, G.; Wallace, P. M., Inverted size-dependence of surface-enhanced raman scattering on gold nanoholes and nanodisk arrays. *Nano Letters* **2008,** *8* (7), 1923-1928.

10.    Hu, J.; Chen, M.; Fang, X.; Wu, L., Fabrication and application of inorganic hollow spheres. *Chemical Society Reviews* **2011,** *40* (11), 5472-5491.

11.    (a) Panepucci, R. R.; Kim, B. H.; Almeida, V. R.; Jones, M. D., Photonic crystals in polymers by direct electron-beam lithography presenting a photonic band gap. *Journal of Vacuum Science & Technology B Microelectronics and Nanometer Structures* **2004,** *22* (6), 3384-3351; (b) Kim, S.; Chong, H.; De la Rue, R. M.; Marsh, J. H.; Bryce, A. C., Electron-beam writing of photonic crystal patterns using a large beam-spot diameter. *Nanotechnology* **2003,** *14,* 1004-1008; (c) Perez-Junquera, A.; Martin, J. I.; Alameda, J. M., One-step fabrication of large area arrays of dots by electron beam lithography. *Microelectronic Engineering* **2007,** *84,* 845-847; (d) Reboud, V.; Kehagias, N.; Sotomayor Torres, C. M.; Zelsmann, M.; Striccoli, M.; Curri, M. L.; Agostiano, A., Spontaneous emission control of colloidal nanocrystals using nanoimprinted photonic crystals. *Applied Physics Letters* **2007,** *90,* 011115-3; (e) Tamborra, M.; Striccoli, M.; Curri, M. L.; Alducin, J. A.; Mecerreyes, D.; Pomposo, J. A.; Kehagias, N.; Reboud, V.; Sotomayor Torres, C. M.; Agostiano, A., Nanocrystal-based luminescent composites for nanoimprinting lithography. *Small* **2007,** *3* (5), 822-828.

12.    Rius Sune, G. Electron beam lithography for nanofabrication. Universitat Autonoma de Barcelona, Barcelona, 2008.

13.    Costner, E. A.; Lin, M. W.; Jen, W.-L.; Willson, C. G., Nanoimprint lithography materials development for semiconductor device fabrication. *Annual Review of Materials Research* **2009,** *39,* 155-180.

14.    Pease, R. F.; Chou, S. Y., Lithography and Other Patterning Techniques for Future Electronics. *Proceedings of the IEEE* **2008,** *96* (2), 248-270.

15.    Pomogailo, A. D.; Kestelman, V. N., Synthetic Methods for Metallopolymer Nanocomposite Preparation. In *Metallopolymer Nanocomposites,* Hull, R.; Osgood, R. M. J.; Parisi, J.; Warlimont, H., Eds. Springer-Verlag Berlin Heidelberg: 2005; pp 117-135.

16.    Ge, J.; He, L.; Goebl, J.; Yin, Y., Assembly of Magnetically Tunable Photonic Crystals in Nonpolar Solvents. *Journal of the American Chemical Society* **2009,** *131* (10), 3484-3486.

17.    (a) Garcia Lopez, M. Self Assembled Photonic-Plasmonic Crystals for Light control at the Nanoscale. Santiago de Compostela, Madrid, 2011; (b) Cole, R. M.; Sugawara, Y.; Baumberg, J. J.; Mahajan, S.; Abdelsalam, M.; Bartlett, P. N., Easily coupled whispering gallery plasmons in dielectric nanospheres embedded in gold films. *Physical Review Letters* **2006,** *97,* 137401.

18.    Rubio-Roy, M.; Vlasin, O.; Pascu, O.; Caicedo, J. M.; Schmidt, M.; Goni, A. R.; Tognalli, N. G.; Fainstein, A.; Roig, A.; Herranz, G., Magneto-optical enhancement by plasmon excitation in nanoparticle/metal structure. *Langmuir special Issue-Plasmonics* **2012,** *submitted.*

19.    (a) Kim, M. H.; Choi, J. Y.; Choi, H. K.; Yoon, S. M.; Park, O. O.; Yi, D. K.; Choi, S. J.; Shin, H. J., Carbon Nanotube Network Structuring Using Two-Dimensional Colloidal Crystal Templates. *Advanced Materials* **2008,** *20* (3), 457-461; (b) Wang, Y.; Angelatos, A. S.; Caruso, F., Template

Synthesis of Nanostructured Materials via Layer-by-Layer Assembly†. *Chemistry of Materials* **2007**, *20* (3), 848-858; (c) Xia;, Y.; Lu;, Y.; kamada;, K.; Gates;, B.; Yin, Y., Macroporous Materials Containing Three-dimensionally Periodic Structures. In *The chemistry of nanostructured materials*, Yang, P., Ed. Worl Scientific Publishing Co.Pte.Ltd.: Singapore, 2003; p 386; (d) Agrawal, M.; Gupta, S.; Stamm, M., Recent developments in fabrication and applications of colloid based composite particles. *Journal of Materials Chemistry* **2011**, *21* (3), 615-627; (e) White, R. J.; Luque, R.; Budarin, V. L.; Clark, J. H.; Macquarrie, D. J., Supported metal nanoparticles on porous materials. Methods and applications. *Chemical Society Reviews* **2009**, *38* (2), 481-494.

20.      (a) Ai, Z.; Deng, K.; Wan, Q.; Zhang, L.; Lee, S., Facile Microwave-Assisted Synthesis and Magnetic and Gas Sensing Properties of Fe3O4 Nanoroses. *The Journal of Physical Chemistry C* **2010**, *114* (14), 6237-6242; (b) Hu, X.; Yu, J. C.; Gong, J., Fast Production of Self-Assembled Hierarchical α-Fe$_2$O$_3$ Nanoarchitectures. *The Journal of Physical Chemistry C* **2007**, *111* (30), 11180-11185; (c) Hu, X.; Yu, J. C., High-Yield Synthesis of Nickel and Nickel Phosphide Nanowires via Microwave-Assisted Processes. *Chemistry of Materials* **2008**, *20* (21), 6743-6749; (d) Chen, S. Q.; Wang, Y., Microwave-assisted synthesis of a Co$_3$O$_4$-graphene sheet-on-sheet nanocomposite as a superior anode material for Li-ion batteries. *Journal of Materials Chemistry* **2010**, *20* (43), 9735-9739.

21.      Pascu, O.; Gich, M.; Herranz, G.; Roig, A., 2D Magnetic Frames Obtained by the Microwave-Assisted Chemistry Approach. *European Journal of   Inorganic Chemistry* **2012**, *DOI: 10.1002/ejic.201101244.*

22.      Rieger, J., The glass transition temperature of polystyrene. Results of a round robin test. *Journal of Thermal Analysis* **1996**, *46,* 965-972.

23.      Suh, K. Y.; Yoon, H.; Lee, H. H.; Khademhosseini, A.; Langer, R., Solventless ordering of colloidal particles through application of patterned elastomeric stamps under pressure. *journal article* **2004**, *85* (13), 2643-2645.

24.      Pascu, O.; Carenza, E.; Gich, M.; Estradé, S.; Peiró, F.; Herranz, G.; Roig, A., Surface reactivity of iron oxide nanoparticles by microwave-assisted synthesis; comparison with the thermal decomposition route. *Journal of Physical Chemistry C* **2012**, *submitted.*

25.      Gündüz, S.; Dinçer, S., Solubility behaviour of polystyrene: thermodynamic studies using gas chromatography. *Polymer* **1980**, *21* (9), 1041-1046.

26.      (a) Wu, H.; Wang, W.; Yang, H.; Su, Z., Crystallization and Orientation of Syndiotactic Polystyrene in Nanorods. *Macromolecules* **2007**, *40* (12), 4244-4249; (b) Gao, X.; Liu, R.; Huang, Y.; Starykov, O.; Oppermann, W., Clathrate (δ) Form Crystal Transitions of Syndiotactic Polystyrene in Atactic Polystyrene Networks. *Macromolecules* **2008**, *41* (7), 2554-2560; (c) Woo, E. M.; Sun, Y. S.; Lee, M. L., Crystal forms in cold-crystallized syndiotactic polystyrene. *Polymer* **1999**, *40* (15), 4425-4429.

# 4

# 3D MAGNETO–PHOTONIC MATERIALS

## Preamble of chapter 4

The addition of a magnetic component into 3D photonic crystal structures –the so-called magneto-photonic crystals (MPCs)– has two interesting effects. On one hand, it breaks time inversion symmetry allowing non-reciprocal effects in light propagation[1]. On the other hand, light is slowed down at frequencies of the photonic band edges, strongly increasing the light-matter interaction and enhancing the magneto-optical response[2]. Along this line it has been demonstrated that the magneto-optical response of one- (1D) and two-dimensional (2D) MPCs is significantly enhanced at band-edge frequencies (presented in Chapter 1.3). The possibility of controlling the light propagation (in all directions) and modifying the magneto-optical spectral response by judicious material's design makes 3D MPCs a very suitable platform for the development of a new generation of fast and compact isolators for optical data transmission and integrated optics. Nevertheless, the achievement of high-quality 3D-MPCs is much more complex and, therefore, the attainment of an optimal magneto-optical response –comparable at least to that of 1D-MPCs– remains a challenging issue.

This challenge set our focus on the fabrication of 3D-MPCs being targeted i) tunability of the magneto-optical spectral response with the magnetic field; ii) the enhancement of magneto-optical response near photonic band-edge frequencies; and iii) possible applications in new integrated optic devices[3]( 1.e.. optical isolators).

To achieve our goals, two approaches have been considered for the fabrication of 3D-MPCs, namely: **(1)** infiltration of opals with *ex-situ* synthesized magnetic nanoparticles and **(2)** deposition/infiltration of opals with *in-situ* synthesized magnetic nanoparticles either by classic sol-gel route or by microwave-assisted sol-gel chemistry.

**(1) Infiltration with ex-situ synthesized magnetic nanoparticles.** By infiltrating self-assembled $Al_2O_3$ inverse opal structures with monodisperse nickel nanoparticles using a vertical lifting method, we fabricated 3D-MPCs which show a sizable enhancement of the magneto-optical signal at frequencies around the stop-band edges of the photonic crystals. The results of the optical and magneto-optical characterization are consistent with the homogeneous magnetic infiltration of the opal structure. The results furthermore demonstrated the potential of 3D-MPCs fabricated using ex-situ prepared NPs , to adapt the magneto-optical spectral response at optical frequencies by appropriate design of the opal structure (varying the periodicity of the structure by different spheres diameters) or magnetic field strength. The drawback of this method was found in the limitation of the content of the magnetic component up to 9%.

**(2) Deposition/infiltration of opals with *in-situ* synthesized magnetic nanoparticles (ferrites).**

A traditional liquid phase sol-gel chemistry is a commonly used route for the fabrication of 3D inverse opals using the direct opal as sacrificial template. Over the dry processes (ALD, CVD,melting) it has the advantages to achieve maximal filling of inorganic materials into the 3D templates voids, a lower cost, and availability for a wide range of inorganic materials (e.g. magnetic ferrites, $MFe_2O_4$, M = Ni, Co, Mn ). By combining the sol-gel chemistry of ferrites with photonic materials, our goal was to fabricate $MnFe_2O_4$ inverse opals. The goal was only partially achieved, first due to the difficulties in obtaining the right phase of $MnFe_2O_4$ inverse spinel. Second, to have a mechanically strong structure without a framework collapse, multiple infiltrations/drying cycles were required and this resulted in the appearance of cracks, preserving the photonic order just along few hundreds of $\mu$m, insufficient for Bragg peak detection. We present these trials while further optimization of the experimental process would be needed to evaluate the method's feasibility for 3D–MPCs fabrication.

**B.** Optimization of sol-gel chemistry route to fabricate magneto-photonic crystals was achieved by microwave-assisted benzyl alcohol route that allowed us the growth of a stoichiometric and homogeneous conformal nanometric coating covering extensive areas—at least in the order of $cm^2$—of the 3D photonic crystals only in a few minutes. The coating was formed by superparamagnetic $MnFe_2O_4$ nanoparticles and did not require any post-synthesis material processing. The resulting materials exhibited unambiguously enhanced magneto-

photonic response at band edge frequencies and a magneto-optical response tunable by magnetic fields. By controlling the precursors' concentration, deposition time, presence of functional groups on opal surface, we achieved a control on the magnetic content up to 30% for direct opals and around 15% for inverse with a detectable photonic band gap.

## 4.1 GENERAL ASPECTS

### 4.1.1 Approaches for the magneto-photonic crystals' fabrication

This chapter presents the fabrication of three dimensional magnetic opals by bottom-up techniques, starting from (direct and inverse) prefabricated blank opals which were subsequently functionalized with magnetic nanoparticles by different strategies.
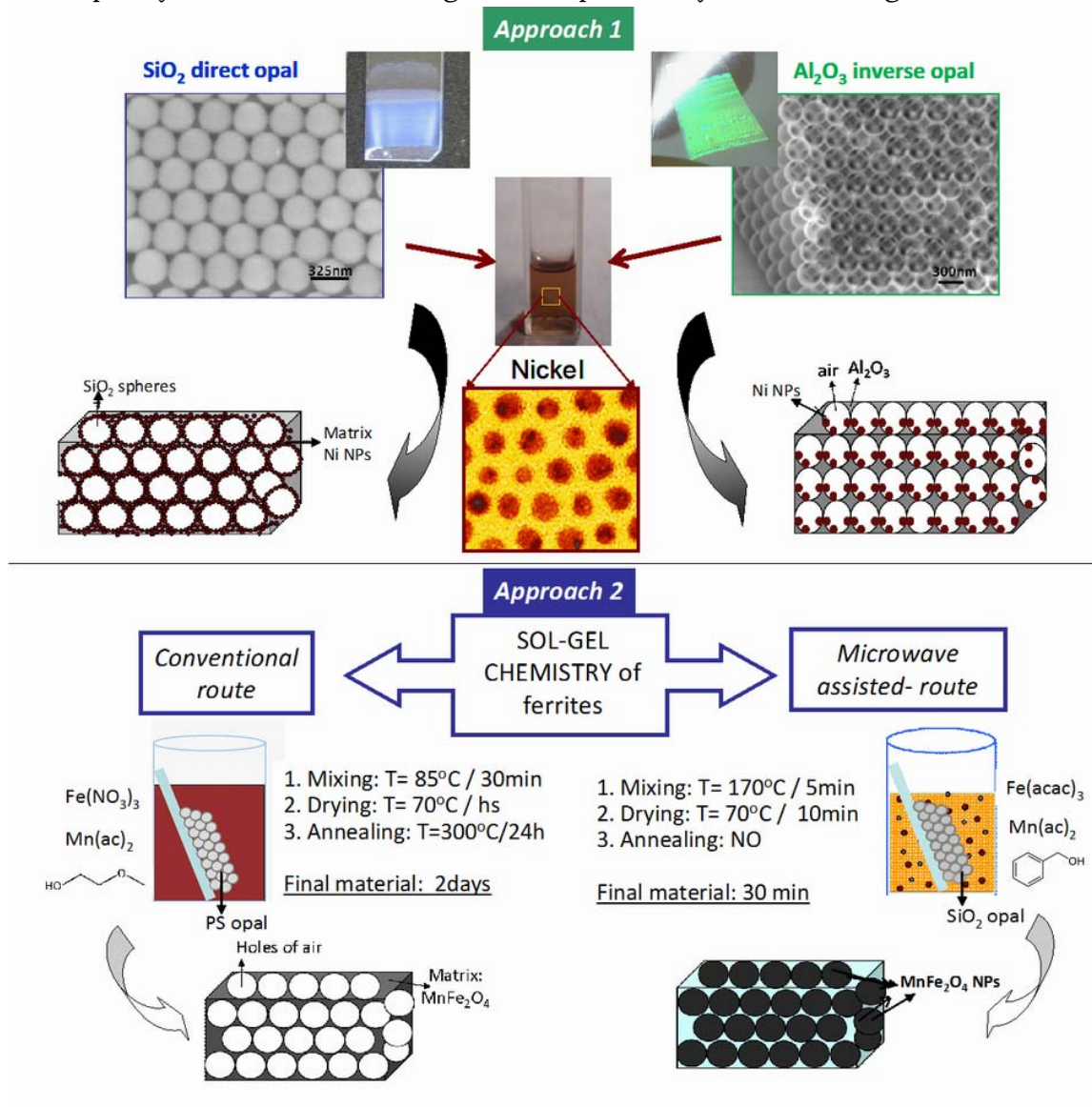


*Figure 4.1. Schematization of the fabrication methods of magneto-photonic materials*

**Approach 1 (Figure 4.1)** consisted of the infiltration of direct/inverse opals with *ex-situ* synthesized Ni nanoparticles (**Chapter 1.2**) by partially filling the voids of the photonic structures with magnetic material.

**Approach 2** relied on the fabrication of MPCs by *in-situ* deposition of magnetic materials. For this, two strategies have been considered (**Figure 4.1**): (1) fabrication of magnetic ferrites inverse opals by conventional sol-gel route; and (2) *in-situ* deposition of magnetic nanoparticles by microwave-assisted sol-gel route. Approach (1) involved the

filling of the voids of a PS direct opal with amorphous solution of $MnFe_2O_4$ sol followed by annealing in order to obtain the crystalline ferrite phase in the matrix framework. In (2), microwave heating was employed to perform *in–situ* sol-gel reaction resulting in the conformal coverage of opals with a crystalline ferrite layer, without the need of a post annealing step.

## 4.1.2 Fabrication of blank direct and inverse opals

Although the prefabricated opals (2D and 3D) used in this thesis were provided by our collaborators at ICMM, a short description of the fabrication methodology is given.

The template material for the fabrication of direct/inverse opals was a self–assembled direct opal, constituted of silica ($SiO_2$) or polystyrene (PS) spheres with diameters of 325/260 nm and 320/300/260 nm, respectively.

The spheres were deposited onto 1 $cm^2$ area hydrophilic glass from a 1% (w/w) solution in ethanol at 55 °C and 60% relative humidity of the environment (in the oven) [4]. $SiO_2$, spheres were synthesized by Stöber method[4]. The self-assembled direct opals have a face-centered cubic (fcc) lattice symmetry with the highest crystalline packing density of 74%. In this geometry, one sphere is in direct contact with 12 surrounding spheres and the space between spheres is around 10% of the sphere's diameter Due to the vertical deposition method (**Figure 4.2a**), the opal grows forming terraces of increasing number of layers (**Figure 4.2b, c**) with a variation of up to 30% in the number of layers especially in the upper part of it[5] Instead in the central part, there is a homogeneous distribution of terraces (**Figure 4.2.d, e**). It is worth to be mentioned that during opal formations, dislocation, vacancies distortions of the local lattice could appear perhaps due to the colloidal polydispersity. Moreover by optical microscopy and SEM can be clearly seen some cracks at every 50-80 μm along rows of spheres which might appear during drying process once the ordering had taken place[5].
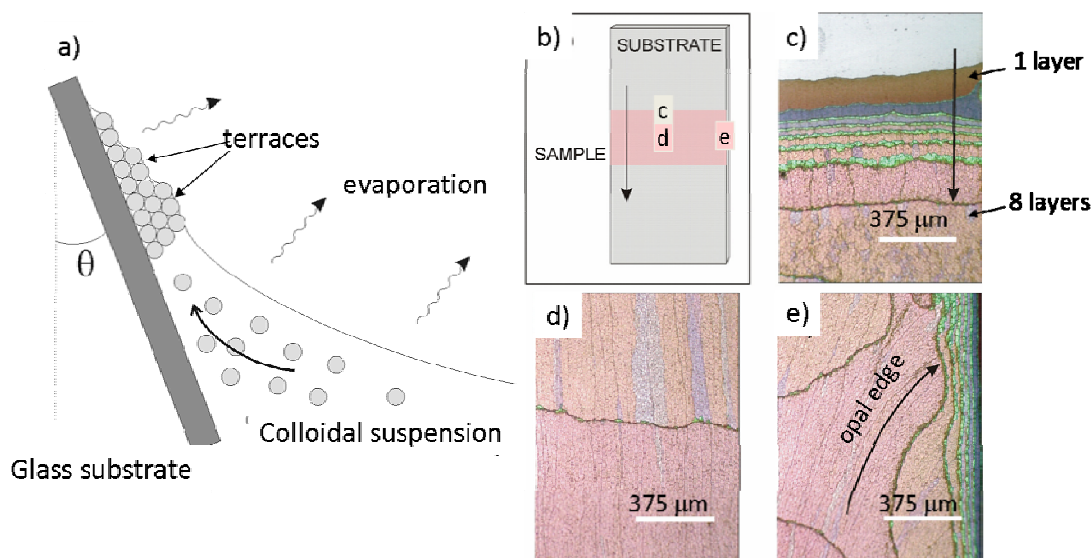


**Figure 4.2.** *Pristine opal formation and morphology[5] (a) fabrication by vertical deposition process. (b)schematic representation of substrate (grey) and sample (pink), the vertical arrow indicating the opal growth direction.(c) upper part of the opal showing variation in layer thickness.(d) central region uniform in thickness and (e) Edge of opal.*

For the fabrication of inverse opals, an $Al_2O_3$ shell was deposited into the PS template (**Figure 4.3.b**) by atomic layer deposition (ALD) providing conformal layers around the polystyrene spheres of controllable thickness. (ALD, Savannah S100 Cambridge NanoTech Inc). Reactants for alumina growth *i.e.,* trimethylaluminum (TMA) and water, were kept at room temperature. The sample, in the ALD vacuum chamber at 90ºC, was exposed to alternate TMA and water pulses (each with duration of 10 ms). Each TMA-water cycle was followed by 5 s waiting time to ensure complete diffusion through the material followed by 5s chamber evacuation. In each ALD cycle, around 1.8 Å was deposited, as estimated by ellipsometry measurements. In our case, 80 cycles of ALD were used, forming an $Al_2O_3$ conformal layer thickness of around 15 nm. Finally, the original polystyrene spheres were removed by dissolution in toluene, leaving spherical voids in the $Al_2O_3$ structure. The resulting replica network had a free volume (air) of more than 74% with a large internal surface/volume ratio. The contact points between the templating particles led to orifices (windows) between the spherical voids (removed particles) and ensured an open, full-continuous 3D network. It is worth mentioning, that during the atomic layer deposition of $Al_2O_3$, the PS sphere shrank (by around 10-20%) and the void diameter of the inverse structure was consequently smaller than the original sphere diameter. In our case, using a PS template of 320 nm sphere diameter, the final inverse opal structure (**Figure 4.3c**) exhibited voids of around 290 nm and connection gate sizes of around 100 nm. The connection gates provided paths for the diffusion of Ni nanoparticles into the opals during impregnation.
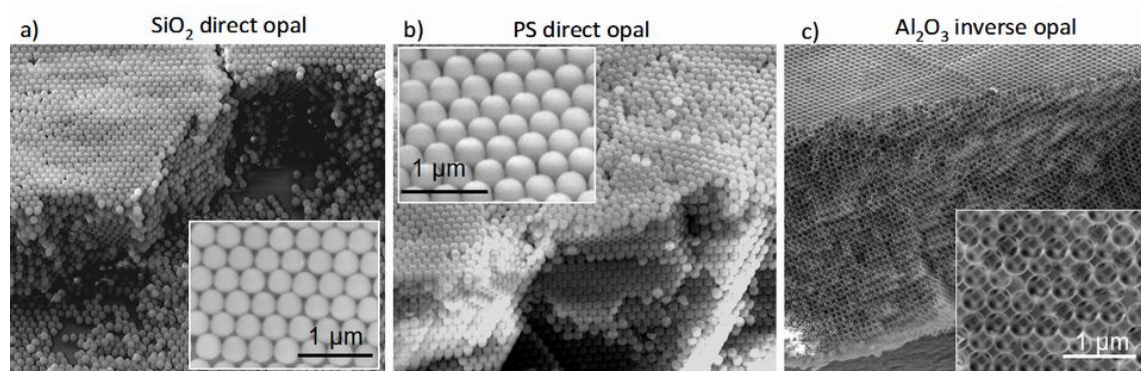


***Figure 4.3*** *SEM images of pristine (blank) opals presenting the fcc structure.used in this thesis for the fabrication of MPCs,*

## 4.1.3 Characterization techniques

**Optical measurements:**

The quality of the blank and magnetic opals was evaluated by optical reflectivity or transmission measurements (**Chapter 6.2 A.ii.7**). The intensity and narowness of the Bragg peak give information about the opal's long-range structural order (narrow with high intensity peak is associated with high quality material). Due to the opal fabrication technique by vertical self-assembly, the opal is considered of good quality when it contains 15-20 layers. Above those values, intrinsic disorder appears and the opal loses the long-range order. Too thin opals, on the other hand, have a very fragile structure due to the weak forces

maintaining the self-assembly and are easier predisposed to cracks and damages during their manipulation.

After the proper infiltration of an opal with the magnetic component (i.e., uniformity within the whole structure), a shift of the Bragg peak position should be observed due to the change in the effective refractive index of the final system and the refractive index contrast (both being related with photonic band gap control). The larger shift associated to larger loaded magnetic component. When the nanoparticles are deposited on the surface of the opal rather than within the structure, no shift of the Bragg peak position and intensity decrease is expected (**Chapter 4.2.3**) due to light absorption and Raleigh's scattering by NPs[6] The diffusive scattering (due to the NPs on the surface) can be avoided by polishing the opal surface[6b] but this is not a good choice since the opal structure can easily be destroyed.

The disappearance or the very low intensity of the Bragg peak in a magnetic opal can be related either to the destruction of the structural photonic order (i.e., disorder in the material causing diffusive scattering) or to a refractive index contrast close to zero[6c] (i.e., the order is preserved while the template and magnetic material have the same refractive index)[7]. The latter is a special case that may occur when the air holes of a direct or inverse opal are partially filled with a magnetic component with high refractive index (e.g. iron oxide). Some simulations have shown that height of the Bragg peak can be decreased and shifted to longer wavelengths by gradually filling the voids of a $SiO_2$ direct opal with maghemite[6c]. Moreover, the peak intensity could be increased again when very large amounts of iron oxide were infiltrated, filling completely the voids thus the average dielectric constant of pores becoming greater than that of the $SiO_2$ spheres[6c]. These findings have also been confirmed by experimental results[6a, 6c] and also observed in our experiments (**Chapter 4.4.3**).

According to the above mentioned, for the fabrication of a magneto-photonic crystal with a pseudo or complete photonic band gap, the following prerequisites have to be fulfilled:

➢ a high-quality blank opal;

➢ the highest possible refractive index contrast between the magnetic and non-magnetic components ;

➢ the superposition of photonic band gap energies with the optical absorption energy of magnetic nanoparticles must be avoided; a photonic band gap position below or above the optical absorption allows a coherent localization of light within the material with minimal absorption losses[8];

➢ the accumulation of nanoparticles on the photonic surface should be avoide;

➢ the effective refractive index ($n_{eff}$) of the final material determines the (pseudo/complete) photonic band gap.


**Magneto-optical measurements:**


Magneto-optical properties of the fabricated 3D-MPCs were examined by performing optical transmittance (OT), circular dichroism (CD) and magnetic circular dichroism (MCD) spectroscopy experiments in a range of wavelengths $\lambda$ = 400–800 nm using a home-made experimental setup[9] (**Chapter 6.2 A.ii.9**). Although Faraday rotation and ellipticity were also recorded, their signal was largely masked by the large magneto-optical contribution of glass

substrates, which made the analysis of the spectra quite difficult. On the contrary, the MCD signal, which is proportional to the Faraday ellipticity[10], was much stronger and was used to track the photonic effects on the magneto-optical spectra. The OT spectra were taken at normal incidence and allowed us to measure the stop-band frequencies of the MPCs.

The MCD data were obtained by using a lock-in amplified detection of the light transmitted through the samples using a photo-elastic modulator. In our setup configuration, the first harmonic of the detector signal was proportional to the dichroic (MCD) signal ($I_{RCP}-I_{LCP})/(I_{RCP} + I_{LCP}$) where $I_{RCP}$ and $I_{LCP}$ are the right- and left-circularly polarized light transmitted through the 3D-MPCs, respectively. We stress that this setup allows the measurement of the optical and magneto-optical spectral response at exactly the same place on the crystals, with a light probe spot size of ~2 mm.

## 4.2 INFILTRATION OF 3D OPALS WITH *EX-SITU* SYNTHESIZED NICKEL NANOPARTICLES

Promising results were earlier reported on 3-D photonic crystals impregnated with a Faraday active transparent liquid[11]. Other approaches, as *in-situ* deposition of magnetic nanoparticles[8b, 12] over 3D photonic structures have revealed some features around the photonic crystal stop-band that have been interpreted generally as a moderate increase of the magneto-optical activity around those frequencies. However to find the enhanced functionality of MPCs, must be considered the factors that strongly influence the magneto-optical behavior of magneto-photonic crystals: the type and amount of magnetic component, opal structure (direct or inverse) and quality (long range structural order).

In this section, we present the magneto-photonic response of 3D opals infiltrated with Ni nanoparticles. By disentangling their intrinsic magneto-optical response from other sources of optical activity, we found a strong modification of the spectral response especially prominent near the photonic band edges.

### 4.2.1. Fabrication methodology

**Infiltration with pre-synthesized nickel nanoparticles**

The studied systems consisted of $SiO_2$ direct and $Al_2O_3$ inverse opals, both infiltrated with monodisperse Ni nanoparticles. For that purpose, two sets of 8 and 15 nm spherical and surfactant-stabilized Ni nanoparticles with good polydispersity of 12% (8 nm, *D_TD.Ni_16*) (**Figure 4.4a**) and 10% (15 nm, *C_TD.Ni_9*) (**Figure 4.4b**) were synthesized by organometallic thermal decomposition method (**Chapter 2.2.1**). The two sets of Ni nanoparticles (8 and 15 nm) were superparamagnetic at room temperature, as indicated by the zero field cool – field cool magnetization curve (**Figure 4.4c**), with blocking temperatures ($T_B$) of 59K and 231K, respectively. The saturation magnetization at 300K was about 18 and 44 emu/g for 8 and 15 nm particles, respectively (**Chapter 2.2.3**).
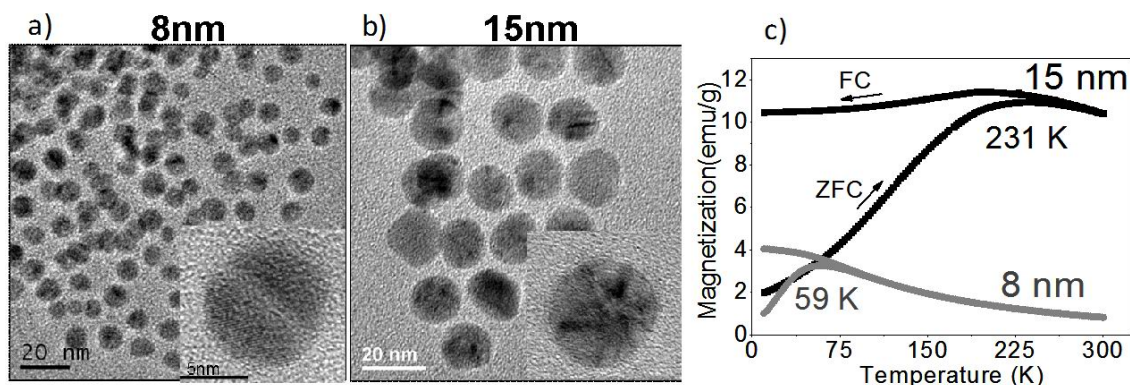
**Figure 4.4** *Infiltrated Ni NPs characteristics: (a-b) TEM images of two sets of Ni NPs with HRTEM of a single particle as insets; (c) the corresponding ZFC-FC magnetization curves at 50 Oe.*

Using these nanoparticles in the form of stable colloidal dispersion, the infiltration was carried out through three methods (**Figure 4.5**) with the aim of comparing the resulted material qualities



1 – Micropipette; 2 – Colloidal dispersion; 3 – SiO$_2$ direct opal;
4 – Glass slide substrate; 5 – Magnet; 6 – Al$_2$O$_3$ inverse opal; 7 – step-motor setup
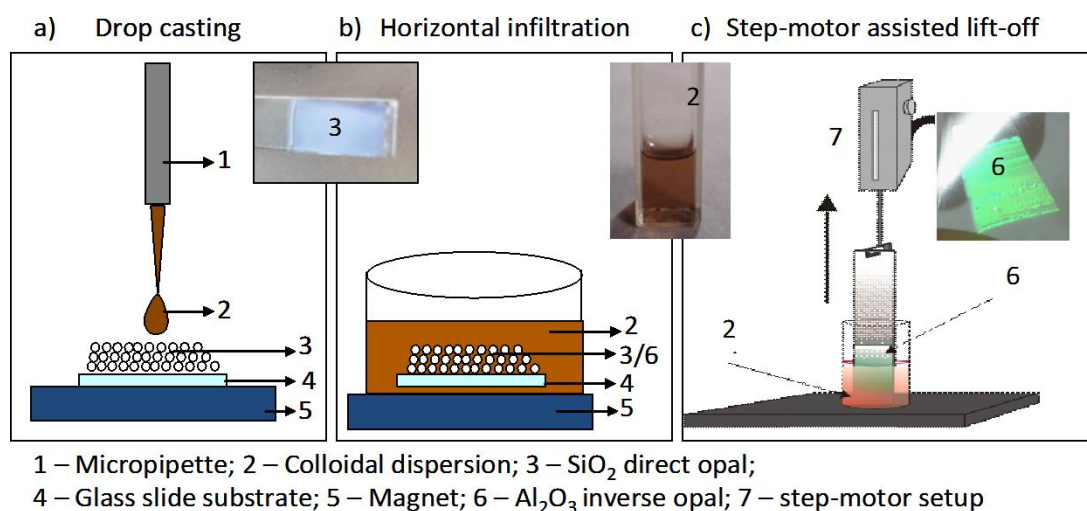
**Figure 4.5** *Infiltration methods using pre-synthesized Ni NPs for MPCs fabrication*

1) For the **drop casting** of magnetic colloids using a micropipette (**Figure 4.5a**), 8 nm Ni NPs with a concentration of $5.1 \times 10^{-3}$ M was used. The opal was made by self-assembly of SiO$_2$ spheres of 325 nm diameter containing 21 layers (surface around 5 mm x 10 mm)

2) **Horizontal infiltration** consisted of the complete immersion of the opal into stable magnetic colloidal dispersion (2 ml) for longer time (10–20 h)(**Figure 4.5b**). Both direct and inverse opals were used. The direct opal was made by self-assembly of SiO$_2$ spheres of 325 nm diameter with 59 layers and infiltrated with hexane dispersion of 8 nm Ni NPs of $1.7 \times 10^{-3}$ M. The Al$_2$O$_3$ inverse opal with a hole diameter of 290 nm and a few layers thickness was infiltrated with hexane dispersion of 8 or 15 nm NPs of $5 \times 10^{-4}$ M.

3) Inverse opals dipped into stable colloidal dispersions were lifted up by a **step-motor assisted dip coating** setup[13] (**Figure 4.5c**). This method was performed in the laboratory of our collaborators at ICMM. For comparison purposes, the same inverse opal and colloidal dispersion concentration was used as in the horizontal infiltration method. The degree and homogeneity of the infiltration of Ni nanoparticles into the inverse opals was controlled by

the lifting-up speed (3.6 mm/h), the number of infiltration cycles, the size and concentration of NPs in the colloidal dispersion.

## 4.2.2. Morphological analysis

Scanning electron microscopy (SEM) was used for the magneto-photonic crystal characterization involving surface and cross-sectional studies. Cross-sectional pictures were instrumental to assess the homogeneity of the infiltration and the calculation of the filling fraction factors (**Chapter 4.2.3**).

### Drop casting and horizontal immersion methods

**Figure 4.6** shows the surfaces of the direct /inverse magneto-photonic materials, fabricated by the drop casting and horizontal immersion methods. In the case of drop casting, the nanoparticles diffusion was minimal or negligible within the template voids because of NPs tendency to accumulate rather at the surface (**Figure 4.6a**). This resulted in the blocking of the surface voids, thus impeding the further diffusion of nanoparticles inside the structure. While the first layer is decorated with NPs (bright spots in the image), they are completely missing in the layers below (**Figure 4.6b**) due to pore closure. In the case of horizontal immersion, the nanoparticles diffused within the structure (**Figure 4.6d, f**) due to the longer infiltration time but in significantly less amount than at the surface (**Figure 4.6c, e**). These observations were confirmed for both direct and inverse opals. When exposed to visible light, the nanoparticles and their agglomerations on the opal surface can not only absorb but scatter the light.

Since we are interested to study the interaction of light with matter within the photonic structure, light scattering must be avoided as much as possible. Because of this, drop casting and horizontal immersing methods were considered not suitable for our purposes.

### Step-motor assisted dip coating method

This method is an improved infiltration process that allows us having an opal surface without agglomerated nanoparticles and a uniform NPs distribution in the matrix can be achieved. Preliminary experiments in our group using the dip-coating method (**Figure 4.5c**) suggested promising results with aqueous dispersion of maghemite nanoparticles infiltrated into $SiO_2$ inverse opal[13b]. Using the same setup, we performed the infiltration in one cycle by dipping $Al_2O_3$ inverse opals into stable hexane colloidal dispersions of 8 and 15 nm Ni NPs ($5 \times 10^{-4}$ M). The resulted materials are presented in **Figure 4.7**. On one hand, **Figure 4.7b, c** noticeably reveals that $Al_2O_3$ forms a very uniform conformal coating on the polystyrene spheres with a thickness of about 15 nm. On the other hand, the tiny bright spots on the spherical surfaces and within the voids –which are better visible in the zoomed image of the inset of **Figure 4.7a, b** are the Ni nanoparticles.
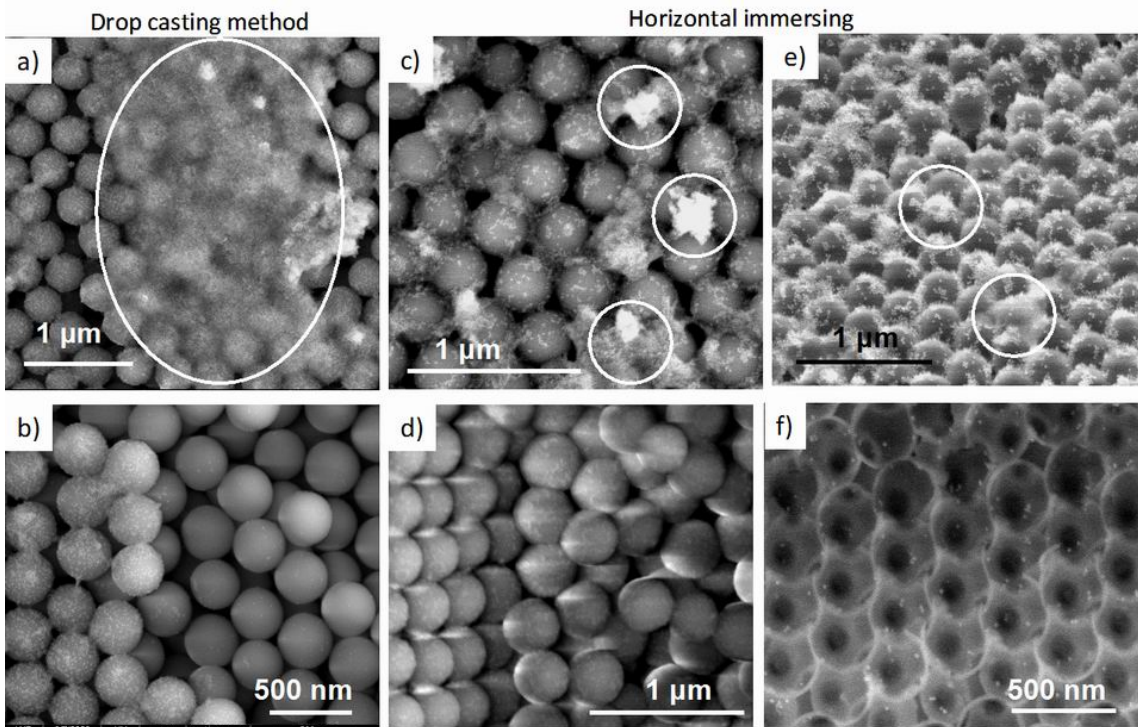
**Figure 4.6.** *Comparison between drop casting (**a, b**) and horizontal infiltration (**c-f**) methods, regarding the loaded magnetic component **a, c, e**) SEM images of the opals surface –first layer, showing high amount of deposited nanoparticles with agglomerations, too (highlighted in white circles) While in drop casting the lower layers do not contain infiltrated NPs (**b**), in the horizontal immersion, the whole layers of the opals are infiltrated with NPs, as can be clearly seen in the cross-section images of the direct (**d**) and inverse(**f**) opal.*

A uniform infiltration can be seen for the 8 nm NPs (**Figure 4.7b**) with no surface accumulation (**Figure 4.7a**). The infiltration efficiency of 15 nm NPs was significantly lower than that of the 8 nm NPs (**Figure 4.7c**), probably due to both the smaller diffusivity and lower total NPs volume/opal surface ratio in the case of the bigger NPs. In order to increase the amount of infiltrated magnetic nanoparticles, further tests were run with a higher concentration of colloidal dispersion ($3 \times 10^{-3}$M) of 8 nm Ni and with more infiltration cycles at the same lifting-up speed. Unfortunately, the infiltration could not be enhanced this way. For instance, two cycles of infiltration at higher dispersion concentration resulted in the accumulation of NPs at the surface rather than within the structure.
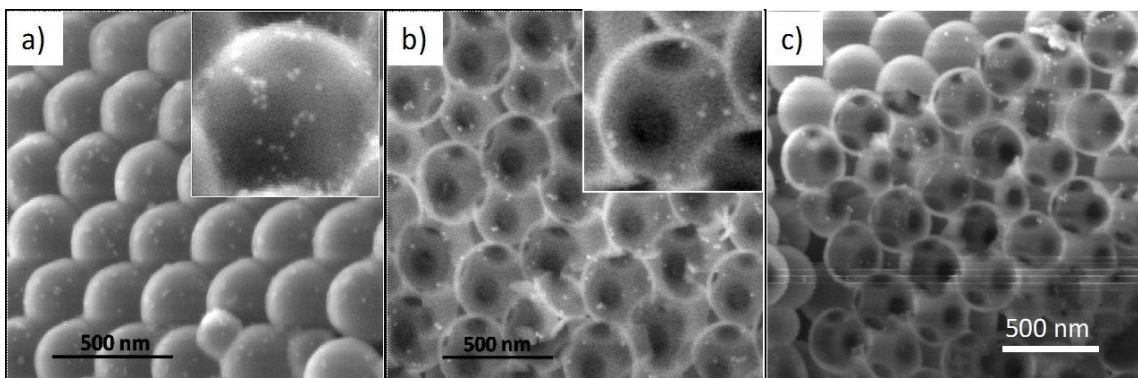


**Figure 4.7.** *SEM images of magnetic opals fabricated by the step-motor assisted dip-coating method (one-cycle infiltration): (**a**) surface and (**b**) cross-section of inverse opal with 8 nm Ni NPs;.(**c**) inverse opal with 15 nm Ni NPs.*

The SEM cross-sectional image of the 3D-MPCs (**Figure 4.7b**) was used to estimate the infiltration homogeneity across the depth of the opals and to determine the void and connecting windows diameters which were found $\sim 288$ nm and $\sim 100$ nm, respectively.

**Calculations of the filling fractions of each component in a binary system (blank inverse opal)**

The values corresponding to the void and connecting window diameters were used to calculate the filling fraction of air ($f_{air}$) and alumina ($f_{Al2O3}$) which were found 0.87 and 0.13, respectively. For their calculation it was taken into account that each sphere has 12 neighbors resulting in 12 connecting windows. Therefore the $Al_2O_3$ layer will be rather a discontinue one, presenting 12 gates, each of around 100 nm diameter. For an easier understanding of the calculations, **Figure 4.8** shows a schematization of the porous inverse matrix.
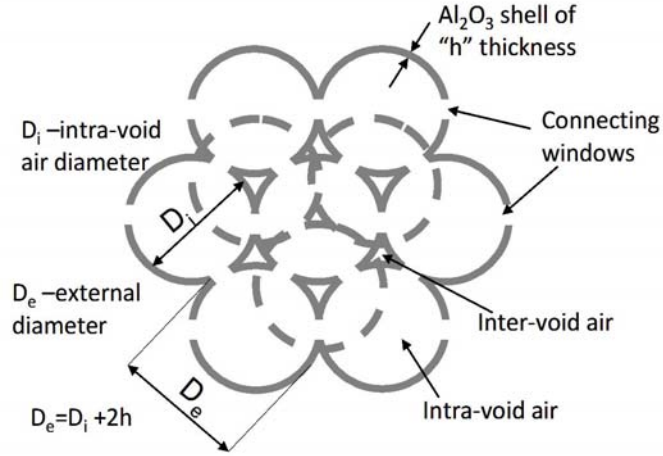


***Figure 4.8.*** *Schematization of two layers of hallow spheres, each sphere being in contact with 12 other spheres (6 in the same layer, 3 in the above and 3 in the below layers), the contact surface representing the connection gates.*

*As a first approximation*, we considered that the template is formed by hollow spheres with diameter $D_e$, ordered in fcc structure, having the filling fraction of 0.74 (74%) of the total volume. By knowing the diameter of the void and the alumina shell thickness (h) the volume of the continuous alumina shell can be expressed by (eq.4.1 )

$$
\left.
\begin{aligned}
V_{sphere} &= \frac{1}{6}\pi D_e^3 = \frac{1}{6}\pi (D_i + 2h)^3 \\[4pt]
V_{air-void} &= \frac{1}{6}\pi D_i^3 \\[4pt]
V_{sphere} &= V_{air-void} + V_{shell}
\end{aligned}
\right\}
V_{shell} = \frac{1}{6}\pi\left[(D_i + 2h)^3 - D_i^3\right]
\qquad \text{(Eq.4.1)}
$$

*In a second approximation* we considered that the connecting window is a planar circle instead of a spherical cap. Thus the volume of the discontinuous alumina shell can be calculated by (eq.4.2) , where $D_{window}$ was measured from SEM images and h is alumina thickness.

$$V_{shell} = V_{Al_2O_3} + 12 \cdot V_{window}$$

$$V_{window} = S_{window}h = \pi\left(\frac{D_{window}}{2}\right)^2 h$$

$$\left.\right\} V_{Al_2O_3} = V_{shell} - 12 \cdot \pi\left(\frac{D_{window}}{2}\right)^2 h \quad (Eq.4.2)$$

Combining these two equations, the real alumina volumes are obtained and subsequently the filing fractions of the discontinued alumina shell and air are given by eqs. 4.3 and 4,4, respectively

$$\text{volume fraction } Al_2O_3 = \frac{V_{Al_2O_3}}{V_{sphere}} \Rightarrow$$

$$\Rightarrow \text{filling fraction } f_{Al_2O_3} = 0.74 \cdot \frac{V_{Al_2O_3}}{V_{sphere}} \quad (Eq.4.3)$$

$$\Rightarrow \text{filling fraction } f_{air} = 0.26 + 0.74 \cdot \left(1 - \frac{V_{Al_2O_3}}{V_{sphere}}\right) \quad (Eq.4.4)$$

The values obtained using these equations are going to be used for the calculation of the filling fraction of magnetic material (**Sections 4.2.3 and 4.4.3**).

## 4.2.3. Functional characterization

**Optical transmittance: stop-band red-shift**

In order to compare the infiltration efficiency of dip coating *versus* horizontal immersion methods, we first performed optical reflection (OR) and transmission (OT) experiments to determine the stop band frequencies of the inverse crystals before and after infiltration. **Figure 4.9** shows the OR for the blank non-infiltrated opal (grey line) as well as the infiltrated opals with both, 8 and15 nm Ni NPs (black lines). We observe that the blank opal exhibits a stop band centered at $\lambda_B \approx 537$ nm, whereas after the infiltration with the Ni nanoparticles the stop band experiences a red-shift. This effect is very weak for the opal infiltrated by horizontal immersion (for both sizes nanoparticles) (**Figure 4.9a, b**) whereas it is substantial (~18nm shift) for the opals infiltrated with 8 nm nanoparticles (**Figure 4.9c**) and around 13 nm for the opal containing 15 nm Ni NPs (**Figure 4.9d**) .
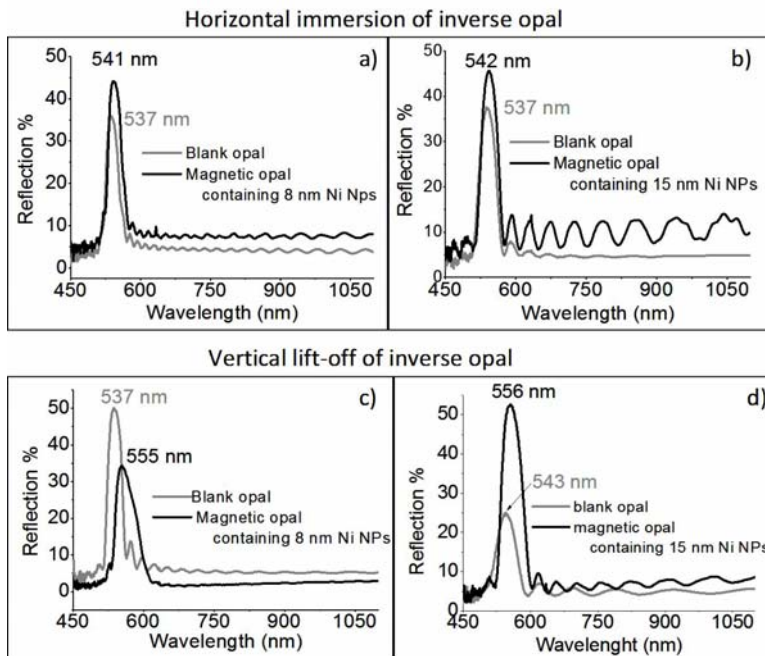


**Figure 4.9** *Comparison between the Bragg peak position of the blank and the magnetic opals fabricated by dip coating method.*

The very small Bragg peak shift for the opals infiltrated by horizontal immersion, as it was expected, is due to the nanoparticles' accumulation on the opal surface. This can cause diffusive scattering, increasing in the same time the reflected light intensity while less light is transmitted through the material, as it was observed in optical spectra. For a uniform infiltration, without surface accumulations of the nanoparticles, the magnitude of the stop band red-shift is directly related to the degree of the opal infiltration. To quantify this parameter, we calculated the effective refractive index ($n_{eff}$) of the material before and after infiltration (material fabricated by step-motor assisted dip coating), from the experimental $\lambda_B$ red-shift using the Bragg law for a *fcc* closed packed structure[14] (eq.4.5).

$$\lambda_B = \left(\frac{8}{3}\right)^{\frac{1}{2}} D n_{eff} \qquad (Eq.4.5)$$

where $D$ is the sphere diameter of the photonic crystal ($D$ = 316,8 nm in our case, which is obtained from the addition of the void diameter −288 nm− plus twice the $Al_2O_3$ shell thickness). From Eq. 4.5 we obtained $n_{eff}$ = 1,039 for the original opal and $n_{eff}$ = 1,073 and 1,044 for the opals infiltrated with Ni nanoparticles of 8 nm and 15 nm, respectively. From these values we could extract the volume fractions $f_{Ni}$ of the infiltrated magnetic nanoparticles by using well known effective medium approximations, i.e., Maxwell–Garnett equation (**Chapter 1.2.3**) (eq.4.6).

$$\frac{n_{eff}^2 - 1}{n_{eff}^2 + 2} = f_{Ni} \frac{n_{Ni}^2 - 1}{n_{Ni}^2 + 2} + f_{Al_2O_3} \frac{n_{Al_2O_3}^2 - 1}{n_{Al_2O_3}^2 + 2} + f_{air} \frac{n_{air}^2 - 1}{n_{air}^2 + 2} \qquad (Eq.\ 4.6)$$

and Bruggeman equation (**Chapter 1.2.3**) (eq.4.7). (

$$0 = f_{Ni} \frac{n_{Ni}^2 - n_{eff}^2}{n_{Ni}^2 + 2 \cdot n_{eff}^2} + f_{Al_2O_3} \frac{n_{Al_2O_3}^2 - n_{eff}^2}{n_{Al_2O_3}^2 + 2 \cdot n_{eff}^2} + f_{air} \frac{n_{air}^2 - n_{eff}^2}{n_{air}^2 + 2 \cdot n_{eff}^2} \qquad (Eq.4.7)$$

where we also used the refractive indices of air ($n_{air}$ = 1) and Ni ($n_{Ni}$ = 1.78)[7]. Using the $f_{air}$ and the $f_{Al2O3}$ values calculated above and the observed red-shift of the gap, the effective filling fraction of Ni has been determined. These estimates were virtually the same for both approaches (Eq. 4.2 and Eq. 4.3), and yielded $f_{Ni-15nm} \approx$ 1.1– 1.3% and $f_{Ni-8nm} \approx$ 9% for the 3D-MPCs infiltrated with 15 nm and 8 nm nanoparticles, respectively. The smaller infiltration observed when using the 15 nm nanoparticles is likely related to the fact that when larger particles or higher concentrations are used, some blocking of the connecting necks of the opal takes place. Indeed, smaller filling fractions are also obtained when using 8 nm Ni nanoparticle dispersions of high enough concentrations ($>10^{-3}$M = 0.1mg Ni NPs/ml solvent). Thus, optimal infiltration of 3D-MPCs requires small enough nanoparticle size and low concentrations.

### Magneto-optical measurements: band-edge enhancement

Once the structural quality of the photonic crystals and the efficiency of the infiltration with the magnetic nanoparticles have been accomplished, the following task was the investigation of their functional optical and magneto-optical properties.

The non-magnetic 3D photonic crystals due to their particular compact *fcc* periodic structure, can exhibit a significant optical activity near the stop band frequencies and thus much of the optical activity of the3D–MPCs may have a non–magnetic origin, resulted from the geometry of the opal structure. To obtain the intrinsic magneto-optical activity of the 3D –MPCs a specific measurement protocol, detailed elsewhere was established[15].

To assess the magneto-photonic effects in the magneto-optical spectral response we recorded the whole series of full hysteresis MCD loops of the 3D-MPCs with 1 nm step resolution, from $\lambda$ = 400 nm to $\lambda$ = 800 nm. The maximum amplitude of each hysteresis loop was then used to compute the system MCD spectral response. As an illustration, we show in **Figure 4.10d** the MCD spectrum measured, while **Figures. 4.10a-c** display the full hysteresis loops at selected wavelengths.
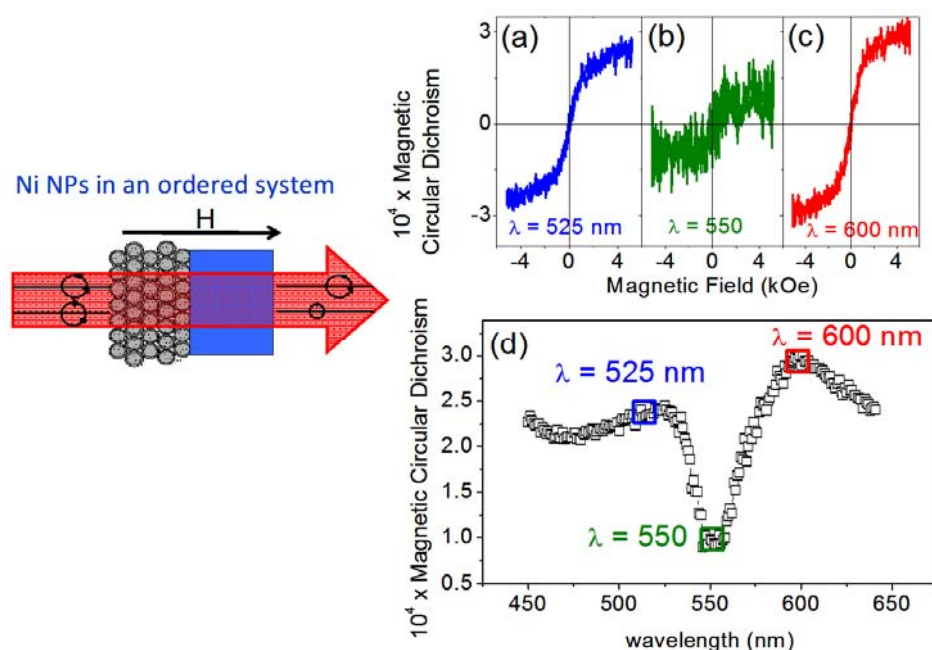


*Figure 4.10. A scheme of the magnetic circular dichroism (MCD) principle and the measured spectrum of an inverse opal infiltrated with 8 nm Ni nanoparticles is shown in (d). The data are obtained from the maximum amplitude of the MCD hysteresis loops (see the panels (a-c) for these loops at three selected wavelengths).*

Once the protocol to measure the intrinsic MCD is established we discuss now the magneto-optical spectral responses of the photonic crystals and their relation to their optical properties. **Figure 4.11** depicts the MCD measurements principles and OT (full symbols) and MCD (empty symbols) spectra obtained at the same spot (diameter ~2 mm) in opals infiltrated with 8 nm and 15 nm nickel nanoparticles. Additionally, **Figure 4.11** shows the MCD spectrum of a sample consisting of 8 nm nanoparticles distributed randomly on a glass substrate (empty squares). This spectrum is the reference of the MCD response of the Ni nanoparticles free of any crystal-induced photonic effect. The figure immediately reveals a deep modification of the MCD spectra of the two 3D-MPCs with respect to that of the randomly distributed Ni nanoparticles.

More specifically, a clear signature is observed of a magneto-optic enhancement in the form of two prominent shoulders in the MCD spectra around the two stop band edge frequencies (which are indicated by arrows). Note that the frequency shift of the optical stop-band positions of the 3D-MPCs infiltrated with 8 nm and 15 nm nanoparticles is perfectly reproduced by the shift of the features of the MCD spectra induced by the photonic band effects.
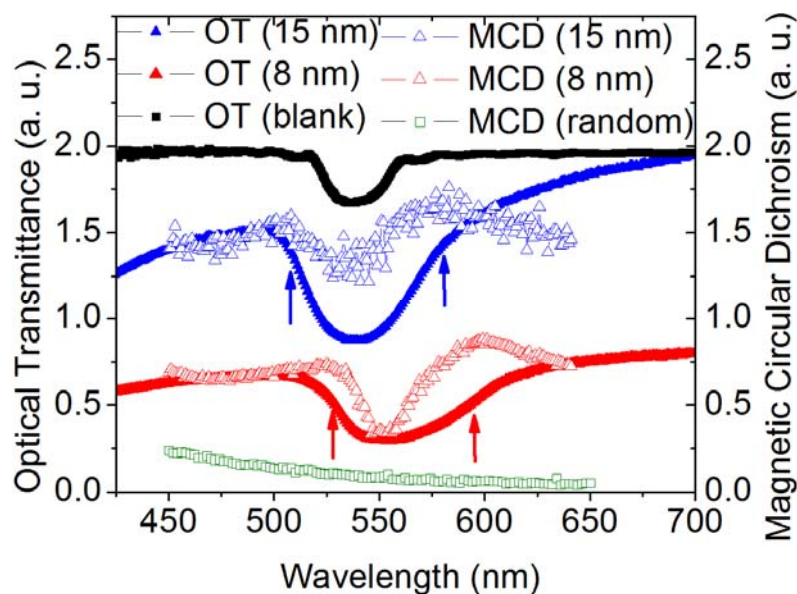


**Figure 4.11** *Optical transmittance (OT) of a non-infiltrated opal (blank) and opals infiltrated with 15 nm and 8 nm Ni nanoparticles. The Figure also shows the magnetic circular dichroism (MCD) spectra of opals infiltrated with nanoparticles as well as the MCD spectra of Ni nanoparticles distributed randomly on a glass substrate. The arrows indicate the location of the magneto-optical enhancement discussed in the text.*

Therefore, the intensive modification of the magneto-optical response in close proximity of the band edge frequencies is in agreement with the theoretical predictions[16] and is a direct consequence of the strong increase of light matter interaction due to photonic band flattening and the resulting reduction of the light group velocity at band edge wavelengths[17] Importantly, such response can be tuned by the applied magnetic field. We finally point out that the photonic effect on magneto-optics in the 3D-MPC infiltrated with 8 nm is slightly larger than that of the one infiltrated with 15 nm, in agreement with the larger impregnation of 8 nm Ni nanoparticles inside the crystal compared to the 15 nm.

Our results show that an optimal infiltration of inverse opals with magnetic nanoparticles is a suitable strategy to customize the magneto-optical spectral response of magnetic materials. We have demonstrated that our approach can be exploited to generate a tailored magneto-optical response that is operative at least in the order of a few millimeters (the probe light spot size in our experiments). This shows that the structural order required to observe the photonic band induced effects is preserved in the same length scale, which makes still more appealing the approach here described for applications using lasers as light sources. We note that the superparamagnetic properties of the nanoparticles ensure an agile response of our system with the magnetic field, at variance with a continuous layer that would lead to hysteretic ferromagnetic behavior with more limited agility.

# 4.3 MnFe$_2$O$_4$ INVERSE OPALS BY CLASSIC SOL–GEL APPROACH

The fabrication of magneto-photonic materials using pre-synthesized magnetic nanoparticles is a suitable approach for preserving the photonic structure and allowing the infiltration of enough magnetic nanoparticles in order to reach a stop band-edge enhancement. However, one drawback of this approach is the limitation of the magnetic component loading up to 10%. To further increase the magnetic component within the photonic structure, other approaches based on the *in-situ* deposition of magnetic materials to fabricate 3D–MPCs were tried. In this section, the fabrication of magnetic ferrite (MnFe$_2$O$_4$) inverse opals by conventional sol-gel route (**Figure 4.1, approach 2 –left panel**) is discussed.

Traditional liquid phase sol-gel chemistry is a commonly used route for the fabrication of 3D inverse opals using the direct opal as sacrificial template[18]. Over the dry processes (atomic layer deposition, chemical vapor deposition, melting) it has the advantages of a greater potential to achieve maximal filling of inorganic materials into the 3D templates voids, a lower cost, and availability for a wide range of inorganic materials[19]. Among other ceramic materials, magnetic ferrites (MFe$_2$O$_4$, M = Ni, Co, Mn, Fe) can be prepared by sol-gel methods[18c, 20].

By combining the sol-gel chemistry of ferrites with photonic materials, our goal was to fabricate MnFe$_2$O$_4$ inverse opals with tunable photonic band gap and enhanced magneto-photonic response. This could only be achieved partially due to the difficulties in obtaining the right phase of MnFe$_2$O$_4$ inverse spinel. To have a mechanically strong structure without a framework collapse, multiple infiltrations/drying cycles were required. Both the optimization of the precursor solution –the sol, for a better and uniform infiltration within the templates voids and the avoidance of residual precursor accumulation at the surface– and the choice of the right sintering temperature (to obtain the desired crystalline phase) presented a challenge.

## 4.3.1 Methodology

Prior to the direct opal infiltration with the Mn ferrite sol, optimization of the experimental sol-gel parameters to obtain the desired MnFe$_2$O$_4$ inverse spinel phase was carried out.

**Sol-gel procedure of MnFe$_2$O$_4$**

**Chemicals:** The reagents, iron (III) nitrate nanohydrate (Fe(NO$_3$)$_3$ x9H$_2$O), Mn(II) acetate tetrahydrated ( Mn(ac)$_2$ 4H$_2$O) and the solvent, 2 methoxyethanol (2methoxyEtOH) were purchased from Sigma-Aldrich and used without further purification.

**Synthesis:** The synthesis was adapted from Lee et al.[18c] and Kim et al.[20a]. A brief description of the typical procedure is the following (**Figure 4.12**): 1 mmol (0.404 g) iron (III) and 0.5 mmol (0.125 g) Mn(II)precursors were mixed in 2 ml of methoxyethanol solvent under magnetic stirring (250 rpm) at 85 °C for 30 min with the formation of the Mn ferrite sol. This gel-like sol was further dried in an oven for a few hours at 70 °C, resulting in an amorphous solid mass of Mn ferrite (reddish powder), followed by sintering at a few

hundreds °C (300, 500 or 700°C) for several hours under air atmosphere to form the crystalline inverse spinel phase.

Several experimental parameters were varied in order to study their effect on crystallographic phase(s) of the final material:

1.  *Precursors total concentrations* of either 1.5 M or 0.75 M at a fixed Fe : Mn molar ratio of 2:1 showed no significant influence on the final material.

2.  *Solvent type and pH.* Using methoxyethanol (solution pH 1) and sintering at 400 °C, a magnetic material was obtained (*SG_3a*). By changing the solvent for ethanol and keeping the other parameters unchanged, no ferrite formation was observed. Using a solution with basic pH (8–9) did not result in a good material.

3.  *Mixing temperature and time.* Operating at mixing times of 30, 60 or 90 min and temperatures of 70 or 85°C did not result in observable changes in the final material.

4.  *Drying temperature.* Drying at 100°C under vacuum for a few hours or at 70 °C in an oven overnight did not cause significant changes in the obtained solid mass. However, the drying temperature had an effect on the infiltrated opal. Due to the weak forces keeping the opal structure, we avoided vacuum drying in order not to damage the photonic template.

5.  *Sintering temperature* played an important role in the final phase formation. Unfortunately, we could not obtain the pure $MnFe_2O_4$ inverse spinel but a mixture of oxides such as iron oxide–hematite ($\alpha$–$Fe_2O_3$), maghemite ($\gamma$–$Fe_2O_3$), magnetite ($Fe_3O_4$) and manganese oxides ($Mn_2O_3$ and $Mn_3O_4$).

A summary of the applied experimental conditions are presented in Table 4.1.
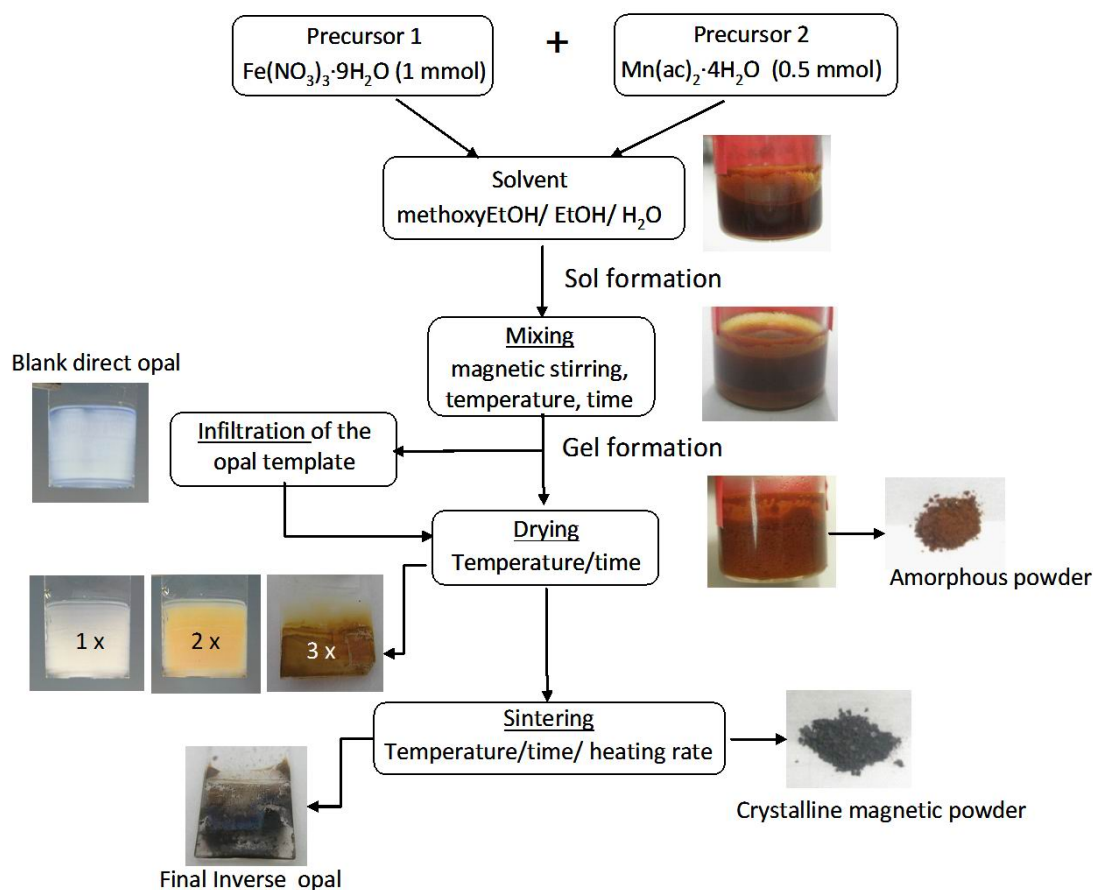


***Figure 4.12.*** *Schematization of the sol-gel chemistry process to prepare $MnFe_2O_4$ inverse opals*

*Table.4.1. Summary of the sol-gel experimental parameters for the synthesis of MnFe$_2$O$_4$*

| label | Fe(III) (mmol) | Mn(II) (mmol) | Solvent (ml) | Mixing, rpm/ T(°C)/t(min) | Drying, T(°C)/t(hs) | Sintering, T(°C)/t(hs) | OBS |
|-------|---------|--------|---------|----------------|----------------|------------------|-----|
| SG_1a | 1 | 0.5 | S1 (1) | 250/70/30 | v 80/1 | 700/5 | |
| SG_1b | 1 | 0.5 | S1 (1) | 250/70/90 | v 100/5 | 700/5 | not magnetic |
| SG_1c | 1 | 0.5 | S1 (2) | 250/70/90 | v 100/5 | 700/5 | |
| SG_2a | 1 | 0.5 | S1 (2) | 250/70/240 | v 100/5 | 500/12 | magnetic |
| SG_2b | 1 | 0.5 | S1 (2) | 250/85/60 | o. 70/night | 500/12 | |
| SG_3a | 1 | 0.5 | S1 (2) | 250/85/60 | o. 70/night | 400/7 | magnetic |
| SG_3b | 1 | 0.5 | S2 (2) | 250/85/60 | o. 70/night | 400/7 | not |
| SG_3c | 1 | 0.5 | S3 (2) | 250/85/60 | o. 70/night | 400/7 | magnetic |
| SG_4a | 1 | 0.5 | S1 (2) | 250/85/60 | o. 70/night | 300/7 | |
| SG_4b | 1 | 0.5 | S1 (2) | 250/85/60 | o. 70/night | 300/12 | magnetic |
| SG_4c | 1 | 0.5 | S1 (2) | 250/85/60 | o. 70/night | 300/24 | |

Where v. – vacuum; o. –oven; S1 –2methoxyethanol; S2–ethanol; S3–water

## Inverse opal fabrication

The experimental conditions that resulted in a magnetic material (**Table 4.1**) were subsequently used for the magnetic inverse opal fabrication (**Figure 4.12**). In a typical procedure, the voids of the PS direct opal were infiltrated with the formed Mn ferrite sol either by step-motor assisted dip-coating (A) or vertical immersion (B) methods. The infiltrated samples were then dried at 70°C for 1 h, followed by sintering in air at 300, 500 or 700°C for several hours. The infiltration cycles, precursors' concentration, sintering temperature and time were varied in order to compare the quality of as-fabricated inverse opals. The applied fabrication conditions are summarized in **Table 4.2**. It is worth noting that by vertically immersing followed by manual lifting up of the opal from the sol solution, the precursor excess on the opal surface was much higher than by step-motor assisted dip-coating. This excess resulted in crystals of the micrometer size which damage the photonic structure (discussed in section 4.3.2).

*Table.4.2. Summary of the inverse opal fabrication procedure*

| Label | Template (D, nm) | Sol formation | | Infiltration | Drying, T(°C)/t(h) | Sintering, T(°C)/t(h) |
|-------|-----------|-----------------|-----------------|--------------|------------|------------|
| | | Reagents | Mixing, rpm/ T(°C)/t(min) | | | |
| SG_4a_PS.1 | | Fe(III)– 1 mmol | | 1 cycle-A | | |
| SG_4a_PS.2 | PS (260) | Mn(II) –0.5 mmol 2methoxyEtOH – 1.5 ml | 250/80/30 | 2 cycles–A | Oven 70/1 | 300/7 |
| SG_4c_PS.3 | | 2methoxyEtOH – 1 ml | | 1 cycle-A | Oven 70/1 | 300/24 |
| SG_4b_PS.4 | PS (320) | Fe(III)– 1 mmol Mn(II) –0.5 mmol | 250/85/30 | 3 cycles-B | Oven 70/1 | 300/12 +500/7 |
| SG_1a_PS.5 | | 2methoxyEtOH – 1 ml | 250/70/30 | 1 cycle-B | Vacuum .80/1 | 700/5 |

## 4.3.2 Structural and morphological analysis of inverse opals

The materials prepared at different sintering temperatures were analyzed by their XRD spectra (**Figure 4.13**). The presence of oxides mixture rather than $MnFe_2O_4$ phase was detected. Our findings are different from what Kim et al[20a] reported using the same reagents and concentrations but annealing in vacuum at 750 °C. Similar results have shown that $MnFe_2O_4$ starts to form above 750 °C [21]. In our materials, independent of the sintering temperature, a mixture of iron and manganese oxides was formed. It has been furthermore reported that $Mn_3O_4$ can be formed by precipitation reaction and annealing at 100 °C and $Mn_3O_4$ and $Mn_2O_3$ coexist after increasing the temperature to 400–500 °C, while only $Mn_2O_3$ can be found above 600 °C[22]. These are in good agreement with our findings. For instance, $Fe_3O_4$ and $Mn_3O_4$ (the corresponding peaks are almost at the same position in the XRD spectra) predominated in the material prepared at 300 °C. At a temperature of 500 °C, the peaks corresponding to both $Mn_2O_3/Mn_3O_4$ could be detected such as the partial transformation of magnetite in maghemite and hematite. The material prepared at 700 °C presented rather $\alpha$-$Fe_2O_3$ and $Mn_2O_3$.
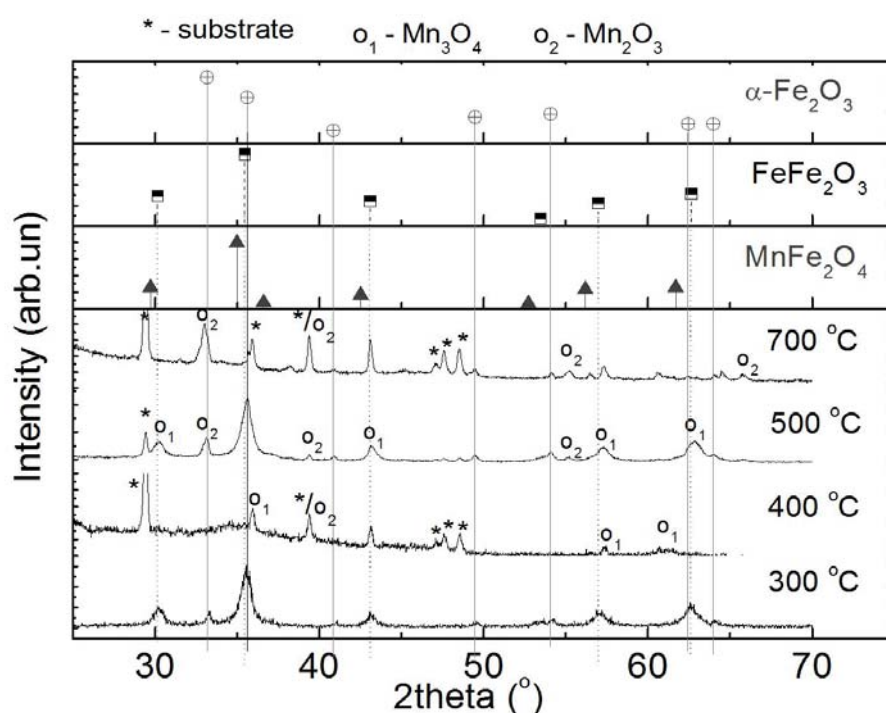


***Figure 4.13.*** *XRD spectra of the materials prepared at different sintering temperatures in comparison with bulk oxides and MnFe₂O₄. The material at 300 °C corresponds to SG_4c; at 400 °C to SG_3a; at 500 °C to SG_2b; and at 700 °C to SG_1c.*

The magnetometry analysis (SQUID), M(H) at room temperature and ZFCFC curves of material prepared at 300 °C/24h (*SG_4c*) is presented **in Figure 4.14**. The magnetization curve revealed no coercivity and remnant magnetization in the absence of magnetic field (inset at low magnetic field) with a high susceptibility. The blocking temperature around 300 K (ZFCFC curve as inset) suggested a nanoparticulate material with a superparamagnetic behavior.

159
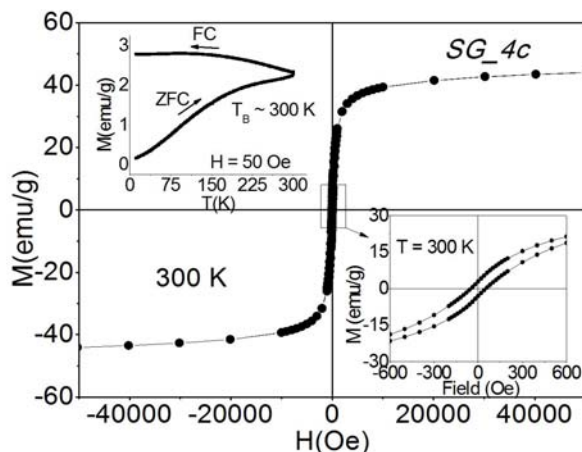
Figure 4.14. Magnetic analysis of the material labeled SG_4c. The left inset corresponds to the ZFCFC curve and the right inset shows a zoom in the hysteresis.

For the fabrication of a magnetic inverse opal, the PS direct opals were infiltrated with the ferrite sol at diffrent experimental parameters presented in Table 4.2. Surprisingly, the resulted material sintered at 300°C in framework form (inverse opal) (Figure 4.15a, b) was rather amorphous compared to the material prepared at the same conditions but in powder form. However, the frameworks prepared at 500°C and 700°C presented more cristallinity and peaks corresponded to the oxides mixture of hematite, maghemite and $Mn_2O_3$ similar with the powder form (Figure 4.15 b-c inset).
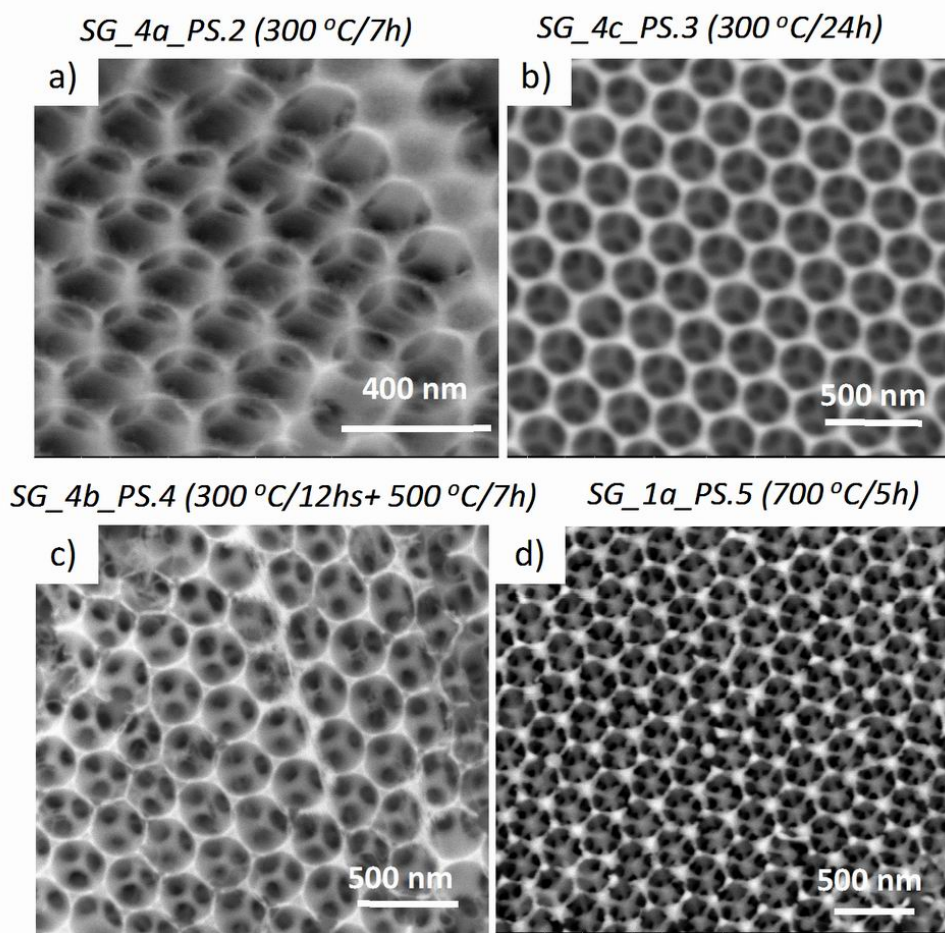


Figure 4.15. SEM images of inverse opals fabricated by sol-gel chemistry of ferrites under different conditions: infiltration using step-motor assisted dip-coating in 2 cycles; (a) and 1 cycle (b); infiltration by vertical immersion of the opal and manually lifted-up 3 cycles (c); 1 cycle. (d).

The analysis of these structures revealed the following features: i) the framework sintered at 300°C (for 7 or 24 hours) showed less contrast in SEM, suggesting rather an amorphous material. This was also confirmed by XRD analysis revealing no crystalline structure **(Figure 4.16a inset)**; ii) By increasing the annealing temperature to 500°C or 700°C, the framework became more crystalline and, as expected, the matrix was formed of a mixture of oxides, not being suitable for our purposes **(Figure 4.16d)**. iii) The step-motor dip coating method seems to be more appropriate for the sol infiltration, leaving the surface of the opal with minimal precursor excess (even for two infiltration cycles) and allowing a uniform infiltration of the voids templates **(Figure 4.16a and inset)**; iv) One cycle of vertical immersion for a few hours with manual lifting up allowed the complete infiltration of the template but also the accumulation of the precursor in excess at the opal surface. This led to the surface crystals growing in rods shape in the micrometer range **(Figure 4.16b)**. When the accumulated precursor amount was increased (e.g. by three infiltration cycles), these crystal rods completely covered the opal surface **(Figure 4.16c and its inset).** Moreover, when the vertical immersion was repeated three times, the infiltration became less efficient due to the higher surface accumulation of the sol that blocked the surface voids and subsequently only a partial template infiltration took place. A possible solution may be the opal surface cleaning (for instance, with ethanol) after each infiltration in order to remove the excess of precursor without causing damage to the structure. v) In both infiltration methods, more cracks appeared in the opal producing ordered structure only below a length scale of about 100 μm **(Figure 4.16a, b,-upper insets)**. This length of the ordered structure is insufficient either for optical measurements (using a laser diameter of around 0.9 mm) or for magneto-optical analysis (using a laser with 2 mm diameter).
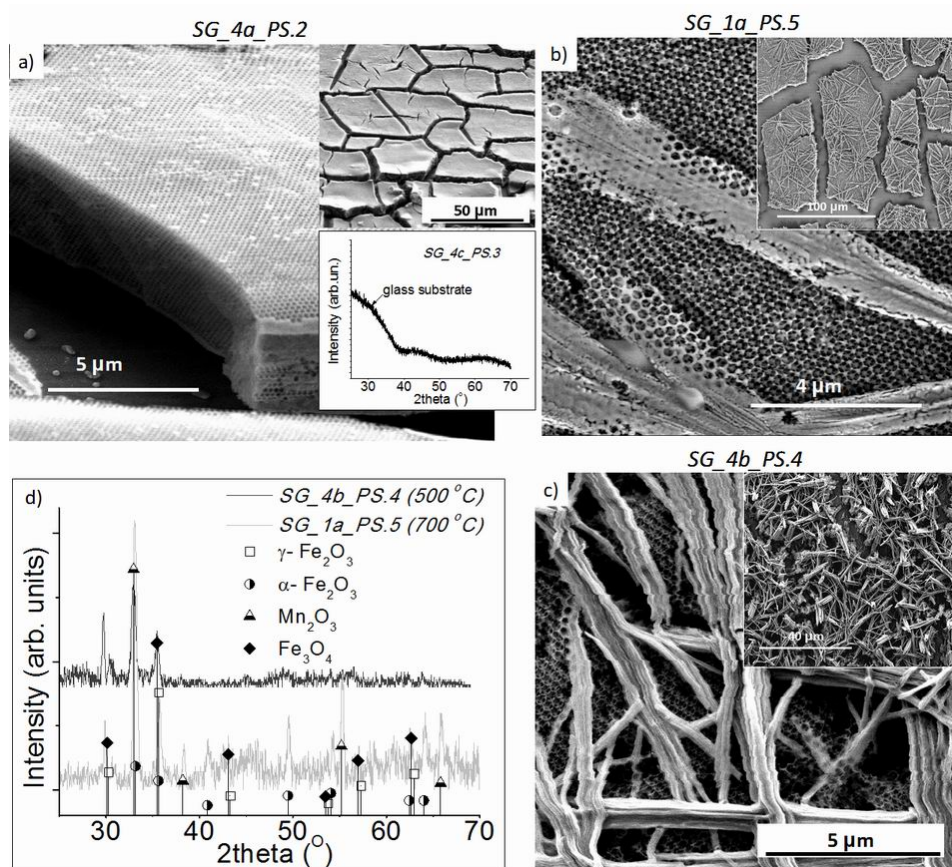
Therefore, although the framework contained the desired inverse spinel phase, the photonic band gap was lost due to the damage on the photonic structure (there is not anymore a long range order). For these reasons, no further optical and magneto-optical measurements for these opals were performed and the strategy of inverse magneto-photonic crystals' fabrication by classic sol-gel chemistry was suspended.

## 4.4 MICROWAVE-ASSSITED *IN – SITU* DEPOSITION OF FERRITE NANOPARTICLES OVER PHOTONIC OPALS

We showed here that microwave chemistry (**Chapter 2.3**) is a very efficient method to achieve fast conformal ultra-thin coating of 2D opals (**Chapter 3.3**) with multivalent complex oxides. Even though magneto-photonics is targeted here, applications to other areas, such as energy, as sensors or catalysis can be envisioned.

In this section we present on a microwave assisted benzyl alcohol route that has allowed us the growth, in just a few minutes, of a stoichiometric and homogeneous conformal nanometric coating covering extensive areas—at least on the order of $cm^2$—of the 3D photonic crystals. The coating is formed by superparamagnetic $MnFe_2O_4$ nanoparticles and does not require any post-synthesis material processing (note that bulk $MnFe_2O_4$ is ferrimagnetic with a Curie temperature of 560 K)[23]. The resulting materials exhibit unambiguously enhanced magneto-photonic response at band edge frequencies and a magneto-optical response tunable by magnetic fields.

### 4.4.1. Magnetic opals fabrication

A non-aqueous benzyl alcohol route for ferrite nanoparticles, adapted from the one first reported by Niederberger[24] was used. The microwave experiments were carried out using a CEM Discover reactor (Explorer 12-Hybrid) operating at a frequency of 2.45 GHz and a power of 200 W. Photonic crystals (direct $SiO_2$ and inverse $Al_2O_3$ opals) (**Table 4.3**) of about 5 mm x 5 mm in size grown on a glass slide substrate were vertically immersed in the reaction solution using a 10 ml closed pressurized vessel. The reaction media contained iron (III) acetylacetonate ($Fe(acac)_3$) and the stoichiometric quantity of manganese(II) acetate ($Mn(ac)_2$) with a total concentration of 0.15 M or 0.3 M in 1.5 ml of anhydrous benzyl alcohol. During a typical run, the power was automatically adjusted to heat the sample to 170°C and the temperature was kept stable for a few minutes. After the reaction took place, the solution was automatically cooled to 60°C by compressed nitrogen, stopping the reaction. The opal surface was cleaned with ethanol and from the reaction media, nanoparticles were

162

separated using the procedure described in **Chapter 2.1.** A schematization of the microwave-assisted deposition is presented in **Figure 4.17**.
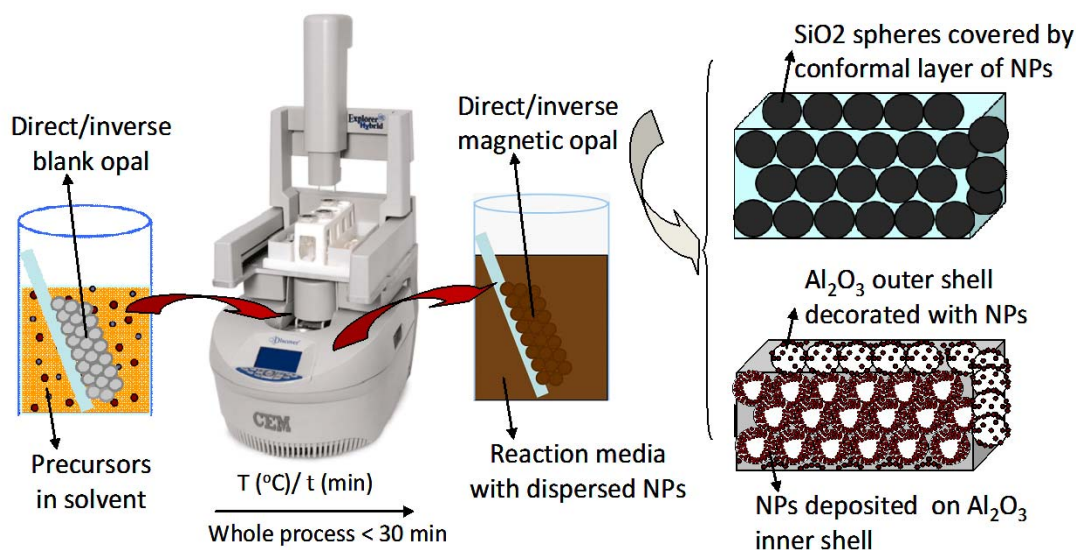


*Figure 4.17.Schematization of the microwave-assisted in –situ deposition process.*

As a reference and for comparison purposes (between nanoparticles in an ordered and disordered system), a thick ($\sim$ 200 nm) layer of randomly distributed $MnFe_2O_4$ nanoparticles (**Figure 4.18a**) was prepared by appropriate conditions in the microwave reactor: 0.15/0.3M precursors ($Fe^{3+}$ and $Mn^{2+}$) concentration in 1.5ml solvent was used to deposit the NPs on a vertically immersed optical glass slide into the microwave reaction solution, in order to have the magneto-optical behavior of NPs in a disordered system. The sample was heated up to 170 °C and the set temperature was kept constant for 5 min. In **Figure 4.18b** we show the X-ray diffractometer, displaying the peaks of the spinel structure. This layer was measured to obtain the saturated magnetic moment ($\sim$50 emu/g, **Figure 4.18c**) close to the bulk value[23].

Although the $MnFe_2O_4$ nanoparticles show ferromagnetic behavior at low temperatures (5K) (**Figure 4.18c–upper inset**) at room temperature they are superparamagnetic (**Figure 4.18c–lower inset**) Zero field cooled and field cooled (50 Oe) magnetization measurements in **Figure 4.18d** show a blocking temperature ($\sim$78 K) compatible with a size of around 5 nm.

For the fabrication of magnetic opals, several experimental parameters were varied to investigate their influence on the final material quality and functionalities (optical and magneto-optical):

➢ Two metal precursor concentrations (0.15 and 0.3M) were used while keeping the same microwave set parameters.

➢ The reaction temperature was chosen to be 170 °C for all the experiments.

➢ The reaction time (at 170 °C) was 5 or 10 minutes while the $t_{irrad}$ had a small variation for every experiment (see discussions **Chapter 2.3.2**) (**Chapter 6.3 Table A.iv.1**)

**MnFe₂O₄ NPs on glass substrate**
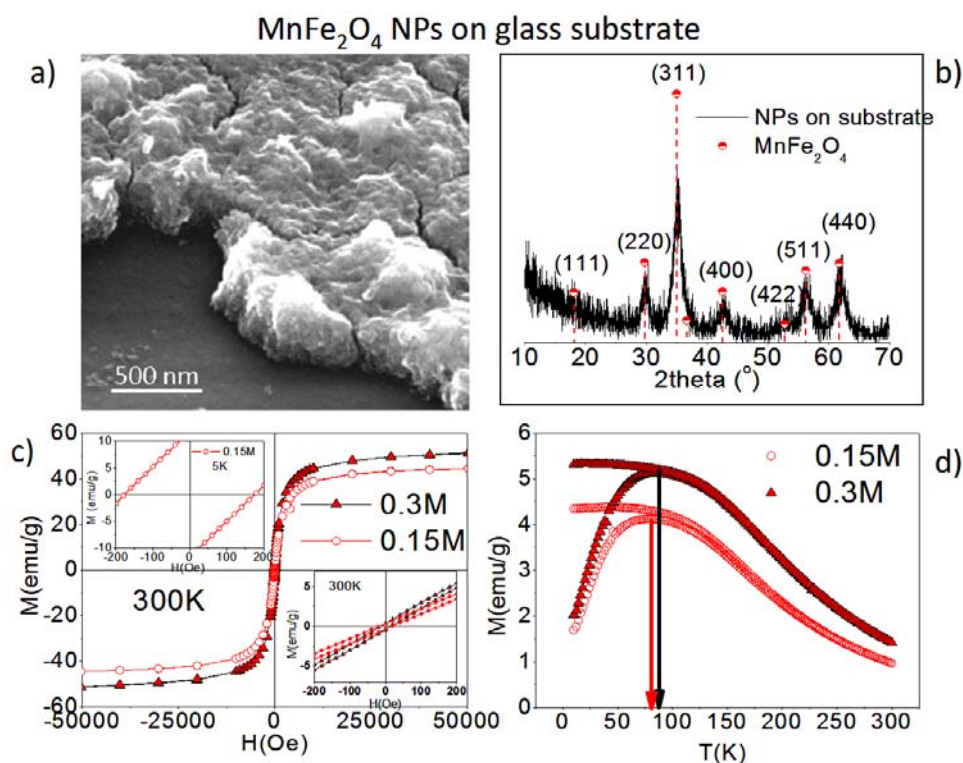
*Figure 4.18.Characteristics of in-situ deposited MnFe₂O₄ NPs on a glass substrate by microwave-assisted deposition approach. (a) SEM image of the prepared NPs film from 0.3M precursors' concentration; (b) XRD spectrum in comparison with the bulk MnFe₂O₄.; (c) M(H) curves at 300 K with two insets: upper zoom of M(H) at 5K and the lower, a zoom of M(H) at 300K; (d) ZFCFC curves at 50 Oe.*

➢ Two types of blank opals with two different opal spheres diameters have been used, namely direct opals made of $SiO_2$ spheres of 326 and 260 nm and $Al_2O_3$ inverse opals with the void diameter of 270 and 234 nm. The final material obtained from the $SiO_2$ direct opal will be labeled as *MW_MD.X*, where MD correspond to magnetic direct opal and X to the experiment number, while the magnetic material obtained from $Al_2O_3$ inverse opals will be labeled as *MW_MI.X* (MI corresponding to magnetic inverse opal

➢ Trietylamine is a catalyst for the condensation reaction[25]. Knowing (Chapter 2.3) that the growth of ferrite nanoparticles is based on the surface condensation reaction, the pristine opal (both direct and inverse) was functionalized with triethyalmine (by vertical immersing,) to study the influence of amine on the magnetic coverage degree.

The summary of the experimental conditions are presented in **Table 4.3** and more detailed data can be found in **Chapter 6.3 Table A.iv.1**

*Table 4.3. Summary of the experimental parameters used for the fabrication of the magnetic opals by microwave-assisted in-situ deposition approach.*

| Material label | Opal type | Spheres (nm) | Precursors Fe(III) (mmol) | M(II) (mmol) | Solvent (ml) | $C_{tot}$ (M) | MW set parameters (200W) T (°C) | time (min) |
|---|---|---|---|---|---|---|---|---|
| *MW_MD.X* | direct | SiO$_2$ (260) SiO$_2$+R3N (260) | Fe(acac)$_3$ (0.15) | Mn(ac)$_2$ (0.075) | | 0.15 | | 5 |
| | | SiO$_2$ (350) | Fe(acac)$_3$ (0.15) | Mn(ac)$_2$ (0.075) | | 0.15 | | 3/5 |
| | | | Fe(acac)$_3$ (0.3) | Mn(ac)$_2$ (0.15) | | 0.3 | | 5/7/10 |
| *MW_MI.X* | inverse | Al$_2$O$_3$ shell of 8.2 nm with the air void of 234 nm | Fe(acac)$_3$ (0.15) | Mn(ac)$_2$ (0.075) | Benzyl alcohol (1.5 ml) | 0.15 | 170 | 5 |
| | | | Fe(acac)$_3$ (0.3) | Mn(ac)$_2$ (0.15) | | 0.3 | | 5 |
| | | Al$_2$O$_3$ +R3N(234) | Fe(acac)$_3$ (0.15) | Mn(ac)$_2$ (0.075) | | 0.15 | | 5 |
| | | Al$_2$O$_3$ shell of 15 nm with the air void of 270 nm | Fe(acac)$_3$ (0.15) | Mn(ac)$_2$ (0.075) | | 0.15 | | 5 |
| | | | Fe(acac)$_3$ (0.3) | Mn(ac)$_2$ (0.15) | | 0.3 | | 5 |

## 4.4.2. Morphology of the magnetic opals

### Evaluation of the magneto-photonic crystal quality

Both iron oxide (magnetite/maghemite) and manganese ferrite (MnFe$_2$O$_4$) nanoparticles were deposited over silica direct opals, while MnFe$_2$O$_4$ was used for the infiltration of Al$_2$O$_3$ inverse opals. For similar microwave experimental parameters (0.15M precursor concentration, 160/170°C reaction time and ~ 8 min irradiation time) we evaluate first the final material quality (for both direct and inverse opals) in terms of the preservation of the structural order, the amount, crystalline phase and uniformity of the *in-situ* formed magnetic component. As can be seen in **Figure 4.19a** the SEM images at lower resolution shows a very good material quality meaning that microwave deposition is a non destructive method preserving the structural order of the original photonic material. The cracks visible at the opal surfaces in **Figure 4.19c, e** after deposition, were already present in the pristine opal (**Chapter 4.1.2**). Moreover, the size of these cracks will have an insignificant effect on the optical and magneto-optical properties (**Chapter 4.4.3**). The preservation of the structure has been observed for all the prepared materials. A closer look on the cross-section of the magneto-photonic material — by further increasing the magnification, reveal the fcc structural order across the whole depth of the opal certifying the suitability of the microwave technology for the fabrication of magneto-photonic materials. Because of the fabrication method the pristine (blank) opal presents a gradient of thickness which in turn influences the microwave magnetic coating thickness. As the central part of the opal shows uniformity in the thickness, the same uniformity in the magnetic coverage has been found in this region and subsequently optimal functional properties, discussed later. It is worth to mention that the quality of the blank opal plays a fundamental role in the morphology and functionality of

the final magneto-photonic structures. If the opal presents cracks and some defects within the structures before any further procedure, they will be magnified after the microwave-assisted synthesis (depending on the magnetic loading), thus damaging the structural order and the functional properties of the magneto-photonic crystal. In consequence, a careful attention was paid firstly in the initial quality of the blank opal
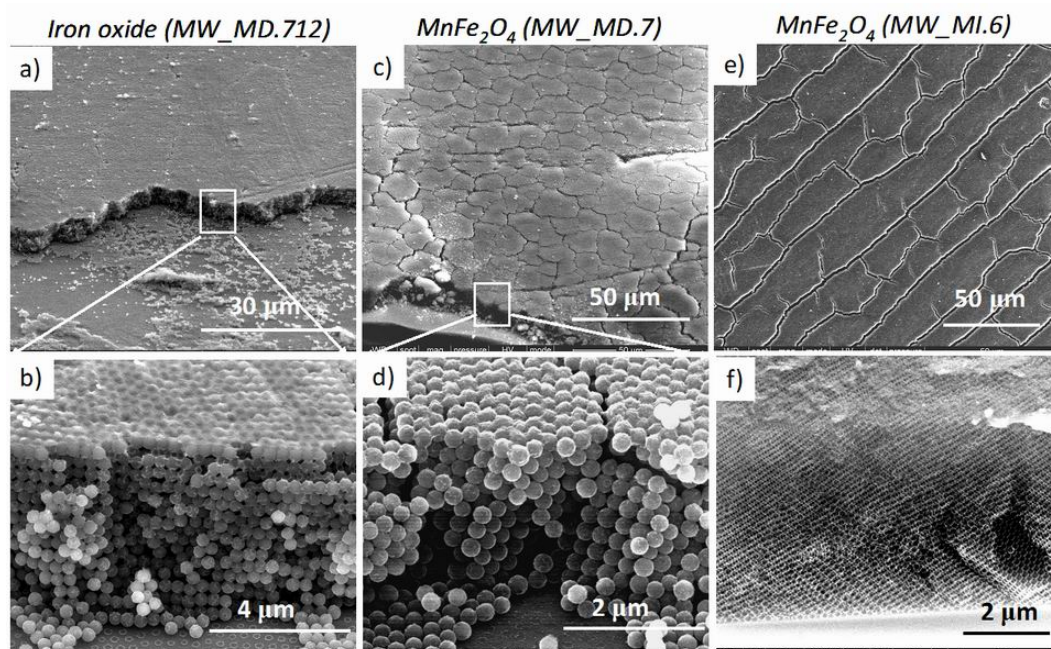


*Figure 4.19. SEM analysis of different types of magneto-photonic crystals. Surface of a direct opal coated with iron oxide NPs (a); and MnFe₂O₄ and (b) and of inverse opal infiltrated with MnFe₂O₄ NP (c) respectively. A closer look on the cross sections of those opals (b, d, f).*

## Influence of precursor type on magnetic deposition

The morphology of direct opals covered with a conformal layer of iron oxide and $MnFe_2O_4$ NPs using similar deposition experimental parameters are presented through their surface and cross-section SEM images (**Figure 4.20**). The images of different points –at the top and middle layers of the direct magneto-photonic crystals revealed a conformal continuous manganese ferrite (*MW_MD.7*) (**Figure 4.20a–d**) and iron oxide (*MW_MD.12*) (**Figure 4.20 c–d**) layers confirming the homogeneous and uniform coverage of the opal structures across its depth. The absence of coating in some particular places, especially at the contact surface between two silica spheres (**Figure 4.20b, d**) highlights the uniformity of the magnetic layer. Moreover, the coating also reaches the deeper part of the crystals (bottom layer)(images not shown). Although similar experimental parameters were used for both depositions, some differences have been observed. The surface of the opal it seems that is covered with a thicker layer of iron oxide NPs. This could be attributed to a different thickness of the opal and also to the precursor's type. As was experimentally observed in the case of nanoparticles synthesis by microwave heating (**Chapter 2.3.3, Figure 2.31**), the same conditions will lead to $MnFe_2O_4$ NPs smaller than iron oxide NPs.
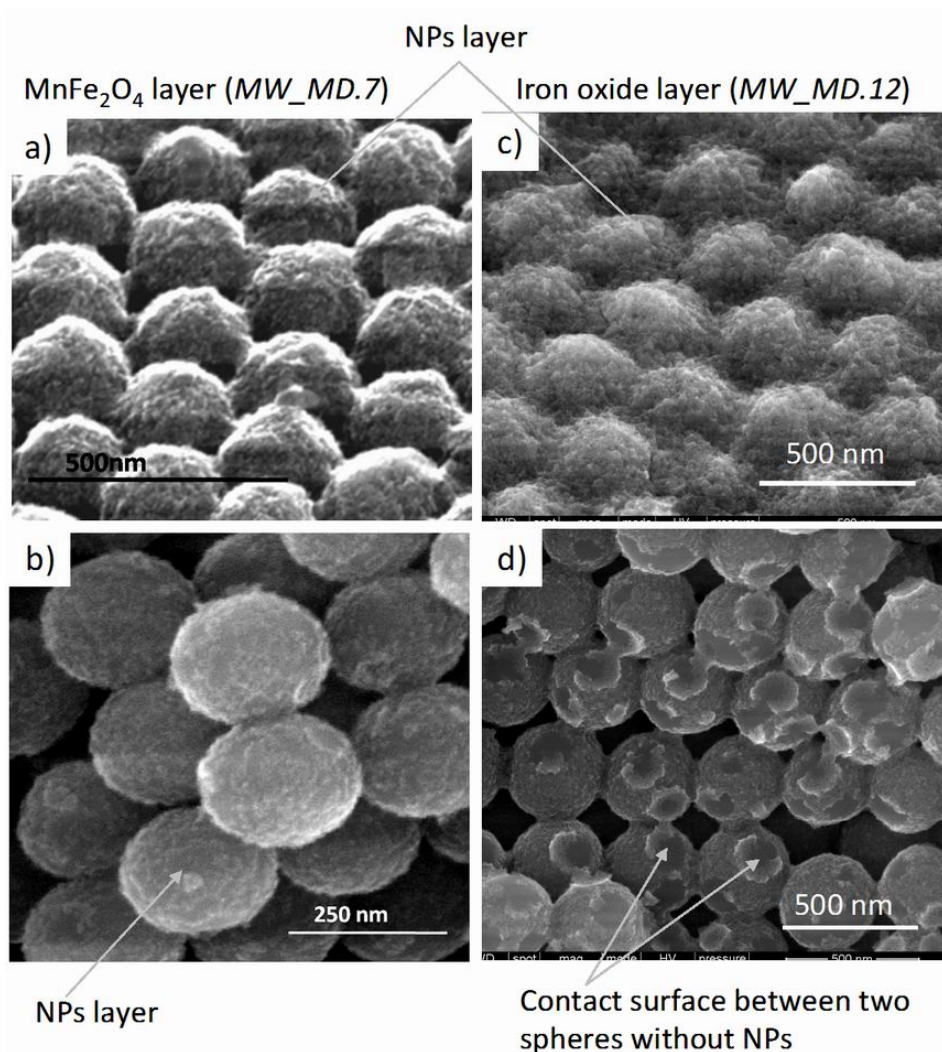
*Figure 4.20.* SEM images of surfaces and cross-sections of a direct opal coated with a layer of MnFe$_2$O$_4$ NPs *(a, b)* and iorn oxide *(c, d)*

### Influence of precursors concentration on magnetic deposition

While in the case of nanoparticles synthesis, higher precursor's concentration will lead to bigger nanoparticles, in the case of opals, a higher coverage degree has been observed, independent of the opal type used, for 0.3M compared to 0.15 M precursors' concentration. **Figure 4.21** presents the surfaces and cross-sections of direct (*MW_MD.6 and 7*) and inverse opals (*MW_MI.2 and 3*), respectively, for the following deposition parameters: 170°C as reaction temperature, 5 min-reaction time with a total irradiation time of 9 ± 1 min. In the case of direct opal, the thickness of the conformal magnetic layer will increase with the concentration (**Figure 4.21.a, b**), while in the case of inverse opal, the voids are filled with more NPs (**Figure 4.21c, d**). The values of the volume fraction of magnetic loading are given in Table 4.4 and 4.5. The surface chemistry is an important part in microwave-assisted deposition. In both direct and inverse opals, the hydroxyl terminated oxide surfaces of the SiO$_2$ and Al$_2$O$_3$ scaffolds are more susceptible to absorb microwave energy than the bulk of the material, activating in this way the opal surfaces by locally increasing the temperature[26] (hot spots) and promoting the nucleation and the growth of the magnetic nanoparticles on

these surfaces. Higher concentration of precursors can promote a higher concentration of nuclei and subsequently a higher adsorption of them on the silica or alumina surface resulting in a higher coverage.
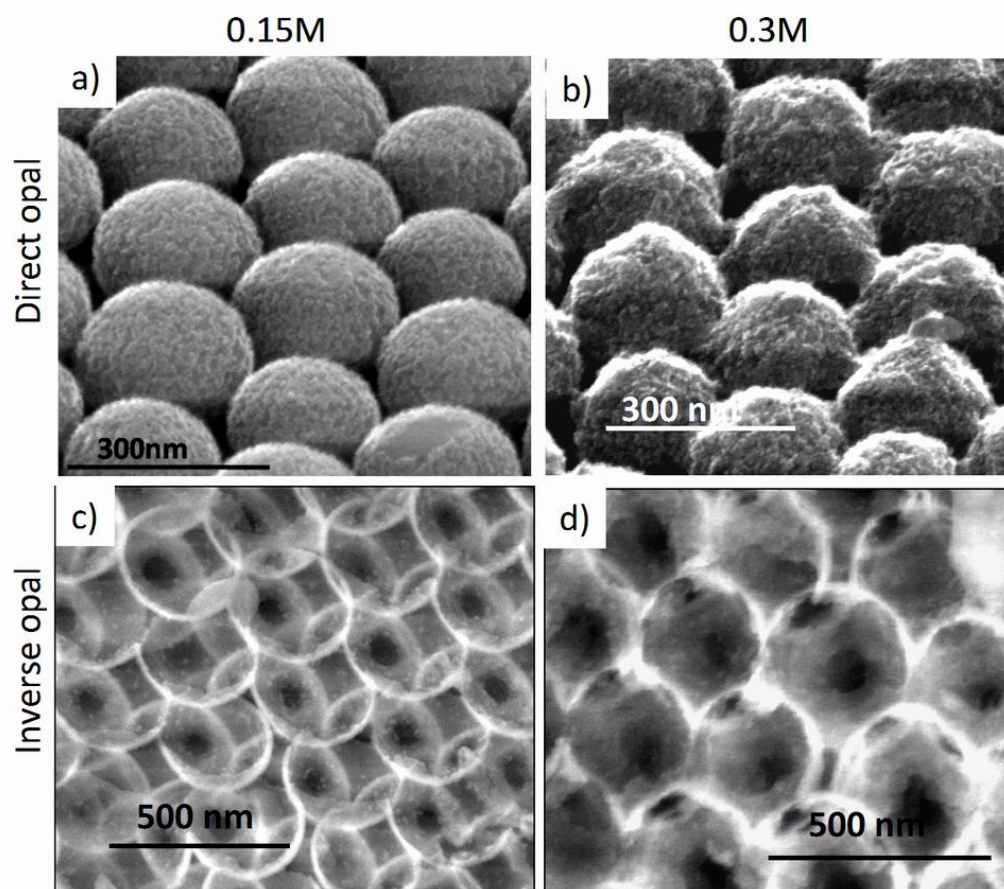


**Figure 4.21** *Influence of different precursors concentration over magnetic loading with MnFe₂O₄ NPs for direct and inverse opals. (**a**) MW_MD.7; (**b**) MW_MD.6; (**c**) MW_MI.3 and (**d**) MW_MI.2*

### Influence of deposition time ($t_{irrad}$)

Another factor that has been found to influence the coverage degree is the total irradiation time and implicitly the reaction time. Employing longer deposition time ($t_{irrad}$) the thickness of the conformal NPs' layer can be increased to such extent that the templates voids are completely filled (**Figure 4.22**) loosing the photonic structure. The same effect was observed in the case of 2D-MPCs using the microwave-assisted deposition approach (**Chapter 3.3**).
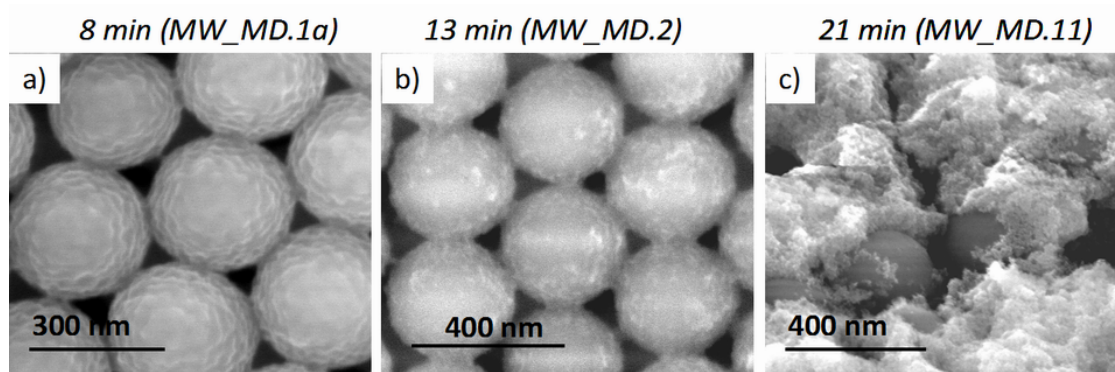


**Figure 4.22.** *Influence of deposition time ($t_{irrad}$) on MnFe₂O₄ NPs coverage degree*

**Influence of amine functionalization on the magnetic coverage**

Based on the previous knowledge about microwave-assisted nanoparticles synthesis (**Chapter 2.3.2**) that i) the growth of the NPs is driven by the chemical reaction of condensation and ii) this reaction can be activated or inhibited by using different types of surfactants (Figure 2.39), our question was what is happening if the pristine opal is functionalized with a chemical compound that influence the condensation reaction. For this purpose  we chose trietylamine, known as a catalyst for the condensation reaction[25]. The pristine opals (SiO$_2$ direct opal and Al$_2$O$_3$ inverse opals) were vertically immersed in trietylamine solution and kept 30 min before magnetic deposition process. In both types of opals, the magnetic loading corresponding to the functionalized opal was higher than in pristine opal, as was expected. Moreover, a much more uniform conformal coverage with the magnetic layer was obtained, either at the surface or in the dipper layers., Even the deposition time for the functionalized opal was longer than for the pristine one, 18 min (*MW_MD.8*) (**Figure 4.23b**) with respect to 12 min (*MW_MD.9*) (**Figure 4.23a**), rather a thick uniform coverage than accumulation of the NPs at the surface was found for the functionalized opal.. The comparison of surfaces and cross-sections of the two direct opals is presented in **Figure 4.23.**
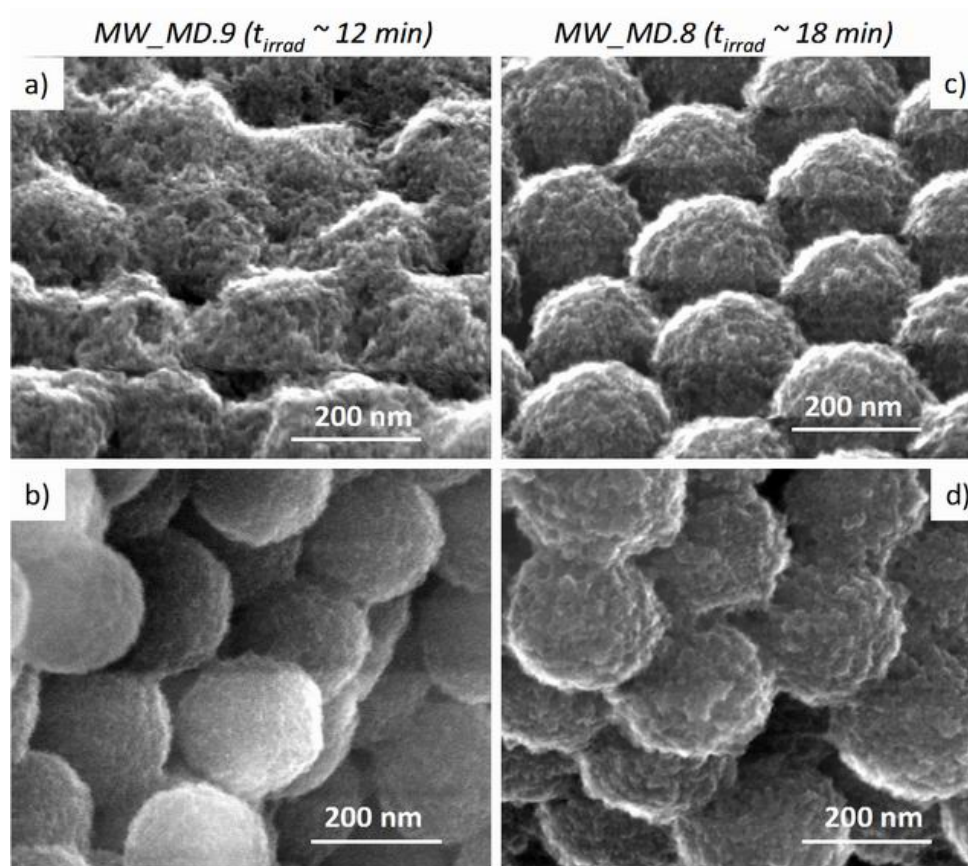


***Figure 4.23*** *Comparison of magnetic deposition on he surfaces (a, c) and cross-sections (b, d) of an opal functionalized (MW_MD.8) and not (MW_MD.9) with trietylemine.*

Similar with the functionalized silica direct opal, the trietylamine promotes the magnetic nanoparticles formation in the voids of alumina inverse opal (**Figure 4.24**). Using 0.15M precursors concentration and similar irradiation time (around 8 min), the magnetic loading

was three times more in the presence of trietylamine (*MW_MI.7*) than without (*MW_MI.6*) (Table 4.5) (**Figure 4.24**).
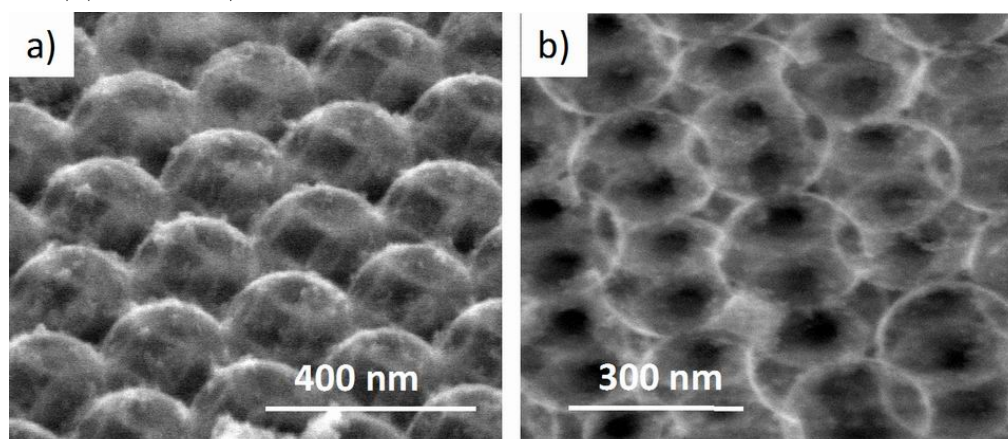


*Figure 4.24. Inverse opal functionalized with triethyalmine (MW_MI.7)*

To conclude, although previous works have also reported fairly high magnetic loads of nanoparticles embedded in direct opals, the homogeneity of the infiltration was not fully addressed and long processing times (>24 h) were required[6c, 8b, 12b]. In contrast, our 3D-MPCs have comparable volume fractions of the magnetic material—up to ~30% for direct and inverse opals, processed at a much faster speed—typically less than 30 min—and forming a quasi-ideal conforming coating and uniform across the opal depth. Additionally, no further thermal treatment of the composite material was required, since the magnetic material exhibited the desired inverse spinel crystalline phase structure ($MnFe_2O_4$ and iron oxide) (Section 4.4.3). Moreover the magnetic coverage degree can be control by precursors concentration, irradiation time and functionalization and with the proper experimental design the original structural order can be maintaining thus demonstrating the versatility of the microwave-assisted deposition method.

## 4.4.3. Structural and chemical analysis of the conformal magnetic coating

A clue to the nature of this uniform conformal coverage is given by the observed superparamagnetic behavior that confirms that the coating is composed of magnetic nanoparticles. This conclusion is further confirmed by transmission electron microscopy (TEM) experiments. **Figure 4.25** displays a TEM image with an expanded view of the top of one of the silica particles forming the direct opal structure of *MW_MD.7* where the ferrite nanoparticles can be observed. The analysis by means of high-resolution TEM confirms the expected cubic spinel structure. Indeed, selected area electron diffraction peaks (**inset of Figure 4.25a**) can be indexed in the $MnFe_2O_4$ inverse spinel phase. A detailed HRTEM analysis was carried out on one of the nanoparticles oriented along the {001}. zone axis (see a magnified detail in **Figure 4.25b**), presenting the {220} and {400} family planes, further confirming the spinel structure.

170
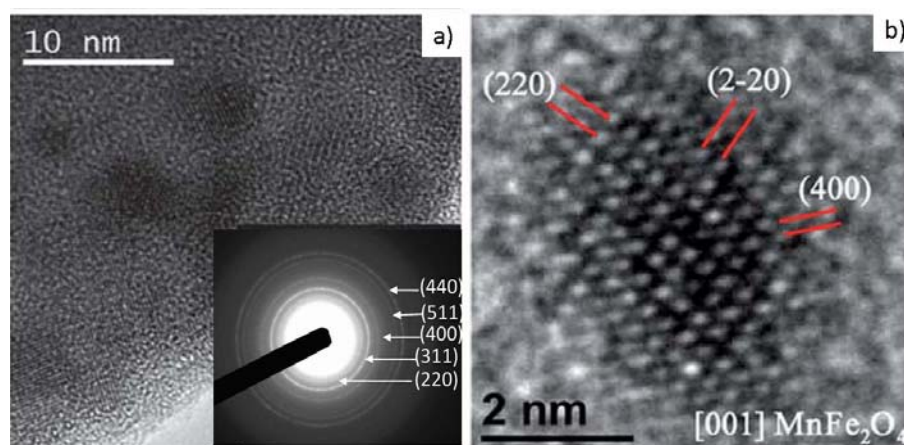
***Figure 4.25*** *High–resolution TEM analysis of one sphere covered by MnFe$_2$O$_4$ NPs (MW_MD.7) **(a)** general image of one silica nanoparticle surface showing high density of crystalline ferrite nanoparticles. The inset corresponds to a selected area electron diffraction pattern obtained on the silica spheres. (b) Magnified detail of one of the inverse spinel nanoparticles.*

Electron energy loss spectroscopy (EELS) also corroborates the coating of the opal surfaces with MnFe$_2$O$_4$ nanoparticles. In **Figure 4.26** an electron energy loss spectroscopy (EELS) line profile has been obtained from the inner (A) to the outer (B) part of the opal. Typical individual spectra obtained on both regions are shown on the right bottom figures. Notice that in the inner part (A), we mainly find the O K–edge corresponding to the SiO$_2$. When approaching to the borders, the Mn and Fe L$_{2,3}$ edges become clearer, meaning that the nanoparticles create a surface shell.
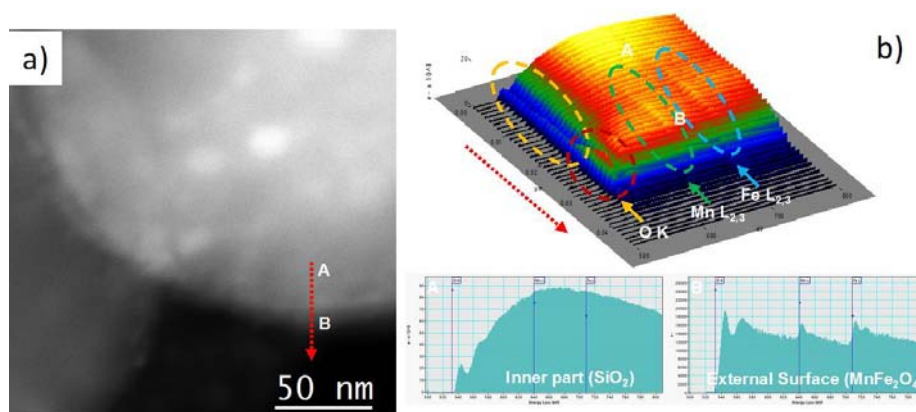


***Figure 4.26.*** *High Angle Annular Dark Field HAADF–STEM image of the SiO$_2$ opal covered with MnFe$_2$O$_4$ NPs (MW_MD.7) **(a)** with EELS profile **(b)***

Furthermore, EELS mappings carried out over a small area of a SiO$_2$ sphere squared showed the presence of Mn and Fe mainly on the external surface of the sphere (**Figure 4.27**).

171
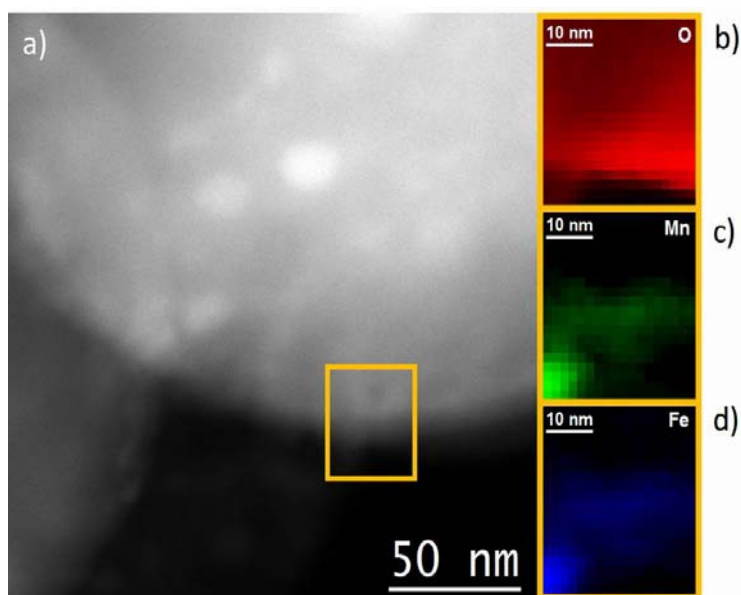
**Figure 4.27** *EELS spectrum image at the surface of a SiO₂ sphere. (a) HAADF image of a SiO₂ sphere with nanoparticles. EELS mappings carried out over the squared area in (a), show the distribution of (b) O, (c) Mn and (d) Fe over this zone.*

## 4.4.4 Materials functionalities (optical and magneto-optical)

### Direct magneto-photonic crystals

The excellent quality of the 3D-MPCs and the optimal with a magnetic layer coating in the central part of the opal revealed by the SEM and TEM images (previous section) anticipates an optimal magneto-photonic response. To assess their functional properties, we have performed optical transmittance (OT) and magnetic circular dichroism (MCD) spectroscopy experiments in a range of wavelengths λ = 400– 800 nm. OT experiments were undertaken to determine the stop-bands of the photonic crystals ($\lambda_B$) and to assess the influence of the magnetic coverage fraction on the optical properties.

We have exploited the different coverage degree exhibited in the same opal to find a magnetic loading with optimal functional properties. **Figure 4.28** presents SEM images of *MW_MD.7* material with different coverage degrees (**Figure 4.28a**) as well as the optical (**Figure 4.28b**) and magneto-optical measurements (**Figure 4.28c**). By doubling the precursors concentration (*MW_MD.6*) the same gradient of coverage have been found along the whole length of opal but at higher degree, as was expected. Both the SEM images or OP spectra of this material are not shown, but the Bragg peaks position and the filing fraction corresponding to different magnetic loadings are presented in **Table 4.4.** As can be clearly observed in the images, the increase of the thickness of magnetic deposited layer resulted in the shift of Bragg peak to longer wavelength but in the same time in decreasing the peak intensity to almost its disappearance (**Figure 4.28b–4**).
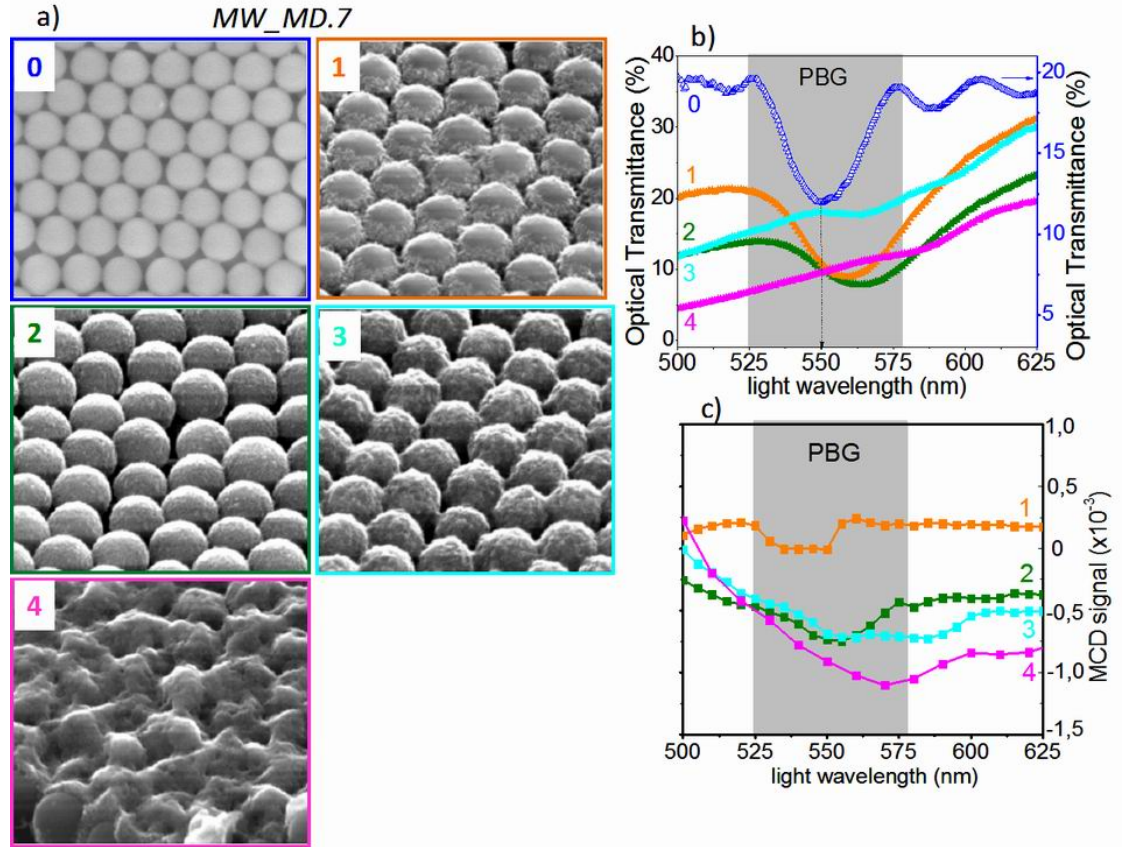
**Figure 4.28.** *The coverage degree and the optical and magneto-optical properties influenced by non-homogeneity in opal thickness: (a) presents SEM images of magneto-photonic crystal, having surfaces with different coverage degree. (b) Optical Transmittance (%) spectra and (c) the magneto-optical response, respectively corresponding to different magnetic coverage.*

As we presented in **Section 4.1.2**, the decrease of the Bragg peak intensity could be originated: i) from the loss or ordered structures; ii) some absorption of light by the magnetic material[6]; iii) the decrease of the refractive index contrast[6c]. We are incline to believe that in this case the decrease of Bragg peak intensity is rather due to the decrease of the contrast refractive index than due to of photonic order loss (SEM images of all the materials confirmed the preservation of the ordered structure). These observations are in good agreement with the simulations made for different infiltration degrees of a silica direct opal with maghemite[6c] (**Section 4.1.3**).

*For a binary system (blank direct SiO₂ opal):*, using the Bragg low (Eq.4.5) and the Maxwell Garnett approximation we calculated first the $n_{eff}$ of every blank opal used in our experiments

$$\frac{n_{eff}^2 - 1}{n_{eff}^2 + 2} = 0.74 \frac{n_{SiO_2}^2 - 1}{n_{SiO_2}^2 + 2} + 0.26 \frac{n_{air}^2 - 1}{n_{air}^2 + 2} \qquad (Eq.4.8)$$

*In the tri-component system (direct magneto-photonic crystal)* the silica spheres are covered with a shell of magnetic nanoparticles. Therefore the air voids of the template will be progressively filled with magnetic component. The silica spheres will have the same filling fraction of 0.74 but the air filling fraction will decrease simultaneously with increasing the magnetic loading, $f_{air} = 0.26 - f_{NPs}$. In addition, knowing the shift of the Bragg peak and the

$n_{SiO2}$ calculated by eq.4.4, the refractive index of $MnFe_2O_4$ NPs[7] $n_{NPs}$ = 2.3, we could extract the volume fractions of the magnetic nanoparticles $(f_{NPs})$ deposited using the eq.4.9.

$$\frac{n_{eff}^2 - 1}{n_{eff}^2 + 2} = 0.74 \frac{n_{SiO_2}^2 - 1}{n_{SiO_2}^2 + 2} + \left(0.26 - f_{NPs}\right) \frac{n_{air}^2 - 1}{n_{air}^2 + 2} + f_{NPs} \frac{n_{NPs}^2 - 1}{n_{NPs}^2 + 2} \qquad (Eq.4.9)$$

Based on these equations (eq. 4.5, 4.8 and 4.9), the calculated values of $n_{eff}$ (for the blank and magnetic opal) with the corresponding magnetic filling fraction are presented in the below table.

*Table.4.4. Optical data of several opals before and after magnetic material deposition*

| Label | $\Phi_{SiO2}$ (nm) | Before deposition (PCs) | | | After deposition (MPCs) | | | |
|---|---|---|---|---|---|---|---|---|
| | | $\lambda_{B-blank}$ (nm) | $n_{eff-blank}$ | $n_{SiO2}$ | $\lambda_{B-MPCs}$ (nm) | $n_{eff}$ | $\varepsilon_{eff}$ | $f_{NPs}$ (% of total pore volume) |
| *MW_MD.1a* | | 760 | 1.330 | 1.463 | 780 | 1.365 | 1.86 | 0.0357 (9.9%) |
| *MW_MD.1b* | 350 | 763 | 1.335 | 1.468 | 810 | 1.417 | 2.00 | 0.0782 (30%) |
| *MW_MD.2* | | | | | 800 | 1.399 | 1.96 | 0.0636 (24.5%) |
| *MW_MD.6–1* | | | | | 571 | 1.345 | 1,81 | 0.0493 (19%) |
| *MW_MD.6–2* | | | | | 574 | 1.352 | 1.83 | 0.0561 (21.6%) |
| *MW_MD.6–3* | | | | | 577 | 1.359 | 1.85 | 0.063 (24%) |
| *MW_MD.6–4* | 260 | 550 | 1.295 | 1.412 | – | – | – | > 25% |
| *MW_MD.7–1* | | | | | 559 | 1.317 | 1.73 | 0.0221 (8.5%) |
| *MW_MD.7–2* | | | | | 563 | 1.326 | 1.76 | 0.0306 (11.8%) |
| *MW_MD.7–3* | | | | | 565 | 1.331 | 1.77 | 0.034 (13.1%) |
| *MW_MD.7–4* | | | | | – | – | – | >15% |

## Inverse magneto-photonic crystals

For the optical characterization of inverse magneto-photonic crystal we applied the same procedure as in **Section 4.2.3**. The interest was the analysis of the influence, first of the precursors' concentration, and second the functionalization of the opal with amine, both correlated with the control of the infiltration degree which will affect the optical and magneto-optical properties.

**Figure 4.29** shows the transmittance spectra of the pristine inverse opals for two voids diameters **(Figure 4.29a,b)** as well as two magnetic opals with different precursors concentrations (*MW_MI.2 and 3*) **(Figure 4.29a)**. In addition, the comparative optical spectra of two magnetic opals, either functionalized with trietylamine (MW_MI.7) or pristine (MW_MD.6), are presented in **Figure 4.29b**. We observed the presence of minima of the transmittance that signals the frequencies at which the stop-bands are centered. Thus, compared with the pristine opals (blanks) the magnetic opals revealed a red-shift of the Bragg peaks due to the increasing magnetic coverage of the structures. As was revealed by cross-sectional SEM images the shell thickness of the magnetic coating becomes larger with a major magnetic loading.

We used these SEM cross-sectional images to determine the voids, connecting windows diameters and alumina shell thickness being found as followings: $D_{void}$ of 270 nm, $D_{window}$ of ~ 80 nm and h = 15 nm for *MW_MI.2 and 3*, while for *MW_MD.6 and 7*, $D_{void}$, $D_{window}$ and h were 234, ~60 and 8.2 nm, respectively. Using the equations eq.4.1-4.4 the

filling fractions $f_{air}$ and $f_{Al2O3}$ of air and alumina, respectively, in the inverse opal structure were calculated to be 0.77 and 0.23 for *MW_MI.2 and 3* and 0.889 and 0.111 for *MW_MI.6 and 7.*

The obtained values were further used to express the magnetic filling fraction factors of the magnetic opals from the $\lambda_{B-MPCs}$ red-shift using the same method as we described previously (Section 4.2.3) and the eq. 4.10.

$$\frac{n_{eff}^2 - 1}{n_{eff}^2 + 2} = f_{NPs}\frac{n_{NPs}^2 - 1}{n_{NPs}^2 + 2} + f_{Al_2O_3}\frac{n_{Al_2O_3}^2 - 1}{n_{Al_2O_3}^2 + 2} + f_{air}\frac{n_{air}^2 - 1}{n_{air}^2 + 2} \qquad (Eq.4.10)$$
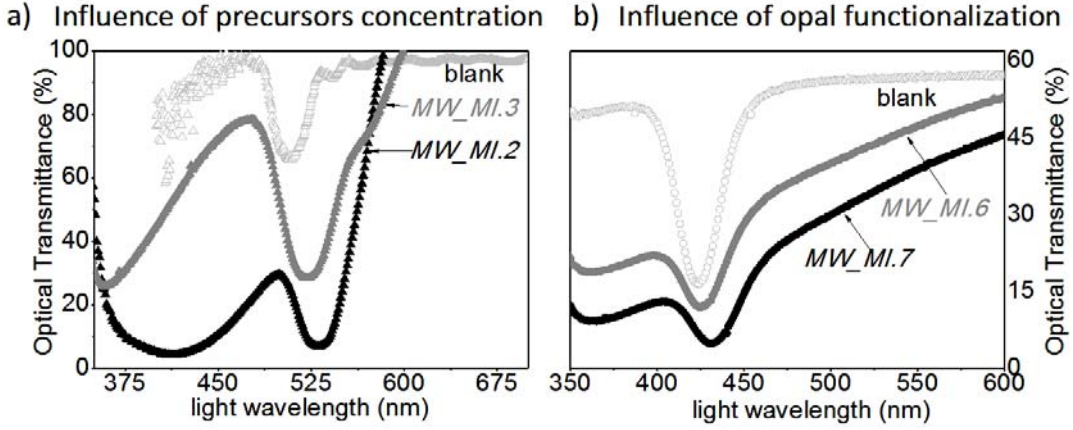


***Figure 4.29*** *Comparison of Bragg peak position of the blanks and the infiltrated opals using different experimental conditions: (a) opals infiltrated with two precursors concentrations of 0.15M (MW_MI.3) and 0.3M (MW_MI.2); (b) infiltration using the same precursor concentration of 0.15M of pristine opal (MW_MI.6) and functionalized opal (MW.MI.7)*

A summary of calculated parameters such as, Bragg peaks before and after infiltration, filling fractions, refractive index of all components, are presented in **Table 4.5**. We show therefore that large magnetic load of the opals can be achieved and that the load can be controlled by the initial concentration of the precursors or by opal functionalization.

*Table 4.5 Optical data of several inverse opals before and after magnetic material deposition*

| Label | $D_e$ (nm) | Before deposition (blank) | | | After deposition (MPCs) | | | |
|---|---|---|---|---|---|---|---|---|
| | | $\lambda_{B-blank}$ (nm) | $n_{eff-blank}$ | $n_{Al2O3}$ | $\lambda_{B-MPCs}$ (nm) | $n_{eff}$ | $\varepsilon_{eff}$ | $f_{NPs}$ (% of total pore volume) |
| *MW_MI.2* | 285 | 508 | 1.092 | 1.44 | 532 | 1.143 | 1.307 | 0.055 (10.8%) |
| *MW_MI.3* | | | | | 522 | 1.122 | 1.26 | 0.033 (6.4%) |
| *MW_MI.6* | 242.2 | 421 | 1.064 | 1.630 | 426 | 1.077 | 1.16 | 0.019 (3%) |
| *MW_MI.7* | | | | | 433 | 1.095 | 1.2 | 0.039 (6.2%) |

To obtain the intrinsic magneto-optic responses of opals—free of the optical activity inherent in their structure[27], we recorded the whole series of full MCD hysteresis loops for wavelengths in the visible range (**Figure 4.30**) and obtained the MCD spectral response from the amplitude of the loops.

Following this approach, we have observed a null MCD spectral signal on the blank inverse or direct opal, as expected from the absence of magnetic content in these samples. We have measured these loops for a range of wavelengths and their intensity being related not only

with the wavelength but also with the amount of magnetic nanoparticles loaded. For instance, in **Figure 4.30** it can be seen the loops at different wavelength of two direct magneto-photonic crystals, loaded with 10% MnFe$_2$O$_4$ NPs (MW_MD.1a) (**Figure 4.30a**) and 30% (MW_MD.1b) (**Figure 4.30b**). Very clear loops showing superparamagnetic behavior present the magnetic opal with 30% of the volume pores filled with NPs.
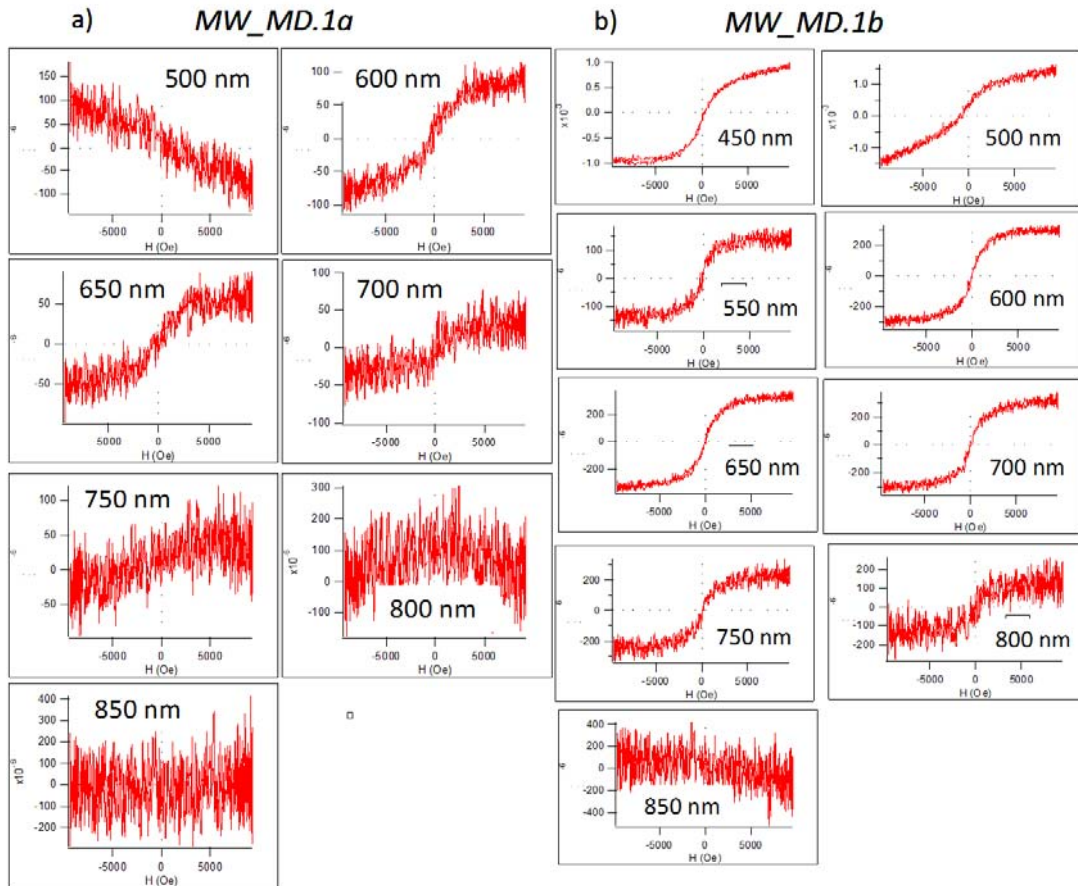


***Figure 4.30*** *MCD hysteresis loops (MCD signal vs. H) recorder at different wavelengths of direct opal loaded with 10% (**a**) and 30% (**b**).magnetic material (MnFe$_2$O$_4$ NPs).*

Plotting the MCD spectral response from the maximum amplitude signal we observed that an intricate structure appeared in the MCD spectra around the stop-band regions for both direct (**Figure 4.28c**) and inverse opals (**Figure 4.31**) indicating that a magneto-photonic response develops due to the interplay of the photonic and magneto-optical properties. To better understand the relationship between the photonic band structure and magneto-optics, we compare the magneto-photonic response of direct and inverse opals. **Figure 4.32** shows the MCD spectra (right axis) of a direct SiO$_2$ opal of 366 nm periodicity and 10.8% filling factor (*MW_MD.7-2*, **Figure. 4.32a**) and two Al$_2$O$_3$ inverse opals of different periodicity, 465 nm with 6.4% filling factor (*MW_MI.3*, **Figure. 4.32b**) and 276 nm with 6.2% (*MW_MI.7*, **Figure. 4.32c**). The figure also includes the OT spectra (left axis) of each of these crystals as well as the MCD spectrum of MnFe$_2$O$_4$ nanoparticles distributed randomly on a glass substrate.
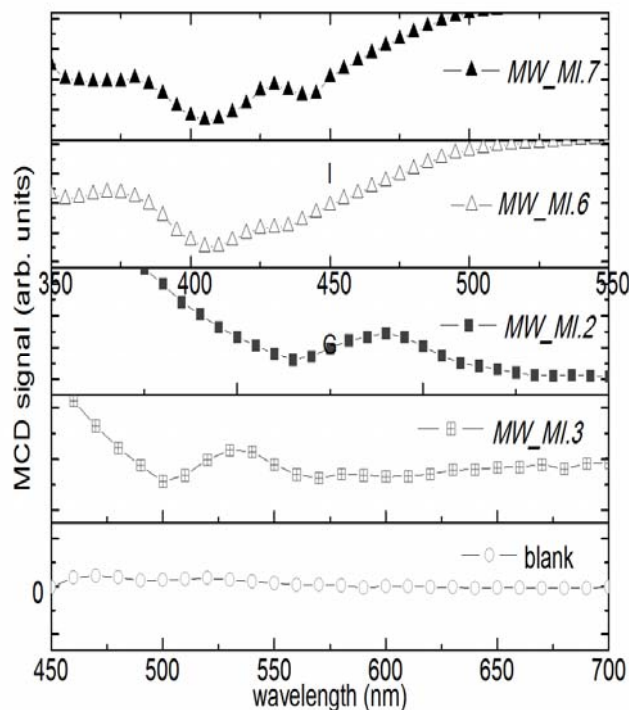
***Figure 4.31*** *Magneto-optical responses of different inverse magneto-photonic crystals in comparison with the blank opal, showing zero response.*

The latter gives the magneto-optical response of $MnFe_2O_4$ nanoparticles in the absence of any photonic effect. A common feature observed for all the magnetic opals is that the MCD response is deeply modified with respect to that of the randomly distributed nanoparticles, indicating that the photonic band structure of the crystals radically influences the magneto-optical properties of the manganese ferrite nanoparticles. Interestingly, we observe that the magneto-optical signal is enhanced at the stop-band edges (even for low filling factor, e.g MW_MI.6 of 2,5%). This signal enhancement is particularly large in the inverse opals, and more specifically for the opal previously functionalized with amine (*MW_MI.7*) where two prominent shoulders are well visible, indicating that in the vicinity of the band-edge frequencies the influence of the photonic structure on the magneto-optics is very intense. An important observation is that the optical transmittance of the inverse opals is larger than that of the direct opal. A huge magneto-photonic effect in combination with a good optical transmittance makes these complex materials very appealing for applications in optical communications. Finally, note that all the materials comprising the photonic structures here described are dielectric and, thus, such structures do not support the propagation of surface plasmon polaritons. Thus, the enhanced magneto-optical response is the result of the strong interaction of light with the structure close to the photonic band frequencies (where the Bragg reflection condition is fulfilled), rather than coupling to plasmons, as recently reported for other systems combining magnetic materials and noble metals[28]. The use of a dielectric photonic crystal to enhance the magneto-optic signal has the advantage of minimizing the optical losses that otherwise would be detrimental for many applications in optical communications.
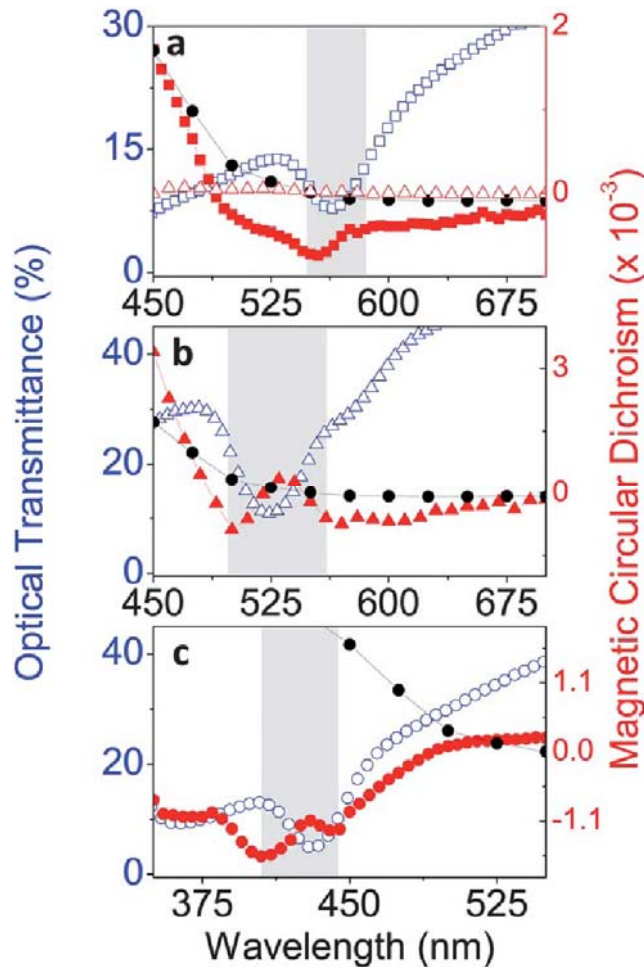
**Figure 4.32**. *MCD and OT spectra obtained in a direct opal D1 (a) and two different inverse opals I1 (b) and I01 (c) with different periodicity. Panel (a) also includes the MCD spectra of a blank opal without magnetic loading (empty red triangles). All of them show anomalous features at the stop band edges (the stop band area is shaded), although the major effects are seen in inverse opals. We show in these figures the spectra of randomly distributed MnFe2O4 nanoparticles (black solid circles) that are the reference of the magneto-optic spectral response free of any magneto-photonic effect.*

Summarizing we have presented an extremely fast and versatile microwave assisted sol–gel route to achieve the conformal coverage of large areas of three-dimensional opals with a superparamagnetic manganese ferrite layer. The use of a ternary oxide for ultra thin coating demonstrates the potential of this methodology to realize three-dimensional structures with complex materials. The resulting materials exhibit unambiguously enhanced magnetophotonic response at band edge frequencies and a magneto-optic response tunable by magnetic fields. The strategy presented here will contribute to the rapidly expanding field of advanced techniques for the fabrication of three-dimensional complex systems needed in different fields such as in photonics, phononics, metamaterials or data storage. The approach could also be relevant for some applications in materials for energy, as for instance in sensors, or in catalysis where a full coverage with functional materials on intricate topologies is crucial to boost the device performance.

# 4.5 REFERECENCES

1.      (a) Wang, Z.; Chong, Y.; Joannopoulos, J. D.; Soljacic, M., Observation of unidirectional backscattering-immune topological electromagnetic states. *Nature* **2009,** *461* (7265), 772-775; (b) Yablonovitch, E., Photonics: One-way road for light. *Nature* **2009,** *461* (7265), 744-745.

2.      (a) Takahashi, K.; Kawanishi, F.; Mito, S.; Takagi, H.; Shin, K. H.; Kim, J.; Lim, P. B.; Uchida, H.; Inoue, M., Study on Magnetophotonic Crystals for Use in Reflection-type Magneto-Optical Spatial Light Modulators. *Journal of Applied Physics* **2008,** *103,* 07B331-3; (b) Boriskina, J.; Erokhin, S.; Granovsky, A.; Vinogradov, A.; Inoue, M., Enhancement of the magnetorefractive effect in magnetophotonic crystals. *Physics of the Solid State* **2006,** *48* (4), 717-721; (c) Fedyanin, A. A.; Aktsipetrov, O. A.; Kobayashi, D.; Nishimura, K.; Uchida, H.; Inoue, M., Enhanced Faraday and nonlinear magneto-optical Kerr effects in magnetophotonic crystals. *Journal of Magnetism and Magnetic Materials* **2004,** *282,* 256-259.

3.      Inoue, M.; Baryshev, A. V.; Khanikaev, A. B.; Dokukin, M. E.; Chung, K.; Heo, J.; Takagi, H.; Uchida, H.; Lim, P. B.; Kim, J., Magnetophotonic materials and their applications. *IEICE TRANS. ELECTRON.* **2008,** *E91-C* (10), 1630-1638.

4.      Galisteo-López, J. F.; Ibisate, M.; Sapienza, R.; Froufe-Pérez, L. S.; Blanco, Á.; López, C., Self-Assembled Photonic Structures. *Advanced Materials* **2011,** *23* (1), 30-69.

5.      Galisteo López, J. F. An Optical Study of Opals based photonic crystals. Universidad Autónoma de Madrid, Madrid, 2005.

6.      (a) Libaersa, W.; Kolaric, B.; Vallée, R. A. L.; Wongd, J. E.; Woutersa, J.; Valeva, V. K.; Verbiest, T.; Clays, K., Engineering colloidal photonic crystals with magnetic functionalities. *Colloids and Surfaces A: Physicochemical and Engineering Aspects* **2009,** *339,* 13-19; (b) Baryshev, A. V.; Kodama, T.; Nishimura, K.; Uchida, H.; Inoue, M., Magneto-Optical Properties of Three-Dimensional Magnetophotonic Crystals. *IEEE Transactions on Magnetics* **2004,** *40* (4), 2829-2831; (c) Grudinkin, S. A.; Kaplan, S. F.; Kartenko, N. F.; Kurdyukov, D. A.; Golubev, V. G., Opal-Hematite and Opal-Magnetite Films: Lateral Infiltration, Thermodynamically Driven Synthesis, Photonic Crystal Properties. *The Journal of Physical Chemistry C* **2008,** *112* (46), 17855-17861.

7.      Lourtioz, J.-M., Photonic Crystals Toward Nanoscale Photonic Devices. 2nd ed.; Springer: 2008.

8.      (a) Blanco, A.; Chomski, E.; Grabtchak, S.; Ibisate, M.; John, S.; Leonard, S. W.; Lopez, C.; Meseguer, F.; Miguez, H.; Mondia, J. P.; Ozin, G. A.; Toader, O.; van Driel, H. M., Large-scale synthesis of a silicon photonic crystal with a complete three-dimensional bandgap near 1.5 micrometres. *Nature* **2000,** *405* (6785), 437-440; (b) Pavlov, V. V.; Usachev, P. A.; Pisarev, R. V.; Kurdyukov, D. A.; Kaplan, S. F.; Kimel, A. V.; Kirilyuk, A.; Rasing, T., Enhancement of optical and magneto-optical effects in three-dimensional opal/$Fe_3O_4$ magnetic photonic crystals. *Applied Physics Letters* **2008,** *93* (7), 072502-3.

9.      (a) Caicedo, J. M.; Dekker, M. C.; Dörr, K.; Fontcuberta, J.; Herranz, G., Strong magnetorefractive and quadratic magneto-optical effects in $(Pr_{0.4}La_{0.6})_{0.7}Ca_{0.3}MnO_3$. *Physical Review B*

2010, *82* (14), 140410; (b) Caicedo, J. M.; et al., Large magnetorefractive effect in magnetite. *New Journal of Physics* **2010,** *12* (10), 103023.

10.      Scott, G. B.; Lacklison, D. E.; Ralph, H. I.; Page, J. L., Magnetic Circular Dichroism and Faraday Rotation Spectra of $Y_3Fe_5O_{12}$. *Physical Review B* **1975,** *12,* 2562 - 2571.

11.      Koerdt, C.; Rikken, G. L. J. A.; Petrov, E. P., Faraday effect of photonic crystals. *Applied Physics Letters* **2003,** *82* (10), 1538-1540.

12.      (a) Šimkiene, I.; Reza, A.; Kindurys, A.; Bukauskas, V.; Babonas, J.; Szymczak, R.; Aleshkevych, P.; Franckevičius, M.; Vaišnoras, R., Magnetooptics of opal crystals modified by cobalt nanoparticles. *Lithuanian Journal of Physics* **2010,** *50* (1), 7-15; (b) Pavlov, V. V.; Usachev, P. A.; Pisarev, R. V.; Kurdyukov, D. A.; Kaplan, S. F.; Kimel, A. V.; Kirilyuk, A.; Rasing, T., Optical study of three-dimensional magnetic photonic crystals opal/Fe3O4. *Journal of Magnetism and Magnetic Materials* **2009,** *321* (7), 840-842.

13.      (a) García, P. D.; Blanco, A.; Shavel, A.; Gaponik, N.; Eychmüller, A.; Rodríguez-González, B.; Liz-Marzán, L. M.; López, C., Quantum Dot Thin Layers Templated on ZnO Inverse Opals. *Advanced Materials* **2006,** *18,* 2768-2772; (b) Caicedo, J. M.; Taboada, E.; Hrabovský, D.; López-García, M.; Herranz, G.; Roig, A.; Blanco, A.; López, C.; Fontcuberta, J., Facile route to magnetophotonic crystals by infiltration of 3D inverse opals with magnetic nanoparticles. *Journal of Magnetism and Magnetic Materials* **2010,** *322* (9-12), 1494-1496.

14.      Minguez, H.; López, C.; Meseguer, F.; Blanco, A.; Vázquez, L.; Mayoral, R.; Ocaña, M.; Fornés, V.; Mifsud, A., Photonic Crystal Properties of Packed Submicrometric $SiO_2$ Spheres. *Applied Physics Letters* **1997,** *71* (9), 1148-1150.

15.      Caicedo, J. M.; Pascu, O.; López-García, M. n.; Canalejas, V. c.; Blanco, A. l.; López, C.; Fontcuberta, J.; Roig, A.; Herranz, G., Magnetophotonic Response of Three-Dimensional Opals. *ACS Nano* **2011,** *5* (4), 2957-2963.

16.      Zvezdin, A. K.; Belotelov, V. I., Magnetooptical properties of two dimensional photonic crystals. *Eur. Phys. J* **2004,** *37,* 479-487.

17.      Galisteo-López, J.; Galli, M.; Patrini, M.; Balestreri, A.; Andreani, L.; López, C., Effective Refractive Index and Group Velocity Determination of Three-Dimensional Photonic Crystals by Means of White Light Interferometry. *Physical Review B* **2006,** *73,* 125103-9.

18.      (a) Goncalves, M. C.; ·, B. J.; Almeida, R. M., Process optimization of sol–gel derived colloidal photonic crystals. *Journal of Sol-Gel Science and Technology* **2007,** *42,* 135–143; (b) Gonçalves, M. C.; Fortes, L. M.; Almeida, R. M.; Chiasera, A.; Chiappini, A.; Ferrari, M., 3-D rare earth–doped colloidal photonic crystals. *Optical Materials* **2009,** *31,* 1315–1318; (c) Lee, E. K.; Kim, W. S.; Lee, K. W.; Lim, H.; Lee, J. I.; Lee, H. G.; Hur, N. H., Enhanced coercivity in sponge magnets with three dimensionally ordered nanopores,. *Solid State Communications* **2009,** *149,* 37-40; (d) Jia, B.; Wu, S.; Li, J.; Gub, M., Near-infrared high refractive-index three-dimensional inverse woodpile photonic crystals generated by a sol-gel process. *Journal of Applied Physics* **2007,** *102,* 096102-3; (e) Stein, A.; Li, F.; Denny, N. R., Morphological Control in Colloidal Crystal Templating of Inverse Opals, Hierarchical Structures, and Shaped Particles. *Chemistry of Materials* **2008,** *20,* 649–666; (f) Lee, J. A.; Ha, S. T.; Choi, H. K.; Shin, D.

O.; Kim, S. O.; Im, S. H.; Park, O. O., Novel Fabrication of 2D and 3D Inverted Opals and their Application. *Small* **2011**, *7* (18), 2581–2586.

19.       Moon, J. H.; Yang, S., Chemical Aspects of Three-Dimensional Photonic Crystals. *Chemical Reviews* **2010**, *110* (1), 547-574.

20.       (a) Kim, K. J.; Lee, H. J.; Park, J. Y., Cationic behavior and the related magnetic and magnetotransport properties of manganese ferrite thin films. *Journal of Magnetism and Magnetic Materials* **2009**, *321*, 3706–3711; (b) Rajic, N.; Ceh, M.; Gabrovsek, R.; Kaucic, V., Formation of NanocrystallineTransition-Metal Ferrites inside a Silica Matrix. *Journal of American Ceramics Society* **2002**, *85* (7), 1719–1724; (c) Li, J.-J.; Zhai, C.-X.; Liu, M.-L., Tailoring the magnetic properties of manganese ferrite with substitution of a small fraction dysprosium for iron. *Solid State Communications* **2005**, *134*, 759–764; (d) Cushing, B. L.; Kolesnichenko, V. L.; O'Connor, C. J., Recent Advances in the Liquid-Phase Syntheses of Inorganic Nanoparticles. *Chemical Reviews* **2004**, *104* (3893-3946); (e) Gopalana, E. V.; Joyb, P. A.; Al-Omaric, I. A.; Kumard, D. S.; Yoshidad, Y.; Anantharaman, M. R., On the structural, magnetic and electrical properties of sol–gel derived nanosized cobalt ferrite. *Journal of Alloys and Compounds* **2009**, *485*, 711–717; (f) Srivastava, M.; Chaubey, S.; Ojha, A. K., Investigation on size dependent structural and magnetic behavior of nickel ferrite nanoparticles prepared by sol–gel and hydrothermal methods. *Materials Chemistry and Physics* **2009**, *118*, 174–180.

21.       Carta, D.; Casula, M. F.; Mountjoyz, G.; Corrias, A., Formation and cation distribution in supported manganese ferrite nanoparticles: an X-ray absorption study. *Physical Chemistry Chemical Physics* **2008**, *10*, 3108–3117.

22.       Wang, Z. H.; Geng, D. Y.; Hu, W. J.; Ren, W. J.; Zhang, Z. D., Magnetic propeeties and exchange bias in $Mn_2O_3/Mn_3O_4$ nancluesters. *Journal of Applied Physics* **2009**, *105*, 07A315-3.

23.       Tang, Z. X.; Sorensen, C. M.; Klabunde, K. J.; Hadjipanayis, G. C., Size-dependent Curie temperature in nanoscale $MnFe_2O_4$particles. *Physical Review Letters* **1991**, *67* (25), 3602.

24.       Bilecka, I.; Kubli, M.; Amstad, E.; Niederberger, M., Simultaneous formation of ferrite nanocrystals and deposition of thin film via a microwave-assisted nonaqueous sol-gel process. *J. Sol-gel Sci. Technol.* **2011**, *57*, 313–322.

25.       Sorgi, K. L., Triethylamine. In *Encyclopedia of Reagents for Organic Synthesis*, 2nd ed.; Paquette, L. A.; Crich, D.; Funchs, P. L.; Molander, G., Eds. John Wiley & Sons: New york, 2010; Vol. 14, p 12094.

26.       (a) Vallee, S. J.; Conner, W. C., Microwaves and Sorption on Oxides: a Surface Temperature Investigation. *Journal of Physical Chemistry B* **2006**, *110*, 15459-15470; (b) Conner, W. C.; Tompsett, G. A., How Could and Do Microwave Influence Chemistry at Interfaces. *Journal of Physical Chemistry B* **2008**, *112*, 2110-2118.

27.       Blanco, A.; López, C.; Mayoral, R.; Míguez, H.; Meseguer, F.; Mifsud, A.; Herrero, J., CdS photoluminescence inhibition by a photonic structure. *AIP* **1998**, *73* (13), 1781-1783.

28.     Belotelov, V. I.; Akimov, I. A.; PohlM; Kotov, V. A.; KastureS; Vengurlekar, A. S.; Gopal, A. V.; Yakovlev, D. R.; Zvezdin, A. K.; BayerM, Enhanced magneto-optical effects in magnetoplasmonic crystals. *Nat Nano* **2011,** *6* (6), 370-376.

# 5

# CONCLUSIONS
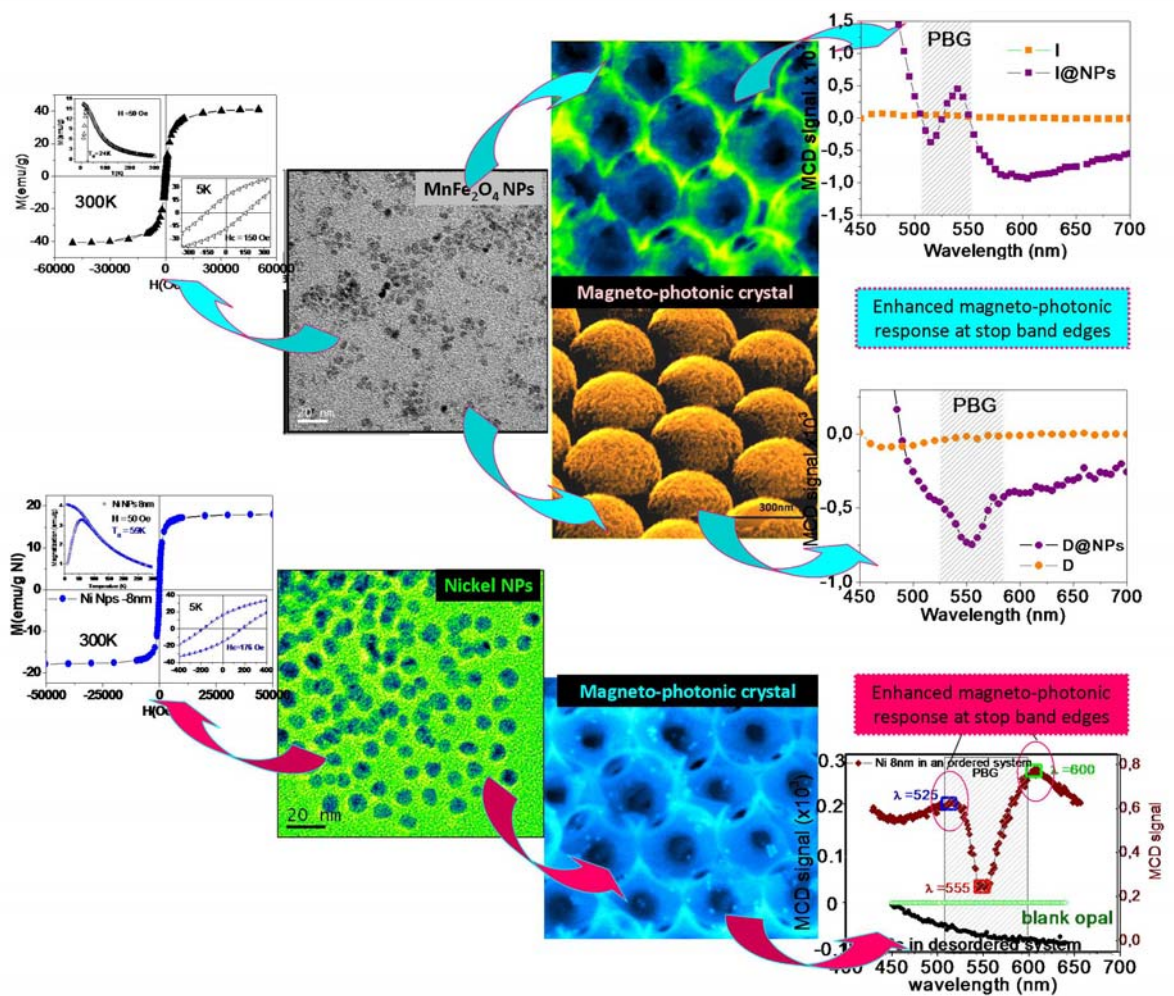
## 5.1 CONCLUSIONS

The main goal of this thesis has been to obtain an optical system responding to a magnetic field by nanocomposing photonic crystal materials (two and three dimensions) with magnetic nanoparticles. Such magneto-photonic crystals (MPCs) could enable firstly, the tunability of photonic band gap spectral position using an external magnetic field, and secondly an enhanced magneto-optical response near photonic band-edge frequencies due to light-matter interaction.

The more specific objectives have been:

1) To synthesize highly crystalline nanoparticles (nickel, iron oxide and manganese ferrite) that are superparamagnetic at room temperature, via chemical methods. The nanoparticles size should be controlled modifying various experimental parameters and their stability in liquid magnetic colloids analyzed.

2) To fabricate 2D and 3D magneto-photonic materials by bottom-up and top-down techniques and to evaluate the quality of the fabricated material by structural, morphological and functional characterizations.

3) To optimize the fabrication of magneto-photonic materials to ensure an appropriate magneto-optical response, namely enhanced magneto-optical response near photonic band-edge frequencies.

The main conclusions are:

❖   The enhancement of the magneto-optical response near the photonic band edges of three dimensional magneto-photonic crystals have been achieved by using two different approaches and this enhancement is dependent on the magnetic field applied. One, involving the functionalization of 3D photonic crystals with *ex-situ* synthesized nickel nanoparticles and the other via *in-situ* conformal deposition of 3D photonic crystals with magnetic ferrites nanoparticles.

❖   A new fabrication method based on microwave-assisted *in-situ* magnetic nanoparticles deposition has been developed for the fabrication of magneto-photonic materials with preservation of the original photonic structure and control of the magnetic content.

❖   Highly crystalline magnetic nanoparticles, superparamagnetic at room temperature and stable as colloids in liquid dispersion have been successfully prepared by chemical methods with the evaluation of the feasibility of each method.

More detailed conclusions are divided according to Thesis objectives:

1.   Synthesis and characterization of magnetic nanoparticles via three chemical synthesis methods.

2.   Fabrication and characterization of two dimensional magneto-photonic materials.

3.   Fabrication and characterization of three dimensional magneto-photonic materials.

*1. Synthesis and characterization of magnetic nanoparticles via three chemical synthesis methods.*

- Mono and polycrystalline nickel nanoparticles in the range of 8-24 nm have been synthesized by thermal decomposition of nickel acetylacetonate precursor in oleylamine in the presence of two surfactants, oleic acid and trioctylphosphine.

- The size, shape and polydispersity of Ni NPs have been controlled by varying experimental parameters such as the molar ratio between the two surfactants, the aging temperature and the heating rate. The presence of both surfactants, one strongly bonded (OAc) and the other weakly bonded (TOP) during synthesis is strongly recommended to prepare nearly spherical nanoparticles with narrow particle size distribution (~ 10%). It has been found that a slow heating rate ~ 12°/min or fluctuations in temperature during aging (on the order of 10°C) increase the polydispersity, producing also faceted nanoparticles, that should better avoided.

- The covalent bond of oleic acid to the Ni nanoparticle surface warranties the long term (up to 2 years for the smaller NPs, below 10 nm by our experience) stability of nanoparticles in non-polar solvents (with polarity index below 3).

- The magnetic properties are influenced by the nanoparticles size; the magnetization saturation varies from 25 emu/g (8 nm) to 56 emu/g (100 nm), the latter being closer to the bulk value of nickel metal (57.6 emu/g). Modeling the nanoparticles with a core (Ni metal)-shell (NiO) model as the cause of the magnetization decrease, a very thin (~1nm) self-limiting oxide (NiO) layer have been calculated for all sizes which is non-detectable by X-ray.

- Magneto-optical spectroscopy in liquid media is a suitable and very fast in-situ testing method for very dilute magnetic colloidal dispersions. A full hysteresis loop can be measured in 1 min for concentrations as low as ~1μg/ml Ni NPs. Moreover, a proper calibration of the magneto-optical signal and careful selection of the wavelength of the probe light allows us to accurately determination of the nanoparticle concentration in the dispersion. We envisage that by exploiting the strong sensitivity of magneto-optical signals to the surface magnetic properties changes in surface chemistry of the nanoparticles could also be monitored.

- By microwave dielectric heating, magnetic nanoparticles with good cristallinity, small size, good polydispersity and comparable magnetic properties to the ones obtained by the thermal decomposition method can be prepared. Our approach, the non-aqueous sol-gel chemistry route in the presence/absence of surfactants allowed us to synthesize stoichiometric ferrites ($MFe_2O_4$, M = Mn, Fe) nanoparticles with superparamagnetic behavior at room temperature in less than 30 minutes, air atmosphere and at moderated temperatures.

- When comparing nanoparticles of similar sizes (6 nm) obtained by thermal decomposition and by microwave routes we found that a relevant difference is the lower surface reactivity of the nanoparticles obtained from the microwave route due to the lower energy crystallographic faceting planes (low Miller indexes) for the microwaves

nanoparticles. Surface reactivity, in addition to particle size and surface area, will influence the interaction of the nanoparticles with its surroundings. Thus the surface differences found can be particularly relevant depending on the targeted final application, especially when long time aggregation or particle growth is undesirable.

-   The size, shape, cristallinity and polydispersity of the ferrite nanoparticles (iron oxide and $MnFe_2O_4$) prepared by microwave-heating route can be controlled by the reaction temperature (from 160 to $200^{o}C$), the irradiation time (7-20 min), the power input (200 or 300W), the precursor concentration and type of surfactant.

-   In contrast to thermal decomposition, in microwave heating it was not possible to vary one of the above mentioned parameters while keeping the others constant, making more difficult the interpretation of the results.

-   It has been found that nanoparticles prepared at $160^{o}C$ have good magnetic properties but those can be improved by performing the synthesis at higher temperature (180 or $200^{o}C$) or by longer irradiations times. Moreover the power input correlated with the heating rate plays a crucial role in nanoparticles cristallinity and polydispersity. A power below 300 W for instance 250 or 200W is recommended, independently of the temperature used.

-   Oleic acid is essential in the thermal decomposition method to control the particle size and to keep the size monodispersity. In microwave route, oleic acid by chemisorptions to the nanoparticles surface seems to inhibit the nanoparticles growth by inactivating their surface: either by decreasing the surface condensation rate, which promote the nanoparticles growth, or decreasing the local surface temperature with respect to the bulk solution by its non-polar tail, transparent to microwave irradiation. On the contrary, more spherical nanoparticles and bigger (up to 11 nm) NPs are obtained without any or in the presence of steric surfactant.

-   Microwave-route has the advantages that the surfactant (steric or electrostatic) can be added either during or after nanoparticles synthesis, allowing the NPs stabilization either in polar or non-polar media.

-   In terms of "eco-design" applied to the fabrication of nanoparticles it can be concluded that the microwave approach yields: i) an energy consumption reduced by a factor of 10; ii) a reduction in the use of environmentally burdening reagents and iii) an overall cost 40 % smaller that thermal decomposition.

-   The promising preliminary results of synthesis of superparamagnetic ferrites nanoparticles using supercritical ethanol have shown the great potential of this sustainable technology in synthesis of inorganic nanoparticles at larger scales.

-   Adapting a wet-chemical synthesis (thermal decomposition) to supercritical ethanol synthesis in a continuous mode, ferrite nanoparticles of ~ 7 nm were prepared from organometallic precursors using ethanol as solvent, and small quantity of oleic acid and oleylamine as surfactants.

*2) Fabrication and characterization of two dimensional magneto-photonic materials.*

- Patterning a polymeric film (Poly(methyl methacrylate)- in silicon substrate) by electron beam or nanoimprint lithography followed with the functionalization with the colloidal dispersion of Ni NPs in hexane has failed because hexane dissolved the polymeric film.

- A second strategy, patterning the magnetic nanocomposites (Poly(methyl methacrylate)- film and nanoparicles) was partially successful. I have been found the proper conditions first to spin a uniform nanocomposites film and second, to pattern it by both lithography methods. Unfortunately the quantity of magnetic nanoparticles in the composite was not sufficient to give neither a magnetic nor magneto-optical signals. But with further optimization of the magnetic nancomposite, this approach is worth to be further studied.

- The fabrication of 2D magnetic frames have been successfully developed by using microwave-assisted deposition over a sacrificial template, made of a monolayer of 1 micron polystyrene spheres.

- Only in a few minutes (2 or 5 min reaction time) at $160^{\circ}$C, a stoichiometric and homogeneous conformal nanometric coating of superparamagnetic nanoparticles was grown onto a 2D template. No post-treatment was required; the sacrificial template was removed simultaneously with the magnetic nanoparticles formation while the structural order at large scale was preserved. Moreover the thickness of the magnetic framework was tuned by controlling the irradiation time.

- Material functionalities (optical and magneto-optical) were not possible to be performed in our laboratory, since the magnetic load was too small and its signal was masked by the noise signal. These structures are, however, very promising and a more detailed study will be performed in the future.

- It was shown that depositing 8 nm Ni or iron oxide NPs onto corrugated gold/dielectric interfaces (cavity or dots array), an enhancement of the magneto-optical activity by up to an order of magnitude can be found for wavelengths that are correlated to the excitation of propagating or localized surface plasmons.

*3) Fabrication and characterization of three dimensional magneto-photonic materials.*

- It was demonstrated that an optimal infiltration (in terms of NPs concentration, NPs size, the speed of the step-motor lifting and infiltration uniformity within the whole structure) of inverse opals with ex-situ synthesized magnetic nanoparticles is a suitable strategy to customize the magneto-optical spectral response of magnetic materials.

- By step-motor assisted dip-coating, 3D –MPCs were fabricated showing a sizable enhancement of the magneto-optical signal at frequencies around the stop-band edges of the photonic crystal due to a structural order at least in the order of a few millimeters (the probe light spot size in our experiments). The results of the optical and magneto-optical characterization were consistent with the homogeneous magnetic infiltration of the opal structure. At the same time, a proper design of the geometrical parameters of the opal structure allows to determine the range of wavelengths for which modification of the spectral response is desired.

- However, a drawback of this approach was the limitation of the loaded magnetic material up to 9% for 8 nm Ni NPs. By using bigger nanoparticles (15 nm), smaller loading was attained due to the blocking the connection windows within the photonic structures.

- This limitation was overcome by developing an alternative *in-situ* deposition method namely, microwave-assisted deposition approach for 3D photonic structures.

- With the proper optimized experimental parameters, microwave-assisted *in–situ* deposition of ferrite nanoparticles not only preserved the original photonic structure but enabled an enhancement of the magneto-optical activity near the edges of the photonic band gap and a magneto–optic response tunable by magnetic fields.

- Similarly with 2D, the magnetic material coverage was conformal, a layer made of superparamagnetic crystalline nanoparticles with small sizes (~ 5–6 nm).

- The degree of coverage and uniformity of magnetic layer could be controlled by precursors' concentration (0.15 and 0.3M have been used) and irradiation time (7–20 min), allowing us a depositing up to 30% magnetic filling fractions.

- In addition, if the pristine opal (direct/inverse) is functionalized with triethylamine, by vertical immersing followed by microwave–assisted deposition, the magnetic coverage is increased ~ three times more, compared to the non treated opal. Trieltylamine promotes the nanoparticles formation of the opal surface due to its catalytic property for the condensation reaction (NPs growth being based on the condensation reaction).

We have demonstrated that microwave assisted sol–gel route is an extremely fast and versatile approach to achieve the fabrication of good quality magneto-photonic materials showing enhanced functionalities. The strategy developed in this Thesis might contribute to the rapidly expanding field of advanced techniques for the fabrication of three-dimensional complex systems needed in different fields such as in photonics, phononics, metamaterials or data storage. The approach could also be relevant for some applications in materials for energy, as for instance in sensors, or in catalysis where a full coverage with functional materials on intricate topologies is crucial to boost the device performance. Moreover the ferrite nanoparticles synthesized by microwave approach, and directly stabilized in aqueous media could be used also for bio-application. In addition, the knowledge and understanding of the influence of some experimental parameters in nanoparticles formation mechanism can open the way for more complex structure preparation.

## 5.2 CONCLUSIONES

El objetivo principal de esta tesis ha sido obtener un sistema óptico que responda a estímulos externos, en concreto, a campos magnéticos, basado en cristales fotónicos (de dos y tres dimensiones) nanocompuestos con nanopartículas magnéticas. Tales cristales magnetofotónicos podrían permitir en primer lugar, los cambios en la posición espectral del bandgap utilizando campos magnéticos externos, y en segundo lugar, permitir respuestas magneto-ópticas aumentadas a determinadas longitudes de onda debido a la interacción luz-materia.

Los objetivos más específicos han sido:

1) sintetizar a través de métodos químicos nanopartículas magnéticas de alta cristalinidad (níquel, óxido de hierro y ferrita de manganeso) que son superparamagnéticas a temperatura ambiente. Se ha buscado controlar el tamaño de las nanopartículas a través de diversos parámetros experimentales y la estabilidad de las soluciones coloidales magnéticas.

2) la fabricación de materiales magneto-fotónicos 2D y 3D mediante técnicas "bottom-up y "top-down" – con evaluación de la calidad de los materiales fabricados a través de la caracterización estructural, morfológica y funcional.

3) optimizar la fabricación de los cristales magneto-fotónicos para garantizar una respuesta magneto-óptica aumentada a longitudes de onda cerca del bandgap óptico.

Las principales conclusiones son las siguientes:

- ❖ Se ha conseguido el aumento de la respuesta magneto-óptica cerca de los bordes del bandgap fotónicos mediante diferentes aproximaciones y este aumento es dependiente del campo magnético aplicado. Se ha logrado tales objetivos mediante la funcionalización de cristales fotónicos 3D con nanopartículas de níquel sintetizadas *ex-situ*. Por otro lado, también se ha llevado a cabo con éxito el depósito *in-situ* con nanopartículas de ferritas magnéticas.

- ❖ Se ha desarrollado un nuevo método de fabricación de cristales magneto-fotónicos basado en el depósito *in situ* de nanopartículas magnéticas asistido por radiaciones de microondas, que preserva la estructura fotónica original y permite el control del contenido magnético depositado.

- ❖ Se han preparado con éxito por diferentes métodos químicos, nanopartículas magnéticas de alta cristalinidad, superparamagnéticas a temperatura ambiente y estables como dispersiones líquidas coloidales, evaluando la viabilidad de cada método.

Las conclusiones más detalladas se dividen de acuerdo con los objetivos de la Tesis:

1. Síntesis y caracterización de nanopartículas magnéticas a través de tres métodos de síntesis química.

2. Fabricación y caracterización de los materiales magnetofotónicos bidimensionales

3. Fabricación y caracterización de los materiales magnetofotónicos tridimensionales

*1. Síntesis y caracterización de nanopartículas magnéticas a través de tres métodos de síntesis química.*

– Se han sintetizado nanopartículas de níquel mono- y poli-cristalinas en el rango de tamaño de 8–24 nm por descomposición térmica del precursor de acetilacetonato de níquel en oleyalmina en presencia de dos tensioactivos, ácido oleico y tioctylphosphina.

– El tamaño, forma y polidispersidad de nanoparticulas de Ni se han controlado mediante la variación de los parámetros experimentales tales como la relación molar entre los dos tensioactivos, la temperatura de reacción y la velocidad de calentamiento. Para preparar nanopartículas casi esféricas con distribución estrecha de tamaños de partícula (~ 10%) se recomienda el uso de dos tensioactivos durante la síntesis, uno que establece un enlace fuerte (OAc) y el otro un enlace más débil (TOP) con la superficie de la nanoparticula. Se ha encontrado que una velocidad de calentamiento lenta ~ 12°/min o fluctuaciones en la temperatura durante de reacción química (del orden de 10°C) aumentan la polidispersidad, produciendo nanopartículas también facetadas, situación que es deseable evitar.

– El enlace covalente del ácido oleico con la superficie de nanopartículas de Ni garantiza la estabilidad a largo plazo (hasta 2 años para las nanoparticulas más pequeñas, por debajo de 10 nm de nuestra experiencia) de las nanopartículas en disolventes no polares (con un índice de polaridad inferior a 3).

– El tamaño de las nanopartículas tiene influencia en las propiedades magnéticas; la magnetización de saturación varía de 25 emu / g (8 nm) a 56 emu / g (100 nm), siendo este último el más cercano al valor del metal de níquel masivo (57.6 emu / g ). Modelando las nanopartículas a través del modelo "core (Ni metal)-shell (NiO)", se ha calculado para todos los tamaños, una capa de auto-limitación de óxido (NiO) muy delgada (~ 1 nm), que no es detectable por rayos-X.

– La espectroscopía magneto-óptica en medios líquidos es un método adecuado y muy rápido para analizar *in situ* dispersiones coloidales magnéticas muy diluidas. Una curva de histéresis completa se puede medir en 1 min (para concentraciones tan bajas como ~ 1μg/ml Ni NPs.). Además, una calibración adecuada de la señal magneto-óptica y una selección cuidadosa de la longitud de onda de la luz permite la determinación con precisión de la concentración de nanopartículas en la dispersión. Se prevé que mediante la explotación de la sensibilidad de las señales magneto-ópticas a los cambios magnéticos de superfície, se podrían estudiar las propiedades de la química de superfície de las nanopartículas.

– Mediante química asistida por radiación microondas, se pueden preparar nanopartículas magnéticas con buena cristalinidad, tamaño pequeño, polidispersidad buena y propiedades magnéticas comparables a las obtenidas por el método de descomposición térmica. Nuestra aproximación, vía química de sol-gel nonacuosa en la presencia / ausencia de tensioactivos, nos permitió sintetizar en menos de 30 minutos nanopartículas de ferritas estequiométricas ($MFe_2O_4$, M = Mn, Fe) con comportamiento superparamagnético a temperatura ambiente, en atmósfera de aire y a temperaturas moderadas.

– Al comparar las nanopartículas de tamaños similares (6 nm) obtenidos por descomposición térmica y por radiación de microondas, encontramos que una diferencia

relevante es la reactividad inferior de la superficie de las nanopartículas obtenidas por microondas, debido a los planos cristalográficas de energía más baja (índices de Miller bajos) que facetan las nanopartículas de microondas. La reactividad de la superficie, además de tamaño de partícula y área superficial, influirá en la interacción de las nanopartículas con su entorno. Así, las diferencias de superficie encontradas pueden ser particularmente relevantes en función de la aplicación específica final, especialmente cuando la agregación de partículas o el crecimiento de partículas son indeseables.

– El tamaño, forma, cristalinidad y polidispersidad de las nanopartículas de ferrita (óxido de hierro y $MnFe_2O_4$) preparadas vía calentamiento por microondas, pueden ser controlados por la temperatura de reacción (de 160 a 200° C), el tiempo de irradiación (7-20 min), la potencia de entrada (200 o 300 W), la concentración de precursor y el tipo de tensioactivo utilizados.

– En contraste con la descomposición térmica, en el calentamiento por microondas no fue posible variar solamente uno de los parámetros antes mencionados sin dejar los restantes inalterados, haciendo así más difícil la interpretación de los resultados.

– Se ha encontrado que las nanopartículas preparadas a 160°C tienen buenas propiedades magnéticas, pero éstas se puede mejorar mediante la realización de la síntesis a temperatura más alta (180 o 200° C) o por tiempos de irradiación más largos. Además, la potencia de entrada correlacionada con la velocidad de calentamiento juega un papel crucial en la cristalinidad de las nanopartículas y la polidispersidad. Se recomienda una potencia por debajo de 300 W, por ejemplo 250 o 200 W, independientemente de la temperatura utilizada.

– El ácido oleico es esencial en el método de descomposición térmica para controlar el tamaño de las partículas y para mantener la monodispersidad del tamaño. En la ruta de microondas, la quimisorción de ácido oleico en la superficie de las nanopartículas parece inhibir el crecimiento de nanopartículas mediante la inactivación de su superficie: bien sea disminuyendo la velocidad de la reacción de condensación en la superficie, que promueven el crecimiento nanopartículas, o bien –en su área no polar, que es transparente a la irradiación de microondas– disminuyendo la temperatura local de la superficie con respecto a la solución. Por el contrario, las nanopartículas más esféricas y más grandes (hasta 11 nm) se obtienen sin tensioactivo o en presencia de un agente tensioactivo estérico.

– La ruta de microondas tiene la ventaja de que el agente tensioactivo (estérico o electrostático) se puede añadir durante o después de la síntesis de nanopartículas, permitiendo la estabilización de NPs ya sea en medios polares o no polares.

– En términos de "diseño ecológico" aplicado a la fabricación de nanopartículas se puede concluir que la aproximación de microondas ofrece: i) un consumo de energía reducido por un factor de 10, ii) una reducción en el uso de reactivos que perjudican el medio ambiente y iii ) un coste global del 40% menor que la descomposición térmica.

– Los prometedores resultados preliminares de la síntesis de nanopartículas de ferritas superparamagnéticas utilizando etanol en condiciones supercríticas, han mostrado el gran

potencial de esta tecnología sostenible en la síntesis de nanopartículas inorgánicas a mayor escala.

– Adaptando una síntesis química en fase líquida (descomposición térmica) a la síntesis en condiciones supercríticas en un modo continuo, nanopartículas de ferrita de ~ 7 nm se prepararon a partir de precursores organometálicos utilizando etanol como disolvente, y una pequeña cantidad de ácido oleico y oleilamina como tensioactivos.

## 2) *Fabricación y caracterización de los materiales magnetofotónicos bidimensionales*

– No se ha logrado la funcionalización, mediante dispersiones coloidales NPs de Ni en hexano, de patrones en capas de polímero (poli (metacrilato de metilo), debido a que el hexano disuelve la película polimérica.

– En una segunda estrategia, los patrones de los nanocompuestos magnéticos (capa de poli (metacrilato de metilo) con nanopartículas) tuvo un éxito parcial. Se han encontrado las condiciones adecuadas para espinear una película uniforme de nanocompuestos así como hacer patrones por ambos métodos de litografía. Por desgracia, la cantidad de nanopartículas magnéticas en el material compuesto no era suficiente para dar señales magnéticas o magneto-ópticas detectables. Sin embargo, con una mayor optimización de los nanocompuestos magnéticos, vale la pena estudiar más a fondo esta aproximación.

– Se ha desarrollado con éxito la fabricación de cristales magnéticos bidimensionales mediante el uso de microondas.

– En tan sólo unos pocos minutos (2 o 5 minutos de tiempo de reacción) a 160°C, se han podido crecer capas nanométricas estequiométricas, conformes y homogéneas de nanopartículas superparamagnéticas sobre una plantilla bidimensional. Sin necesitar un tratamiento posteior, la plantilla de sacrificio se pudo eliminar simultáneamente con la formación de nanopartículas magnéticas, mientras que el orden a gran escala se pudo conservar. Además, se pudo controlar el espesor de la capa magnética mediante el control del tiempo de irradiación.

– Debido a la muy débil carga magnética no se pudieron caracterizar las funcionalidades del material (ópticas y magneto-ópticas). Estas estructuras son, sin embargo, muy prometedoras y merecen un estudio más detallado que se realizará en el futuro.

– Se ha demostrado que depositar nanoparticulas de Ni o de óxido de hierro de 8 nm sobre interfícies corrugadas de oro / dieléctrico (matriz de cavidades o nanodiscos), permite aumentar la actividad magneto-óptica hasta un orden de magnitud para las longitudes de onda que estén en correspondencia con la excitación de plasmones de superfície.

## 3) *Fabricación y caracterización de los materiales magnetofotónicos tridimensionales*

– Se demostró que una infiltración óptima (en términos de concentración y tamaño de nanoparticulas, la velocidad de la elevación del motor y la uniformidad de la infiltración dentro de la estructura) de ópalos inversos con nanopartículas magnéticas sintetizadas *ex-*

*situ* es una estrategia adecuada para sintonizar la respuesta espectral magneto-óptica de los materiales magnéticos.

– Mediante dip coating asistido por un motor paso a paso, fueron fabricados cristales magnetofotónicos mostrando un aumento considerable de la señal magneto-óptica a longitudes de onda cerca del bandgap fotónico. Ello implica un orden estructural en escalas de al menos unos pocos milímetros (que es el tamaño del spot de la luz de análisis en nuestros experimentos). Los resultados de la caracterización óptica y magneto-óptica fueron consistentes con una infiltración magnética homogénea en la estructura de los ópalos. Al mismo tiempo, un diseño adecuado de los parámetros geométricos de la estructura de ópalo permite determinar el intervalo de longitudes de onda para el cual se desea la modificación de la respuesta espectral.

– Sin embargo, un inconveniente de este método fue la limitación del material magnético infiltrado, hasta un 9% para nanopartículas de Ni de 8 nm. El uso de nanopartículas de un tamaño mayor (15 nm), implica una menor infiltración debido al bloqueo de las ventanas de conexión dentro de las estructuras fotónicas.

– Esta limitación fue superada gracias al desarrollo de un método alternativo de depósito *in situ*, mediante el depósito de nanopartículas asistido por microondas.

– Con los parámetros experimentales optimizados, el depósito *in situ* asistido por microondas de nanopartículas de ferrita – no sólo conserva la estructura original, sino que permite un aumento de la actividad magneto-óptica cerca de los bordes de la banda bandgap fotónica y una respuesta magneto-óptico sintonizable por los campos magnéticos.

– De forma similar a los 2D, la cobertura de material magnético fue conformal, compuesta de una capa de nanopartículas superparamagnéticas cristalinas con tamaños pequeños (~ 5-6 nm).

– El grado de cobertura y uniformidad de la capa magnética se puede controlar la concentración de los precursores (0.15 y 0.3 M se han utilizado) y el tiempo de irradiación (7-20 min), cosa que permitió incrementar el grado de infiltración hasta un 30%.

– En el depósito asistido por microondas, la funcionalización de los ópalos (directos o inversos) con trietilamina promueve la formación de nanopartículas en la superficie debido a su propiedad catalítica para la reacción de condensación (nanopartículas crecen por una reacción de condensación).

Hemos demostrado que la ruta de sol-gel asistida por microondas es un método extremadamente rápido y versátil para lograr la fabricación de magnetofotónicos de alta calidad. La estrategia desarrollada en esta tesis representa una contribución relevante al campo de las técnicas avanzadas para la fabricación de sistemas tridimensionales complejos que son necesarios en diferentes campos como la fotónica, fonónica, los metamateriales o el almacenamiento de datos. Esta metodología también podría ser relevante para algunas aplicaciones en materiales para energía, sensores, o en catálisis, donde para un rendimiento óptimo de los dispositivos se requiere un recubrimiento completo con materiales funcionales en topologías complejas. Además, las nanopartículas de ferrita sintetizadas por esta vía y estabilizadas directamente en medios acuosos podrían utilizarse también para bio-

aplicaciones. Además, el conocimiento y la comprensión de la influencia de algunos parámetros experimentales en los mecanismos de formación de las nanopartículas pueden abrir el camino para la preparación de estructuras más complejas.

# 5.3 CONCLUZII

Scopul principal al acestei teze a fost obținerea un sistem optic care răspunde la un stimula esterior, cum ar fi un câmp magnetic.folosind un material cristal fotonic (bi și tridimensiuni) funcționalizat cu nanoparticule magnetice. Un astfel de cristal magneto-fotonic (MPC) ar putea permite pe de o parte, controlarea poziției spectrale a benzii fotonice intersize cu ajutorul unui câmp magnetic extern și pe de altă parte un rapuns magneto-optic crescut corespunzator frecventelor apropiate de banda interzisă, datorită interacțiunii lumina-materie

        Principalele obiective specifice au fost:

1) Sinteza prin metode chimice de nanoparticule de inaltă cristalinitate (nichel, oxid de fier și ferita de mangan), care sunt superparamagnetice la temperatura camerei. Dimensiunea nanoparticule să fie controlata prin modificarea diversilor parametrii experimentali și analiza stabilitatii nanoparticlulor in coloizi lichizi magnetici.

2) Fabricarea materialelor magneto-fotonice di si trimensionale prin tehnicile¨bottom-up¨si ¨top-down¨ cu evaluarea calitatii materialului fabricat prin caracterizări structurale, morfologice și funcționale.

4) Optimizarea corespunzătoare a fabricarii materialului magneto-fotonic pentru a obtine un răspuns magneto-optic creascut

Principalele concluzii sunt:

❖   S-a obtinut un raspuns magneto-optic crescut pentru frecventele de langa banda interzisa in cazul unui material cristal magneto-fotonic tridimensional fabricat prin doua cai distincte si acest raspuns se poate controla prin intensitatea campului magnetic. O cale a implicat functionalizarea cristalului fotonic 3D cu nanoparticule de nichel sintetizate *ex-situ* și cealalta depunerea conformala cu nanoparticule magnetice de ferrita sintetizate *in-situ* cu ajutorul microundelor.

❖   A fost dezvoltate o noua metoda de fabricatie bazate pe utilizaera microundelor ca si sursa de incalzire pentru a realiza reactia chimica cu fomarea nanoparticulelor *in-situ* in interiorul structurii fotonice. Mai mult, structura ordonata a materialului original s-a pastrat si s-a putut controla grosimea stratului de nanoparticule depuse.

❖   Nanoparticule magnetice de mare cristalinitate, superparamagnetice la temperatura camerei și stabile ca coloizi lichid au fost sinteizate cu succes prin trei metode chimice, cu evaluarea de fezabilitatii fiecărei metode.

Concluzii mai detaliate sunt împărțite în funcție de obiectivele tezei:

1. Sinteza și caracterizarea de nanoparticule magnetice prin intermediul celor trei metode chimice de sinteza.

2. Fabricarea și caracterizarea materialelor magneto-fotonice bidimensionale

3. Fabricarea și caracterizarea materialelor magneto-fotonice tridimensionale

## 1. Sinteza şi caracterizarea nanoparticulelor magnetice

– Nanoparticule de nichel mono şi policristaline, cu dimensiuni intre 8–24 nm au fost sintetizate prin descompunerea termică a precursorului acetilacetonat de nichel în oleyalminea, în prezenţa a doi surfactanti, acid oleic şi troctylphosphina.

– Dimensiunea, forma şi polidispersitatea annoparticulelor au fost controlate prin diferiti parametrii experimentale, cum ar fi raportul molar între cei doi surfactanti, de reactie şi viteza de încălzire. Prezenţa, în cursul sintezei a două tensioactivi, un puternic legat (acidul oleic) şi celalalt sab legat (TOP) este recomandat in scopul obtinerii ne nanoparticule aproape sferice, cu polidispersityate mica (~ 10%). Experimental s-a constatt ca a incalzire mai lenta~ $12^o$/min sau fluctuaţii de temperatură în timpul perioadei de reactie chimica (in jurul a $10^oC$) creşte polidispersitatea sistemului, si de asemenea produce nanoparticule faţetate side aceea este mai bine daca se pot evita.

– Legăturile covalente facute de acidul oleic cu suprafata nanoparticulei de Ni asigura stabilitatea lor in solventi organici (cu polaritate pana la 3) pe termen lung (pana la foi ani).
– proprietatile magentice sunt influentate de dimensiune; magnetizatia de saturatie variaza de la 25 la 56 emu/g, ultima fiind aproape de valoarea de bulk a Ni (57.6 emu/g). Prin modelarea nanoparticulelor cu un miez metalic si o scoarta nonmagnetica (NiO), s-a calculat un strat autolimitant de oxid de ~ 1 nm nedetectabil pentru rzele X.

– Spectroscopia magneto-optica in mediu lichid este o metoda de testare potrivita si foarte rapida pentru sistemele coloidale foarte diluate. A bukla de histereza se poate masura intr-un minut, detectandu-se concnetratii pana la 1µg/ml. Mai mult, printr-o calibrare corespunzatoare si selectionarea cu grija a unei longitudi de unda a laserului folosit, se poate determina cu acuratete conentratian unei dispersii colodale. Subliniem ca explotand senzitivitatea ridicata a semnalului magneto-optic la schimbarile magnetice de la suprafata, se poater monitoriza chimia suprafetei nanoparticulelor.

– folosind microundele ca si sursa de incalzire, se pot sintetiza particule magnetice de buna calitate, dimensiuni reduse si proprietati magentice comparabile cu cele obtinute prin decompozitia termica. Abordarea noastra, chimia de sol-gel neapos in presenta/absenta surfactantilor, ne-a permis sinteza stoechiometrica a feritelor ($Mfe_2O_4$, M= Mn, Fe), superparamagentice la temperatura camerei, in mai putin de 30 minute , in mediu ambiental si la o temperatura nu foarte inalta.

– comparand nanoparticule de 6 nm, obtinute prin cele doua metode (descompunera termica si cu ajutorul microundelor) am descoperit ca suprafata nanoparticulelor este foarte diferita in ce priveste reactivitatea, si mai precis cele fabricate cu ajutorul microundelor au o reactivitatea mica a suprafetei. Reactivitaea suprafetei, alaturi de dimensiune si aria influenteaza interactiunea nanoparticulelor cu mediul din jur. Diferenta in reactivitaea poate fi importanta pentru unele aplicatii, mai ales daca se prefera evitarea fomarii aglomeratelor pe termen lung.

– dimensiunea, forma, cristalinitatea si polidispersitatea se pot controla cu ajutorul parametrilor : temperatura de reactie ( de la 160 la $200^oC$), timpul iradierarii ( 7-20

minute), puterea folosita (200 sau 300W), concentratia precursorilor sau tipul surfactantatlui folosit.

- spre deosebire de descompunerea termica in sinteza cu microunde, nu a fost posibila modificarea unui singur parametru experimetal in timp ce restul au ramas constanti,facadn interpreatrea rezultatelor mult mai dificila.

- S-a gasit ca nanoparticulele obtinute la temperature de $160^{\circ}C$ au proprietati magentice bune, dar care pot fi imbunatatite prin sinteza la o temperatura mai inalta sau un timp mai lung. Mai mult, puterea microundelor, corelata cu viteza de incalzire joaca un rol crucial in cristalinitatea nanoparticulor precum si in polidispersitatea lor. O putere mai mica de 300W, 200 - 250W este recomndata.

- Acidul oleic este esential pentru controlul dimensiunii si monodispersitatii in descompunerea termica. In metoda microundelor, se pare ca acidul oleic prin chemisorbtia la suprafata nanoparticuelor impiedica cresterea acestora prin dezactivarea suprafetei: sau prin scaderea rata reactiei de condesare ce promoveaza cresterea cristalelor, sau scade temperatura suprafetei in comparatie cu temperature mediului ambient. Opus, particule mai sferice si cu dimensiuni mai mari (pana la 11 nm) s-au obtinut in lipsa unui surfactant steric sau in presenta unuia electrostatic.

- Metoda microundelor are avantajul ca surfactantul se poate adauga la inceput reactiei sau dupa ce nanoparticuelel s-au format, permitand in felul acesta stabilizarea lor direct in mediu polar sau apolar.

- in termeni de ¨eco-design¨ aplicat la fabricarea nanoparticulelor se pot conclude urmatoarele desprea metoda cu microunde: i) un consum energetic reduc de 10 ori; ii) reducera reactantilor daunatori mediului; un cost cu 40% reduc comparativ cu descompunera termica.

- Resultatele prelimire promitatoare in ce priveste sinteza nanoparticulelor magnetic folosind conditiile supercritice au aratat marele potential al tehnologiei supercritice in fabricarea de nanoparticule inorganice la scalal mai mare.

- adptand sinteza clasica pentru conditiile supercritice in mod continuu, s-au obtinut nnaoparticule de ferrita de ~ 7 nm plecand de la precursor organometalic, uitlizand etanolul ca si solvent si o cantitate redusa de surfactanti.

*2. Fabricarea şi caracterizarea materialelor magneto-fotonice bidimensionale*

-Structurarea unui film polimeric (polimetil metracrilat) cu ajutorul fasciculi de electroni urmat de functionalizarea structurii cu dispersia de nanoparticule in hexan, a esuat deoarece hexanul dizolva polimerul.

- a doua strategia folosita, structurarea unui nanocompozit a avut un succes partial. Am gasit conditiile potrivite , 1) pentru a obtine un film uniform de nanocompozit si 2) pentru a –l srucutra cu metodele litografice, dar din pacate cantitatea de material magnetic inglobata in nanocompozit nu a fost suficienta ca sa dea un semnal magneto-optic. Dar cu optimizari viitoare aceasta abordarea merita sa fie studiata.

– cadru magnetic bidimensional a fost obtinut cu succes prin dezvoltarea unei noi metode de depozitare in situ a unui material magnetic peste un sablon, format dintr-un strat de sfere de polistire de 1μm diametry.

– in numai cateva minute ( 2-5 minute) la o temperatura de 160°C s-a obtinut o acoperire confomrala si uniforma cu un strat de nanoparticule superparamagnetice peste sablonneffind necesar un tratament posterior, deoarece sablonul se dizolva in timpul procesului de acoperire dar cu mentinrea strucutrii fotonice. Grasimea stratului depus s-a putut controla cu ajutorul timpului de iradiere folosit.

– functionalitatea materialui (optica si magneto-optica) nu a putut fii masurata din cauza insuficientei cantitati magentice, semnalul fiind mascat de semnalului zgomotlui. Dar oricum aceste strcuturi sunt interesante si vor fi studiate indetalait in viitor.

– S-a aratat ca prin depozitarea particulelor de 8 nm de nichel si oxid de fier peste suprafete ondulate aur/dielectric ( matrice de cavitati sau dot) se poate obtine activitate magneto-optica crescuta cu un odrdin de magnitudine pentru lungimile de unda corelate cu excitarea plasmonilor de suprafata.

### 3   Fabricarea si caracterizarea materialelor magneto-fotonice tridimensionale

–S-a demonstrat ca o infiltrare optima (in termeni de concentratie de nanoparticule, dimensiunea lor, viteza de ridicare a probei din lichidul coloidal, uniformitatea infiltrarii in toata structura fotonica) a opalului invers cu particule magnetice, sintetizate *ex-situ* este o abordarea potrivita pentru a personaliza raspunsul spectral magneto-optic al materialullui magnetic.

– prin metoda ¨dip-coating¨cu ajutorul uni motor in pasi, am fabricat cristale magneto-fotonice tridimensionale prezentand un semnal magneto-optic crescut pentru frecvente aproape de banda interzia, prin presenta unei structuri odonater pe u suprafata de cativa mm (diametrul fasciculului de laser folost in experimenteel noastere). Rezultatele caracterizarilor optice simagneto-optice au fost consistente cu o infiltrare unfirma a opalului cu particulele magnetice. In acelasi timp, un design geometric corespunzator a opalului permite determinrea regiunii de lungimi de unda penteru care se doreste modificarea rapsunsului.

– Totusi aceasta metoda este limitata la infiltrarea unei cantitati de material magnetic prea mare ( posibil pana la 9% pentru nanoparticule de 8 nm). Folosind dimensiuni mai mari de nanoparticule, o infiltrarea inferioara s-a obtinut, din cauza blocarii ferestrelor ce conecteaza spatiile goale din opal.

– Aceste limitari au fost depasite prin dezvoltarea metodei de depzitare *in-situ* cu ajutorul microundelor.

– cu optimizarea corespunzatoare a parametrilor experimentali, depozitarea de nanoparticule superparamagnetice de ferrita nu numai ca pastreaza structura opalului original dar si creste functionalitatea raspunslui magneto-optic pentru frecventele in apropierea benzii interzise si permite controlarea raspunsului cu ajutorul campului magnetic.

- similar cu materialul bidimensional, acoperirea a fost conformala, uniforma formand un strate de nanoparticule de dimensiuni reduse ( ~ 5-6 nm).

- gradul de acoperire s-a putut controla cu ajutorul concentratiei de precursori ( utilizandu-se 0.15 sau 0.3 M) si timpului de iradiere (7-20 nm) permitandu-ne depositarea unei cantitati magnetice de pana la 30%.

- Daca opalul original a fost functionalizat cu trietilamina, prin simpla imersare a opalului in compusul organic lichid, s-a crescut acoperirea magnetica de 3 ori. Trietilamine fiind un catalizator pentru reactie de condensarea, promoveaza cresterea nanoparticulele pe suprafata opalului (condensarea guvarnand procesul de crestere).


Am demonstrat ca metoda folosing microundele este o abordare extrem de rapida si multilaterala pentru a fabrica cristale magneto-fotonice de foarte buna calitate cu o functionalitate crescuta. Strategia dezvoltata in aceasta Teza poate contribuii la rapida dezvoltare a tehnicilor avansate folosite pentru fabricarea sistemelor complexe tridimensionale, necesare in domenii cum ar fi, fotonica, fononica, metamateriale sau stocarea de date. Aceasta metoda poate fi folosita si pentru alte aplicatii cum ar fi materiale pentru enrgie, senzori, cataliza unde o acoperire completa a unor arhitecturi complicate cu materiale functionale este cruciala pentru a creste performanta materialului. Mai mult, nanoparticulele de ferrita, direct stabilizate in mediu polar (apa) pot fi ulizate in aplicatii bio. Cunostintele si intelegrea influentei unor parametrii experimentali implicati in mecanismul de formare a annoparticulelor poate deschide noi cai pentru prepararea unor strucutri mmult mai complexe.

# 6
# ANNEXES

# *6.1* LIST OF PUBLICATIONS DERIVED FROM THESIS

1. **Pascu, O.**; Caicedo, J.M.; Fontcuberta, J.; Herranz, G.; Roig, A. Magneto-optical characterization of colloidal dispersions. Application to nickel nanoparticles. *Langmuir* **2010**, *26(15)*, 12548-12552.

2. Chen, D-X. **Pascu, O.**; Roig, A.; Sanchez, A. Size analysis and magnetic structure of nickel nanoparticles. *Journal of Magnetism and Magnetic Materials* **2010**, *322(24)*, 3834-3840.

3. Caicedo, J.M.; **Pascu, O.**; Fontcuberta, J.; Herranz, G.; Roig, A.; Canalejas, V.; López, M.;López, C.; Blanco, A. Magnetophotonic response of three dimensional opals. *ACS Nano* **2011**, *5(4)*, 2957-2963.

4. **Pascu, O.**; Caicedo, J.M.; Fontcuberta, J.; Herranz, G.; Roig, A.; Canalejas, V.; López, M.;López, C.; Blanco, A. Ultrathin conformal coating for complex photonic structures. *Nanoscale* **2011**, *3*, 4811-4816.

5. **Pascu, O.**; Gich, M.; Herranz, G.; Roig, A. 2D magnetic complex geometries by microwave assisted sol-gel chemistry. *European Journal of Inorganic Chemistry* **2012**, *DOI:10.1002/ejic.201101244.*

6. **Oana Pascu**, Elisa Carenza, Martí Gich, Sònia Estradé, Francesca Peiró, Gervasi Herranz and Anna Roig A. Surface reactivity of iron oxide nanoparticles by microwave synthesis; Comparison with thermal decomposition route. *Journal of Physical Chemistry C* **2012** (Submitted).

7. M. Rubio-Roy, O. Vlasin, **O. Pascu**, J.M. Caicedo, M. Schmidt, A. R. Goñi, N. G. Tognalli, A.Fainstein, A. Roig, G. Herranz. Magneto-optical enhancement by plasmon excitations in nanoparticle/metal structures, *Langmuir* **2012** (Submitted)

# Magneto-Optical Characterization of Colloidal Dispersions. Application to Nickel Nanoparticles

Oana Pascu, José Manuel Caicedo, Josep Fontcuberta, Gervasi Herranz,* and Anna Roig*

*Institut de Ciència de Materials de Barcelona (ICMAB-CSIC), Campus de la UAB, 08193 Bellaterra, Catalonia, Spain*

*Received March 24, 2010. Revised Manuscript Received June 16, 2010*

We report here on a fast magneto-optical characterization method for colloidal liquid dispersions of magnetic nanoparticles. We have applied our methodology to Ni nanoparticles with size equal or below 15 nm synthesized by a ligand stabilized solution-phase synthesis. We have measured the magnetic circular dichroism (MCD) of colloidal dispersions and found that we can probe the intrinsic magnetic properties within a wide concentration range, from $10^{-5}$ up to $10^{-2}$ M, with sensitivity to concentrations below 1 $\mu$g/mL of magnetic Ni particles. We found that the measured MCD signal scales up with the concentration thus providing a means of determining the concentration values of highly diluted dispersions. The methodology presented here exhibits large flexibility and versatility and might be suitable to study either fundamental problems related to properties of nanosize particles including surface related effects which are highly relevant for magnetic colloids in biomedical applications or to be applied to in situ testing and integration in production lines.

## Introduction

Nanoparticle colloidal dispersions have important applications in various technological areas including information technology, biotechnology and energy/environmental related technologies. For the specific case of magnetic colloids two different applications can be highlighted, namely, the biomedical applications (contrast agents MRI, magnetic hyperthermia therapies, and guided drug delivery, among others)[1] and the fabrication of novel magneto-photonic colloidal crystals.[2-4] For both these applications, high quality materials are needed either to have a better understanding of the size-dependent properties of the magnetic nanoparticles or to allow the control of the collective behavior of the nanoparticle assembly. Consequently, synthetic methods producing nanoparticles uniform in composition, size, shape, internal structure, and surface chemistry are needed to reduce the complexity of the system. Over the last 10 years, enormous advances have been made toward improving nanoparticle's fabrication procedures. High quality nanoparticles, in terms of the requirements mentioned above, can be synthesized by high temperature thermal decomposition of organometallic compounds resulting in colloidal dispersions of the nanoparticles in organic media.[5-8] A drawback of this method is the low amount of material produced in each batch, typically on the order of 100 mg. On the other hand, nanoparticles are commonly dispersed in liquids in a wide range of applications, and appropriate tools to characterize them in such environments are rather scarce. Moreover, because of the growing interest of magnetic colloids used for biomedical applications, there is a need of techniques to measure diluted concentrations of magnetic nanoparticles and to correlate the magnetic response of these liquids with particle aggregation or surface particle functionalization. The work presented here is a contribution toward these purposes. Thus, the possibility of using a fast magnetic characterization technique able to probe small quantities of material dispersed in liquid carriers is of enormous interest. Beyond these applications, surface modifications have found widespread applications in medicine. Therefore the development of a suitable technique to sensitively monitor changes in the electronic configuration and eventually the magnetic response of nanomaterials is crucial.

Facing these challenges, we report here on a convenient methodology based on a magneto-optical setup that allows a quick characterization of magnetic particles stabilized in liquid media. The methodology is based on the magnetic circular dichroism (MCD) spectroscopy, which measures the relative difference of optical absorption between right- and left-circularly polarized light as a function of the wavelength.[9,10] In non magnetic materials this difference is null, but in magnetic materials the MCD signal is proportional to the value of the net magnetization. The procedure outlined here allows a magnetic characterization that, depending on specific experimental conditions such as the maximum applied magnetic field or type of magnetic source, may be even a few orders of magnitude faster than the commonly used SQUID magnetometry.[11] An additional advantage is the possibility of analyzing

*Corresponding authors. E-mail: gherranz@icmab.es; roig@icmab.es.

(1) Parak, W. J.; Gerion, D.; Pellegrino, T.; Zanchet, D.; Micheel, C.; Williams, S. C.; Boudreau, R.; Le Gros, M. A.; Larabell, C. A.; Alivisatos, A. P. *Nanotechnology* **2003**, *14*, R15.
(2) Ge, J. P.; He, L.; Goebl, J.; Yin, Y. D. *J. Am. Chem. Soc.* **2009**, *131*, 3484.
(3) Ge, J. P.; Hu, Y. X.; Yin, Y. D. *Angew. Chem., Int. Ed.* **2007**, *46*, 7428.
(4) Xu, X. L.; Friedman, G.; Humfeld, K. D.; Majetich, S. A.; Asher, S. A. *Chem. Mater.* **2002**, *14*, 1249.
(5) Liu, H. T.; Owen, J. S.; Alivisatos, A. P. *J. Am. Chem. Soc.* **2007**, *129*, 305.
(6) Sun, S.; Zeng, H.; Robinson, D. B.; Raoux, S.; Rice, P. M.; Wang, S. X.; Li, G. *J. Am. Chem. Soc.* **2004**, *126*, 273.
(7) Sun, S.; Anders, S.; Thomson, T.; Baglin, J. E. E.; Toney, M. F.; Hamann, H. F.; Murray, C. B.; Terris, B. D. *J. Phys. Chem. B* **2003**, *107*, 5419.
(8) Park, J.; Jin, J.; Gu, S.; Kwon, S. G.; Jang, Y.; Hyeon, T. *Angew Chem. Int. Ed.* **2007**, *46*, 4630.

(9) Stephens, P. J. *Annu. Rev. Phys. Chem.* **1974**, *25*, 201.
(10) Caldwell, D.; Thorne, J. M.; Eyring, H. *Annu. Rev. Phys. Chem.* **1971**, *22*, 259.

(11) In our particular set up, a complete MCD hysteresis loop can be obtained as fast as 1s. A typical magnetization loop in a SQUID takes more than $10^3$ s. The main reason for this extremely different time responses is that in magnetooptics the information on the magnetic state comes from the interaction of light with matter, whereas in a SQUID extracting the magnetic information requires the sample to be moved between a couple of detector coils, which is a much slower process. On the other hand, SQUIDs use superconductive coils, and our MCD system is based on an electromagnet, in which the fields can be cycled much more rapidly.

in situ the magnetic properties of nanoparticle colloidal dispersions in industrial production lines, whereas such liquid environments are complex to be dealt using other magnetic characterization tools. Finally, and not less important, is the fact that MCD spectroscopy provides information that is not accessible by SQUID magnetometry, since the spectral MCD response probes the electronic structure of the system with photons of different energies. We have, therefore, a means to directly monitor changes of the electronic structure with the nanoparticle size. To demonstrate the potentiality of such approach, we used a model system consisting of nickel nanoparticles of two different sizes dispersed in hexane. The sensitivity of the technique has been identified (in our setup to be about 1 $\mu$g/mL of magnetic particles) and a linear relationship of the magneto-optical response with the concentration is observed. Beyond these methodological developments, our data suggest that size effects are present in the magnetooptic response of nanometric Ni particles thus indicating significant electronic structure modifications.

## Materials and Methods

**Materials.** The following reagents were used in the chemical synthesis as received, without any further purification: nickel(II) acetylacetonate (Ni(acac)$_2$, 95% Aldrich, ref. 283657), oleylamine (tech.gr., 70%, Aldrich, ref. 07805), trioctylphosphine (TOP, tech. gr., 90%, Aldrich, ref. 117854), oleic acid (reagent gr., ≥99% (GC), Sigma-Aldrich, ref. 01008), *n*-hexane anhydrous (95%, Sigma-Aldrich, ref. 296090), and ethanol absolute (Panreac).

**Nickel Nanoparticles (Ni NPs) Synthesis.** Nickel nanoparticles were synthesized by high-temperature solution-phase method adapting the procedures reported by Chen et al.[12] and Murray et al.[13] In a typical synthesis, 1 mmol (0.257 g) of Ni(acac)$_2$ was added to 7 mL of oleylamine, 2 mmol (0.63 mL) of oleic acid, and 1 mmol (0.45 mL) of TOP, and the mixture was heated to 130 °C and stirred magnetically under a flow of high purity argon. During the heating, the mixture is changing color, from blue-turquoise to very clear green. The mixture was kept for 20 min at 130 °C. Afterward, it was further heated up to 250 °C and maintained at this temperature for additional 30 min. The color of the solution changed from green to dark green and finally to black. After cooling to room temperature, the nanoparticles were precipitated by adding extra ethanol, followed by centrifugation. The resulting black precipitate can be redispersed in an organic nonpolar solvent. The precipitate was dried in an oven (at 70 °C) overnight and weighted. Finally, the as-synthesized nickel nanoparticles were kept in a hexane concentrated dispersion of known concentration. For the as-described synthesis (molar ratio of precursor:oleic acid:TOP = 1:2:1, $T_1$ = 130 °C, $T_2$ = 250 °C), slightly faceted Ni nanoparticles with an average size of 15 nm were obtained. Changing just one synthetic parameter at the time (temperature and/or surfactants molar ratio) we were able to tune the size of the nickel nanoparticles from 8 to 150 nm (see the Supporting Information, Figure S1). In this work, we will focus on nanoparticles with average diameters of 8 and 15 nm. The 8 nm spherical nanoparticles were produced by using a molar ratio of precursor to oleic acid to TOP that equals to 1:1:2.

A concern is whether the conditions for the nanoparticles synthesis outlined here may induce the formation of an antiferromagnetic NiO thin layer at the surface. To check this issue, we dried samples of 8 nm nanoparticles overnight at 70 °C either under oxygen or argon atmosphere. Subsequent measurements of the magnetization at 5 K of both samples (see Figure S2 in the

Supporting Information file) indicated that their saturation magnetization values are virtually identical. In addition, we note that SQUID experiments performed after field-cooling conditions ($H$ = 50 kOe) conditions, particularly sensitive to exchange bias, indicate that the loops are well centered at zero-field (see the inset in Figure S2), and thus, there is no evidence of exchange bias and, by extension, of the formation of an antiferromagnetic (likely NiO) surface layer in any of the two samples. Finally, we also note that particles in hexane are even more protected since this solvent is not oxidizing and is commonly used to prevent nanoparticle oxidation.

**Characterization of the Nickel Nanoparticles.** Transmission electron microscopy (TEM) and X-ray diffraction (XRD) were used for morphological and structural characterization. TEM images were obtained with a JEOL JEM-1210 electron microscope, operating at 120 kV. The HRTEM images and selected area diffraction patterns (SADP) were captured using a JEOL JEM-2011, operating at 200 kV. The sample was prepared by depositing a drop of dilute nanoparticles hexane dispersion ($1.7 \times 10^{-3}$ M = 0.1 mg/mL) onto a TEM carbon grid and allow the solvent to evaporate. Mean diameter and polydispersity of each system were determined by adjusting to a Gaussian distribution a particle size histogram of over 300 counts measured from TEM images using the imageJ software.

X-ray diffraction patterns of colloidal dispersions were performed placing 100 $\mu$L Ni nanoparticle colloidal dispersions (concentration 10 mg/mL for 8 nm Ni NPs and 5 mg/mL for 15 nm Ni NPs) in a thin capillary (0.2 mm) and using a Bruker-AXS D8 Advanced model diffractometer with cupper K$\alpha$ incident radiation ($\lambda$ = 1.54 Å) and a GADDS bi dimensional detector (collimator 0.3 mm, conditions 40 KV and 40 mA).

The weight percentage of surfactants on the nanoparticle surface was determined by thermogravimetric analysis (TGA; see the Supporting Information, Figure S3). Solid samples (approximately 10 mg) were characterized with a Mettler Toledo TGA/SDRA 851E with the following setup: heating rate 10°/min and temperature range 30−800 °C under a N$_2$ flux. It was found that the quantity of surfactant (calculated in the temperature range 200−600 °C) was of 18.7% for the 8 nm particles and of 8.6% for the 15 nm particles.

**Dynamic Light Scattering (DLS).** Hydrodynamic size (metal core with surfactants shell and a layer of solvent close to the particle) of the 8 and 15 nm Ni NPs suspended in organic media was investigated with a Zetasizer Nano ZS from Malvern Instruments equipped with a He/Ne 633 nm laser for the concentrations range $1.7 \times 10^{-4}$−$5.1 \times 10^{-3}$ M. The DLS peak position and width was the same after three consecutive runs for all concentrations. We have also checked that there are not differences in the DLS peak position measured prior and after the MCD experiments and that the peak position does not change after applying a constant magnetic field for one hour. We thus conclude that the colloidal systems are stable, the particles are individually dispersed and do not cluster and that the application of magnetic fields does not affect the distribution of nanoparticles in the colloidal dispersions during the MCD experiments in the range of fields used here (see the Supporting Information, S4).

**Magnetic circular dichroism (MCD)** spectroscopy was performed using the homemade experimental setup illustrated (see the Supporting Information, S5).[14] The sample reservoir was placed between the poles of an electromagnet. Light from a 150 W Xe arc lamp (Zolix Technology) is dispersed by a monochromator

(12) Chen, Y.; Peng, D. L.; Lin, D.; Luo, X. *Nanotechnology* **2007**, *18*, 505703.
(13) Murray, C. B.; Sun, S.; Doyle, H.; Betley, T. *MRS Bull.* **2001**, 985.

(14) Hrabovský, D.; Caicedo, J. M.; Herranz, G.; Infante, I. C.; Sánchez, F.; Fontcuberta, J. *Phys. Rev. B* **2009**, *79*, 052401.

(Zolix l-150), collimated, and then linearly polarized by the action of a Glan-Thompson prism, which is rotated 45° with respect to the modulator axis of a photoelastic modulator (PEM). After the PEM, the light is transmitted through the sample (with a typical light beam diameter of about ~2 mm) and then goes, toward a detector. The signal from this detector is brought to a lock-in amplifier synchronized to the frequency of the PEM retardation angle. It can be demonstrated that, in this setup configuration, one can measure the MCD signal by inspection of the first harmonic of the detector signal.[9,10]

The magneto-optical measurements were performed by placing 1.5 mL of colloidal dispersions in a glass square cuvette for which the optical path was 1 cm (see Figure S5 in the Supporting Information). These experiments were carried out for the following concentrations; for 8 nm Ni NPs: $1.7 \times 10^{-4}$ M (0.0083 mg/mL Ni), $1.7 \times 10^{-3}$ M (0.083 mg/mL Ni), $2.6 \times 10^{-3}$ M (0.1264 mg/mL Ni), $4 \times 10^{-3}$ M (0.1938 mg/mL Ni), and $5.1 \times 10^{-3}$ M (0.25 mg/mL Ni) and for 15 nm Ni NPs: $1.7 \times 10^{-4}$ M (0.0092 mg/mL Ni), $1.7 \times 10^{-3}$ M (0.092 mg/mL Ni), $2.6 \times 10^{-3}$ M (0.1404 mg/mL Ni), $4 \times 10^{-3}$ M (0.2149 mg/mL Ni), and $5.1 \times 10^{-3}$ M (0.28 mg/mL Ni). Notice that all of the molar concentrations are reported in the basis of moles of Ni atoms and that for concentrations given in mg/mL Ni the amount of surfactant has been corrected. Those concentrations represent volume fractions of nanoparticles in colloidal dispersion in the range of 0.9−30 ppm. The amount of magnetic material used for the analysis was of 0.012 mg for the most diluted sample and of 0.12 mg for the most concentrated one. The background magneto-optical spectroscopic signal was subtracted from the raw experimental data by recording the spectra of glass cuvette filled with bare hexane solvent. The subtraction was made assuming that the background and the nanoparticle magneto-optical signals are additive.

Magnetic characterization was performed with a quantum interference device (SQUID) magnetometer (Quantum Design MPMS5XL). The sample was prepared using a plastic capsule filled with compacted cotton which was impregnated with 500 $\mu$L Ni solution of 10 mg/mL 8 nm Ni NPs giving 4.1 mg of Ni (30 times more solid material than the amount used for the magnetooptics characterization in the most concentrated sample). Magnetization data is presented in units of emu/g Ni (after correcting the weighted sample by the mass of surfactant).

## Results and Discussion

**Morphological, Structural, and Surface Characterization.** Nickel nanoparticles were synthesized as described above. Representative TEM images and particle size distribution histograms are shown in Figure 1. Transmission electron microscope (TEM) revealed nanoparticles with a mean size of 8 nm (12% polydispersity) and 15 nm (10% polydispersity) respectively. From TEM images it can be observed that the shape of nanoparticles is changing slightly as the size decreases becoming less faceted and more spherical. This is in agreement with previous reports.[13] Multiple crystalline domain orientations can be appreciated in the HRTEM image of 15 nm Ni NPs (see the Supporting Information, S6) and the SAED image (S6 inset) revealed a multispot pattern with the spots equally distant from the center which could be associated with multiple-twinned NPs. This observation is supported by the crystallite size value resulting from the Scherrer formula of the (111) diffraction peak which is about half the size of that found from TEM. Similar observations
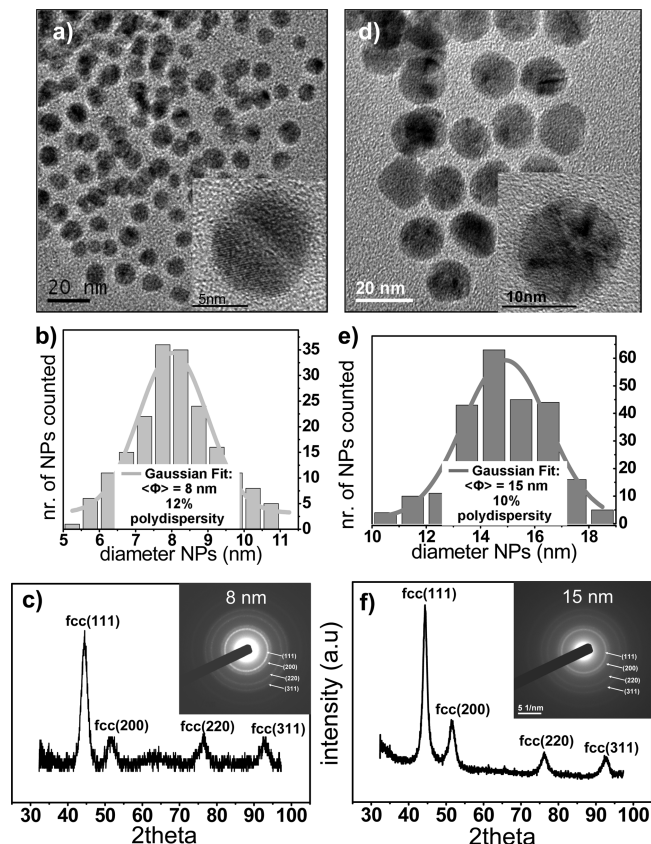
(15) Winnishofer, H.; Rocha, T. C. R.; Nunes, W. C.; Sokolovsky, L. M.; Knobel, M.; Zanchet, D. *ACS Nano* **2008**, *2*, 1313.
(16) Johnston-Peck, A. C.; Wang, J.; Tracy, J. B. *ACS Nano* **2009**, *3*, 1077.

**Figure 1.** (a) TEM image of 8 nm Ni NPs. The inset shows the HRTEM image of a single particle; scale bar is 5 nm. (b) Particle size distribution histogram fitted to a Gaussian function, (c) X-ray liquid diffraction pattern of 8 nm Ni NPs. The inset shows a selected-area electron diffraction pattern (SADP). d) TEM image of 15 nm Ni NPs. The inset shows the HRTEM image of a single particle; scale bar is 10 nm. (e) Particle size distribution histogram fitted to a Gaussian function. f) X-ray liquid diffraction pattern of 15 nm Ni NPs. The inset shows a SADP.

were reported by other authors.[15,16] X-ray diffraction (XRD) patterns of the colloidal solution exhibits four characteristic peaks corresponding to the fcc nickel lattice planes (111), (200), (220), and (311). No presence of peaks characteristic of crystalline nickel oxide could be detected. SADP images show continuous rings that could be indexed to the same fcc nickel crystalline planes, (111), (200), (220), and (311), as in XRD spectrum (see Figure 1).

**Magneto-Optical Characterization: Magnetic Circular Dichroism.** In a first set of experiments, we established that the range of concentrations for which our magneto-optical setup was able to probe the properties of the Ni nanoparticle dispersions was within a $10^{-5}−10^{-2}$ M concentration range. We verified that the concentrations below $10^{-5}$ M were too diluted and the magneto-optical signal too weak to be properly analyzed, even though still sufficient to be measured, whereas for concentrations above $10^{-2}$ M the magnetic field ($|\mathbf{H}| \leq 6$ kOe) promoted the aggregation of nanoparticles in clusters thereby distorting the magnetic hysteresis loops and precluding the analysis of the intrinsic nanoparticle properties. Figure 2 shows the recorded magneto-optical loops for the two extreme concentrations, $10^{-5}$ and $10^{-2}$ M. In particular we appreciate in this Figure that the loop measured at a concentration $10^{-2}$ M shows an anomalous shape (the upper and lower branches of the loops do not coincide) that departs significantly from the superparamagnetic behavior observed for more diluted dispersions.
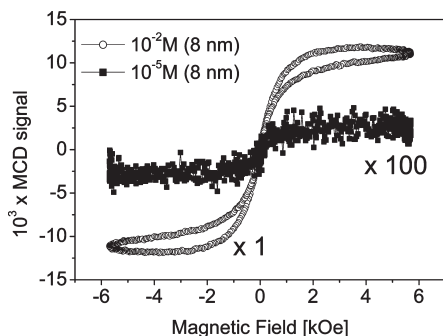
**Figure 2.** The recorded magneto-optical loops of 8 nm Ni NPs colloidal dispersions for the two extreme concentrations, $10^{-5}$ and $10^{-2}$ M. The data corresponding to $10^{-5}$ M are magnified by a factor 100.

Once determined the concentration window within which we can detect the intrinsic magneto-optical properties of colloidal suspensions, we have carried out measurements for five different concentrations, namely $1.7 \times 10^{-4}$, $1.7 \times 10^{-3}$, $2.6 \times 10^{-3}$, $4 \times 10^{-3}$, and $5.1 \times 10^{-3}$ M. For each concentration, two different sets of colloidal suspensions were measured; one set for Ni nanoparticles with size 8 nm and the other for 15 nm sizes.

We have measured the spectral dependence of the magneto-optical hysteresis loops (in Figure S7 of the Supporting Information we display the loops recorded at selected wavelengths for the two sets of particles with concentration $1.7 \times 10^{-3}$ M). As expected, the magnitude of the loops is a strong function of the probe light wavelength, and this spectral dependence is discussed below. It is immediately evident from these measurements that the data can provide straightforward information on some magnetic characteristics of the system namely, remnant magnetization and coercive and anisotropy fields. In particular, we observe that for the investigated nanoparticle sizes the remnant magnetization is less than about 1% of the saturated value and that the coercive field is virtually null, indicating that the colloidal dispersions exhibit a superparamagnetic behavior even with the short time scale of the measure. We should note that due to the superparamagnetic properties of these liquids, the application of any magnetic field during the synthesis of the nanoparticles does not affect the shape of the magneto-optical loops, since the colloidal dispersions loose their magnetic memory, and the moments of the nanoparticles are randomly oriented at zero field once the magnetic field is removed.

On the other hand, size effects can be evidenced by the different anisotropy fields observed for the two systems. This is better appreciated in Figure 3, where we plot the normalized magneto-optical hysteresis loops of the two sets of nanoparticle dispersions measured at a wavelength $\lambda = 425$ nm. We observe that the field necessary to saturate the magnetization of the set with nanoparticles with size 15 nm is around 1.5 kOe, whereas the anisotropy field of the set of nanoparticles (8 nm) is much higher, of the order of 5 kOe. In Figure 3 we have also plotted the normalized magnetization loops obtained at room temperature from a SQUID magnetometer, the two techniques give superimposable normalized loops. We see, as expected, that both the magneto-optical and the SQUID hysteresis loops confirm that the set of smaller nanoparticle dispersions are magnetically much harder than the bigger nanoparticles.

Additionally, from SQUID measurements (Figures S8a and S8b, Supporting Information), we observe that the magnetization value is strongly dependent on the size of the nanoparticles being 18 emu/g Ni for the 8 nm Ni NPs and 42 emu/g for 15 nm Ni NP
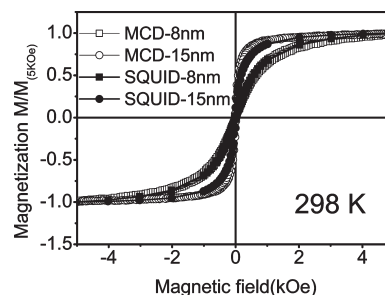


**Figure 3.** Comparison of the normalized loops obtained by the two techniques, SQUID and MCD. Hysteresis loops were taken at 298 K for 8 and 15 nm Ni NPs, respectively.
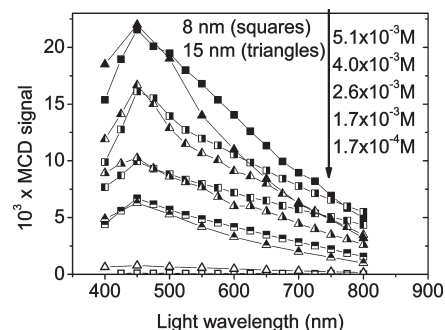


**Figure 4.** Magneto-optical signal as a function of wavelength and as a function of Ni NPs colloidal dispersion concentration for the two sets of nanoparticles.

(closer to the Ni bulk value $M_s$ = 56.7 emu/g). Some of us have interpreted recently such effects in terms of a size-dependent magnetic structure in the Ni nanoparticles[17] (see also Figures S8c and S8d in the Supporting Information file).

We discuss now the wavelength dependence of the saturated magneto-optical signal measured for different light wavelengths within the range 400 nm $< \lambda <$ 800 nm. In Figure 4 we have plotted these spectra for the five different concentrations ($1.7 \times 10^{-4}$, $1.7 \times 10^{-3}$, $2.6 \times 10^{-3}$, $4 \times 10^{-3}$, and $5.1 \times 10^{-3}$ M) and the two different nanoparticle sizes. As described above, to obtain the saturated value we proceeded to subtract from the raw measured signal the background magneto-optical signal, arising from the contributions of the glass container and hexane solvent. The spectral dependence of the MCD signal is displayed in Figure 4. We observed in this Figure that for all concentrations and nanoparticle sizes the spectral shape is very similar and exhibits a maximum at wavelengths $\lambda \approx 450$ nm and photon energies $E \approx$ 2.75 eV. The presence of features of the Ni optical dielectric response close to this energy has been reported previously (see, e.g., Figure 3 of ref 18. and Figure 4 of ref 19.).

From the experimental spectral response displayed in Figure 4 we can select an optimal spectral region for which we observe the highest sensitivity to MCD. This is relevant if we want to use the recorded MCD signal as a means to determine the concentration of a given colloidal dispersion of Ni nanoparticles. Note that the MCD is proportional to the net magnetization and, therefore, any eventual nonmagnetic or antiferromagnetic shell forming on the nanoparticle signal does not contribute to the magneto-optical

(17) Chen, D.-X.; Pascu, O; Roig, A.; Sanchez, A., submitted
(18) Amekura, H.; Takeda, Y.; Kishimoto, N. *Thin Solid Films* **2004**, *464−465*, 268–272.
(19) Visnovský, S.; Parizek, V; Nyvlt, M.; Kielar, P; Prosser, V.; Krishnan, R. *J. Magn. Magn. Mater.* **1993**, *127*, 135–139.

**Figure 5.** (a) Linear dependence of the magneto-optical response as a function of the Ni concentration measured at $\lambda = 450$ nm for both the 8 and 15 nm subsets. (b) Linear dependence of the magneto-optical response as a function of the Ni concentration measured at different wavelengths for the 8 nm subset.
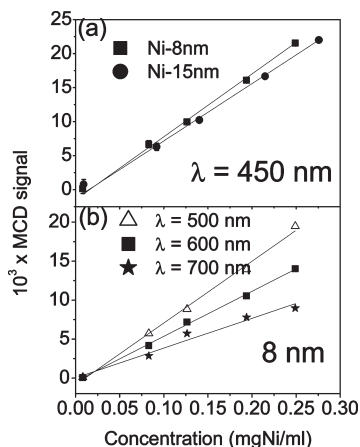
signal. To illustrate the potentiality of this methodology, we have plotted in Figure 5a for each set of dispersions (8 and 15 nm) the values of the MCD signal measured at $\lambda \approx 450$ nm at the five different concentrations shown in Figure 4. Figure 5a evidence that a linear relationship can be established between the recorded MCD and the concentration of Ni nanoparticles. The same linear relationship is observed for any other wavelength, the only effect being a change of the slope (see Figure 5b). The error bar in Figure 5a is around 5% of the average MCD value for the more diluted concentrations while it goes to around 1% for the more concentrated dispersions. These experiments confirm that the methodology presented here is a powerful and straightforward means to determine with large accuracy the concentration of Ni nanoparticles dispersed in liquid media. We emphasize that for our specific experimental conditions, given the sensitivity of the MCD set up to detect signals below $10^{-3}$ (see Figure 2), our method can detect concentrations as small as 1 $\mu$g/mL.

Finally, we note that the MCD signals depend slightly on the nanoparticles size. Indeed, from Figure 4 we observe that the MCD at wavelengths $\lambda \geq 450$ nm is somewhat higher for the 8 nm NPs than for the 15 nm ones. This trend is just the opposite of the measured magnetization (see Figure S8a of the Supporting Information), thus reflecting that MCD contains richer information than the magnetization, which integrates spin-dependent density of states, and indicates that both the magnetization and dielectric response become extensive properties in nanosize particles. This observation is also at the root of the distinct slope of the sensitivity curves shown in Figure 4. Detailed understanding of these effects is beyond of the scope of this manuscript but it

clearly shows that the magneto-optic technique here described is extremely sensitive to size effects and thus it may be well suited to explore the effect of a specific surface functionalization on the properties of magnetic nanoparticles or to in situ monitor chemical reactions.

## Conclusions

In summary, we have presented a fast and versatile methodology to characterize the magnetic properties of magnetic nanoparticles in colloidal dispersion using magneto-optical spectroscopy. Using this method, intrinsic properties such as magnetic anisotropy as well as coercive fields can be obtained straightforwardly. In addition, we show that proper calibration of the magneto-optical signal and careful selection of the wavelength of the probe light can yield a high sensitivity to highly diluted concentrations of magnetic nanoparticles colloidal dispersions allowing the accurate determination of the nanoparticle concentration. The flexibility of the method presented here makes it suitable for the in situ test of colloidal dispersions that are used in such state in specific applications and also its integration in mass-scale analysis in production lines. The capabilities of the experimental approach presented here can be largely expanded if the strong sensitivity of magneto-optical signals to the surface magnetic properties is properly exploited. For instance, real-time MCD monitoring could be used to track in situ chemical reactions that modify the surface state of the nanoparticles and the physical properties of the nanoparticles, as is the case of thiol-functionalized Au nanoparticles.[20] From a broader perspective, we have shown that MCD of colloidal suspensions may provide new information on the spectral dielectric response of non interaction magnetic nanoparticles.

**Supporting Information Available:** Details of HRTEM image, thermogravimetric analysis, dynamic light scattering, as well as SQUID magnetometry (zero-field and nonzero field curves) and magneto-optical experiments performed on the nanoparticle systems. This information is available free of charge via the Internet at http://pubs.acs.org/.

(20) Crespo, P.; Litrán, R.; Rojas, T. C.; Multigner, M.; De la Fuente, J. M.; Sánchez-López, J. C.; García, M. A.; Hernando, A.; Penadés, S.; Fernández, A. *Phys. Rev. Lett.* **2004**, *93*, 087204.

# Size analysis and magnetic structure of nickel nanoparticles

D.-X. Chen [a,*], O. Pascu [b], A. Roig [b], A. Sanchez [c]

[a] ICREA and Departament de Física, Universitat Autònoma de Barcelona, 08193 Bellaterra, Spain
[b] Institut de Ciència de Materials de Barcelona (ICMAB), CSIC, 08193 Bellaterra, Spain
[c] Departament de Física, Universitat Autònoma de Barcelona, 08193 Bellaterra, Spain

## ARTICLE INFO

## ABSTRACT

The size distribution of an assembly of fcc nickel nanoparticles is studied by measuring the temperature dependent magnetization curves fitted by a uniform model and a core–shell model, both based on the Langevin function for superparamagnetism with a log-normal particle volume distribution. The uniform model fits lead to a spontaneous magnetization $M_s$ much smaller than the $M_s$ for bulk nickel and to particle sizes larger than the ones evaluated by transmission electron microscopy; the core–shell model fits can result in a correct size distribution but the $M_s$ in the core becomes significantly greater than the $M_s$ for bulk nickel. It is concluded that there is a core–shell magnetic structure in nickel particles. Although the enhanced $M_s$ in the core may be related to the narrowing of the energy bands of 3d electrons in small fcc nickel particles, the modeling values of $M_s$ are over large compared with previous calculations on nickel clusters of different structures, which implies possible existence of an exchange interaction between the core and the shell, which is not considered in the simple core–shell model.

© 2010 Elsevier B.V. All rights reserved.

## 1. Introduction

Ferrimagnetic or ferromagnetic fine particles present rich physical phenomena and also serve as a key element in many technologies, including recent developments in fields such as magnetic separation, drug delivery, hyperthermia treatments and magnetic resonance imaging contrast agents [1], which have followed earlier applications in magnetic recording and ferromagnetic liquids [2,3]. In most cases, a knowledge of size distribution of the fine particles is crucially important for the proper working of a particular application.

The magnetic particle size distribution of powder samples may be determined from the measurements of magnetization curve based on the theory of superparamagnetism, first proposed by Bean and co-workers [4–6]. This theory defines a dilute assembly of ferromagnetic particles as superparamagnetic if the particles are single domain and when the thermal energy at the temperature of the experiment is sufficient to equilibrate the magnetization of the assembly in a time shorter than that of the experiment. The reduced magnetization $M(H)$ curve of the superparamagnetic assembly is expressed by the Langevin function

$$L(x) = \coth x - 1/x, \tag{1}$$

where $x = \mu_0 m_0 H / k_B T$, with $m_0$, $k_B$, and $T$ being the particle magnetic moment, the Boltzmann constant, and temperature,

respectively [6]. Thus, the particle moment may be determined by magnetic measurements, from which the particle volume may be obtained as $m_0/M_s$ if the saturation magnetization $M_s$ is known.

The saturation magnetization of particles $M_s$ was first thought to be the same as for the bulk material that had the same composition and structure as the particles. However, already in 1968, $M_s$ of many acicular $\gamma-Fe_2O_3$ polycrystalline particles was measured at room temperature, and it was found that $M_s$ decreased with decreasing the average crystallite size determined from X-ray diffraction (XRD) line broadening measurements using the Scherrer relation [7]. This phenomenon was explained by assuming the crystallites to be separated by a nonmagnetic grain shell on the order of 0.6 nm thick. A similar effect was found for single-domain superparamagnetic $Fe_3O_4$ particles in ferromagnetic liquids; their magnetization curve could be correlated to the superparamagnetic theory only when the size distribution of the suspended particles was considered with their volumetric concentration corrected for the formation of a nonmagnetic surface mantle one-unit-cell thick [8]. Such surface mantle was later called the magnetically dead layer with respect to the magnetic core [9]. The differences in magnetic structure between the surface layer and the core have been an interesting topic in physics [10–13].

A frequently adopted approach since then has been to assume the particles with a certain size distribution to have the same $M_s$ as the bulk and to determine by magnetic measurements a "magnetic size", which is significantly smaller than the physical size obtained from transmission electron microscopy (TEM) data. In recent years, however, in the determination of particle sizes by magnetic measurements, a paramagnetic susceptibility term has

---

been incorporated to the superparamagnetic term, and the magnetically determined sizes of $Fe_3O_4$ or $\gamma-Fe_2O_3$ nanoparticles are found to be in agreement with the sizes determined by TEM or XRD techniques [14–16]. In [17], we have completed this approach by proposing a core–shell model and a uniform model, both based on the Langevin function with a log-normal particle volume distribution, and by performing careful fits to experimental data of iron-oxide nanoparticles. It has been found that the core–shell model gives particle sizes consistent with the TEM or XRD sizes, while the sizes determined by the uniform model are larger with a wider distribution. The core–shell model has been used for the size analysis of superparamagnetic iron-oxide particles, which could be used potentially as contrast agents of magnetic resonance imaging [18].

In this work, we will use the methodology developed in [17] to study ferromagnetic nickel nanoparticles, to be compared with experimental and theoretical results on similar particles already published in the literature [19–29]. We will show that our particles display interesting magnetic features different from ferrimagnetic iron-oxide nanoparticles.

## 2. Experimental

### 2.1. Synthesis of nickel nanoparticles

Nickel nanoparticles were synthesized by thermal decomposition of a nickel organometallic precursor, adapting the method reported in [27]. For the studied particles, 1 mmol of $Ni(acac)_2$ was added to 7 ml oleylamine and 3 mmol trioctylphosphine, and the mixture was heated to 130 °C and stirred magnetically under a flow of high purity argon gas for 20 min, and then further heated to 250 °C and maintained at this temperature for 30 min. After cooling to room temperature, the nanoparticles were precipitated by adding excessive ethanol, followed by centrifugation. The as-prepared precipitate was dried at 70 °C overnight then weighted. To prevent oxidation, the as-synthesized nickel nanoparticles were kept as a concentrated dispersion in hexane of a known concentration.

### 2.2. Characterization of nanoparticles

TEM and XRD were used for morphological and structural characterization of the nanoparticles. TEM images were obtained using a JEOL JEM-2011 electron microscope, operating at 200 kV. The sample was prepared by depositing a drop of dilute nanoparticles hexane dispersion onto a TEM carbon grid followed by room temperature drying. A representative TEM image is shown in Fig. 1, where we see that most particles are roughly spherical.

XRD was performed for a powder sample by a Rigaku diffractometer with Cu Kα incident radiation ($\lambda = 0.154$ nm). The resulting pattern is shown in Fig. 2, from which four peaks are observed corresponding to the (1 1 1), (2 0 0), (2 2 0), and (3 1 1) planes of fcc structure of lattice parameter 0.354 nm (very near the standard value 0.352 nm for bulk nickel). The average crystallite size may be determined from XRD pattern using the Scherrer relation with a shape factor of 4/3 for spherical particles [30]

$$D_{XRD} = \frac{4k\lambda}{3\Delta(2\theta)\cos\theta}, \tag{2}$$

where Scherrer constant $k=0.9$, the peak is centered at $2\theta$, and $\Delta(2\theta)$ (rad) is the width of the peak at half maximum intensity. The $D_{XRD}$ determined from the (1 1 1), (2 0 0), (2 2 0), and (3 1 1) peaks is 5.2, 3.4, 5.2, and 4.5 nm, respectively.
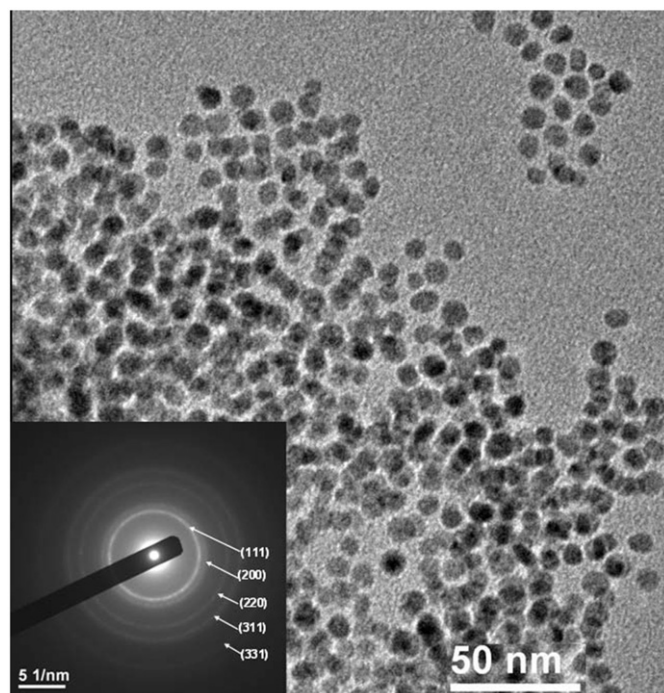


**Fig. 1.** TEM image of studied nanoparticles. The inset is a selected area electron diffraction pattern with indexed planes.
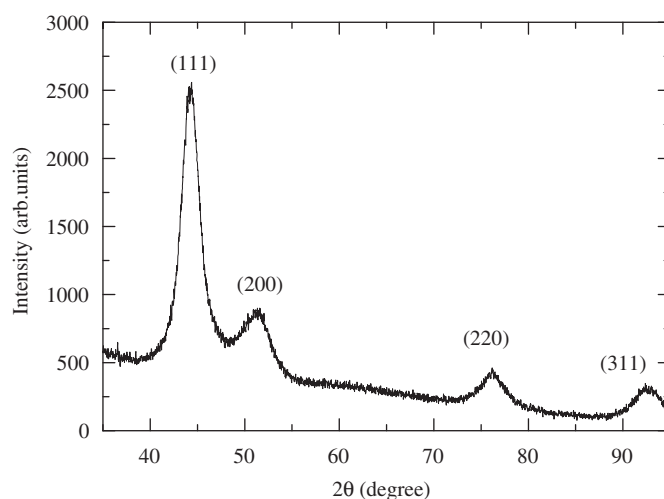


**Fig. 2.** The X-ray diffraction pattern of studied nanoparticles.

### 2.3. Magnetic measurements

The magnetic measurements were performed with a superconducting quantum interference device (SQUID) magnetometer, which was carefully calibrated by using a Pd standard sample. The nickel sample was powder packed in a plastic capsule. The zero-field and field (3 kA/m) cooled measurements were carried out for one sample during warming at a measuring applied field $H_a = 3$ kA/m. The results are shown in Fig. 3, from which we see that the external susceptibility $M/H_a$ increases and then decreases with increasing temperature $T$ for the zero-field cooled case, whereas it decreases monotonically with $T$ for the field cooled case and that both curves merge at $T > 75$ K.

Another sample was prepared with more caution concerning the powder mass (to get more accurate magnetization) and its
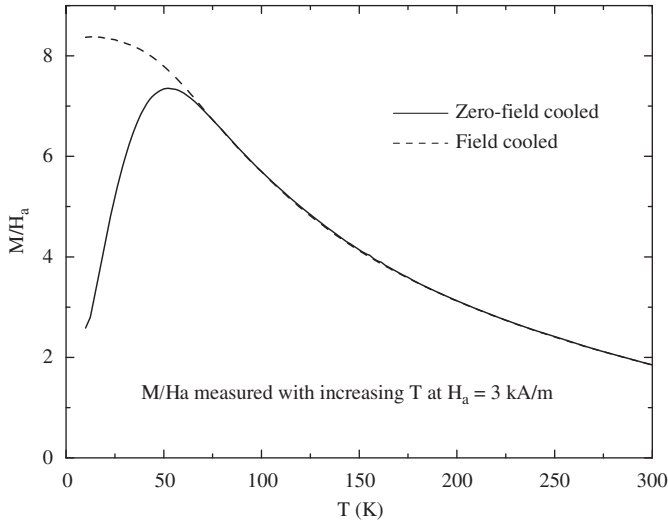
**Fig. 3.** External susceptibility $M/H_a$ of a powder sample measured at $H_a=3$ kA/m as a function of increasing temperature $T$, after cooling at $H_a=0$ and 3 kA/m.
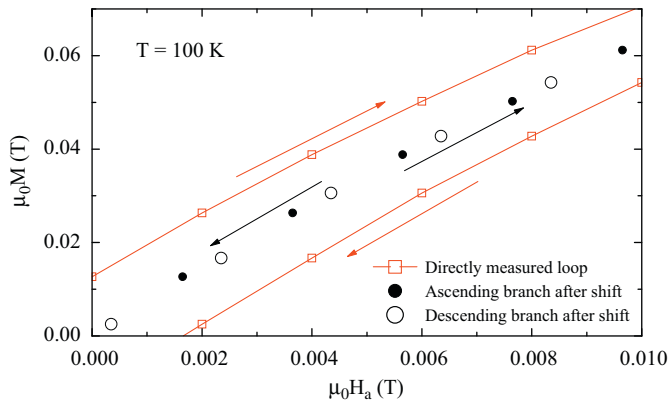


**Fig. 4.** The correction to $M(H_a)$ loop obtained from SQUID magnetometric measurements, showing how the unphysical measured loop (low-field portion) is shifted to a reversible magnetization curve.

dispersion (to reduce demagnetizing effects) and used for the measurements of magnetization loops at $T=100$, 200, 300, and 400 K. In the data treatment, a shift of $\pm 0.00165$ T was performed for the ascending and descending applied field $\mu_0 H_a$ to correct the effects of remanence of the SQUID superconducting magnet, so that the magnetic reversibility of the measured sample could be accurately checked.

A comparison between the directly recorded and corrected hysteresis loops in a low-field region is shown in Fig. 4. Owing to the irreversible magnetization of the superconducting wire of which the magnet of the SQUID magnetometer is wound, the field at the magnet center is produced not only by the current flowing through the wire, from which the field reading is calculated, but also by the poles in the magnetized wire itself, which gives an error in the field measurements. According to the critical-state model [31], the magnetization of the wire will be along the field produced by the transport current when the current decreases from a large value as in our case. Thus, the poles will produce a negative demagnetizing field at the magnet center when the total field sweeps from a large positive value in the descending branch. As a result, by cycling the field between $\pm 5$ T, the directly measured $M(H_a)$ of a paramagnetic sample will become a

hysteresis loop corresponding unphysically to a negative energy loss, as shown in Fig. 4. Such a loop is corrected to a reversible one after a shift determined by the calibration of the SQUID magnetometer with a paramagnetic Pd standard sample. This correction is essential at low $|H_a|$ only.

Moreover, a demagnetizing correction was performed to convert the applied field $H_a$ to the internal field $H$ in the sample by using

$$H = H_a - N_m M, \tag{3}$$

where magnetometric demagnetizing factor $N_m=0.02$ was taken (see below) [32]. After such corrections, the $\mu_0 M$ vs $\mu_0 H$ loops are plotted in Fig. 5 by solid (ascending branch) and open circles (descending branch).

For calculating magnetization, the mass fraction $(1-f_m)$ of surfactants on the surface of dried nanoparticles was obtained by thermogravimetric analysis (TGA). A powder sample of about 10-mg mass was measured with a Mettler Toledo TGA/SDTA 851 at heating rate 10 °C/min in a temperature range 30–800 °C under flowing $N_2$.

The original data given by the magnetometer were the moment $m$ of the sample in emu units. The formula to calculate $\mu_0 M$ in SI units is $\mu_0 M = 4\pi m\rho/(10\,000 w f_m)$, where $f_m=0.83$ is obtained from TGA data and $w$ and $\rho$ are the sample mass and the density of nickel (8.9 g/cm$^3$), respectively, in cgs units.
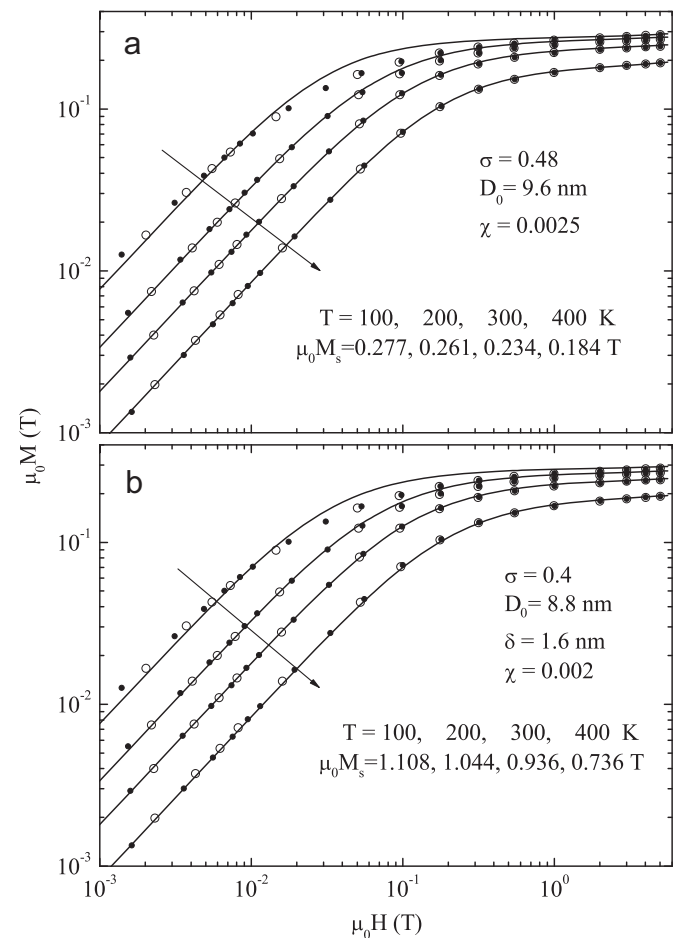


**Fig. 5.** The magnetization $M$ versus field $H$ loops (solid and open circles for ascending and descending branches, respectively) of a powder sample measured at $T=100$, 200, 300, and 400 K and their fits (lines) by the uniform model (a) and the core–shell model (b). Arrows indicate the direction of increasing $T$.

## 3. Model fits to magnetization curves

### 3.1. Uniform and core–shell models

To fit the $\mu_0 M$ versus $\mu_0 H$ curves, we assume that all particles are spherical without mutual interaction and the particle volume $v$ distribution by volume follows the log-normal probability density function

$$p(v; \mu, \sigma) = \frac{1}{\sqrt{2\pi}\sigma v} \exp\left[-\frac{(\ln v - \mu)^2}{2\sigma^2}\right], \qquad (4)$$

where $\mu$ and $\sigma$ are the mean and the standard deviation of $\ln v$. For convenience, we define

$$\mu \equiv \ln v_0 = \ln(\pi D_0^3/6), \qquad (5)$$

where $v_0$ and $D_0$ are the median volume and its corresponding diameter, respectively.

The uniform model assumes all the particles to have the same spontaneous magnetization $M_s$ (equal to the average saturation magnetization of the superparamagnetism for the entire particle assembly) and the same paramagnetic susceptibility $\chi$. Magnetization $M$ as a function of field $H$ is contributed by the superparamagnetism and paramagnetism of all the particles with a volume distribution $p(v; \mu, \sigma)$ and is expressed by

$$M(H) = \int_0^\infty p(v; \mu, \sigma)[M_s L(x) + \chi H]\, dv, \qquad (6)$$

where $L(x)$ is expressed by Eq. (1) with

$$x = \mu_0 M_s v H / k_B T. \qquad (7)$$

The core–shell model assumes that each particle has an inner single-domain core with spontaneous magnetization $M_s$ and an outer paramagnetic shell of susceptibility $\chi$ and thickness $\delta$, if the particle diameter $D > 2\delta$. Writing the volumes of a particle, its core, and its shell as $v$, $v_c$, and $v_s$, respectively, we have in general $v = v_c + v_s = \pi D^3/6$ and $v_c = 0$ if $D < 2\delta$ and $v_c = \pi(D - 2\delta)^3/6$ otherwise. Thus, $M(H)$ is contributed by the core superparamagnetism and the shell paramagnetism of all the particles with a volume distribution $p(v; \mu, \sigma)$ and is expressed by

$$M(H) = \int_0^\infty p(v; \mu, \sigma) v^{-1}[M_s v_c L(x) + v_s \chi H]\, dv, \qquad (8)$$

where $L(x)$ is expressed by Eq. (1) with

$$x = \mu_0 M_s v_c H / k_B T. \qquad (9)$$

These uniform and core–shell models have been explained in greater detail in [17]. Most researchers used the Langevin function to fit superparamagnetic magnetization curves of particle systems without considering a paramagnetic contribution (i.e., $\chi = 0$) and a magnetic core–shell structure. Although such model fits cannot be good according to our experience, we will call the model used in, for example, [24,26] without explicitly mentioning a core–shell structure as a uniform model for simplicity. Our core–shell model is a completion of some previous models where a core–shell structure was considered, and essentially different from a popular model by which the problem was treated self-inconsistently leading to a magnetic size even smaller than the size of the core, as already discussed in [17]. Moreover, our core–shell structure is a magnetic one that may not be seen morphologically, which is different from cases where the core and shell are made of different materials [20,28].

### 3.2. Model fits

Using Eq. (6) to calculate numerically the magnetization curve of the uniform model for given values of $T$, we fix the values of the Boltzmann constant $k_B = 1.38 \times 10^{-23}$ J/K and the permeability of free space $\mu_0 = 4\pi \times 10^{-7}$ H/m, and change the values of parameters $\sigma, D_0, \chi$, and $M_s(T)$ iteratively until the measured $\mu_0 M$ vs. $\mu_0 H$ curves for $T = 300$ and 400 K are best fitted with a proper demagnetizing correction of $N_m = 0.02$. Then, we fix the same data for $\sigma, D_0$, and $\chi$ and change $M_s(T)$ for $T = 100$ and 200 K until the low and high field portions of the measured $\mu_0 M$ vs. $\mu_0 H$ curves are best fitted. All the four fitting curves are plotted as solid lines in Fig. 5(a), with fitting parameters listed.

For the core–shell model fits using Eq. (8), the values of $M_s(T)$ are set as four times those for the uniform model (as explained below), and the fitting curves are plotted in Fig. 5(b), with all fitting parameters listed. It should be noted that the data for $T = 100$ and 200 K cannot be well fitted by using the same set of $\sigma, D_0, \delta$, and $\chi$ as those used for higher temperatures. Since $\sigma$ and $D_0$ should be $T$ independent for the same assembly of particles and the effect of $\chi$ is small, this implies that at least $\delta$ should change with $T$ and $H$ if a core–shell model is still applied. Physically, this may be a consequence of the interaction occurring between the core and the shell, which will be discussed in Section 4.6.

It is necessary to make an explanation on the demagnetizing correction. In the measurements of our superparamagnetic powder, the magnetic moment and the applied field are measured accurately since the SQUID magnetometer has been properly calibrated and the field error owing to the magnetization of the superconducting wire has been corrected. However, there is still a demagnetizing effect to be considered. This effect can be neglected when the magnetic particles are very loosely packed, as in the case of [17], but it cannot in most cases. We propose a way to determine $N_m$ in the present work by measuring $M(H)$ curves at more than two different $T$ values and fitting them logically with the same set of parameters. It is shown that the fitting can be well done only when $N_m$ is incorporated as an extra parameter, so that proper $N_m$ is determined for the measured sample. Our experience shows that $N_m$ cannot be larger than 0.02. Such a small $N_m$ value comes from loosely packed particles in the sample; $N_m = 0.02$ gives a rough estimate of the volume fraction of the nickel particles in the sample, which is about 0.1 in the present case.

It is important to mention that such a demagnetizing correction was not performed in most works on magnetic properties of assemblies of magnetic fine particles, so that low-field superparamagnetic susceptibility $\chi_0$ obeying the Curie law was modified to one obeying the Curie–Weiss law. In our case, the Curie law may be expressed by $\mu_0^2 M_s^2 / \chi_0 \propto T$ [17], where the average values of $\mu_0 M_s$ in particles is given in Fig. 5(a) and $\chi_0$ may be obtained from the experimental $M/H$ at $\mu_0 H \approx 0.004$ T. A comparison of $\mu_0^2 M_s^2 / \chi_0$ vs. $T$ before and after demagnetizing correction is shown in Fig. 6. We see that the Curie–Weiss relation $\mu_0^2 M_s^2 / \chi_0 \propto (T - T_c)$ with $T_c < 0$ is changed into the Curie relation by the demagnetizing correction.

### 3.3. Size distribution

The log-normal probability density function $p(v; \mu, \sigma)$ of the particle volume distribution by volume, expressed by Eq. (4), may be converted into the probability density function of the particle diameter distribution by volume,

$$p(D) = \frac{3}{\sqrt{2\pi}\sigma D} \exp\left[-\frac{9(\ln D - \ln D_0)^2}{2\sigma^2}\right], \qquad (10)$$

where particle diameter
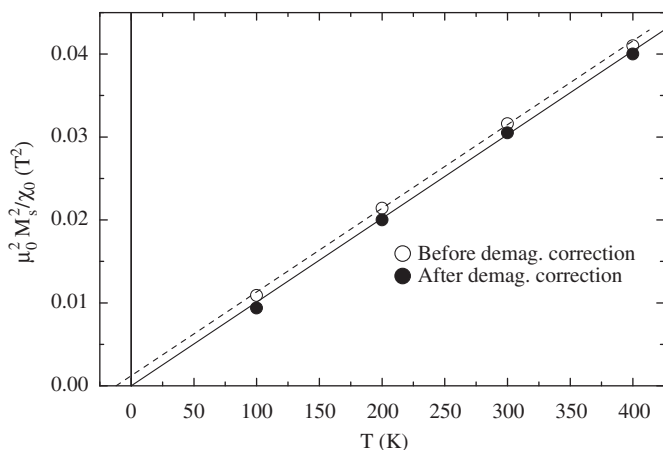
$$D = (6v/\pi)^{1/3}. \qquad (11)$$

**Fig. 6.** Influence of demagnetizing correction on $M_s^2/\chi_0$ vs. $T$ relation. The solid and dashed lines show the linear relations of the Curie and the Curie–Weiss laws, respectively.
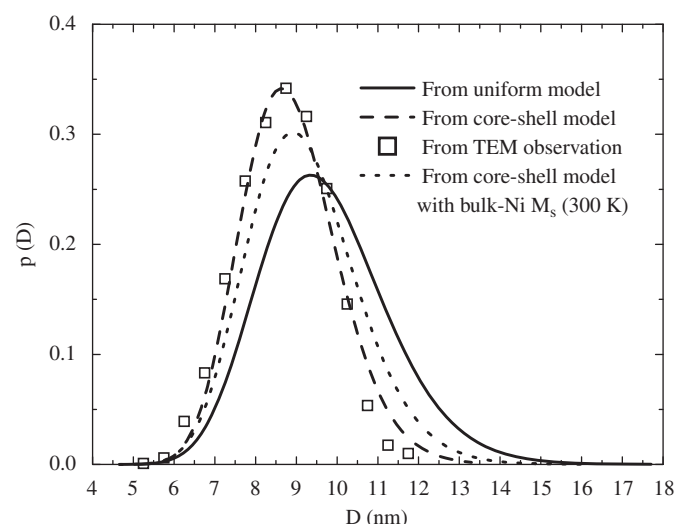


**Fig. 7.** Particle size distribution by volume obtained from magnetization curve fits by the uniform (solid line) and core–shell models (dashed line) and from TEM images (open squares). The dotted line is obtained from the core–shell model fit at $T=300$ K with $\mu_0 M_s = 0.607$ T, the value of bulk nickel.

The $p(D)$ vs $D$ curves calculated from $D_0=9.6$ nm and $\sigma = 0.48$ for the uniform model fits and from $D_0=8.8$ nm and $\sigma = 0.4$ for the core–shell model fits are plotted in Fig. 7 by solid and dashed lines, respectively. We see that the former distribution is wider than the latter with its maximum located at larger $D$. The square symbols are the size distribution by volume evaluated by measuring more than 550 nanoparticles from the TEM image in Fig. 1; it shows a good coincidence with the dashed line. In fact, the fitting parameters of the core–shell model have been chosen iteratively by comparing the modeling distribution curve with the TEM results.

# 4. Discussion

## 4.1. Polycrystalline nanoparticles

Since the X-ray intensity is proportional to the total particle volume and the peak width is directly related to the particle size, the particle diameter determined directly from XRD patterns

using the Scherrer relation is the particle-volume-weighted average diameter [17]

$$D_{vd} = \int_0^\infty p(v; \mu, \sigma) D(v) \, dv. \tag{12}$$

$D_{vd}=8.9$ nm is calculated using $D_0=8.8$ nm and $\sigma = 0.4$ for the core–shell model fits, which is consistent with TEM observation. This $D_{vd}$ is roughly twice the average $D_{RXD}=4.6$ nm for the crystallites, so that the nickel particles shown in the TEM images are polycrystalline in general. This is different from the case of ferrimagnetic iron-oxide particles, whose particles observed in TEM are single crystals [17,18].

Since $D_{XRD}$ determined from the $(2\,0\,0)$ peak is significantly smaller than that determined from the $(1\,1\,1)$ peak, the crystallites seem to have a cube-like shape.

## 4.2. Superparamagnetism

As shown in Fig. 5, there is no hysteresis occurring in the magnetization loops for $T$ between 100 and 400 K, i.e., the thermal energy is sufficient to equilibrate the magnetization at each field value in the time of experiment, so that the assembly of the studied nickel nanoparticles may be superparamagnetic in this $T$ range. Being polycrystalline, each particle is a single magnetic domain, since after a proper demagnetizing correction, the measured magnetization curves at $T=300$ and 400 K can be well fitted by the uniform model of superparamagnetism with the same set of parameters. However, to further confirm the superparamagnetism, the magnetization curves at lower $T$ should also be well fitted with the same set of $D_0$ and $\sigma$ values, since the sizes of the particles should not be $T$ dependent, and both $D_0$ and $\sigma$ parameters should define a size distribution that is consistent with the one determined by TEM measurements. These two requirements may be fulfilled by using the core–shell model fits, as discussed below.

## 4.3. Model fits and particle sizes

The uniform model fits lead to over-large $D_0$ and $\sigma$, which results in a wider particle size distribution centered at a larger $D$ compared with the TEM size distribution (Fig. 7). As shown in [17], the same magnetization curve may be equally well fitted by either the uniform model or the core–shell model, and the $D_0$ and $\sigma$ obtained by the core–shell model fitting are smaller than those obtained by the uniform model fitting. Increasing the shell thickness $\delta$ and the $M_s$ in the core to fit the magnetization curves by the core–shell model, we find a set of parameters listed in Fig. 5(b) that are best in agreement with the TEM data.

The advantage of the core–shell model over the uniform model is not shown by a better fitting quality to the $M(H)$ curves but by the obtained size distribution to be closer to the TEM data. In principle, an increase in $M_s$ could be compensated by a decrease in $v_c$ to maintain constant $M_s v_c$ in Eq. (9), so that a size distribution that is most close to the TEM one may be obtained by changing both freely. However, in order to maintain the same distribution of $M_s v_c$, the increase in $M_s$ and decrease in $v_c$ have to be realized by increasing $\delta$ and decreasing $D_0$ and $\sigma$ simultaneously. The reason for $D_0$ and $\sigma$ determined from the core–shell model fits to be smaller than those from the uniform model can be understood as follows. In the core–shell model, the contribution of the shell of a certain thickness to superparamagnetism is removed, and the shell occupies a larger volume fraction in smaller particles than in larger particles. As a result, the total particle size distribution with smaller $D_0$ and $\sigma$ obtained by the core–shell model fits will give

practically the same $M_s v_c$ distribution as that obtained by uniform model fits with larger $D_0$ and $\sigma$.

## 4.4. Magnetic structure

The goodness of the core–shell model fits indicates the existence of a core–shell magnetic structure in the nickel nanoparticles.

Different from the case of ferrimagnetic iron oxide, for which the $M_s$ in the core is the same as that for the bulk, the $M_s$ in the core of nickel nanoparticles can be greater than its bulk value. The $\mu_0 M_s(T)$ data points resulting from the uniform and core–shell model fits are drawn in Fig. 8, where, for comparison, a solid curve is plotted for bulk nickel, calculated from

$$M_s(T) = M_s(0)[1 - 0.15(T/T_c)^{3/2} - 0.85(T/T_c)^{5/2}]^{1/3}, \qquad (13)$$

where $M_s(0) = 0.65\,\mathrm{T}$ and $T_c = 630\,\mathrm{K}$ [33], and the dashed and dotted curves are drawn artificially for the uniform and core–shell model results to have the same $T_c$ as the bulk. We see that although the $M_s$ for the uniform model is always much smaller than that for the bulk, the $M_s$ in the core could be significantly larger.

This difference in magnetic structure between ferromagnetic and ferrimagnetic nanoparticles suggests the difference in the nature of magnetic ordering. As described in [34], the magnetic ordering in ferrimagnetic iron oxides results from the local superexchange interaction between the 3d electrons of iron ions with certain magnetic moments through the oxygen ions in between, and when the surface effects reduce the interaction so that $M_s$ becomes zero in a surface layer, $M_s$ in the core remains its bulk value. The detailed mechanisms for the zero $M_s$ in the surface layer were studied in [10–13].

For ferromagnets, however, $M_s(0)$ comes from the 3d electrons itinerant among the atoms, so that the discrete energy levels for isolated atoms are extended to certain spin-up and spin-down energy bands splitted by exchange field. Since both bands are partially overlapped in energy, so that the spontaneous magnetic moment per ion, given by the difference in the number of electrons in the spin-up and the spin-down bands, is about $0.6\mu_B$, which is much smaller than $2\mu_B$ ($\mu_0 M_s \approx 2.1\,\mathrm{T}$), expected by 2 vacancies in the 3d shell of nickel atom [34]. For a nano-sized particle, the spin-up and spin-down bands should be energetically narrower than those for the bulk with less overlap in the same exchange field, so that $\mu_0 M_s(0)$ being between 0.65 and 2.1 T may be expected. The core–shell model fits indicate that such an

enhancement in $M_s$ occurs only in the core, and they should require that the exchange effects be weakened (or even change the sign to antiferromagnetic coupling) near the particle surface, leading to a very small $M_s$ in the shell. As to the paramagnetism, it should be Pauli paramagnetism resulting from the band structure, so that $\chi$ is approximately temperature independent [34].

## 4.5. Comparison with previous works

The temperature dependence of $M_s$ shown in Fig. 8 deduced from the core–shell model fits is qualitatively similar to that found in [26], where magnetization of nickel nanoparticles of average diameter 3 nm was detected by Kerr ellipticity at $T > 300\,\mathrm{K}$, and explained by quantum Monte-Carlo simulations considering Ising spins in a nanocube [22]. However, fitting the experimental $M(H,T)$ by a uniform model without considering a size distribution, the authors of [26] obtained a spontaneous magnetic moment per ion to be $2.5\mu_B$ per atom, which is a value 10 times larger than our result without physical basis.

$M_s$ of nickel particles was found to decrease quickly with decreasing particle size in [19], which is consistent with our results. By Langevin function fitting with a uniform model in [24], $M_s$ of nickel nanoparticles of TEM size about 3.3 nm was found approximately the same as that of bulk nickel with "magnetic" size about 5 nm. This seems to be consistent with our results, since the disagreement between the two sizes could be resolved by a core–shell model fit to get $M_s$ in the core much larger than $M_s$ of bulk nickel. $M_s$ of nickel nanoparticles in silica gel was found to be about 90% of $M_s$ of bulk nickel for particle sizes between 3 and 10 nm in [20]. This would help to understand the magnetic structure in nickel particles by showing significant influence of silica gel if it is further confirmed.

In a study of nickel nanoparticles [28], a synthesis procedure similar to ours was adopted with polycrystalline fcc grains obtained. Since the high-field magnetization was found to be, similarly to our case, significantly smaller than that for bulk nickel, the existence of an amorphous antiferromagnetic NiO shell was assumed. The shell thickness was estimated to be around 1 nm by assuming the bulk-nickel $M_s$ value in the core and using the densities for bulk nickel and bulk NiO in the core and the shell, respectively. Different from that approach, we have assumed the particles are pure nickel and determined the shell thickness by careful uniform and core–shell model fits to the entire magnetization curves with the same set of $D_0$ and $\sigma$ parameters at different temperatures, and comparing the resulting size distribution with TEM measurements, so that the thicker shell is found with the $M_s$ in the core to be greater than that for the bulk nickel. We should emphasize that using the bulk-nickel $M_s$ for the core, not only the core–shell model fit gives overlarge $D_0$ and $\sigma$, but the resultant $D_0$ and $\sigma$ are also unphysically $T$ dependent. As an example, we show the size distribution curve (dotted line) obtained by the core–shell model fit at $T = 300\,\mathrm{K}$ with $\mu_0 M_s = 0.607\,\mathrm{T}$ in Fig. 7.

## 4.6. Possible exchange interaction between the core and the shell

The $M_s$ in the core resultant from the core–shell model fits is significantly larger than what was measured and calculated for small nickel clusters in [35–37]. The magnetism from the atom to the bulk in nickel clusters was studied by measuring the clusters deflections of a molecular beam in an inhomogeneous magnetic field in [35] and the measurements were improved in [36]. According to [36], the spontaneous moment per atom decreases from 1.8 to $0.68\mu_B$ with increasing the atom number per cluster from 5 to 740, showing a tendency of further decrease at even
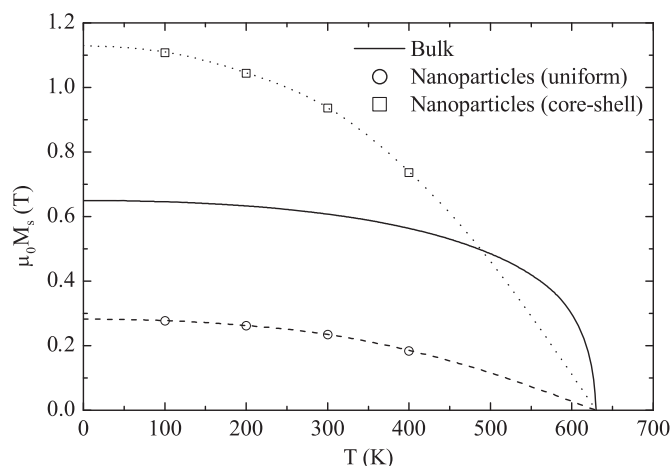


**Fig. 8.** Spontaneous magnetization $M_s$ as a function of temperature $T$. Symbols are for the nickel nanoparticles obtained from model fits in Fig. 4(a) and (b) and solid line is for the bulk nickel calculated from Eq. (13).

larger atom numbers. The variation up to a cluster of 60 atoms was explained by calculating the spin-polarized electronic structure with a self-consistent tight-binding method considering 3d, 4s, and 4p valence electrons [37]. The core of our nickel particles of diameter $D_0 - 2\delta = 5.6$ nm contains about $10^4$ atoms, which is one order of magnitude more than the upper limit studied in [35,36], and corresponds to a moment of $1.04\mu_B$ per atom. This over-large $M_s$ in the core might be related to the difference in atomic structure; the clusters have quite different structures from fcc as in our case. But more reasonably, the resultant over-large $M_s$ in the core may be a consequence of interaction between the core and the shell, which is not considered in our core–shell model.

The large $M_s$ variation in ferromagnetic nanoparticles is a new phenomenon that has to be properly explained. Its explanation turns out to be difficult, since unlike the case of ferrites whose magnetic ordering occurs among 3d electrons localized in each iron ion, the band theory explaining magnetic ordering of ferromagnets itself is defined for the whole body with ignored local variation of magnetization. The spherical particles consisting of few cubic crystallites suggest the existence of a spherical amorphous shell containing oxygen atoms with an antiferromagnetic properties. If this is true, the discovered magnetic core–shell structure would be directly linked to a core–shell microstructure, and the magnetization rotations in the core would not only be driven by the applied field but also be impeded by an opposite exchange field owing to the exchange interaction between the ferromagnetic core and the antiferromagnetic shell. As a result, the low-field susceptibility of the assembly should be reduced from what is calculated from the Langevin function without considering the core–shell interaction. If the exchange field is relatively larger for smaller particles than for larger particles, then smaller particles contribute to the reduction of susceptibility more than larger particles. In this case, the large increase in $\delta$ and $M_s$ required to explain the anomalous size distribution may be partially replaced by the effect of the exchange field. In other words, the required $M_s$ in the core can be smaller if the exchange interaction between the core and the shell is considered. If such an interaction is $T$ and $H$ dependent, then the anomalies occurring in the low-$T$ $M$ vs. $H$ curves, formally explained by a $T$ and $H$ dependent $\delta$, may be understood on a more fundamental level.

## 5. Conclusion

A core–shell model developed for the study of ferrimagnetic oxide nanoparticles is used for metallic ferromagnets. Values of $M_s$ in the core larger than its bulk value may result from the model fits to obtain a correct particle size distribution, which is different from the case of ferrimagnets, whose $M_s$ is the same for the core and the bulk. Such a difference in model fits reflects the difference in magnetic ordering mechanism. The magnetic ordering in oxide ferrites is due to the superexchange interaction between neighboring spins of iron ions, with fixed moments, through oxygen ions, whereas for metallic ferromagnets, it comes from the slip of spin-up and spin-down bands of the entire body by direct exchange interaction. The bands for nanoparticles are energetically narrower than those for the bulk, so that $M_s(0)$ for the former is larger than for the latter. However, the mechanism of magnetic core–shell structure in ferromagnetic nanoparticles is unclear, and the resultant $M_s$ in the core is over large compared

with previous calculations on nickel clusters. Nevertheless, if the core and the shell may be regarded as ferromagnetic and antiferromagnetic, respectively, then the difficulty of over-large $M_s$ in the core may be overcome by considering the exchange interaction between the core and the shell.

## Acknowledgments

## References

[1] Q.A. Pankhurst, J. Connolly, S.K. Jones, J. Dobson, J. Phys. D Appl. Phys. 36 (2003) R167.
[2] G. Bate, in: E.P. Wohlfarth (Ed.), Ferromagnetic Materials, vol. 2, North-Holland, Amsterdam1980, p. 381.
[3] S.W. Charles, J. Popplewell, in: E.P. Wohlfarth (Ed.), Ferromagnetic Materials, vol. 2, North-Holland, Amsterdam1980, p. 509.
[4] C.P. Bean, J. Appl. Phys. 26 (1955) 1381.
[5] C.P. Bean, I.S. Jacobs, J. Appl. Phys. 27 (1956) 1448.
[6] C.P. Bean, J.D. Livingston, J. Appl. Phys. 30 (1959) 120S.
[7] A.E. Berkowitz, W.J. Schule, P.J. Flanders, J. Appl. Phys. 39 (1968) 1261.
[8] R. Kaiser, G. Miskolczy, J. Appl. Phys. 41 (1970) 1064.
[9] R.E. Rosensweig, Ferrohydrodynamics, Cambridge University Press, Cambridge, 1985, p. 60.
[10] J.M.D. Coey, Phys. Rev. Lett. 27 (1971) 1140.
[11] R.H. Kodama, A.E. Berkowitz, E.J. McNiff Jr., S. Foner, Phys. Rev. Lett. 77 (1996) 394.
[12] B. Martinez, X. Obradors, Ll. Balcells, A. Rouanet, C. Monty, Phys. Rev. Lett. 80 (1998) 181.
[13] H. Kachkachi, M. Dimian, Phys. Rev. B 66 (2002) 174419.
[14] A. Millan, A. Urtizberea, N.J.O. Silva, F. Palacio, V.S. Amaral, E. Snoeck, V. Serin, J. Magn. Magn. Mater. 312 (2007) L5.
[15] R.C. Woodward, J. Heeris, T.G.St. Pierre, M. Saunders, E.P. Gilbert, M. Rutnakornpituk, Q. Zhang, J.S. Riffle, J. Appl. Cryst. 40 (2007) s495.
[16] P.P. Vaishnava, U. Senaratne, E.C. Buc, R. Naik, V.M. Naik, G.M. Tsoi, L.E. Wenger, Phys. Rev. B 76 (2007) 024413.
[17] D.-X. Chen, A. Sanchez, E. Taboada, A. Roig, N. Sun, H.-C. Gu, J. Appl. Phys. 105 (2009) 083924.
[18] D.-X. Chen, N. Sun, H.-C. Gu, J. Appl. Phys. 106 (2009) 063906.
[19] W. Gong, H. Li, Z. Zhao, J. Chen, J. Appl. Phys. 69 (1991) 5119.
[20] C. Estournes, T. Lutz, J. Happich, T. Quaranta, P. Wissler, J.L. Guille, J. Magn. Magn. Mater. 173 (1997) 83.
[21] X. Sun, A. Gutierrez, M.J. Yacaman, X. Dong, S. Jin, Mater. Sci. Eng. A286 (2000) 157.
[22] D. Gerion, A. Hirt, I.M.L. Billas, A. Chatelain, W.A. de Heer, Phys. Rev. B 62 (2000) 7491.
[23] P. Zhang, F. Zuo, F.K. Urban III, A. Khabari, P. Griffiths, A. Hosseini-Tehrani, J. Magn. Magn. Mater. 225 (2001) 337.
[24] F.C. Fonseca, G.F. Goya, R.F. Jardim, R. Muccillo, N.L.V. Carreo, E. Longo, E.R. Leite, Phys. Rev. B 66 (2002) 104406.
[25] H. Amekura, H. Kitazawa, N. Kishimoto, Nucl. Instr. Methods Phys. Res. B 219–220 (2004) 825.
[26] H. Amekura, Y. Fudamoto, Y. Takeda, N. Kishimoto, Phys. Rev. B 71 (2005) 172404.
[27] Y. Chen, D.L. Peng, D. Lin, X. Luo, Nanotechnology 18 (2007) 505703.
[28] A.C. Johnston-Peck, J. Wang, J. Tracy, ACSNANO 3 (2009) 1077.
[29] F. Davar, Z. Fereshteh, M. Salavati-Niasari, J. Alloys Compd. 476 (2009) 797.
[30] J.I. Langford, D. Louër, P. Scard, J. Appl. Cryst. 33 (2000) 964.
[31] D.-X. Chen, R.B. Goldfarb, J. Appl. Phys. 66 (1989) 2489.
[32] D.-X. Chen, J.A. Brug, R.B. Goldfarb, IEEE Trans. Magn. 27 (1991) 3601.
[33] M.D. Kuz'min, Phys. Rev. Lett. 94 (2005) 107204.
[34] S. Chikazumi, Physics of Ferromagnetism, Oxford University Press, 1997.
[35] I.M.L. Billas, A. Chatelain, W.A. de Heer, Science 265 (1994) 1682.
[36] S.E. Apsel, J.W. Emmert, J. Deng, L.A. Bloomfield, Phys. Rev. Lett. 76 (1996) 1441.
[37] F. Aguilera-Granja, S. Bouarab, M.J. Lopez, A. Vega, J.M. Montejano-Carrizales, M.P. Iniguez, J.A. Alonso, Phys. Rev. B 57 (1998) 12469.

# Magnetophotonic Response of Three-Dimensional Opals

José Manuel Caicedo,[†] Oana Pascu,[†] Martín López-García,[‡] Víctor Canalejas,[‡] Álvaro Blanco,[‡] Cefe López,[‡] Josep Fontcuberta,[†] Anna Roig,[†,*] and Gervasi Herranz[†,*]

[†]Institut de Ciència de Materials de Barcelona (ICMAB-CSIC), Campus UAB, E08193, Bellaterra, Spain and [‡]Instituto de Ciencia de Materiales de Madrid (ICMM-CSIC), Calle Sor Juana Inés de la Cruz 3, Madrid 28049, Spain

Photonic crystals are materials in which the permittivity is periodically modulated on the scale of the optical wavelength, giving rise to a deep modification of the spectral optical response.[1–3] The addition of a magnetic component into these structures, the so-called magnetophotonic crystals (MPCs), has two main interesting effects. On one hand, it breaks time inversion symmetry, allowing nonreciprocal effects in light propagation.[4,5] On the other hand, light is slowed at frequencies of the photonic band edges, strongly increasing the light—matter interaction and enhancing the magneto-optical response.[6–8] The possibility of controlling the light propagation and modifying the magneto-optical spectral response by judicious material design makes the MPCs a very suitable platform for the development of a new generation of fast and compact isolators for optical data transmission and integrated optics.[9]

Along this line it has been demonstrated that the magneto-optical response of one- (1D) and two-dimensional (2D) MPCs is significantly enhanced at band edge frequencies.[10,11] This remarkable result has prompted the investigation of 3D-MPCs in which the periodicity in the three directions could lead to a complete photonic bandgap in the optical region, with an added functionality.[10,12,13] Nevertheless, the achievement of high-quality 3D-MPCs is much more complex and, therefore, the attainment of an optimal (magneto-) optical response—comparable at least to that of 1D-MPCs—remains a challenging issue.[14,15] Early reports on the magneto-optical characterization of 3D-MPCs has revealed some features around the photonic crystal stop-band that have been interpreted generally as a moderate increase of the magneto-optical activity around those frequencies.[16–18] However, little attention has been paid to the eventual occurrence of optical activity in 3D-MPC opals due to their structure and its relevance with respect to the intrinsic

**ABSTRACT** Three-dimensional magnetophotonic crystals (3D-MPCs) are being postulated as appropriate platforms to tailor the magneto-optical spectral response of magnetic materials and to incorporate this functionality in a new generation of optical devices. By infiltrating self-assembled inverse opal structures with monodisperse nickel nanoparticles we have fabricated 3D-MPCs that show a sizable enhancement of the magneto-optical signal at frequencies around the stop-band edges of the photonic crystals. We have established a proper methodology to disentangle the intrinsic magneto-optical spectra from the nonmagnetic optical activity of the 3D-MPCs. The results of the optical and magneto-optical characterization are consistent with a homogeneous magnetic infiltration of the opal structure that gives rise to both a red-shift of the optical bandgap and a modification of the magneto-optical spectral response due to photonic bandgap effects. The results of our investigation demonstrate the potential of 3D-MPCs fabricated following the approach outlined here and offer opportunities to adapt the magneto-optical spectral response at optical frequencies by appropriate design of the opal structure or magnetic field strength.

**KEYWORDS:** photonic crystals · magnetic nanoparticles · magneto-optic enhancers · optical activity

magneto-optical properties. Promising results were earlier reported on 3D photonic crystals impregnated with a Faraday-active transparent liquid.[11,19] Here we present the magnetophotonic response of 3D opals infiltrated with Ni nanoparticles. By exploiting newly developed methodologies to disentangle their intrinsic magneto-optical response from other sources of optical activity, we find a strong modification of the spectral response especially prominent near the photonic band edges.

## RESULTS AND DISCUSSION

**Al₂O₃ Inverse Opals Infiltrated with Ni Nanoparticles.** The 3D-MPCs systems studied consist of $Al_2O_3$ inverse opals infiltrated with monodisperse Ni nanoparticles. For that purpose, two sets of 8 and 15 nm spherical and surfactant-stabilized Ni nanoparticles with good polydispersity of 12% (8 nm (Figure 1a and b)) and 10% (15 nm, data not shown) were synthesized by organometallic thermal decomposition method.[20] The two sets of Ni particles were superparamagnetic at room temperature, as indicated by the zero field
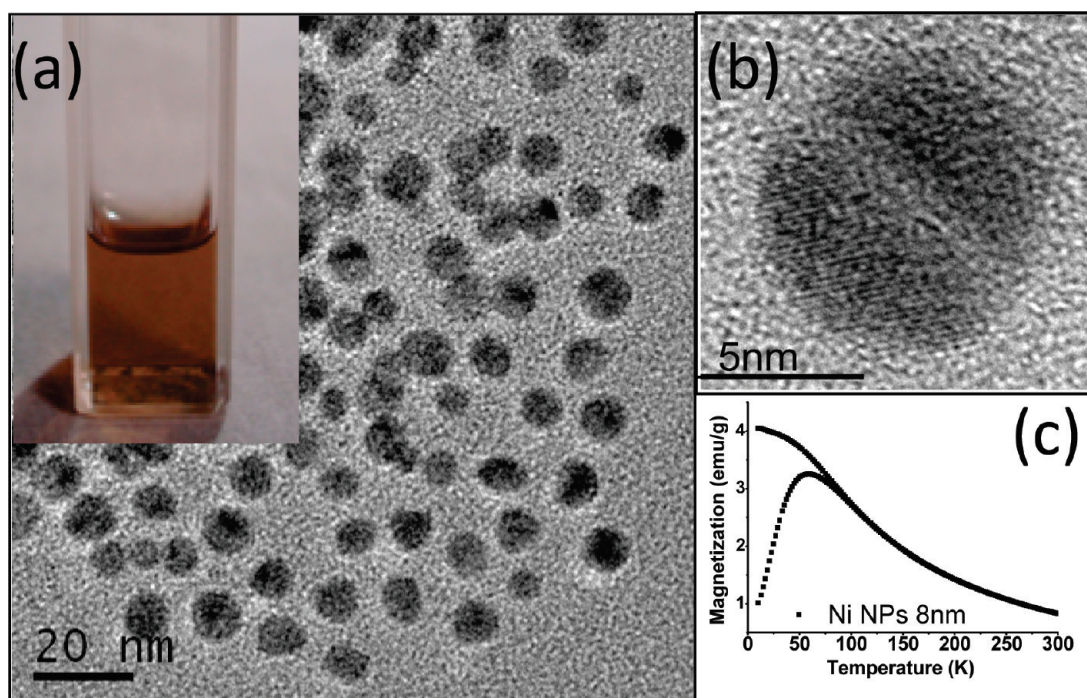
**Figure 1.** (a) Transmission electron microscopy (TEM) image of 8 nm Ni nanoparticles used for the infiltration and the corresponding stable colloidal dispersion image (inset). (b) High-resolution TEM image of a single 8 nm Ni nanoparticle. (c) Zero-field and field (50 Oe) magnetization *versus* temperature curves.

cooled−field cooled magnetization curve corresponding to 8 nm Ni nanoparticles (Figure 1c), with a blocking temperature ($T_B$) of 59 K. The saturation magnetization at 300 K was about 18 and 44 emu/g for 8 and 15 nm particles, respectively (not shown). Using these nanoparticles, the infiltration was done by dipping the inverse opals, described below, into stable colloidal dispersions (see the inset of Figure 1a) by using a step-motor-assisted dip-coating set up.[21,22]

The inverse opals were fabricated by self-assembly of polystyrene spheres (diameter 320 nm) onto hydrophilic glass substrates by standard vertical deposition.[23] Subsequently, conformal $Al_2O_3$ layers with controllable thickness were grown by atomic layer deposition (ALD) around the polystyrene spheres. To leave spherical voids in the $Al_2O_3$ structure, the original organic spheres were removed by dissolution with toluene. The resulting inverse opal was infiltrated with Ni nanoparticles as described above. Figure 2a shows a scanning electron microscope (SEM) overview picture of a typical Ni-infiltrated sample where the three-dimensional fcc compact stacking of the spherical opal units can be clearly appreciated. The same figure also allows discerning the hollow spheres that were broken during the sample preparation, revealing the inverse opal structure. Figure 2b shows an SEM image of the surface of the infiltrated opal. On one hand, Figure 2b noticeably reveals that $Al_2O_3$ forms a very uniform conformal coating on the polystyrene spheres. On the other hand, the tiny bright spots on the spherical surfaces—which are more visible in the zoomed image of the inset of Figure 2b—are the Ni nanoparticles.

SEM cross-sectional images of the 3D-MPCs (Figure 2c) were used to estimate the infiltration homogeneity across the depth of the opals and to determine the void (~288 nm) and the connecting neck (~100 nm) sizes, which are used for filling fraction calculations, $f_{air}$ = 0.87 and $f_{Al2O3}$ = 0.13, of air and alumina, respectively. The original contact points of the polystyrene spheres are clearly visible as the smaller windows in the inverse structure (Figure 2c). The zoom included in the inset of Figure 2c again unambiguously shows the presence of the Ni nanoparticles appearing as small bright spots across the image. This figure reveals also that the $Al_2O_3$ coating is homogeneous and has a thickness of about 15 nm.

**Optical Transmittance: Stop-Band Red-Shift.** The optical and magneto-optical properties of these 3D-MPCs were examined by performing optical transmittance (OT), circular dichroism (CD), and magnetic circular dichroism (MCD) spectroscopy experiments in the range of wavelengths $\lambda$ = 400−800 nm. Although Faraday rotation and ellipticity were also recorded, their signals were largely masked by the large magneto-optical contribution of glass substrates, which made the analysis of the spectra quite difficult. On the contrary, the MCD signal, which in our configuration is proportional to the Faraday ellipticity,[24] was much stronger and was used to track the photonic effects on the magneto-optical spectra. The OT spectra were taken at normal incidence and allowed us to measure the stop-band frequencies of the MPCs. The CD and MCD data were obtained by using a lock-in amplified detection of the light transmitted through the samples using a photoelastic
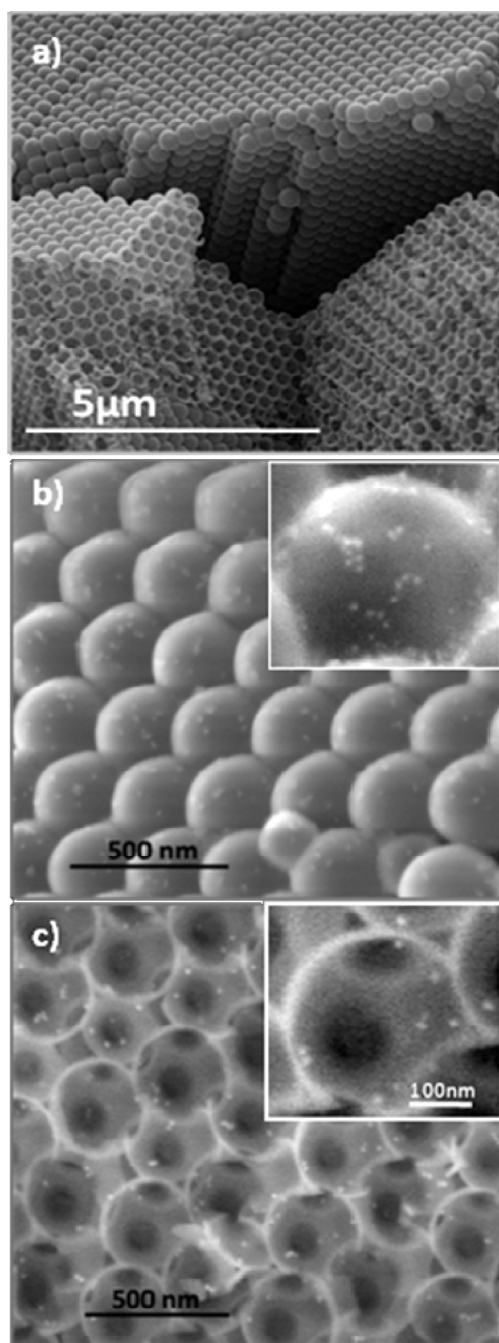
**Figure 2. Scanning electron microscopy images of the opal after infiltration with 8 nm Ni nanoparticles: (a) overview, (b) surface, and (c) cross-section.**

modulator.[20,25,26] In our setup configuration, the first harmonic of the detector signal is proportional to the dichroic (CD or MCD) signal $(I_{RCP} - I_{LCP})/(I_{RCP} + I_{LCP})$, where $I_{RCP}$ and $I_{LCP}$ are the right and left circularly polarized light transmitted through the 3D-MPCs, respectively. We stress that this setup allows the measurement of the optical and magneto-optical spectral response at exactly the same place on the crystals, with a light probe spot size of $\sim$2 mm.[27]

We first performed OT experiments to determine the stop-band frequencies of the crystals. Figure 3 (left axis)

shows the OT for the blank non-infiltrated opal (solid squares) as well as the opals infiltrated with 15 and 8 nm nanoparticle (solid triangles). We note that in Figure 3 the OT and MCD spectra are given in arbitrary units and have been shifted in order to facilitate their visual inspection. This data treatment, however, does not alter at all the conclusions of the combined analysis of the OT and MCD spectral responses discussed below. We observe in Figure 3 that the blank opal exhibits a stop band centered at $\lambda_B \approx 537$ nm, whereas after the infiltration with the Ni nanoparticles the stop band experiences a red-shift. This effect is very weak for the opal infiltrated with 15 nm nanoparticles, whereas it is substantial ($\sim$18 nm shift) for the opals infiltrated with 8 nm nanoparticles. The magnitude of the stop-band red-shift is directly related to the degree of the opal infiltration. To quantify this parameter, we calculated the effective refractive index ($n_{eff}$) of material before and after infiltration, from the experimental $\lambda_B$ red-shift using the Bragg law for a fcc closed packed structure:[28]

$$\lambda_B = 2(2/3)^{1/2}Dn_{eff} \qquad (1)$$

where $D$ is the sphere diameter of the photonic crystal ($D = 316.8$ nm in our case, which is obtained from the addition of the void diameter (288 nm) plus twice the $Al_2O_3$ shell thickness). From eq 1 we obtained $n_{eff} = 1.039$ for the original opal and $n_{eff} = 1.073$ and 1.044 for the opals infiltrated with Ni nanoparticles of 8 and 15 nm, respectively. From these values we could extract the volume fractions $f_{Ni}$ of the infiltrated magnetic nanoparticles by using well-known effective medium approximations, i.e., the Maxwell–Garnett equation[29]

$$\frac{n_{eff}^2 - 1}{n_{eff}^2 + 2} = f_{Ni}\frac{n_{Ni}^2 - 1}{n_{Ni}^2 + 2} + f_{Al_2O_3}\frac{n_{Al_2O_3}^2 - 1}{n_{Al_2O_3}^2 + 2} + f_{air}\frac{n_{air}^2 - 1}{n_{air}^2 + 2} \qquad (2)$$

and Bruggeman equation[30]

$$0 = f_{Ni}\frac{n_{Ni}^2 - n_{eff}^2}{n_{Ni}^2 + 2n_{eff}^2} + f_{Al_2O_3}\frac{n_{Al_2O_3}^2 - n_{eff}^2}{n_{Al_2O_3}^2 + 2n_{eff}^2} + f_{air}\frac{n_{air}^2 - n_{eff}^2}{n_{air}^2 + 2n_{eff}^2} \qquad (3)$$

where we also used the refractive indices of air ($n_{air} = 1$) and bulk Ni ($n_{Ni} = 1.78$). Using the $f_{air}$ and the $f_{Al2O3}$ values described above and the observed red-shift of the gap, the effective filling fraction of Ni has been determined. These estimates were virtually the same for both approaches, eq 2 and eq 3, and yielded $f_{Ni-15 nm} \approx 1.1-1.3\%$ and $f_{Ni-8 nm} \approx 9\%$ for the 3D-MPCs infiltrated with 15 and 8 nm nanoparticles, respectively. The smaller infiltration observed when using the 15 nm nanoparticles is likely related to the fact that when larger particles or higher concentrations are used, some blocking of the connecting necks of the opal takes place. Indeed, smaller filling fractions are also obtained when using 8 nm Ni nanoparticle dispersions of high enough concentrations ($>10^{-3}$ M =
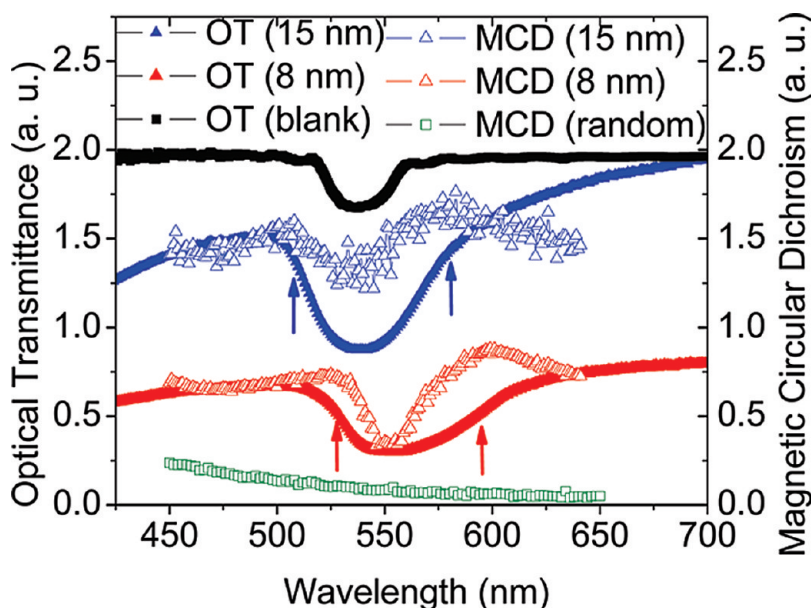
**Figure 3.** Optical transmittance (OT) of a non-infiltrated opal (blank) and opals infiltrated with 15 and 8 nm Ni nanoparticles. The figure also shows the magnetic circular dichroism (MCD) spectra of opals infiltrated with nanoparticles as well as the MCD spectra of Ni nanoparticles distributed randomly on a glass substrate. The arrows indicate the location of the magneto-optical enhancement discussed in the text.
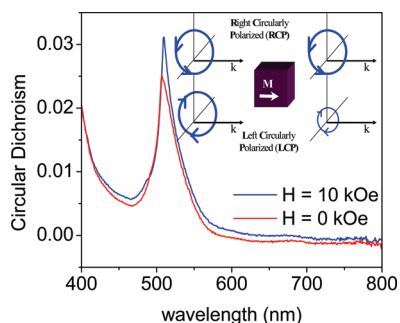


**Figure 4.** Circular dichroism (CD) spectra at zero field and at field $H$ = 10 kOe of an inverse opal infiltrated with 8 nm Ni nanoparticles. The sketch in the inset shows the principle of the CD experiment.

0.1 mg Ni NPs/mL solvent). Thus, optimal infiltration of 3D-MPCs requires small enough nanoparticle size and concentrations.

**Magneto-optical Characterization: Band-Edge Enhancement.** Once the structural quality of the photonic crystals and the efficiency of the infiltration with the magnetic nanoparticles have been assessed, we turn now to the investigation of their functional optical and magneto-optical properties. Following the commonly used approach,[31] we performed CD experiments by recording the intensity of the light transmitted though the opals (see inset of Figure 4) while sweeping the wavelengths in the absence of any magnetic field. For nonoptically active systems a null CD signal should be expected, but due to their particular compact fcc periodic structure, photonic crystals can indeed exhibit a significant CD near the stop-band frequencies, especially at off-normal incidence.[32,33] Here we show that
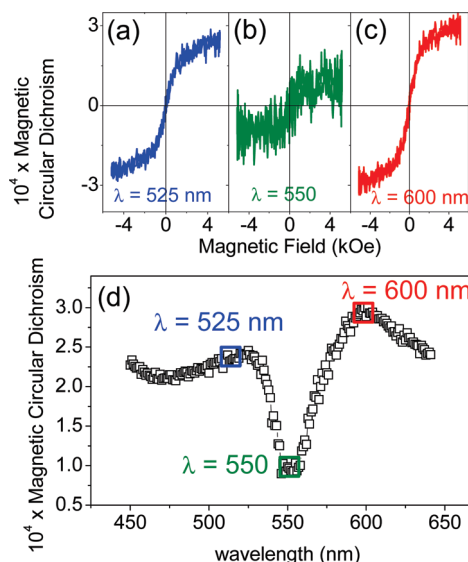


**Figure 5.** Magnetic circular dichroism (MCD) spectrum of an inverse opal infiltrated with 8 nm Ni nanoparticles is shown in (d). The data are obtained from the maximum amplitude of the full MCD hysteresis loops (see panels (a)−(c) for these loops at three selected wavelengths).

this effect can be quite large even at normal incidence. Indeed, we see in Figure 4 that the CD spectrum of the opal infiltrated with 8 nm Ni nanoparticles is significantly large around the stop band. The application of a field of $H$ = 10 kOe (well above the saturation field on the Ni nanoparticles) induces only an additional moderate increase of around 30% of the CD response. Thus, much of the optical activity of these 3D-MPCs has a nonmagnetic origin; it results from the geometry of the opal structure, and thus this technique does not allow

disentangling the distinct contributions to the optical activity. We used then a proper strategy in order to determine the intrinsic magneto-optical response of the crystals. For that purpose, and in order to have the complete information on their magneto-optical properties, we recorded the whole series of full hysteresis MCD loops of the 3D-MPCs with 1 nm step resolution, from $\lambda$ = 400 nm to $\lambda$ = 800 nm. The maximum amplitude of each hysteresis loop was then used to compute the MCD spectral response. As an illustration, we show in Figure 5d the MCD spectrum measured using this procedure, while Figure 5a−c displays the full hysteresis loops at selected wavelengths.

Once the protocol to measure the intrinsic MCD is established, we discuss now the magneto-optical spectral responses of the photonic crystals and their relation to their optical properties. Figure 3 depicts the OT (left axis) and MCD (right axis) spectra obtained at the same spot (diameter ~2 mm) in opals infiltrated with 8 and 15 nm nickel nanoparticles. Additionally, Figure 3 shows the MCD spectrum of a sample consisting of 8 nm nanoparticles distributed randomly on a glass substrate (empty squares). This spectrum is the reference of the MCD response of the Ni nanoparticles free of any crystal-induced photonic effect. Figure 3 immediately reveals a deep modification of the MCD spectra of the two 3D-MPCs with respect to that of the randomly distributed Ni nanoparticles. More specifically, a clear signature is observed of a magneto-optic enhancement in the form of two prominent shoulders in the MCD spectra around the two stop-band edge frequencies (which are indicated by arrows). Note that the frequency shift of the optical stop-band positions of the 3D-MPCs infiltrated with 8 and 15 nm nanoparticles is perfectly reproduced by the shift of the features of the MCD spectra induced by the photonic band effects. Therefore, the intensive modification of the magneto-optical response in close proximity of the band edge frequencies is in agreement with the theoretical predictions[11] and is a direct consequence of the strong increase of light matter interaction due to photonic band flattening and the resulting reduction of the light group velocity at band edge wavelengths.[34] Importantly such response can be tuned by the applied magnetic field. We finally point out that the photonic effect on magneto-optics in the 3D-MPC infiltrated with 8 nm is slightly larger than that of the one infiltrated with 15 nm nanoparticles (Figure 3), in agreement with the larger impregnation of Ni nanoparticles inside the crystal in that case compared to the former.

## CONCLUSIONS

Our results show that an optimal infiltration of inverse opals with magnetic nanoparticles is a powerful strategy to customize the magneto-optical spectral response of magnetic materials. We have demonstrated that our approach can be exploited to generate a tailored magneto-optical response that is operative at least on the order of a few millimeters (the probe light spot size in our experiments). This shows that the structural order required to observe the photonic band induced effects is preserved in the same length scale, which makes still more appealing the approach here described for applications using lasers as light sources. We note that the superparamagnetic properties of the nanoparticles ensure an agile response of our system with the magnetic field, at variance with thin-layer infiltration, where a continuous layer would lead to hysteretic ferromagnetic behavior with more limited agility.

At the same time, a proper design of the geometrical parameters of the opal structure allows the determination at will of the range of wavelengths for which modification of the spectral response is desired. All these features are basic prerequisites for the development of novel optical devices in the field of optical data transmission and processing. As a possible further development in the field, one of the major advances would be to establish whether suitable strategies could be set to increase further the magnetic material content in the opal structures and analyze the impact of larger filling fraction factors in the optical spectral response.

## MATERIALS AND METHODS

**Fabrication of the Inverse Opals.** The template material for the fabrication of the inverse opals was a self-assembled direct opal constituted of polystyrene spheres with 320 nm diameter. These direct opals were assembled by vertical deposition onto a hydrophilic glass substrate. Subsequently, an $Al_2O_3$ shell was infiltrated into this template by atomic layer deposition (ALD),[3] providing conformal layers around the polystyrene spheres of controllable thickness. In each ALD cycle around 1.8 Å was deposited. In our case, 80 cycles of ALD were used, forming an $Al_2O_3$ conformal layer thickness of around 15 nm (see also Figure 2c). Finally, the original polystyrene spheres were removed by dissolution in toluene, leaving spherical voids in the $Al_2O_3$ structure. The final inverse opal structure exhibited connection gate sizes of around 100 nm at the areas where initially the polystyrene spheres were in contact (Figure 2c). These connection gates provided the paths for the diffusion of Ni nanoparticles into the opals during the impregnation.

**Synthesis of Ni Nanoparticles.** Nickel nanoparticles were synthesized by a high-temperature solution-phase method adapting the procedures reported by Chen et al.[35] and Murray et al.[36] In a typical synthesis, 1 mmol (0.257 g) of $Ni(acac)_2$ was added to 7 mL of oleylamine, 2 mmol (0.63 mL) of oleic acid, and 1 mmol (0.45 mL) of trioctylphosphine, and the mixture was heated to 130 °C and stirred magnetically under a flow of high-purity argon. The mixture was kept for 20 min at 130 °C. Afterward, it was further heated up to 250 °C and maintained at this temperature for an

additional 30 min. After cooling to room temperature, the nanoparticles were precipitated by adding extra ethanol, followed by centrifugation. The resulting black precipitate can be redispersed in an organic nonpolar solvent. The precipitate was dried in an oven (at 70 °C) overnight and weighed. Finally, the as-synthesized nickel nanoparticles were kept in a hexane concentrated dispersion of known concentration.

**Infiltration with Magnetic Nanoparticles.** The infiltration was done by dipping the inverse opals into stable colloidal dispersions of two sets of Ni nanoparticles—with size 8 and 15 nm, respectively—and a concentration of $5 \times 10^{-4}$ M (0.03 mg Ni/mL). The degree and homogeneity of the infiltration of the Ni nanoparticles into the inverse opals was controlled by the lifting-up speed (3.6 mm/h in our case), the number of infiltration cycles, and the size and concentration of the nanoparticles in the colloidal dispersion. As described in the main text, SEM cross-sectional pictures (Figure 2c) were instrumental to assess the homogeneity of the infiltration and the calculation of the filling factor fractions.

**Circular Dichroism and Magnetic Circular Dichroism Spectroscopy.** It was performed using a homemade experimental setup.[37,38] The sample reservoir was placed between the poles of an electromagnet. Light from a 150 W Xe arc lamp (ZolixTechnology) was dispersed by a monochromator (Zolix I-150), collimated, and then linearly polarized by the action of a Glan-Thompson prism, which is rotated 45° with respect to the modulator axis of a photoelastic modulator (PEM). After the PEM, the light was transmitted through the sample (with a typical light beam diameter of about ~2 mm) and then went toward a detector. The signal from this detector was brought to a lock-in amplifier synchronized to the frequency of the PEM retardation angle. It can be demonstrated that, in this setup configuration, one can measure the CD and MCD signals by inspection of the first harmonic of the detector signal.

## REFERENCES AND NOTES

1. Yablonovitch, E. Inhibited Spontaneous Emission in Solid-Stated Physics and Electronics. *Phys. Rev. Lett.* **1987,** *58*, 2059–2062.
2. Johnson, S. G.; Joannopoulos, J. D. *Photonic Crystals: The Road from Theory to Practice*; Kluwer: Boston, 2001.
3. Galisteo-López, J. F.; Ibisate, M.; Sapienza, R.; Froufe-Pérez, L. S.; Blanco, A.; López C. Self-Assembled Photonic Structures. *Adv. Mater.* **2011,** *23*, 30−69.
4. Yablonovitch, E. Photonics: One Way Road for Light. *Nature.* **2009,** *461*, 744–745.
5. Wang, Z.; Chong, Y.; Joannopoulos, J. D.; Soljačić, M. Observation of Unidirectional Backscattering-Immune Topological Electromagnetic States. *Nature* **2009,** *461*, 772–775.
6. Takahashi, K.; Kawanishi, F.; Mito, S.; Takagi, H.; Shin, K. H.; Kim, J.; Lim, P. B.; Uchida, H.; Inoue, M. Study on Magnetophotonic Crystals for Use in Reflection-type Magneto-Optical Spatial Light Modulators. *J. Appl. Phys.* **2008,** *103*, 07B331–07B331-3.
7. Boriskina, J. V.; Erokhin, S. G.; Granovsky, A. B.; Vinogradov, A. P.; Inoue, M. Enhancement of the Magnetorefractive Effect in Magnetophotonic Crystals. *Phys. Solid State.* **2006,** *48*, 717–721.
8. Fedyanin, A. A.; Aktsipetrov, O. A.; Kobayashi, D.; Nishimura, K.; Uchida, H.; Inoue, M. Enhanced Faraday and Nonlinear Magneto-Optical Kerr Effects in Magnetophotonic Crystals. *J. Magn. Magn. Mater.* **2004,** *282*, 256–259.
9. Kato, H.; Matsushita, T.; Takayama, A.; Egawa, M.; Nishimura, K.; Inoue, M. Properties of One-Dimensional Magnetophotonic Crystals for Use in Optical Isolator Devices. *IEEE Trans. Magn.* **2002,** *38*, 3246–3248.
10. Inoue, M.; Fujikawa, R.; Baryshev, A.; Khanikaev, A.; Lim, P. B.; Uchida, H.; Aktsipetrov, O; Fedyanin, A.; Murzina, T.; Granovsky, A. Magnetophotonic Crystals. *J. Phys. D: Appl. Phys.* **2006,** *39*, R151–R161.
11. Zvezdin, A. K.; Belotelov, V. I. Magnetooptical Properties of Two Dimensional Photonic Crystals. *Eur. Phys. J. B* **2004,** *37*, 479–487.
12. Mekis, A.; Chen, J. C.; Kurland, I.; Fan, S.; Villeneuve, P.; Joannopoulos, J. D. High Transmission Through Sharp Bends in Photonic Crystal Waveguides. *Phys. Rev. Lett.* **1996,** *77*, 3787–3790.
13. Noda, S.; Tomoda, K.; Yamamoto, N.; Chutinan, A. Full Three-Dimensional Photonic Bandgap Crystals at Near-Infrared Wavelengths. *Science* **2000,** *289*, 604–606.
14. Liu, N.; Guo, H.; Fu, L.; Kaiser, S.; Schweizer, H.; Giessen, H. Three-Dimensional Photonic Metamaterials at Optical Frequencies. *Nat. Mater.* **2008,** *7*, 31–37.
15. Fang, M.; Volotinen, T. T.; Kulkarni, S. K.; Belova, L.; Rao, K. V. Effect of Embedding $Fe_3O_4$ Nanoparticles in Silica Spheres on the Optical Transmission Properties of Three-Dimensional Magnetic Photonic Crystals. *J. Appl. Phys.* **2010,** *108*, 103501–103501-6.
16. Pavlov, V. V.; Usachev, P. A.; Pisarev, R. V.; Kurdyukov, D. A.; Kaplan, S. F.; Kimel, A. V.; Kirilyuk, A.; Rasing, Th. Enhancement of Optical and Magneto-Optical Effects in Three-Dimensional Opal/$Fe_3O_4$ Magnetic Photonic Crystals. *Appl. Phys. Lett.* **2008,** *93*, 072502–072503.
17. Šimkiene, I.; Reza, A.; Kindurys, A.; Bukauskas, V.; Babonas, J.; Szymczak, R.; Aleshkevych, P.; Franckevicius, M.; Vaišnoras, R. Magnetooptics of Opal Crystals Modified by Cobalt Nanopartilces. *Lith. J. Phys.* **2010,** *50*, 7–15.
18. Pavlov, V. V.; Usachev, P. A.; Pisarev, R. V.; Kurdyukov, D. A.; Kaplan, S. F.; Kimel, A. V.; Kirilyuk, A.; Rasing, Th. Optical Study of Three-Dimensional Magnetic Photonic Crystals Opal/$Fe_3O_4$. *J. Magn. Magn. Mater.* **2009,** *321*, 840–842.
19. Koerdt, C.; Rikken, G. L. J. A.; Petrov, E. P. Faraday Effect of Photonic Crystals. *Appl. Phys. Lett.* **2003,** *82*, 1538–1540.
20. Pascu, O.; Caicedo, J. M.; Fontcuberta, J.; Herranz, G.; Roig, A. Magneto-Optical Characterization of Colloidal Dispersions. Application to Nickel Nanoparticles. *Langmuir* **2010,** *26*), 12548–12552.
21. García, P. D.; Blanco, A.; Shavel, A.; Gaponik, N.; Eychmüller, A.; Rodríguez-González, B.; Liz-Marzán, L. M.; López, C. Quantum Dot Thin Layers Templated on ZnO Inverse Opals. *Adv. Mater.* **2006,** *18*, 2768–2772.
22. Caicedo, J. M.; Taboada, E.; Hrabovsky, D.; Lopez-Garcia, M.; Herranz, G.; Roig, A.; Blanco, A.; Lopez, C.; Fontcuberta, J. Facile Route to Magnetophotonic Crystals by Infiltration of 3D Inverse Opals with Magnetic Nanoparticles. *J. Magn. Magn. Mater.* **2010,** *322*, 1494–1496.
23. Jiang, P.; Bertone, J. F.; Hwang, K. S.; Colvin, V. L. Single-Crystal Colloidal Multilayers of Controlled Thickness. *Chem. Mater.* **1999,** *11*, 2132–2140.
24. Scott, G. B.; Lacklison, D. E.; Ralph, H. I.; Page, J. L. Magnetic Circular Dichroism and Faraday Rotation Spectra of $Y_3Fe_5O_{12}$. *Phys. Rev. B* **1975,** *12*, 2562–2571.
25. Stephens, P. J. Magnetic Circular Dichroism. *Annu. Rev. Phys. Chem.* **1974,** *25*, 201–232.
26. Caldwell, D.; Thorne, J. M.; Eyring, H. Magnetic Circular Dichroism. *Annu. Rev. Phys. Chem.* **1971,** *22*, 259–278.
27. By performing the optical and magneto-optical measurements on exactly the same location we avoided the effects associated with any eventual infiltration spatial inhomogeneities in the photonic crystals.
28. Minguez, H.; López, C.; Meseguer, F.; Blanco, A.; Vázquez, L.; Mayoral, R.; Ocaña, M.; Fornés, V.; Mifsud, A. Photonic Crystal Properties of Packed Submicrometric $SiO_2$ Spheres. *Appl. Phys. Lett.* **1997,** *71*), 1148–1150.
29. Garnett, J. C. M. Colours in Metal Glasses and in Metallic Films. *Philos. Trans. R. Soc. London, Ser. A* **1904,** *203*, 385–420.

30. Bruggeman, D. A. G. Berechnung verschiedener physikalischer Konstanten von heterogenen Substanzen. I. Dielektrizitätskonstanten und Leitfähigkeiten der Mischkörper aus Isotropen Substanzen. *Ann. Phys. (Leipzig)* **1935,** *416*, 636–664.

31. Mason, W. R. *Magnetic Circular Dichroism Spectroscopy*; Wiley: New York, 2007.

32. Gottardo, S.; Burresi, M.; Geobaldo, F.; Pallavidino, L.; Giorgis, F.; Wiersma, D. S. Self-Alignment of Liquid Crystals in Three-Dimensional Photonic Crystals. *Phys. Rev. E.* **2006,** *74*), 040702–040702-4.

33. Reza, A.; Simkiene, I.; Vaisnoras, R.; Lopez, C.; Golmayo, D.; Babonas, J. Optical Anisotropy of Synthetic Opals. *Photonics Nanostruct.* DOI: 10.1016/j.photonics.2010.10.003.

34. Galisteo-López, J.; Galli, M.; Patrini, M.; Balestreri, A.; Andreani, L.; López, C. Effective Refractive Index and Group Velocity Determination of Three-Dimensional Photonic Crystals by Means of White Light Interferometry. *Phys. Rev. B* **2006,** *73*, 125103–125103-9.

35. Chen, Y.; Peng, D. L.; Lin, D.; Luo, X. Preparation and Magnetic Properties of Nickel Nanoparticles via the Thermal Decomposition of Nickel Organometallic Precursor in Alkylamines. *Nanotechnology* **2007,** *18*, 505703–505708.

36. Murray, C. B.; Sun, S.; Doyle, H.; Betley, T. Colloidal Synthesis of Nanocrystals and Nanocrystals Superlatices. *IBM J. Res. Dev.* **2001,** 47–56.

37. Caicedo, J. M.; Dekker, M. C.; Dörr, K.; Fontcuberta, J.; Herranz, G. Strong Magnetorefractive and Quadratic Magneto-Optical Effects in $(Pr_{0.4}La_{0.6})_{0.7}Ca_{0.3}MnO_3$. *Phys. Rev. B* **2010,** *82*, 140410–140414.

38. Caicedo, J. M.; Arora, S. K.; Ramos, R.; Shvets, I. V.; Fontcuberta, J.; Herranz, G. Large Magnetorefractive Effect in Magnetite. *New J. Phys.* **2010,** *12*, 103023–103023-8.

**PAPER**

# Ultrathin conformal coating for complex magneto-photonic structures†

**Oana Pascu,[a] José Manuel Caicedo,[a] Martín López-García,[b] Víctor Canalejas,[b] Álvaro Blanco,[b] Cefe López,[b] Jordi Arbiol,[ac] Josep Fontcuberta,[a] Anna Roig[*a] and Gervasi Herranz[*a]**

We report on an extremely fast and versatile synthetic approach, based on microwave assisted sol–gel chemistry, that allows a conformal nanometric coating of intricate three-dimensional structures. Using this methodology, we have achieved a conformal coverage of large areas of three-dimensional opals with a superparamagnetic manganese ferrite layer, yielding magneto-photonic crystals with excellent quality. The use of a ternary oxide for the ultrathin coating demonstrates the potential of this methodology to realize three-dimensional structures with complex materials that may find applications beyond photonics, such as energy, sensing or catalysis.

## 1. Introduction

Keeping long-range structural order along the three dimensions (3D) is essential for the development of composite systems for different emerging areas, including metamaterials, magnonics, phononics and photonics.[1–4] Opals are one example of 3D ordering of sub-micronic spheres that have received much attention in recent years and which have strongly impacted the field of photonics. Fine tailoring of the photonic band gap and/or achieving new functionalities requires an appropriate coating of the 3D-opal structure by suitable materials while keeping the required high quality 3D structures. This is extremely challenging.[1,5,6] The most widespread methods to obtain 3D composite structures are atomic layer deposition, thermal chemical vapor deposition, electrodeposition[7] as well as deposition in aqueous solutions.[8–10] These methods, however, are limited by either the amount of available reagents and their relatively simple chemical formulations or the required long unpractical processing times.[8] We show here that microwave chemistry[11,12] is a very efficient method to achieve fast conformal ultrathin coating of opals with multivalent complex oxides, adding new functionalities to these photonic structures. Even though magnetophotonics is targeted here, applications to other areas, such as energy, as sensors or catalysis can be envisioned.

The addition of functional materials into photonic structures is an emergent field of research. In particular, the incorporation of magnetic materials in photonic crystals gives rise to intriguing new possibilities, including non-reciprocal optical effects[13] and large magneto-optical responses at the stop-band edge frequencies[14–16] with large potential in applications for optical communications. The promising results reported for one- (1D) and two-dimensional (2D) magneto-photonic crystals (MPCs)[17,18] have spurred research on 3D photonic crystals, in which the periodicity in the three dimensions should allow a better integration in devices with an enhanced functionality.[6,7,17,19] Nevertheless, efforts aimed at the achievement of 3D-MPCs are challenged by the difficulty of having the required high-quality long-range structure along the three directions in space and high magnetic content.[9,20–24]

Here, we report on a microwave assisted benzyl alcohol route that has allowed us the growth, in just a few minutes, of a stoichiometric and homogeneous conformal nanometric coating covering extensive areas—at least on the order of cm²—of the 3D photonic crystals. The coating is formed by superparamagnetic $MnFe_2O_4$ nanoparticles and does not require any post-synthesis material processing (note that bulk $MnFe_2O_4$ is ferrimagnetic with a Curie temperature of ~560 K).[25] The resulting materials exhibit unambiguously enhanced magneto-photonic response at band edge frequencies and a magneto-optical response tunable by magnetic fields.

## 2. Experimental section

### 2.1 Microwave synthesis protocol

A non-aqueous benzyl alcohol route for ferrite nanoparticles, adapted from the one first reported by Niederberger,[12] was used. The microwave experiments were carried out using a CEM Discover reactor (Explorer 12-Hybrid) operating at a frequency of 2.45 GHz and a power of 200 W. Photonic crystals (direct $SiO_2$ and inverse $Al_2O_3$ opals) of about 5 mm × 5 mm in size grown on a glass slide substrate were vertically immersed in the reaction solution using a 10 ml closed pressurized vessel. The reaction media contained 0.3 mmol (sample I2) or 0.15 mmol (samples D1

*[a]Institut de Ciència de Materials de Barcelona (ICMAB-CSIC), Campus UAB, E08193 Bellaterra, Spain. E-mail: gherranz@icmab.es; roig@icmab.es*
*[b]Instituto de Ciencia de Materiales de Madrid (ICMM-CSIC), Calle Sor Juana Inés de la Cruz 3, Madrid, 28049, Spain*
*[c]Institució Catalana de Recerca i Estudis Avançats (ICREA), E08010 Barcelona, Spain*

and I1) of iron(III) acetylacetonate (Fe(acac)$_3$) and the stoichiometric quantity of manganese(II) acetate (Mn(ac)$_2$) with a total concentration of 0.3 M or 0.15 M in 1.5 ml of anhydrous benzyl alcohol. During a typical run, the power is automatically adjusted to heat the sample to 170 °C and the temperature is kept stable for 5 min. After the reaction takes place, the solution is automatically cooled to 60 °C by compressed nitrogen. Temperature and pressure are controlled by a volume independent infrared sensor.

## 2.2 Fabrication of direct and inverse opals

SiO$_2$ direct opals were fabricated by vertical deposition onto 1 cm width hydrophilic glass from a 1% (w/w) solution in ethanol at 55 °C and 60% relative humidity of the environment (in the oven). SiO$_2$ spheres of 260 nm diameter, synthesized by the Stöber method,[26] were used for the opal fabrication. Regarding the fabrication of Al$_2$O$_3$ inverse opals, direct opals of 320 nm (I1 and I2) and 276 nm (I1′) polystyrene spheres constituted the template for the inverse opal. The spheres were assembled by vertical deposition onto a hydrophilic glass substrate followed by infiltration of Al$_2$O$_3$ by atomic layer deposition (ALD, Savannah S100 Cambridge NanoTech Inc). Reactants for alumina growth, i.e., trimethylaluminium (TMA) and water, were kept at room temperature. The sample, in the ALD vacuum chamber at 90 °C, was exposed to alternate TMA and water pulses (each with a duration of 10 ms). Each TMA–water cycle was followed by 5 s waiting time to ensure complete diffusion through the sample followed by 5 s chamber evacuation. The rate of alumina growth was about 0.18 nm per cycle as estimated by ellipsometry measurements. In our case, 80 cycles of ALD were used, forming an Al$_2$O$_3$ layer around 15 nm thickness. The inverse opals were produced by dissolving the polystyrene spheres with toluene.

## 2.3 Electron microscopy analysis

Transmission electron microscopy (TEM) was used for morphological and structural characterization. The high-resolution TEM images were obtained with a Jeol2010F field emission gun microscope working at 200 keV with a point to point resolution of 0.19 nm. The sample was prepared by scratching the coated opals and dispersing them in ethanol. Subsequently, after an ultrasound bath, a few drops of the solution were deposited on a TEM carbon grid, allowing the solvent to evaporate. During this TEM preparation, a significant portion of the oxide coating on the spheres was detached and, indeed, we observed in the TEM images a large amount of nanoparticles over the filaments of the carbon grids, probably deposited there after being separated from the opal surface during the preparation. Selected area diffraction patterns (SADP) were captured using a JEOL JEM-2011, operating at 200 kV.

SEM images were acquired using a Quanta FEI 200F microscope in low vacuum mode with a cone LOW kV P.L.A. type with 500 μm aperture. The working conditions were: an acceleration voltage of 10–20 kV, an electron beam spot of 2–2.5, a pressure of 50 Pa and a distance of 5–6 mm.

## 2.4 Magnetic circular dichroism

It was performed using a homemade experimental setup.[27,28] The sample on a holder was placed between the poles of an electromagnet. Light from a 150 W Xe arc lamp (ZolixTechnology) is dispersed by a monochromator (Zolix l-150), collimated, and then linearly polarized by the action of a Glan-Thompson prism, which is rotated 45° with respect to the modulator axis of a photo-elastic modulator (PEM). After the PEM, the light is transmitted through the sample (with a typical light beam diameter of about ∼2 mm) and then goes toward a detector. The signal from this detector is brought to a lock-in amplifier synchronized to the frequency of the PEM retardation angle. It can be demonstrated that, in this setup configuration, one can measure the CD and MCD signals by inspection of the first harmonic of the detector signal.

## 3. Results and discussion

### 3.1 Microwave coating of opals

Microwave heating represents an attractive non-conventional energy source to perform chemical synthesis due to the high acceleration of the chemical reaction and the high yield obtained.[29,30] It is based on the ability of some compounds to absorb electromagnetic energy and to transform it into heat. While a domestic microwave has a multimode cavity producing a non-homogeneous heating of the cavity, the one for chemical synthesis is specially designed for a single mode, resulting in a uniform heating of the cavity. Compared to other conventional heating methods (heating plates and oil bath), the microwave radiation affects only the solvent and reactants, passing through the reaction vessel without heating it and avoiding any temperature gradients. While non-polar substances are not heated, microwaves produce a rapid, intense heating of polar substances permitting to have selective heating modes. In addition, microwaves induce molecular vibration and a subsequent temperature increase causing a greater movement of the molecules, a higher diffusivity and collision probability. Based on the heating selectivity and the increase of the molecular motion, complex nanostructured materials can be fabricated, as for instance, infiltration/doping of a structured/porous material with *in situ* synthesized secondary phase.[29,30] As a particular case, in this work we present *in situ* deposition of ferrite nanoparticles on preformed photonics crystals. The solvent used, benzyl alcohol, was employed for the first time as a microwave absorbing substance for iron oxide nanoparticle synthesis by Niederberger.[31] The preformed photonic crystals used by us were SiO$_2$ direct opals and Al$_2$O$_3$ inverse opals. In both cases, the hydroxyl terminated oxide surfaces of the Al$_2$O$_3$ and SiO$_2$ scaffolds are more susceptible to absorb microwave energy than the bulk of the material, activating in this way the opal surfaces and promoting the nucleation and the growth of the magnetic nanoparticles on these surfaces.

Before attempting the microwave-assisted growth of MnFe$_2$O$_4$ in photonic structures, the synthesis of self-standing ferrite nanoparticles has been optimized by adapting the non-aqueous sol–gel chemical reaction first reported by Niederberger *et al.*[9,32] Details of the synthesis as well as the material characterization are included in the Experimental section in the ESI†. By means of X-ray diffraction and magnetometry we identified the spinel structure of the nanoparticles with a mean diameter of ∼5 nm (Fig. S1, ESI†). Pristine opals, direct (SiO$_2$) and inverse (Al$_2$O$_3$), with a period of 366 nm and 465 nm, respectively, and volumes of

~5 mm × 5 mm × ~0.5 μm were grown on glass slides by using known procedures.[26,33] Pristine direct opals have been labeled as D0 and inverse ones as I0. To load the opals with magnetic content, they were immersed in the reaction microwave vessel using iron(III) acetylacetonate and manganese(II) acetate as precursors. Two metal precursor concentrations were investigated while keeping the same microwave setup parameters: D1 and I1 refer to direct and inverse magnetic opals using a 0.15 M concentration and I2 when the concentration was 0.3 M.

Fig. 1 shows a series of scanning electronic microscopy (SEM) pictures of direct (Fig. 1a and b) and inverse (Fig. 1c and d) opals. The inspection of the images of the surface (Fig. 1a and c) and the cross-section (Fig. 1b and d) allows us to confirm the homogeneous and uniform coverage of the opal structures. The absence of coating in some particular places highlights the uniformity of the magnetic layer. For instance, the white circle at the right-hand side lower corner of Fig. 1a (direct opal) shows a small area where the coating is not complete; the coating is also absent in the contact points between two opal spheres (see Fig. 1b). Cross-sectional SEM pictures displayed in Fig. 1b–d show that the coating also reaches the deeper part of the

crystals. Indeed SEM images obtained at different points over the cross-section—at the top, middle and bottom layers of the photonic crystals—show the continuous manganese ferrite layer visible until the bottom part of the direct opal (Fig. 2). A clue to the nature of this uniform conformal coverage is given by the observed superparamagnetic behavior that confirms that the coating is composed of magnetic nanoparticles. This conclusion is further confirmed by transmission electron microscopy (TEM) experiments. Fig. 1e displays a TEM image with an expanded view of the top of one of the silica particles forming the direct opal structure of Fig. 1a, where the ferrite nanoparticles can be observed. The analysis by means of high-resolution TEM confirms the expected cubic spinel structure. Indeed, selected area electron diffraction peaks (inset of Fig. 1e) can be indexed in the $MnFe_2O_4$ inverse spinel phase. A detailed HRTEM analysis was carried out on one of the nanoparticles oriented along the [001] zone axis (see a magnified detail in Fig. 1f), presenting the {220} and {400} family planes, further confirming the spinel structure. Electron energy loss spectroscopy (EELS) also corroborates the coating of the opal surfaces with $MnFe_2O_4$ nanoparticles (see Fig. S2 and S3 in the ESI†).

Previous works have also reported fairly high magnetic loads of nanoparticles embedded in direct opals, although the homogeneity of the infiltration was not fully addressed and long processing times (>24 h) were required.[8,9,23] In contrast, our 3D-MPCs have comparable volume fractions of the magnetic material—up to ~50% for direct opals, processed at a much faster speed—typically less than 30 min—and forming a quasi-ideal conforming coating. Additionally, no further thermal treatment of the composite material was required, since the magnetic material exhibited the desired inverse spinel crystalline phase structure ($MnFe_2O_4$). The degree of magnetic coverage



Fig. 1 Surface and cross-sectional SEM images have been obtained for direct (a and b) as well as inverse opals (c and d). Surface and cross-sectional SEM pictures assess the quality and uniformity of this coverage. (e) High-resolution TEM general image of one silica nanoparticle surface showing high density of crystalline ferrite nanoparticles. The inset corresponds to a selected area electron diffraction pattern obtained on the silica spheres. (f) Magnified detail of one of the inverse spinel nanoparticles.



Fig. 2 (a) Overview SEM picture of direct opal (D1). Cross-sectional SEM pictures of the upper (b), middle (c) and bottom (d) layers of the photonic crystals. These images prove that the conformal $MnFe_2O_4$ magnetic coating is uniform across the depth of the photonic crystals.

could be achieved by controlling either the opal thickness or the duration of the reaction. First, the opal fabrication method by vertical colloidal self-assembly deposition yields opals with different thicknesses which in turn influences the microwave magnetic coating thickness. We have exploited this feature to find a magnetic loading with optimal functional properties. Fig. S4 in the ESI† presents SEM images of D1 material with different coverage degrees (a) as well as the optical (b) and magneto-optical measurements (c). On the other hand, Fig. S5 in the ESI† shows 3D-SiO$_2$ opals coated with $\gamma$-Fe$_2$O$_3$ nanoparticles where the influence of the reaction time on the degree of magnetic material coverage can be observed.

## 3.2 Optical and magneto-optical characterization

The excellent quality of the 3D-MPCs and the optimal coating with a magnetic layer revealed by the SEM and TEM images of Fig. 1 and 2 anticipates an optimal magneto-photonic response. To assess their functional properties, we have performed optical transmittance (OT) and magnetic circular dichroism (MCD) spectroscopy experiments in a range of wavelengths $\lambda = 400$–800 nm.[34] The spectra were taken at the same place (spot size $\approx$ 2 mm) to avoid the effects associated with any eventual spatial inhomogeneity.
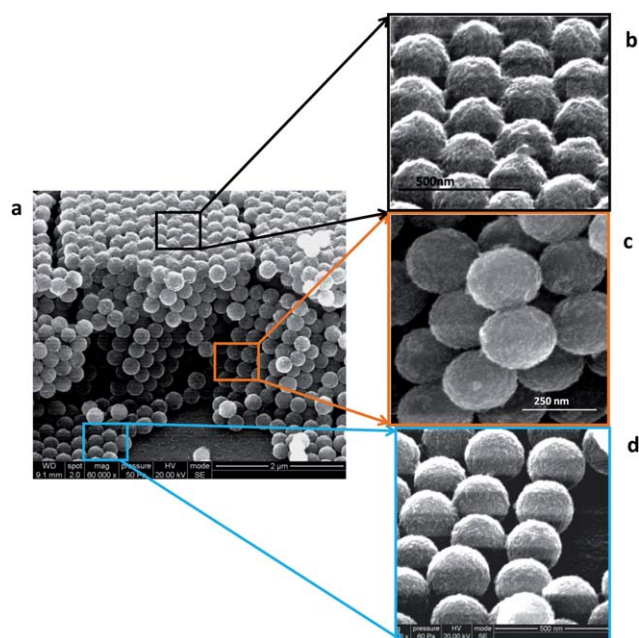
OT experiments were undertaken to determine the stop-bands of the photonic crystals and to assess the influence of the magnetic coverage fraction on the optical properties. Although similar results were found in direct opals (see Fig. S4b in the



**Fig. 3** Optical transmission (a) and magnetic circular dichroism (MCD) (b) data of the inverse opal structures I0–I2. I0 is the blank opal without magnetic content, whereas I1 and I2 are opals with different concentrations of magnetic loading (see the text). The different degrees of coating (see SEM pictures on panels (c–e) on the cross-section of the infiltrated inverse opals) and the resulting different amounts of magnetic material infiltration can be monitored by optical measurements through the progressive red-shift of the optical stop band (a). The inset of (b) shows a MCD hysteresis loop measured at $\lambda = 600$ nm. The maximum value of these loops (at $H = 1$ Tesla) for each wavelength was used to plot the MCD spectra shown in (b).

ESI†), here we focus on the results obtained in the series of inverse opals (I0–I2). Fig. 3a shows the transmittance spectra of the pristine inverse opal (I0) as well as two magnetic opals with different concentrations (I1 and I2). We observe in Fig. 3a the presence of minima of the transmittance that signals the frequencies at which the stop-bands are centered. Thus the pristine I0 opal has the stop band centered on $\lambda_B \approx 517$ nm, whereas for the magnetic opals I1 and I2 the stop-bands are centered on $\lambda_B \approx 524$ nm and $\lambda_B \approx 534$ nm, respectively, revealing a red-shift due to the increasing magnetic coverage of the structures. Indeed, an inspection of the cross-sectional SEM images (Fig. 3c–e) demonstrates clearly how the shell thickness of the magnetic coating becomes larger with a major magnetic loading. We used these SEM cross-sectional images to determine the void ($\sim$300 nm) and the connecting window ($\sim$100 nm) diameters as well as the filling fractions $f_{air} = 0.87$ and $f_{Al2O3} = 0.13$ of air and alumina, respectively, in the inverse opal structures. These data were then used to quantify the magnetic filling fraction factors of the magnetic opals from the $\lambda_B$ red-shift using the same method as we described previously,[35] yielding $f_{I1} = 0.0287$ (4.7% of the available pore volume) and $f_{I2} = 0.0704$ (11.5%) for I1 and I2, respectively. We show therefore that large magnetic load of the opals can be achieved and that the load can be controlled by the initial concentration of the precursors.

To obtain the intrinsic magneto-optic response of opals—free of the optical activity inherent in their structure (ref. 36)—we recorded the whole series of full MCD hysteresis loops for wavelengths in the visible range and obtained the MCD spectral response from the amplitude of the loops. Following this approach, we have observed a null MCD spectral signal on the blank inverse opal I0, as expected from the absence of magnetic content in this sample (Fig. 3b). Instead, the samples loaded with the magnetic content (I1 and I2) exhibit MCD loops (inset of Fig. 3b). We have measured these loops for a range of wavelengths and plot the MCD spectral response from their amplitude signal (open circles, Fig. 3b). We observe that an intricate structure appears in the MCD spectra around the stop-band regions (Fig. 3a), indicating that a magneto-photonic response develops due to the interplay of the photonic and magneto-optical properties.

To better understand the relationship between the photonic band structure and magneto-optics, we compare the magneto-photonic response of direct and inverse opals. Fig. 4 shows the MCD spectra (right axis) of a direct SiO$_2$ opal of 366 nm periodicity and 10.4% filling factor (D1, Fig. 4a) and two Al$_2$O$_3$ inverse opals of different periodicity, 465 nm with 4.7% filling factor (I1, Fig. 4b) and 276 nm with 0.6% (labeled as I'1, it was processed in the same conditions as I1, Fig. 4c). Fig. 4 also includes the OT spectra (left axis) of each of these crystals as well as the MCD spectrum of MnFe$_2$O$_4$ nanoparticles distributed randomly on a glass substrate. The latter gives the magneto-optical response of MnFe$_2$O$_4$ nanoparticles in the absence of any photonic effect. A common feature observed for all the magnetic opals is that the MCD response is deeply modified with respect to that of the randomly distributed nanoparticles, indicating that the photonic band structure of the crystals radically influences the magneto-optical properties of the manganese ferrite nanoparticles. Interestingly, we observe that the magneto-optical signal is enhanced at the stop-band edges (even for very low
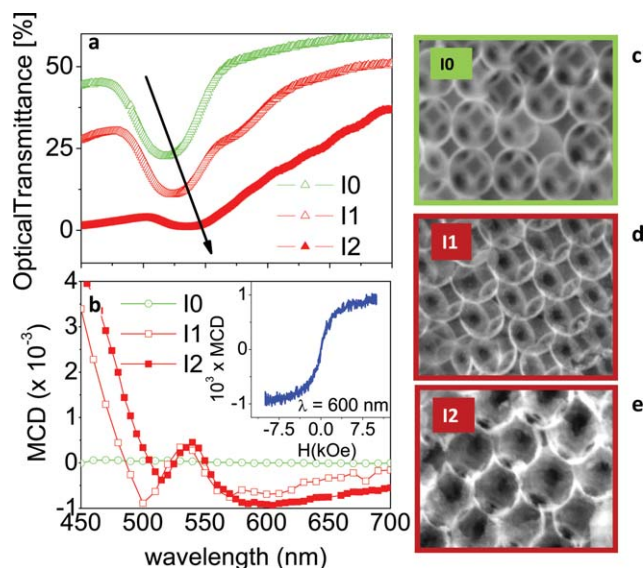
**Fig. 4** MCD and OT spectra obtained in a direct opal D1 (a) and two different inverse opals I1 (b) and I′1 (c) with different periodicity. Panel (a) also includes the MCD spectra of a blank opal without magnetic loading (empty red triangles). All of them show anomalous features at the stop band edges (the stop band area is shaded), although the major effects are seen in inverse opals. We show in these figures the spectra of randomly distributed $MnFe_2O_4$ nanoparticles (black solid circles) that are the reference of the magneto-optic spectral response free of any magneto-photonic effect.

filling factor), as observed in the shaded areas of Fig. 4. This signal enhancement is particularly large in the inverse opals, and more specifically for the opal I′1 where two prominent shoulders are well visible, indicating that in the vicinity of the band-edge frequencies the influence of the photonic structure on the magneto-optics is very intense. An important observation is that the optical transmittance of the inverse opals is larger than that of the direct opal. A huge magneto-photonic effect in combination with a good optical transmittance makes these complex materials very appealing for applications in optical communications.

Finally, note that all the materials comprising the photonic structures here described are dielectric and, thus, such structures do not support the propagation of surface plasmon polaritons. Thus, the enhanced magneto-optical response is the result of the strong interaction of light with the structure close to the photonic band frequencies (where the Bragg reflection condition is

fulfilled), rather than coupling to plasmons, as recently reported for other systems combining magnetic materials and noble metals.[37] The use of a dielectric photonic crystal to enhance the magneto-optic signal has the advantage of minimizing the optical losses that otherwise would be detrimental for many applications in optical communications.

## 4. Conclusions and outlook

We have presented an extremely fast and versatile microwave assisted sol–gel route to achieve the conformal coverage of large areas of three-dimensional opals with a superparamagnetic manganese ferrite layer. The use of a ternary oxide for ultrathin coating demonstrates the potential of this methodology to realize three-dimensional structures with complex materials. The resulting materials exhibit unambiguously enhanced magneto-photonic response at band edge frequencies and a magneto-optic response tunable by magnetic fields. The strategy presented here will contribute to the rapidly expanding field of advanced techniques for the fabrication of three-dimensional complex systems needed in different fields such as in photonics, phononics, metamaterials or data storage. The approach could also be relevant for some applications in materials for energy, as for instance in sensors, or in catalysis where a full coverage with functional materials on intricate topologies is crucial to boost the device performance.

## References

1 M. Farsari and B. N. Chichkov, *Nat. Photonics*, 2009, **3**, 450–452.
2 V. V. Kruglyak, S. O. Demokritov and D. Grundler, *J. Phys. D: Appl. Phys.*, 2010, **43**, 264001.
3 E. Yablonovitch, *Nature*, 2009, **461**, 744–745.
4 J. B. Pendry, D. Schurig and D. R. Smith, *Science*, 2006, **312**, 1780–1782.
5 A. Blanco, E. Chomski, S. Grabtchak, M. Ibisate, S. John, S. W. Leonard, C. Lopez, F. Meseguer, H. Miguez, J. P. Mondia, G. A. Ozin, O. Toader and H. M. van Driel, *Nature*, 2000, **405**, 437–440.
6 S. Noda, K. Tomoda, N. Yamamoto and A. Chutinan, *Science*, 2000, **289**, 604–606.
7 X. Yu, Y.-J. Lee, R. Furstenberg, J. O. White and P. V. Braun, *Adv. Mater.*, 2007, **19**, 1689–1692.
8 S. A. Grudinkin, S. F. Kaplan, N. F. Kartenko, D. A. Kurdyukov and V. G. Golubev, *J. Phys. Chem. C*, 2008, **112**, 17855–17961.
9 V. V. Pavlov, P. A. Usachev, R. V. Pisarev, D. A. Kurdyukov, S. F. Kaplan, A. V. Kimel, A. Kirilyuk and Th. Rasing, *Appl. Phys. Lett.*, 2008, **93**, 072502–072503.

10  A. V. Baryshev, T. Kodama, K. Nishimura, H. Uchida and M. Inoue, *J. Appl. Phys.*, 2004, **95**, 7336–7338.

11  I. Bilecka and M. Niederberger, *Nanoscale*, 2010, **2**, 1358–1367.

12  I. Bilecka, M. Kubli, E. Amstad and M. Niederberger, *J. Sol-Gel Sci. Technol.*, 2011, **57**, 313–322.

13  Z. Wang, Y. Chong, J. D. Joannopoulos and M. Soljačić, *Nature*, 2009, **461**, 772–775.

14  K. Takahashi, F. Kawanishi, S. Mito, H. Takagi, K. H. Shin, J. Kim, P. B. Lim, H. Uchida and M. Inoue, *J. Appl. Phys.*, 2008, **103**, 07B331.

15  J. V. Boriskina, S. G. Erokhin, A. B. Granovsky, A. P. Vinogradov and M. Inoue, *Phys. Solid State*, 2006, **48**, 717–721.

16  A. A. Fedyanin, O. A. Aktsipetrov, D. Kobayashi, K. Nishimura, H. Uchida and M. Inoue, *J. Magn. Magn. Mater.*, 2004, **282**, 256–259.

17  M. Inoue, R. Fujikawa, A. Baryshev, A. Khanikaev, P. B. Lim, H. Uchida, O. Aktsipetrov, A. Fedyanin, T. Murzina and A. Granovsky, *J. Phys. D: Appl. Phys.*, 2006, **39**, R151–R161.

18  A. K. Zvezdin and V. I. Belotelov, *Eur. Phys. J. B*, 2004, **37**, 479–487.

19  A. Mekis, J. C. Chen, I. Kurland, S. Fan, P. Villeneuve and J. D. Joannopoulos, *Phys. Rev. Lett.*, 1996, **77**, 3787–3790.

20  N. Liu, H. Guo, L. Fu, S. Kaiser, H. Schweizer and H. Giessen, *Nat. Mater.*, 2008, **7**, 31–37.

21  M. Fang, T. T. Volotinen, S. K. Kulkarni, L. Belova and K. V. Rao, *J. Appl. Phys.*, 2010, **108**, 103501–103506.

22  I. Šimkiene, A. Reza, A. Kindurys, V. Bukauskas, J. Babonas, R. Szymczak, P. Aleshkevych, M. Franckevicius and R. Vaišnoras, *Lith. J. Phys.*, 2010, **50**, 7–15.

23  V. V. Pavlov, P. A. Usachev, R. V. Pisarev, D. A. Kurdyukov, S. F. Kaplan, A. V. Kimel, A. Kirilyuk and Th. Rasing, *J. Magn. Magn. Mater.*, 2009, **321**, 840–842.

24  J. M. Caicedo, E. Taboada, D. Hrabovsky, M. Lopez-Garcıa, G. Herranz, A. Roig, A. Blanco, C. Lopez and J. Fontcuberta, *J. Magn. Magn. Mater.*, 2010, **322**, 1494–1496.

25  Z. X. Tang, C. M. Sorensen, K. J. Klabunde and G. C. Hadjipanayis, *Phys. Rev. Lett.*, 1991, **67**, 3602.

26  J. F. Galisteo-López, M. Ibisate, R. Sapienza, L. S. Froufe-Perez, A. Blanco and C. López, *Adv. Mater.*, 2011, **23**, 30–69.

27  J. M. Caicedo, M. C. Dekker, K. Dörr, J. Fontcuberta and G. Herranz, *Phys. Rev. B: Condens. Matter Mater. Phys.*, 2010, **82**, 140410–140414.

28  J. M. Caicedo, S. K. Arora, R. Ramos, I. V. Shvets, J. Fontcuberta and G. Herranz, *New J. Phys.*, 2010, **12**, 103023–103028.

29  A. de la Hoz, A. Diaz-Ortiz and A. Moreno, *Chem. Soc. Rev.*, 2005, **34**, 164–178.

30  P. Lidstrom, J. Tierney, B. Wathey and J. Westman, *Tetrahedron*, 2001, **57**, 9225–9283.

31  N. Pinna, S. Grancharov, P. Beato, P. Bonville, M. Antonietti and M. Niederberger, *Chem. Mater.*, 2005, **17**, 3044–3049.

32  I. Bilecka and M. Niederberger, *Chem. Commun.*, 2008, 886–888.

33  P. Jiang, J. F. Bertone, K. S. Hwang and V. L. Colvin, *Chem. Mater.*, 1999, **11**, 2132–2140.

34  O. Pascu, J. M. Caicedo, J. Fontcuberta, G. Herranz and A. Roig, *Langmuir*, 2010, **26**, 12548–12552.

35  J. M. Caicedo, O. Pascu, M. López-García, V. Canalejas, A. Blanco, C. López, J. Fontcuberta, A. Roig and G. Herranz, *ACS Nano*, 2011, **5**, 2957–2963.

36  A. Blanco, C. López, R. Mayoral, H. Míguez, F. Meseguer and J. Herrero, *Appl. Phys. Lett.*, 1998, **73**, 1781–1783.

37  V. I. Belotelov, I. A. Akimov, M. Pohl, V. A. Kotov, S. Kasture, A. S. Vengurlekar, A. V. Gopal, D. R. Yakovlev, A. K. Zvezdin and M. Bayer, *Nat. Nanotechnol.*, 2011, **6**, 370–376.

## SHORT COMMUNICATION

# 2D Magnetic Frames Obtained by the Microwave-Assisted Chemistry Approach

# Oana Pascu,[a] Martí Gich,[a] Gervasi Herranz,[a] and Anna Roig*[a]

Microwave chemistry is becoming a very attractive synthesis technique in many areas of synthetic chemistry. In particular, the utilization of this method to fabricate nanostructured materials is a fast growing research area with immense potential. Similarly, the use of sacrificial scaffolds has been demonstrated as an effective route to achieve intricate 2D and 3D porous architectures. Here, we present an extremely fast and versatile synthetic approach based on microwave heating to fabricate complex macroporous magnetic frames using sacrificial templates. In just a few minutes, a stoichiometric and homogeneous conformal nanometric coating of superparamagnetic nanoparticles was grown onto a 2D monolayer formed by self-assembled polystyrene colloids. No post-treatment was required, the sacrificial polystyrene template was removed simultaneously as the magnetic nanoparticles formed, and large-scale structural order was preserved.

## Introduction

Fabrication of nanostructured materials by using sacrificial scaffolds, against which another material is deposited by mimicking the original template, has been demonstrated as effective and versatile approach towards achieving complex 2D and 3D porous architectures.[1–2] Among those, 2D or 3D arrays of inorganic hollow spheres can display interesting optical, optoelectronic, magnetic, electric, or catalytic properties.[3] For such applications, the preservation of the long-range order of the nanostructure is essential. Templating over polymer colloids is a commonly used strategy to achieve long-range order, although it presents the drawback of having to remove the template either by solvent dissolution, etching, or calcination, which in turn could damage the intended hollow structure.

Microwave energy is becoming a very attractive tool in all areas of synthetic chemistry. It has been used not only for organic[4] and inorganic[5] nanoparticle synthesis but also for the fabrication of high-quality nanocrystals and large-scale defect-free complex nanostructures with controllable morphologies and surfaces.[6] Other intricate nanoarchitectures, such as nanoporous materials,[7] superstructures,[6] or 3D magneto photonic opals[8] have also been reported.

In this communication, we describe a facile and fast microwave-assisted sol–gel chemical approach to produce two-dimensional hollow magnetic frames using sacrificial templates. The method has allowed us to grow, in just a few minutes, a stoichiometric and homogeneous conformal nanometric coating of manganese ferrite on a polystyrene template over an area of half a square centimeter. No post-treatment was required – the sacrificial template is removed simultaneously with the formation of magnetic nanoparticles.

## Results and Discussion

The fabrication of complex nanostructures by microwave heating is becoming an area of intense research and great potentiality in synthetic chemistry. In addition to drastically decreasing the time for the synthesis, the technique offers a combination of kinetics and selectivity characteristics that can be used advantageously, such as: (i) the acceleration of the chemical reaction rate, (ii) the heating selectivity – polar substances absorb electromagnetic radiation and are intensively heated while the non-polar ones do not absorb it, and (iii) the high diffusivity of the molecular species in solution facilitates the conformal deposition onto intricate frames. We have recently demonstrated some of those features on the fabrication of three-dimensional magnetic photonic crystals by microwave synthesis, where direct $SiO_2$ and inverse $Al_2O_3$ photonic crystals have been uniformly infiltrated with in situ synthesized magnetic oxide nanoparticles.[8]

Here, we describe the conformal coverage with small superparamagnetic $MnFe_2O_4$ nanoparticles of a 2D structure resulting from self-assembled polystyrene (PS) spheres coated with a thin $Al_2O_3$ layer (10 nm). A schematic representation of the synthesis steps and the resulting magnetic frame is displayed in Scheme 1.

The two-dimensional polystyrene colloidal template, vertically immersed in a solution containing the solvent and the organometallic precursors, was subjected to microwave

[a] Institut de Ciència de Materials de Barcelona (ICMAB-CSIC)
Campus UAB,
08193 Bellaterra, Spain
Fax: +34-93-5805729
E-mail: roig@icmab.es

WILEY ONLINE LIBRARY

# SHORT COMMUNICATION

O. Pascu, M. Gich, G. Herranz, A. Roig
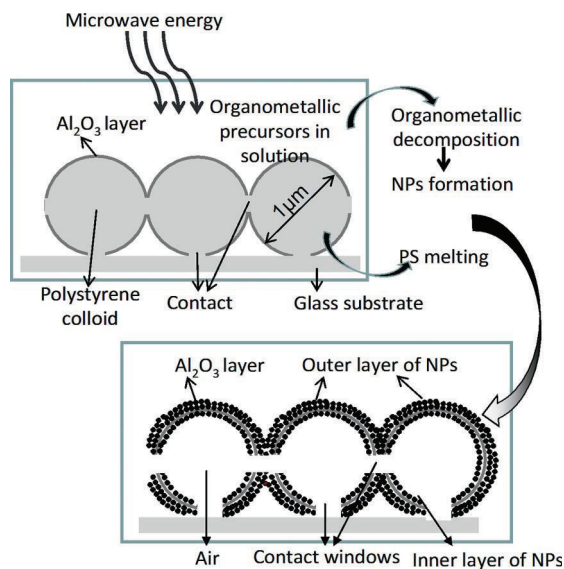


Scheme 1. Schematic representation of the fabrication process.

radiation for a few minutes. The solvent (benzyl alcohol), being a polar substance, absorbs the microwave radiation and increases its temperature, which promotes the decomposition of the organometallic precursor and nanoparticle formation. By coating the PS spheres with a thin layer of an oxide ($Al_2O_3$ in this case), we gain two additional advantageous effects. Firstly, because PS has a glass transition at about 95–100 °C[9] and starts melting above this temperature,[10] the PS template melts during the microwave synthesis at 160 °C and thus the $Al_2O_3$ frame keeps the mechanical stability of the structure. Secondly, the hydroxy surface terminations of the alumina efficiently absorb the microwave energy, which activates the surface and selectively promotes nucleation and growth of the magnetic nanoparticles on it. Thus, a final 2D hollow structure with a conformal magnetic coating is obtained. When the 2D template is made only of PS spheres, a non polar compound, the coating is not effective, and the template is not mechanically strong during particle deposition.

Prior to the discussion of the characteristics of the magnetic frames, the characterization of the nanoparticles is reported. As explained in the Experimental Section, non-attached $MnFe_2O_4$ nanoparticles could be separated from the reaction media by adding oleic acid once the reaction had taken place and thus stable colloidal dispersions in hexane were obtained after centrifugation and washing steps.[11] Transmission electron microscopy (Figure 1a) reveals small nanoparticles with good polydispersity and a rather irregular shape. A size distribution, fitted to a Gaussian function, gives an average size of $4.0 \pm 0.8$ nm (Figure 1b). The low polydispersity in the distribution of particle sizes is most probably a consequence of the rather uniform formation of nuclei as well as the uniform nanoparticle growth in the microwave reactor. The powder X-ray diffractogram (inset of Figure 1a) and selected area electron diffraction pattern (SADP) (Figure 1c) can be indexed with that of the cubic inverse spinel manganese ferrite phase (ICDD PDF075-

0035). The magnetic properties of the nanoparticles were evaluated by measuring the magnetization vs. the magnetic field strength at 300 K (Figure 1d) and the zero-field-cooled (ZFC), field-cooled (FC) magnetization curves (Figure 1d inset) vs. temperature. The absence of remnant magnetization at room temperature indicates the superparamagnetic character of the nanoparticles. The low blocking temperature at 26 K corresponds to very small nanoparticles, which is in agreement with the TEM data.
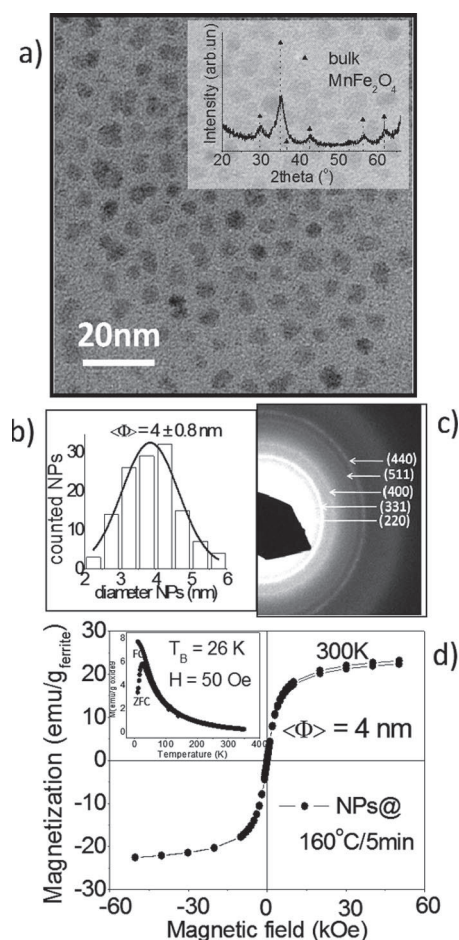


Figure 1. $MnFe_2O_4$ nanoparticles stabilized in organic media. (a) TEM image of monodisperse nanoparticles stabilized with oleic acid; the inset shows the powder X-ray diffratogram of these nanoparicles, (b) size distribution fitted to a Gaussian function, (c) the corresponding electron diffraction pattern, (d) magnetometry data; M(H) at room temperature and ZFC–FC curves at 50 Oe.

With regard to the 2D magnetic frames, the first observation is that the thickness of the coating can be controlled by the duration of the chemical reaction. Scanning electron microscopy (SEM) was used to study the surface of the magnetic frames at different reaction times (Figure 2). The PS template covered by the thin $Al_2O_3$ shell (about 10 nm) presents a very smooth surface (Figure 2a and inset). The reaction at 160 °C for 2 min results in partial coverage of the template (bright spots on the sphere surface) (Figure 2b and inset). The reaction with the same precursor concentration (0.1 M) at the same temperature (160 °C) but with a

longer reaction time (5 min) produces a complete conformal coating (Figure 2c). Higher magnification (inset of Figure 2c) confirms that the layer is conformal, continuous and consists of small nanoparticles. By increasing the reaction time to 10 min, the coverage increases to such an extent that the nanostructures are no longer evident and a continuous film is formed instead.

At that point, if the growth continues, every sphere starts pushing against its neighbors, and cracks begin to appear in the nanostructure, as clearly seen in Figure 2d.

The next issue addressed is what happens to the PS template during the chemical reaction that forms the nanoparticles. A close observation of the pristine template reveals that the PS spheres are in contact, and, therefore, the alumina will not be deposited on these contact areas (see Scheme 1 and Figure 2a). Because PS is not very soluble in benzyl alcohol,[12] we assume that the disappearance of the PS during microwave heating results from a melting process.
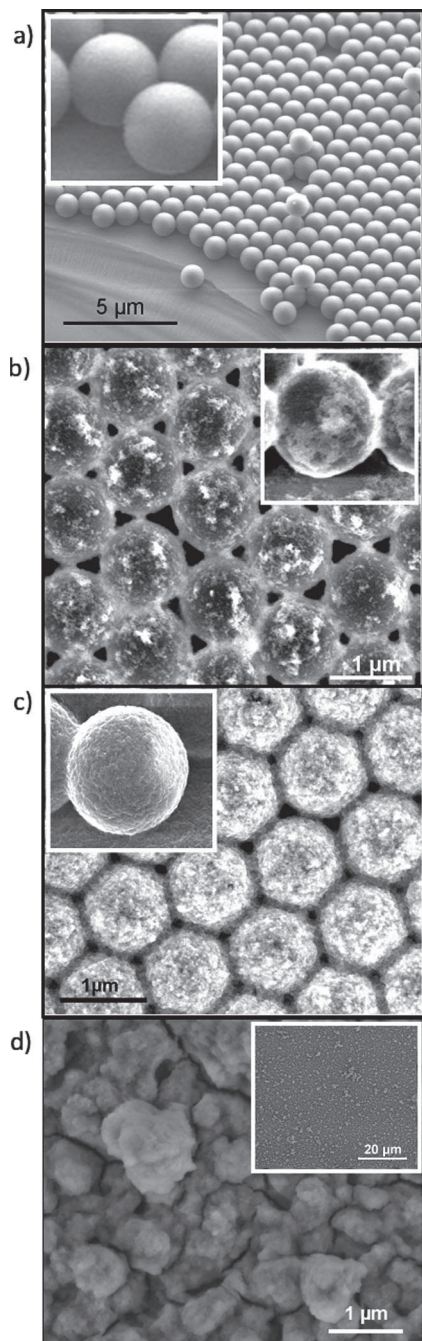


Figure 2. The various coverage thicknesses depending on the duration of the chemical reaction are visualized by SEM micrographs. (a) The pristine opal; a higher magnification is included in the inset. (b) Partial magnetic coverage of the opal obtained at 160 °C/2 min; the inset shows one sphere in more detail. (c) Homogeneous magnetic coverage of the 2D template obtained at 160 °C/5 min; the inset shows in better detail the conformal uniform coating as a single sphere. (d) A thick magnetic film is formed at 160 °C/10 min over the 2D template; the inset shows a smaller magnification (scale bar 20 μm) of the film surface.
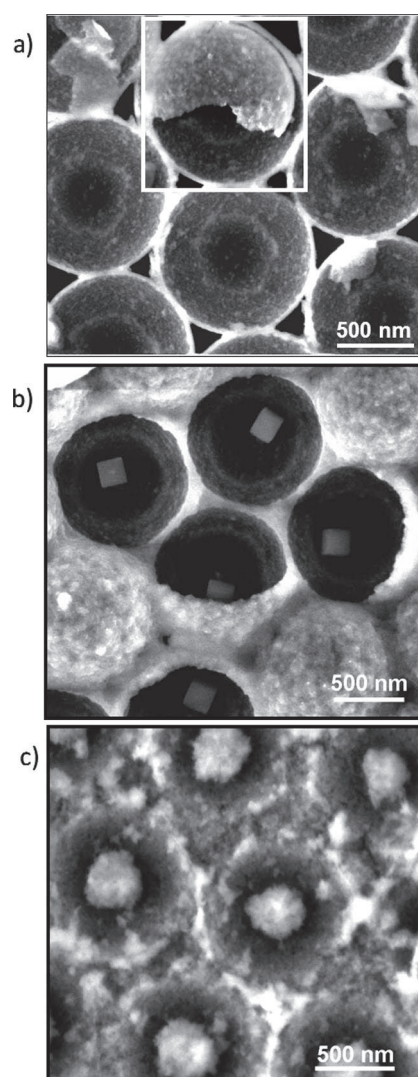


Figure 3. SEM images of the transversal section across the spheres, which reveals the morphology within the hollow spheres. (a) The material with a bright $Al_2O_3$ shell (160 °C/2 min); the white spots uniformly distributed on the inner wall are nanoparticles. (b) Spheres with a thicker deposition within the spheres (5 min reaction). The cube inside is made of PS melted and recrystallized during the reaction. (c) After a 10-min chemical reaction under microwaves MW, the PS spheres disappear completely. The white spots inside the spheres are nanoparticle aggregates.

# SHORT COMMUNICATION

O. Pascu, M. Gich, G. Herranz, A. Roig

Since the microwave experiment is a very fast process – the full cycle does not take longer than 15 min – we can also safely assume that the melting of the PS and the nucleation and growth of the nanoparticles occur simultaneously. When the PS melts, the contact areas between two PS spheres become contact windows, which allows the diffusion of the organometallic precursors inside the spheres and consequently the formation of nanoparticles at the inner side of the alumina takes place. This could be verified by the images taken from a transversal section across the templates (Figure 3). In the case of a 2-min reaction, it can be seen that the PS is only partially melted, and a small quantity of nanoparticles uniformly distributed (bright spots) inside the spheres can be observed (Figure 3a). By increasing the reaction time to 5 min, more nanoparticles are deposited on the outer shell and inner shell, a large fraction of the PS is melted, which leaves big voids, and a

small fraction of the PS recrystallizes at the center of the spheres in the form of small cubes (Figure 3b).[13] For a 10-min reaction time, the majority of the PS is melted, and large aggregates of nanoparticles accumulate at the center of the sphere (Figure 3c). To certify the coverage of the PS colloidal template with magnetic material, elemental analysis by energy dispersive X-ray spectroscopy (EDX) of the different materials was performed (Figure 4). The spectrum of the pristine template on a glass substrate is displayed in Figure 4a; naturally, iron and manganese peaks are not present. Figure 4b shows the spectrum, obtained at 160 °C over 10 min, of a thick magnetic film that completely covers the template, in which the Fe and Mn peaks are clearly visible. Figure 4c-A corresponds to the spectra (the scanned area represented by the square A of the template covered by a thinner ferrite layer, prepared at 160 °C over 5 min, and the intensity of the Fe and Mn peaks is smaller than in the previous case. Finally, Figure 4c-B corresponds to the spectrum of a cube inside the sphere (marked with a white cross), which reveals that no Mn and Fe is present in this area.

## Conclusions

We have reported on a facile, rapid, and inexpensive microwave-assisted approach to fabricate large areas of high–quality, hollow, two-dimensional magnetic frames using sacrificial colloidal templates. We have proved that in addition to short reaction times, the technique offers other characteristics in terms of reaction kinetics, molecular diffusion, and selectivity, which can be used to enhance the potentiality of such a synthetic chemistry approach. The method has allowed the growth, in just a few minutes, of a stoichiometric and homogeneous conformal nanometric manganese ferrite coating of tenths of square millimeters. The coating thickness can be controlled by controlling the time of the reaction. No post-treatment was required – the sacrificial template is removed simultaneously as the magnetic nanoparticle coating is formed.

## Experimental Section

**Microwave Synthesis:** The microwave experiments were carried out by using a CEM Discover reactor (Explorer 12-Hybrid) operating at a frequency of 2.45 GHz and with a power of 200 W. The template, polystyrene beads covered with a thin $Al_2O_3$ layer grown by atomic layer deposition, self-assembled in one monolayer with an area of 5 × 5 mm onto a glass slide substrate, were vertically immersed in the reaction solution by using a 10-mL closed pressurized vessel. The reaction media contained the organometallic precursors, iron(III) acetylacetonate [Fe(acaca)$_3$] and manganese(II) acetate [Mn(ac)$_2$] (molar ratio of Fe/Mn = 2:1) with a total concentration of 0.1 M in anhydrous benzyl alcohol (1.5 mL). During a typical run, the power was automatically adjusted to heat the sample to 160 °C, and the temperature was kept stable for 2, 5, or 10 min. After the reaction took place, the solution was automatically cooled to 50 °C by compressed nitrogen. The temperature and the pressure were controlled by a volume-independent infrared sensor.



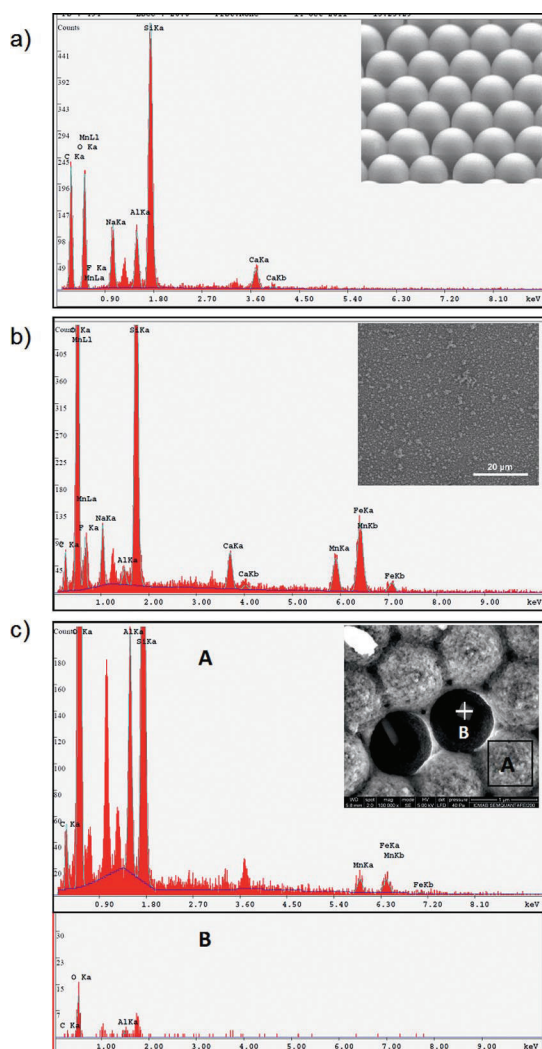Figure 4. EDX spectra for different materials: (a) the template of pristine PS + $Al_2O_3$ on a glass substrate; (b) magnetic film completely covering the template obtained at 160 °C/10 min; (c-A) spectra corresponding to the template covered by a ferrite layer at 160 °C/5 min. (c-B) spectra for the cube inside the sphere, no Mn and Fe are present.

The $Al_2O_3$ layer was deposited by ALD (Savanah 100 system by Cambridge Nanotech). Reactants for alumina growth, i.e. trimethylaluminum (TMA) and water were kept at room temperature. The PS monolayer was placed in the ALD chamber at 100 °C, under a $N_2$ flow of 20 sccm and exposed to continuous TMA and water pulses (0.15 s each). Every TMA/water cycle was followed by a waiting time of 8 s, to ensure the complete reaction of the species on the exposed surface of the sample. Hundred cycles were performed as the rate of alumina growth is about 0.1 nm per cycle, which yields an alumina layer of 10 nm. Non-attached nanoparticles were also separated from the reaction media. Briefly, the reaction solution was mixed with excess EtOH (in a volume ratio of 1:3) and surfactant (20 µL, oleic acid for organic dispersion) followed by centrifugation at 6000 rpm for 30 min. The supernatant was discharged, and the precipitate redispersed in hexane (2 mL) containing oleic acid (10 µL) followed by centrifugation at 6000 rpm for 15 min. No precipitate was separated, and the stable dark brown solution was used for further analysis.

**Material Characterization:** TEM micrographs were obtained with a JEOL JEM-1210 electron microscope, operating at 120 kV. The selected area diffraction patterns were captured by using a JEOL JEM-2011, operating at 200 kV. The samples were prepared by depositing a drop of diluted nanoparticle dispersion in hexane onto a TEM grid and by letting the solvent evaporate. The mean diameter and polydispersity of each system were determined by fitting a particle size histogram of over 200 counts measured from TEM images to a Gaussian distribution by using the imageJ software. Template SEM images were acquired by using a Quanta FEI 200F microscope in low vacuum mode with a cone LOW kV P.L.A. with a 500-µm aperture. The working conditions were: acceleration voltage 5 kV, electron beam spot 2, pressure 40 Pa, and distance 5–6 mm. For the EDX analysis, 10–15 kV, a spot of 2.5–3, and a distance of 10 mm were used. Magnetic characterization was performed with a quantum interference device (SQUID) magnetometer (Quantum Design MPMS5XL). The sample was prepared by using a gelatin capsule filled with compacted cotton impregnated with 150 µL of a hexane dispersion of nanoparticles, which gave a mass of 1.2 mg (magnetic material without surfactant).

## Acknowledgments

[1] a) M. H. Kim, J. Y. Choi, H. K. Choi, S. M. Yoon, O. O. Park, D. K. Yi, S. J. Choi, H. J. Shin, *Adv. Mater.* **2008**, *20*, 457–461; b) Y. Wang, A. S. Angelatos, F. Caruso, *Chem. Mater.* **2008**, *20*, 848–858.

[2] a) Y. Xia, Y. Lu, K. Kamada, B. Gates, Y. Yin in *The Chemistry of Nanostructured Materials* (Ed.: P. Yang), Worl Scientific, Singapore, **2003**, pp. 69–101; b) M. Agrawal, S. Gupta, M. Stamm, *Mater. Chem.* **2011**, *21*, 615–627; c) R. J. White, R. Luque, V. L. Budarin, J. H. Clark, D. J. Macquarrie, *Chem. Soc. Rev.* **2009**, *38*, 481–494.

[3] a) J. Hu, M. Chen, X. Fang, L. Wu, *Chem. Soc. Rev.* **2011**, *40*, 5472–5491; b) J. M. Campelo, D. Luna, R. Luque, J. M. Marinas, A. A. Romero, *ChemSusChem* **2009**, *2*, 18–45.

[4] a) L. Perreux, A. Loupy, *Tetrahedron* **2001**, *57*, 9199–9223; b) V. Polshettiwar, M. N. Nadagouda, R. S. Varma, *Aust. J. Chem.* **2009**, *62*, 16–26.

[5] a) M. Tsuji, S. Hikino, M. Matsunaga, Y. Sano, T. Hashizume, H. Kawazumi, *Mater. Lett.* **2010**, *64*, 1793–1797; b) T. Yamauchi, Y. Tsukahara, T. Sakata, H. Mori, T. Yanagida, *Nanoscale* **2010**, *2*, 515–523; c) L. Xiao, H. Shen, R. von Hagen, J. Pan, L. Belkoura, S. Mathur, T. Kawaic, Y. Wada, *Chem. Commun.* **2010**, *46*, 6509–6511; d) P. Nekooi, M. Akbari, M. K. Amini, *Int. J. Hydrogen Energy* **2010**, *35*, 6392–6398; e) I. Bilecka, M. Kubli, E. Amstad, M. Niederberger, *J. Sol-Gel Sci. Technol.* **2011**, *57*, 313–322; f) C. Gonzales-Arellano, A. M. Balu, R. Luque, D. J. Macquarrie, *Green Chem.* **2010**, *12*, 1995–2002.

[6] a) Z. Ai, K. Deng, Q. Wan, L. Zhang, S. Lee, *J. Phys. Chem. C* **2010**, *114*, 6237–6242; b) X. Hu, J. C. Yu, J. Gong, *J. Phys. Chem. C* **2007**, *111*, 11180–11185; c) X. Hu, J. C. Yu, *Chem. Mater.* **2008**, *20*, 6743–6749; d) S. Q. Chen, Y. Wang, *J. Mater. Chem.* **2010**, *20*, 9735–9739; e) C. Gonzales-Arellano, R. Luque, D. J. Macquarrie, *Chem. Commun.* **2009**, *30*, 4581–4583.

[7] a) G. A. Tompsett, W. C. Conner, K. S. Yngvesson, *ChemPhysChem* **2006**, *7*, 296–319; b) C. Yacou, A. Ayral, A. Giroir-Fendler, M.-L. Fontaine, A. Julbe, *Microporous Mesoporous Mater.* **2009**, *126*, 222–227.

[8] O. Pascu, J. M. Caicedo, M. Lopez-Garcia, V. Canalejas, A. Blanco, C. Lopez, J. Fontcuberta, A. Roig, G. Herranz, *Nanoscale* **2011**, *3*, 4811–4816.

[9] J. Rieger, *J. Therm. Anal.* **1996**, *46*, 965–972.

[10] K. Y. Suh, H. Yoon, H. H. Lee, A. Khademhosseini, R. Langer, *Appl. Phys. Lett.* **2004**, *85*, 2643–2645.

[11] O. Pascu, E. Carenza, M. Gich, G. Herranz, A. Roig, submitted.

[12] S. Gündüz, S. Dinçer, *Polymer* **1980**, *21*, 1041–1046.

[13] a) X. Gao, R. Liu, Y. Huang, O. Starykov, W. Oppermann, *Macromolecules* **2008**, *41*, 2554–2560; b) H. Wu, W. Wang, H. Yang, Z. Su, *Macromolecules* **2007**, *40*, 4244–4249; c) E. M. Woo, Y. S. Sun, M. L. Lee, *Polymer* **1999**, *40*, 4425–4429.

Received: November 7, 2011
Published Online: ■

# SHORT COMMUNICATION

O. Pascu, M. Gich, G. Herranz, A. Roig

The fabrication of porous magnetic nanoarchitectures by microwave heating is reported. In addition to drastically decreasing the time for the synthesis, other characteristics of the technique, i.e. reaction kinetics, diffusivity and selectivity, have been exploited.

## 6.2. ANNEX ii –brief description of characterization techniques and the protocol used

*Magnetic nanoparticles analysis.* Since several analysis techniques (**XRD, TGA, SQUID**) require the sample in the powder form, it was needed to transfer the nanoparticles from colloidal dispersion (the usual storage was in 2ml hexane dispersion with a known concentration) in the dry from, by the following procedure: 500 µl dispersion of around 10 mg/ml concentration was evaporated in an Ependorf tube, using a vacuum dryer in a several filling/drying cycles in order to obtained 500 µl hexane dispersion of around 40 mg/ml concentration. From this solution, a volume of 50 to 200 µl colloidal dispersion (depending on the technique) was evaporated directly on the sample holder. The details are written in the description of each technique (see below). A suggestion is that the evaporation to be performed at room temperature in vacuum or in the hood to avoid the errors regarding the exact weight value of the analyzed material, since the Ependorf tube and other holders (e.g. gelatin tubes for SQUID) can modify their weight by heating.

### A.ii.1 X-ray diffraction patterns (XRD)

*Nickel nanoparticles,* the X-ray diffraction patterns were performed in liquid form, by placing 100 µl colloidal dispersions (concentration about 10 mg/ml for 8 nm Ni NPs and 5mg/ml for 15 nm Ni NPs) in a thin borosilicate capillary tubes[a] (0.2 mm) and using a BRUKER-AXS D8 (ICMAB) Advanced model diffractometer with cupper K$\alpha$ incident radiation ($\lambda_{K\alpha 1}$=1.54 Å) and a GADDS bi dimensional detector (collimator 0.3 mm, conditions 40 KV and 40 mA). The higher sensitivity of this instrument allows measuring very small amounts of sample. It is commonly named microdiffractometer. The experimental time is much shorter than with the Rigaku diffractometers (seconds vs. minutes/hours). It measures discrete frames of 30 2$\theta$ degrees. To study larger ranges of 2$\theta$, several frames are measured and then they are overlapped (that is why the background may not be constant). For nickel, the 2$\theta$ range was 30–100 degrees.

*Iron oxide and manganese ferrite nanoparticles:,* the X-ray diffractograms of powder material were measured with a Rigaku, "rotaflex" RU-200B model using a Cu anode with $\lambda_{K\alpha 1}$=1.5406 Å and $\lambda_{K\alpha 2}$=1.5444 Å (ICMAB) in the 2$\theta$ range of 20–70 degree ($^{o}$) using a step of 0.02\/min. The amount of sample for analysis with Rigaku diffractometers has to be enough to cover a circular glass substrate of 2.5 cm in diameter. For a lower amount of sample, the contribution of the glass substrate appears in the diffractogram. Due to the very small quantity of material (nanoparticles) obtained in one batch, the nanoparticles to measure (not exactly in dried powder form) were prepared by evaporating directly on the sample holder (preferably in one cycle), of 100–200 µl concentrate hexane colloidal dispersion(like a ferrofluid) obtaining more a film of nanoparticles.

---

[a] *Borosilicate capillary tube:* is preferred because absorb less amount of radiation compared to silicate (boron has a lower atomic number  than silicon). The tube width for microdiffraction has to be small enough not to disturb significantly the diffraction intensity but at the same time, it has to be wide enough so it can be filled with the liquid overcoming the capillary pressures.

MAUD program (Materials analysis using diffraction) with the Rietveld refinement method was used to fit experimental diffractograms and to extract information from the material such as crystallite size, crystalline cell dimensions, strain, etc. An experimental resolution function was obtained from the refinement of a quartz reference in order to take into account the instrumental broadening.

### A.ii.2 Transmission electron microscope images (TEM)

TEM images were obtained with a JEOL JEM-1210 electron microscope, operating at 120 kV (ICMAB). The HRTEM images and selected area diffraction patterns (SADP) were captured using a JEOL JEM-2011, operating at 200 kV (UAB) The sample was prepared by depositing a drop of dilute (very slight brown color) nanoparticles hexane dispersion onto a TEM carbon grid and letting the solvent to evaporate at room temperature.

The size distribution was calculated by fitting the size histogram of at least 200 nanoparticles (from TEM images) with a Gaussian function. The standard deviation ($\sigma$) is defined as the root of the average of the squares of the differences of all the observations from their mean value, and the polidispersity of the distribution (P) is defined as the percentage of the standard deviation ($\sigma$) related to the mean value.

$$\sigma = \sqrt{\frac{\sum(value_i - mean \cdot value)^2}{mean \cdot value}} \qquad P = \frac{\sigma}{mean \cdot value} \cdot 100$$

Cryo transmission electron microscopy experiments were performed on aqueous suspensions of magnetic nanoparticles at an iron concentration of 10 mM. A drop of suspension was put on Quantifoil® grid where a perforated foil is used to bear an ultra-thin carbon support foil to minimize the total specimen thickness. The drop was blotted with filter paper and the grid was rapidly quenched into liquid ethane in order to produce "vitreous" ice, without formation of crystals. Then the grid was transferred into the TEM microscope (JEM-2011 operating at 200 kV, UAB) where the temperature is kept under -140 °C with liquid nitrogen during the imaging.

### A.ii.3 Scanning electron microscope images (SEM)

SEM images were acquired using a Quanta FEI 200F microscope (ICMAB) in low vacuum mode with a cone LOW kV P.L.A. type with 500 μm aperture. For the analysis of opals materials (2D or 3D) on glass substrate (without covering with a Au layer), the working conditions were usually: low vacuum conditions, an acceleration voltage of 5-20 kV, an electron beam spot of 2-2.5 a pressure of 50 Pa and a distance of 5-6 mm. Due to the presence of magnetic nanoparticles on silica or polystyrene surface, the sample was conducting, being very difficult to focus. Therefore the working conditions, varied from sample to sample, but better images were acquired working with a lower acceleration voltage (5, 10KV) and smaller beam spot.

### A.ii.4 Thermogravimetry analysis (TGA)

The weight percentage of surfactants on the nanoparticle surface was determined using a METTLER TOLEDO TGA /SDRA 851E device. The solid samples (approx. 10 mg for Nickel and around 4 mg for ferrite nanoparticles) were characterized with the following setup: heating rate of $10°$/min, in the temperature range $30\,°C$ $-800\,°C$ under a $N_2$ or Ar flux. Similar with XRD, the material to analyze was evaporated directly on alumina cresol from a concentrated nanoparticles colloidal dispersion. To fill the cresol it was needed around 50 µl dispersion (one cycle). Therefore, to avoid a time consuming sample preparation (too many filling-drying cycles) and to reach the minimum 4 mg material using fewer steps, 100 µl dispersion of around 40 mg/ml concentration it is suggested to be used.

### A.ii.5 Infrared spectra (IR)

Infrared spectra were acquired using a PerkinElmer FT-IR Spectrum One with U-ATR (Universal Attenuated Total Reflectance) accessory having a diamond tip and zinc selenide crystal under the tip. The spectrum, with a 4 $cm^{-1}$ resolution, was recorded between 650 and 4000 $cm^{-1}$ using 4 scans. A drop (10µl) of concentrated (> 10 mg/ml) nanoparticles colloidal dispersion was placed on the support; the solvent (hexane) was let to evaporate and after, the measurement was performed.

### A.ii.6 Dynamic Light Scattering (DLS)

Dynamic light scattering (also known as PCS – Photon Correlation Spectroscopy) measures brownian motion and relates it to the size of the particles. It does this by illuminating the particles with a 633 nm laser and analysing the intensity fluctuations in the scattered light at 173°. The calculated hydrodynamic size is defined as the diameter of a sphere which has the same Brownian motion as the analyzed particle, independently of the particle shape. This diameter corresponds to the particle together with the molecules strongly adsorbed onto its surface (surfactants, electrolytes and solvent.). Therefore, the hydrodynamic size is always larger than the size observed by TEM. Furthermore, the scattering intensity depends on the sixth power of the particle radius (intensity $\propto$ $r^6$) meaning that the larger particles contribute more to the average size than the smaller ones. It is worth to be mentioned that DLS technique is very sensitive to any particle in suspension (e.g. dust) and therefore a careful attention has to be paid in the sample preparation, to avoid as much as possible impurities within the colloidal dispersion (that may cause interferences during the DLS measurements).

The hydrodynamic diameter of the nanoparticles (nickel, iron oxide, Mn ferrite) suspended in organic media (usually hexane) / water were investigated with a Zetasizer Nano ZS from Malvern Instruments equipped with a He/Ne 633 nm laser (ICMAB). 1.5 ml of a diluted colloidal dispersion (around $10^{-3}M$ concentration) was placed in a quarts cuvette and three consecutive runs of 15 scans each run for all the nanoparticles were performed. Care was taken that the DLS maximum peak position and width was the same for all runs and the media of the row data for the size distribution vs. volume % was represented using *ORIGIN* programme. Regarding the time stability experiments, a comparison between the

DLS maximum peak position of the as prepared nanoparticles colloidal dispersion and after a few month was made.

## A.ii.7 Optical measurments

Reflection measurements were performed in the laboratory of ICMM (Madrid) using a BRUKER IFS 66/S spectrometer, connected to a microscope IRSCOPE II Bruker. The light beam with diameter of 0.9 mm (normal to the probe surface) allowed the measurement of Bragg peak spectral position by detecting the reflected beam from the material.

## A.ii.8 Superconductive quantum interference device (SQUID)

Magnetic characterization was performed with a superconductive quantum interference device (SQUID) magnetometer (Quantum Design MPMS5XL). The evaluation of the magnetic properties comprises the measurement of the magnetization *vs.* the applied magnetic field at a constant temperature (300 K and 5K) (M(H) curves) and *vs.* the temperature at a constant applied magnetic field (50 Oe) (ZFC–FC curves).The sample was prepared using a gelatine (1.5 cm length and 0.5 cm diameter; water soluble) filled with compacted cotton impregnated with 150-200 µl of a hexane dispersion of nanoparticles giving a mass of around 4 mg Nickel and 2 mg Ferrite (magnetic material + surfactant). The magnetization values were reported per mass of magnetic material by subtracting the mass of surfactant as measured in TGA experiments.

## A.ii.9 Magnetic circular dichroism (MCD) spectroscopy

The measurements were performed using the home made experimental setup illustrated in the Figure. A.ii.9. The sample was placed between the poles of an electromagnet. Light from a 150W Xe arc lamp (Zolix Technology) is dispersed by a monochromator (Zolix 1-150), collimated, and then linearly polarized by the action of a Glan-Thompson prism, which is rotated 45◦ with respect to the modulator axis of a photoelastic modulator (PEM). After the PEM, the light is transmitted through the sample (with a typical light beam diameter of about ~2 mm) and then goes, towards a detector. The signal from this detector is brought to a lock-in amplifier synchronized to the frequency of the PEM retardation angle. It can be demonstrated that in this setup configuration, one can measure the MCD signal by inspection of the first harmonic of the detector signal.

In our particular setup, a complete MCD hysteresis loop can be obtained as fast as 1s. A typical magnetization loop in a SQUID takes more than 103 s. The main reason for this extremely different time response is that in magnetooptics, the information of magnetic state comes from the interaction between light and matter; in SQUID, extraction of the magnetic information requires moving of the sample between a couple of detector coils, that is a much slower process. On the other hand, SQUID uses superconductive coils contrary to our MCD system that is based on an electromagnet in which the fields can be much more rapidly cycled.
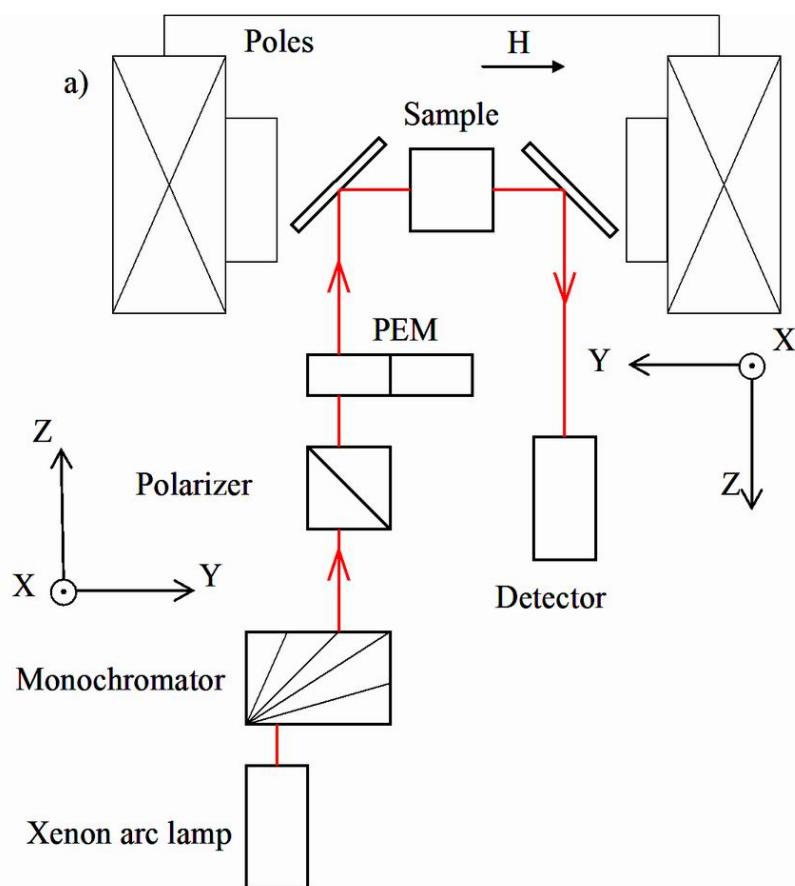
**Figure A.ii.9** *MCD spectroscopy measurement setup*

**Magnetic colloids/opals measurements**

*Magnetic colloids (Ni NPs/hexane).*The magneto-optical measurements were performed in a range of wavelengths $\lambda$ = 400– 800 nm, by placing 1.5 ml of colloidal dispersions in a glass square cuvette for which the optical path was 1cm. These experiments were carried out for the following concentrations; for 8 nm Ni NPs: $1.7 \times 10^{-4}$M (0.0083 mg/ml Ni), $1.7 \times 10^{-3}$M (0.083 mg/ml Ni), $2.6 \times 10^{-3}$M (0.1264 mg/ml Ni), $4 \times 10^{-3}$M (0.1938 mg/ml Ni) and $5.1 \times 10^{-3}$M (0.25 mg/ml Ni) and for 15 nm Ni NPs: $1.7 \times 10^{-4}$M (0.0092 mg/ml Ni), $1.7 \times 10^{-3}$M (0.092 mg/ml Ni) , $2.6 \times 10^{-3}$M (0.1404 mg/ml Ni), $4 \times 10^{-3}$M (0.2149 mg/ml Ni) and $5.1 \times 10^{-3}$M (0.28 mg/ml Ni). Notice that all the molar concentrations are reported in the basis of moles of Ni atoms and that for concentrations given in mg/ml Ni, the amount of surfactant has been corrected. Those concentrations represent volume fractions of nanoparticles in colloidal dispersion in the range of 0.9 ppm to 30 ppm. The amount of magnetic material used for the analysis was of 0.012 mg for the most diluted sample and of 0.12 mg for the most concentrated one. The background magneto-optical spectroscopic signal was subtracted from the raw experimental data by recording the spectra of glass cuvette filled with bare hexane solvent over the entire range of analyzed wavelengths. The subtraction was made assuming that the background and the nanoparticle magneto-optical signals are additives.

*Blank /magnetic opals measurement.* The same setup as for magnetic colloids was used. The opal was placed between the electromagnetic poles in such a way that the incident beam light to be normal to opal surface. Measurements were carried out in transmission, allowing to be taken in the same place both the optical transmittance and magneto-optical spectra, avoiding thus additional effects associated with any eventual spatial inhomogeneity.

# 6.3. Tables with detailed experimental conditions

**6.3. A.iii.1** *Ni nanoparticles synthesis by thermal decomposition.*

**6.3. A.iii.2** *Calculation of self-limiting surface oxide barrier of one Ni nanoparticle.*

**6.3. A.iii.3** *Absorbing properties of different organic solvent at the microwave reactor frequency of 2.54 GHz.*

**6.3. A.iii.4** *Ferrites (MnFe$_2$O$_4$ and iron oxide) nanoparticles synthesis by microwave-assisted non-hydrolytic sol-gel chemistry.*

**6.3. A.iv.1** *Magnetic opal fabrication by microwave-assisted in-situ deposition approach*

**A.iii.1** *Detailed experimental data for Ni nanoparticles synthesis by thermal decomposition*

| Material label | Experimental parameters | | | | | | | | Characterization data | | | | | | | |
|---|---|---|---|---|---|---|---|---|---|---|---|---|---|---|---|---|
| | Mixing T/time | T1 (°C)/min | T2 (°C)/min | Ni(acac)$_2$ (mmol) | OAc (mmol) | TOP (mmol) | Solvent (OAm) (mL) | Obs | $\langle\Phi\rangle_{XRD}$ (nm) | $\langle\Phi\rangle_{TEM}$ (nm) | $\langle\Phi\rangle_{HYD}$ as prep (nm) | $\langle\Phi\rangle_{HYD}$ after* (nm) | Weight loss % | Ms (emu/g) 298K | $T_B$ (K) | Hc (Oe) at 5K |
| A_TD.Ni_1 | 24°C/20 | 130/20 | 250/30 | 2 | 4 | 2 | 14 | o.1 | 7.15 | 19.3 ± 3.3 | – | – | – | 34.6 | >RT | – |
| A_TD.Ni_2 | 23°C/20 | 130/20 | 250/30 | 1 | 2 | 1 | 7 | o.2 | 7.09 | 17 ± 2 | – | 37.8±10 531±129 | – | – | – | – |
| A_TD.Ni_3 | 23°C/20 | 130/20 | 250/30 | 2 | 4 | 2 | 14 | o.3 | 7.4 | 21.4 ± 2.2 | – | 24.4±5.6 615±150 | – | 38.7 | 290 | 183 |
| A_TD.Ni_4 | – | 130/20 | 250/30 | 2 | 4 | 2 | 14 | o.4 | 7.5 | 15.5 ± 1.3 | – | 24.4±5 295±59 | 8.6 | 43.3 | >RT | – |
| A_TD.Ni_14 | – | 130/20 | 250/30 | 2 | 4 | 2 | 14 | o.14 | 7.4 | 24.2 ± 3.8 | – | – | – | – | – | – |
| B_TD.Ni_5 | 24°C/20 | 130/20 | 250/30 | 2 | – | – | 14 | – | – | – | – | – | – | – | – | – |
| B_TD.Ni_6 | – | 130/20 | 250/30 | 2 | – | – | 14 | – | 11.9 | 101 ± 10 | – | – | – | 56 | – | – |
| C_TD.Ni_7 | – | 130/20 | 215/30 | 2 | 4 | 2 | 14 | – | – | – | – | – | – | – | – | – |
| C_TD.Ni_8 | – | 170/20 | 215/30 | 2 | 4 | 2 | 14 | – | – | – | – | – | – | – | – | – |
| C_TD.Ni_9 | – | 170/20 | 250/30 | 1 | 2 | 1 | 7 | o.9 | 6.97 | 14.9 ± 1.6 | 24.5±7 | | 9.2 | 54.55 | 233.7 | 182 |
| C_TD.Ni_15 | – | 170/20 | 250/30 | 1 | 2 | 1 | 7 | o.15 | 7.6 | 19.6 ± 1.7 | – | – | – | – | – | – |
| D_TD.Ni_10 | – | 130/20 | 250/30 | 2 | 6 | – | 14 | o.10 | 24.5 | 150 | – | – | 1.54 | 53.6 | – | – |
| D_TD.Ni_11 | – | 130/20 | 250/30 | 2 | – | 6 | 14 | o.11 | 4.3 | 8 ± 1 | | 73 &295 | 17.97 | 24.7 | 52 | – |
| D_TD.Ni_12 | – | 130/20 | 250/30 | 2 | 2 | 4 | 14 | o.12 | 4.5 | 8.8 ± 1.4 | | 41±11.3 296±100 | 17.69 | 26.6 | 74 | – |
| D_TD.Ni_13 | – | 130/20 | 250/30 | 2 | 3 | 3 | 14 | o.13 | 5.3 | 11.1 ± 1.5 | | 255±106 | 14.77 | 32.8 | 161 | – |
| D_TD.Ni_16 | – | 130/20 | 250/30 | 2 | 2 | 4 | 14 | o.16 | 4.5 | 8 ± 0.9 | 20±2.5 | 21.4±6 296±121 | 17.97 | 25.8 | 57 | 300 |

o.1 – it was a variation of T2: 210 – 250°C during 30 min ; o.2 – T2 was maintained constant at 248°C ; o.3 – it was a variation of T2: 210 – 250°C during 30 min
o.4 – T2 was maintained constant at 246°C ; o.14 – it was a variation of T2: 243 – 255°C during 30 min ; o.9 – T2 was maintained constant at 250°C
o.15 – it was a variation of T2: 250 – 265°C during 30 min; o.10 – T2 was maintained constant at 250°C ; o.11 – it was a variation of T2: 245 – 255°C during 30 min;
o.12 – T2 was maintained constant at 246°C ; o.13 – T2 was maintained constant at 250°C ; o.16 – T2 was maintained constant at 250°C
* DLS measurements after 2 and half years of storage in powder form

| A.iii.2. Calculation of self-limiting surface oxide barrier of one Ni nanoparticle. |
|---|

$$m_T = N_P \cdot m_P \text{ (emu)} \Rightarrow m_P = \frac{m_T}{N_P}$$

$$m_P = Ms \cdot \frac{4}{3}\pi R_m^3 \Rightarrow m_P^{1/3} = \left(Ms \cdot \frac{4}{3}\pi\right)^{1/3} (R - d_0)$$

$m_P = $ magnetic moment of aNP

$m_P = $ measured by SQUID (emu)

$R_m = R - d_0$

$R_m = $ magnetic radius of aNP

$R = $ geometrical radius of aNP

$d_0 = $ non − ferromagnetic layer

$$N_P = \frac{mass}{\frac{4}{3}\pi R^3 \cdot \rho_{bulk}}$$

mass = of the sample (g)

**A.iii.3** *Absorbing properties of different organic solvent at the microwave reactor frequency of 2.54 GHz : tanδ – loss tangent ($\varepsilon''/\varepsilon'$=tanδ), $\varepsilon'$- dielectric constant, $\varepsilon''$- dielectric loss*

| Organic solvent | tanδ at 2.45 GHz | $\varepsilon'$ | $\varepsilon''$ |
|---|---|---|---|
| Ethylene glycol | 1.350 | 37.0 | 49.950 |
| Ethanol | 0.941 | 24.3 | 22.866 |
| DMSO | 0.825 | 45.0 | 37.125 |
| 2-Propanol | 0.799 | 18.3 | 14.622 |
| 1-Propanol | 0.757 | 20.1 | 15.216 |
| Formic Acid | 0.722 | 58.5 | 42.237 |
| Benzyl alcohol | 0.667 | 13 | 8.671 |
| Methanol | 0.659 | 32.6 | 21.483 |
| Nitrobenzene | 0.589 | 34.8 | 20.497 |
| 1-Butanol | 0.571 | 17.1 | 9.764 |
| Isobutanol | 0.522 | 15.8 | 8.248 |
| 2-Butanol | 0.447 | 15.8 | 7.063 |
| 2-Methoxyethanol | 0.410 | 16.9 | 6.929 |
| 0-Dichlorobenzene | 0.280 | 9.9 | 2,772 |
| Acetic acid | 0.174 | 6.2 | 1.079 |
| Water | 0.123 | 80.4 | 9.889 |
| Chlorobenzene | 0.101 | 2.6 | 0.263 |
| Chloroform | 0.091 | 4.8 | 0.437 |
| Acetonitrile | 0.062 | 37.5 | 2.325 |
| Acetone | 0.054 | 20.7 | 1.118 |
| THF | 0.047 | 7.4 | 0.348 |
| Toluene | 0.040 | 2.4 | 0.096 |
| Hexane | 0.020 | 1.9 | 0.038 |

**A.iii.4** Detailed experimental data for ferrites nanoparticles synthesis by microwave–assisted sol–gel chemistry

| | precursors | | surfactants | | Solvent (mL) | MW set parameters | | | $t_{irrad}$ (min) | Characterization data | | | | | | |
|---|---|---|---|---|---|---|---|---|---|---|---|---|---|---|---|---|
| | | | | | | | | | | MnFe$_2$O$_4$ | | | | | | |
| Material label | Fe(acac)$_3$ (mmol) | Mn(ac)$_2$ (mmol) | Oac (mmol) | Oam (mmol) | | $T_{set}$ (°C) | $t_{set}$ (min) | $P_{max}$ (W) | | $\langle\Phi\rangle_{TEM}$ (nm) | $\langle\Phi\rangle_{HYD}$ as prep (nm) | $\langle\Phi\rangle_{HYD}$ after• (nm) | Weight loss % | Ms (emu/g) 298K | $T_B$ (K) | Hc (Oe) at 5K |
| A_MW.MnFe$_2$O$_4$_5.1 | 0.15 | 0.075 | 0.45 | 0.45 | 1.5 | 160 | 5 | 200 | 8' | – | 10.1 ± 3 | 11.7 ± 4.7 | – | – | – | – |
| A_MW.MnFe$_2$O$_4$_5.2 | 0.15 | 0.075 | 0.45 | – | 1.5 | 160 | 5 | 200 | 10'6" | 3.9±0.7 | 10.1 ± 3.1 | 11.7 ± 4.3 | 55.1 | 41[a] | 24 | – |
| A_MW.MnFe$_2$O$_4$_5.3 | 0.15 | 0.075 | 0.3 | 0.15 | 1.5 | 160 | 5 | 200 | 11'49" | 3.1±0.8 | 15.6 ± 1.6 | 11.7 ± 3.6 | – | – | 20.2 | – |
| A_MW.MnFe$_2$O$_4$_4.2 | 0.15 | 0.075 | 0.45 | – | 1.5 | 160 | 2 | 200 | 4'22" | 3.2±0.5 | 10.1 ± 3.8 | 11.7 ± 3.4 | – | – | – | – |
| A_MW.MnFe$_2$O$_4$_4.3 | 0.15 | 0.075 | 0.45 | – | 1.5 | 160 | 45" | 200 | 3'57" | 3.2±0.5 | 11.7 ± 2 | 11.7 ± 3.7 | 34.9 | 16[a] | 18.5 | – |
| A_MW.MnFe$_2$O$_4$_8.4 | 0.15 | 0.075 | 0.45 | – | 1.5 | 160 | 5 | 200 | 11'13" | 3.2±0.4 | 10.1 ± 2.8 | 11.7 ± 3.7 | – | – | – | – |
| B_MW.MnFe$_2$O$_4$_2.1 | 0.15 | 0.075 | – | – | 1.5 | 160 | 10 | 200 | 21' | 4.9±0.8 | 13.5 ± 4.8 | 15.7 ± 9 | 39.35 | 44[a] | 28 | 150 |
| B_MW.MnFe$_2$O$_4$_8.2 | 0.45 | 0.225 | – | – | 4.5 | 160 | 2 | 200 | 9'20" | 3.8±0.8 | 8.7 ± 3 | 8.7 ± 3 | – | – | – | – |
| B_MW.MnFe$_2$O$_4$_8.5 | 0.1 | 0.05 | – | – | 1.5 | 160 | 5 | 200 | 14'39" | 3.8±0.8 | 8.7 ± 2.1 | 6.5 ± 2.1 | – | – | 26 | – |
| B_MW.MnFe$_2$O$_4$_8.6 | 0.3 | 0.15 | – | – | 4.5 | 160 | 3 | 200 | 6'39" | – | 8.7 ± 2.4 | 8.7 ± 2.4 | – | – | – | – |

| | Iron oxide ($\gamma$–$Fe_2O_3$/ $Fe_3O_4$) | | | | | | | | | | | | | | | |
|---|---|---|---|---|---|---|---|---|---|---|---|---|---|---|---|---|
| *Material label* | Fe(acac)$_3$ (mmol) | Fe(acac)$_2$ (mmol) | Oac (mmol) | DTAB (mmol) | Solvent (ml) | $T_{set}$ (°C) | $t_{set}$ (min) | $P_{max}$ (W) | $t_{irrad}$ (min) | $<\Phi>_{TE}$ M (nm) | $<\Phi>_{HYD}$ as prep (nm) | $<\Phi>_{HYD}$ after 10 m. (nm) | Weight loss % | Ms (emu/g) 298K | $T_B$ (K) | Hc (Oe) at 5K |
| *C_MW.iron oxide_6.16* | 0.23 | 0.12 | 0.69 | – | 4.5 | 160 | 5 | 200 | 21' | – | 18 ± 7.3 | 21 ± 7.5 | – | – | – | – |
| *C_MW.iron oxide_6.17* | 0.23 | 0.12 | 0.69 | – | 4.5 | 160 | 5 | 200 | 17' | 6 ± 1 | 16 ± 5.7 | 16 ± 3.9 | – | 9 [b] | 60 | 309 |
| *C_MW.iron oxide_6.18* | 0.23 | 0.12 | 0.69 | – | 4.5 | 160 | 3 | 200 | 10' | 5 ± 1.1 | 11.7 ± 4 | 13.5 ± 8 | – | 44[b] | 46 | 300 |
| *D_MW.iron oxide_6.1* | 0.225 | – | 0.675 | – | 1.5 | 160 | 10 | 200 | 16' | – | – | – | – | – | – | – |
| *D_MW.iron oxide_6.2* | 0.675 | – | 2.025 | – | 4.5 | 160 | 5 | 200 | 9' | 6.7 ± 2 | – | 11 | 28 | 48[a] | 119 | 356 |
| *D_MW.iron oxide_6.3* | 0.675 | – | 2.025 | – | 4.5 | 160 | 8 | 200 | 12'15 s | 7.7 ± 2.3 | 32.7 ± 10 | 1281 | – | 35.6[b] | 173 | – |
| *D_MW.iron oxide_6.4* | 1.35 | – | 4.05 | – | 4.5 | 160 | 5 | 200 | 8' | – | 47 | – | – | – | – | – |
| *D_MW.iron oxide_6.5* | 0.675 | – | 2.025 | – | 4.5 | 160 | 5 | 200 | 17'20 s | – | 10.8 ± 3 | Obs.1 | – | – | – | – |
| *D_MW.iron oxide_6.6* | 0.45 | – | 1.35 | – | 4.5 | 160 | 3 | 200 | 10'50 s | 5.5 ± 1.4 | 10.8 ± 3 | 10.8 ± 3 | – | 13[b] | 62 | 450 |
| *D_MW.iron oxide_6.7* | 0.32 | – | 1.25 | – | 4.2 | 160 | 10 | 200 | 24' | – | 15.7 ± 4.2 | 18.2 ± 4.6 | – | – | – | – |
| *D_MW.iron oxide_6.8* | 0.32 | – | 1.25 | – | 4.2 | 160 | 10 | 200 | 17'20 s | – | 10.8 ± 2.7 | 18.2 ± 6 | – | – | – | – |
| *D_MW.iron oxide_6.9* | 0.32 | – | 1.25 | – | 4.2 | 160 | 5 | 200 | 10'33 s | – | 10.8 ± 3.6 | 11.7 ± 4.3 | – | – | – | – |
| *D_MW.iron oxide_6.10* | 0.35 | – | 1.05 | – | 4.5 | 160 | 3 | 200 | 16'2s | 6.3 ± 1.2 | 11.7 ± 3 | – | – | – | – | – |
| *D_MW.iron oxide_6.11* | 0.35 | – | 1.05 | – | 4.5 | 160 | 5 | 200 | 20'23 s | 7.3 ± 2.1 | 13.5 ± 5.5 | – | – | – | – | – |
| *D_MW.iron oxide_6.12* | 0.35 | – | 1.05 | – | 4.5 | 160 | 3 | 200 | 14'40 s | – | 17 ± 3.2 | 1990 | – | – | – | – |
| *D_MW.iron oxide_6.13* | 0.35 | – | 1.05 | – | 4.5 | 160 | 1'30s | 200 | 10'22 s | 4.5 ± 2.1 | 10.1 ± 3.3 | 10.8 ± 3.9 | – | – | – | – |

| Material label | Fe(acac)$_3$ (mmol) | Fe(acac)$_2$ (mmol) | Oac (mmol) | DTAB (mmol) | | T$_{set}$ (°C) | t$_{set}$ (min) | P$_{max}$ (W) | t$_{irrad}$ (min) | $\langle\Phi\rangle_{TE}$ M (nm) | $\langle\Phi\rangle_{HYD}$ as prep (nm) | $\langle\Phi\rangle_{HYD}$ after 10 m. (nm) | Weight loss % | Ms (emu/g) 298K | T$_B$ (K) | Hc (Oe) at 5K |
|---|---|---|---|---|---|---|---|---|---|---|---|---|---|---|---|---|
| *D_MW.iron oxide_6.14* | 0.35 | – | 1.05 | – | 4.5 | 160 | 5 | 200 | 25' | 8.3 ± 2.5 | 11.7 ± 3.5 | 13.5 ± 5.3 | – | – | – | – |
| *D_MW.iron oxide_6.15* | 0.35 | – | 1.05 | – | 4.5 | 160 | 5 | 200 | 15' | 6.3 ± 1.5 | 12.5 ± 3.3 | 12.5 ± 3.2 | 39.1 | 59[a] | 66 | 250 |
| *D_MW.iron oxide_6.22* | 0.35 | – | 1.05 | – | 4.5 | 140 / 160 / 180 / 200 | 3 / 3 / 3 / 3 | 300 | 25'33 s | 11 ± 2 | 13.5 ± 3.8 | 50.8 ± 14.6 2 months | 25 | 55.5[a] | 181 | 400 |
| *D_MW.iron oxide_6.23* | 0.35 | – | 1.05 | – | 4.5 | 200 | 5 | 300 | 8' | 4 ± 0.8 | 10.1 ± 3.4 | 10.1 ± 5 | – | 9.6[b] | 34 | 580 |
| *D_MW.iron oxide_6.26* | 0.35 | – | – | 0.875 | 4.5 | 180 | 5 | 300 | 7'20s | 7.8 ± 2.3 | – | 59 ± 18.7 | – | – | – | – |
| *D_MW.iron oxide_6.27* | 0.35 | – | – | 0.875 | 4.5 | 200 | 15 | 300 | 19' | 11.2±2.3 | 50.8±21.7 | 50.8±21.7 2 months | – | 23[b] | >RT | 50 |
| *D_MW.iron oxide_6.28* | 0.35 | – | 0.875 | – | 4.5 | 200 | 15 | 300 | 17'34 s | 5.5 ± 1.4 | 15.7±5.5 | 458.7±74 2 months | – | 40.9[b] | 78 | 350 |
| *D_MW.iron oxide_6.29* | 0.35 | – | 0.525 | 0.35 | 4.5 | 200 | 15 | 300 | 19' | 8.3±1.75 | 18.2 ± 8 | 18.2 ± 6 | – | – | – | – |
| *D_MW.iron oxide_6.30* | 0.35 | – | 0.35 | 0.525 | 4.5 | 200 | 15 | 300 | 19'20 s | 9.3 ± 1.3 | 18.2 ± 8 | 825.8±153 | – | – | – | – |
| *D_MW.iron oxide_6.31* | 0.35 | – | 0,875 | 0 +Au | 4.5 | 200 | 15 | 300 | 22' | 7.8 ± 2.3 | – | 15.7±4 | – | – | – | – |
| *D_MW.iron oxide_6.32* | 0.35 | – | 0.525 | 0.35 +Au | 4.5 | 200 | 15 | 300 | 21'30 s | 7.8 ± 2.3 | – | – | – | – | – | – |
| *E_MW.iron oxide_2.12* | 0.3 | 0.15 | – | – | 3 | 160 | 3 | 200 | 12' | – | – | – | – | – | – | – |
| *E_MW.iron oxide_2.13* | 0.3 | 0.15 | – | – | 4.5 | 160 | 3 | 200 | 11' | 6.1 ± 1.4 | 15.7 ± 5.1 | 24.3 ± 4.9 | 16.6 | 57.6[a] | 56 | 231 |

| Material label | Fe(acac)$_3$ (mmol) | Fe(acac)$_2$ (mmol) | Oac (mmol) | DTAB (mmol) | | T$_{set}$ (°C) | t$_{set}$ (min) | P$_{max}$ (W) | t$_{irrad}$ (min) | $\langle\Phi\rangle_{TE}$ M (nm) | $\langle\Phi\rangle_{HYD}$ as prep (nm) | $\langle\Phi\rangle_{HYD}$ after 10 m. (nm) | Weight loss % | Ms (emu/g) 298K | T$_B$ (K) | Hc (Oe) at 5K |
|---|---|---|---|---|---|---|---|---|---|---|---|---|---|---|---|---|
| E_MW.iron oxide_6.19 | 0.35 | – | – | – | 4.5 | 160 | 5 | 300 | 6'30s | 3.5 ± 0.7 | 11.7 ± 3.7 | 11.7 ± 3.8 | 20 | 35[a] | 30 | 252 |
| E_MW.iron oxide_6.20 | 0.35 | – | – | – | 4.5 | 180 | 5 | 300 | 7'10s | 4.4 ± 0.6 | 21 ± 8 | 24.4±10 | – | – | – | – |
| E_MW.iron oxide_6.21 | 0.35 | – | – | – | 4.5 | 200 | 5 | 300 | 8' | 5.5 ± 0.8 | 21 ± 7.4 | 24.3±11.3 3 months | – | – | – | – |
| E_MW.iron oxide_6.24 | 0.35 | – | – | – | 4.5 | 180 | 5 | 300 | 7'30s | 4 ± 0.7 | 10.1 ± 2.7 | 13.5 ± 4.2 | – | – | – | – |
| E_MW.iron oxide_6.25 | 1.4 | – | – | – | 18 | 160 | 5 | 300 | 17'20 s | – | 10.1 ± 3.7 | 32.7 ±14.7 | – | – | – | – |
| E_MW.iron oxide_6.33 | 0.35 | – | – | – | 4.5 | 200 | 15 | 300 | 21' | 6.8 ± 1.3 | 10.1 ± 4.3 | 10.1 ± 4.3 2 months | – | 12[b] | 64 | – |

[a] – refers to Ms corresponding to emu/g magnetic core without the surfactant mass
[b] – refers to Ms corresponding to emu/g material (the mass of magnetic core + the mass of surfactant )
t$_{set}$ – the time at setpoint (T$_{set}$)

A.iv.1 Detailed experimental data for magnetic opal fabrication by microwave–assisted in–situ deposition approach

| Material label | Blank opal (label) | Spheres (Φ nm) | precursors | | Solvent (ml) | $C_{tot}$ (M) | MW set parameters | | | $t_{irrad}$ (min) | Bragg peak | |
| --- | --- | --- | --- | --- | --- | --- | --- | --- | --- | --- | --- | --- |
| | | | Fe(III) (mmol/mg) | M(II) (mmol/mg) | | | T(°C) | t (min) | Power (W) | | Before (nm) | After (nm) |
| MW_MD.1a | $SiO_2\_086$ | SiO2 (350) | $Fe(acac)_3$ 0.3/0.106 | $Mn(ac)_2$ 0.15/0.037 | Benzyl alcohol (1.5 ml) | 0.3 | 170 | 5 | | 8 | 760 | 780 |
| MW_MD.1b | $SiO_2\_050a$ | | | | | | | 5+5 | | 19'50s | 763 | 810 |
| MW_MD.2 | $SiO_2\_050b$ | | | | | | | 10 | | 13'28s | 763 | 800 |
| MW_MD.3 | $SiO_2\_06$ | | | | | | | 7 | | 15 | 793 | – |
| MW_MD.4 | $SiO_2\_VIL123T$ | $SiO_2(290)$ | | | | | | 7 | | 9 | 620 | – |
| MW_MD.5 | $SiO_2\_G2L137$ | $SiO_2(250)$ | | | | | | 10 | | 12'22s | – | – |
| MW_MD.6 | $SiO_2\_239a$ | $SiO_2(260)$ | $Fe(acac)_3$ 0.15/0.054 | $Mn(ac)_2$ 0.075/0.018 | Benzyl alcohol (1.5 ml) | 0.15 | | 5 | | 9'16s | 550 | 571 |
| MW_MD.7 | $SiO_2\_239b$ | | | | | | | 5 | | 8'18s | 550 | 563 |
| MW_MD.8 | $SiO_2\_241a+$ R3N | | | | | | | 5 | | 17'40s | 556 | – |
| MW_MD.9 | $SiO_2\_241b$ | | | | | | | 5 | | 12'25s | 559 | – |
| MW_MD.10 | $SiO_2\_078a$ | SiO2 (350) | | | | | 145 | 5 | 200 | 21 | 768 | – |
| MW_MD.11 | $SiO_2\_078b$ | | | | | | 157 | 5 | | 21 | 768 | – |
| MW_MD.12 | $SiO_2\_083a$ | | $Fe(acac)_3$ 0.3/0.106 | $Fe(acac)_2$ 0.15/0.038 | Benzyl alcohol (3 ml) | 0.15 | 160 | 3 | | 8 | 768 | – |
| MW_MD.13 | $SiO_2\_083b$ | | | | | | | 5 | | 10'4s | 768 | – |
| MW_MI.1 | E300.2P2 | $Al_2O_3$ shell of 15 nm, void of 270 | $Fe(acac)_3$ 0.3/0.106 | $Mn(ac)_2$ 0.15/0.037 | Benzyl alcohol (1.5 ml) | 0.3 | 170 | 10 | | 15'50s | 506 | 528 |
| MW_MI.2 | E300.1P1 | | | | | | | 5 | | 10 | 508 | 533 |
| MW_MI.3 | E300.3P1 | | $Fe(acac)_3$ 0.15/0.054 | $Mn(ac)_2$ 0.075/0.018 | | 0.15 | | 5 | | 8'50s | | 522 |
| MW_MI.4 | PS.244.a | $Al_2O_3$ shell of 8.2 nm, void of 234 +R3N | $Fe(acac)_3$ 0.3/0.106 | $Mn(ac)_2$ 0.15/0.037 | | 0.3 | | 5 | | 7'25s | 418 | 424 |
| MW_MI.5 | PS.244.b | | $Fe(acac)_3$ 0.15/0.054 | $Mn(ac)_2$ 0.075/0.018 | | 0.15 | | 5 | | 7'43s | 421 | 424 |
| MW_MI.6 | PS.243.a | | | | | | | 5 | | 8'12s | 421 | 426 |
| MW_MI.7 | PS.243.b | | | | | | | 5 | | 8'9s | 421 | 433 |

# CURRICULUM VITAE

## OANA PASCU

***PERSONAL DATA***

**Date and place of birth:** 16/11/1976, Bistriţa
**Nationality:** Romanian
**Passport**: 12123968
**Civil state**: Married
**Address:** Rambla de Brasil 42, 5/4, 08028 Barcelona, Catalonia
**Phone:** +34 645508155
**e-mail:** opascu@icmab.es; oana.t.pascu@gmail.com
**web:** www.icmab.es/nn

***ACADEMIC BACKGROUND***

- **European Ph.D. in Materials Science (doctoral student)**
  *Thesis topic: Synthesis of magnetic nanoparticles and strategies toward magnetophotonic crystals materials*
  Dept. of Crystallography & Dept. of Magnetic Materials and Functionalised Oxides
  Institute of Materials Science of Barcelona (ICMAB-CSIC), Bellaterra, Catalonia, Spain
  Jan 2009 – May 2012 (expected)
  Supervisors: Anna Roig and Gervasi Herranz

- **European Master (M.Sc.) in Chemical and Process Engineering**
  *Thesis: Smart microcapsules*
  Dept. of Chemical Engineering, University Rovira i Virgili, Tarragona, Catalonia, Spain
  2006 – 2007
  Supervisor: Marta Giamberini

- **Master (M.Sc.) in Cell Biotransformations**
  *Thesis: Bile salts study on biological interfaces*
  Dept. of Biology and Geology, Babes-Bolyai University, Cluj-Napoca, Romania
  2003 – 2004
  Supervisor: Maria Tomoia-Cotisel

- **Bachelor (B.Sc.) in Physical Chemistry**
  *Project: Adsorption and micellisation study of bile salts by measurements of surface tension*
  Dept. of Physical-Chemistry, Babes-Bolyai University, Cluj-Napoca, Romania
  1995 – 1999

***EDUCATIVE AND RESEARCH STAGES***

- Institute of Condensed Matter Chemistry of Bordeaux (ICMCB-CNRS)
  Supercritical Fluids Group, Bordeaux, France
  *Research: Fabrication of 3D inverse magnetic photonic crystals by sol-gel in supercritical fluids media*
  March 2011 – Jun 2011
  Supervised by Cyril Aymonier
  Grant given by Government of Catalonia

- 'Bio-Image' Summer School (Ecole Normal Superieure; UNESCO)
  Paris, France
  *Poster: Atomic Force Microscopy Studies of Langmuir-Blodgett Films. The influence of aluminum substrate on dipalmitoyl phosphatidylcholine nanolayers*

# Oana Pascu

Rambla de Brasil 42, 5/4, 08028 Barcelona • +34 645508155 • opascu@icmab.es
July 2005
Scholarship given by UNESCO

## WORK EXPERIENCE

- **Ph.D-assistant**

  Babes-Bolyai University, Dep. of Chemistry and Chemical Engineering

  Cluj-Napoca, Romania

  Studying the behavior of micro- and nanostructures built-up from biosurfactants on fluid interfaces; teaching experience in thermodynamics, biophysics and problem solving.

  October 2004 – September 2006

## TECHNICAL KNOWLEDGE

- Scanning Electron Microscopy (SEM), Optical Microscopy (OM); (autonomous user)
- Electron beam lithography (EBL), Nanoimprint Lithography (NIL);
- Dynamic Light Scattering (DLS); (autonomous user)
- Spectrophotometry (UV-VIS, IR) ; (autonomous user)
- (Manipulation of reactors working at supercritical conditions; (autonomous user)
- Organic synthesis of polymers (elastomers);
- Chemical synthesis of magnetic nanoparticles;
- Microwave-assisted inorganic synthesis;
- Microsoft Office, ChemDraw, Originlab.

## LANGUAGES

| Language | written | reading | conversation |
|----------|---------|---------|--------------|
| Spanish  | good    | good    | fluent       |
| English  | good    | good    | fluent       |
| French   | basic   | basic   | poor         |
| Hungarian| average | average | good         |

## PARTICIPATION IN RESEARCH PROJECTS

**2008-2010**: Project (ES) 'CRIMAFOT – Towards a new generation of synthesised photonic crystals/CSIC Intramural Border Project' (PIF 08-016).

**2007-2012**: Project (ES) 'CONSOLIDER NANOSELECT – Advanced materials and nanotechnology for electric, electronic and innovative magnetoelectronic devices and systems' (CSD 2007-00041).

**2006-2007**: Project (EU) 'IMPULSE – Integrated Multiscale Process Units With Locally Structured Elements (NMP-2-CT-2005-011816).

**2005-2006**: Project (RO) 'Basic research and development of nanostructured systems with applications in biomolecular recognition at fluid interfaces' (CNCSIS no.15/178/2005-2008).

## PUBLICATIONS IN JOURNALS

1. **Pascu, O.**; Gich, M.; Herranz, G.; Roig, A. 2D magnetic complex geometries by microwave-assisted sol-gel chemistry. *European Journal of Inorganic Chemistry* **2012**, *DOI: 10.1002/ejic.201101244.*

2. **Pascu, O.**; Marre, S.; Aymonier, C.; Roig, A. Continuous supercritical ethanol synthesis of monodispersed magnetic nanoparticles. Manuscript in progress

# Oana Pascu

Rambla de Brasil 42, 5/4, 08028 Barcelona • +34 645508155 • opascu@icmab.es

3. **Oana Pascu**, Elisa Carenza, Martí Gich, Sònia Estradé, Francesca Peiró, Gervasi Herranz and Anna Roig A. Surface reactivity of iron oxide nanoparticles by microwave synthesis; Comparison with thermal decomposition route. *Journal of Physical Chemistry C* **2012** (Submitted).

4. **Pascu, O.;** Caicedo, J.M.; Fontcuberta, J.; Herranz, G.; Roig, A.; Canalejas, V.; López, M.; López, C.; Blanco, A. Ultrathin conformal coating for complex photonic structures. *Nanoscale* **2011,** *3*, 4811-4816.

5. Caicedo, J.M.; **Pascu, O.;** Fontcuberta, J.; Herranz, G.; Roig, A.; Canalejas, V.; López, M.; López, C.; Blanco, A. Magnetophotonic response of three dimensional opals. *ACS Nano* **2011**, *5(4)*, 2957-2963.

6. **Pascu, O**.; Caicedo, J.M.; Fontcuberta, J.; Herranz, G.; Roig, A. Magneto-optical characterization of colloidal dispersions. Application to nickel nanoparticles. *Langmuir* **2010**, *26(15)*, 12548-12552*.*

7. Chen, D-X. **Pascu, O.;** Roig, A.; Sanchez, A. Size analysis and magnetic structure of nickel nanoparticles. *Journal of Magnetism and Magnetic Materials* **2010**, *322(24)*, 3834-3840.

8. **Pascu, O**.; Garcia-Valls, R.; Giamberini, M**.** Interfacial polymerization of an epoxy resin and carboxylic acids for the synthesis of microcapsules. *Polymer International* **2008**, *57(8)*, 995-1006.

9. Tomoaia-Cotisel, M.; Pop, V-D.; Tomoaia, G.; Mocanu, A.; Racz, Cs.; Ispas, C.R.; **Pascu, O.;** Borostean, O.C. Atomic force microscopy studies of Langmuir-Blodgett films. 4. The influence of aluminum substrate on dipalmitoyl phosphatidylcholine nanolayers. *Chemia L* 2005, *1*, 23-37.

10. Tomoaia-Cotisel, M.; Racz, Cs.; Tomoaia, G.; Floare, C.; Totos, R.; Bobos, L.; **Pascu, O**.; Dumitru, A. Molecular structure and monolayer properties of some carotenoids. *Chemia L* 2005, *1*, 39-45.

## *ATTENDANCES TO CONGRESSES, CONFERENCES AND MEETINGS*

Pascu, O.; Caicedo, J.M.; Fontcuberta, J.; Herranz, G.; Roig, A.; Canalejas, V.; López, M.; López, C.; Blanco, A.
  Intrinsic magneto-optical response of 3D inverse photonic-crystals infiltrated with magnetic nanoparticles (**oral presentation**)
  2D and 3D magnetic frames by microwave-assisted sol-gel chemistry approach (**poster**)
  *International Symposium on Advanced Complex Inorganic Nanomaterials (ACIN)*, Namur (Belgium), 11-14 September 2011.

Pascu, O.; Caicedo, J.M.; Fontcuberta, J.; Herranz, G.; Roig, A**.**
  Fabrication of 3D magneto-photonic crystals using *ex-situ* synthesized magnetic nanoparticles (**oral presentation**)
  Magnetic decoration of photonic crystals via microwave-assisted non-aqueous sol-gel chemistry (**poster**)
  *2nd International Conference in Multifunctional, Hybrid and Nanomaterials (HYMA)*, Strasbourg (France), 6-10 March 2011.

Pascu, O.; Caicedo, J.M.; Fontcuberta, J.; Herranz, G.; Roig, A.; Canalejas, V.; López, M.; López, C.; Blanco**,** A.
  3D magneto-photonic crystals (**poster**)
  *Photonic and Electromagnetic Crystal Structures (PECS IX)*, Granada (Spain), 26-30 September 2010.

# Oana Pascu

Rambla de Brasil 42, 5/4, 08028 Barcelona • +34 645508155 • opascu@icmab.es

Pascu, O.; Caicedo, J.M.; Fontcuberta, J.; Herranz, G.; Roig, A.
  Fabrication and characterization of magneto-photonic crystals (**oral presentation**)
  *NANOSELECT (Annual meeting)*, Girona (Spain), 14-16 July 2010.

Pascu, O.; Caicedo, J.M.; Fontcuberta, J.; Herranz, G.; Roig, A.; López, M.; López, C.;
Blanco, A.
  Synthesis and characterisation of nickel nanoparticles for advanced photonic structures
  (**oral presentation**)
  *12<sup>th</sup> International Ceramics Congress (CIMTEC)*, Montecatini Terme (Italy), 6-11 June
2010.

Pascu, O.; Caicedo, J.M.; Fontcuberta, J.; Herranz, G.; Roig, A.; López, M.; López, C.;
Blanco, A.
  Fabrication of 3D magneto-photonic crystals by infiltration with magnetic nanoparticles
(**poster**)
  *Materials Research Society (Spring Meeting)*, San Fransisco (CA), 5-9 April 2010.

Pascu, O.; Caicedo, J.M.; Fontcuberta, J.; Herranz, G.; Roig, A.
  Synthesis and magneto-optical characterization of magnetic nanoparticles for advanced
  photonic structures (**poster**)
  *NANOSELECT (Workshop)*, Barcelona (Spain), 9-10 July 2009.

*I like cooking, listening music (classic, jazz, oldies), dancing, doing sport. I am enthusiastic,
friendly, honest, hardworker, with a great dedication to teaching, helping people and always
open to learn new things.*

**If you would like references, please adress yourself to the following persons:**

*Anna Roig (roig@icmab.es)*
*Gervasi Herranz (gherranz@icmab.es)*
*Cyril Aymonier (aymonier@icmcb-bordeaux.cnrs.fr)*